UNDERSTANDING NICKEL CATALYSIS AT THE MOLECULAR LEVEL: INSIGHTS INTO C-O FUNCTIONALIZATION AND ELECTRON TRANSFER EVENTS

Craig Day

UNIVERSITAT ROVIRA i VIRGILI

Understanding Nickel Catalysis at the Molecular Level: Insights into C-O Functionalization and Electron Transfer Events

Craig Day

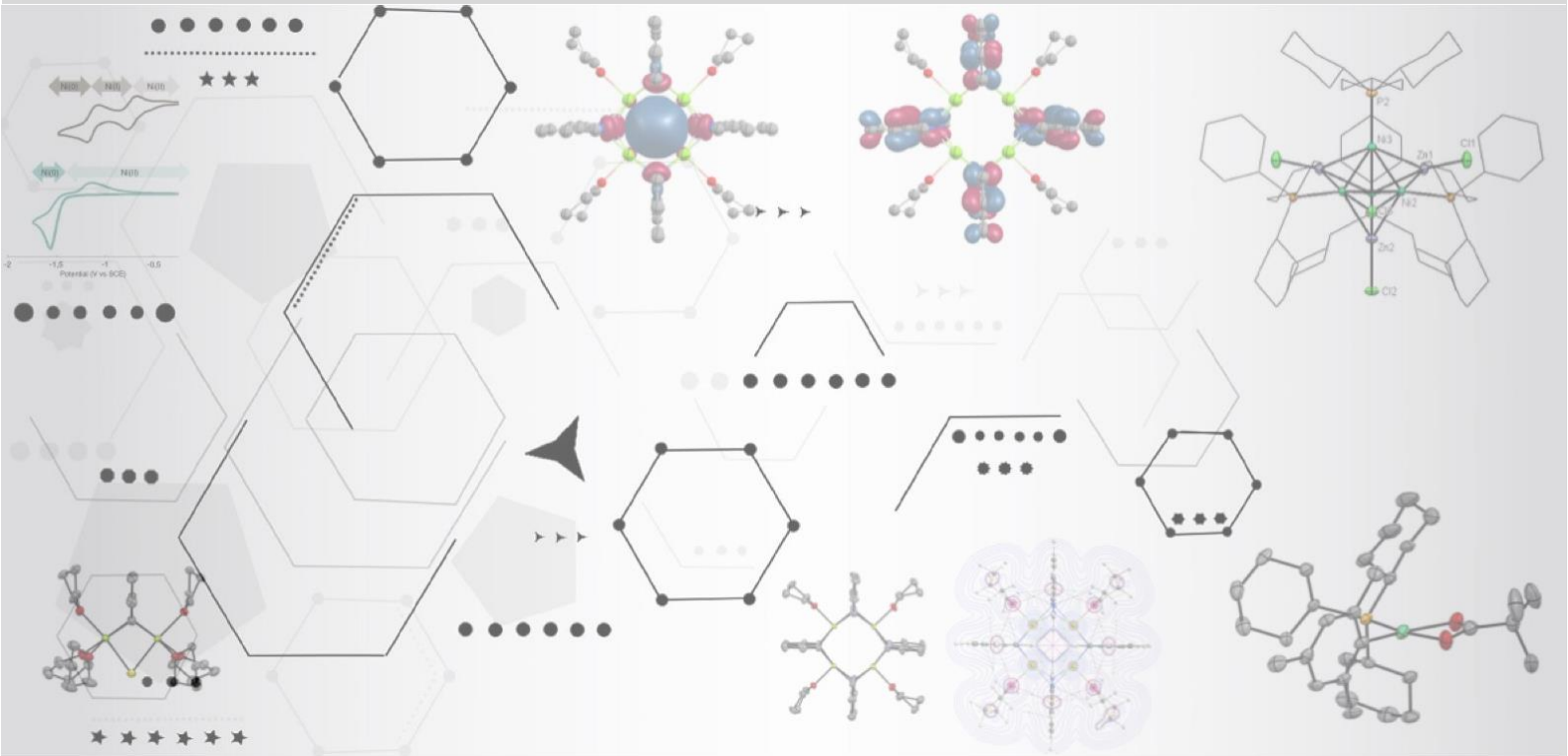

DOCTORAL THESIS
2022

UNIVERSITAT ROVIRA I VIRGILI
UNDERSTANDING NICKEL CATALYSIS AT THE MOLECULAR LEVEL: INSIGHTS INTO C-O FUNCTIONALIZATION AND ELECTRON TRANSFER EVENTS
Craig Day

UNIVERSITAT ROVIRA I VIRGILI
UNDERSTANDING NICKEL CATALYSIS AT THE MOLECULAR LEVEL: INSIGHTS INTO C-O FUNCTIONALIZATION AND ELECTRON TRANSFER EVENTS
Craig Day

Understanding Nickel Catalysis at the Molecular Level: Insights into C-O Functionalization and Electron Transfer Events

Craig Day

Doctoral Thesis

Supervised by Prof. Ruben Martin Romo

Institute of Chemical Research of Catalonia (ICIQ)

Universitat Rovira i Virgili (URV)

Department of Analytical Chemistry & Organic Chemistry

Tarragona, 2022

UNIVERSITAT ROVIRA I VIRGILI
UNDERSTANDING NICKEL CATALYSIS AT THE MOLECULAR LEVEL: INSIGHTS INTO C-O FUNCTIONALIZATION AND ELECTRON TRANSFER EVENTS
Craig Day

UNIVERSITAT ROVIRA I VIRGILI

ICIQ
Institut Català d'Investigació Química

Prof. Dr. Ruben Martín, Group Leader of the the Institute of Chemical Research of Catalonia (ICIQ) ,

STATES, that the present Doctoral Thesis entitled: **Understanding Nickel Catalysis at the Molecular Level: Insights into C-O functionalization and electron-transfer events**, presented by Craig Day to receive the degree of Doctor, has been carried out under his supervision at the Institute of Chemical Research of Catalonia (ICIQ).

Tarragona, April 20th 2022

PhD Thesis Supervisor

Prof. Rubén Martín

UNIVERSITAT ROVIRA I VIRGILI
UNDERSTANDING NICKEL CATALYSIS AT THE MOLECULAR LEVEL: INSIGHTS INTO C-O FUNCTIONALIZATION AND ELECTRON TRANSFER EVENTS
Craig Day

Table Contents

List of Publications

Contributions covered in this thesis:

1. **Day, C. S.**; Somerville, R. J.; Martin, R. Deciphering the Dichotomy Exerted by Zn(II) in the Catalytic sp^2 C–O Bond Functionalization of Aryl Esters at the Molecular Level. *Nat. Catal.* **2021**, 4, 124-133. Article
2. **Day, C. S.**; Do, C. D.;† Odena, C.;† Benet-Buchholz, J.; Xu, L.; Foroutan-Nejad, C.; Hopmann, K. H.; Martin, R. "A Room Temperature-Stable Magnesium Electride" *Under Review; JACS*
3. **Day, C. S.**; Angel R. G.;† Ton, S. J.;† Gogoi. A.;† Gutierreze. O.; Martin, R. ¨Elucidating Electron Transfer Events for Polypyridine Ligated Nickel Complexes¨ *Submitted Nat Cat*

Contributions not covered in this thesis:

4. **Day, C. S.**;† Fawcett, A.;† Chatterjee, R.; Hartwig, J. F.* "Mechanistic Investigation of the Iron-Catalyzed Azidation of Alkyl C(sp^3)–H Bonds with Zhdankin's λ^3-Azidoiodane" *J. Am. Chem. Soc.* **2021**, 143 (39), 16184–16196. Article
5. Wen-Jun, Y.; **Day, C. S.**; Rucinski, A, J, B.; Martin, R. ¨ Geminal Difluoroalkanes via Hydro-Difluoroalkylation of Unactivated Olefins¨ *Submitted ACIE*
6. Tortajada Navarro, Andreu;† Correia, José Tiago;† Serrano, Eloisa;† Monleon, Alicia;† Tampieri, Alberto; **Day, C. S.**; Julia-Hernandez, Francisco; Martin, R. "Ligand-Controlled Regiodivergent Catalytic Amidation of Unactivated Secondary Alkyl Bromides." *ACS Catal.* **2021**, 11 (16), 10223–10227. Communication
7. Wen-Jun, Y.; **Day, C. S.**; Martin, R. ¨Site-Selective Defluorinative sp^3 C–H Alkylation of Secondary Amides¨ *J. Am. Chem. Soc.* **2021**, 143, 17, 6395-6400. Communication
8. Davies, J; Janssen-Müller, D; Zimin, D; **Day, C. S.**; Yanagi, T; Elfert, J; Martin, R ¨Ni-Catalyzed Carboxylation of Aziridines en Route to β-Amino Acids¨ *J. Am. Chem. Soc.* **2021**, 141, 13, 4949-4954. Communication
9. Sun, S;† Talavera, L;† Spieß, P; **Day, C. S.**; Martin, R ¨Sp^3 Bis-Organometallic Reagents via Catalytic 1,1-Difunctionalization of Unactivated Olefins¨ *Angew. Chem. Int. Ed.* **2021**, 60 (21), 11740-11744. Communication
10. Cong, F.; Lv, X.; **Day C. S.**; Martin, R. ¨Dual Catalytic Strategy for Forging sp^2–sp^3 and sp^3–sp^3 Architectures via β-Scission of Aliphatic Alcohol Derivatives¨ *J. Am. Chem. Soc.* **2020**, 142, 49, 20594–20599. Communication
11. Zu, W.; **Day, C. S.**; Wei, L.; Jia, X.; Xu, L. ¨Dual Aminoquinolate Diarylboron and Nickel Catalysed Metallaphotoredox Platform for Carbon-Oxygen Bond Construction.¨ *Chem. Commun.* **2020**, *56* (59), 8273–8276.

†*These authors contributed equally*

In preparation:

12. Zimin, D.; Wakeling, M.; Janssen-Müller, D; **Day C. S.;** Martin, R. ¨Nickel Catalyzed Aziridine Hydroalkenylation¨
13. Cong, F.; Mega, R. S.;† Chen, J.;† **Day C. S.;**† Martin, R. ¨Forging Trifluoromethylated module by sp^3 C–C cleavage via Structurally Diverse Feedstocks¨
14. Lyonnet, J.; Davies, J; **Day C. S.;** Sahoo, B.; Duan, Y.; Martin, R. ¨Kinetically Controlled Carboxylation of Secondary Alkyl Bromides Through Dual Photoredox and Nickel Catalysis¨
15. **Day, C. S.;** Ton, S. J.;† McGuire, R. T.;† Foroutan-Nejad, C.; Martin, R. “Facile reductive elimination from a sterically encumbered Ni-polypyridine complex”

Acknowledgements

The last 3 and a half years of my PhD at the ICIQ have been an unforgettable experience. From working on exciting research projects and meeting amazing people, to isolation during COVID-19 lockdowns or going to UC Berkeley; I'm incredibly grateful for the opportunity to have shared these times with many great scientists and people who have helped me tremendously along the way.

First and foremost, I'd like to thank my PhD supervisor Ruben Martin who has helped guide me through some of the most challenging but exciting years of my life. I could not have asked for a better supervisor during my PhD I'm incredibly grateful for your full support and trust in me to freely pursue research projects and new directions throughout my PhD, leading to some really exciting discoveries! Before joining the group I would have never imagined I'd be studying a magnesium electride nor half of the other projects I've tackled while here. Working with you has let me grow as a scientist and person and I've always felt tremendous support, both in a professional and personal capacity. Thank you for the great advice throughout my PhD and for giving me every opportunity to prove myself and succeed. I will look back on the time of working with you fondly!

Secondly, I'd like to thank John Hartwig for letting me come to his group for 6 months even with COVID-19 and his lab working in shifts. Right from the first emails, I felt incorporated into the group and always received prompt and helpful insight. Working in the group was an unforgettable experience, with everyone there being incredibly kind, driven and intelligent. Undoubtedly, I developed tremendously in those months, from sitting in on your organometallics course to the multiple problems sessions discussing everything from total synthesis to main-group bonding. Working on the Fe-catalyzed azidation project was an extremely enriching experience with the multiple meetings to discuss mechanistic possibilities and further experiments. I really appreciate the opportunity and working there has is one of the highlights of my PhD.

I'd also like to thank my committee members, Professors John Hartwig, Cristina Nevado, and Marcos Suero for accepting our invitation to read and assess my work. Travelling during this time isn't trivial and I greatly appreciate the time and effort.

None of this work would have been possible without European Union's Horizon 2020 under the Marie Curie PREBIST grant agreement 754558 for the PhD fellowship providing me with the financial support to allow me to carry out my research.

Thank you to the collaborators involved in the research chapters: Rosie Somerville, Cuong Dat Do, Carlota Odena, Jordi Benet-Buchholz, Liang Xu, Cina Foroutan-Nejad, Kathrin Hopmann, Stephanie Ton, Angel Renteria Gomez, Achyut Gogoi, and Osvaldo Gutierrez. Your involvement has been very rewarding and has elevated the impact of these studies greatly. In addition, Alex Fawcett, who worked on the Fe-catalyzed azidation project at John's lab before I arrived. While we never got to meet in person, the skype calls were always very productive, and I appreciate the time spent discussing ideas and working on the manuscript.

I'm grateful to Ingrid Mateu, Sergio Sopena, and David Sádaba for keeping the lab running smoothly over the years and being so friendly and kind. I'm also tremendously grateful for the ICIQ research support units which really streamlined the research done. A particular thank you to Jordi Benet-Buchholz whom is the greatest crystallographer I have met and an absolute pleasure to work with. Getting high-quality X-ray data of the Mg-electride complex was a difficult number of months but you were amazing to work with! I really enjoyed getting to know you and our conversations over the years. Of course, the other support staff were also amazing and a huge thank you to Marta, and Eduardo for helping me with many other crystal structures, Isra and Kerman for your help with NMR experiments, Georgiana for help with the EPR experiments, and Mariona for help with UV-VIS and Stern-Volmer quenching studies. I've been really fortunate to have spent a lot of time with each of you for the various techniques and your expertise so thank you for being so kind and sharing your knowledge!

I would also like to thank my lab mates who kept me sane for the last two years and provided a place I looked forward to going each and every day. A big thank you to those that welcomed me when I first arrived in Spain. Marino Börjesson, Daniel Janssen-Muller, Antonio García and Ciro Romano, thank you for the nights out at La Cantonada and around Tarragona. Thanks to Yiting Gu, Andreu Tortajada, Raul Martin and Rosie Somerville for showing me the ropes when I first arrived. A huge shoutout

to Hongfei Yin, Basudev Sahoo, Liang Xu, Shang-Zheng Sun, José Tiago, Victoria Rendón, and Jessica Giacoboni for the times at Quattros or the late nights in the lab and at El Cau together and for the great friendships we built. I'll cherish those memories and miss you all. Yaya Duan, you're such a kind and welcoming person and thank you for hosting me for hotpot. Christopher Sandford, we had great discussions about electrochemistry and chemistry in general, looking forward to seeing the future work from your group. Bradley Higginson and Julien Lyonnet for having me over at your houses over the years, It's always a great time hanging out with you two. Carlota Odena, thanks for sharing the glovebox with me, it was a pleasure to have worked with you and best of luck on your PhD. Dmitry Zimin, my favorite Russian, thank you for sharing your culture with me and the secrets of Russian pancakes. I always enjoy your company at lunch. Jacob Davies, I'm really grateful that you've been around throughout my PhD as a calm and collected voice, I appreciate all the feedback you've shared with me. Fei Cong, it has been great to share my PhD with you, from nights out dancing at El Cau with Antoni to hotpot and other celebrations. Wen-Jun Yue, thank you for all the great discussions about chemistry and life in general, wish you luck in the future! Xinyang Lyu and Jinhong Chen, it was great to get to know the two of you. Good luck with the rest of your PhDs! Riccardo Mega, Matthew Wakeling, and Jesús Rodrigalvarez it was great to get to know you and unfortunate that we only overlapped briefly. Best of luck in the future. I've really enjoyed my time as a Martini and am thankful for all of the other group members for making the atmosphere a great place to be.

To the Hartwig group members, I really appreciate that I was made a part of the group. Going out for hikes or drinks were some highlights of my time there. A particular thank you to my jogging buddies Jason Ma and Yehao Qiu. Thanks to Kyoungmin Choi for all the late nights in the lab during the evening shifts and drinks after work. A big thank you to the other lab members of 709 Masha Elkin and Christina Pierson it was great to get to know you all. Even though the lab leaked water and my fumehood half worked I would gladly go back to 709 again. A shoutout to Brandon Bloomer for helping with measuring the formation of N_2 gas for the azidation project but also in general for all the discussions about chemistry and life. It was great to have come during the 2022 class of, Jake Shi, Jeremy Nicolai, Jenna Manske, Isaac Joyner, Nicodemo Ciccia, and John Brunn you guys were really kind and hopefully will keep the atmosphere the same. Thanks you Isaac Yu for hosting hotpot and Reichi Chen for the

drives back home, I really enjoyed myself and my time with you two. Thanks to Jake Wilson for hosting us back at his place for more drinks and the good times. Eric Kalkman, Connor Delaney, and Erik Romero for the detailed discussions about kinetics, organometallics or anything else for that matter.

I'd also like to thank my past mentors that helped get me prepared for this journey, namely Deryn Fogg, Michael Organ, Derek Wilson, Tom Baker and Arturo Orellana. I've been fortunate to take away important lessons from each of you, be it hard work, critical thinking, the importance of a tough skin, and to be kind, compassionate and passionate. Jee Kwak, Minhao Zhang, and Faizan Rasheed, thank you for being such great friends and for your support and grounding perspectives. You guys have been like family to me.

My family who has always been there, Mom, Dad, Mike, Em, Jess thank you for your endless support. If I ever have a problem, I know you have my back which has allowed me to push myself to pursue the unknown. Chara, I am looking forward to a life of ball with you. To Stephanie, thank you for supporting me throughout this journey. I love you. The hardest part of doing this was being apart from you and I'm looking forward to that being behind us.

In the field of observation, chance favors the prepared mind. - Louis Pasteur

Preface

The entirety of the work presented in this dissertation has been carried out at the Institute of Chemical Research of Catalonia (ICIQ) during the period of January 2019 to June 2022 under the supervision of Professor Ruben Martin. The thesis contains five chapters: a general introduction, three research chapters, and the last chapter with a general conclusion of all the research work. Each of the research chapter includes a brief introduction and the aim of the respective topic, followed by a discussion of the experimental results, mechanistic analysis, conclusions, and experimental sections. The relevant references and their numbering are independently organized by chapters.

The first chapter deals with a general introduction of the background of the Ni-catalyzed cross-coupling reactions. A particular focus is on Ni-catalyzed C-O functionalization reactions and reductive cross-electrophiles coupling reactions.

The second chapter, "*Deciphering the dichotomy exerted by Zn (II) in the catalytic sp^2 C–O bond functionalization of aryl esters at the molecular level*", describes the mechanistic study of Ni-catalyzed Negishi cross-coupling reactions of aryl esters with aryl zinc reagents. This work provides access to on-cycle mononuclear oxidative addition complexes and studies their reactivity and decomposition pathways. During this work we uncover intriguing reactivity of Zn(II) salts that result in parasitic ligand scavenging, oxidation events, and the formation of NiZn clusters. We provide evidence that coordinating solvents disrupt these processes and offer insight for designing more efficient Ni-catalyzed reactions. The results of this chapter have been published in *Nat Catal.* **2021**, *4* (2), 124-133, in collaboration with Dr. Rosie Somerville.

The third chapter, "*A Room Temperature-Stable Magnesium Electride",* describes the synthesis of highly-reduced bipyridyl magnesium complexes possessing intriguing electronic properties, unique bonding geometries and to our knowledge is the first magnesium stabilized electride reported. These complexes serve as unconventional homogeneous reductants due to their high solubility, modular redox potentials and the formation of insoluble, non-coordinating by-products upon oxidation. The applicability of these reductants are showcased by accessing low valent $(bipy)_2Ni(0)$ metal species that are otherwise challenging. The results of this chapter are currently under review,

and performed in collaboration with Cuong Dat Do, Carlota Odena, Jordi Benet-Buchholz, Liang Xu, Cina Foroutan-Nejad and Kathrin Hopmann.

The fourth chapter, "*Elucidating Electron Transfer Events for Polypyridine Ligated Nickel Complexes*", presents factors responsible for key elementary steps of electron transfer in disproportionation, comproportionation and reduction for polypyridine ligated nickel complexes. A representative example of pseudohalide and halide ligated Ni(II) complexes are studied in which a change in anionic ligand results in significantly different reactivity during electron transfer events. While Ni(II)-halides react by comproportionation with Ni(0) complexes to form Ni(I) species, we identify that Ni(II)-pseudohalides are unreactive and the corresponding Ni(I)-pseudohalides react by disproportionation. Factors responsible for disproportionation or comproportionation are further investigated electrochemically and computationally. The implications of these findings are related to the formation of off-cycle species, reduction events and catalysis, suggesting a blueprint for the development of future nickel-catalyzed reactions. The results of this chapter are under review, and performed in collaboration with Stephanie Ton, Angel Renteria Gomez, Achyut Gogoi, and Osvaldo Gutierrez.

General conclusions are of this Doctoral Thesis are presented in Chapter 5.

Abbreviations & Acronyms

DMA = *N*,*N*-Dimethylacetamide

PCy_3 = Tricyclohexylphosphine

^{t}Bu = *tert*-Butyl

SOMO = Singly occupied molecular orbital

QTAIM = Quantum theory of atoms in molecules

bipy = 2,2'-Bipyridine

XRD = X-ray diffraction

DFT = Density functional theory

EN = Electronegativity

THF = Tetrahydrofuran

^{t}AmOMe = *tert*-Amyl ethyl ether

PhMe = Toluene

TMDSO = Tetramethyldisiloxane

COD = 1,5-Cyclooctadiene

NaO^tBu = Sodium tert-butoxide

SIPr = 1,3-Bis(2,6-diisopropylphenyl)imidazolidine

OPiv = Pivalate

Ar = Aryl

Nep = Neopentylglycol ester

Bpin = 4,4,5,5-Tetramethyl-1,3,2-dioxaboronic ester

NHC = *N*-Heterocyclic carbene

dcype = Ethylenebis(dicyclohexylphosphine)

dcypt = 3,4-Bis(dicyclohexylphosphino)thiophene)

dtbpe = 1,2-Bis(diisopropylphosphino)ethane

OAc = Acetate

DMF = *N*,*N*-Dimethylformamide

PPh_3 = Triphenylphosphine

DMPU = *N*,*N*′-Dimethylpropyleneurea

4,4-OMe-bipy = 4-4'-Dimethoxy-2-2'-bipyridine

box = Bisoxazoline

DME = Ethylene glycol dimethyl ether

dtbppy = 4,4′-Di-*tert*-butyl-2,2′-dipyridyl

acac = Acetylacetonate

ΔG = Gibbs free energy

BDFE = Bond dissociation free energy

tol = Tolyl

phen = 1,10-Phenanthroline

pyrox = Bisoxazoline

dppe = 1,2-Bis(diphenylphosphino)ethane

SCE = Saturated calomel electrode

SET = Single electron transfer

Cp = Cyclopentadienyl

$P(OPh)_3$ = Triphenyl phosphite

MeCN = Acetonitrile

Dipp = 2,6-Diisopropylphenyl

IPr = 1,3-Bis(2,6-diisopropylphenyl)imidazol-2-ylidene)

equiv = Equivalent

r.t. = Room temperature

m = *Meta*

o = *Ortho*

p = *Para*

t = *Tert*

Abstract

The chemical industry is reliant on metal catalysts for the production of pharmaceuticals, fuels, commodity chemicals, and modern materials. Earth-abundant metals such as nickel are emerging as attractive, more sustainable alternatives to traditional precious-metal catalysts due to their abundance and distinct reactivity compared to their counterparts. Notably, nickel catalysts offer similar reactivity to palladium catalysts that the pharmaceutical industry is dependent on. In addition, nickel has the added possibility to easily access open-shell electronic configurations and react as a harder, more electropositive and smaller analogue. These properties allow nickel to activate a range of typically inert electrophiles, or undergo single electron reactions which palladium catalysts are generally poorly suited for. This has led to the extensive development of reductive cross-coupling reactions which leverage the ability of nickel to partake in single electron oxidation or reduction events along with activating electrophiles by single electron transfer. A hallmark of reductive cross-coupling reactions, as an alternative to traditional cross-coupling reactions, is the wide scope of available electrophiles, improved functional group tolerance and operational simplicity compared to the use of nucleophilic organometallic reagents, making cross-electrophile-coupling reactions highly attractive to synthetic chemists.

Chemists have also developed innovative technologies for the functionalization of typically inert bonds which take advantage of the hard and electropositive nature of nickel to cleave C(sp^2)-O bonds. Utilizing simple and readily available phenol-derived precursors in place of aryl halide electrophiles opens a range of untraditional electrophiles for the construction of molecular complexity. The ability to activate previously inert bonds offers new synthetic strategies to target molecules and streamline their synthesis while reducing waste. In line with our groups interests in Ni-catalyzed cross-coupling reactions, this thesis will focus on the mechanistic understanding and catalytic implications of key nickel catalyzed reactions in C(sp^2)-O functionalization and reductive cross-coupling.

The first research chapter focuses on studying the mechanism of C(sp^2)-O bond functionalization of aryl esters in combination with aryl zinc reagents (Scheme 1). Initially we developed a protocol to access monomeric oxidative addition complexes

ligated with monodentate PCy_3 ligands in which the ester is bound in the κ^1 or κ^2 binding modes. The stoichiometric reactivity and decomposition pathways of these complexes is investigated which support that these Ni(II) complexes rapidly undergo transmetallation with aryl zinc reagents to afford biaryl complexes. We further identify an intriguing impact of Zn(II) on the catalytic transformation in which Zn(II) salts react in ligand scavenging, oxidation reactions and in the formation of NiZn clusters. With a comprehensive understanding of fundamental steps within the catalytic cycle, we provide evidence for the role of coordinating solvents in catalysis and disrupting decomposition.

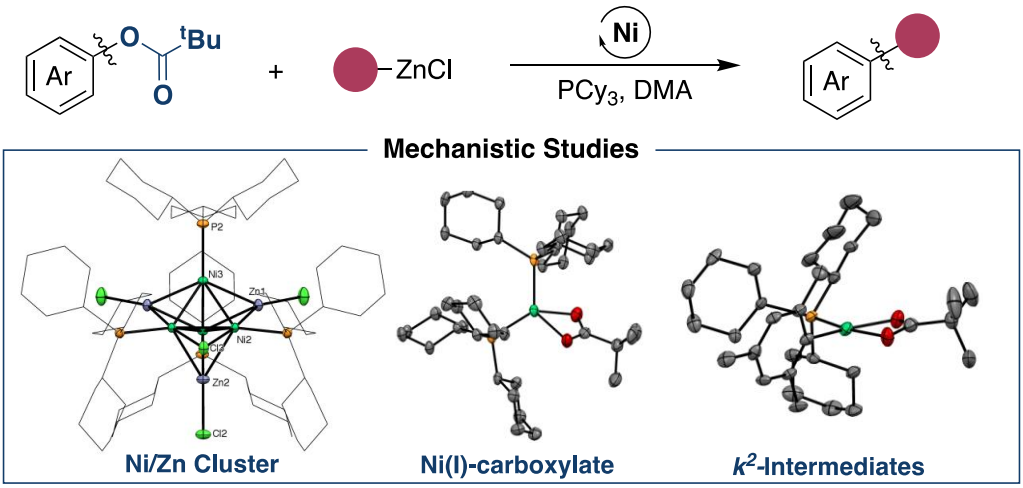

Scheme 1. Reaction scheme of the model C(sp^2)-O functionalization reaction studied and key complexes crystallized.

The following chapter then studies the effect of strong reductants on reductive coupling reactions employing redox active ligands in which the interaction between strongly reducing magnesium metal and polypyridine ligated nickel complexes is studied and a highly reduced bipyridine magnesium complex is isolated (Scheme 2). This complex possesses intriguing electronic properties, unique bonding geometries and to our knowledge is the first magnesium stabilized electride reported. Additionally, these complexes can act as homogeneous reductants due to their high solubility and the resulting formation of insoluble, non-coordinating by-products upon oxidation. The utility of these complexes is showcased by accessing otherwise challenging low valent metal complexes.

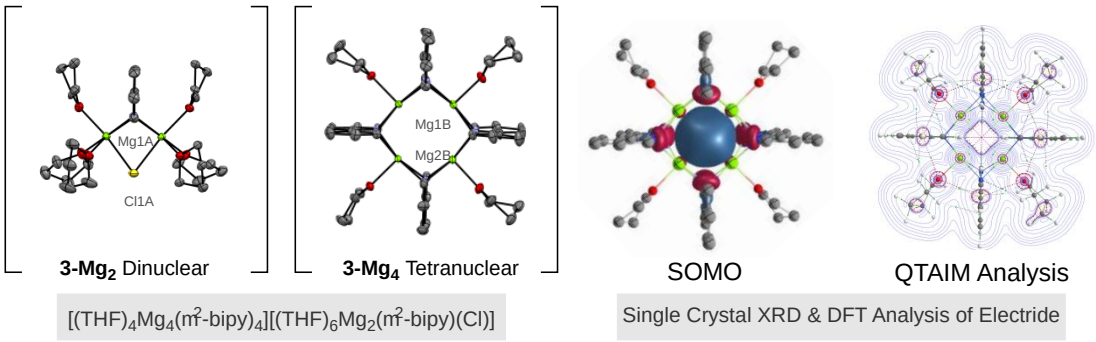

Scheme 2. Highly reduced Mg-polypyridine complexes.

The final chapter focuses on studying factors that contribute to electron transfer events such as comproportionation, disproportionation and reduction for polypyridine ligated nickel complexes (Scheme 3). Representative examples of pseudohalide and halide ligated Ni(II) complexes are studied in which a change in anionic ligand results in significantly different reactivity during electron transfer events. While Ni(II)-halides react by comproportionation with Ni(0) complexes to form Ni(I) species, we identify that Ni(II)-pseudohalides are unreactive and the corresponding Ni(I)-pseudohalides which can be transiently generated by anion exchange from Ni(I) halide complexes react by disproportionation. Factors responsible for disproportionation or comproportionation are further investigated electrochemically and computationally. The implications of these findings are related to the formation of off-cycle species, reduction events and catalysis, suggesting a blueprint for the development of future nickel-catalyzed reactions.

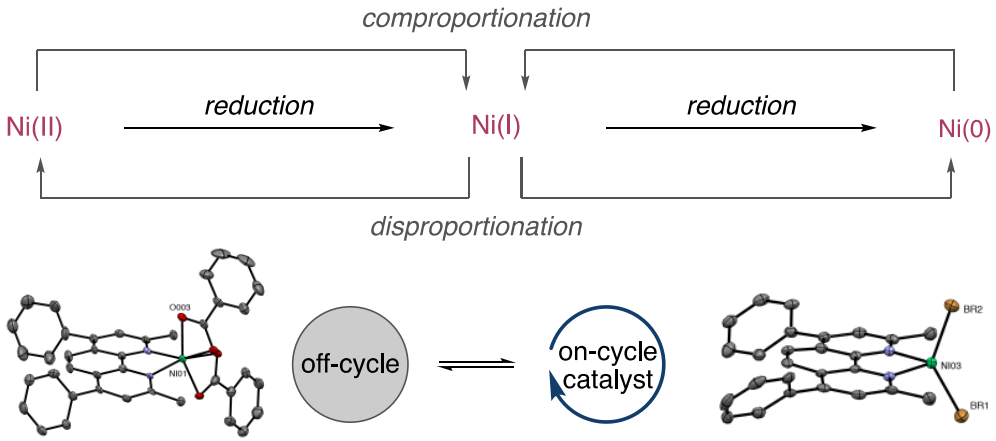

Scheme 3. Reactions of disproportionation, comproportionation, and reduction events interconnecting nickel complexes and the possible implications of these results to on-cycle or off-cycle species during catalysis.

In conclusion, we have identified new fundamental organometallic reactivity and key organometallic intermediates that are relevant for the development of synthetic methodologies and for future mechanistic investigations.

Chapter 1: General Introduction

1.1 General Introduction

1.1.1 Transition-Metal-Catalyzed Reactions

Transition-metal-catalyzed reactions have revolutionized organic synthesis in the way chemists synthesize medicine, fuels, commodity chemicals, and modern materials. The foundations for many of these reactions are rooted in fundamental organometallic chemistry which has led to the development of modern methodologies for rapid and reliable construction of C-C and C-heteroatom bonds. The importance of these highly efficient, mild, and functional group tolerant metal-catalyzed reactions has been recognized by three Nobel Prizes in Chemistry over the last two decades (Figure 1.1). The Nobel Prize in Chemistry was shared in 2001 between William S. Knowles and Ryoji Noyori for work on ¨chirally catalyzed hydrogenation reactions¨ and K. Barry Sharpless for ¨chirally catalyzed oxidation reactions¨. Yves Chauvin, Robert H. Grubbs and Richard R. Schrock were also awarded a Nobel Prize in Chemistry in 2005 ¨for the development of the metathesis method in organic synthesis¨ and then in 2010, Richard F. Heck, Ei-ichi Negishi, and Akira Suzuki were awarded the Prize for ¨palladium-catalyzed cross couplings in organic synthesis¨.

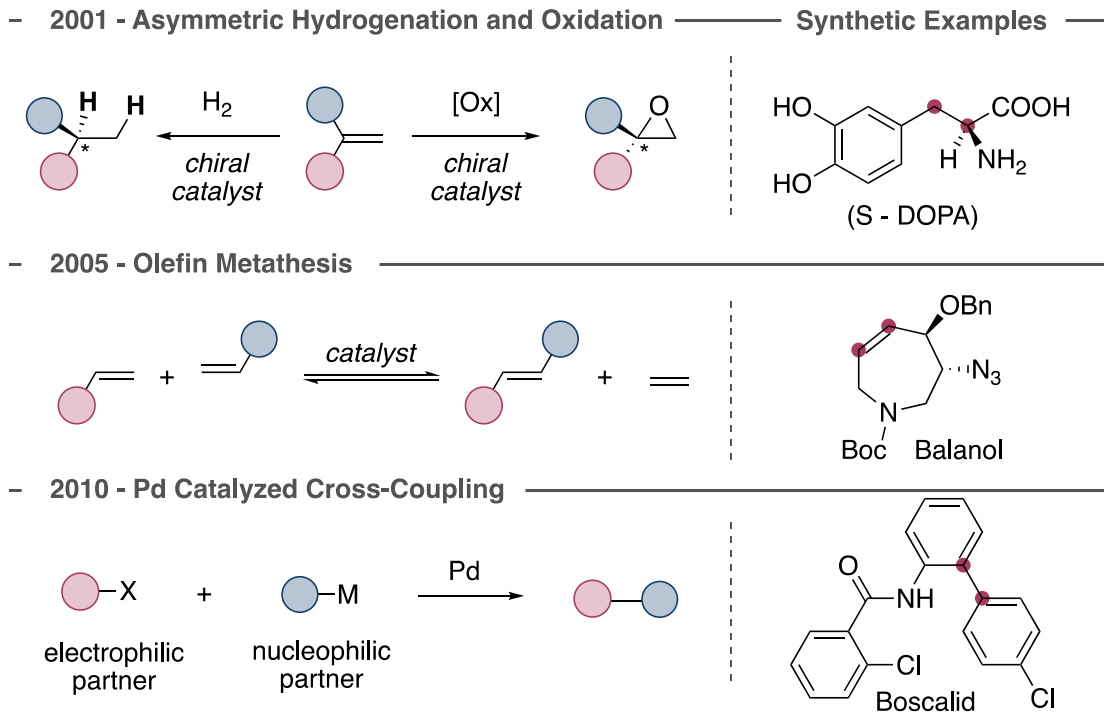

Figure 1.1 Nobel Prizes in Chemistry for the development of transition-metal-catalyzed reactions over the last two decades.

Notably, understanding the mechanistic underpinning of these reactions was essential to their widespread adoption and for the further development of these powerful methodologies.

1.1.2 Group 10 Metal-Catalyzed Reactions

The impact of palladium-catalyzed cross-coupling reactions on organic synthesis can hardly be underestimated, accounting for over 40% of carbon-carbon bond-forming reactions in the synthesis of pharmaceuticals.[1] Part of this success can be attributed to the simplicity and reliability of the catalytic transformations, in which three steps are commonly encountered (Figure 1.2).[2] First, a low valent transition metal undergoes oxidative addition of an electrophile which increases the coordination number and oxidation state of the metal by two. This is followed by transmetallation by a nucleophilic (often organometallic) reagent which substitutes the metal-halide bond and is subsequently followed by reductive elimination to form the desired cross-coupled product and regenerate the low valent metal catalyst.[3-6]

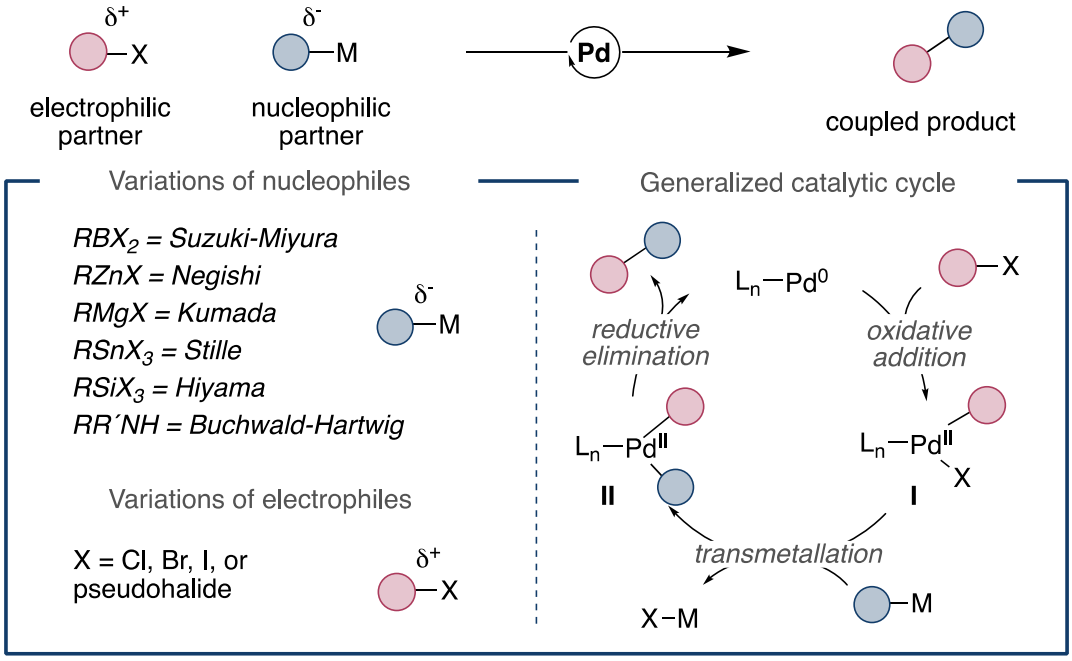

Figure 1.2 Traditional palladium-catalyzed cross-coupling reactions.

1.1.2 Properties of Nickel

Despite the significant advances realized, there remain many unsolved challenges in palladium-catalyzed reactions such as the ability to activate challenging electrophiles or efficiently couple C(sp^3) carbon fragments.[7-8] These limitations stem from the fundamental reactivity of palladium complexes as relatively soft, large, and electronegative when compared to its first-row counterparts. Addressing the limitations of activating strong σ bonds, nickel complexes can more easily stabilize odd or even oxidation states, have lower reduction potentials and are less electronegative, which make them attractive candidates to undergo challenging oxidative addition reactions (Figure 1.3).[6,8-10] Furthermore, considering the coupling of C(sp^3) carbon fragments, the smaller atomic radius of nickel typically results in more strained transition states when forming agostic interactions with C-H bonds that enable β-hydride elimination.[11-13] Slow β-hydride elimination from Ni-alkyl complexes therefore allows further productive reactivity and limits the formation olefinic side-products. Therefore, all of these features make nickel-complexes particularly attractive candidate as catalysts for the development of new metal-catalyzed reactions.

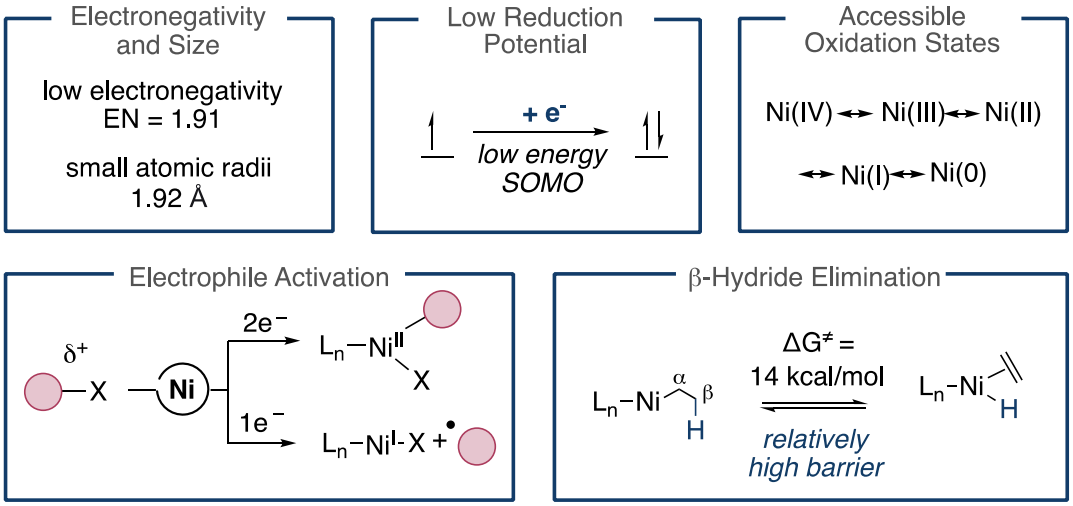

Figure 1.3 Properties of nickel complexes.

1.1.3 Nickel-Catalyzed C(sp^2)-O Functionalization

These properties of Ni as a hard and electropositive transition-metal have resulted in the development of metal-catalyzed C(sp^2)-O bond cleavage reactions that are beyond reach with palladium or platinum catalysts.[14-16] While the use of aryl sulfonates is common in palladium catalysis, the functionalization of stronger C-O bonds such as aryl ethers or esters is possible with nickel catalysts. Undoubtably, the ability to

transform phenol derived electrophiles offers use of unconventional yet readily abundant feedstocks instead of traditional aryl halides.

Pioneering work in this field can be attributed to Yamamoto and Wenkert who discovered that Ni(0) complexes can cleave C(sp^2)-O bonds (Figure 1.4).[17-20] Yamamoto published a series of organometallic articles highlighting cleavage of the acyl C(sp^2)-O bond (path a) or the carboxylate C(sp^2)-O bond (path b). The authors reported selectivity based primarily on the choice of ester in which phenyl esters were prone to react at the acyl C-O bond while vinyl esters reacted preferentially at the carboxylate C-O bond. Additionally, the authors noted that modifying the ligand influenced selectivity between the two pathways.[17-18] Wenkert further demonstrated aryl or vinyl methyl ethers can undergo Kumada-Corriu-type cross coupling reactions with Grignard reagents to afford alkylated or arylated products.[19-20]

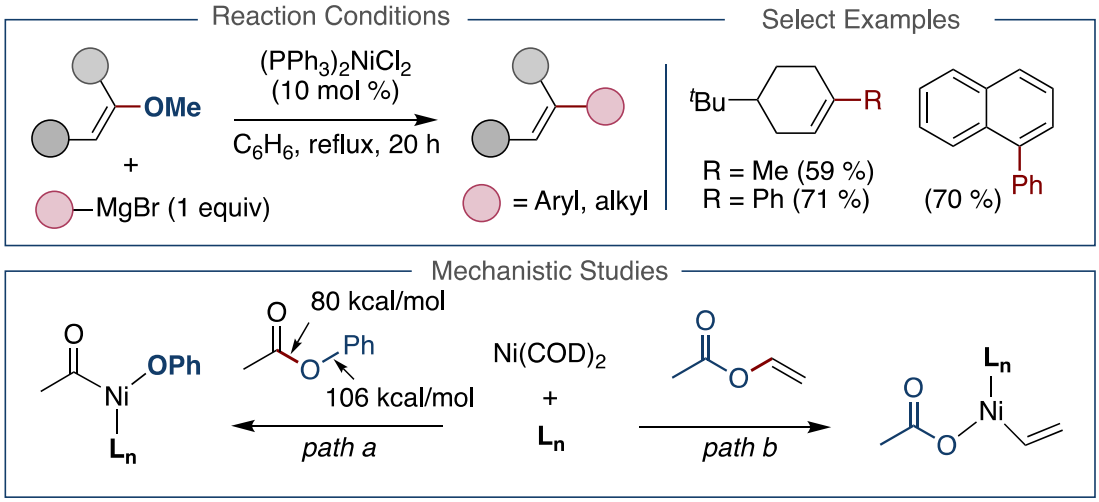

Figure 1.4 Pioneering studies on the mechanism of nickel-catalyzed C(sp2)-O cleavage and catalytic applications.

While these early studies supported the viability of C(sp^2)-O electrophiles in nickel-catalyzed reactions, it was not until the last two decades that the preparative aspects of these transformations have been sufficiently explored. In 2004 Dankwardt reported a more general transformation of aryl ethers than that developed by Wenkert by employing alkyl phosphines in combination with a nickel catalyst that provided improved reactivity (Figure 1.5, **a**).[21] These studies served as the inspiration for the development of milder and more functional group tolerant conditions by Shi and Garg which transformed aryl esters into biaryl compounds with less reactive organozinc or organoboron reagents (Figure 1.5, **b** and **c**).[22-24] Of the aryl esters studied, aryl pivalates were found to be ideal. As the earlier studies by Yamamoto suggest, a major undesired

side reaction in these transformations is cleavage of the weaker acyl C(sp^2)-O bond (Figure 1.4, path a) which calculations of phenylacetate determine to be 80 kcal/mol vs 106 kcal/mol of C(sp^2)-O cleavage of the ester.[25] Bulky aryl pivalates therefore aid in preventing acyl C(sp^2)-O cleavage due to the increased steric hinderance which results in the desired ester cleavage and productive catalysis.

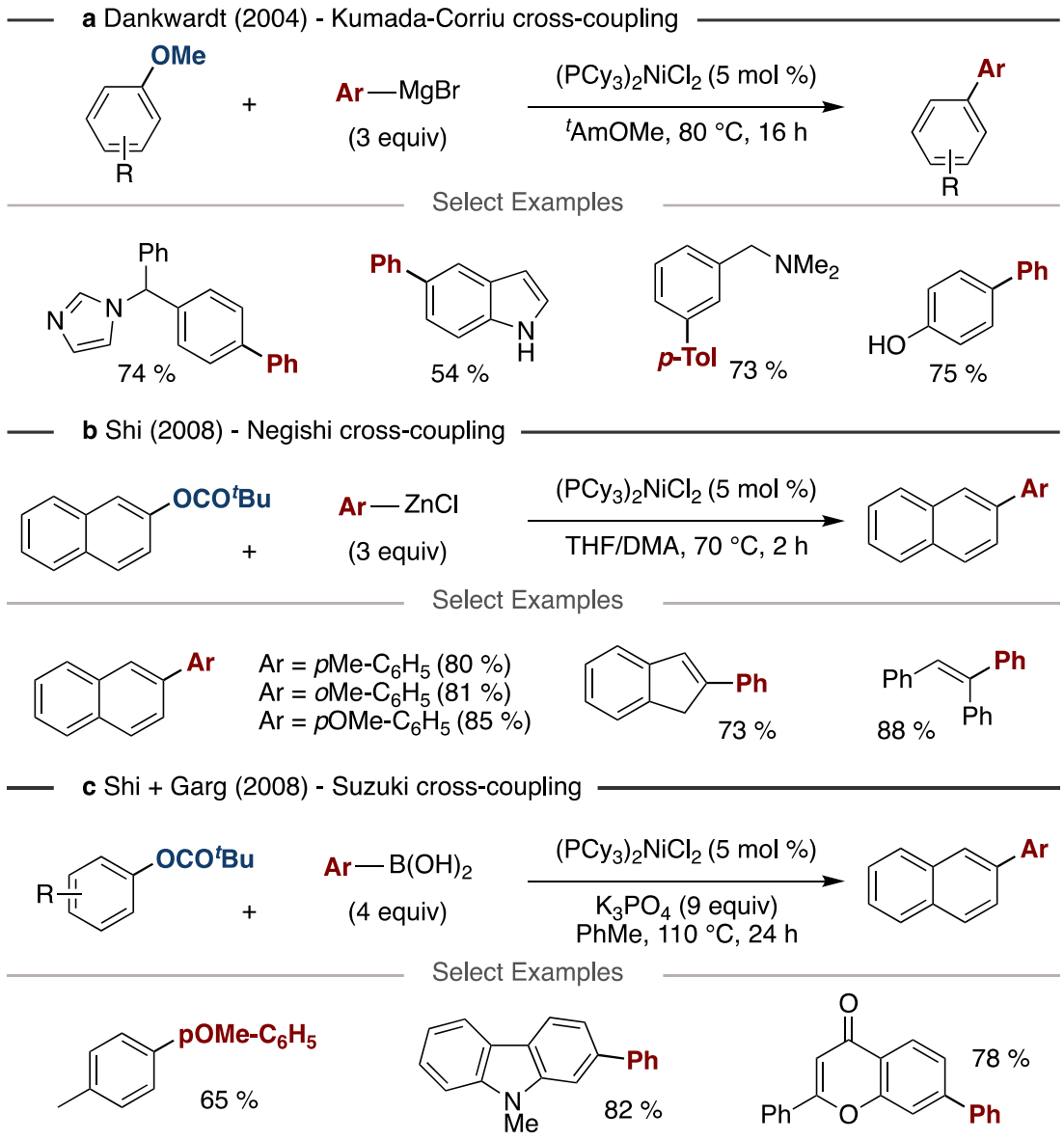

Figure 1.5 Significant advances in C(sp^2)-O bond cleavage reactions to form C(sp^2)-C(sp^2) bonds. **a**, Reinvestigation of Kumada-Corriu cross-coupling reactions by Dankwardt. **b**, Negishi cross-coupling reaction developed by the Shi lab.[24] **c**, Suzuki cross-coupling reaction developed independently by Shi and Garg.[22-23]

Later studies have expanded on these developments in both preparative terms and the mechanistic understanding of C(sp^2)-O functionalization reactions. Notable examples

include the reduction of aryl ethers and esters,[26-30] borylation[31-32] silyation[33] and stanylation[34] reactions (Figure 1.6).

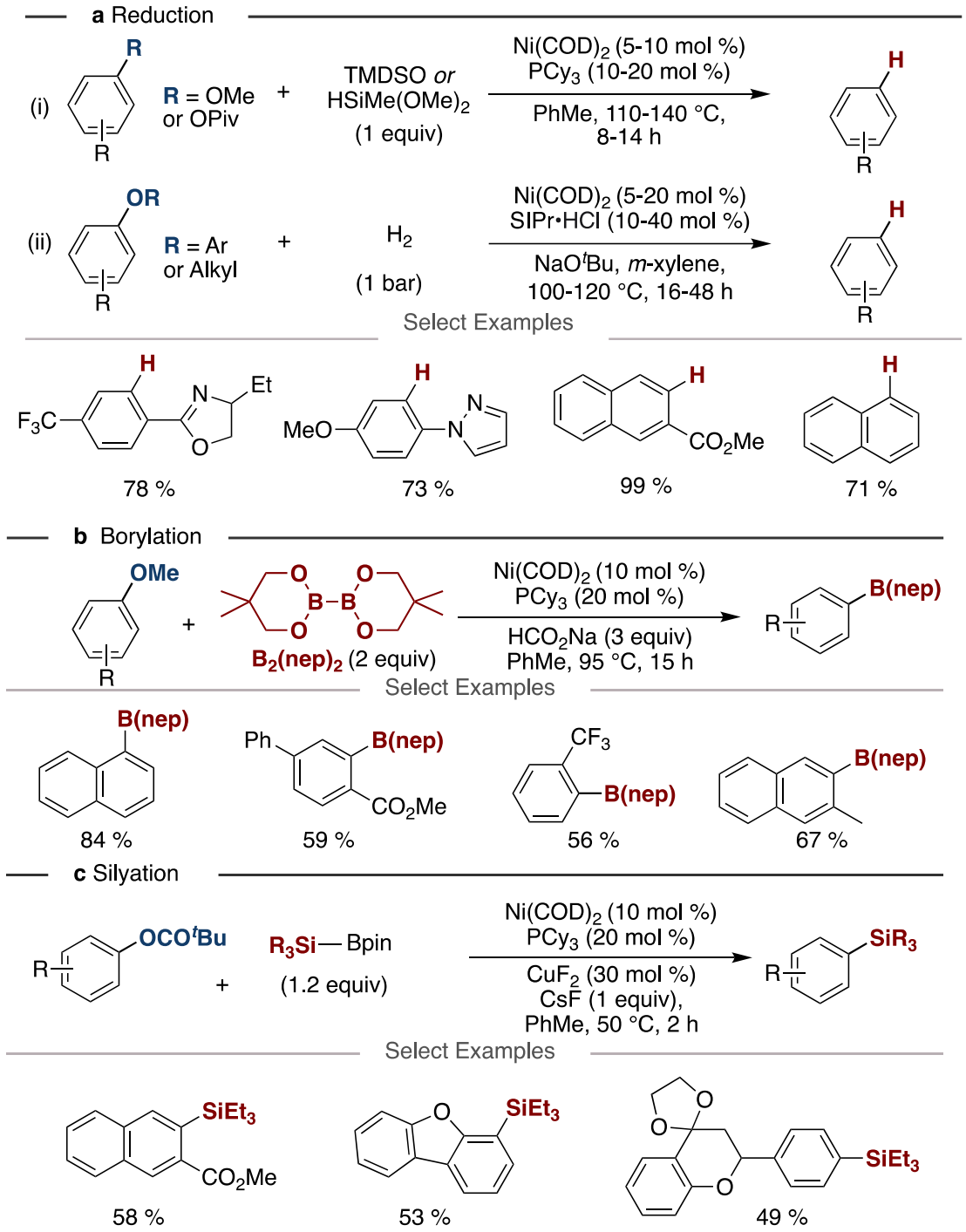

Figure 1.6 Advances in C(sp^2)-O bond functionalization reactions. **a**, Examples of diaryl ether and alkyl aryl ether reduction. **b**, Borylation of aryl alkyl ethers **c**, Silyation of aryl alkyl ethers.

Mechanistic studies into C(sp^2)-O cleavage reactions have primarily studied systems using strongly donating NHC or alkyl phosphine ligated complexes as these have proven the most successful.[35] Stoichiometric studies reacting aryl esters with

phosphine ligated Ni(0) complexes have allowed isolation of well-defined oxidative addition complexes. Examples by Itami include the reaction of $Ni(COD)_2$ with bidentate phosphines dcype or dcypt and π-extended napthyl pivalates at 100 °C to form (dcype)Ni(Ar)(κ^1-OPiv) **1** or (dcypt)Ni(Ar)(κ^1-OPiv) **2** (Figure 1.7, a).[36-37] Examples by Love described the activation of non π-extended aryl esters with dtbpe at room temperature in 1.5 hours to form a discrete (dtbpe)Ni(Ar)(κ^1-OAc) complex **3** (Figure 1.7, b).[38] Later work by our group studied oxidative addition with monodentate phosphine PCy_3, in which PCy_3 bound Ni(0) complexes were demonstrated to react with π-extended aryl esters rapidly at room temperature (Figure 1.7, C).[39] Interestingly off-cycle, dimeric complexes such as $[Ni(PCy_3)]_2(\mu,\eta^2$-2-naphthyl)(μ-OPiv)] **4** were formed, which was suggested to occur from the comproportionation reaction of $(PCy_3)_nNi(Ar)(OPiv)$ (n = 1 or 2) with Ni(0).

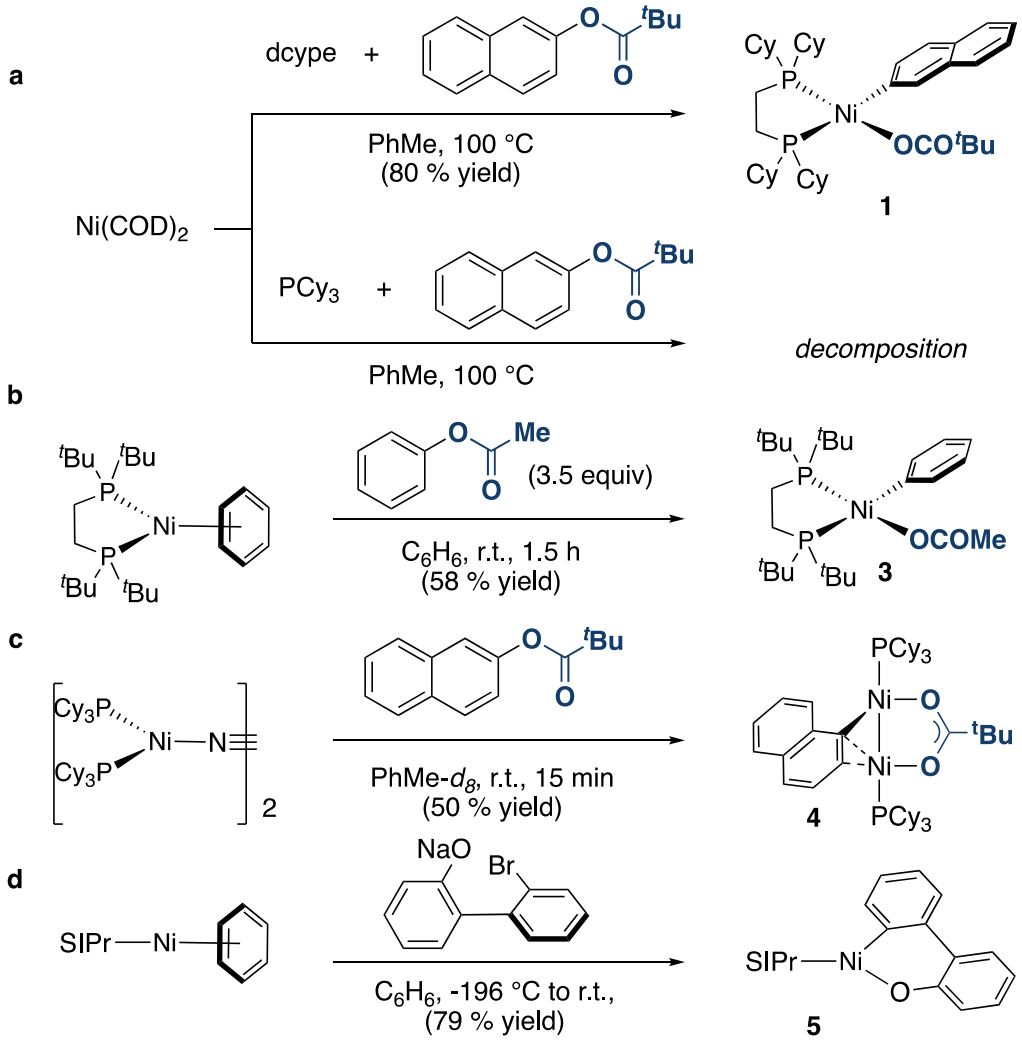

Figure 1.7 Advances in mechanistic understand of C(sp^2)-O bond functionalization reactions. **a-b**, Well-defined examples of oxidative addition of aryl esters with nickel ligated bidentate phosphines. **c**, Oxidative addition with monodentate phosphines

forming dimeric Ni complex. **d**, Indirect synthesis of the oxidative addition complex with aryl ethers and NHC ligated nickel complexes.

DFT studies performed by Houk for PCy_3 ligated Ni(0) complexes supported a traditional Ni(0/II) oxidative addition of aryl esters which was proposed to occur via a five-centered transition state that invokes interactions between the aryl π-system and an extra Ni-O bond.[40-41] Mechanistic studies on the hydrogenolysis of diaryl ethers by Hartwig with NHC ligated Ni complexes supported a traditional Ni(0/II) cycle in which oxidative addition is rate limiting. While the proposed oxidative addition complex could not be accessed by direct oxidative addition to an aryl ether, the authors provide an indirect synthesis from SIPr ligated Ni(0) and an aryl bromide with a pendant methoxide group which forms the proposed product of oxidative addition as a stable metallacycle **5** (Figure 1.7d).[30] Studies on methyl aryl ether cleavage however are complicated by the tendency of the resulting oxidative addition complex (L)Ni(OMe)(Ar) (Figure 1.8, **I)** to undergo rapid β-hydride elimination which forms formaldehyde and a (L)Ni(H)(Ar) complex **II** that can reductively eliminate arene.[42-43] Studies by Agapie on hydrogenolysis of aryl methyl ethers with NHC ligated nickel complexes supported C(sp^2)-OMe cleavage via a Ni(0) oxidative addition to the aryl methyl ether followed by β-hydride elimination and reductive elimination from the resultant (NHC)Ni(H)(Ar) complex.[42] Subjecting deuterated substrate Ar-OCD_3 to the standard catalytic reaction conditions saw nearly full deuterium incorporation into the product Ar-D (Figure 1.8, left). Interestingly, the reaction did not work in the absence of H_2 which led the authors to propose the role of H_2 was to form the catalytically active species, likely by hydrogenation of COD from the precatalyst $Ni(COD)_2$ as indicated previously by Hartwig in their diaryl ether studies.[30]

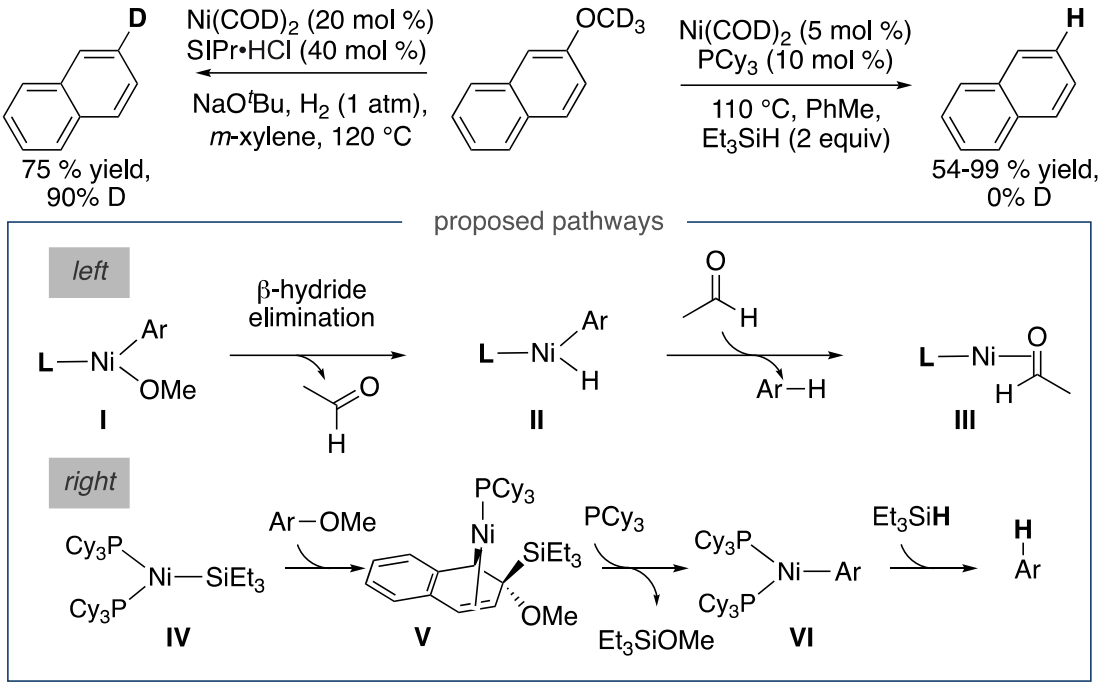

Figure 1.8 Divergent reactivity proposed for reduction of aryl methyl ethers with proposed pathways responsible for instability of aryl methyl ether Ni oxidative addition complexes and the proposed Ni(I) silane pathway.

Mechanistic studies by our lab[43] on reductive cleavage of aryl methyl ethers using silanes supported an alternative mechanism with Ni(I) intermediates. While oxidative addition from the aryl methyl ether to PCy_3-Ni(0) was shown to occur under mild conditions, the analogous experiments using deuterium labelled substrates found no deuterium incorporation in the product with Et_3SiH as the reductant (Figure 1.8, right). Further experiments were performed by monitoring the reaction which revealed an induction period involving consumption of Et_3SiH which tentatively supported the formation of a Ni(I)-silane complex **IV**. Additional evidence for this was provided by EPR analysis of the reaction mixture that revealed characteristic signals for Ni(I) species over the reaction time course. DFT analysis of a Ni(0/II) or a Ni(I) mechanism supported the possibility of the latter with $(PCy_3)_2$Ni-$SiEt_3$ as the active catalytic species.

1.1.4 Nickel-Catalyzed Reductive Cross-Coupling Reactions

Reductive coupling reactions between electrophiles date back to sodium-mediated dimerization of alkyl halides discovered by Wurtz[44] and the Cu-mediated homocoupling of aryl halides by Ullmann (Figure 1.9).[45] While these reactions are conceptually interesting by reacting two electrophiles, these dimerization reactions are limited by their low functional group tolerance as a result of the harsh reaction

conditions required for the reaction to occur. Modern synthetic methodologies have since leveraged this concept of coupling two electrophiles into powerful technologies to construct molecular building blocks. First row transition-metals such as nickel have excelled in this area due to the properties of nickel outlined in section 1.1.2, in which nickel complexes can more easily stabilize odd or even oxidation states, have lower reduction potentials and react in both single-electron or two-electron pathways.

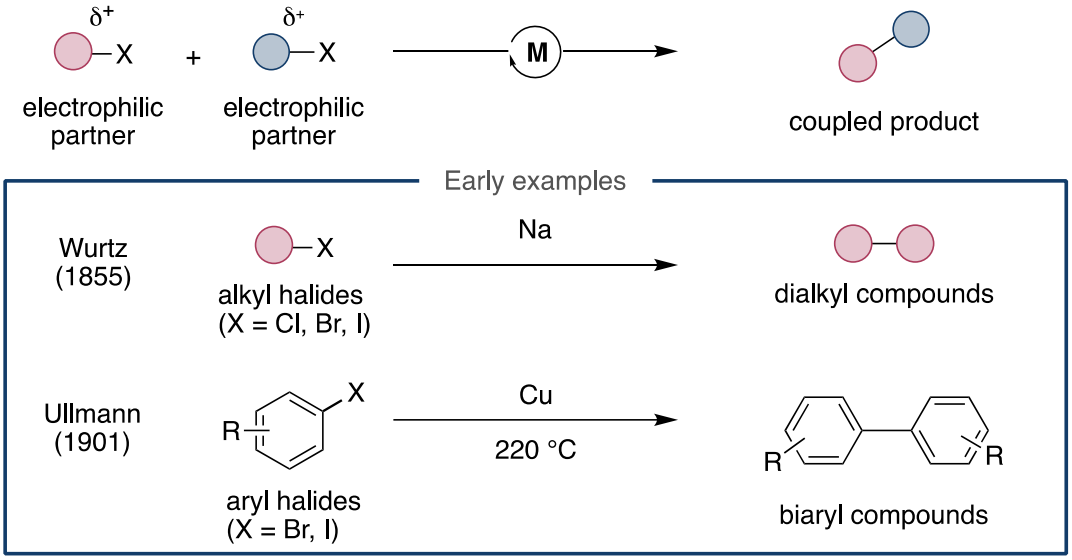

Figure 1.9 Cross-electrophile coupling reactions and early examples of cross-electrophile homocoupling reactions with alkyl halides or aryl halides.

A significant challenge in the development of reductive cross-coupling reactions relates back to the early examples of aryl or alkyl homocoupling reactions. As such, homocoupling can compete with the desired cross-electrophile coupling, particularly if the coupling partners share similar reactivity and reduction potentials. Strategies to selectively engage the cross-coupling partners have been developed to minimize these challenges such as the addition of one reagent in excess, electronically differentiating the starting materials, matching electronic and steric properties, and formulating catalytic cycles that undergo oxidative addition by two different mechanisms. These developments now offer efficient and mild reaction conditions by catalytic formation of reactive organometallic complexes which are operationally easy to setup and have increased functional group tolerance.

Early work in nickel-catalyzed reductive coupling was performed by Semmelhack who reacted aryl bromides with $Ni(COD)_2$ in DMF to form biaryl compounds.[46] Later, Kumada published the homocoupling of aryl bromides using a PPh_3 ligated nickel catalyst and Zn in DMF.[47] While these reactions offered a mild approach to form

symmetric biaryl compounds, few of these early methodologies were synthetically useful. Nevertheless, in the past two decade nickel-catalyzed reductive cross-coupling reactions have offered improved synthetic utility (Figure 1.10). An early report by Durandetti and coworkers in 2007 demonstrated a nickel-catalyzed reductive cross-coupling between α-choloroesters and aryl iodides using Mn as a reductant.[48] Weix et. al. expanded the scope of these reactions to alkyl iodides and aryl halides utilizing a Ni(II) precatalyst and bipyridine ligands.[49] Significant efforts have been spent to expand the scope of these transformations with examples by Weix,[50-52] Gong,[53-57] and Molander.[58-59] Advances in asymmetric biaryl reductive coupling reactions are notably distinct from the reaction between compounds of differing hybridization. Particularly interesting advances to access these compounds have been developed by Weix et al[60] through the merger of a duel Ni/Pd catalytic system which is effective for the coupling of aryl/vinyl bromides with aryl/vinyl triflates to form asymmetric biaryls and dienes.

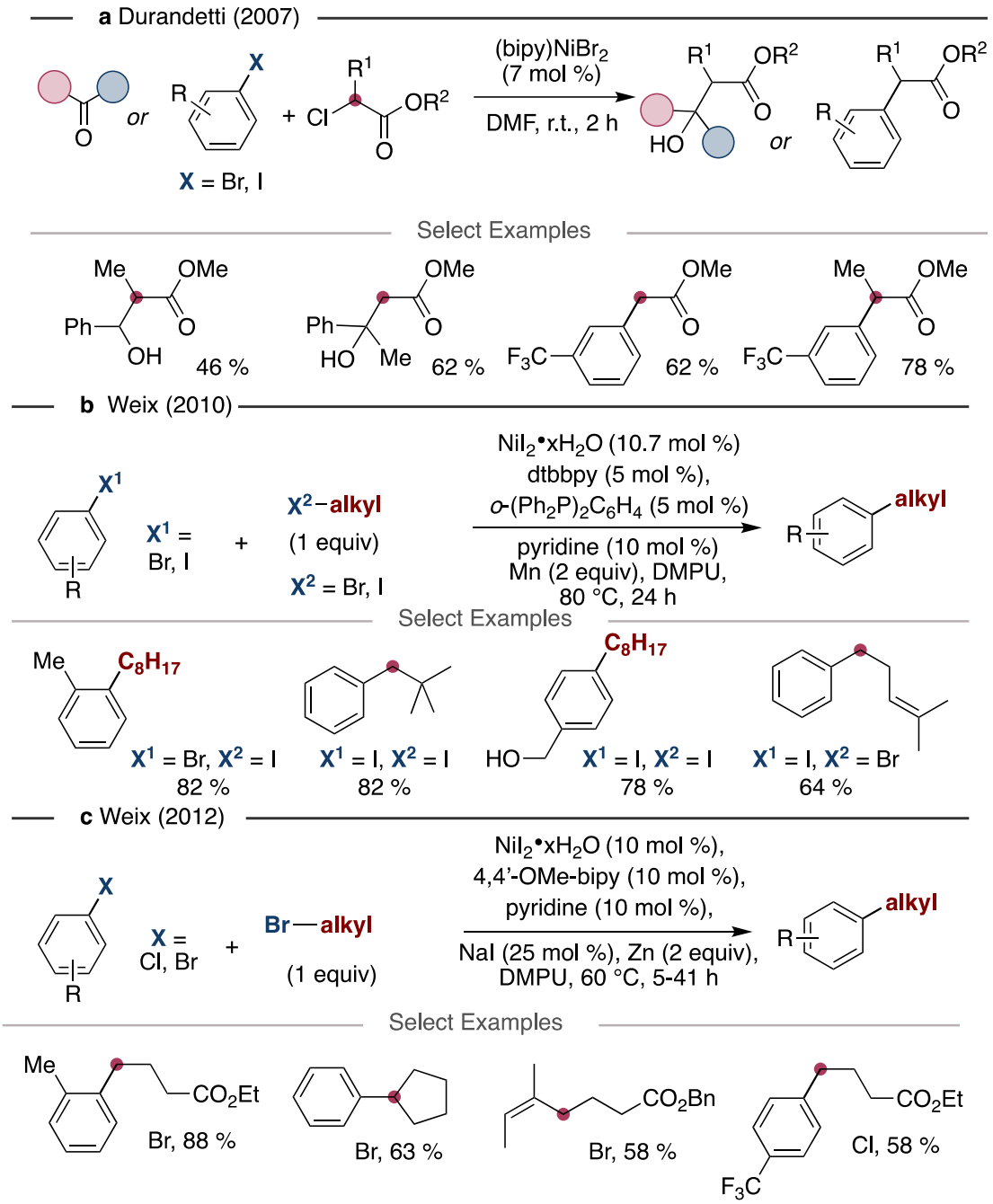

Figure 1.10 Early nickel-catalyzed reductive cross-coupling reactions between C(sp^2) and C(sp^3) fragments. **a**, coupling of α-chloroesters with aryl halides of ketones. **b-c**, coupling of aryl halides with alkyl halides.

Mechanistic investigations of these reactions have proposed either a radical chain mechanism or a sequential reduction mechanism.[50,61-62] In a sequential reduction mechanism, aryl halide electrophiles are proposed to undergo oxidative addition by Ni(0) complex **A** to afford Ni(II) oxidative addition species **B** (Figure 1.11). This complex then undergoes one electron reduction by a reductant to form Ni(I)-aryl

complex **C**,[63] which subsequentially undergoes single electron transfer to an alkyl halide electrophile in a radical-rebound process. The Ni(III) intermediate **D**[64-68] then undergoes rapid reductive elimination to form the desired coupling product and regenerates the Ni(I)-halide complex **E** which can be reduced to Ni(0) complex **A** and restart the catalytic cycle.

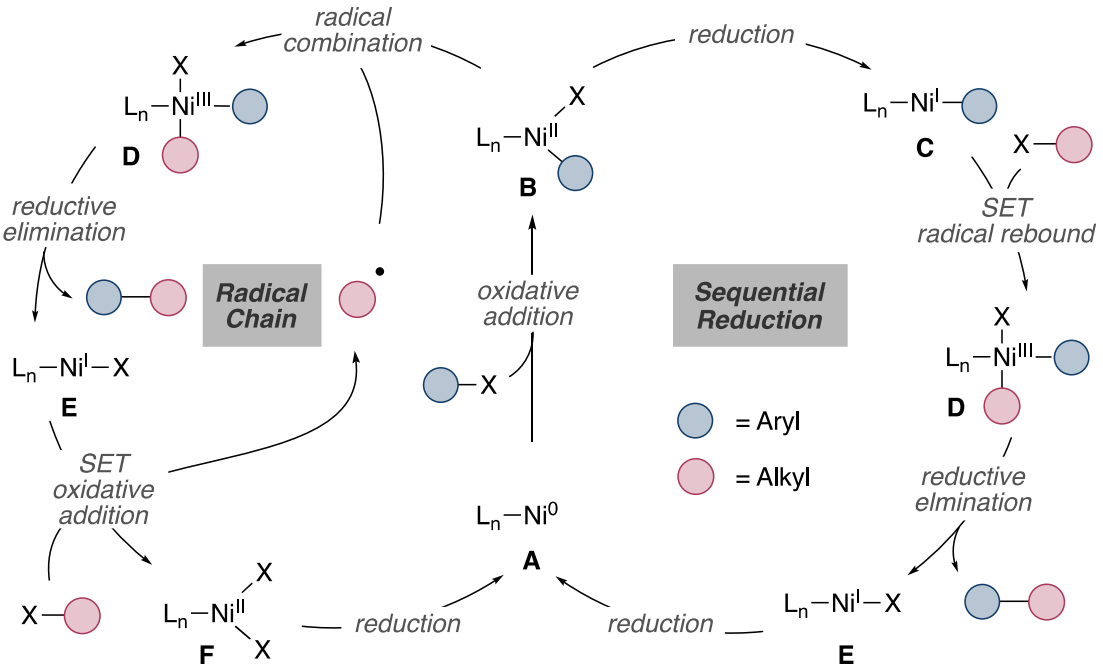

Figure 1.11 Proposed pathways for radical chain mechanisms and sequential reduction mechanisms.

Radical chain reactions are believed to occur by similar reactivity (Figure 1.11, left). The same initial step of oxidative addition from Ni(0) complex **A** to an aryl halide occurs to form Ni(II) oxidative addition complex **B**. Differing from the sequential reduction mechanism, the oxidative addition complex reacts directly with an open-shell alkyl radical to form Ni(III) complex **D** which rapidly undergoes reductive elimination to form the product and a Ni(I)-halide **E**. The resultant Ni(I)-halide reacts with the alkyl halide electrophile to form Ni(II)-halide complex **F** and an alkyl radical which escapes the solvent cage.[69]

Mechanistic experiments supporting either radical chain or sequential reduction mechanisms have been studied by multiple groups.[69-78] Examples demonstrating Ni(I) halides undergoing single electron transfer with alkyl electrophiles have been reported by Fu in which (Ph-Box)$Ni^{I}Br$ **6** undergoes halogen atom abstraction with α-bromoketone in DME at −60 °C in an estimated second-order rate constant: > 104 $M^{-1}s^{-1}$ to form (Ph-Box)$Ni^{II}Br_2$ **7** and a mixture of isomeric organic products derived

from homocoupling (Figure 1.12, a).[71] Reacting $[(dtbbpy)NiCl]_2$ **8** or $[(neocuproine)_2Ni]Cl$ **9** with trityl chloride, Hazari demonstrated quantitative formation of the trityl dimer alongside the respective $(dtbbpy)NiCl_2$ **10** or $(neocuproine)NiCl_2$ **11** complexes formed. Conversely, $[(dtbbpy)NiCl]_2$ was found to be unreactive towards aryl iodides.[73] DFT studies by Gutierrez and Molander have studied Ni-acac and bipyridine systems in wherein tertiary alkyltrifluoroborate salts independently generate tertiary alkyl radicals from homolytic cleavage that may undergo either inner-sphere reductive elimination for Ni-bipy systems or an outer sphere reductive elimination for Ni-acac manifolds.[77]

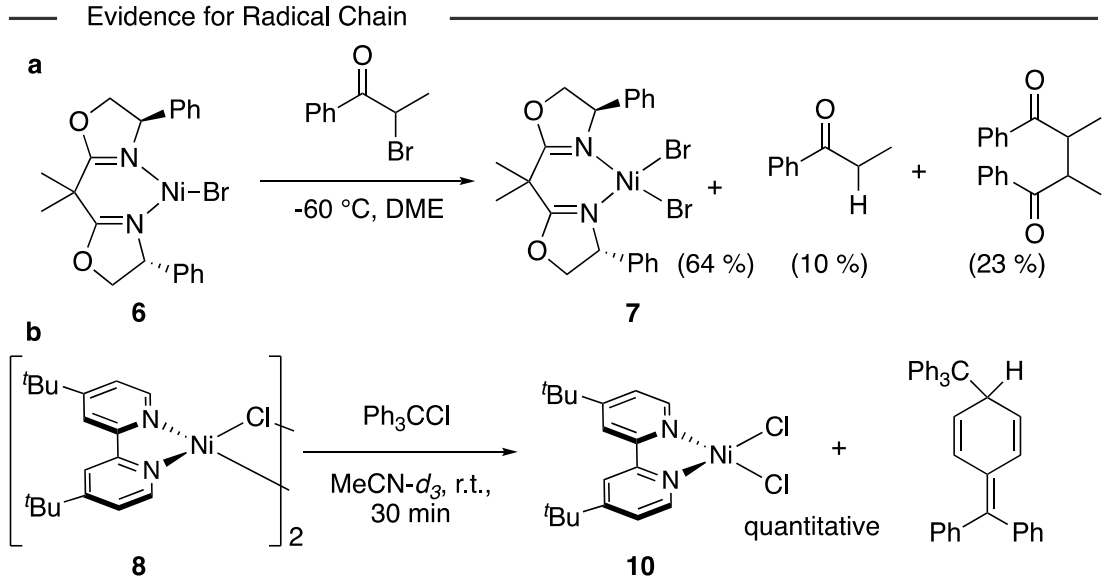

Figure 1.12 Stoichiometric reactions providing evidence of radical chain reactions. **a**, Reaction of (Ph-Box)NiBr with an α-bromo ketone. **b,** Reaction of $[(dtbbpy)NiCl]_2$ with trityl chloride.

Evidence supporting a sequential reduction mechanism have also been provided by Diao[74-75] in which electrochemical reduction of (bipy)Ni(mesityl)(Br) **12** was performed to generate $[(bipy)Ni(mesityl)(Br)]^{\bullet-}$ **13** in the presence of various electrophiles (Figure 1.13). A linear trend was found comparing the $\Delta G^{\ddagger}$ of the reactions to the bond dissociation free energy (BDFE) of the carbon-halogen bond. In these studies, aryl bromides were found to be unreactive and reaction with cyclohexyl chloride proceeded slowly but 1-phenylethyl chloride or alkyl bromides and iodides occurred at modest rates.

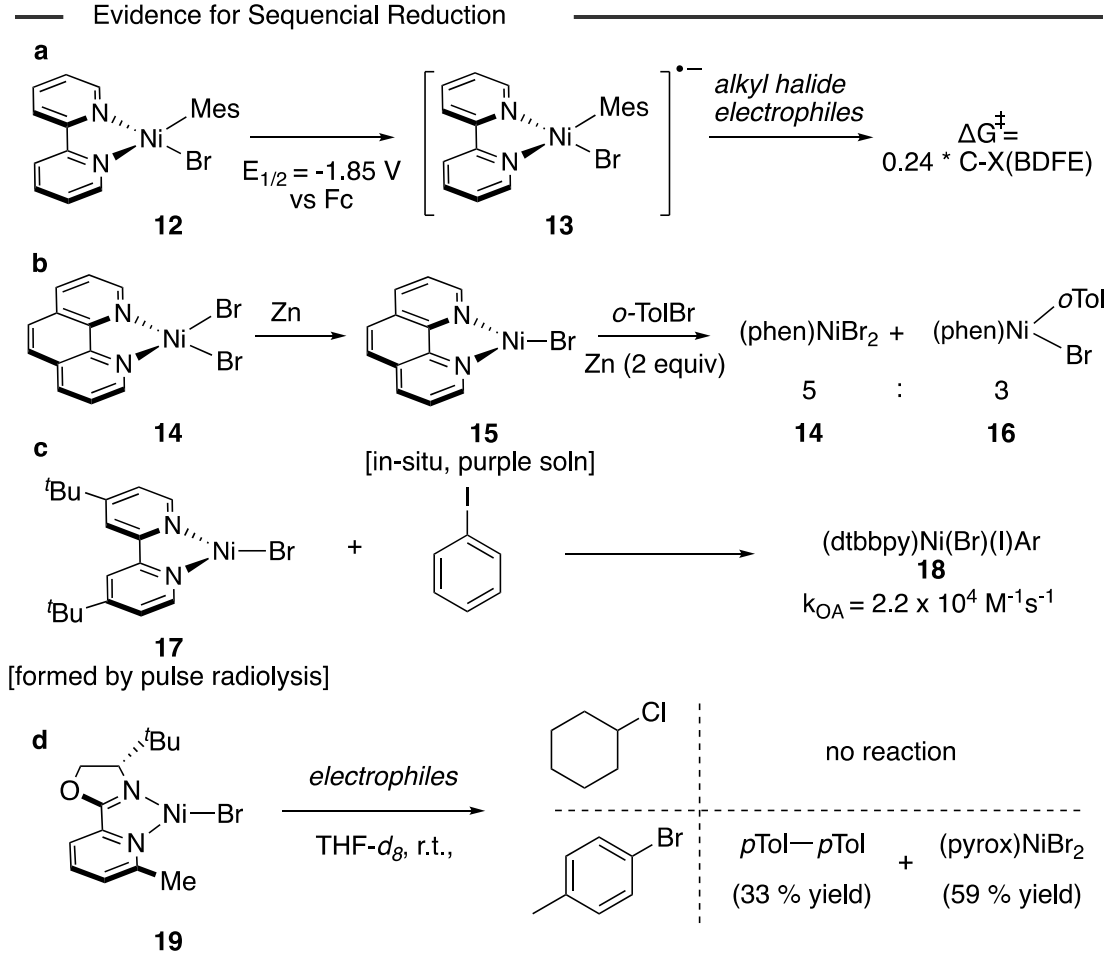

Figure 1.13 Stoichiometric reactions providing evidence of sequential reduction reactions. **a**, Electrochemical formation of [(bipy)Ni(Br)(Mes)]$^{\bullet-}$ and reaction with alkyl halides. **b**, Insitu formation of (phen)NiBr and reaction with aryl bromides. **c**, In-situ formation of (dtbbpy)NiBr and reaction with aryl iodides. **d**, Stoichiometric reaction of (pyrox)NiBr with alkyl chlorides and aryl bromides.

Diao also demonstrated (phen)NiBr$_2$ **14** could be in-situ reduced to form (phen)NiBr **15** with metallic zinc, which subsequently reacts with aryl bromides preferentially over alkyl bromides.[76] Determining the fate of nickel species formed from oxidative addition of **15** to *o*-tolyl bromide allowed the identification of (phen)NiBr$_2$ **14** and (phen)Ni(*o*-tolyl)Br **16** in a 5:3 ratio, likely via a putative Ni(III) complex. These resultant species are proposed to be reduced to a Ni(I)-aryl complex that later on reacts with the alkyl bromide. Nevado also proposed in an experimental and computational study that aryl iodides can react with dtbbpy ligated Ni(I) iodide complexes to form a Ni(III) complex which is then reduced to a Ni(I) aryl complex which activates the tertiary alkyl iodide.[79] Pulse radiolysis experiments by MacMillan supported this claim, in which in-situ generated (dtbbpy)NiBr **17** was shown to react

with aryl iodides with a rate of oxidative addition of k_{OA} = 2.2 x 10^4 $M^{-1}s^{-1}$ to form (dtbbpy)Ni(*o*-tolyl)(I)(Br).[80] Interestingly, they note (dtbbpy)NiBr **17** may dimerize en route to $[(dtbbpy)NiBr]_2$ which results in no reactivity. Further stoichiometric studies by Nocera support that Ni(I)-halides can undergo direct oxidative addition with aryl halides in which they synthesized and studied a mixed Ni(I/II) complex $[(dtbbpy)Ni(Cl)(quinuclidine)]_2Cl$ that reacted with aryl bromides.[81] Studies of pyrox ligated nickel complex have shown that (pyrox)NiBr **19** also reacts with aryl bromides but not with cyclohexyl chloride.[75]

1.1.5 Reduction and Electron Transfer Events in Nickel Catalysis

While electrochemical values vary depending on conditions, the general range of Ni(II/I) and Ni(I/0) reduction for phosphine, NHC, or polypyridine ligated nickel complexes can be compared as: $Ni(dppe)_2$ **20** (-1.08 V vs SCE for Ni(II/I) and -1.26 V vs SCE for Ni(I/0)), [82] (IPr)Ni(Cp) **21** (-1.04 V vs SCE for Ni(II/I) and -1.44 V vs SCE for Ni(I/0)),[83] and $(bipy)_2Ni$ **22** (-1.24 V vs SCE for Ni(II/0)) (Figure 1.14).[84]

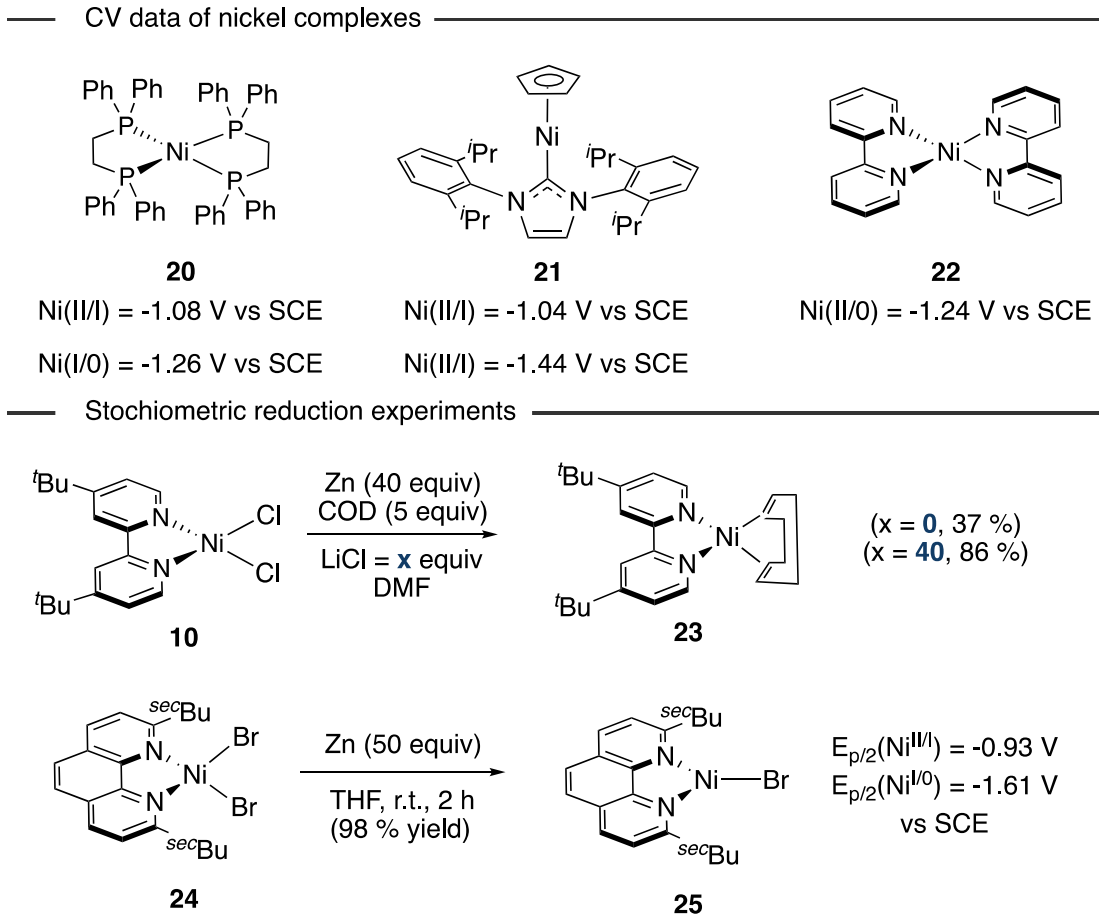

Figure 1.14 Electrochemical data of phosphine, NHC, and polypyridine ligated nickel complexes and stoichiometric reductions of the latter.

With polypyridine ligands proving to be among the most used ligands in reductive coupling reactions, it is not suprising that chemists have been challenged to unravel their role in Ni-catalyzed endeavors. In the stoichiometric reduction of (dtbbpy)$NiCl_2$ **10** with Zn to Ni(0), Weix et al found LiCl assisted reduction en route to (dtbbpy)Ni(COD) **23**.[85] This observation builds on literature precedent in which LiCl assists in the formation of organozinc reagents from organic halides by forming soluble zincates.[86-89] Studying the mechanism of reductive 1,2-dicarbofunctionalization of alkenes, Diao et al performed the stoichiometric reduction of 2,9 *sec*-butyl disubstituted phenanthroline (phen*) ligated nickel dibromide complexes **24** with zinc and found reduction to the Ni(I) bromide **25** occurs rapidly.[76] Cyclic voltammograms of (phen*)$NiBr_2$ **24** displayed reduction peaks at $E_{p/2}$ = -0.93 V vs SCE and -1.61 V vs SCE for Ni(II/I) and Ni(I/0) reductions respectively. The low Ni(II/I) reduction is consistent with previous studies by Sauvage et al in which the CV of interlocking 2,9-disubstituted phenanthroline ligated nickel complexes displayed a Ni(II/I) reduction at -0.18 V vs SCE which the authors suggest is due to the greater stabilization of the tetrahedral geometry.[90-91]

1.1.6 Comproportionation and Disproportionation of Nickel Complexes

An overlooked and poorly understood example of electron transfer is in comproportionation and disproportionation reactions. In these reactions, two nickel complexes in different oxidations states converge to a single oxidation state via comproportionation reactions or two complexes of the same oxidation state react to form products of different oxidation states via disproportionation reactions (Figure 1.15). The study of these reactions dates back to 1964 in a report by Heimbach in which $(PPh_3)_2NiCl_2$ **26** and $(PPh_3)_4Ni$ **27** react by comproportionation forming $(PPh_3)_3NiCl$ **28**.[92] Heimbach also demonstrated the reverse disproportionation reaction could be induced by the addition of π-accepting phosphite ligands to $(PPh_3)_3NiCl$ **28**, in which $(P(OPh)_3)_2NiCl_2$ **29** and $(P(OPh)_3)_4Ni$ **30** are formed. The generality of comproportionation between Ni(0) and Ni(II) to form stable Ni(I) complexes has been expanded to other phosphine ligands,[92-96] NHCs,[97] and polypyridine ligands.[73,98] Comproportionation reactions can be visualized as the low valent Ni(0) complex acting as a reductant, and the Ni(II) complex acting as an oxidant which results in the formation of a Ni(I) complex. The reasoning behind π-acids inducing

disproportionation from Ni(I) to Ni(0) and Ni(II) is their ability to stabilize the low valent Ni(0) complexes.[99] However, insight into disproportionation occurring without the addition of π-acidic ligands is still poorly defined.

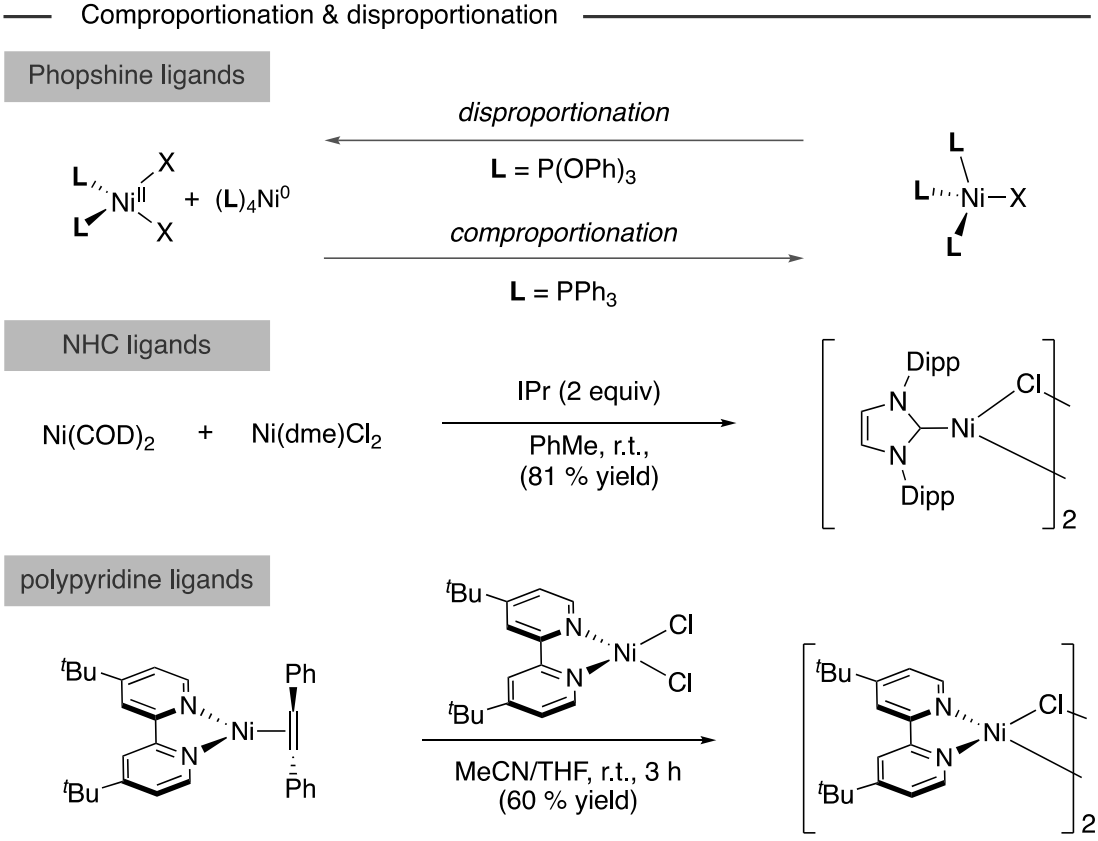

Figure 1.15 Examples of comproportionation and disproportionation reactions.

1.2 General Aim of this Thesis

Nickel-catalyzed cross-coupling reactions have become a powerful tool to assemble molecular complexity from a broad range of coupling partners including strong σ C-O bonds. While the extensive preparative use of nickel catalysts has led to a qualitative understanding of reactivity, a quantitative mechanistic understanding remains significantly underdeveloped which hampers further advances in the field. Such mechanistic studies, however, are challenging to perform due to the ability of nickel complexes to readily undergo one or two electron reactions and the paramagnetism of many nickel complexes. This thesis therefore aims to expand our understanding of nickel-catalyzed reactions at the molecular level with a focus on the activation of strong C(sp^2)-O bonds and reductive coupling reactions that use polypyridine ligands.

The first research chapter will focus on a detailed mechanistic study of nickel-catalyzed Negishi cross-coupling reactions of aryl pivalates in which key on-cycle intermediates present during aryl ester functionalization reactions remained elusive. In this chapter, we synthesize and study these on-cycle intermediates and disclose overlooked reactions between Ni and Zn to provide a full mechanistic picture of the reaction. The second research chapter describes an investigation into the use of reducing Mg in reductive cross-electrophile couplings with redox active ligands. In this investigation, we identify the bipyridine ligands are directly reduced by Mg to the dianion and a unique Mg cluster is formed which exists as the first room temperature stable magnesium electride reported to date. The bonding and chemistry of this complex is interrogated and applications as a readily handled reductant are disclosed. The final research chapter covers a systematic study into disproportionation and comproportionation of polypyridine ligated nickel complexes. This work studies the influence of anionic ligands in governing disproportionation or comproportionation and their implications in catalysis.

1.3 References

1. Magano, J.; Dunetz, J. R. Large-Scale Applications of Transition Metal-Catalyzed Couplings for the Synthesis of Pharmaceuticals. *Chem. Rev.* **2011,** *111* (3), 2177-2250.

2. Johansson Seechurn, C. C. C.; Kitching, M. O.; Colacot, T. J.; Snieckus, V. Palladium-Catalyzed Cross-Coupling: A Historical Contextual Perspective to the 2010 Nobel Prize. *Angew. Chem. Int. Ed.* **2012,** *51* (21), 5062-5085.

3. Campeau, L.-C.; Hazari, N. Cross-Coupling and Related Reactions: Connecting Past Success to the Development of New Reactions for the Future. *Organometallics* **2019,** *38* (1), 3-35.

4. Wu, X.-F.; Anbarasan, P.; Neumann, H.; Beller, M. From Noble Metal to Nobel Prize: Palladium-Catalyzed Coupling Reactions as Key Methods in Organic Synthesis. *Angew. Chem. Int. Ed.* **2010,** *49* (48), 9047-9050.

5. Hazari, N.; Melvin, P. R.; Beromi, M. M. Well-defined nickel and palladium precatalysts for cross-coupling. *Nature Reviews Chemistry* **2017,** *1* (3), 0025.

6. Tasker, S. Z.; Standley, E. A.; Jamison, T. F. Recent advances in homogeneous nickel catalysis. *Nature* **2014,** *509* (7500), 299-309.

7. Diccianni, J.; Lin, Q.; Diao, T. Mechanisms of Nickel-Catalyzed Coupling Reactions and Applications in Alkene Functionalization. *Acc. Chem. Res.* **2020,** *53* (4), 906-919.

8. Diccianni, J. B.; Diao, T. Mechanisms of Nickel-Catalyzed Cross-Coupling Reactions. *Trends in Chemistry* **2019,** *1* (9), 830-844.

9. Roy, L. E.; Jakubikova, E.; Guthrie, M. G.; Batista, E. R. Calculation of One-Electron Redox Potentials Revisited. Is It Possible to Calculate Accurate Potentials with Density Functional Methods? *J. Phys. Chem. A* **2009,** *113* (24), 6745-6750.

10. Poli, R.; Cacelli, I. Orbital Splitting and Pairing Energy in Open-Shell Organometallics: A Study of Two Families of 16-Electron Complexes [Cp_2M] (M = Cr, Mo, W) and [$CpM(PH_3)$] (M = Co, Rh, Ir). *Eur. J. Inorg. Chem.* **2005,** *2005* (12), 2324-2331.

11. Leatherman, M. D.; Svejda, S. A.; Johnson, L. K.; Brookhart, M. Mechanistic Studies of Nickel(II) Alkyl Agostic Cations and Alkyl Ethylene Complexes: Investigations of Chain Propagation and Isomerization in (α-diimine)Ni(II)-Catalyzed Ethylene Polymerization. *J. Am. Chem. Soc.* **2003,** *125* (10), 3068-3081.

12. Xu, H.; White, P. B.; Hu, C.; Diao, T. Structure and Isotope Effects of the β-H Agostic (α-Diimine)Nickel Cation as a Polymerization Intermediate. *Angew. Chem. Int.*

Ed. **2017,** *56* (6), 1535-1538.

13. Xu, H.; Hu, C. T.; Wang, X.; Diao, T. Structural Characterization of β-Agostic Bonds in Pd-Catalyzed Polymerization. *Organometallics* **2017,** *36* (21), 4099-4102.

14. Su, B.; Cao, Z.-C.; Shi, Z.-J. Exploration of Earth-Abundant Transition Metals (Fe, Co, and Ni) as Catalysts in Unreactive Chemical Bond Activations. *Acc. Chem. Res.* **2015,** *48* (3), 886-896.

15. Cornella, J.; Zarate, C.; Martin, R. Metal-catalyzed activation of ethers via C–O bond cleavage: a new strategy for molecular diversity. *Chem. Soc. Rev.* **2014,** *43* (23), 8081-8097.

16. Tobisu, M.; Chatani, N. Cross-Couplings Using Aryl Ethers via C–O Bond Activation Enabled by Nickel Catalysts. *Acc. Chem. Res.* **2015,** *48* (6), 1717-1726.

17. Junichi, I.; Takakazu, Y.; Akio, Y. Selective Cleavage of C–O Bonds in Esters Through Oxidative Addition to Nickel(0) Complexes. *Chem. Lett.* **1976,** *5* (10), 1091-1094.

18. Yamamoto, T.; Ishizu, J.; Kohara, T.; Komiya, S.; Yamamoto, A. Oxidative addition of aryl carboxylates to nickel(0) complexes involving cleavage of the acyl-oxygen bond. *J. Am. Chem. Soc.* **1980,** *102* (11), 3758-3764.

19. Wenkert, E.; Michelotti, E. L.; Swindell, C. S. Nickel-induced conversion of carbon-oxygen into carbon-carbon bonds. One-step transformations of enol ethers into olefins and aryl ethers into biaryls. *J. Am. Chem. Soc.* **1979,** *101* (8), 2246-2247.

20. Wenkert, E.; Michelotti, E. L.; Swindell, C. S.; Tingoli, M. Transformation of carbon-oxygen into carbon-carbon bonds mediated by low-valent nickel species. *J. Org. Chem.* **1984,** *49* (25), 4894-4899.

21. Dankwardt, J. W. Nickel-Catalyzed Cross-Coupling of Aryl Grignard Reagents with Aromatic Alkyl Ethers: An Efficient Synthesis of Unsymmetrical Biaryls. *Angew. Chem. Int. Ed.* **2004,** *43* (18), 2428-2432.

22. Guan, B.-T.; Wang, Y.; Li, B.-J.; Yu, D.-G.; Shi, Z.-J. Biaryl Construction via Ni-Catalyzed C−O Activation of Phenolic Carboxylates. *J. Am. Chem. Soc.* **2008,** *130* (44), 14468-14470.

23. Quasdorf, K. W.; Tian, X.; Garg, N. K. Cross-Coupling Reactions of Aryl Pivalates with Boronic Acids. *J. Am. Chem. Soc.* **2008,** *130* (44), 14422-14423.

24. Li, B.-J.; Li, Y.-Z.; Lu, X.-Y.; Liu, J.; Guan, B.-T.; Shi, Z.-J. Cross-Coupling of Aryl/Alkenyl Pivalates with Organozinc Reagents through Nickel-Catalyzed C□O Bond Activation under Mild Reaction Conditions. *Angew. Chem. Int. Ed.* **2008,** *47* (52),

10124-10127.

25. Li, Z.; Zhang, S.-L.; Fu, Y.; Guo, Q.-X.; Liu, L. Mechanism of Ni-Catalyzed Selective C−O Bond Activation in Cross-Coupling of Aryl Esters. *J. Am. Chem. Soc.* **2009,** *131* (25), 8815-8823.

26. Álvarez-Bercedo, P.; Martin, R. Ni-Catalyzed Reduction of Inert C−O Bonds: A New Strategy for Using Aryl Ethers as Easily Removable Directing Groups. *J. Am. Chem. Soc.* **2010,** *132* (49), 17352-17353.

27. Cornella, J.; Gomez-Bengoa, E.; Martin, R. Combined experimental and theoretical study on the reductive cleavage of inert C-O bonds with silanes: ruling out a classical Ni(0)/Ni(II) catalytic couple and evidence for Ni(I) intermediates. *J. Am. Chem. Soc.* **2013,** *135* (5), 1997-2009.

28. Tobisu, M.; Yamakawa, K.; Shimasaki, T.; Chatani, N. Nickel-catalyzed reductive cleavage of aryl–oxygen bonds in alkoxy- and pivaloxyarenes using hydrosilanes as a mild reducing agent. *Chem. Commun.* **2011,** *47* (10), 2946-2948.

29. Sergeev, A. G.; Hartwig, J. F. Selective, Nickel-Catalyzed Hydrogenolysis of Aryl Ethers. *Science* **2011,** *332* (6028), 439-443.

30. Saper, N. I.; Hartwig, J. F. Mechanistic Investigations of the Hydrogenolysis of Diaryl Ethers Catalyzed by Nickel Complexes of N-Heterocyclic Carbene Ligands. *J. Am. Chem. Soc.* **2017,** *139* (48), 17667-17676.

31. Zarate, C.; Manzano, R.; Martin, R. Ipso-Borylation of Aryl Ethers via Ni-Catalyzed C–OMe Cleavage. *J. Am. Chem. Soc.* **2015,** *137* (21), 6754-6757.

32. Nakamura, K.; Tobisu, M.; Chatani, N. Nickel-Catalyzed Formal Homocoupling of Methoxyarenes for the Synthesis of Symmetrical Biaryls via C–O Bond Cleavage. *Org. Lett.* **2015,** *17* (24), 6142-6145.

33. Zarate, C.; Martin, R. A Mild Ni/Cu-Catalyzed Silylation via C–O Cleavage. *J. Am. Chem. Soc.* **2014,** *136* (6), 2236-2239.

34. Gu, Y.; Martín, R. Ni-Catalyzed Stannylation of Aryl Esters via C−O Bond Cleavage. *Angew. Chem. Int. Ed.* **2017,** *56* (12), 3187-3190.

35. Yu, D.-G.; Li, B.-J.; Shi, Z.-J. Exploration of New C−O Electrophiles in Cross-Coupling Reactions. *Acc. Chem. Res.* **2010,** *43* (12), 1486-1495.

36. Muto, K.; Yamaguchi, J.; Lei, A.; Itami, K. Isolation, Structure, and Reactivity of an Arylnickel(II) Pivalate Complex in Catalytic C–H/C–O Biaryl Coupling. *J. Am. Chem. Soc.* **2013,** *135* (44), 16384-16387.

37. Takise, R.; Muto, K.; Yamaguchi, J.; Itami, K. Nickel-Catalyzed α-Arylation of

Ketones with Phenol Derivatives. *Angew. Chem. Int. Ed.* **2014,** *53* (26), 6791-6794.

38. Desnoyer, A. N.; Friese, F. W.; Chiu, W.; Drover, M. W.; Patrick, B. O.; Love, J. A. Exploring Regioselective Bond Cleavage and Cross-Coupling Reactions using a Low-Valent Nickel Complex. *Chem. Eur. J.* **2016,** *22* (12), 4070-4077.

39. Somerville, R. J.; Hale, L. V. A.; Gómez-Bengoa, E.; Burés, J.; Martin, R. Intermediacy of Ni–Ni Species in sp^2 C–O Bond Cleavage of Aryl Esters: Relevance in Catalytic C–Si Bond Formation. *J. Am. Chem. Soc.* **2018,** *140* (28), 8771-8780.

40. Hong, X.; Liang, Y.; Houk, K. N. Mechanisms and Origins of Switchable Chemoselectivity of Ni-Catalyzed C(aryl)–O and C(acyl)–O Activation of Aryl Esters with Phosphine Ligands. *J. Am. Chem. Soc.* **2014,** *136* (5), 2017-2025.

41. Zhang, S.-Q.; Taylor, B. L. H.; Ji, C.-L.; Gao, Y.; Harris, M. R.; Hanna, L. E.; Jarvo, E. R.; Houk, K. N.; Hong, X. Mechanism and Origins of Ligand-Controlled Stereoselectivity of Ni-Catalyzed Suzuki–Miyaura Coupling with Benzylic Esters: A Computational Study. *J. Am. Chem. Soc.* **2017,** *139* (37), 12994-13005.

42. Kelley, P.; Lin, S.; Edouard, G.; Day, M. W.; Agapie, T. Nickel-Mediated Hydrogenolysis of C–O Bonds of Aryl Ethers: What Is the Source of the Hydrogen? *J. Am. Chem. Soc.* **2012,** *134* (12), 5480-5483.

43. Cornella, J.; Gómez-Bengoa, E.; Martin, R. Combined Experimental and Theoretical Study on the Reductive Cleavage of Inert C–O Bonds with Silanes: Ruling out a Classical Ni(0)/Ni(II) Catalytic Couple and Evidence for Ni(I) Intermediates. *J. Am. Chem. Soc.* **2013,** *135* (5), 1997-2009.

44. Wurtz, A. Ueber eine neue Klasse organischer Radicale. *Justus Liebigs Ann. Chem.* **1855,** *96* (3), 364-375.

45. Ullmann, F.; Bielecki, J. Ueber Synthesen in der Biphenylreihe. *Berichte der deutschen chemischen Gesellschaft* **1901,** *34* (2), 2174-2185.

46. Semmelhack, M. F.; Helquist, P. M.; Jones, L. D. Synthesis with zerovalent nickel. Coupling of aryl halides with bis(1,5-cyclooctadiene)nickel(0). *J. Am. Chem. Soc.* **1971,** *93* (22), 5908-5910.

47. Zembayashi, M.; Tamao, K.; Yoshida, J.-i.; Kumada, M. Nickel-phosphine complex-catalyzed homo coupling of aryl halides in the presence of zinc powder. *Tetrahedron Lett.* **1977,** *18* (47), 4089-4091.

48. Durandetti, M.; Gosmini, C.; Périchon, J. Ni-catalyzed activation of α-chloroesters: a simple method for the synthesis of α-arylesters and β-hydroxyesters. *Tetrahedron* **2007,** *63* (5), 1146-1153.

49. Everson, D. A.; Shrestha, R.; Weix, D. J. Nickel-Catalyzed Reductive Cross-Coupling of Aryl Halides with Alkyl Halides. *J. Am. Chem. Soc.* **2010,** *132* (3), 920-921.

50. Everson, D. A.; Jones, B. A.; Weix, D. J. Replacing Conventional Carbon Nucleophiles with Electrophiles: Nickel-Catalyzed Reductive Alkylation of Aryl Bromides and Chlorides. *J. Am. Chem. Soc.* **2012,** *134* (14), 6146-6159.

51. Anka-Lufford, L. L.; Prinsell, M. R.; Weix, D. J. Selective Cross-Coupling of Organic Halides with Allylic Acetates. *J. Org. Chem.* **2012,** *77* (22), 9989-10000.

52. Wotal, A. C.; Weix, D. J. Synthesis of Functionalized Dialkyl Ketones from Carboxylic Acid Derivatives and Alkyl Halides. *Org. Lett.* **2012,** *14* (6), 1476-1479.

53. Yin, H.; Zhao, C.; You, H.; Lin, K.; Gong, H. Mild ketone formation via Ni-catalyzed reductive coupling of unactivated alkyl halides with acid anhydrides. *Chem. Commun.* **2012,** *48* (56), 7034-7036.

54. Qiu, C.; Yao, K.; Zhang, X.; Gong, H. Ni-catalyzed reductive coupling of α-halocarbonyl derivatives with vinyl bromides. *Org. Biomol. Chem.* **2016,** *14* (48), 11332-11335.

55. Wang, S.; Qian, Q.; Gong, H. Nickel-Catalyzed Reductive Coupling of Aryl Halides with Secondary Alkyl Bromides and Allylic Acetate. *Org. Lett.* **2012,** *14* (13), 3352-3355.

56. Jia, X.; Zhang, X.; Qian, Q.; Gong, H. Alkyl–aryl ketone synthesis via nickel-catalyzed reductive coupling of alkyl halides with aryl acids and anhydrides. *Chem. Commun.* **2015,** *51* (51), 10302-10305.

57. Chen, H.; Jia, X.; Yu, Y.; Qian, Q.; Gong, H. Nickel-Catalyzed Reductive Allylation of Tertiary Alkyl Halides with Allylic Carbonates. *Angew. Chem. Int. Ed.* **2017,** *56* (42), 13103-13106.

58. Molander, G. A.; Traister, K. M.; O'Neill, B. T. Reductive Cross-Coupling of Nonaromatic, Heterocyclic Bromides with Aryl and Heteroaryl Bromides. *J. Org. Chem.* **2014,** *79* (12), 5771-5780.

59. Molander, G. A.; Traister, K. M.; O'Neill, B. T. Engaging Nonaromatic, Heterocyclic Tosylates in Reductive Cross-Coupling with Aryl and Heteroaryl Bromides. *J. Org. Chem.* **2015,** *80* (5), 2907-2911.

60. Ackerman, L. K. G.; Lovell, M. M.; Weix, D. J. Multimetallic catalysed cross-coupling of aryl bromides with aryl triflates. *Nature* **2015,** *524* (7566), 454-457.

61. Zhao, Y.; Weix, D. J. Enantioselective Cross-Coupling of meso-Epoxides with Aryl

Halides. *J. Am. Chem. Soc.* **2015,** *137* (9), 3237-3240.

62. Ren, Q.; Jiang, F.; Gong, H. DFT study of the single electron transfer mechanisms in Ni-Catalyzed reductive cross-coupling of aryl bromide and alkyl bromide. *J. Organomet. Chem.* **2014,** *770*, 130-135.

63. Amatore, C.; Jutand, A. Rates and mechanism of biphenyl synthesis catalyzed by electrogenerated coordinatively unsaturated nickel complexes. *Organometallics* **1988,** *7* (10), 2203-2214.

64. Anderson, T. J.; Jones, G. D.; Vicic, D. A. Evidence for a NiI Active Species in the Catalytic Cross-Coupling of Alkyl Electrophiles. *J. Am. Chem. Soc.* **2004,** *126* (26), 8100-8101.

65. Jones, G. D.; Martin, J. L.; McFarland, C.; Allen, O. R.; Hall, R. E.; Haley, A. D.; Brandon, R. J.; Konovalova, T.; Desrochers, P. J.; Pulay, P.; Vicic, D. A. Ligand Redox Effects in the Synthesis, Electronic Structure, and Reactivity of an Alkyl−Alkyl Cross-Coupling Catalyst. *J. Am. Chem. Soc.* **2006,** *128* (40), 13175-13183.

66. Fischer, C.; Fu, G. C. Asymmetric Nickel-Catalyzed Negishi Cross-Couplings of Secondary α-Bromo Amides with Organozinc Reagents. *J. Am. Chem. Soc.* **2005,** *127* (13), 4594-4595.

67. Arp, F. O.; Fu, G. C. Catalytic Enantioselective Negishi Reactions of Racemic Secondary Benzylic Halides. *J. Am. Chem. Soc.* **2005,** *127* (30), 10482-10483.

68. Lin, X.; Sun, J.; Xi, Y.; Lin, D. How Racemic Secondary Alkyl Electrophiles Proceed to Enantioselective Products in Negishi Cross-Coupling Reactions. *Organometallics* **2011,** *30* (12), 3284-3292.

69. Biswas, S.; Weix, D. J. Mechanism and Selectivity in Nickel-Catalyzed Cross-Electrophile Coupling of Aryl Halides with Alkyl Halides. *J. Am. Chem. Soc.* **2013,** *135* (43), 16192-16197.

70. Schley, N. D.; Fu, G. C. Nickel-Catalyzed Negishi Arylations of Propargylic Bromides: A Mechanistic Investigation. *J. Am. Chem. Soc.* **2014,** *136* (47), 16588-16593.

71. Yin, H.; Fu, G. C. Mechanistic Investigation of Enantioconvergent Kumada Reactions of Racemic α-Bromoketones Catalyzed by a Nickel/Bis(oxazoline) Complex. *J. Am. Chem. Soc.* **2019,** *141* (38), 15433-15440.

72. Weix, D. J. Methods and Mechanisms for Cross-Electrophile Coupling of Csp^2 Halides with Alkyl Electrophiles. *Acc. Chem. Res.* **2015,** *48* (6), 1767-1775.

73. Mohadjer Beromi, M.; Brudvig, G. W.; Hazari, N.; Lant, H. M. C.; Mercado, B. Q.

Synthesis and Reactivity of Paramagnetic Nickel Polypyridyl Complexes Relevant to C(sp^2)–C(sp^3)Coupling Reactions. *Angew. Chem. Int. Ed.* **2019,** *58* (18), 6094-6098.

74. Lin, Q.; Fu, Y.; Liu, P.; Diao, T. Monovalent Nickel-Mediated Radical Formation: A Concerted Halogen-Atom Dissociation Pathway Determined by Electroanalytical Studies. *J. Am. Chem. Soc.* **2021,** *143* (35), 14196-14206.

75. Wagner, C. L.; Herrera, G.; Lin, Q.; Hu, C. T.; Diao, T. Redox Activity of Pyridine-Oxazoline Ligands in the Stabilization of Low-Valent Organonickel Radical Complexes. *J. Am. Chem. Soc.* **2021,** *143* (14), 5295-5300.

76. Lin, Q.; Diao, T. Mechanism of Ni-Catalyzed Reductive 1,2-Dicarbofunctionalization of Alkenes. *J. Am. Chem. Soc.* **2019,** *141* (44), 17937-17948.

77. Yuan, M.; Song, Z.; Badir, S. O.; Molander, G. A.; Gutierrez, O. On the Nature of C(sp^3)–C(sp^2) Bond Formation in Nickel-Catalyzed Tertiary Radical Cross-Couplings: A Case Study of Ni/Photoredox Catalytic Cross-Coupling of Alkyl Radicals and Aryl Halides. *J. Am. Chem. Soc.* **2020,** *142* (15), 7225-7234.

78. Wang, X.; Ma, G.; Peng, Y.; Pitsch, C. E.; Moll, B. J.; Ly, T. D.; Wang, X.; Gong, H. Ni-Catalyzed Reductive Coupling of Electron-Rich Aryl Iodides with Tertiary Alkyl Halides. *J. Am. Chem. Soc.* **2018,** *140* (43), 14490-14497.

79. Shu, W.; García-Domínguez, A.; Quirós, M. T.; Mondal, R.; Cárdenas, D. J.; Nevado, C. Ni-Catalyzed Reductive Dicarbofunctionalization of Nonactivated Alkenes: Scope and Mechanistic Insights. *J. Am. Chem. Soc.* **2019,** *141* (35), 13812-13821.

80. Till, N. A.; Oh, S.; MacMillan, D. W. C.; Bird, M. J. The Application of Pulse Radiolysis to the Study of Ni(I) Intermediates in Ni-Catalyzed Cross-Coupling Reactions. *J. Am. Chem. Soc.* **2021,** *143* (25), 9332-9337.

81. Sun, R.; Qin, Y.; Ruccolo, S.; Schnedermann, C.; Costentin, C.; Nocera, D. G. Elucidation of a Redox-Mediated Reaction Cycle for Nickel-Catalyzed Cross Coupling. *J. Am. Chem. Soc.* **2019,** *141* (1), 89-93.

82. Tsou, T. T.; Kochi, J. K. Mechanism of oxidative addition. Reaction of nickel(0) complexes with aromatic halides. *J. Am. Chem. Soc.* **1979,** *101* (21), 6319-6332.

83. Berning, D. E.; Noll, B. C.; DuBois, D. L. Relative Hydride, Proton, and Hydrogen Atom Transfer Abilities of [HM(diphosphine)$_2$]PF_6 Complexes (M = Pt, Ni). *J. Am. Chem. Soc.* **1999,** *121* (49), 11432-11447.

84. Henne, B. J.; Bartak, D. E. Metal-vapor synthesis and electrochemistry of bis(bipyridyl)nickel(0). *Inorg. Chem.* **1984,** *23* (3), 369-373.

85. Huang, L.; Ackerman, L. K. G.; Kang, K.; Parsons, A. M.; Weix, D. J. LiCl-

Accelerated Multimetallic Cross-Coupling of Aryl Chlorides with Aryl Triflates. *J. Am. Chem. Soc.* **2019,** *141* (28), 10978-10983.

86. Krasovskiy, A.; Malakhov, V.; Gavryushin, A.; Knochel, P. Efficient Synthesis of Functionalized Organozinc Compounds by the Direct Insertion of Zinc into Organic Iodides and Bromides. *Angew. Chem. Int. Ed.* **2006,** *45* (36), 6040-6044.

87. Koszinowski, K.; Böhrer, P. Formation of Organozincate Anions in LiCl-Mediated Zinc Insertion Reactions. *Organometallics* **2009,** *28* (3), 771-779.

88. Feng, C.; Cunningham, D. W.; Easter, Q. T.; Blum, S. A. Role of LiCl in Generating Soluble Organozinc Reagents. *J. Am. Chem. Soc.* **2016,** *138* (35), 11156-11159.

89. Jess, K.; Kitagawa, K.; Tagawa, T. K. S.; Blum, S. A. Microscopy Reveals: Impact of Lithium Salts on Elementary Steps Predicts Organozinc Reagent Synthesis and Structure. *J. Am. Chem. Soc.* **2019,** *141* (25), 9879-9884.

90. Dietrich-Buchecker, C. O.; Guilhem, J.; Kern, J.-M.; Pascard, C.; Sauvage, J.-P. Molecular Structures of a Monovalent and a Divalent Nickel Catenate: Competition between Metal Orbital Requirements and Geometrical Constraints Imposed by the Ligand. *Inorg. Chem.* **1994,** *33* (16), 3498-3502.

91. Dietrich-Buchecker, C. O.; Kern, J.-M.; Sauvage, J.-P. An air-stable d^9 nickel(I) catenate: stabilisation of monovalent nickel by interlocked macrocyclic ligands. *J. Chem. Soc., Chem. Commun.* **1985,** (12), 760-762.

92. Heimbach, P. Changes in the Coordination Number of Ni(0) and Ni(I) Compounds. *Angew. Chem. Int. Ed.* **1964,** *3* (9), 648.

93. Fischer, E. O.; Palm, C. ‹ber Aromatenkomplexe von Metallen, XVII. Cyclopentadienyl-metall-carbonyle des Nickels. *Chem. Ber.* **1958,** *91*, 1725-1731.

94. Tilney-Bassett, J. F. 115. Cyclopentadienylnickel–acetylene complexes. *J. Chem. Soc.* **1961,** (0), 577-581.

95. Cundy, C. S.; Nöth, H. Metal-boron compounds: XI. Complexes derived from reactions of bis(triphenylphosphine)(π-ethylene)nickel with alkyl and boron halides. *J. Organomet. Chem.* **1971,** *30* (1), 135-143.

96. Porri, L.; Gallazzi, M. C.; Vitulli, G. Complexes of nickel(I) with triphenylphosphine. *Chem. Commun.* **1967,** (5), 228-228.

97. Dible, B. R.; Sigman, M. S.; Arif, A. M. Oxygen-Induced Ligand Dehydrogenation of a Planar Bis-μ-Chloronickel(I) Dimer Featuring an NHC Ligand. *Inorg. Chem.* **2005,** *44* (11), 3774-3776.

98. Ting, S. I.; Garakyaraghi, S.; Taliaferro, C. M.; Shields, B. J.; Scholes, G. D.;

Castellano, F. N.; Doyle, A. G. 3d-d Excited States of Ni(II) Complexes Relevant to Photoredox Catalysis: Spectroscopic Identification and Mechanistic Implications. *J. Am. Chem. Soc.* **2020,** *142* (12), 5800-5810.

99. Beattie, D. D.; Lascoumettes, G.; Kennepohl, P.; Love, J. A.; Schafer, L. L. Disproportionation Reactions of an Organometallic Ni(I) Amidate Complex: Scope and Mechanistic Investigations. *Organometallics* **2018,** *37* (9), 1392-1399.

Chapter 2: Deciphering the Dichotomy Exerted by Zn(II) in the Catalytic sp^2 C–O Bond Functionalization of Aryl Esters at the Molecular Level

Published as: Day, C. S.; Somerville, R. J.; Martin, R. Deciphering the dichotomy exerted by Zn(II) in the catalytic sp^2 C–O bond functionalization of aryl esters at the molecular level. *Nat. Catal.* **2021**, *4* (2), 124-133.

Author Contribution: C.S.D. designed and carried out all of the chemical reactions and analyzed the data. R.J.S. participated in preliminary experiments. C.S.D. and R.M. conceived and designed the experiments as well as prepared the manuscript. All authors contributed to discussions, commented and edited the manuscript.

2.1 General Introduction

2.1.1 Phenol Derived Electrophiles in Nickel Catalysis

Phenol derived electrophiles have emerged as a stable, readily synthesized and abundant cross-coupling partner for a range of metal-catalyzed reactions. While aryl sulfonates have historically found success in palladium-catalyzed cross-coupling reactions, these catalysts are unable to be extended to C–O electrophiles with strong σ-bonds. As Chapter 1 covers, nickel complexes offer a smaller, more electropositive analogue to Pd catalysts, and due to these properties, nickel catalysts have found success activating strong C(sp^2)–O electrophiles. Preparative methodologies have now been developed for C-C and C-heteroatom bond forming reactions that have taken particular advantage of the functionalization of aryl pivalate electrophiles (Figure 2.1).

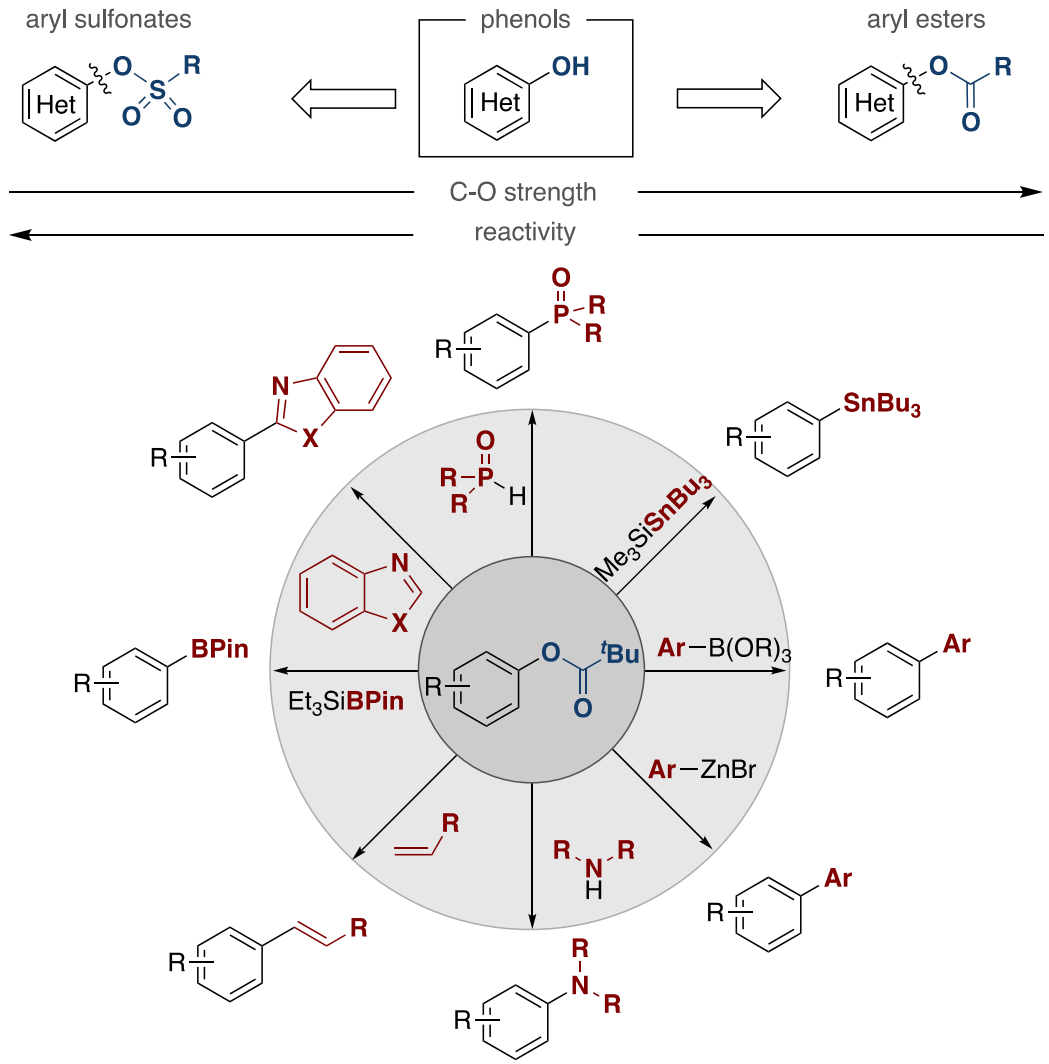

Figure 2.1. C(sp^2)-O electrophiles and catalytic reactions that have been developed to functionalize aryl pivalate into value added compounds.

2.1.2 Aryl Esters in Nickel Catalyzed Negishi Cross-Coupling Reactions

Analyzing the literature of nickel-catalyzed C(sp^2)-O functionalization reactions, an interesting trend emerged where Negishi cross-coupling reactions were rarely reported beyond an early example by Shi.[1] This observation is in sharp contrast to the wide variety of C-C bond forming reactions using Grignard or organoboron coupling reagents.[2-5] The conditions Shi had developed for the cross-coupling of aryl pivalate esters with aryl zinc reagents used $(PCy_3)_2NiCl_2$ as a precatalyst in a THF/DMA solvent mixture at 70 °C. Other examples of Negishi cross-coupling reactions of C(sp^2)-O electrophiles include a report by Uchiyama[6] in which aryl methyl ethers were coupled with Ar-$ZnMe_3Li_2$ using $(PCy_3)_2NiCl_2$ as a precatalyst in toluene at room temperature.

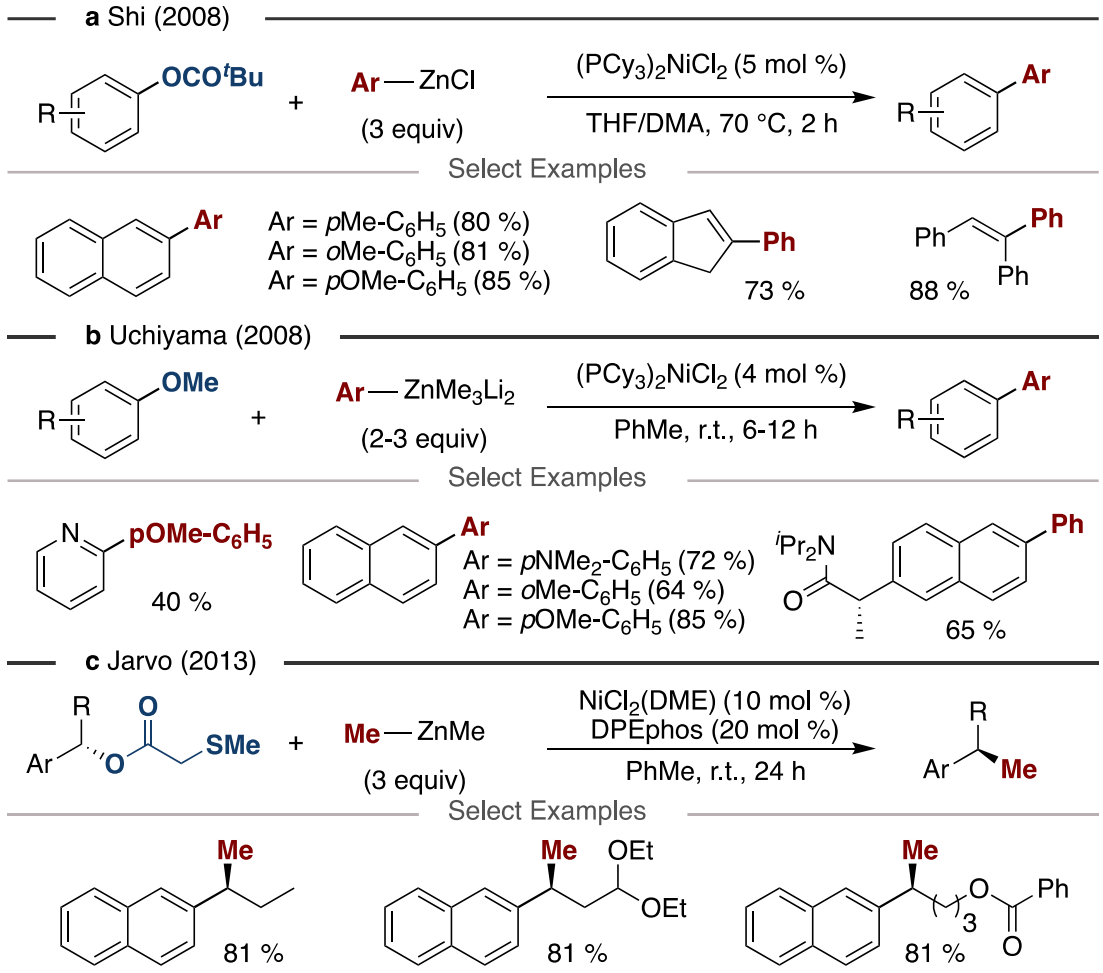

Figure 2.2. Examples of Negishi cross-coupling of C(sp^2)-O electrophiles. a, Negishi cross-coupling of aryl pivalates. b, Aryl methyl ether Negishi cross-coupling with electron rich organozinc reagent. c, Directed Negishi cross-coupling with electron rich organozinc of benzylic esters.

The authors note that their reaction required the use of Ar-$ZnMe_3Li_2$ and attempts to coupling 2-methoxynapthalene with PhZnX (X = Br, Cl, or Ph) afforded no product and only recovered starting material. Jarvo also reported a Ni-catalyzed Negishi cross-coupling of benzylic methyl ethers via a traceless directing group strategy with Lewis acids aiding oxidative addition. The authors found that a protocol based on 20 mol % ligand, Xantphos or DPEphos and $NiCl_2$(DME) (10 mol %) with dialkyl zinc reagents Me_2Zn or Et_2Zn in THF at room temperature afforded the best results.[7-8] Considering these few reports, and the scarcity of Ni-catalyzed Negishi cross-coupling reactions via C(sp^2)-O cleavage reactions, we suspected unidentified challenges may exist originating from the speciation of organozinc species.

2.1.3 Organozinc Speciation in Negishi Catalyzed Cross-Coupling Reactions

The importance of organozinc speciation and additive effects has been well-studied in palladium catalyzed cross-coupling reactions.[9] In a study of Pd-catalyzed Negishi cross-coupling reactions of alkyl zinc reagents, Organ performed double titration experiments to investigate Zn speciation during catalysis that supported that zincate species were involved in transmetallation.[10] A LiBr free solution of ^{n}BuZnBr was coupled with 3-bromo-1-phenylpropane using Pd-PEPPSI-IPr. No coupling was observed until ca. 1 equiv of LiBr was added, and at 1.4 equiv of LiBr quantitative conversion was achieved. This supported $RZnBr_3Li_2$ as the active transmetallating species. Alternatively, $ZnBr_2$ has been proposed to coordinate with the active $L_nPd(0)$ catalyst to form inactive heterobimetallic Pd-ZnX_2 complexes. Indirect support for this was proposed by studying the cross-coupling of 4-bromo-N,N-dimethylaniline using nucleophilic $^nBu_2Zn$, in which titration of $ZnBr_2$ saw loss in activity.[11]

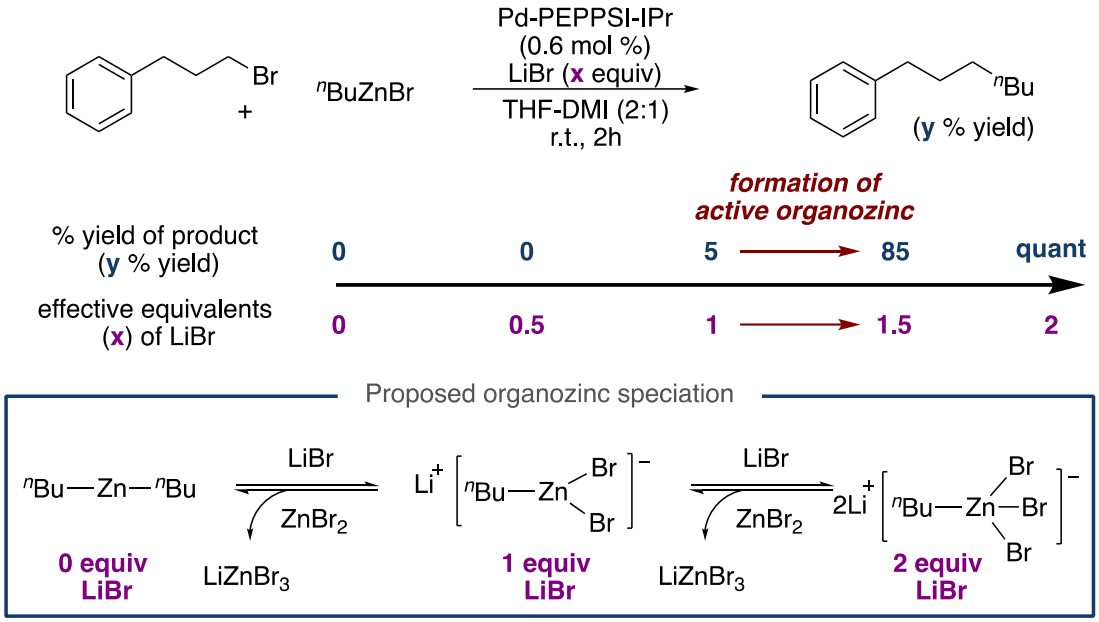

Figure 2.3. Proposed zinc speciation dependent on varied quantities of LiBr or $ZnBr_2$.

2.2 General Aim of the Project

At the onset of this project, phenol derived aryl pivalates had been heavily explored in preparative methodologies as an innovative alternative to aryl halides for C-C bond construction. However, significant mechanistic ambiguity remained about the pathway by which these reactions operated at the molecular level. Inspiration to understand the catalytic functionalization of non-π-extended aryl esters was provided by Shi and co-workers,[1] who reported the nickel-catalyzed cross-coupling of aryl pivalate esters with arylzinc reagents using tricyclohexylphosphine (PCy_3) as the most effective ligand (Scheme 2.1). Outlined below are aspects relevant to studying the mechanism of Ni-catalyzed reactions of non-π-extended aryl esters. Although oxidative addition of aryl esters by nickel (0) complexes were predicted to form mononuclear oxidative addition complexes $(PCy_3)_nNi(OPiv)(Ar)$ (n = 1 or 2) as key intermediates in cross-coupling reactions,[12-15] their identity and carboxylate coordination mode remain unexplored. In addition, the role of zinc(II) speciation on the reaction outcome was unclear, even though they are known to be beneficial in Ni-catalyzed redox-neutral and reductive cross-coupling reactions.[16-19] Additionally, the importance of amide solvents such as dimethylacetamide (DMA) are critical for the successful cross-coupling but, its impact on catalytic activity remains unclear. The latter aspects represent under-appreciated contributions to the success of many Ni-catalyzed cross-coupling reactions.[20-22] We therefore believed these studies would provide new knowledge in the functionalization of strong sigma C–O bonds and nickel-catalyzed Negishi cross-coupling reactions.

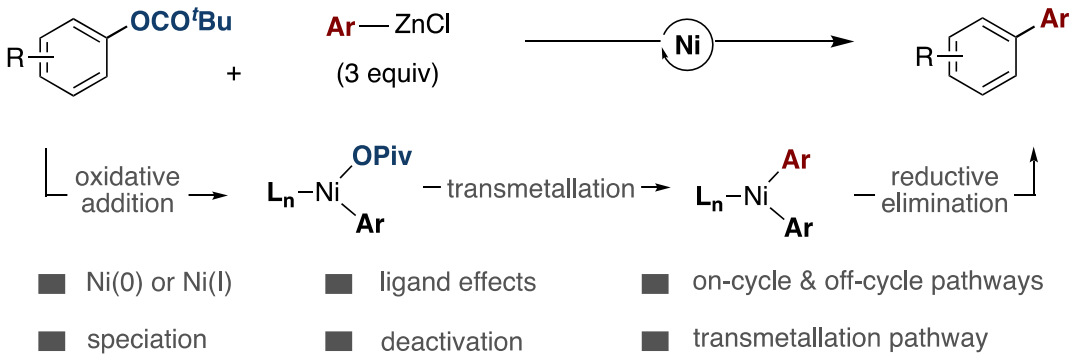

Scheme 2.1. General reaction being studied and the ambiguity surrounding catalytic activity.

2.3 Deciphering the Dichotomy Exerted by Zn(II) in the Catalytic *sp*^{2} C–O Bond Functionalization of Aryl Esters at the Molecular Level

2.3.1 Synthesis and Characterization of Oxidative Addition Complexes

At the start of our studies, on-cycle oxidative addition complexes formed from the direct reaction between Ni(0) complexes and aryl esters were only reported with bidentate phosphines such as dcype[23-24] and activated π-extended aryl esters (Scheme 2.2. complex **1**). While the choice of phosphine ligand can modify chemo and regioselectivity in C(*sp*^{2})–O cleavage reactions,[14,25-26] we wanted to further investigate the reactivity of widely implemented monodentate PCy_3 ligands with non π-extended systems. Our group had previously reported a mechanistic study on the Ni(0)/ PCy_3-catalyzed silylation of aryl esters and disclosed the formation of an unexpected off-cycle dinickel oxidative addition complex (Scheme 2.2, complex **2**), which highlight one of the differences in reactivity between monodentate vs bidentate ligands in the reactions of aryl pivalates.[12] Kinetic studies of these dinickel complexes supported that dinickel complex **2** undergoes disproportionation to form the on-cycle mononuclear aryl-Ni(II)(OPiv) species **I** which then reacts by transmetallation. However, these studies and many others have focused on C(sp^2)-O cleavage of π-extended aryl esters due to their enhanced reactivity which is proposed to originate from the aromatic ring aiding binding of Ni(0) prior to C-O cleavage.[27] Experimental evidence for the reactions of less-reactive, non-π-extended arenes is therefore lacking, and hence our studies began by developing a robust synthetic route to mononuclear aryl–Ni(II)(OPiv) species **I** (Scheme 2.2.).

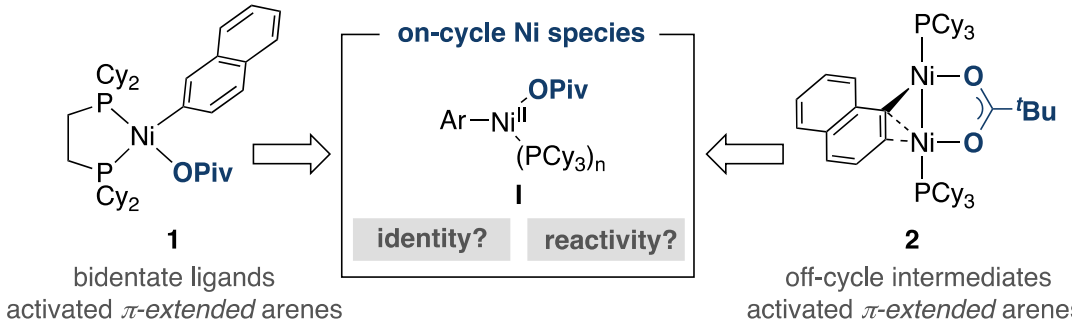

Scheme 2.2. Direct oxidative addition complexes formed from the reaction of Ni(0) and aryl pivalates.

Envisioning a synthesis to mononuclear aryl–Ni(II)(OPiv) species **I**, we believed that the direct oxidative addition of aryl esters to Ni(0) would result in a mixture of products since if oxidative addition to aryl–Ni(II)(OPiv) occurred, it would be immediately followed by rapid comproportionation with unreacted Ni(0) to form an analogue of **2** (Scheme 2.2). [12] We therefore targeted an independent synthesis via anion exchange, as complexes $(PCy_3)_2Ni(aryl)Cl$ (**4a-c,** a = *o*-MeC_6H_4, b = *p*-MeC_6H_4, c = *p*-$CF_3C_6H_4$) could easily be prepared from the reaction between aryl chloride (**3a-c**) and Ni(0).[28-29] Following the anion exchange of **4a** with KOPiv in THF by ^{31}P NMR, we could access **5a** in 62 % yield after 16 h. The stability of **5a** is proposed to originate from the bulky ortho methyl group which prevents axial coordination and helps limit associative decomposition pathway.[30-31] This observation gains support, comparing the synthesis of **5a** to **5b** and **5c** which are much less stable and were synthesized in low yields, with lower reaction times (7h and 3h respectively), and with additional phosphine ligand added to help stabilize the complexes from dissociative decomposition pathways. Crystallization of **5b** and **5c** allowed the comparison of sterically similar but electronically distinct complexes (*p*CF_3 σ = 0.54, *p*Me σ = -0.17). Comparing the Ni-C bond lengths, the more electron-rich complex **5b** contained slightly longer Ni-C bonds than in electron-deficient **5c** (1.897(2) Å vs 1.8865(16) Å). Interestingly, **5b** shows a slight distortion from the P-Ni-P plane, with bonding interactions resembling that of a κ^2-O pivalate ligand (2.7202(16) Å) being formed via the antibonding d_{x2-y2} orbital while κ^1-O complex **5a** contains a nearly perfect square planar geometry with no interaction between the oxygen atom of the carbonyl group at the pivalate fragment and nickel center (Ni–O = 3.0958(12) Å).

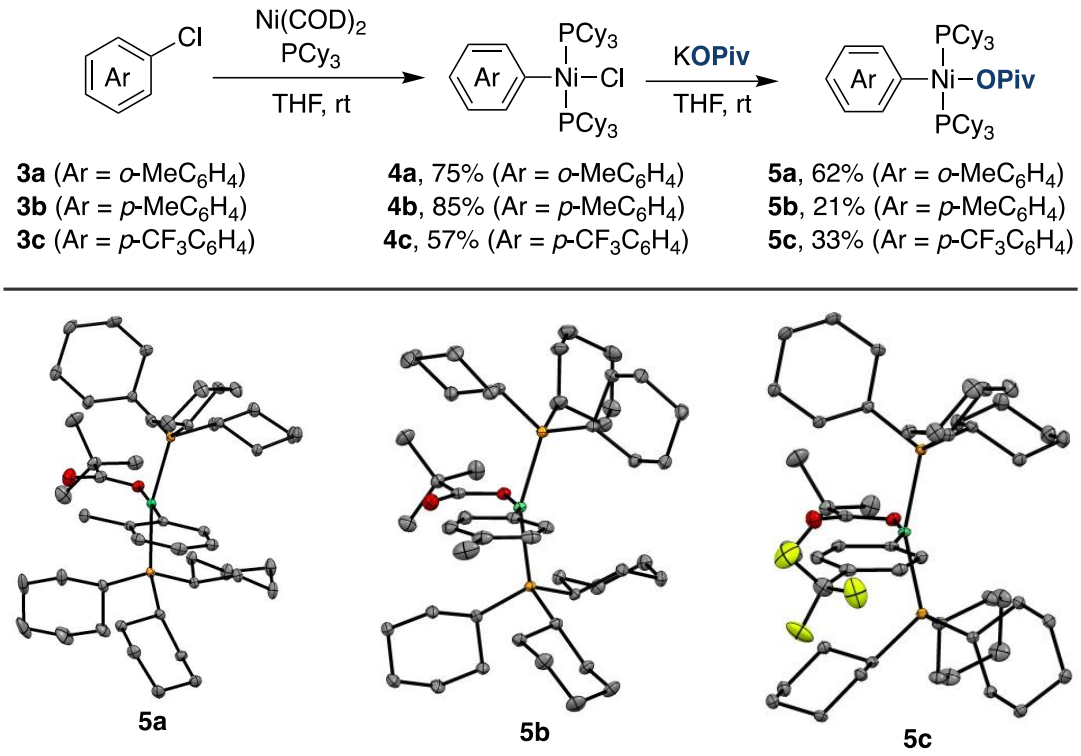

Figure 2.4. Indirect synthesis of monomeric oxidative addition complexes.

With a robust synthetic route to mononuclear κ^1-O oxidative addition complexes, we had spectroscopic handles to investigate if these complexes are generated by the direct oxidative addition between a Ni(0) complex and an aryl ester. Reacting a source of Ni(0), $[Ni(PCy_3)_2]_2N_2$, with *o*-tolyl pivalate in C_6D_6 at room temperature (Figure 2.5) and monitoring the speciation of nickel by ^{31}P NMR spectroscopy (reference: 85% H_3PO_4) revealed the expected dinickel oxidative addition complex **6a** formed as the major species (δ = 24.1 ppm) which could be confirmed by X-ray diffraction but also identified an upfield signal at δ = 37.7 ppm. This signal at 37.7 ppm is consistent with the formation of mononuclear κ^1-O oxidative addition complex **5a**, which displays ^{31}P NMR signals as a 1:1 ratio with PCy_3 (δ = 13.1 ppm).

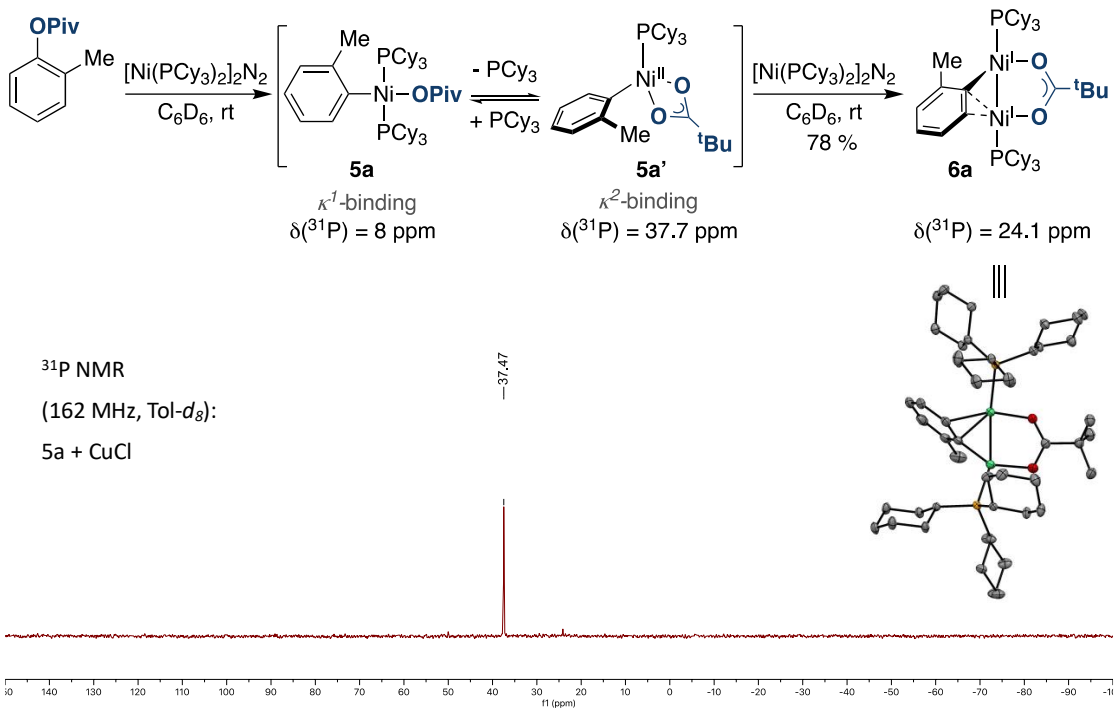

Figure 2.5. Direct oxidative addition to form monomeric oxidative addition complexes and a dinuclear nickel complex. ^{31}P NMR spectrum of 5a + CuCl shown.

The ^{31}P NMR spectrum of **5a** displaying a 1:1 ratio of PCy_3 to complex suggested that the solid state κ^1-O structure obtained crystallographically undergoes PCy_3 dissociation in solution to form a κ^2-O congener **5a'** which would be in equilibrium with the κ^1-O complex **5a**. Indeed, performing variable temperature ^{31}P NMR experiments, a new signal at 8 ppm was observed upon cooling to only 15 °C which would correspond to the κ^1-O bis(PCy_3) complex **5a**. Other experiments to probe the solution speciation of **5a** were performed by reacting **5a** with phosphine scavenger CuCl in C_6D_6 in which only the signal at δ = 37.5 ppm remained (Figure 2.5). With these results, we propose that monomeric, κ^2-O bound pivalate oxidative addition complexes such as **5a'** are formed in the reaction of monodentate phosphines PR_3-Ni(0) with aryl pivalates. The generation of these κ^2-O bound complexes, may support their superior reactivity and popularity in nickel-catalyzed cross-coupling reactions of aryl pivalates[32-35] as κ^2-O bound complexes would be more electrophilic than their bis ligated counterparts and show enhanced reactivity to carbogenic nucleophiles and hence accelerate transmetallation. While thus far we have demonstrated strong spectroscopic evidence for in-situ generated mononuclear (PCy_3)Ni(Ar)(κ^2-OPiv) complexes, we aimed to provide access to isolate these complexes as a discrete entity to study in a well-defined setting due to their relevance in direct oxidative addition and catalysis. We expected however, that the lack of an extra σ-donating PCy_3 ligand

compared to **5a-c** would drastically reduce the stability of these complexes. Early synthetic attempts to access these κ^2-OPiv complexes by scavenging PCy_3 from **5a** were unsuccessful as concentrated solutions underwent rapid decomposition, likely owing to the bridging capability of pivalate ligands to induce decomposition. Attempting to access a more robust complex, we targeted the mesityl variant of **5a** which would shield both axial coordination sites of nickel to further prevent associative decomposition pathways.

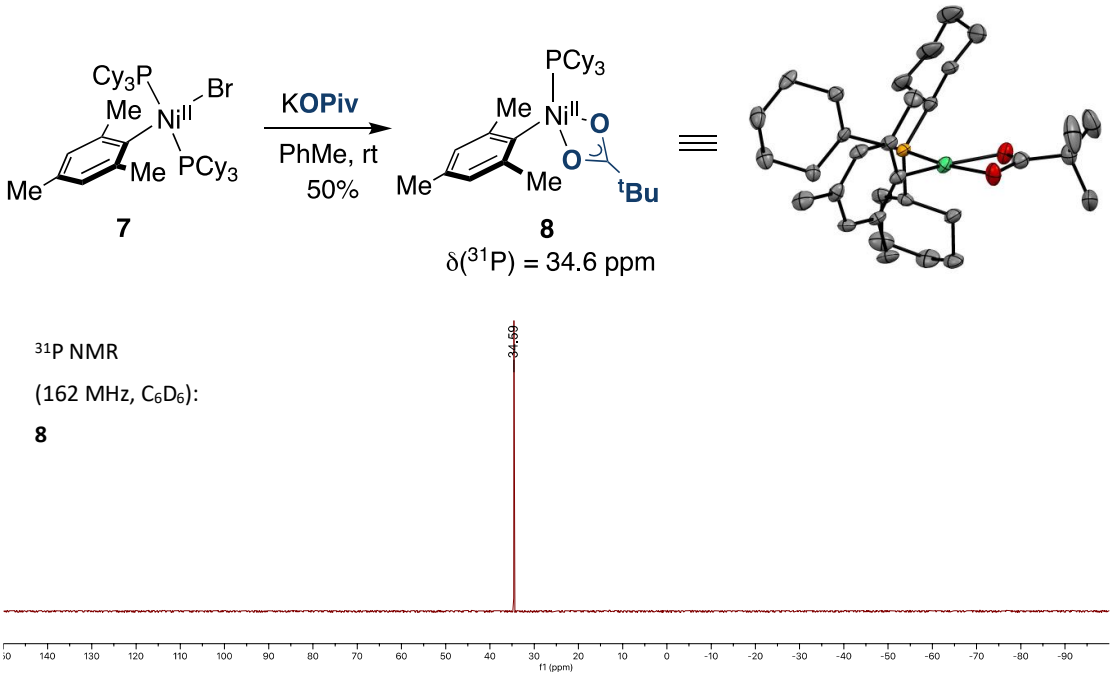

Figure 2.6. Indirect synthesis of $(PCy_3)_2Ni(Mes)(\kappa^2\text{-OPiv})$ via anion metathesis. Crystal structure and ^{31}P NMR spectrum of **8** shown.

Synthesis of $(PCy_3)_2Ni(Mes)Br$ (Mes, mesityl) **7**, and then subsequent anion metathesis with KOPiv indeed provided access to the targeted κ^2-O pivalate complex **8** in 50% yield (Figure 2.6). Single crystal XRD of **8** unambiguously identified the κ^2-O binding mode of the pivalate ligand, in which **8** possessed a planar, four-coordinate geometry with symmetric Ni-O bonds. The two similar C–O bond lengths (1.280(7) and 1.272(8) Å) also indicate significant π-delocalization. Interestingly, the P–Ni bond is shorter in **8** (2.1615(18) Å) compared to κ^1-O complex **5a** (2.2699(4) and 2.2693(4) Å) suggesting the P–Ni bond is strengthened after phosphine dissociation from bis-ligated **5a** due to the more electron deficient Ni-center. The unambiguous characterization of κ^1-O and κ^2-O pivalate complexes **5a-c** and **8** represents significant progress in our understanding of nickel-catalyzed cleavage of aryl esters and offers

indirect understanding to the mechanism of related C-O electrophiles such as aryl carbamates.

2.3.2 Studying Disproportionation

With these oxidative addition complexes $(PCy_3)_nNi(aryl)OPiv$ (Figure 2.4, **5a-c**) in hand, we then began to study their stability as it would provide information into decomposition pathways for on-cycle intermediates. Notably, during the synthesis of complexes **5a-c** we noticed the formation of paramagnetic species with a key signal at δ_H = 27 ppm. These paramagnetic species were formed both in the indirect synthesis from anion metathesis or upon concentrating isolated **5a** with PCy_3 removed with phosphine scavenger CuCl. The formation of these paramagnetic complexes indirectly supported disproportionation reactions to form Ni(I) species with a presumed structure $Ni(I)(OPiv)(PCy_3)_n$, which we believed would be facilitated by the pivalate ligands that could act to bridge two nickel atoms. As understanding the decomposition pathways would provide direct insight into designing more robust catalytic conditions and improve catalyst turnover,[21,36] we began synthetic investigations into the speculated Ni(I)-pivalate complexes.

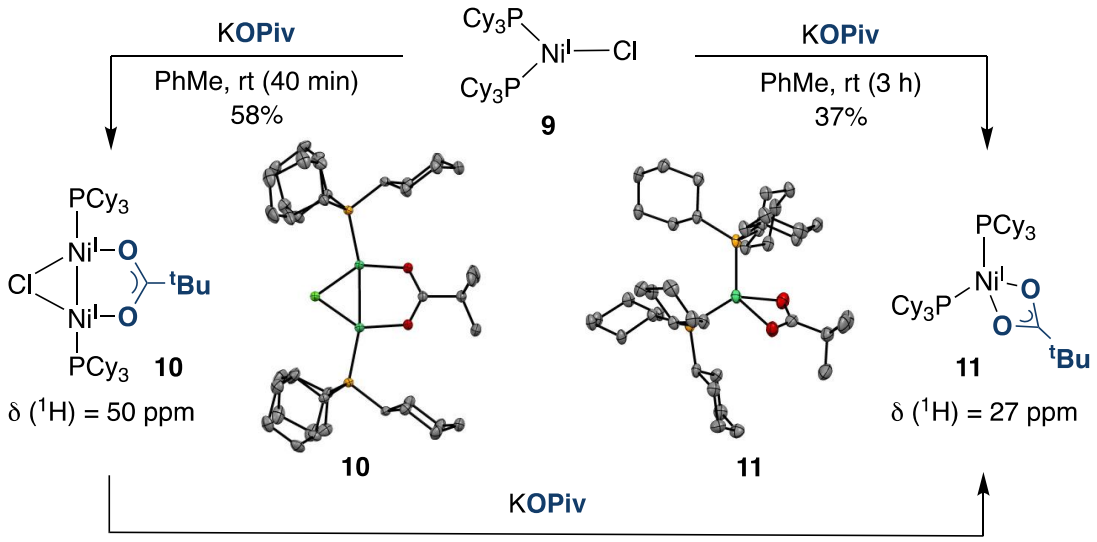

Figure 2.7. Indirect synthesis of Ni(I)-pivalate complexes.

While reviewing the literature for similar complexes, we discovered that there were no Ni(I)-carboxylate complexes synthesized with monodentate phosphine ligands, which we speculated may be due to the poorer stabilization when compared to diphosphine[37] or N-heterocyclic carbene[38] analogues. Envisioning an analogous route to Ni(I)-pivalate complexes as the Ni(II) complexes, we began our investigations by

reacting $(PCy_3)_2NiCl$ **9** with potassium pivalate in toluene in which bridged $[(PCy_3)Ni]_2(\mu\text{-Cl})(\mu\text{-OPiv})$ (**10**) and monomeric $[(PCy_3)_2Ni(\kappa^2\text{-OPiv})]$ (**11**) complexes could be accessed in 60% and 37% yield respectively depending on the reaction time. These structures were unambiguously characterized by single crystal XRD analysis (Figure 2.7). Comparison of the crystallographic data between the Ni(I)-pivalate and Ni(II)- κ^2-O pivalate complexes, reveals that **11** contains a distorted tetrahedral geometry compared to the square planar geometry of **8** with a similar κ^2-O binding to **8**. Considering the Ni-O and carbonyl C-O stretching distances of **11** and **8** also reveals subtle differences. Ni(I) species **11** possesses elongated Ni–O bonds (avg of 2.1245 Å vs 1.984 Å) and shorter C–O bonds (avg of 1.258 vs 1.276 Å). This is tentatively ascribed to a poorer orbital overlap of the distorted tetrahedral geometry in **11** as opposed to the square planar geometry of **8**. The relevance of Ni(I) species such as **11** in decomposition of on-cycle Ni(II)-aryl pivalate complexes was confirmed by comparing the paramagnetic ^1H NMR of **11** at δ_H = 27 ppm, which correlated to the previously unidentified signals formed when concentrating phosphine free solutions of **5a** or during the direct oxidative addition of Ni(0) with *o*-tolyl pivalate. Together, these results support facile decomposition of on-cycle $(PCy_3)_nNi(aryl)OPiv$ complexes to deactivated, off-cycle Ni(I)-pivalate species. As such for productive catalysis, these on-cycle oxidative addition complexes should rapidly be intercepted via their corresponding coupling partner or transformed into a more stable intermediate to limit these intrinsic decomposition pathways.

2.3.3 Unravelling the Influence of Zn on Catalyst Turnover

With the above observations regarding the instability of $(PCy_3)_nNi(aryl)OPiv$ complexes, and the successful cross-coupling in the presence of RZnCl supports that transmetallation kinetically outcompetes decomposition pathways. Considering the Schlenk equilibrium of $ZnCl_2$, $ZnAr_2$ and ArZnCl along with the buildup of zinc(II) salts during catalyst turnover we began investigating the interactions of these species on the catalytic cycle. Zinc salts are commonly found as additives or indirectly formed during transmetallation or reduction events in a wide variety of nickel-catalyzed cross-coupling reactions, however, their influence of reactivity often ill-defined,[16,18-19,39] and new understanding into the role of zinc salts may provide important insight into related nickel-catalyzed reactions. Therefore, we began our investigations by studying the influence of $ZnCl_2$ on the nickel species within the catalytic cycle. As $ZnCl_2$ is often

used as a Lewis acid, one may presume that it may assist in the catalytic reaction by coordination to the aryl ester to weaken the C-O bond and facilitate oxidative addition to Ni(0). However, reacting $[Ni(PCy_3)_2]_2N_2$ with *o*-tolyl pivalate in THF-d_8 in the presence of $ZnCl_2$ resulted in no conversion of *o*-tolyl pivalate (Figure 2.8). Interestingly, this supported an alternative interaction between $ZnCl_2$ and Ni(0). Consistent with this proposal, reacting $[Ni(PCy_3)_2]_2N_2$ with $ZnCl_2$ at room temperature in THF-d_8 saw rapid conversion of $[Ni(PCy_3)_2]_2N_2$ by ^{31}P NMR spectroscopy with the formation of PCy_3 ligated zinc complexes $[(PCy_3)ZnCl_2]_2$ (**13**), $(PCy_3)_2ZnCl_2$ (**14**) and formation of $(PCy_3)_2NiCl$ **9** in 76% yield due to oxidation of Ni(0) to Ni(I). This oxidation reaction between Zn(II) and Ni(0) is consistent with the reported redox potentials of $ZnCl_2$ ($E_{red}(Zn(II)/Zn(0)) = -1.002$ V vs SCE; $E_{red}(Ni(II)/Ni(0)) = -1.25$ V vs SCE).[40] Crystallization of the reaction mixture also revealed the formation of an unorthodox Ni-Zn cluster $Zn_3Ni_4Cl_4P_3C_{73}H_{99}$ (**12**).

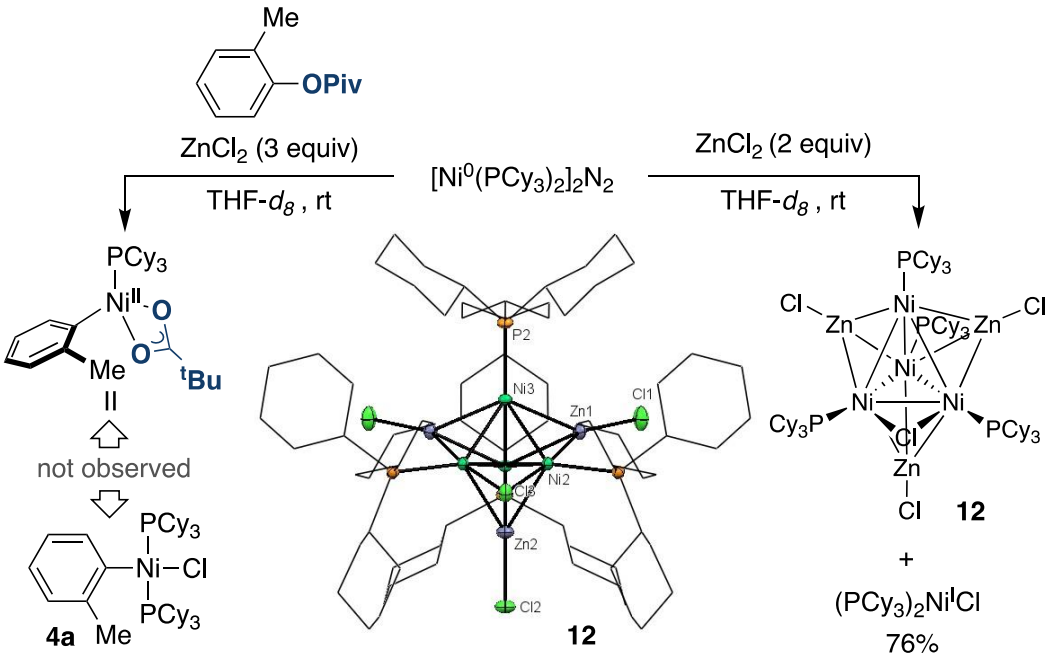

Figure 2.8. Comparison of Ni(0) oxidative addition to aryl pivalates with and without $ZnCl_2$ present.

The above experiments not only support a direct interaction between Ni(0) and Zn(II) but also suggest that these interactions have likely been overlooked in a range of Ni-catalyzed reactions. A closer look at the crystallographic data of **12** demonstrate six Ni-Zn bonds and three Ni-Ni bonds with the latter Ni-Ni bonds being slightly longer than their Ni-Zn counterparts (average of 2.526 versus 2.428). Additionally, the nickel atoms are ligated by four PCy_3 ligands. Considering the formal oxidation states of the atoms in **12**, it consists of three Zn(I) atoms, three Ni(0) atoms, and a single Ni-Cl bond

which contains a bridging chloride atom. Notably, there is a lack of any Zn-Zn interactions, which contrasts the 12 Ni-Zn bonds and indirectly supports that initial Ni-Zn adducts precedes the formation of **12**. Such an adduct would also provide an intermediate for redox interactions between Ni(0) and Zn(II), as this adduct would contain short intermetallic distances and allow for halide bridges that would both favour electron transfer. The formation of **12** may be explained by a formal hard-hard interaction between electron-rich d^{10} Ni(0) center and an electrophilic $3d^{10}$ Zn(II) center. The similar hardness of Zn(II) and Ni(0)[41] would also rationalize the phosphine exchange reactions observed in the formation of $[(PCy_3)ZnCl_2]_2$ (**13**) and $(PCy_3)_2ZnCl_2$ (**14**). This ligand sequestering may be particularly problematic under catalytic conditions, as excess Zn(II) salts may sequester the ancillary ligand of the active metal catalyst and lead to nickel nanoparticles with little to no catalytic activity.[42]

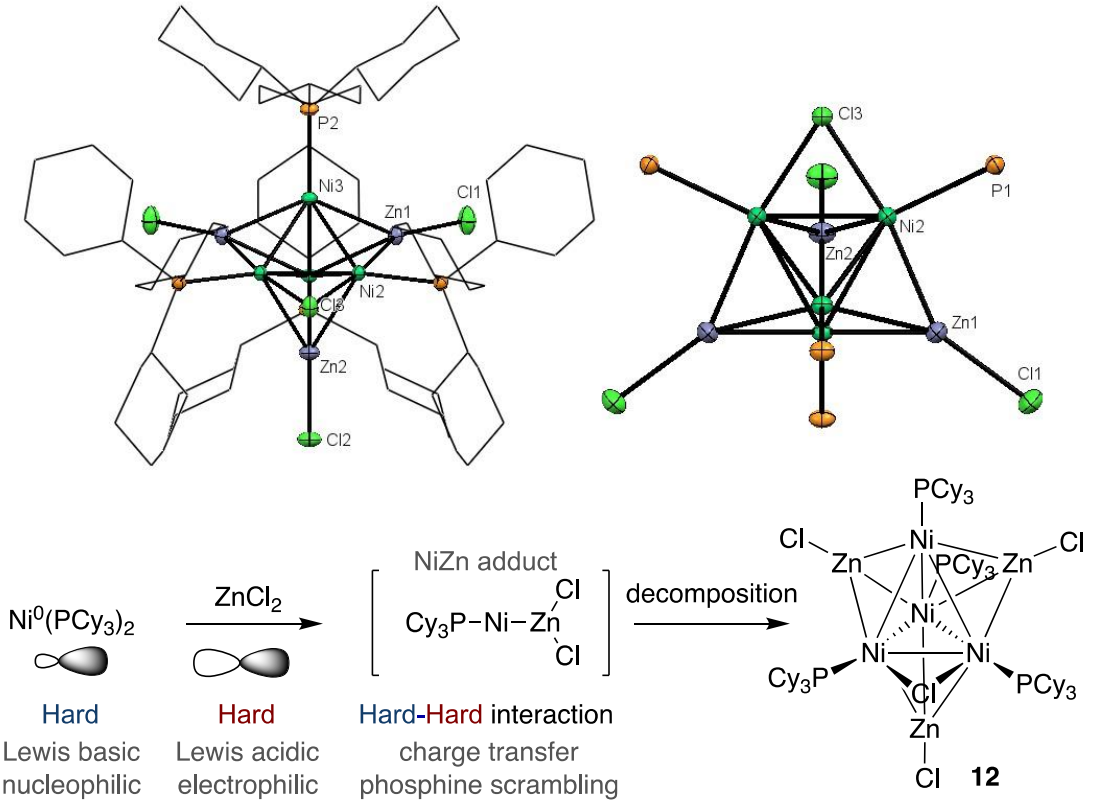

Figure 2.9. Crystallographic depiction of complex **12** and a proposed pathway for its formation.

Reviewing the literature, related Pd-Zn species to **12** have been proposed[11,43] based on DFT,[44-47] spectroscopic studies,[45] and qualitative mass spectrometric analysis,[48] the unambiguous identification of **12** represents evidence of Ni-Zn species being formed within the context of nickel-catalyzed reactions. We further expect that these Ni-Zn adducts may be at least partially responsible for the lack of popularity and high catalyst

loadings of nickel-catalyzed Negishi-type cross-coupling reactions with phosphine ligands compared to Pd-catalyzed protocols.[16,49-50] Comparing the fundamental properties of these two atoms, Pd-Zn adducts may be less likely to form due to the soft-hard mismatch between Pd(0) and Zn(II), along with the higher electronegativity of Pd compared to Ni (2.2 vs 1.9) and weaker metal-ligand bonds typically found in first row metals compared to later metals (Ni^0–PH_3 = 23.0 kcal mol^{-1}; Pd^0–PH_3 = 41.8 kcal mol^{-1})[51] which would result in less ligand exchange between Pd and Zn species when compared to Ni and Zn species (Figure 2.9).

Together, these results support the notion that a number of deactivation or decomposition pathways may come into play with Ni-catalyzed reactions using Zn salts such as redox reactions, ligand sequestering or direct catalyst decomposition. While the experiments in Figure 2.8 highlight detrimental reactivity between Ni(0) and Zn(II), we wondered how other catalytic intermediates interacted with zinc salts. As such, we turned our attention to the reaction between oxidative addition complex **5a** and $ZnCl_2$. Monitoring the reaction, we observed complete conversion of **5a** to Ni(II)-(aryl)(Cl) complex **4a** at room temperature in THF-d_8 (<10 min) supporting the notion that anion exchange may be involved in the catalytic cycle. Analogous reactivity was observed with Ni(I) complex $(PCy_3)_2Ni(OPiv)$ **11**, which rapidly formed $(PCy_3)_2NiCl$ **9**. Noteworthy is that in both reactions with either **5a** or **11**, PCy_3 ligated Zn(II) salts are formed as complexes **13** and **14** (Figure 2.10). Quantification of ^{31}P NMR spectroscopy identified 47 % of PCy_3 was bound to Zn(II) complexes when **5a** was reacted with $ZnCl_2$, supporting that ligand sequestering plays a significant role in these reactions systems.

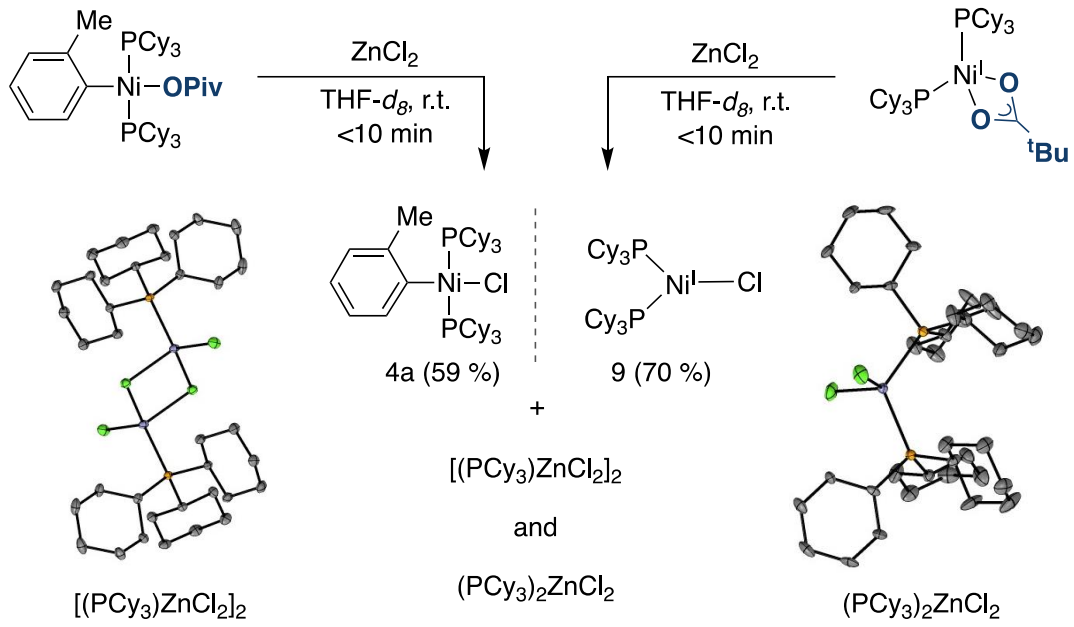

Figure 2.10. Rapid anion exchange from Ni-OPiv to Ni-Cl species, along with the formation of PCy_3 ligated zinc complexes.

Indeed, this deleterious impact of Zn(II) species on catalyst turnover may already be frequently encountered[16,18-19,22,39,52] in Ni-catalyzed cross-electrophile coupling reactions which use stochiometric quantities of Zn to trigger redox processes. Probing if these stochiometric experiments correlated to catalytic conditions, we then investigated the speciation of the standard catalytic conditions by reacting 3-benzophenone pivalate with PhZnCl. Quantitative analysis of the reaction mixture by MALDI mass spectrometry identified mass fragments for Ni-Zn adduct [$PCy_3NiZnCl_2$] (472.2 m/z), Ni(0)(PCy_3)$_2$ (618.5 m/z), and Zn/PCy_3 complexes **13** and **14**. More quantitative data could be obtained about speciation by quantitative ^{31}P NMR spectroscopy. Notably, 50 % of PCy_3 was bound to zinc species **13** and **14** with no signals of oxidative addition complexes of type (PCy_3)$_2$Ni(Ar)X (X = OPiv or Cl) or of dinickel complexes observed (Figure S18). Together with the previous stochiometric experiments, these findings support the dynamic behavior of phosphine ligands during catalysis which shuttle between Ni and Zn complexes. Further aiming to study the relevance of Ni(I) species on the reaction outcome, we monitored the catalytic reaction by ^{1}H NMR in which we were unable to detect Ni(I) complexes (PCy_3)$_2$NiCl (**9**) and (PCy_3)$_2$NiOPiv (**11**). We presume their lack of detection is due to their ability to rapidly transmetalate with PhZnCl to prevent buildup during catalysis,[52-54] which was indirectly supported by the ability of (PCy_3)$_2$NiCl (**9**) to act as a competent precatalyst under the standard catalytic conditions.

2.3.4 Transmetalation of Well-Defined Ni(II) Complexes

Classical catalytic cycles proposed for Ni-catalyzed cross-coupling reactions of aryl esters support transmetallation between the aryl–Ni(II)(OPiv) oxidative addition complex and organometallic reagent prior to reductive elimination. [14-15,24,55] However, the experiments outlined in figure 2.10 support anion metathesis with $ZnCl_2$ may precede transmetallation. To further investigate this possibility, we monitored the reaction between **5a** and 0.50 equivalents of PhZnCl·LiCl by ^{1}H NMR spectroscopy, forming biaryl product **15** in 37 % yield and $(PCy_3)_2Ni(o\text{-tolyl})(Cl)$ **4a** as the sole remaining nickel species. Further addition of PhZnCl·LiCl led to additional biaryl product **15**, which led us to question of transmetallation occurred from **4a** or **5a**. Therefore, we investigated if transmetallation could occur in the absence of $ZnCl_2$ by reacting **5a** or **8** with Ph_2Zn which cleanly delivered biaryl products **15** or **16**. These experiments confirm that transmetallation can occur from either Ni-Cl, κ^1- or κ^2-ester intermediates (Figure 2.11). Inspired by a recent report by Bedford[42] in the role of diphosphine ligated zinc species in iron-catalyzed Negishi cross-coupling reactions, we wondered if transmetallation was assisted by the formation of PCy_3 ligated PhZnCl. To investigate this possibility, PhZnCl was reacted with 1 equivalent of PCy_3 to form $[(PCy_3)Zn(Cl)(Ph)]_2$ (**17**). Control experiments were then performed by reacting **5a** with **17** in which the biaryl product **15** also formed rapidly. These results support the possibility that $[(PCy_3)Zn(Cl)(Ph)]_2$ (**17**) may offer an organozinc species with improved solubility and more electron rich character compared to unligated species.

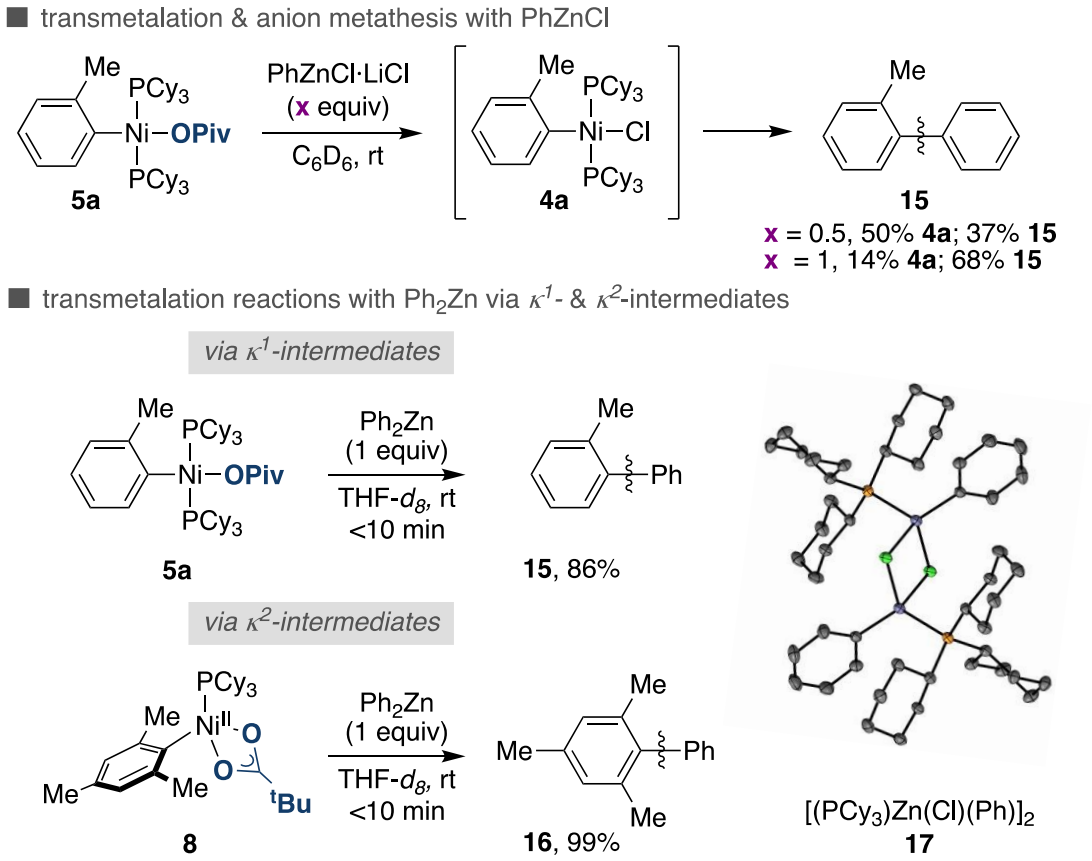

Figure 2.11. Transmetallation and anion metathesis of Ni(II)-pivalate and Ni(II)-chloride complexes with PhZnCl·LiCl and Ph_2Zn.

Taken together, this data supports Bedford's[42] previous findings that Zn(II) salts are not spectators in metal-catalyzed cross-coupling reactions and effect multiple catalytic steps. While zinc salts have been shown to be involved in ligand sequestering, redox events, and formation of Ni-Zn clusters that may compromise catalytic activity, these salts also partake in anion exchange to form stable Ni-Cl species that may precede transmetalation.

2.3.5 Unravelling the Influence of Amide Solvents on Catalytic Activity

While care must be taken to not overinterpret the data presented above, it was apparent that decomposition and deactivation pathways should be significantly problematic for catalyst turnover and yet they appeared to make a minor contribution to C-C bond formation in catalysis. This begged the question as to how other variables may affect the reaction outcome. Investigating the literature on nickel-catalyzed cross-coupling reactions,[20-22] it became apparent that a significant number of transformations rely on coordinating amide solvents,[16-19] including the coupling of aryl esters.[1,56-57] Anticipating then amide solvents such as DMA play an important role in the reaction

outcome, we began to investigate how it impacted the catalytic transformation. While C-O cleavage does not occur with $ZnCl_2$ present (Figure 2.8) but transmetallation occurs rapidly at room temperature (Figure 2.11), we suspected DMA is able to stabilize Ni(0) and Zn(II) species prior to oxidative addition. For these experiments we also suspected that oxidative addition was turnover limiting in the reaction. The validity of these hypotheses were then investigated by monitoring the standard catalytic conditions in the presence and absence of DMA and, replacing DMA with alternative coordinating ligands and by comparing the initial rate of the cross-coupling reaction between a set of electronically different aryl pivalates.

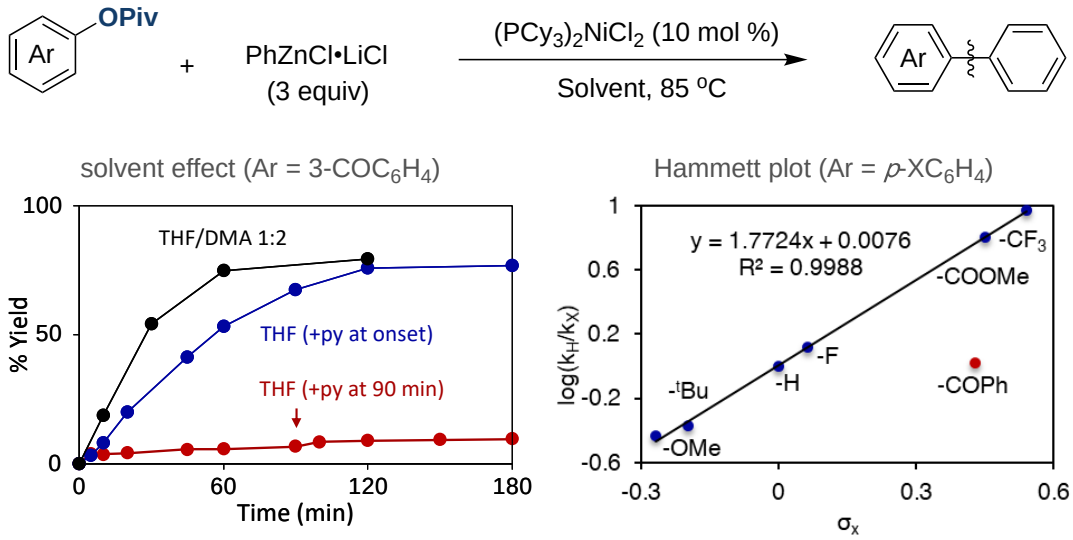

Figure 2.12. The effect of solvent choice on the reaction outcome and a Hammett plot of electronically varied aryl pivalates.

As shown in Figure 2.12, the cross-coupling reaction was faster with electron deficient aryl pivalates and slower with electron rich aryl pivalates. Plotting $\log(k_H/K_X)$ to the corresponding Hammett values of the aryl pivalate resulted in a slope of 1.77. Together these results support a concerted oxidative addition as the turnover-limiting step for the Negishi cross-coupling of non-π-extended aryl pivalates. Perhaps more importantly, upon removing DMA from the reaction solvent minor amounts of cross-coupled product was observed, likely owing to the formation of Ni-Zn adducts and Ni oxidation. This hypothesis was further investigated by performing the stochiometric reaction between $[Ni(PCy_3)_2]_2N_2$ and *o*-tolyl pivalate in the presence of $ZnCl_2$ in a THF-d_8/DMF-d_7 solvent mixture. Consistent with amide solvents stabilizing Ni(0) and Zn(II) species, we observed $(PCy_3)_2NiCl$(*o*-tolyl) (**4a**) in 16% yield, along with unreacted Ni(0) and trace amounts of ligand-sequestering complexes **13** and **14**. These results provide

strong support for the use of a DMA/THF mixtures under the standard conditions and the importance of DMA for catalyst turnover. Speculating if the role of DMA is to act as a ligand to bind Ni(0) and Zn(II), we questioned if the use of toxic amide based solvents may not be necessary for catalyst turnover if they could be replaced by an appropriate sacrificial ligand. If successful, alternative, more industrially friendly solvent systems could be implemented. Among the various possibilities, we speculated that pyridine may act as a small, yet strongly coordinating ligand and may display similar reactivity to amide solvents in the reaction condition. Furthermore, this would provide further mechanistic evidence that the high dielectric constant of DMA does not play an important role in the reaction outcome (pyridine = 12.4 versus DMA = 37.8). As depicted in Figure 2.12, the addition of stochiometric quantities of pyridine to the standard catalytic conditions in only THF recovered catalyst activity and provide similar yields to the previous THF/DMA solvent mixture. To investigate if the reaction between Ni(0) and Zn(II) constituted a deactivation or decomposition event, we attempted to reactivate the activate catalytic species by performing the reaction first in THF and then added pyridine after 90 minutes. If the formation of Ni-Zn clusters is reversible and regenerate Ni(0), than the addition of pyridine would recapture the active Ni(0) complex and restore catalyst activity. However, monitoring the reaction, we did not observe any increase in yield suggesting that while an initial Ni-Zn adduct may be reversibly formed, the downstream formation of Ni-Zn clusters is irreversible. These studies were indirectly supported by stochiometric studies in which in-situ generated Ni-Zn clusters were treated with excess PCy_3 and COD to attempt to stabilize transient Ni(0) species, however, we were unable to observe any Ni(0) species by ^{31}P or ^{1}H NMR spectroscopy in the crude reaction mixture (Figure. S7).

We believe together that these results suggest that the impact of Zn(II) salts and coordinating additives or solvents may have been overlooked in nickel-catalyzed reactions. Reviewing the literature, this notion gains further support as the inhibitory effect of Zn(II) salts on the reductive aryl transfer reactions[58] and nickel-catalyzed halogenation of enol triflates[59] have been noted with the addition of DMAP improving the catalytic activity. Additional poisoning experiments found that $ZnCl_2$ was indeed deleterious to the Ni-catalyzed C–O silylation of aryl esters. These examples likely do not exist in isolation and we speculate that related scenarios likely exist in a wide variety of nickel-catalyzed reactions that Zn additives are used, such as reductive coupling protocols.[18-19,60] We believe these findings highlight that while electrophilic zinc salts

appear to undergo undesired reactions with low-valent nickel species such as ligand sequestering, redox processes, along with deactivation and decomposition pathways, we also provide solutions to circumvent these undesired reactions in order to improve catalytic turnover.

2.4 Conclusions

While nickel catalysts have had immense success in the construction of C-C and C-heteroatom bond forming reactions, the mechanism by which these reactions operate is often overlooked. This study provides insight into the on-cycle and off-cycle speciation in C(sp^2)-O cleavage reactions of aryl esters which were previously unknown. We demonstrate oxidative addition of non-π-extended aryl esters to Ni(0) complexes ligated by PCy_3 ligands forms κ^1-O or κ^2-O bound $(PCy_3)_nNi(aryl)(OPiv)$ complexes which undergo decomposition to Ni(I) species $(PCy_3)_2Ni(OPiv)$. We also provide evidence that zinc(II) species in the reaction can undergoing halide exchange with on-cycle Ni-pivalate complexes, undergoing ligand sequestering events, facilitate decomposition or deactivation pathways, or triggering productive transmetallation. This multifaceted effect of zinc salts shows a significant reliance on solvent choice in which Zn(II) salts react with Ni(0) complexes in weakly ligating solvents and the reaction between Zn(II) and Ni(0) are disrupted with more coordinating solvents. Given the general uptake zinc salts have found in reductive cross-electrophile coupling reactions, one may envision these processes follow similar reactivity to those described in this study. Taken together, we believe the results reported within this work will promote nickel-catalyzed cross-coupling reactions from a preparative and mechanistic standpoint.

Future studies may find the inhibitory effect of entities that act as “Lewis bases” are likely a general challenge in reactions that rely on low valent metals and studies to highlight these interactions will be invaluable to future reaction development. The merits of similar studies have been reported in the literature which have uncovered the inhibitory effect of π-acidic olefin ligands such as COD on many Ni-catalyzed reactions in which avoiding these ligands promotes faster reaction rates. Likewise, future studies could be expanded to investigate the reactivity of various Ni(0) species in the presence of Zn(II) salts. Alternatively, the reactivity observed with aryl esters could be compared and contrasted to other C-O electrophiles.

2.5 References

1. Li, B.-J.; Li, Y.-Z.; Lu, X.-Y.; Liu, J.; Guan, B.-T.; Shi, Z.-J. Cross-Coupling of Aryl/Alkenyl Pivalates with Organozinc Reagents through Nickel-Catalyzed C−O Bond Activation under Mild Reaction Conditions. *Angew. Chem. Int. Ed.* **2008,** *47* (52), 10124-10127.

2. Quasdorf, K. W.; Tian, X.; Garg, N. K. Cross-Coupling Reactions of Aryl Pivalates with Boronic Acids. *J. Am. Chem. Soc.* **2008,** *130* (44), 14422-14423.

3. Guan, B.-T.; Wang, Y.; Li, B.-J.; Yu, D.-G.; Shi, Z.-J. Biaryl Construction via Ni-Catalyzed C−O Activation of Phenolic Carboxylates. *J. Am. Chem. Soc.* **2008,** *130* (44), 14468-14470.

4. Guan, B.-T.; Xiang, S.-K.; Wu, T.; Sun, Z.-P.; Wang, B.-Q.; Zhao, K.-Q.; Shi, Z.-J. Methylation of arenesviaNi-catalyzed aryl C–O/F activation. *Chem. Commun.* **2008,** (12), 1437-1439.

5. Dankwardt, J. W. Nickel-Catalyzed Cross-Coupling of Aryl Grignard Reagents with Aromatic Alkyl Ethers: An Efficient Synthesis of Unsymmetrical Biaryls. *Angew. Chem. Int. Ed.* **2004,** *43* (18), 2428-2432.

6. Wang, C.; Ozaki, T.; Takita, R.; Uchiyama, M. Aryl Ether as a Negishi Coupling Partner: An Approach for Constructing C−C Bonds under Mild Conditions. *Chem. Eur. J.* **2012,** *18* (12), 3482-3485.

7. Wisniewska, H. M.; Swift, E. C.; Jarvo, E. R. Functional-Group-Tolerant, Nickel-Catalyzed Cross-Coupling Reaction for Enantioselective Construction of Tertiary Methyl-Bearing Stereocenters. *J. Am. Chem. Soc.* **2013,** *135* (24), 9083-9090.

8. Tollefson, E. J.; Dawson, D. D.; Osborne, C. A.; Jarvo, E. R. Stereospecific Cross-Coupling Reactions of Aryl-Substituted Tetrahydrofurans, Tetrahydropyrans, and Lactones. *J. Am. Chem. Soc.* **2014,** *136* (42), 14951-14958.

9. Eckert, P.; Sharif, S.; Organ, M. G. Salt to Taste: The Critical Roles Played by Inorganic Salts in Organozinc Formation and in the Negishi Reaction. *Angew. Chem. Int. Ed.* **2021,** *60* (22), 12224-12241.

10. Achonduh, G. T.; Hadei, N.; Valente, C.; Avola, S.; O'Brien, C. J.; Organ, M. G. On the role of additives in alkyl–alkyl Negishi cross-couplings. *Chem. Commun.* **2010,** *46* (23), 4109.

11. Eckert, P.; Organ, M. G. The Role of LiBr and $ZnBr_2$ on the Cross-Coupling of Aryl Bromides with Bu2Zn or BuZnBr. *Chem. Eur. J.* **2019,** *25* (69), 15751-15754.

12. Somerville, R. J.; Hale, L. V. A.; Gómez-Bengoa, E.; Burés, J.; Martin, R. Intermediacy of Ni–Ni Species in sp^2 C–O Bond Cleavage of Aryl Esters: Relevance in Catalytic C–Si Bond Formation. *J. Am. Chem. Soc.* **2018,** *140* (28), 8771-8780.

13. Li, Z.; Zhang, S.-L.; Fu, Y.; Guo, Q.-X.; Liu, L. Mechanism of Ni-Catalyzed Selective C−O Bond Activation in Cross-Coupling of Aryl Esters. *J. Am. Chem. Soc.* **2009,** *131* (25), 8815-8823.

14. Hong, X.; Liang, Y.; Houk, K. N. Mechanisms and Origins of Switchable Chemoselectivity of Ni-Catalyzed C(aryl)–O and C(acyl)–O Activation of Aryl Esters with Phosphine Ligands. *J. Am. Chem. Soc.* **2014,** *136* (5), 2017-2025.

15. Quasdorf, K. W.; Antoft-Finch, A.; Liu, P.; Silberstein, A. L.; Komaromi, A.; Blackburn, T.; Ramgren, S. D.; Houk, K. N.; Snieckus, V.; Garg, N. K. Suzuki−Miyaura Cross-Coupling of Aryl Carbamates and Sulfamates: Experimental and Computational Studies. *J. Am. Chem. Soc.* **2011,** *133* (16), 6352-6363.

16. Haas, D.; Hammann, J. M.; Greiner, R.; Knochel, P. Recent Developments in Negishi Cross-Coupling Reactions. *ACS Catal.* **2016,** *6* (3), 1540-1552.

17. Tortajada, A.; Juliá-Hernández, F.; Börjesson, M.; Moragas, T.; Martin, R. Transition-Metal-Catalyzed Carboxylation Reactions with Carbon Dioxide. *Angew. Chem. Int. Ed.* **2018,** *57* (49), 15948-15982.

18. Weix, D. J. Methods and Mechanisms for Cross-Electrophile Coupling of Csp^2 Halides with Alkyl Electrophiles. *Acc. Chem. Res.* **2015,** *48* (6), 1767-1775.

19. Everson, D. A.; Weix, D. J. Cross-Electrophile Coupling: Principles of Reactivity and Selectivity. *J. Org. Chem.* **2014,** *79* (11), 4793-4798.

20. Tasker, S. Z.; Standley, E. A.; Jamison, T. F. Recent advances in homogeneous nickel catalysis. *Nature* **2014,** *509* (7500), 299-309.

21. Hazari, N.; Melvin, P. R.; Beromi, M. M. Well-defined nickel and palladium precatalysts for cross-coupling. *Nature Reviews Chemistry* **2017,** *1* (3), 0025.

22. Diccianni, J.; Lin, Q.; Diao, T. Mechanisms of Nickel-Catalyzed Coupling Reactions and Applications in Alkene Functionalization. *Acc. Chem. Res.* **2020,** *53* (4), 906-919.

23. Desnoyer, A. N.; Friese, F. W.; Chiu, W.; Drover, M. W.; Patrick, B. O.; Love, J. A. Exploring Regioselective Bond Cleavage and Cross-Coupling Reactions using a Low-Valent Nickel Complex. *Chem. Eur. J.* **2016,** *22* (12), 4070-4077.

24. Muto, K.; Yamaguchi, J.; Lei, A.; Itami, K. Isolation, Structure, and Reactivity of an Arylnickel(II) Pivalate Complex in Catalytic C–H/C–O Biaryl Coupling. *J. Am.*

Chem. Soc. **2013,** *135* (44), 16384-16387.

25. Chatupheeraphat, A.; Liao, H.-H.; Srimontree, W.; Guo, L.; Minenkov, Y.; Poater, A.; Cavallo, L.; Rueping, M. Ligand-Controlled Chemoselective C(acyl)–O Bond vs C(aryl)–C Bond Activation of Aromatic Esters in Nickel Catalyzed C(sp^2)–C(sp^3) Cross-Couplings. *J. Am. Chem. Soc.* **2018,** *140* (10), 3724-3735.

26. Guo, L.; Rueping, M. Decarbonylative Cross-Couplings: Nickel Catalyzed Functional Group Interconversion Strategies for the Construction of Complex Organic Molecules. *Acc. Chem. Res.* **2018,** *51* (5), 1185-1195.

27. Brauer, D. J.; Krueger, C. Bonding of aromatic hydrocarbons to nickel(0). Structure of bis(tricyclohexylphosphine)(1,2-η^2-anthracene)nickel(0)-toluene. *Inorg. Chem.* **1977,** *16* (4), 884-891.

28. Isaeva, L. S.; Drogunova, G. I.; Peregudov, A. S.; Kravtsov, D. N. Arylbis(triphenylphosphinyl)nickel carboxylates. *Bull. Acad. Sci. USSR, Div. Chem. Sci.* **1988,** *37* (1), 153-157.

29. Christian, A. H.; Müller, P.; Monfette, S. Nickel Hydroxo Complexes as Intermediates in Nickel-Catalyzed Suzuki–Miyaura Cross-Coupling. *Organometallics* **2014,** *33* (9), 2134-2137.

30. Chatt, J.; Shaw, B. L. 345. Alkyls and aryls of transition metals. Part III. Nickel(II) derivatives. *J. Chem. Soc.* **1960**, 1718.

31. Standley, E. A.; Smith, S. J.; Müller, P.; Jamison, T. F. A Broadly Applicable Strategy for Entry into Homogeneous Nickel(0) Catalysts from Air-Stable Nickel(II) Complexes. *Organometallics* **2014,** *33* (8), 2012-2018.

32. Desnoyer, A. N.; Love, J. A. Recent advances in well-defined, late transition metal complexes that make and/or break C–N, C–O and C–S bonds. *Chem. Soc. Rev.* **2017,** *46* (1), 197-238.

33. Su, B.; Cao, Z.-C.; Shi, Z.-J. Exploration of Earth-Abundant Transition Metals (Fe, Co, and Ni) as Catalysts in Unreactive Chemical Bond Activations. *Acc. Chem. Res.* **2015,** *48* (3), 886-896.

34. Tobisu, M.; Chatani, N. Cross-Couplings Using Aryl Ethers via C–O Bond Activation Enabled by Nickel Catalysts. *Acc. Chem. Res.* **2015,** *48* (6), 1717-1726.

35. Zarate, C.; van Gemmeren, M.; Somerville, R. J.; Martin, R., Chapter Four - Phenol Derivatives: Modern Electrophiles in Cross-Coupling Reactions. In *Adv. Organomet. Chem.*, Pérez, P. J., Ed. Academic Press: 2016; Vol. 66, pp 143-222.

36. Campeau, L.-C.; Hazari, N. Cross-Coupling and Related Reactions: Connecting

Past Success to the Development of New Reactions for the Future. *Organometallics* **2019,** *38* (1), 3-35.

37. Diccianni, J. B.; Hu, C. T.; Diao, T. Insertion of CO_2 Mediated by a (Xantphos)Ni^{I}–Alkyl Species. *Angew. Chem. Int. Ed.* **2019,** *58* (39), 13865-13868.

38. Witzke, R. J.; Tilley, T. D. A two-coordinate Ni(i) silyl complex: CO_2 insertion and oxidatively-induced silyl migrations. *Chem. Commun.* **2019,** *55* (46), 6559-6562.

39. Diccianni, J. B.; Diao, T. Mechanisms of Nickel-Catalyzed Cross-Coupling Reactions. *Trends in Chemistry* **2019,** *1* (9), 830-844.

40. Bontempelli, G.; Corain, B.; De Nardo, L. Electrochemical reduction of dicyanobis(tertiary phosphine)nickel(II) complexes. *J. Chem. Soc., Dalton Trans.* **1977,** (19), 1887-1891.

41. Crabtree, R. H., *The Organometallic Chemistry of the Transition Metals*. John Wiley & Sons: 2014; Vol. 6.

42. Messinis, A. M.; Luckham, S. L. J.; Wells, P. P.; Gianolio, D.; Gibson, E. K.; O'Brien, H. M.; Sparkes, H. A.; Davis, S. A.; Callison, J.; Elorriaga, D.; Hernandez-Fajardo, O.; Bedford, R. B. The highly surprising behaviour of diphosphine ligands in iron-catalysed Negishi cross-coupling. *Nat. Catal.* **2019,** *2* (2), 123-133.

43. Oeschger, R. J.; Chen, P. A Heterobimetallic Pd–Zn Complex: Study of a d^8–d^{10} Bond in Solid State, in Solution, and in Silico. *Organometallics* **2017,** *36* (8), 1465-1468.

44. Chass, G. A.; O'Brien, C. J.; Hadei, N.; Kantchev, E. A. B.; Mu, W.-H.; Fang, D.-C.; Hopkinson, A. C.; Csizmadia, I. G.; Organ, M. G. Density Functional Theory Investigation of the Alkyl–Alkyl Negishi Cross-Coupling Reaction Catalyzed by N-Heterocyclic Carbene (NHC)–Pd Complexes. *Chem. Eur. J.* **2009,** *15* (17), 4281-4288.

45. Abdiaj, I.; Huck, L.; Mateo, J. M.; de la Hoz, A.; Gomez, M. V.; Díaz-Ortiz, A.; Alcázar, J. Photoinduced Palladium-Catalyzed Negishi Cross-Couplings Enabled by the Visible-Light Absorption of Palladium–Zinc Complexes. *Angew. Chem. Int. Ed.* **2018,** *57* (40), 13231-13236.

46. García-Melchor, M.; Fuentes, B.; Lledós, A.; Casares, J. A.; Ujaque, G.; Espinet, P. Cationic Intermediates in the Pd-Catalyzed Negishi Coupling. Kinetic and Density Functional Theory Study of Alternative Transmetalation Pathways in the Me–Me Coupling of $ZnMe_2$ and trans-[$PdMeCl(PMePh_2)_2$]. *J. Am. Chem. Soc.* **2011,** *133* (34), 13519-13526.

47. Álvarez, R.; de Lera, A. R.; Aurrecoechea, J. M.; Durana, A. Bimetallic

Intermediates in the Formation of Nucleophilic Allenylzincs from Allenylpalladiums: A DFT Study. *Organometallics* **2007,** *26* (11), 2799-2802.

48. Böck, K.; Feil, J. E.; Karaghiosoff, K.; Koszinowski, K. Catalyst Activation, Deactivation, and Degradation in Palladium-Mediated Negishi Cross-Coupling Reactions. *Chem. Eur. J.* **2015,** *21* (14), 5548-5560.

49. Johansson Seechurn, C. C. C.; Kitching, M. O.; Colacot, T. J.; Snieckus, V. Palladium-Catalyzed Cross-Coupling: A Historical Contextual Perspective to the 2010 Nobel Prize. *Angew. Chem. Int. Ed.* **2012,** *51* (21), 5062-5085.

50. Negishi, E.-i. Magical Power of Transition Metals: Past, Present, and Future (Nobel Lecture). *Angew. Chem. Int. Ed.* **2011,** *50* (30), 6738-6764.

51. Craciun, R.; Vincent, A. J.; Shaughnessy, K. H.; Dixon, D. A. Prediction of Reliable Metal−PH3 Bond Energies for Ni, Pd, and Pt in the 0 and +2 Oxidation States. *Inorg. Chem.* **2010,** *49* (12), 5546-5553.

52. Lin, Q.; Diao, T. Mechanism of Ni-Catalyzed Reductive 1,2-Dicarbofunctionalization of Alkenes. *J. Am. Chem. Soc.* **2019,** *141* (44), 17937-17948.

53. Mohadjer Beromi, M.; Brudvig, G. W.; Hazari, N.; Lant, H. M. C.; Mercado, B. Q. Synthesis and Reactivity of Paramagnetic Nickel Polypyridyl Complexes Relevant to C(sp^2)–C(sp^3)Coupling Reactions. *Angew. Chem. Int. Ed.* **2019,** *58* (18), 6094-6098.

54. Mohadjer Beromi, M.; Nova, A.; Balcells, D.; Brasacchio, A. M.; Brudvig, G. W.; Guard, L. M.; Hazari, N.; Vinyard, D. J. Mechanistic Study of an Improved Ni Precatalyst for Suzuki–Miyaura Reactions of Aryl Sulfamates: Understanding the Role of Ni(I) Species. *J. Am. Chem. Soc.* **2017,** *139* (2), 922-936.

55. Zhang, S.-Q.; Taylor, B. L. H.; Ji, C.-L.; Gao, Y.; Harris, M. R.; Hanna, L. E.; Jarvo, E. R.; Houk, K. N.; Hong, X. Mechanism and Origins of Ligand-Controlled Stereoselectivity of Ni-Catalyzed Suzuki–Miyaura Coupling with Benzylic Esters: A Computational Study. *J. Am. Chem. Soc.* **2017,** *139* (37), 12994-13005.

56. Correa, A.; Martin, R. Ni-Catalyzed Direct Reductive Amidation via C–O Bond Cleavage. *J. Am. Chem. Soc.* **2014,** *136* (20), 7253-7256.

57. Correa, A.; León, T.; Martin, R. Ni-Catalyzed Carboxylation of C(sp^2)– and C(sp^3)–O Bonds with CO_2. *J. Am. Chem. Soc.* **2014,** *136* (3), 1062-1069.

58. Isshiki, R.; Inayama, N.; Muto, K.; Yamaguchi, J. Ester Transfer Reaction of Aromatic Esters with Haloarenes and Arenols by a Nickel Catalyst. *ACS Catal.* **2020,** *10* (5), 3490-3494.

59. Hofstra, J. L.; Poremba, K. E.; Shimozono, A. M.; Reisman, S. E. Nickel-Catalyzed

Conversion of Enol Triflates into Alkenyl Halides. *Angew. Chem. Int. Ed.* **2019,** *58* (42), 14901-14905.

60. Gu, J.; Wang, X.; Xue, W.; Gong, H. Nickel-catalyzed reductive coupling of alkyl halides with other electrophiles: concept and mechanistic considerations. *Organic Chemistry Frontiers* **2015,** *2* (10), 1411-1421.

61. Zarate, C.; Martin, R. A Mild Ni/Cu-Catalyzed Silylation via C–O Cleavage. *J. Am. Chem. Soc.* **2014,** *136* (6), 2236-2239.

62. Liu, C.; Ni, Q.; Bao, F.; Qiu, J. A simple and efficient protocol for a palladium-catalyzed ligand-free Suzuki reaction at room temperature in aqueous DMF. *Green Chemistry* **2011,** *13* (5), 1260-1266.

63. Semba, K.; Ohtagaki, Y.; Nakao, Y. Arylboration of 1-Arylalkenes by Cooperative Nickel/Copper Catalysis. *Org. Lett.* **2016,** *18* (16), 3956-3959.

64. Ceder, R.; Muller, G.; Sales, J.; Vidal, J.; Neibecker, D.; Tkatchenko, I. Catalytic dimerization of ethylene to 1-butene by square-planar nickel complexes. *J. Mol. Catal.* **1991,** *68* (1), 23-31.

65. Goel, R. G.; Henry, W. P.; Jha, N. K. Reinvestigation of tricyclohexylphosphine complexes of zinc(II) and cadmium(II) halides. Preparation, characterization, and phosphorus-31 nuclear magnetic resonance and vibrational spectroscopic studies. *Inorg. Chem.* **1982,** *21* (7), 2551-2555.

66. Moers, F. G.; Langhout, J. P. A spectroscopic study of zinc(II), cadmium(II) and mercury(II) complexes with tricyclohexylphosphine as ligand. *Recl. Trav. Chim. Pays-Bas* **1973,** *92* (9), 996-1002.

67. Krasovskiy, A.; Knochel, P. Convenient Titration Method for Organometallic Zinc, Magnesium, and Lanthanide- Reagents. *Synthesis* **2006,** *2006* (5), 0890-0891.

68. Burchat, A. F.; Chong, J. M.; Nielsen, N. Titration of alkyllithiums with a simple reagent to a blue endpoint. *J. Organomet. Chem.* **1997,** *542* (2), 281-283.

2.6 Experimental Section

2.6.1 General Considerations

Solvents. Reactions were carried out under N_2 in a glovebox or on a Schlenk line, in solvents (THF, Et_2O, toluene) that had been dried and degassed using an Innovative Technologies solvent purification system, then stored under N_2 over 4 Å molecular sieves for at least 16 h prior to use. Pentane was degassed by bubbling with N_2 and stored under N_2 over 4 Å molecular sieves for at least 16 h prior to use. C_6D_6, C_7D_8, DMF-d_7, THF-d_8, (Eurisotop) were freeze/pump/thaw degassed (4x) and likewise stored under N_2 over 4 Å molecular sieves for at least 16 h prior to use.

Reagents. [$Ni(COD)_2$] and PCy_3 were purchased from Strem Chemicals. Trimethoxylbenzene (TMB) was purchased from TCI Chemicals. Potassium pivalate (KOPiv), and cobaltocene were purchased from Alfa Aesar. Triphenylphosphine oxide, zinc dichloride ($ZnCl_2$), pyridine, Ph_2Zn and $(PCy_3)_2NiCl_2$ were purchased from Aldrich. Salts $ZnCl_2$, and KOPiv were dried at 150 ºC under high vacuum overnight. All other reagents were purchased from commercial sources and used without further purification. Pivalates *o*-tolyl pivalate,[2] *p*-trifluoromethylphenyl pivalate,[61] *p*-methoxyphenyl pivalate,[2] *p*-tertbutylphenyl pivalate,[61] phenyl pivalate,[3] *p*-methylesterphenyl pivalate,[1] *p*-fluorophenyl pivalate,[3] *p*-benzophenonephenyl pivalate,[1] were synthesized according to literature procedures.[61] Other reagents or products biphenyl,[62] phenyl *o*-toluene,[62] PhZnCl·LiCl[1] were synthesized according to literature procedures. Complexes $(PCy_3)_2NiCl$(*o*-tolyl),[63] $(PCy_3)_2NiCl$(*p*-tolyl),[63] $(PCy_3)_2NiCl$(*p*-trifluoromethylphenyl),[29] were synthesized following modified literature procedures using 5 equivalents of aryl chloride. Complexes $(PCy_3)_2NiBr$(Mesityl),[64] $(PCy_3)_2NiCl$,[54] $[(PCy_3)ZnCl_2]_2$[65] and $(PCy_3)_2ZnCl_2$[66] were synthesized according to literature procedures. Titration of Grignards,[67] organozinc[67] or organolithium[68] reagents used were performed according to literature procedures.

Analytical methods. Flash chromatography was performed with Sigma Aldrich technical grade silica gel 60 (230-400 mesh). Thin layer chromatography was carried out using Merck TLC Silica gel 60 F254. NMR spectra were recorded on Bruker Avance Ultrashield 300, 400, or 500 MHz spectrometers, with chemical shifts reported

in parts per million (ppm) and coupling constants, *J*, reported in hertz. Quantitative NMR experiments were performed with d1 set to 10s (^{1}H), 1.0s (^{1}H para), 30s (^{31}P) respectively. Gas chromatographic analyses were performed on an Agilent 6890N gas chromatograph with an FID detector. IR spectra were obtained with a Bruker FT-IR Alpha spectrometer. MALDI-TOF mass spectra were collected on a Bruker Autoflex MALDI-TOF mass spectrometer. Samples were prepared by the dried-droplet protocol, from solutions containing the charge-transfer matrix pyrene or DCTB in THF.

2.6.2 Synthesis and Characterization of Organometallic Complexes

Synthesis of $(PCy_3)_2Ni(o\text{-Tol})(OPiv)$ 5a

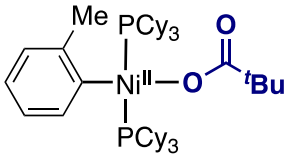

In the glovebox, $(PCy_3)_2Ni(o\text{-Tol})Cl$ (235 mg, 0.32 mmol) was added to a 10 mL vial with KOPiv (51 mg, 1.3 equiv.). A stir bar was added, then the vial was charged with 8 mL of THF turning the orange powder to a red/orange solution. After 16 hours the solvent was removed and dissolved in minimal toluene to give a gold/red solution. This solution was filtered through a pipette plug of celite with green solid being filtered off and an orange/red solution collected. The solvent was again removed to give an orange/red powder and washed with cold (-36 ºC) pentane (1 mL x 3) to give $(PCy_3)_2Ni(o\text{-Tol})OPiv$ **5a** (154 mg, 62% yield) as a yellow powder.

^{1}H NMR (400 MHz, C_7D_8): δ 7.48 (m, 1H, Ar sp^2-C*H*), 6.79 (m, 3H, Ar sp^2-C*H*), 3.52 (s, 3H, Tol *o*-C*H3*), 2.4-0.8 (m, 78H, PCy_3 C*H*). **^{31}P{^{1}H} NMR** (162 MHz, C_6D_6): δ 37.76 (s), 13.10 (s). **^{13}C{^{1}H}** (126 MHz, C_7D_8) δ 144.6, 126.9(2xC_{Ar}), 123.3(2xC_{Ar}), 39.5, 34.5, 33.2, 32.4, 31.7, 30.5, 29.3, 28.1, 27.0, 22.8, 14.3.
EA Calcd. C, 71.02; H, 10.18; N, 0; Found: C, 72.22; H, 9.71; N, 0.12
IR 1595 cm^{-1} (strong), 1565 cm^{-1} (weak)

$(PCy_3)_2Ni(p\text{-Tol})(OPiv)$ 5b

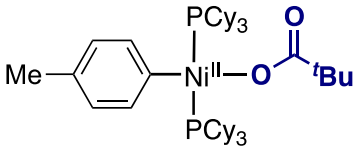

In the glovebox, $(PCy_3)_2Ni(p\text{-Tol})Cl$ (103 mg, 0.14 mmol) was added to a 10 mL vial with KOPiv (25 mg, 1.5 equiv.) and PCy_3 (27 mg, 0.7 equiv.). A stirbar was added, then the vial was charged with 3 mL of THF turning the orange powder to a red/orange solution. After 7 h, the solvent was removed and dissolved in minimal toluene to give a gold/red solution. This solution was filtered through a pipette plug of celite with green solid being filtered off and an orange/red solution collected. The solvent was removed to give an orange/red powder and washed with cold (-36 ºC) pentane (1 mL x 2) to give $(PCy_3)_2Ni(pTol)OPiv$ **5b** (24 mg, 21% yield) as a yellow powder.

^1H NMR (400 MHz, C_6D_6): δ 7.72 (d, $^3J_{HH}$ = 7.7 Hz, 2H, Ar sp^2-C*H*), 6.85 (d, $^3J_{HH}$ = 6.8 Hz, 2H, Ar sp^2-C*H*), 2.19 (s, 3H, Tol *p*-C*H3*), 2.1 – 1.0 (m, 83H, PCy_3 C*H*). **$^{31}P\{^1H\}$ NMR** (162 MHz, C_6D_6): δ 37.58 (br s), 13.02 (br s). **$^{13}C\{^1H\}$** (126 MHz, C_7D_8): δ 138.0, 128.4(2xC_{Ar}), 128.35(2xC_{Ar}), 39.5, 32.8, 30.6, 28.0, 27.5, 26.9, 20.8.
EA Calcd. C, 71.02; H, 10.18; N, 0; Found: C, 69.97; H, 9.58; N, 0.12
Note: Samples were unstable at room temperature preventing long carbon measurements

$(PCy_3)_2Ni(p CF_3\text{-Ph})(OPiv)$ 5c

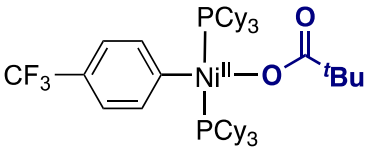

In the glovebox, $(PCy_3)_2Ni(pCF_3\text{-Ph})Cl$ (108 mg, 0.14 mmol) was added to a 10 mL vial with KOPiv (26 mg, 1.5 equiv.) and PCy_3 (29 mg, 0.8 equiv.). A stirbar was added, then the vial was charged with 3 mL of THF turning the orange powder to a red/orange solution. After 3 hours, the solvent was removed and dissolved in minimal toluene to give a gold/red solution. This solution was filtered through a pipette plug of celite with green solid being filtered off and an orange/red solution collected. The solvent was again removed to give an orange/red powder and washed with cold (-36 ºC) pentane (0.7 mL x 3) to give $(PCy_3)_2Ni(pCF_3\text{-Ph})(OPiv)$ **5c** (39 mg, 33% yield) as a yellow

powder.

^{1}H NMR (400 MHz, C_7D_8) δ 7.87 (s, 2H, Ar sp^2-C*H*), 2.04 – 0.98 (m, 88H, PCy_3 C*H*). **^{31}P NMR** (162 MHz, C_7D_8) δ 32.40 (br s), 11.92 (br s). **^{19}F NMR** (376 MHz, C_7D_8) δ -61.60 (s). **^{13}C NMR** (101 MHz, C_7D_8) δ 138.3, 121.0, 32.9, 30.5, 28.0, 26.9, 22.8, 20.4, 14.2.

Note a: -Ar ^{13}C signals overlap with C_7D_8 precluding assignment of -CF_3 carbon

Note b: Samples were unstable at room temperature in solution preventing long carbon measurements

$(PCy_3)_2$Ni(*p*-Tol)(OPiv) 8

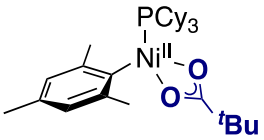

In the glovebox, $(PCy_3)_2$Ni(Mesityl)Br (146 mg, 0.18 mmol) was added to a 10 mL vial with KOPiv (69 mg, 3.1 equiv.). A stirbar was added, then the vial was charged with 7.5 mL of toluene forming a red solution. After 4 hours, the solution was filtered through a pipette plug of celite and the solvent was removed to provide a red solid. This solid was then washed onto a frit with cold pentane (-36 ºC) and washed (0.3 ml x 2, -36 ºC) to give (PCy_3)Ni(Mesityl)OPiv **8** (50 mg, 50% yield) as a red powder.

^{1}H NMR (500 MHz, C_6D_6): δ 6.57 (s, 2H, Ar sp^2-C*H*), 3.53 (s, 6H, Mes *o*-CH_3), 2.26 (s, 3H, Mes *p*-CH_3), 2.12 (d, $^{3}J_{HH}$ = 12.6 Hz, 6H, PCy_3 CH_2) 1.9 – 1.3 (m, 18H, PCy_3 CH_2) 1.20 (s, 9H, OPiv CH_3), 1.16 – 0.95 (m, 9H, PCy_3 CH_2) . **^{31}P{^{1}H} NMR** (202 MHz, C_6D_6): δ 34.59 (s). **^{13}C{^{1}H}** (126 MHz, C_6D_6) δ 143.5, 132.7 (2xC_{Ar}), 125.8 (2xC_{Ar}), 33.5, 33.4, 29.8, 27.9, 27.9, 27.0, 26.6, 26.2, 22.7, 20.6, 14.3.

EA Calcd. C, 68.70; H, 8.55; N, 0; Found: C, 68.30; H, 9.13; N, 0.12

IR 1615 cm^{-1} (medium)

[$(PCy_3)_2Ni^I_2(\mu\text{-}Cl)(\mu\text{-}OPiv)$] 10

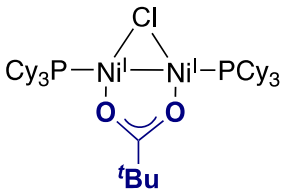

In the glovebox, $(PCy_3)_2Ni(Cl)$ (129 mg, 0.20 mmol) was added to a 10 mL vial with KOPiv (133 mg, 5 equiv.). A stirbar was added, and then the vial was charged with 3 mL of toluene forming a yellow solution. After 1 hours, the green solution with a blue suspension was filtered through a pipette plug of celite and the solvent was removed to provide a green solid. This solid was then washed with cold pentane (0.5 ml x 2, -36 ^oC) to give [$(PCy_3)_2Ni^I_2(\mu\text{-}Cl)(\mu\text{-}OPiv)$] **10** (46 mg, 58% yield) as a green powder.

^{1}H NMR (500 MHz, C_7D_8): δ 50.03 (br s, 4H), 6.0 - 0 (m, 87H),
Due to the paramagnetic nature of **10**, and accompanied line broadening, **^{31}P** and **^{13}C NMR** are not reported
EA Calcd. C, 60.44; H, 9.28; N, 0; Found: C, 62.32; H, 10.11; N, 0.21
IR 1615 cm^{-1} (weak)

$(PCy_3)_2Ni^I(OPiv)$ 11

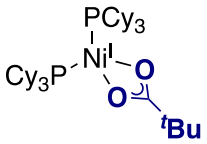

In the glovebox, $(PCy_3)_2Ni(Cl)$ (110 mg, 0.17 mmol) was added to a 10 mL vial with KOPiv (105 mg, 5 equiv.). A stirbar was added, then the vial was charged with 4 mL of toluene forming a yellow solution. After 3 hours, the green solution with a blue suspension was filtered through a pipette plug of celite and the solvent was removed to provide a green solid. This solid was then washed with cold pentane (0.5 ml x 2, -36 ^oC) to give $(PCy_3)_2Ni^I(OPiv)$ **11** (41 mg, 37 % yield) as a green powder.

^{1}H NMR (500 MHz, C_6D_6): δ 27.16 (br s, 4H), 6.3 - 0 (m, 84H)

Due to the paramagnetic nature of **10**, and accompanied line broadening, **^{31}P** and **^{13}C NMR** are not reported

EA Calcd. C, 68.33; H, 10.49; N, 0; Found: C, 62.09; H, 9.46; N, 0.13

IR 1615 cm^{-1} (weak), 1526 cm^{-1} (strong)

[(PCy$_3$)Zn(Cl)(Ph)]$_2$ 17

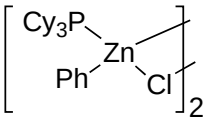

In the glovebox, $ZnCl_2$ (35 mg, 0.26 mmol) and Ph_2Zn (56 mg, 1 equiv.) was added to a 10 mL. A stirbar was added, then the vial was charged with 2 mL of THF forming a clear solution. PCy_3 (143 mg, 2 equiv.) was dissolved in 1 mL of THF and added dropwise where a white precipitate began to form. After 30 minutes, the solvent was removed and filtered to give a white solid. The solid was then washed with cold Et_2O (0.3 mL x 2, -36 ºC) and pentane (0.5 mL x 3, -36 ºC) to give [(PCy$_3$)ZnCl$_2$]$_2$ **17** (76 mg, 32 %) as a white powder.

^{1}H NMR (400 MHz, THF-d_8) δ 7.60 – 7.48 (m, 2H), 7.15 – 6.94 (m, 3H), 1.91 (d, J = 8.0 Hz, 9H), 1.68 – 1.56 (m, 2H), 1.54 – 1.07 (m, 16H). **^{31}P{^{1}H} NMR** (162 MHz, THF-d_8): δ 8.54 (s). **^{13}C NMR** (101 MHz, THF-d_8) δ 139.4, 127.4, 126.2, 32.4, 31.3, 31.2, 28.5, 28.4, 27.3.

NMR data of [(PCy$_3$)ZnCl$_2$]$_2$ 13 & (PCy$_3$)$_2$ZnCl$_2$ 14 are given below for convenience.

[(PCy$_3$)ZnCl$_2$]$_2$ 13. ^{1}H NMR (400 MHz, THF-d_8) δ 2.28 – 1.94 (m, 20H), 1.81 (dt, J = 6.2, 3.1 Hz, 11H), 1.66 – 1.47 (m, 12H), 1.32 (dd, J = 12.2, 9.4 Hz, 21H**). ^{31}P NMR** (162 MHz, THF-d_8) δ 64.05, 5.84. **^{13}C NMR** (101 MHz, THF-d_8) δ 31.9, 31.8, 30.5, 28.4, 28.3, 15.8.

(PCy$_3$)$_2$ZnCl$_2$ 14. ^{1}H NMR (400 MHz, THF-d_8) δ 1.95 (s, 19H), 1.70 (dd, J = 13.6, 6.0 Hz, 9H), 1.37 (dd, J = 72.0, 11.0 Hz, 37H). **^{31}P NMR** (162 MHz, THF-d_8) δ 65.86, 8.80. **^{13}C NMR** (101 MHz, THF-d_8) δ 32.3, 31.2, 28.5, 28.4, 27.3.

Tabulated IR Stretches of carboxylate stretches (C=O)

5a 1595 cm^{-1} (strong), 1565 cm^{-1} (weak)

8 1616 cm^{-1} (medium)

10 1615 cm^{-1} (weak)

11 1615 cm^{-1} (weak)

See Figure S27. for stacked IR spectra

2.6.3 Stochiometric Reactions with Well-Defined Organometallic Species.

Monitoring Oxidative Addition of $[Ni(PCy_3)_2]N_2$ to *o*-Tolyl Pivalate by ^1H NMR

In the glovebox, a solution of *o*-tolyl pivalate (5.4 mg, 0.03 mmol) and trimethoxybenzene (TMB) was dissolved in 1 mL C_6D_6 in a 3 mL vial. The solution was then added to a J. Young NMR tube, and the initial integration ratio of *o*-tolyl pivalate and TMB was measured. The solution was brought back into the glovebox and added to a stirred solution of $[(PCy_3)_2Ni]_2N_2$ (18 mg, 0.02 mmol) in 0.5 mL C_6D_6 and monitored by quantitative ^1H NMR.

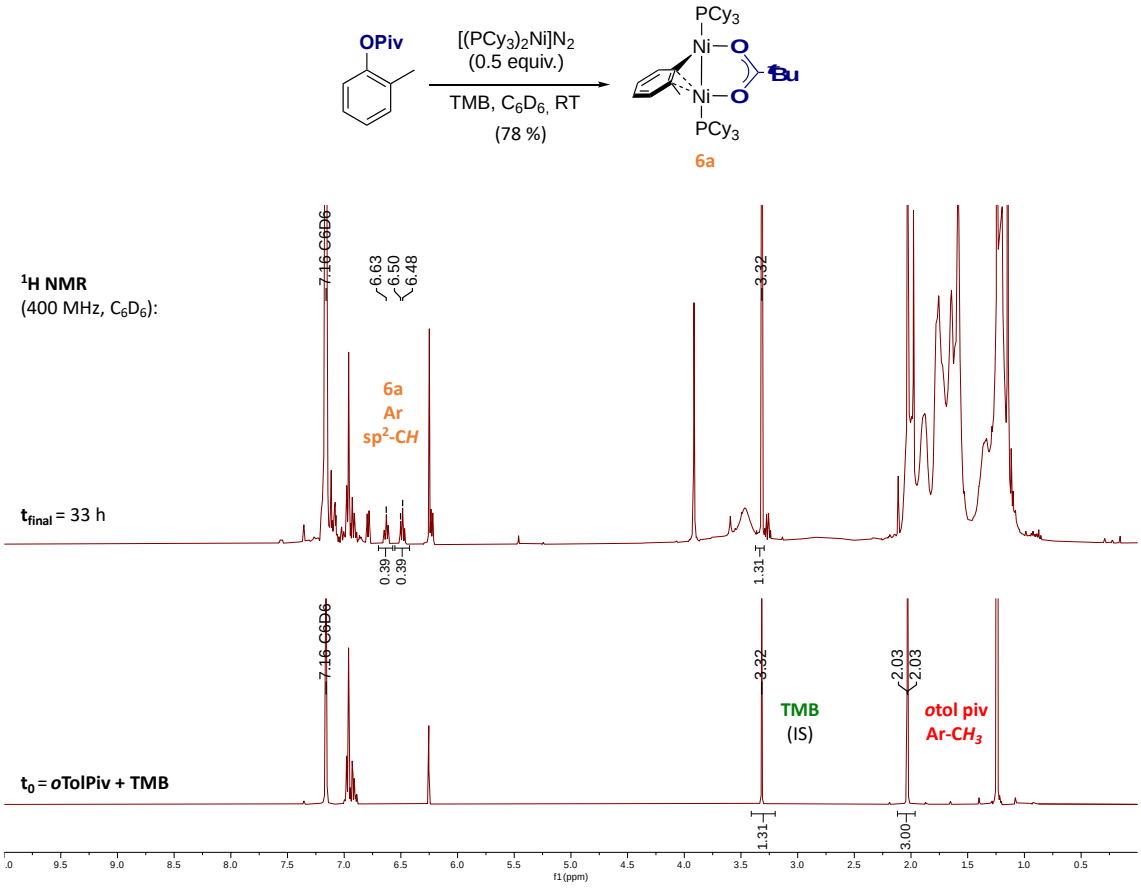

Figure S1. ^1H spectra (C_6D_6, 400 MHz) of the oxidative addition of Ni(0) to *o*-tolyl pivalates generating **6a**

Monitoring Oxidative Addition of $[Ni(PCy_3)_2]N_2$ to *o*-Tolyl Pivalate by ^{31}P NMR

In the glovebox, a solution of *o*-tolyl pivalate (8.3 mg, 0.04 mmol) in 0.5 mL C_6D_6 was added dropwise to a stirred solution of $[(PCy_3)_2Ni]_2N_2$ (27 mg, 0.02 mmol) in 0.5 mL C_6D_6. The reaction was then transferred to a J. Young NMR tube and monitored by ^1H and ^{31}P NMR spectroscopy.

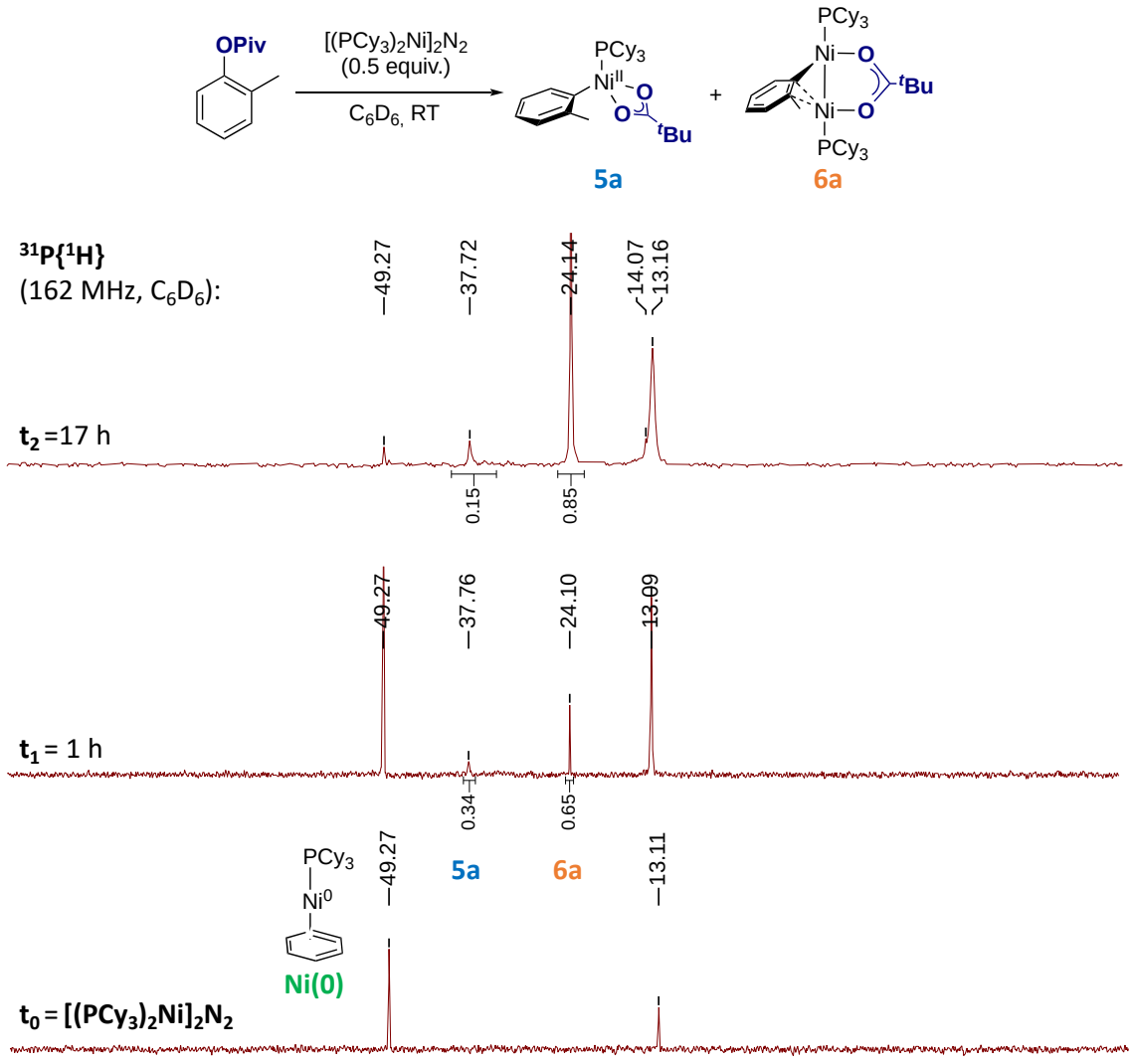

Figure S2. ^{31}P spectra (C_6D_6, 400 MHz) of the oxidative addition of Ni(0) to *o*-tolyl pivalate generating **5a** (blue) and **6a** (orange). PCy_3: δ = 13.1 ppm

Monitoring Comproportionation Between Ni(II) (Mesityl)(Pivalate) and $[Ni(PCy_3)_2]_2N_2$ by ^1H NMR with Internal Standard TMB

In the glovebox, $(PCy_3)Ni(OPiv)(Mesityl)$ **8** (10.2 mg, 0.018 mmol) and trimethoxybenzene (TMB) (1.2 mg) were dissolved in 1 mL C_6D_6 in a 3 mL vial. This solution was then added to a J. Young NMR tube, and the initial integration ratio of **8** and TMB was measured. This solution was then added to $[(PCy_3)_2Ni]_2N_2$ (11.5 mg, 0.09 mmol) and monitored by ^1H NMR spectroscopy.

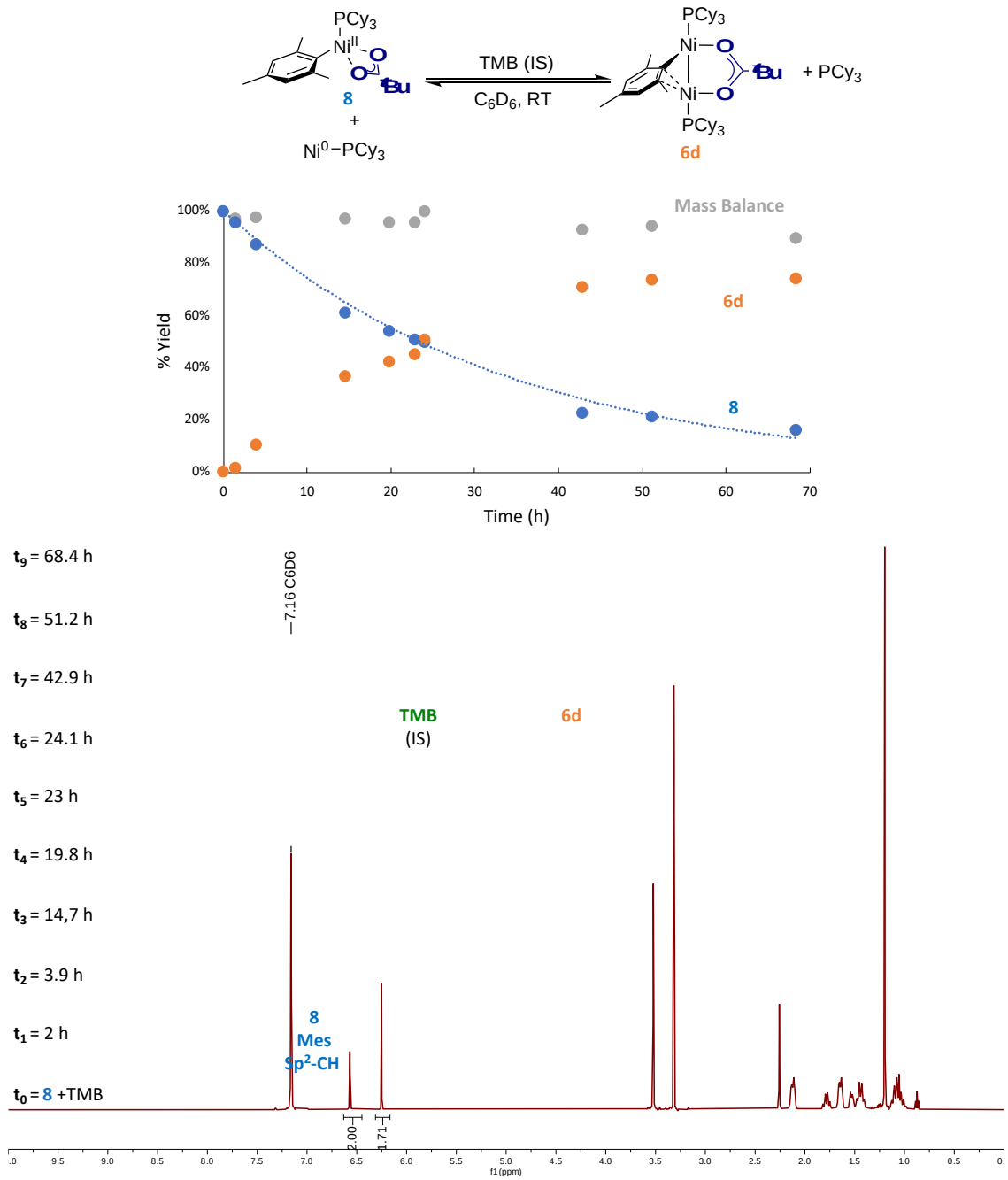

Figure S3. ^1H spectra (C_6D_6, 400 MHz) and corresponding graph of the comproportionation reaction between **8** (blue) and **Ni(0)** to **6d** (orange) (internal standard = TMB (green)).

Lack of Oxidative Addition of $[Ni(PCy_3)_2]N_2$ to *o*-Tolyl Pivalate with $ZnCl_2$

In the glovebox, *o*-tolyl pivalate (7.7 mg, 0.04 mmol), trimethoxybenzene (TMB) (2.7 mg) and $ZnCl_2$ (4.7 mg, 0.034 mmol) were dissolved in 1 mL THF-d_8 in a 3 mL vial. The solution was then added to a J. Young NMR tube, and the initial integration ratio of *o*-tolyl pivalate and TMB was measured. This solution was then added dropwise to a stirred solution of $[(PCy_3)_2Ni]_2N_2$ (13.0 mg, 0.01 mmol) in 0.5 mL THF-d_8. The solution was then added back to the J. Young NMR tube and monitored by ^{1}H NMR analysis.

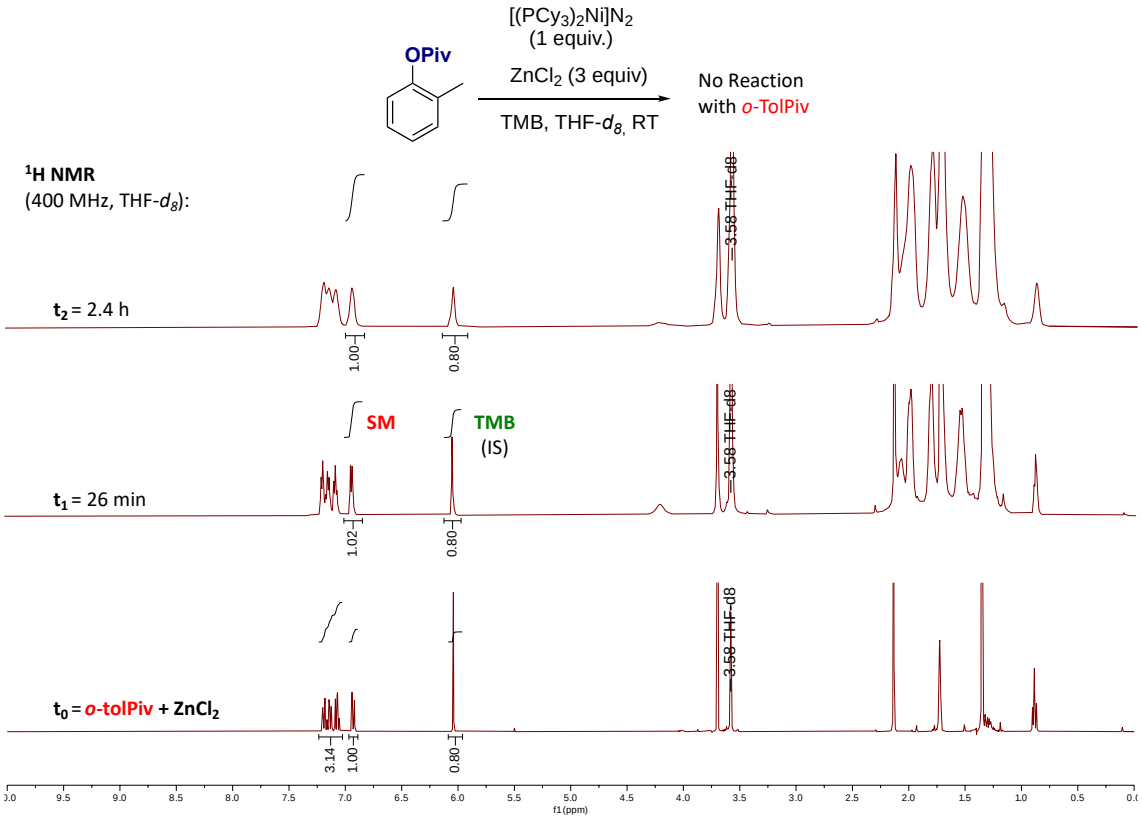

Figure S4. ^{1}H spectra (THF-d_8, 400 MHz) of $ZnCl_2$ preventing oxidative addition between *o*-tolyl pivalate (red) and Ni(0) (internal standard = TMB (green)).

Lack of Oxidative Addition of $(PCy_3)_2NiCl$ to *o*-Tolyl Pivalate

In the glovebox, $(PCy_3)_2NiCl$ (14.4 mg, 0.02 mmol), trimethoxybenzene (TMB) (1.6 mg) and were dissolved in 1 mL C_6D_6 in a 3 mL vial. The solution was then added to a J. Young NMR tube, and the initial integration ratio of $(PCy_3)_2NiCl$ and TMB was measured. This solution was then added dropwise to a stirred solution of *o*-tolyl pivalate (6.4 mg, 0.03 mmol) in 0.5 mL C_6D_6. The solution was then added back to the J. Young NMR tube and monitored by ^1H NMR analysis. After 24 h, the solution was heated at 50 °C for 20 h where no conversion of *o*-tolyl pivalate was observed.

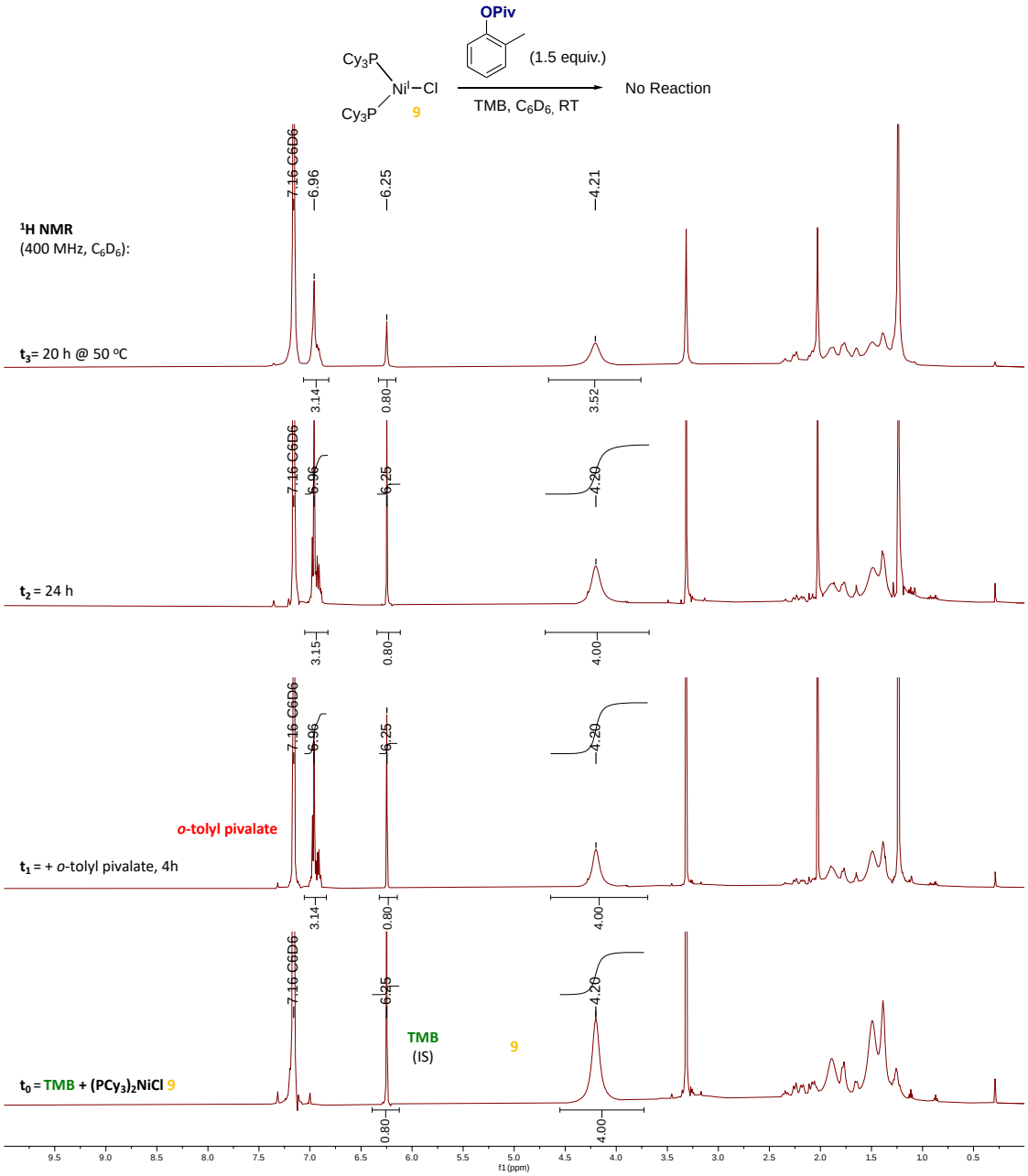

Figure S5. ^1H spectra (C_6D_6, 400 MHz) of $(PCy_3)_2NiCl$ (yellow) unable to undergo oxidative addition with *o*-tolyl pivalate (red) (internal standard = TMB (green)).

Reaction of $[Ni(PCy_3)_2]N_2$ and $ZnCl_2$ Monitored by ^{31}P NMR

In the glvebox, $[(PCy_3)_2Ni]_2N_2$ (18.0 mg, 0.01 mmol) was dissolved in 1 mL THF-d_8 in a 3 mL vial. The solution was then added to a J. Young NMR tube with a sealed capillary of PPh_3O, and the initial integration ratio of $[(PCy_3)_2Ni]_2N_2$ and PPh_3O was measured. This solution was then brought back into the glovebox and added to a 4 mL vial with $ZnCl_2$ (3.9 mg, 0.03 mmol). A colour change from red to brown was observed within 2 minutes. The solution was then added back to the J. Young NMR tube and analyzed by ^{31}P NMR spectroscopy within 10 minutes.

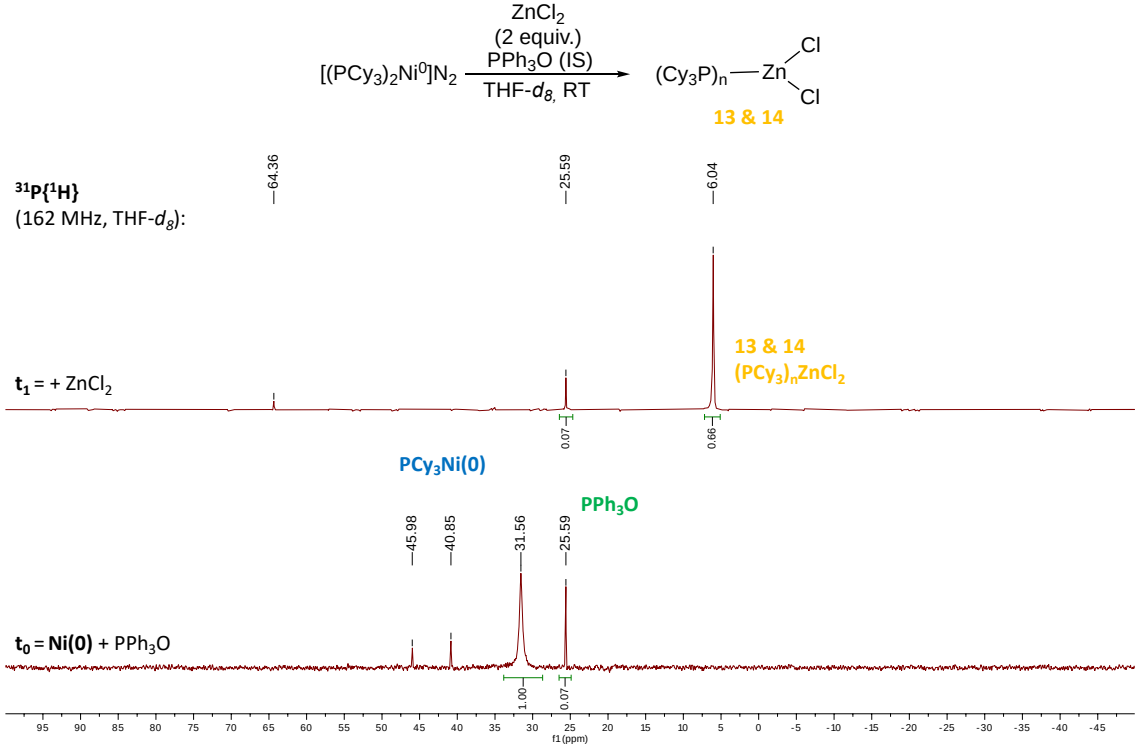

Figure S6. ^{31}P spectra (THF-d_8, 162 MHz) of $ZnCl_2$ reacting directly with Ni(0) (blue) forming $(PCy_3)_nZnCl_2$ (yellow) (standard = PPh_3O (green)).

Probing Reversibility of NiZn Cluster Formation

In the glovebox, $[(PCy_3)_2Ni]_2N_2$ (17.3 mg, 0.01 mmol) was dissolved in 1 mL THF-d_8 in a 3 mL vial with a stir bar. To the stirred solution, a solution of $ZnCl_2$ (3.9 mg, 0.029 mmol) in 1 mL THF-d_8 was added and then 20 minutes later PCy_3 (19.8 mg, 0.071 mmol) and cyclooctadiene (6.2 mg, 0.057 mmol) were added. The solution was then transferred to a J. Young NMR tube and measured by ^1H and ^{31}P NMR analysis. The solution was then heated at 80 ºC for 1 h and measured by ^1H and ^{31}P NMR analysis again. No signals corresponding to Ni(0) species $Ni(COD)_2$ or $[(PCy_3)_2Ni]_2N_2$ were visible by ^1H NMR or ^{31}P NMR.

Control experiments: (1) In the glovebox, $[(PCy_3)_2Ni]_2N_2$ (12.4 mg, 0.01 mmol) was dissolved in 1 mL THF-d_8 in a 3 mL vial with a stir bar and to the stirred solution cyclooctadiene (4.3 mg, 0.04 mmol) was added. The solution gradually turned yellow and was then transferred to a J. Young NMR tube and measured by ^{31}P and ^1H NMR analysis. No signals corresponding to $[(PCy_3)_2Ni]_2N_2$ were visible by ^{31}P NMR, but instead signals of $Ni(COD)_2$ formed.

(2) In the glovebox, $[(PCy_3)_2Ni]_2N_2$ (14.0 mg, 0.01 mmol) was dissolved in 1 mL THF-d_8 in a 3 mL vial with a stirbar. To the stirred solution, a solution of $[(PCy_3)ZnCl]_2$ (9.5 mg, 0.02 mmol/Zn) and PCy_3 (6.2 mg, 0.02 mmol) in 1 mL THF-d_8 were added. The solution was then transferred to a J. Young NMR tube and measured by ^1H and ^{31}P NMR analysis. Signals corresponding to Ni(0) $[(PCy_3)_2Ni]_2N_2$ were visible by ^{31}P NMR.

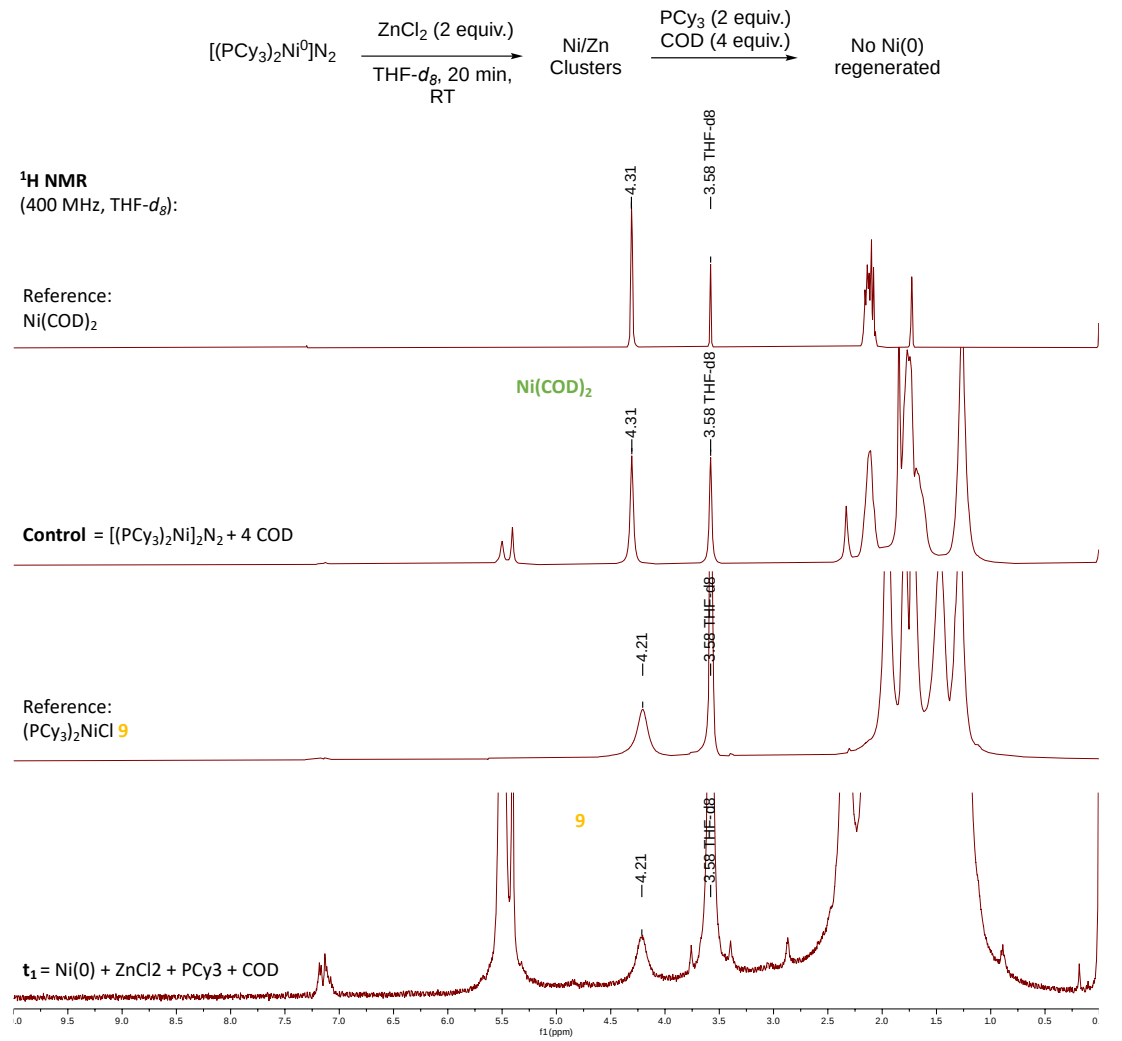

Figure S7. ^{1}H spectra (THF-d_8, 400 MHz) of $ZnCl_2$ reacting with Ni(0) and added ligand not regenerating Ni(0) species.

Reaction of $[Ni(PCy_3)_2]N_2$ and $ZnCl_2$ by ^1H Paramagnetic NMR

In the glovebox, $[(PCy_3)_2Ni]_2N_2$ (11.6 mg, 0.01 mmol) was dissolved in 0.8 mL THF-d_8 in a 3 mL vial and added to $ZnCl_2$ (3.0 mg, 0.02 mmol). The solution was then added to a J. Young NMR tube with a sealed capillary of cobaltocene in C_7D_8, and analyzed by ^1H paramagnetic NMR within 10 minutes. The capillary of cobaltocene was previously calibrated against a pure sample of **9** in 0.8 mL THF-d_8.

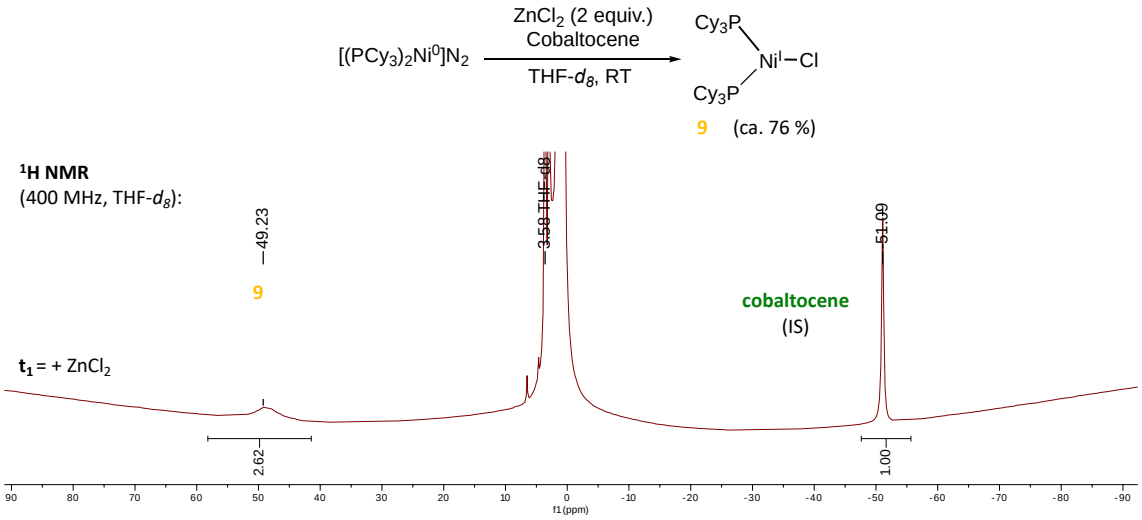

Figure S8. ^1H paramagnetic spectra (THF-d_8, 400 MHz) of $ZnCl_2$ reacting directly with Ni(0) (standard = cobaltocene capillary (green)).

Monitoring the Reaction of $(Cy_3P)_2Ni(I)OPiv$ and $ZnCl_2$ by Paramagnetic ^1H NMR

In the glovebox, $(PCy_3)_2Ni(OPiv)$ **11** (7.5 mg, 0.01 mmol), was dissolved in 0.8 mL THF-d_8 in a 3 mL vial. The solution was then added to a J. Young NMR tube with a sealed capillary of cobaltocene in C_7D_8, and the initial integration ratio of **11** and cobaltocene was measured. This solution was then brought back into the glovebox and added to a 4 mL vial with $ZnCl_2$ (3.1 mg, 0.02 mmol). A color change from green to yellow was observed within seconds. The solution was then added back to the J. Young NMR tube and analyzed by ^1H paramagnetic NMR within 10 minutes.

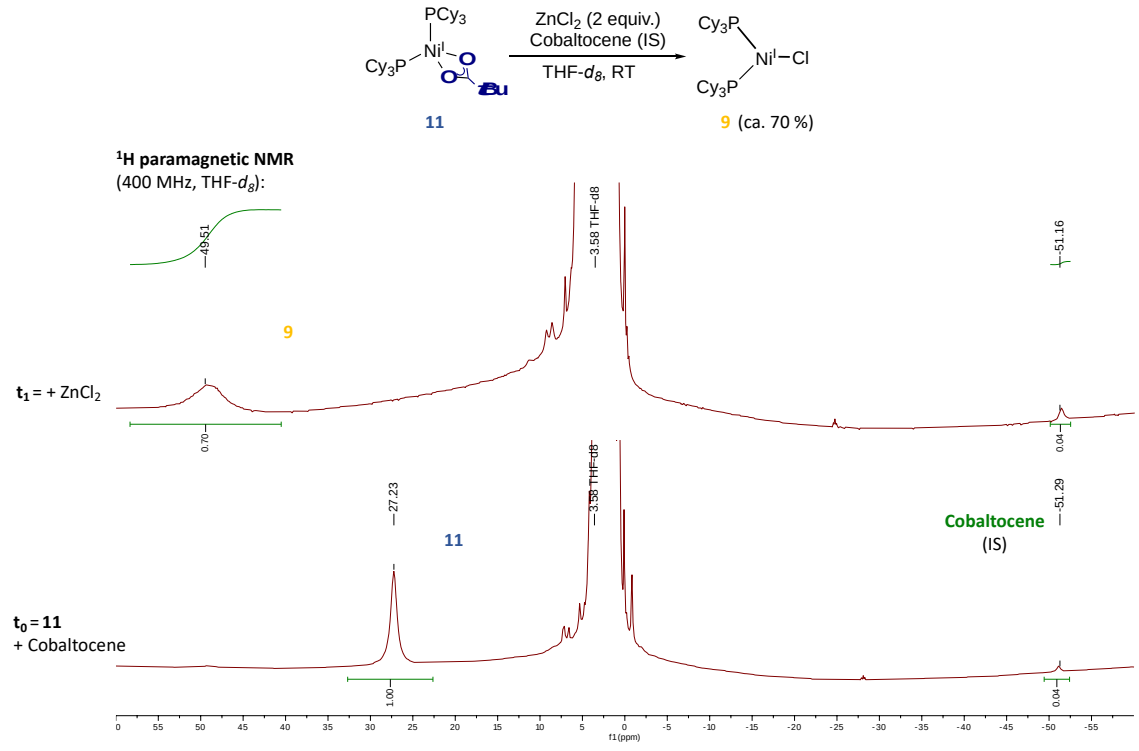

Figure S9. ^1H paramagnetic spectra (THF-d_8, 400 MHz) of $ZnCl_2$ reacting with **11** (standard = cobaltocene capillary (green)).

Monitoring the Reaction of (*o*-tolyl)Ni(PCy$_3$)$_2$OPiv and ZnCl$_2$ by ^{1}H & ^{31}P NMR with Internal Standard PPh$_3$O and TMB

In the glovebox, (PCy$_3$)$_2$Ni(OPiv)(*o*Tol) **5a** (9.0 mg, 0.01 mmol), and trimethoxybenzene (TMB) (0.7 mg) were dissolved in 1 mL THF-d_8 in a 3 mL vial. The solution was then added to a J. Young NMR tube with a sealed capillary of PPh$_3$O in C$_7$D$_8$, and the initial integration ratio of **5a** to TMB and PPh$_3$O was measured. This solution was then brought back into the glovebox and added to a 4 mL vial with ZnCl$_2$ (3.0 mg, 0.02 mmol). A colour change from orange to yellow was observed within seconds. The solution was then added back to the J. Young NMR tube and analyzed by quantitative ^{1}H and ^{31}P NMR.

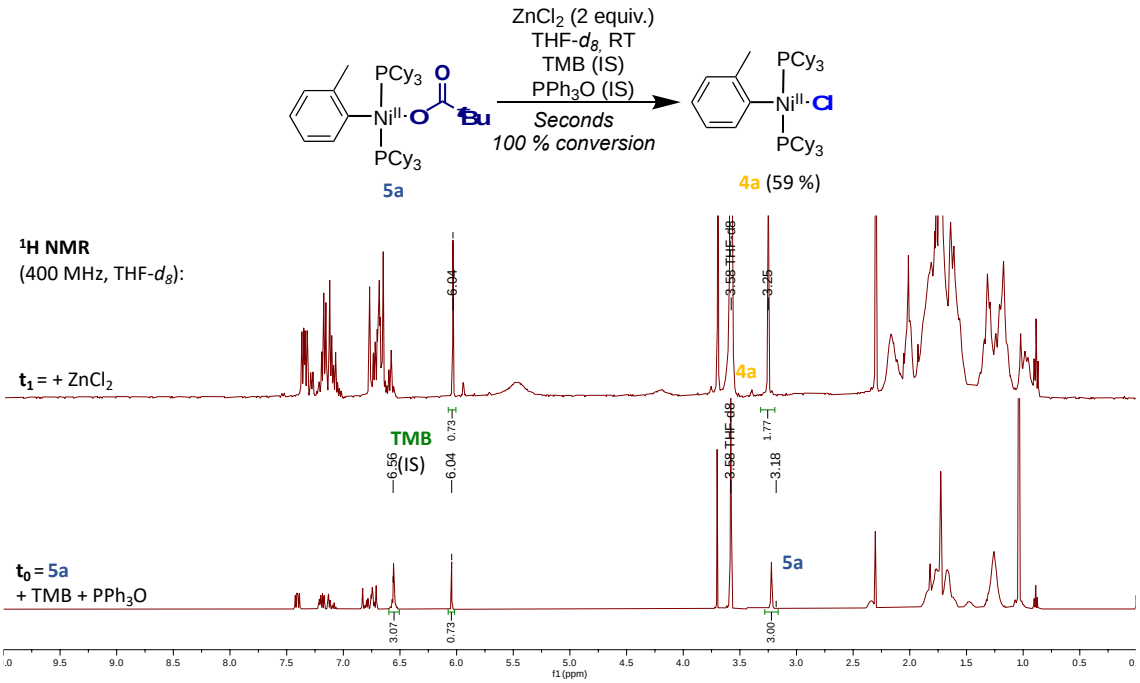

Figure S10. ^{1}H spectra (THF-d_8, 400 MHz) of ZnCl$_2$ reacting with **5a** (blue) (internal standard = TMB (green)).

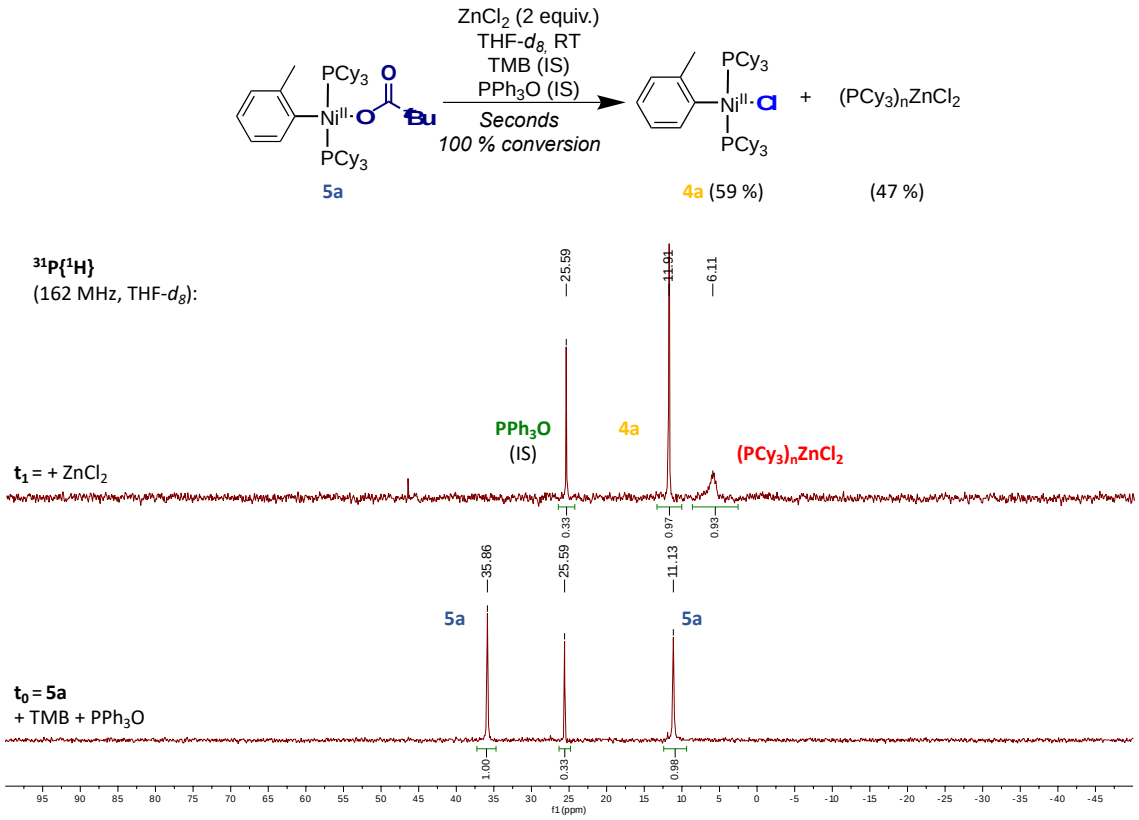

Figure S11. ^{31}P spectra (THF-d_8, 162 MHz) of $ZnCl_2$ reacting with **5a** (blue) (standard = PPh_3O (green)).

Monitoring the Reaction of (*o*-tolyl)Ni(PCy$_3$)$_2$OPiv and PhZnCl·LiCl analyzed by ^{1}H and ^{31}P NMR

In the glovebox, (PCy$_3$)$_2$Ni(OPiv)(*o*Tol) **5a** (15.7 mg, 0.019 mmol) and trimethoxybenzene (TMB) (2.3 mg) were dissolved in 1 mL C_6D_6. The solution was then added to a J. Young NMR tube, and the initial integration ratio of **5a** and TMB was measured. To this solution, a titrated solution of PhZnCl·LiCl in THF (10 µL, 0.99 M, 0.5 equiv) was added and the resulting solution analyzed by ^{1}H and ^{31}P NMR showing complete conversion of **5a**, formation of **4a** and cross-coupled products. To this solution a further addition of PhZnCl·LiCl (10 µL, 0.99 M, 0.5 equiv) was performed and was measured by ^{1}H and ^{31}P NMR.

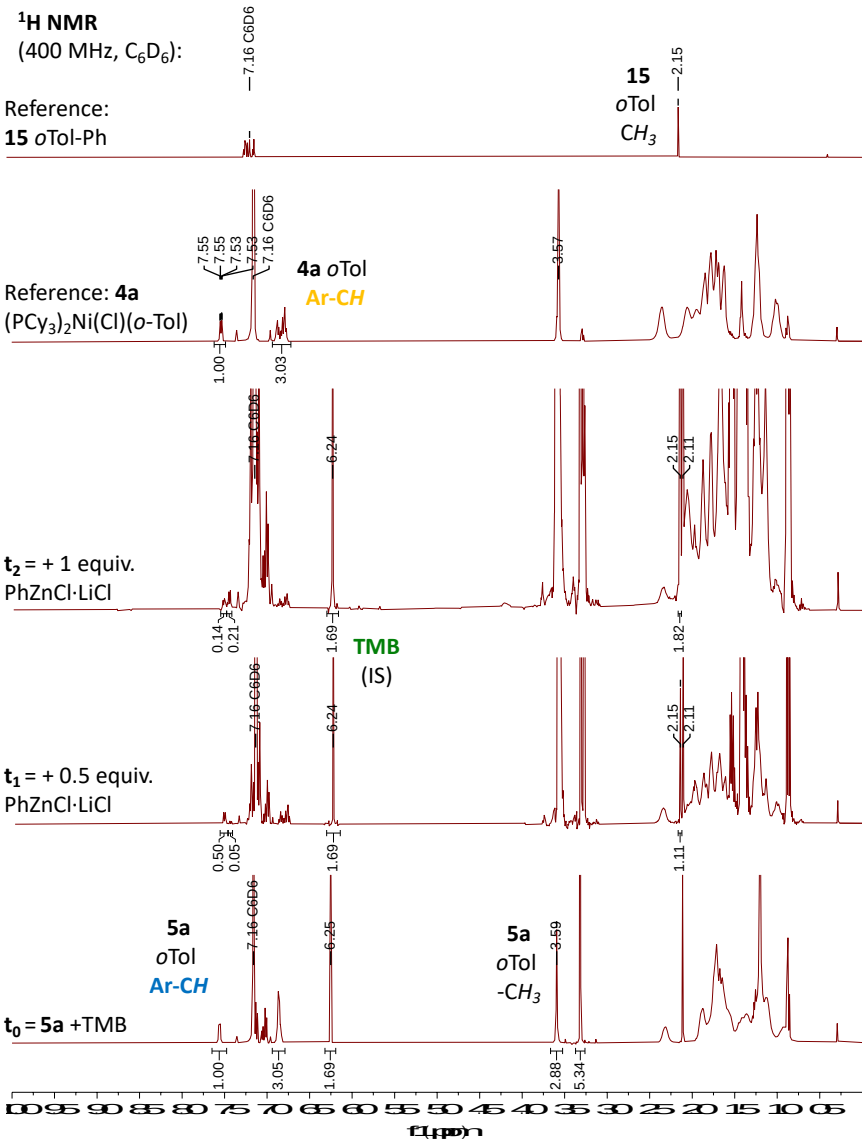

Figure S12. ^{1}H NMR spectra of the reaction between **5a** (blue) and PhZnCl·LiCl at 0.5 equivalents and 1 equivalents of PhZnCl·LiCl with reference spectra of **4a** (yellow) and coupled organic phenyl-*o*-toluene **15**.

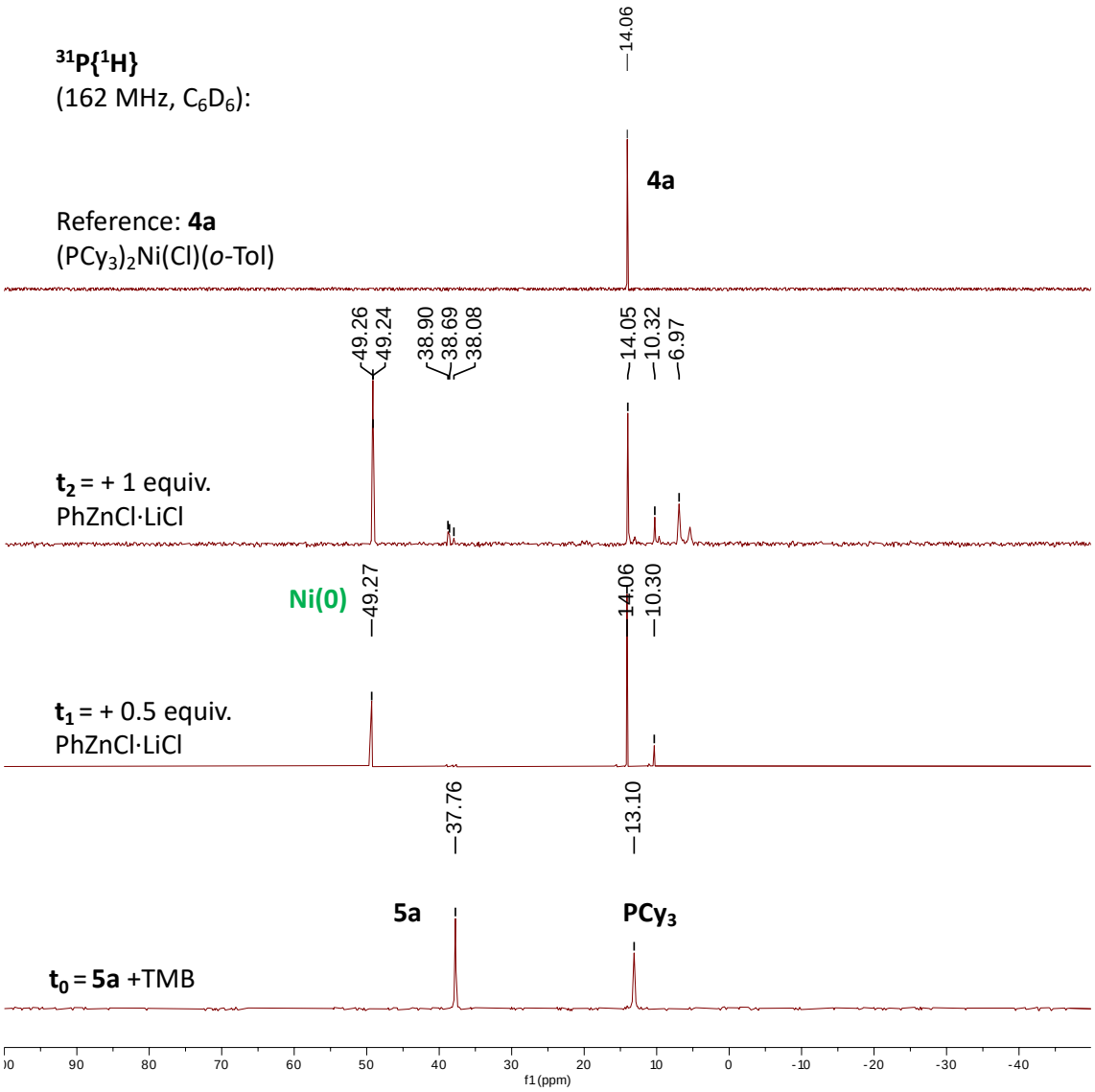

Figure S13. ^{31}H NMR spectra of the reaction between **5a** (blue) and PhZnCl·LiCl at 0.5 equivalents and 1 equivalents of PhZnCl·LiCl with reference spectrum of **4a** (yellow).

Monitoring the Reaction of (*o*-tolyl)Ni(PCy$_3$)$_2$OPiv and Ph$_2$Zn by ^{1}H NMR

In the glovebox, (PCy$_3$)$_2$Ni(OPiv)(*o*Tol) **5a** (13.4 mg, 0.02 mmol) and trimethoxybenzene (TMB) (1.6 mg) were dissolved in 1 mL THF-d_8. The solution was then added to a J. Young NMR tube, and the initial integration ratio of **5a** and TMB was measured. Ph$_2$Zn (4.0 mg, 0.02 mmol) in 0.5 mL THF-d_8 was then added dropwise to a stirred solution of **5a** where the solution turned from orange to brown. The resulting solution was then added back to the J. Young NMR tube and analyzed by ^{1}H NMR within 10 minutes.

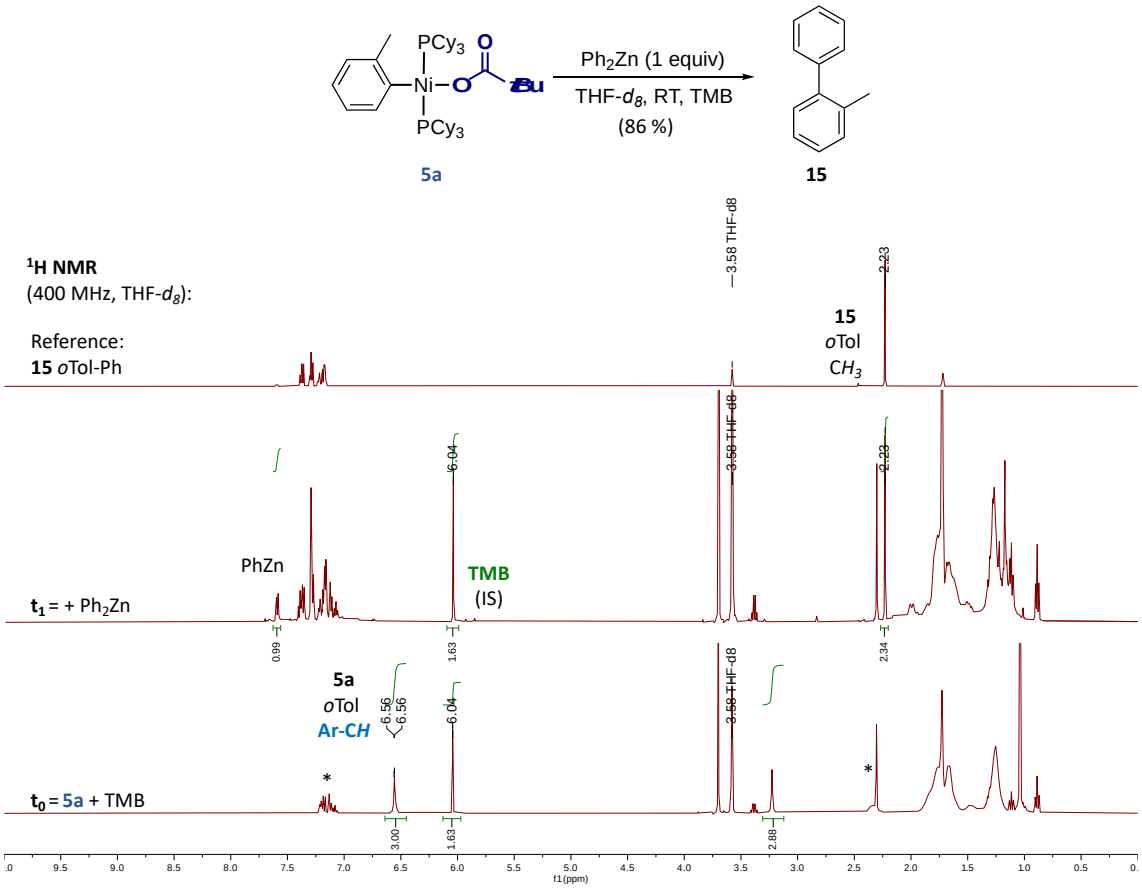

Figure S14. ^{1}H NMR spectra of the reaction between **5a** (blue) and Ph$_2$Zn with internal standard TMB and reference spectrum of phenyl *o*-toluene (yellow). Residual toluene solvent is denoted: (*).

Monitoring the Reaction of (mesityl)Ni(PCy$_3$)k^2–OPiv and Ph$_2$Zn by ^{1}H NMR

In the glovebox, (PCy$_3$)$_2$Ni(OPiv)(Mesityl) **8** (12.8 mg, 0.02 mmol) and trimethoxybenzene (TMB) (1.6 mg) were dissolved in 1 mL THF-d_8. The solution was then added to a J. Young NMR tube, and the initial integration ratio of **8** and TMB was measured. Ph$_2$Zn (5.7 mg, 0.02 mmol) in 0.5 mL THF-d_8 was then added dropwise to a stirred solution of **8** where the solution turned from orange to dark red. The resulting solution was then added back to the J. Young NMR tube and analyzed by ^{1}H NMR within 10 minutes.

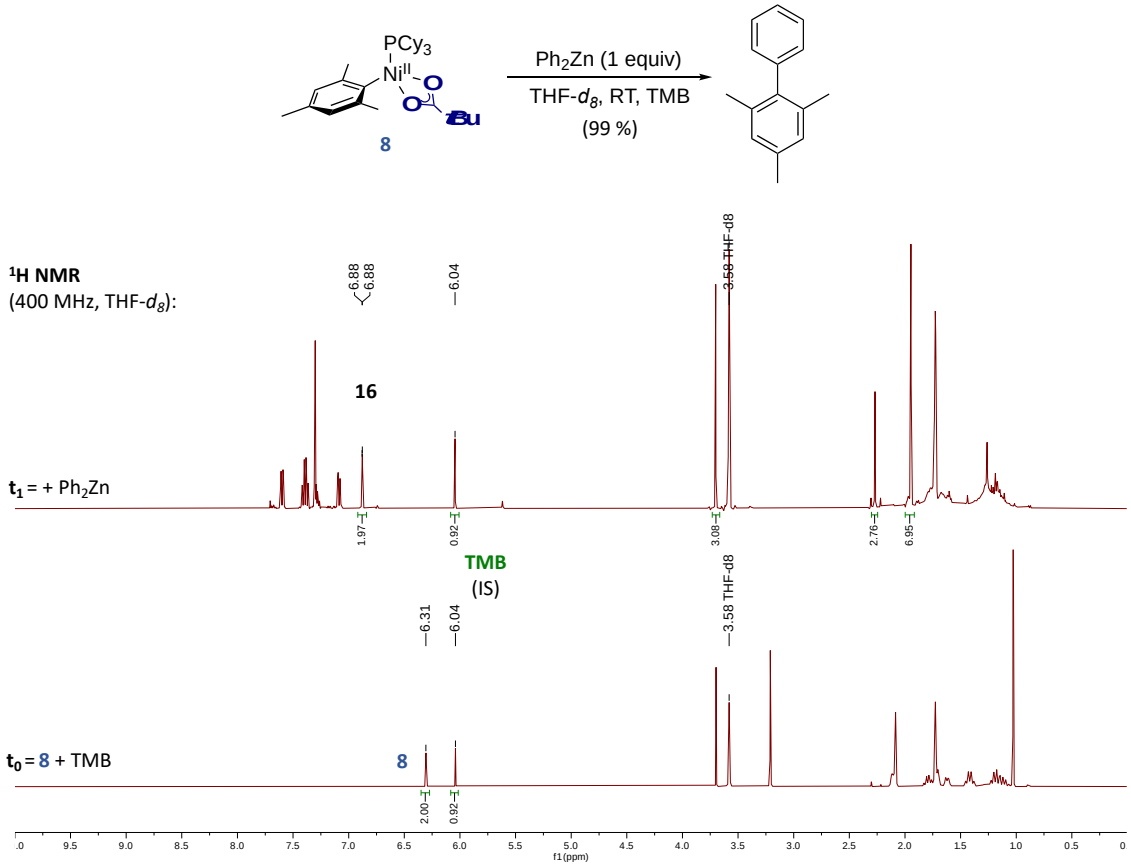

Figure S15. ^{1}H NMR spectra of the reaction between **8** (blue) and Ph$_2$Zn (internal standard = TMB (green)).

Monitoring the Reaction of (*o*-tolyl)Ni(PCy$_3$)$_2$OPiv and PCy$_3$-PhZnCl by ^{1}H NMR with Internal Standard TMB

In the glovebox, (PCy$_3$)$_2$Ni(OPiv)(*o*Tol) **5a** (10.0 mg, 0.01 mmol) and trimethoxybenzene (TMB) (1.0 mg) were dissolved in 1 mL THF-d_8. The solution was then added to a J. Young NMR tube, and the initial integration ratio of **5a** and TMB was measured. [(PCy$_3$)ZnClPh]$_2$ (5.7 mg, 0.01 mmol) in 0.5 mL THF-d_8 was then added dropwise to a stirred solution of **5a** where the solution turned from orange to brown. The resulting solution was then added back to the J. Young NMR tube and analyzed by ^{1}H NMR within 10 minutes.

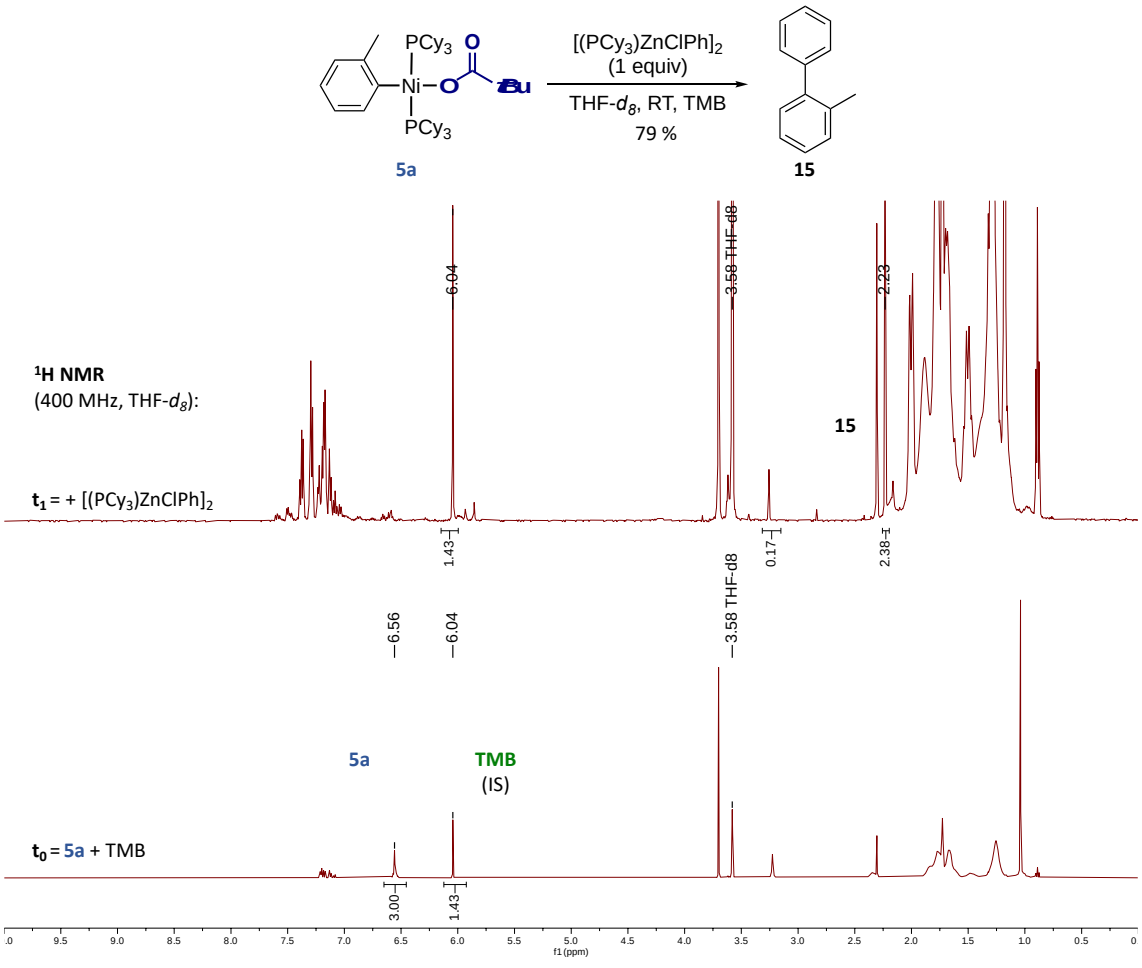

Figure S16. ^{1}H NMR spectra of the reaction between **5a** (blue) and [(PCy$_3$)ZnClPh]$_2$ (internal standard = TMB (green)).

2.6.4 Ni-Catalyzed Cross-Coupling Reactions of Aryl Pivalates with Organozinc Derivatives: Kinetic and Spectroscopic Analysis

Representative Procedure for Cross-Coupling of Aryl Pivalates with PhZnCl for Hammett Analysis. In the glovebox, $ZnCl_2$ (86 mg, 0.63 mmol) is added to a 10 mL Schlenk flask in 0.5 mL THF with a stirbar. To this solution, PhLi (0.3 mL, 1.9 M) is added dropwise then the solution left to stir for 30 minutes. Separately, $Ni(COD)_2$ (5.1 mg, 0.02 mmol) and PCy_3 (11.3 mg, 0.04 mmol) are added to a 4 mL vial with a stirbar in 0.5 mL THF and let to stir for 30 minutes. To the solution of PhZnCl, are added the aryl pivalate (0.19 mmol) and dodecane (45 µL, internal standard for GC analysis) with 1 mL DMA. An aliquot was removed for GC-FID analysis to establish the starting ratio of aryl pivalate to dodecane. This solution is then preheated to 90 ºC and charged with the premixed PCy_3-$Ni(COD)_2$ solution. Aliquots were removed periodically, quenched with potassium trispyrazolylborate (KTp) in THF (10 mg/mL), and analyzed by GC-FID.

Procedure for Cross-Coupling of Aryl Pivalates with PhZnCl using DMA:THF 2:1 for GC and MALDI-MS analysis. In the glovebox, $ZnCl_2$ (175 mg, 1.28 mmol) is added to a 10 mL Schlenk flask in 1 mL THF with a stirbar. To this solution, PhLi (0.6 mL, 1.9 M) is added dropwise then the solution left to stir for 30 minutes. To this solution, 3-benzophenone pivalate (108 mg, 0.38 mmol) and dodecane (90 µL, internal standard for GC analysis) are added with 2 mL DMA. An aliquot was removed for GC-FID analysis to establish the starting ratio of aryl pivalate to dodecane. This solution is then preheated to 85 ºC and charged with $(PCy_3)_2NiCl_2$ (26 mg, 0.04 mmol). Aliquots were removed periodically, quenched with KTp in THF (10 mg/mL), and analyzed by GC-FID. Separately, aliquots were mixed with DCTB (10 mg/mL) and pyrene (10 mg/mL) in 1:10 v/v ratios of matrix/analyte and spotted onto a MALDI target and analyzed by MALDI-MS.

Procedure for Cross-Coupling of Aryl Pivalates with PhZnCl in THF adding pyridine after 90 minutes. The representative procedure is the same as above except THF is added in place of DMA and pyridine (0.2 mL, 2.5 mmol) was added after 90 minutes. The system was sealed when aliquots were not being taken to prevent solvent loss.

Procedure for Cross-Coupling of Aryl Pivalates with PhZnCl in THF/ with pyridine from onset The representative procedure is the same as above except pyridine (0.2 mL, 2.5 mmol) was added to the PhZnCl after it was stirred for 30 minutes and 1.8

mL THF was added during the addition with dodecane.

Procedure for Cross-Coupling of Aryl Pivalates with PhZnCl using DMA:THF 2:1 for ^{31}P and ^{1}H Paramagnetic Analysis In the glovebox, $ZnCl_2$ (173.4 mg, 1.28 mmol) is added to a 10 mL Schlenk flask in 1 mL THF with a stirbar. To this solution, PhLi (0.6 mL, 1.9 M) is added dropwise then the solution left to stir for 30 min. 3-benzophenone (108.9 mg, 0.38 mmol) and PPh_3O (2 mg, reference for ^{31}P NMR) was added with 2 mL DMA. $(PCy_3)_2NiCl_2$ (24.2 mg, 0.04 mmol) is added then the solution is transferred to a J. Young NMR tube. The J. Young NMR tube was then heated at 85 ^{o}C and periodically analyzed by ^{31}P and ^{1}H paramagnetic NMR.

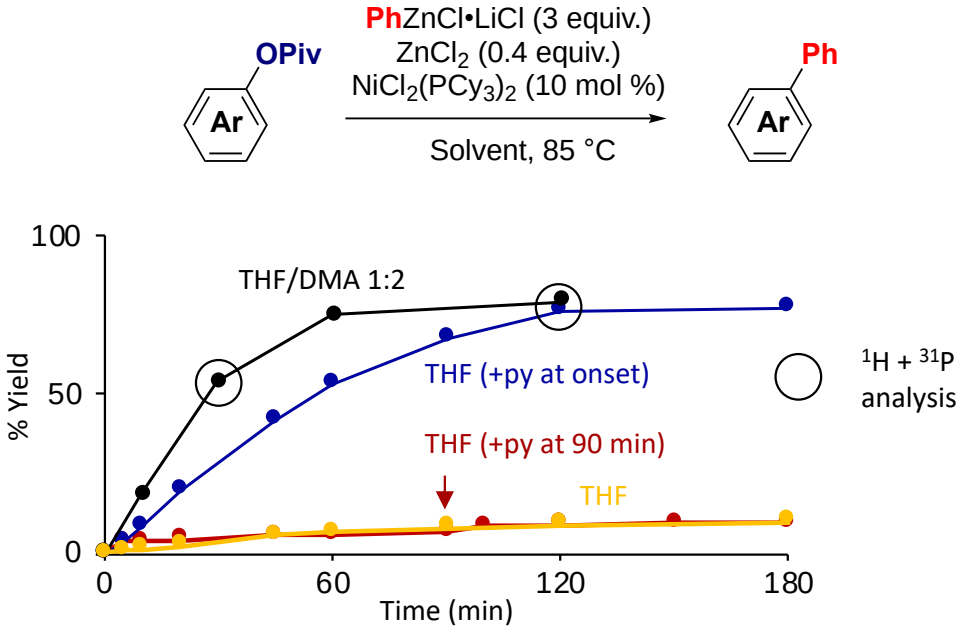

Figure S17. Changing the solvent system with circled timepoints being measured by ^{1}H paramagnetic and ^{31}P NMR spectra shown below.

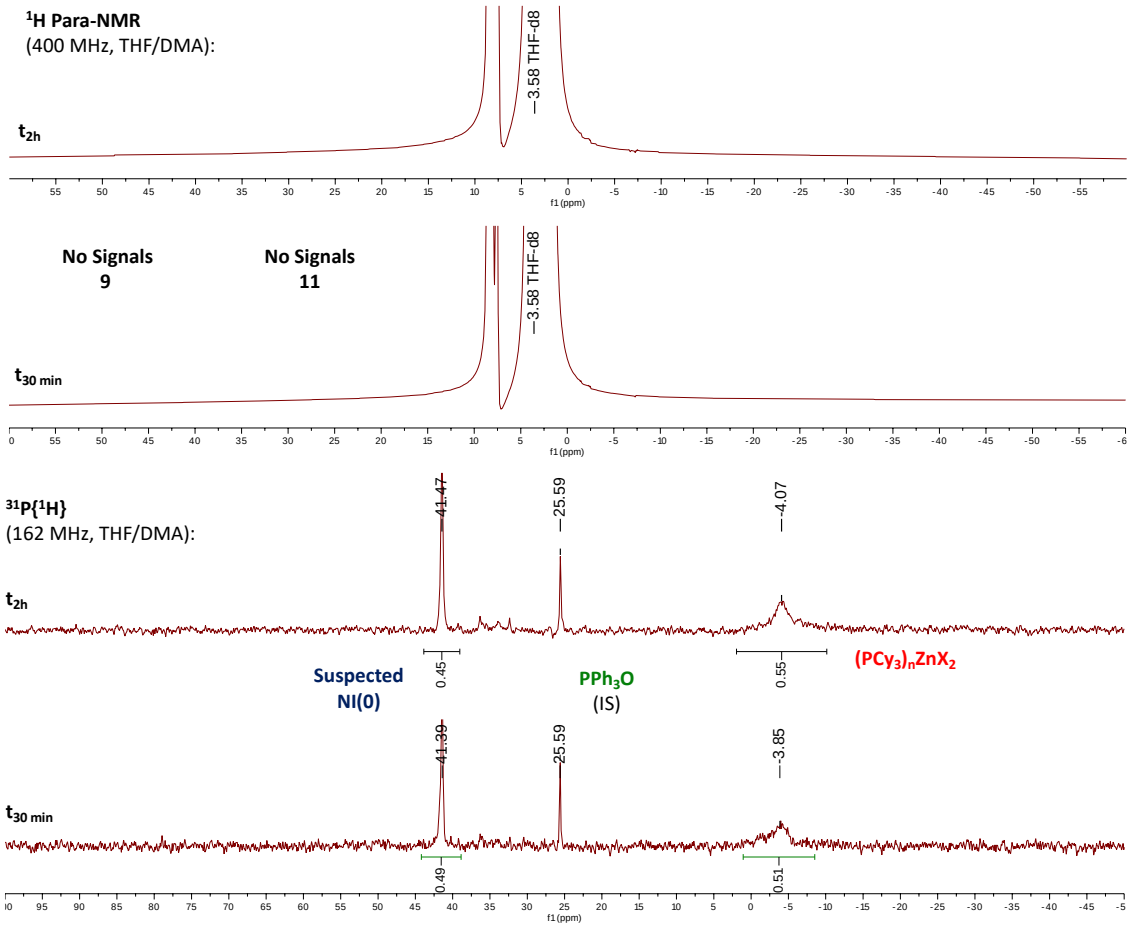

Figure S18. ^{1}H paramagnetic (top) lacking signals of **9** and **11** and ^{31}P NMR spectra (bottom) of $(PCy_3)_nZnCl_2$ at 30 min and 2 hours (solvent: THF/DMA 1:2).

Suggested Speciation During Catalysis in DMA:THF 2:1 by ^{31}P-NMR Analysis

To assign the catalytic resting states, different ^{31}P spectra were recorded in the solvent system of DMA:THF 2:1 with PPh_3O as an internal standard without lock or shim.

(a) PCy_3ZnCl_2 (14.0 mg, 0.02 mmol) in DMA:THF (1 mL, 2:1 ratio)

(b) $[(PCy_3)_2Ni]_2N_2$ (11.6 mg, 0.01 mmol) in DMA:THF (1 mL, 2:1 ratio)

- Without $ZnCl_2$ present, small signals around δ 41.40 ppm present

(c) $[(PCy_3)_2Ni]_2N_2$ (10.6 mg, 0.01 mmol) added to solution of (a)

- As phosphine is scavenged, signal of δ 41.74 ppm becomes more apparent

(d) $ZnCl_2$ (11.4 mg, 0.08 mmol) added to solution of (c)

- Shift of $(PCy_3)_nZnCl_2$ signal as additional $ZnCl_2$ is added is consistent with upfield, and broad chemical shift of $(PCy_3)_nZnX_2$ during catalysis

Additional experiments were conducted with UV-VIS to match the resting state species were inconclusive, which we attributed to a change in speciation at the low concentrations of UV-VIS measurements.

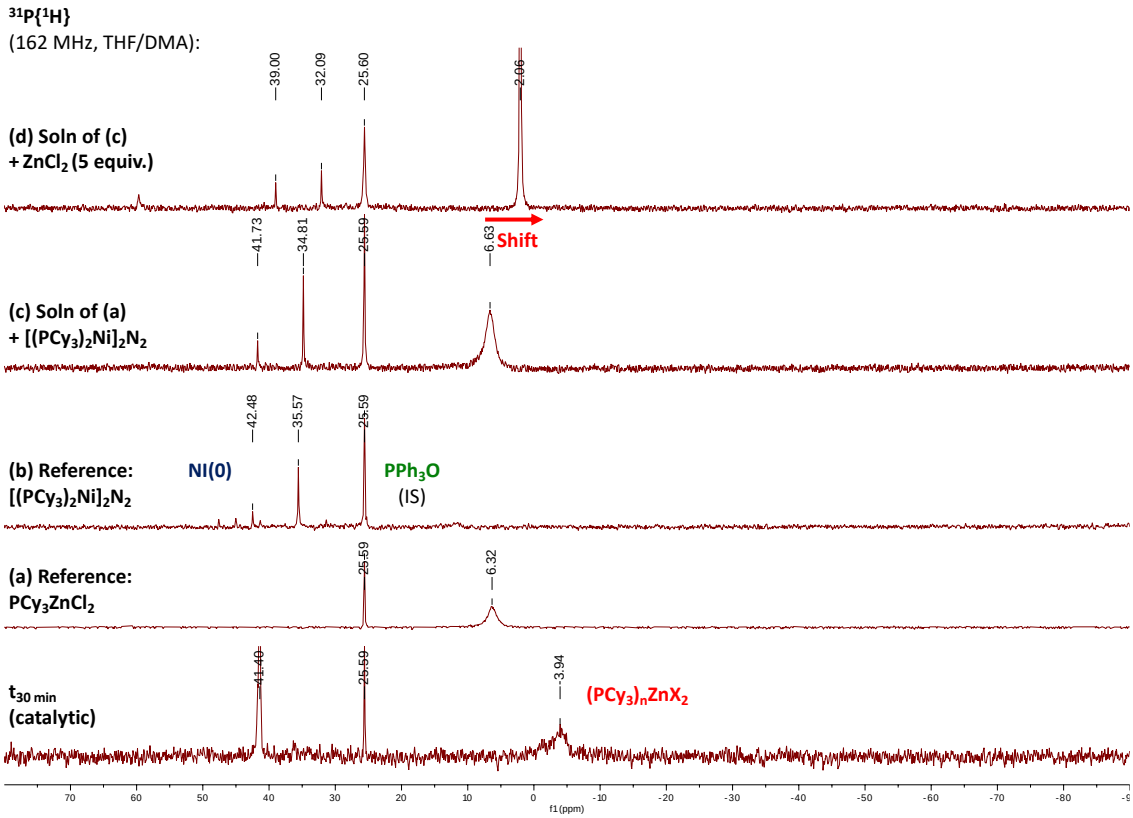

Figure S19. ^{31}P NMR spectra (bottom) of $(PCy_3)_nZnCl_2$ at 30 min and different mixtures to identify the resting state species (solvent: THF/DMA 1:2) with reference PPh_3O (green).

Oxidative Addition of $[(PCy_3)_2Ni]_2N_2$ to *o*-Tolyl Pivalate with $ZnCl_2$ in DMF-d_7/THF-d_8

In the glovebox, *o*-tolyl pivalate (8.1 mg, 0.04 mmol), trimethoxybenzene (TMB) (3.0 mg) and $ZnCl_2$ (4.7 mg, 0.034 mmol) were dissolved in 1 mL DMF-d_7 in a 3 mL vial. The solution was then added to a J. Young NMR tube, and the initial integration ratio of *o*-tolyl pivalate and TMB was measured. This solution was then added to a suspension of $[(PCy_3)_2Ni]_2N_2$ (13.1 mg, 0.01 mmol) in 0.5 mL DMF-d_7. The suspension was added back to the J. Young NMR tube and analyzed by ^1H and ^{31}P NMR, which identified no ^{31}P NMR signals due to insolubility of $[(PCy_3)_2Ni]_2N_2$. The sample was brought back into the glovebox and 1 mL THF-d_8 was added which aided solubilizing $[(PCy_3)_2Ni]_2N_2$ and was then monitored by ^{31}P and ^1H NMR analysis.

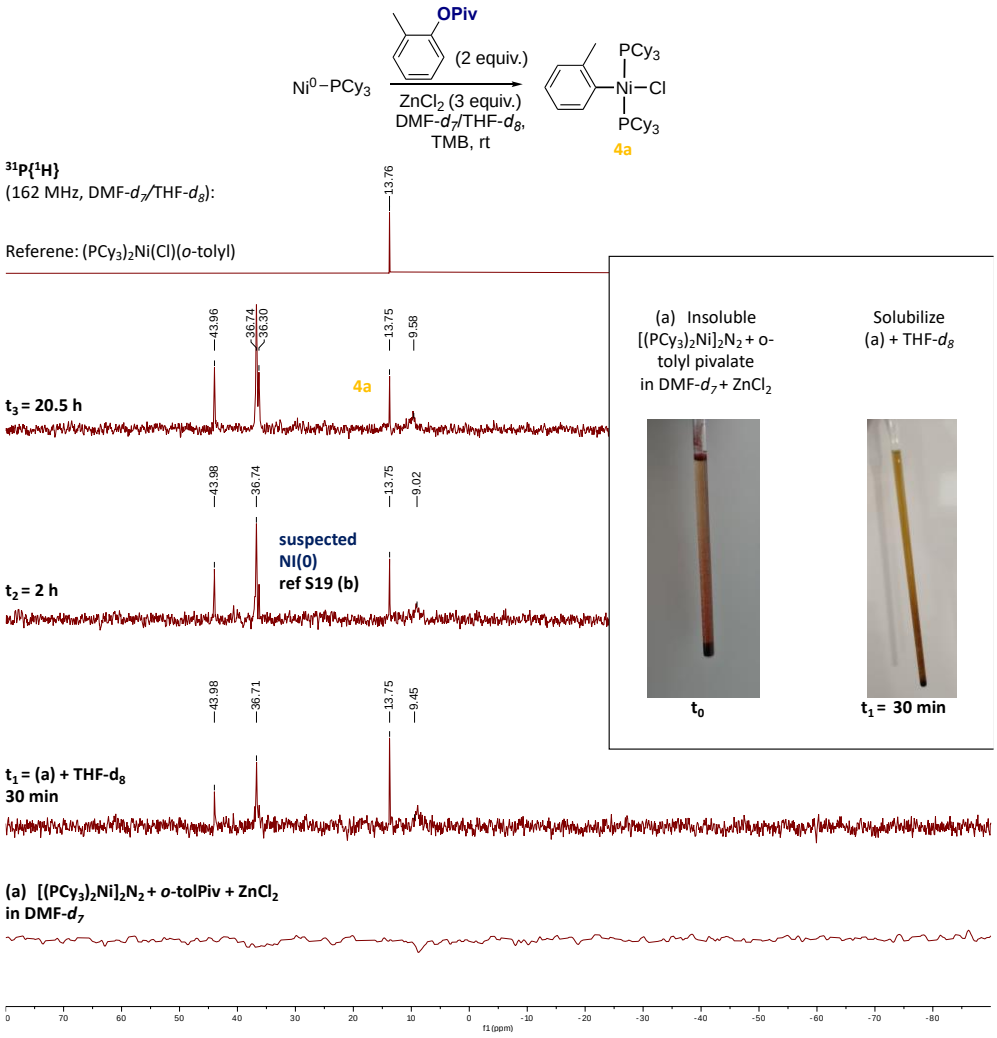

Figure S20. ^{31}P NMR spectra (DMF-d_7/THF-d_8, 162 MHz) of oxidative addition with $[(PCy_3)_2Ni]_2N_2$ to o-tolyl pivalate in the presence of $ZnCl_2$ forming $(PCy_3)_2Ni(Cl)$(*o*-tolyl). Right box indicating insolubility of $[(PCy_3)_2Ni]_2N_2$, which is solubilized by adding THF-d_8. $(PCy_3)_2Ni(Cl)$(*o*-tolyl) (yellow) and suspected Ni(0) (grey).

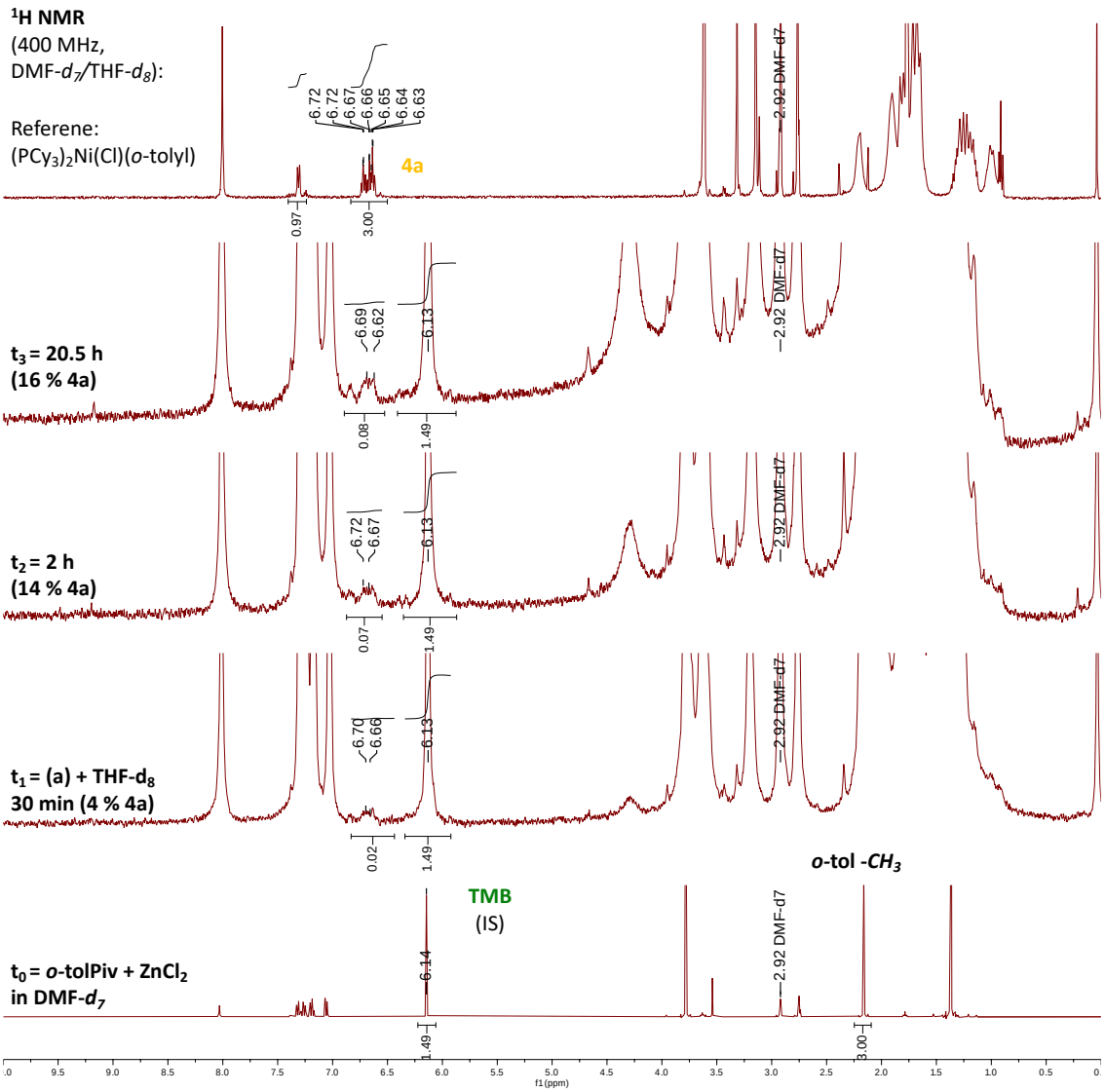

Figure S21. ^{1}P NMR spectra of $[(PCy_3)_2Ni]_2N_2$ + o-tolyl pivalate + $ZnCl_2$ in DMF-d_7/THF-d_8. $(PCy_3)_2Ni(Cl)$(*o*-tolyl) (yellow) and internal standard TMB (green).

Cross-Coupling Reactions With Precatalyst $(PCy_3)_2NiCl$ & $ZnCl_2$ Poisoning Experiments

Procedure for Cross-Coupling of Aryl Pivalates with PhZnCl for using $(PCy_3)_2NiCl$. In the glovebox, $ZnCl_2$ (175 mg, 1.28 mmol) is added to a 10 mL Schlenk flask in 1 mL THF with a stirbar. To this solution, PhLi (0.6 mL, 1.9 M) is added dropwise then the solution left to stir for 30 minutes. To this solution, 3-benzophenone pivalate (111 mg, 0.38 mmol) and dodecane (90 μL, internal standard for GC analysis) are added with 2 mL DMA. An aliquot was removed for GC-FID analysis to establish the starting ratio of aryl pivalate to dodecane. This solution is then preheated to 85 ºC and charged with $(PCy_3)_2NiCl$ (26 mg, 0.04 mmol). An aliquot was removed after 2 h and quenched with KTp in THF (10 mg/mL), and analyzed by GC-FID (100 % conversion, 65 % yield).

Procedure for Silylation of Aryl Pivalates with $Et_3SiBPin$ without $ZnCl_2$. In the glovebox, CsF (38 mg, 0.25 mmol), CuF_2 (7.6 mg, 0.075 mmol), 2-naphthyl pivalate (57 mg, 0.25 mmol) and dodecane (50 μL, internal standard for GC analysis) were added to a 10 mL Schlenk flask in 1 mL toluene with a stirbar. To this solution, PCy3 (14.0 mg, 0.05 mmol), Ni(COD) (6.9 mg, 0.025 mmol), and $Et_3SiBpin$ (73 mg, 0.03 mmol) were added with 2 mL more toluene and an aliquot was removed for GC-FID analysis to establish the starting ratio of aryl pivalate to dodecane. This solution is then warmed in a preheated oil bath at 50 ºC and let stir for 16 h. An aliquot was removed and quenched with KTp in THF (10 mg/mL), and analyzed by GC-FID (100 % conversion, 89 % yield).

Procedure for Silylation of Aryl Pivalates with $Et_3SiBPin$ without $ZnCl_2$. The representative procedure is the same as above except $ZnCl_2$ (34 mg, mmol) is added after $Et_3SiBPin$ (3 % conversion, 0 % yield).

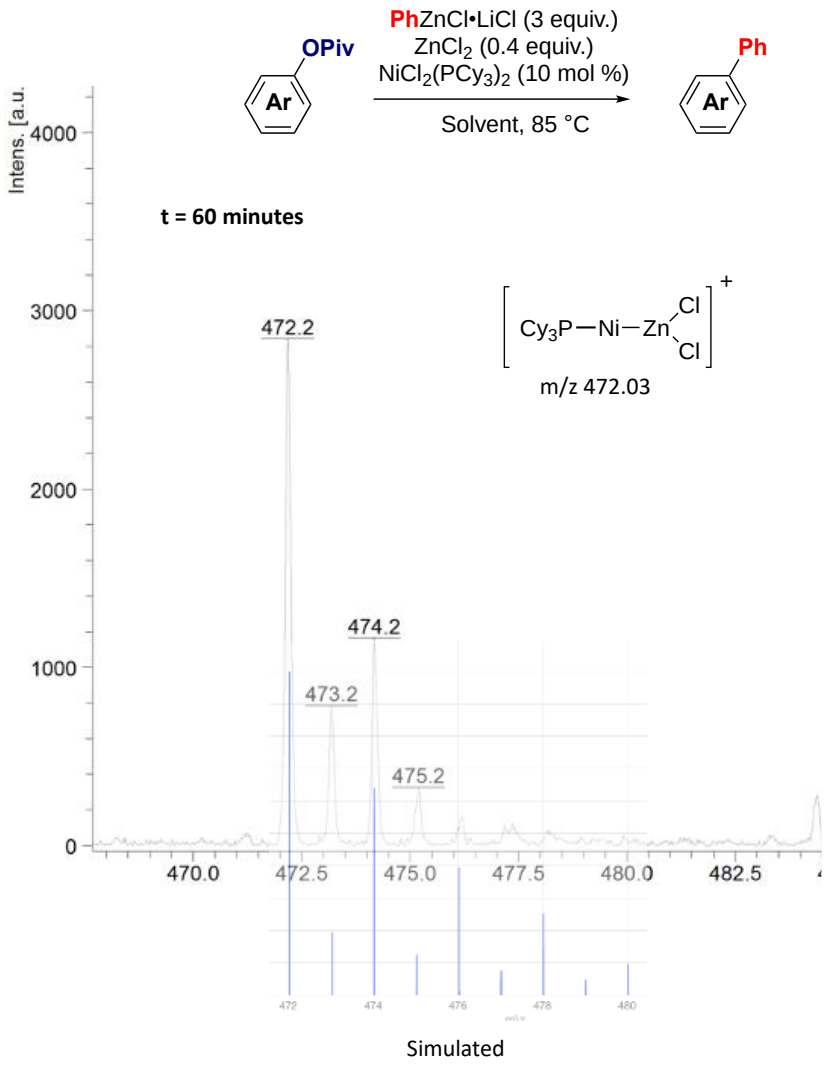

Figure S22. MALDI-TOF MS spectra of $(PCy_3)NiZnCl_2$ from the reaction mixture at 1 hour with the simulated isotope pattern overlaid below.

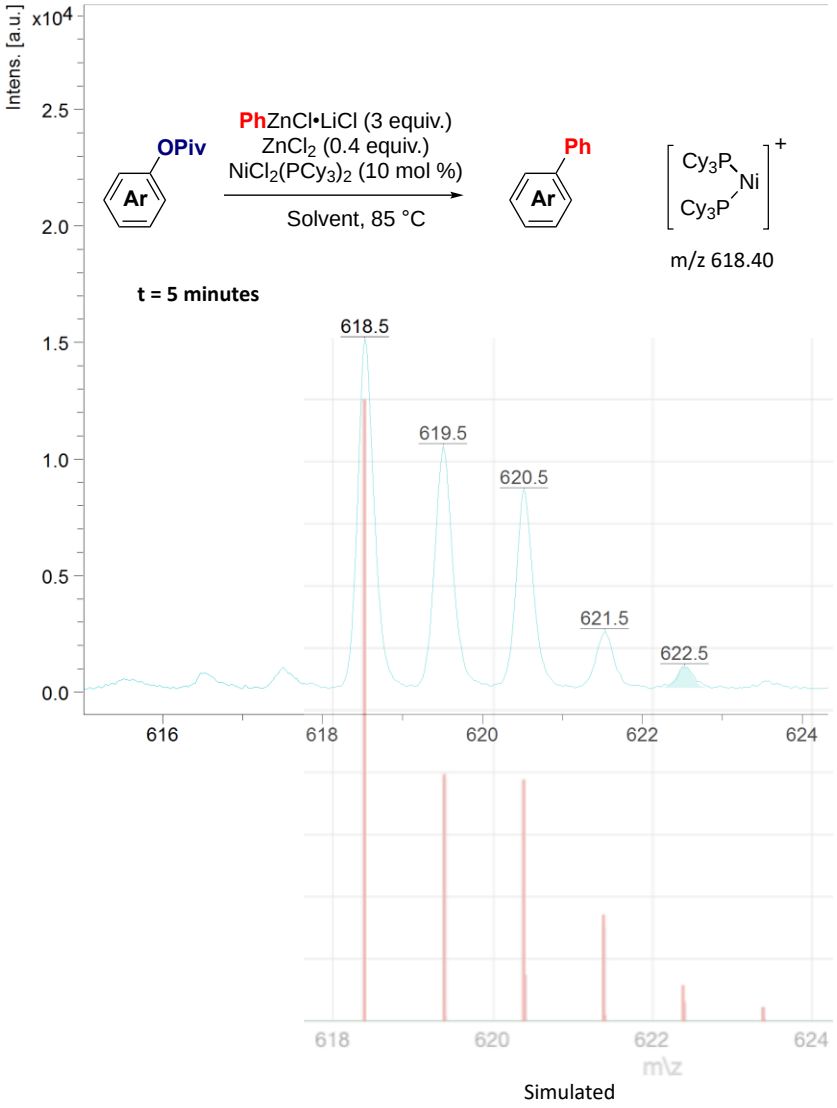

Figure S23. MALDI-TOF MS spectra of $(PCy_3)_2Ni$ from the reaction mixture at 5 minutes with the simulated isotope pattern overlaid below.

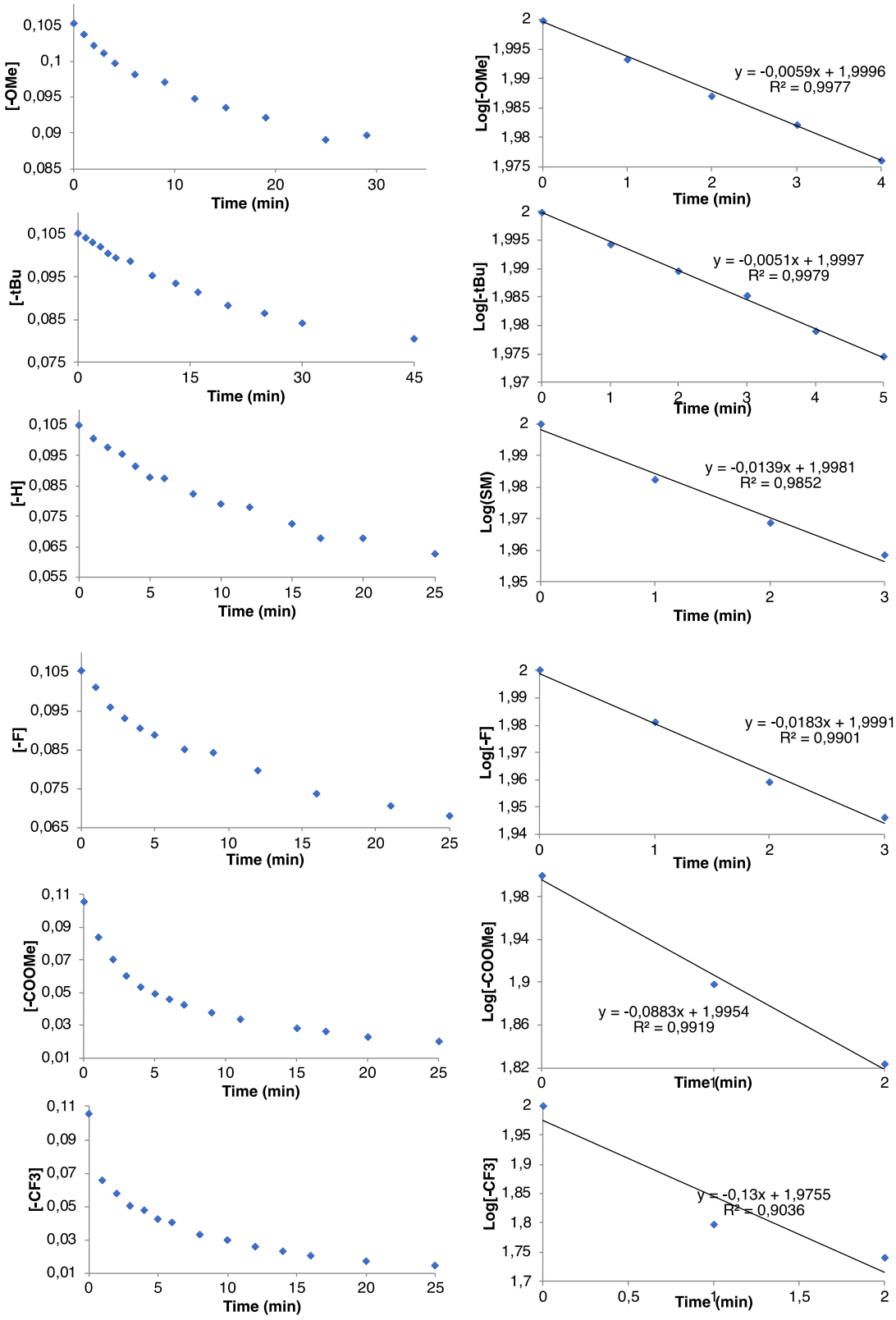

Figure S24. Kinetics data used for the Hammett Plot. R^2 determined from linear regression model in Excel

2.6.5 Characterization

EPR and IR Spectra

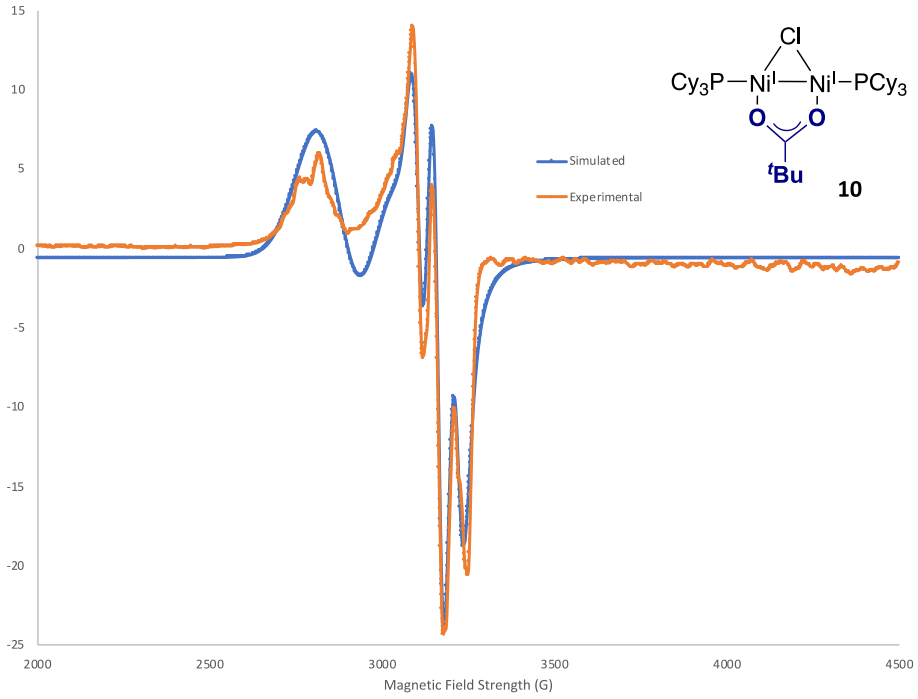

Figure S25. EPR spectrum of $[(PCy_3)Ni]_2(\mu\text{-Cl})(\mu\text{-OPiv})$ **10**, Ni(a) $g_x = 2.09131$, $g_y = 2.15579$, $g_z = 2.39462$, Ni(b) $g_x = 2.96782$, $g_y = 2.12308$, $g_z = 2.43851$.

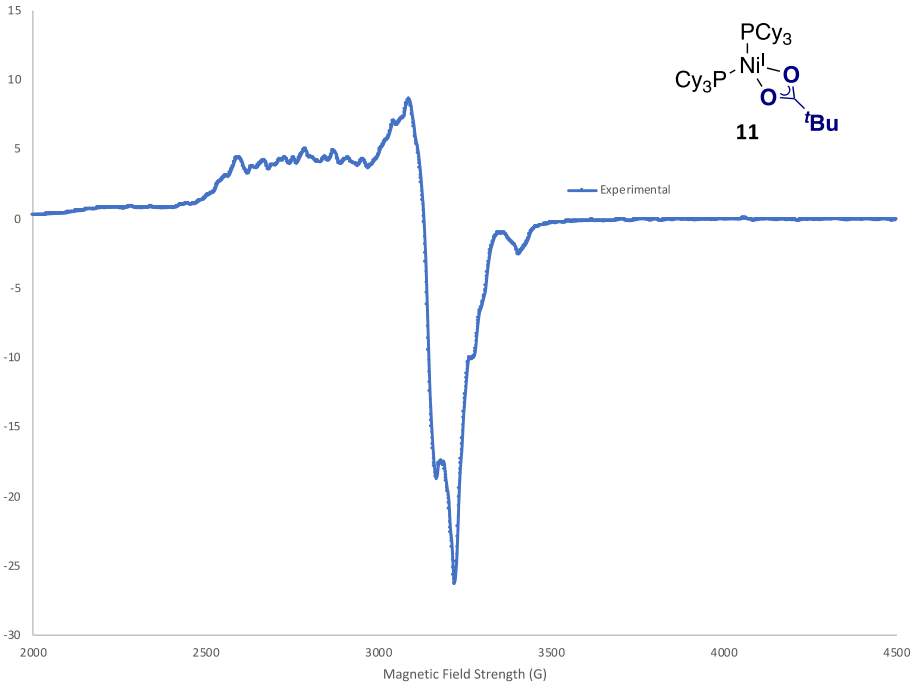

Figure S26. EPR spectrum of $(PCy_3)_2Ni(\kappa^2\text{-OPiv})$ **11** without modeling.

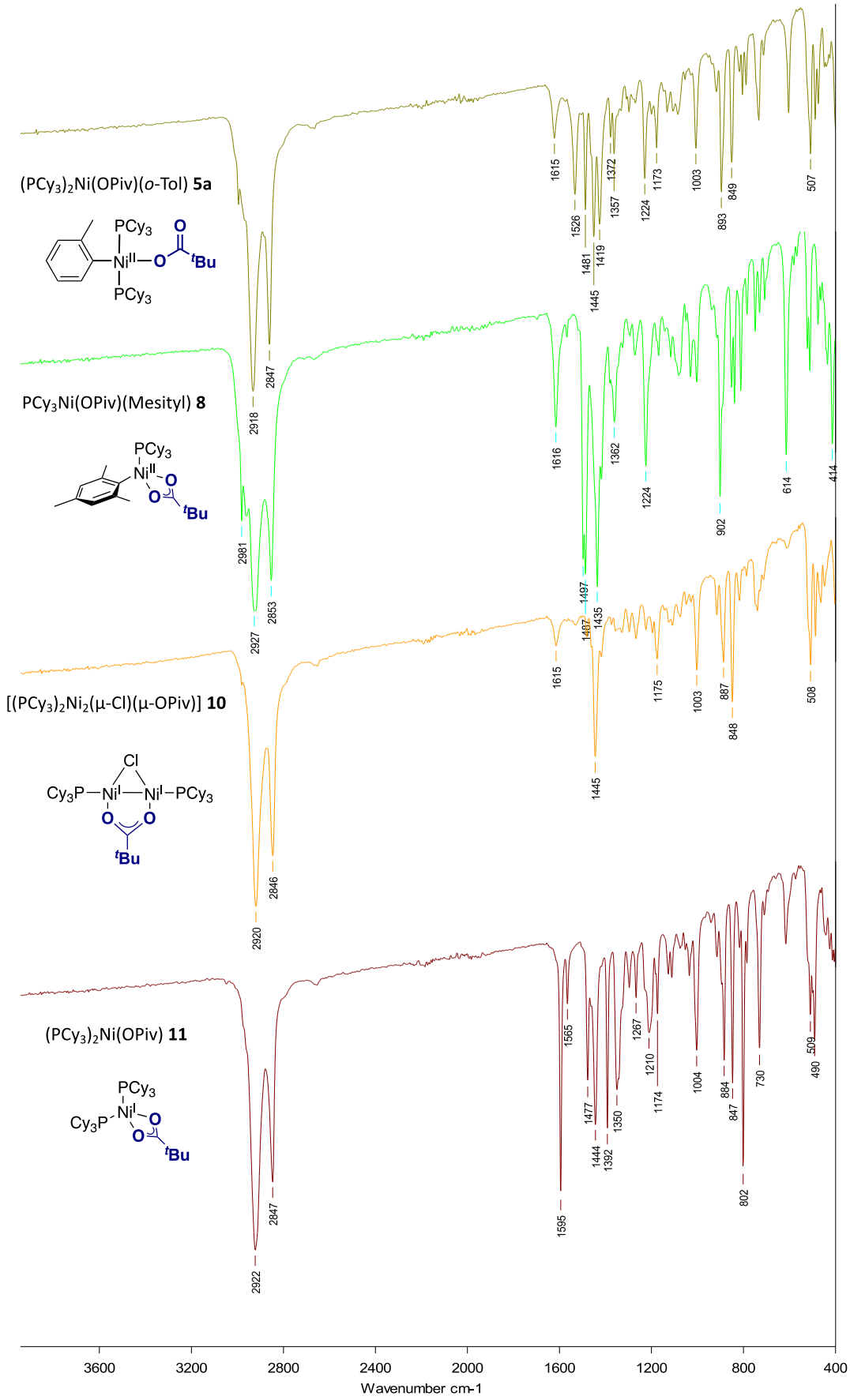

Figure S27. Stacked IR spectra of complexes **5a**, **8**, **10**, and **11**.

NMR Spectra of Synthesized Complexes

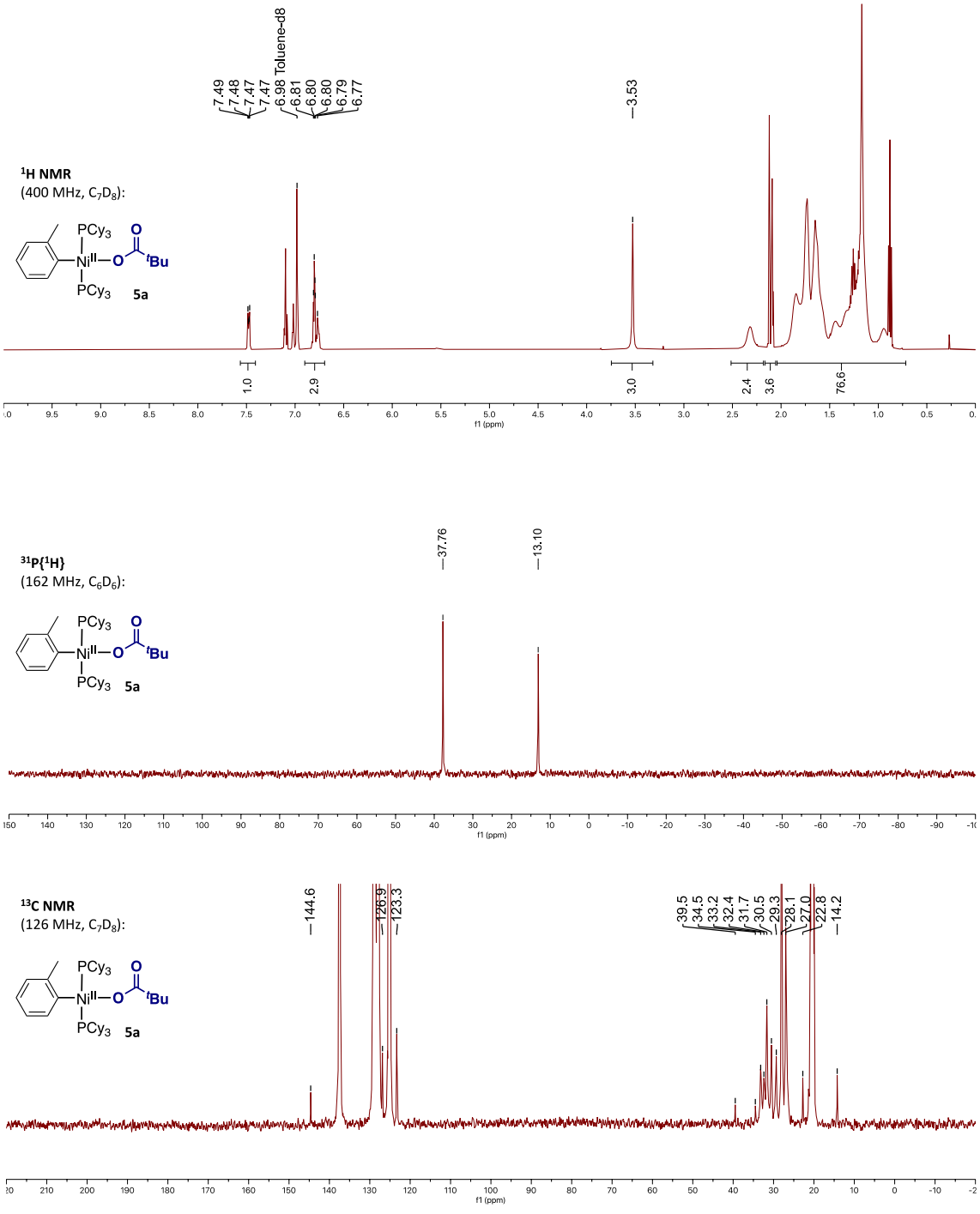

Figure S28. NMR spectra (C_7D_7, 400 MHz) of $(PCy_3)_2Ni(o\text{-Tol})(OPiv)$ **5a**.

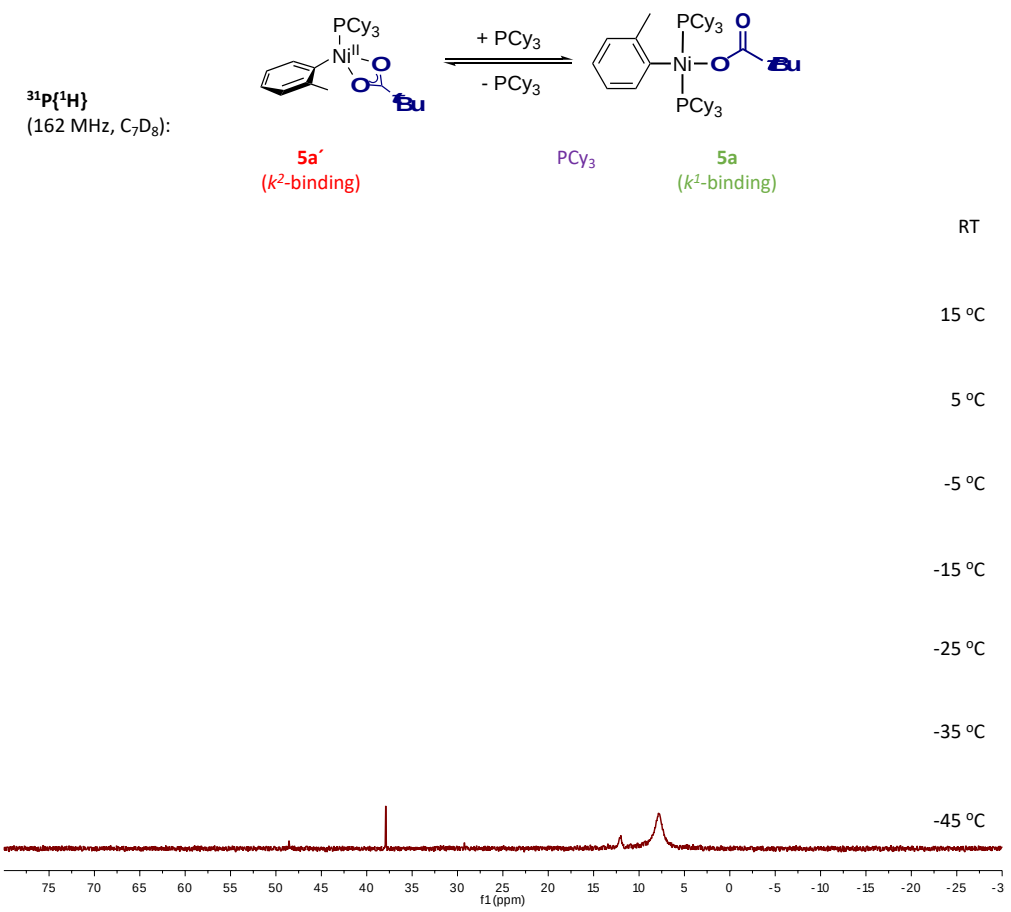

Figure S29. Variable temperature ^{31}P NMR spectra (C_7D_8, 162 MHz) of $(PCy_3)_2Ni(o\text{-}Tol)(OPiv)$ **5a**.

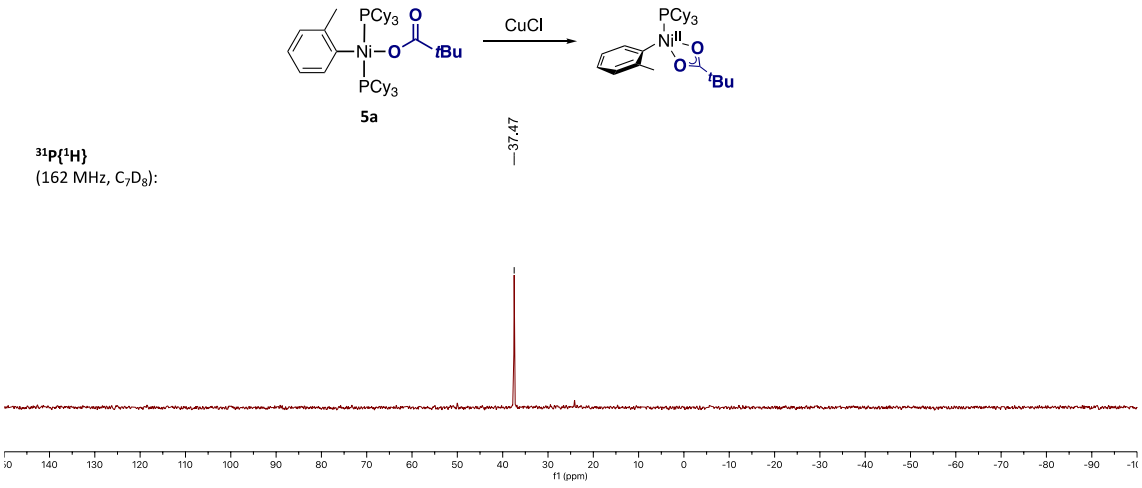

Figure S30. ^{31}P NMR spectra (C_7D_8, 162 MHz) of $(PCy_3)_2Ni(o\text{-}Tol)(OPiv)$ **5a** after adding CuCl, thus illustrating κ^2-O speciation in solution.

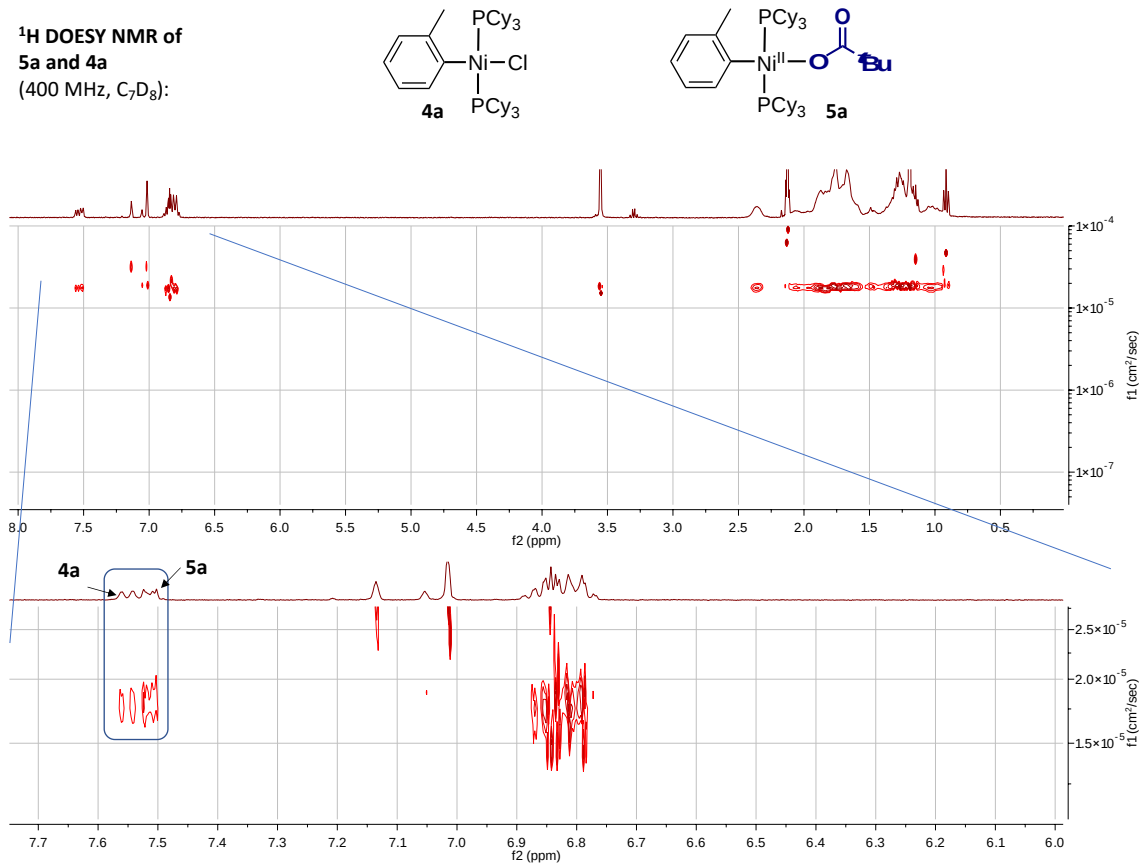

Figure S31. DOSY ^{1}H NMR spectra (C_7D_8, 400 MHz) of $(PCy_3)_2Ni(o\text{-Tol})(OPiv)$ **5a** and $(PCy_3)_2Ni(Cl)(o\text{-Tol})$ **4a** illustrating monomeric speciation in solution

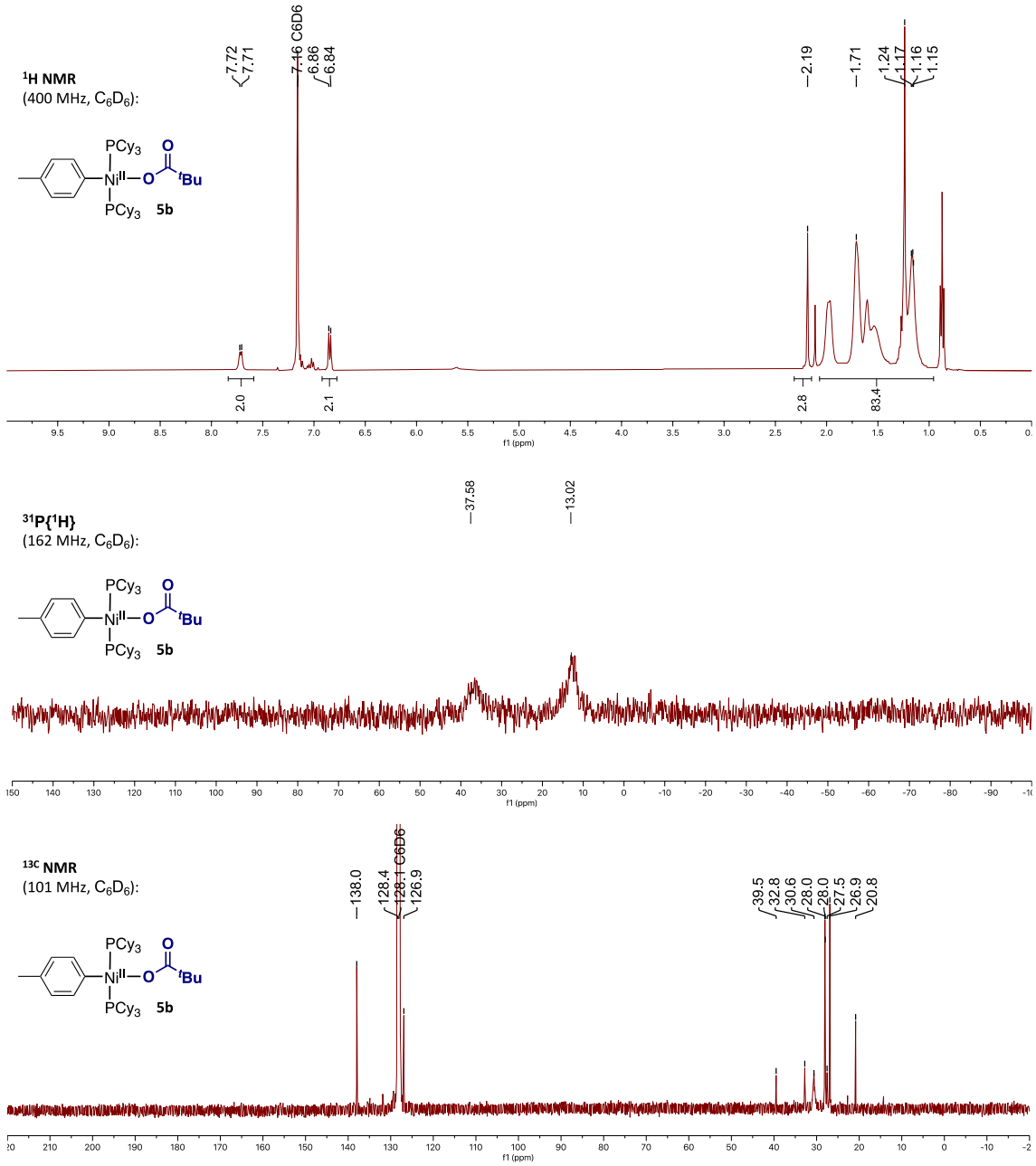

Figure S32. NMR spectra (C_6D_6, 400 MHz) of $(PCy_3)_2Ni(o\text{-Tol})(OPiv)$ **5a**.

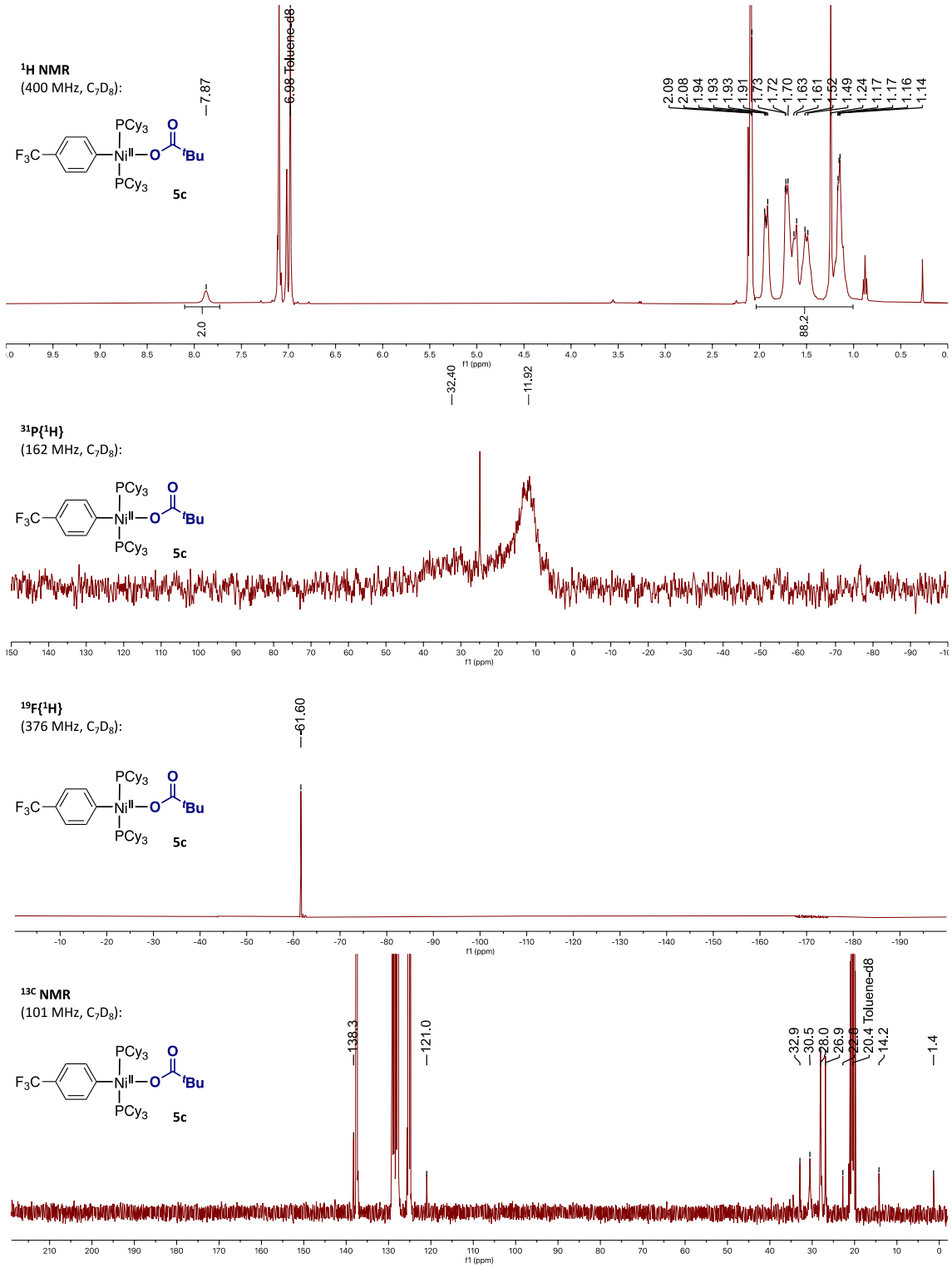

Figure S33. NMR spectra (C_7D_8, 400 MHz) of $(PCy_3)_2Ni(p CF_3\text{-}Ph)(OPiv)$ **5c**.

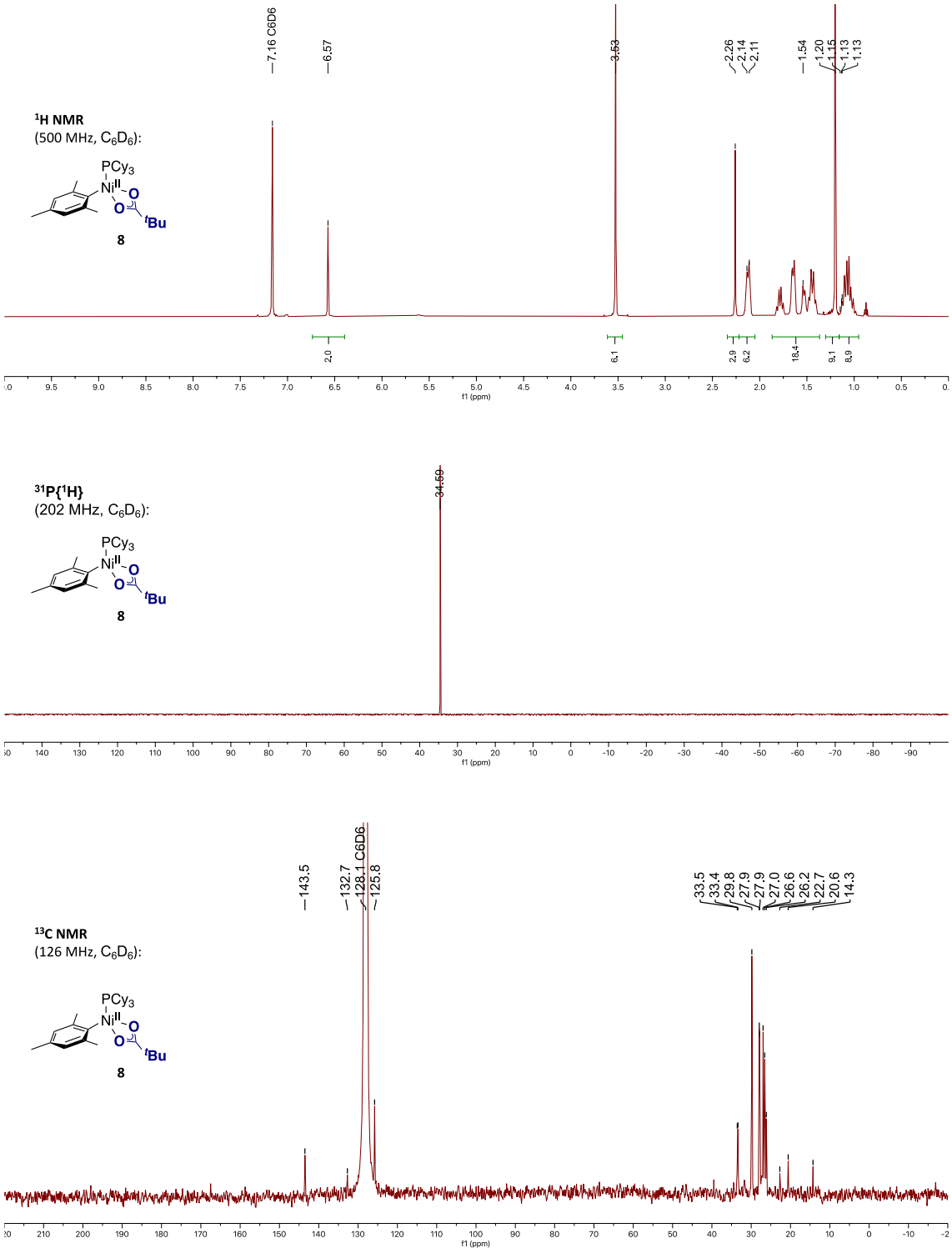

Figure S34. NMR spectra (C_6D_6, 500 MHz) of $(PCy_3)_2Ni(Mesityl)(OPiv)$ **8**.

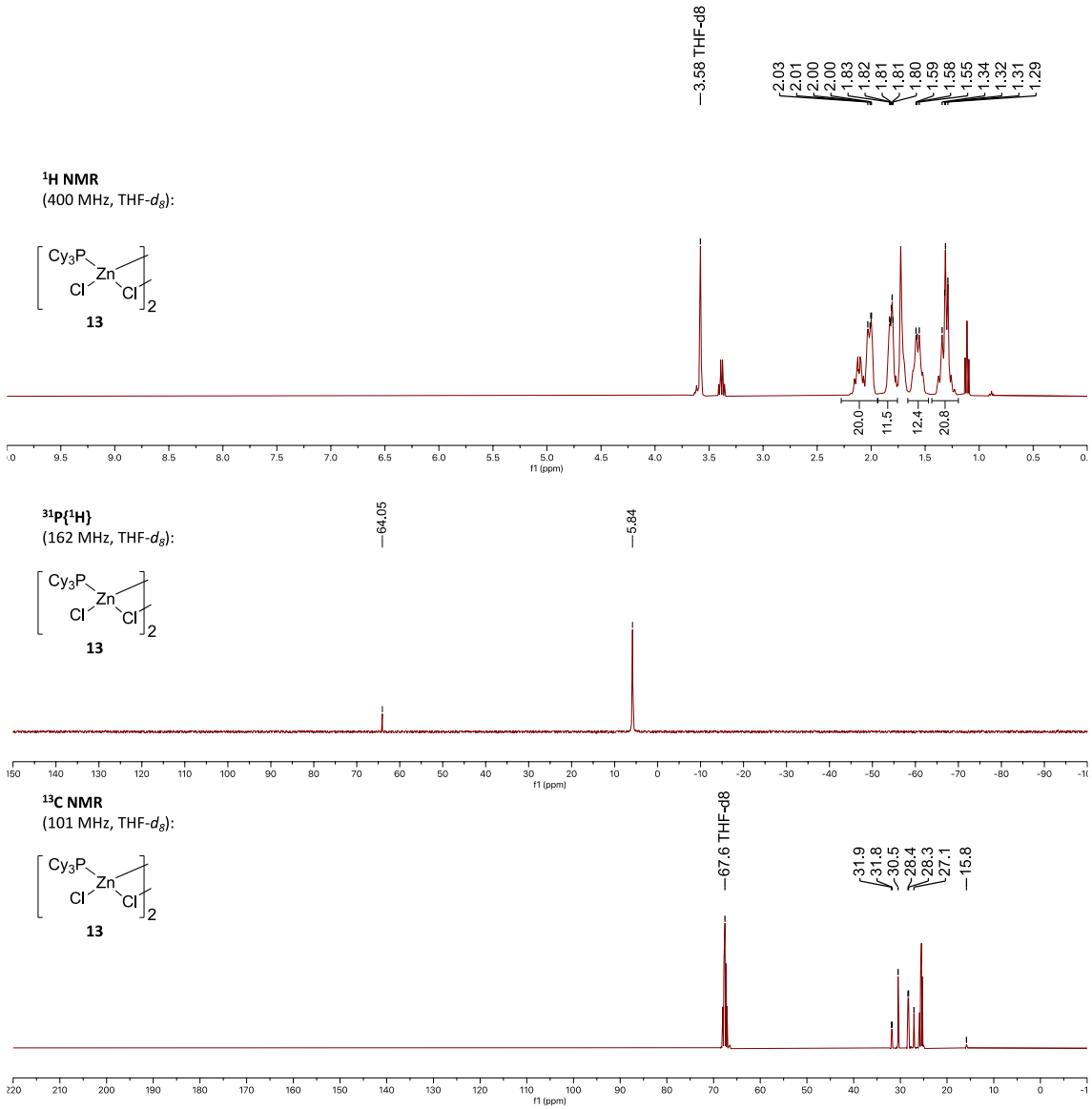

Figure S35. NMR spectra (THF-d_8, 400 MHz) of $[(PCy_3)ZnCl_2]_2$ **13**.

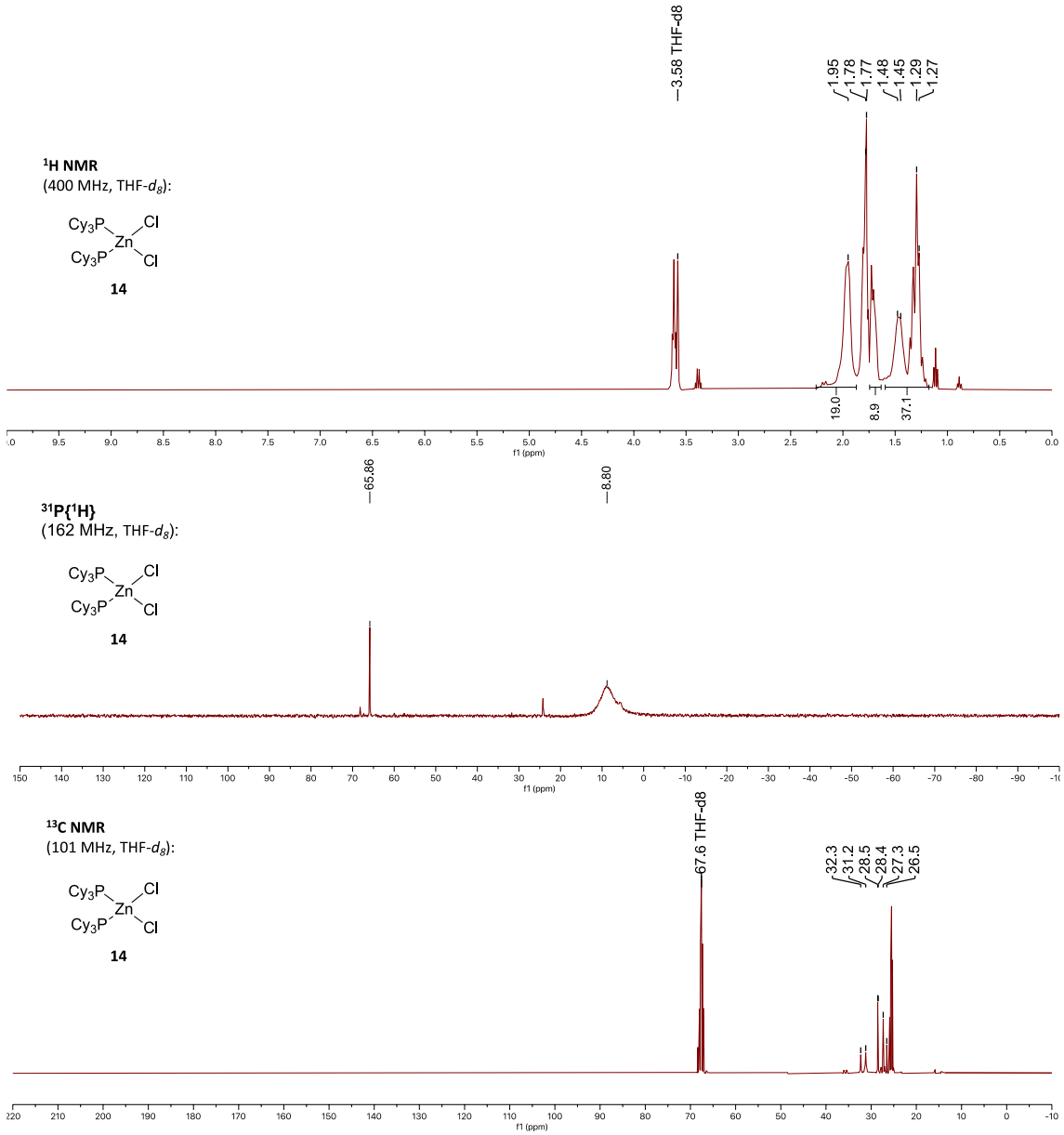

^{1}H NMR
(400 MHz, THF-d_8):

14

^{31}P{^{1}H}
(162 MHz, THF-d_8):

14

^{13}C NMR
(101 MHz, THF-d_8):

14

Figure S36. NMR spectra (THF-d_8, 400 MHz) of $(PCy_3)_2ZnCl_2$ **14**.

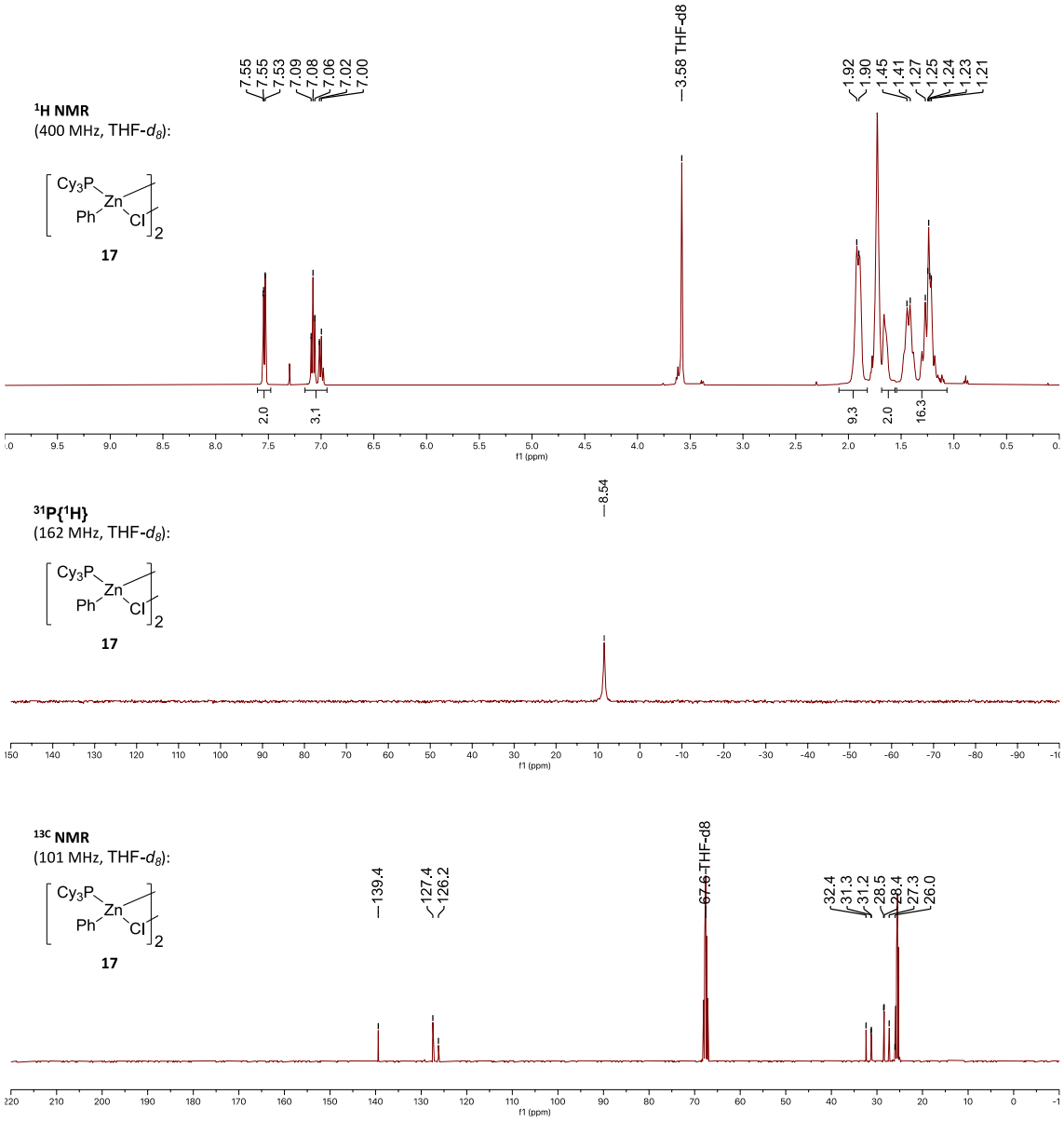

Figure S37. NMR spectra (THF-d_8, 400 MHz) of $[(PCy_3)Zn(Cl)(Ph)]_2$ **17**.

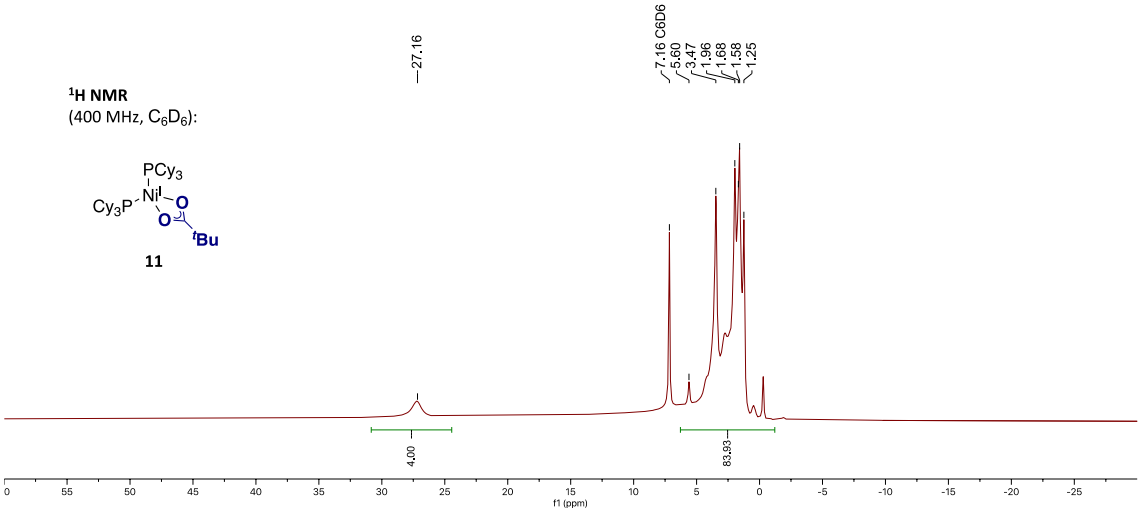

Figure S38. ^{1}H NMR spectrum (C_6D_6, 400 MHz) of $(PCy_3)_2Ni(OPiv)$ **11**.

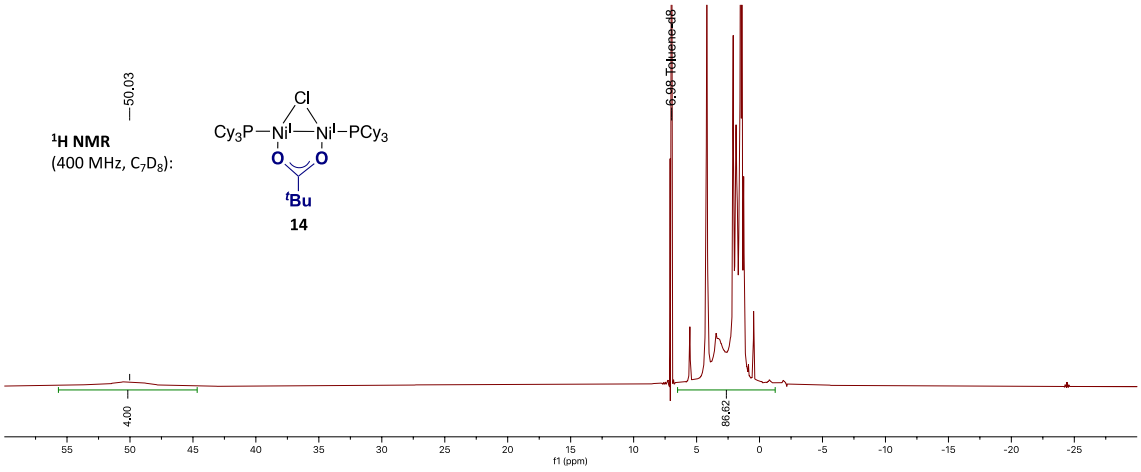

Figure S39. ^{1}H NMR spectrum (C_7D_8, 400 MHz) of $[(PCy_3)Ni]_2(\mu\text{-Cl})(\mu\text{-OPiv})$ **10**.

Crystallographic Data

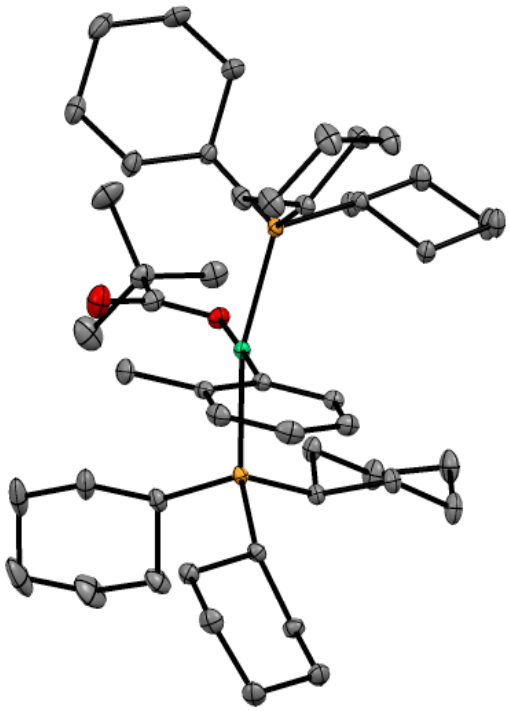

Figure S40. ORTEP Diagram $(PCy_3)_2Ni(o\text{-Tol})(OPiv)$ **5a** CCSD deposition number **2017448**

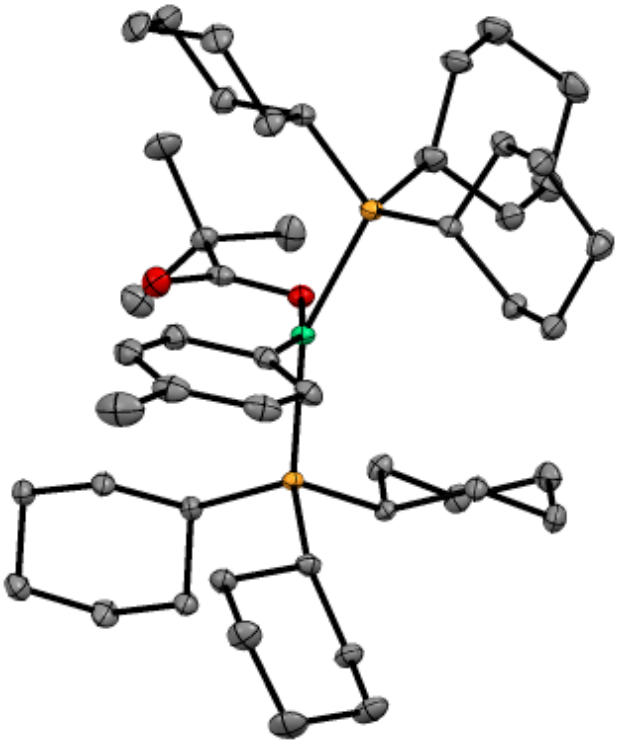

Figure S41. ORTEP Diagram of $(PCy_3)_2Ni(p\text{-Tol})(OPiv)$ **5b.** CCSD deposition number **2017449**

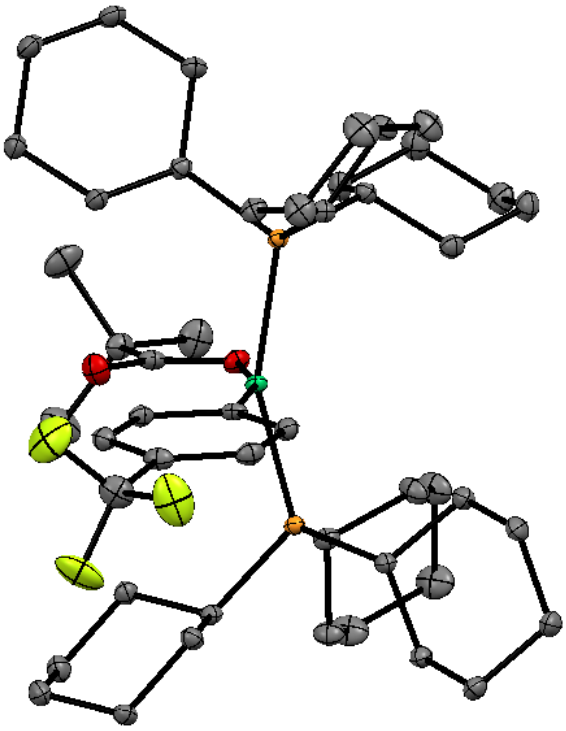

Figure S42. ORTEP Diagram of $(PCy_3)_2Ni(p CF_3\text{-}Ph)(OPiv)$ **5c.** CCSD deposition number **2017447**

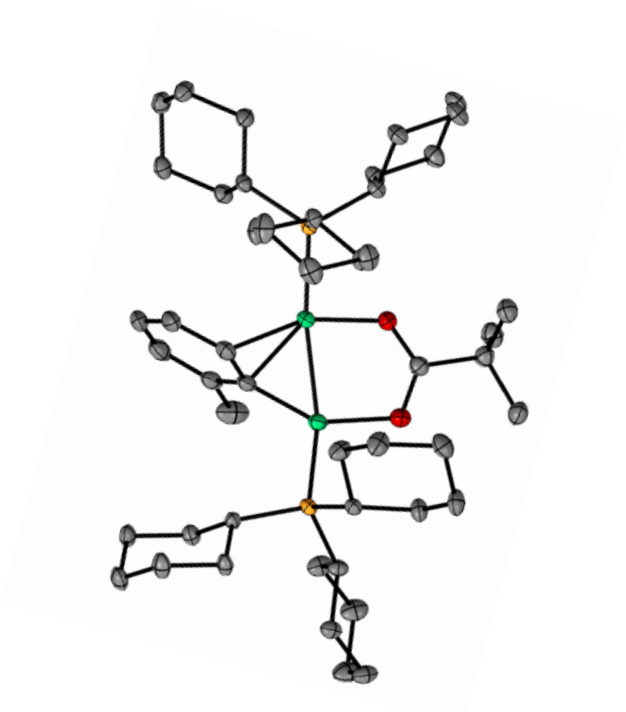

Figure S43. ORTEP Diagram of [Ni(PCy3)]2(μ-η2-1-*o*tolyl)(μ-OPiv) **6a.** CCSD deposition number **2017442**

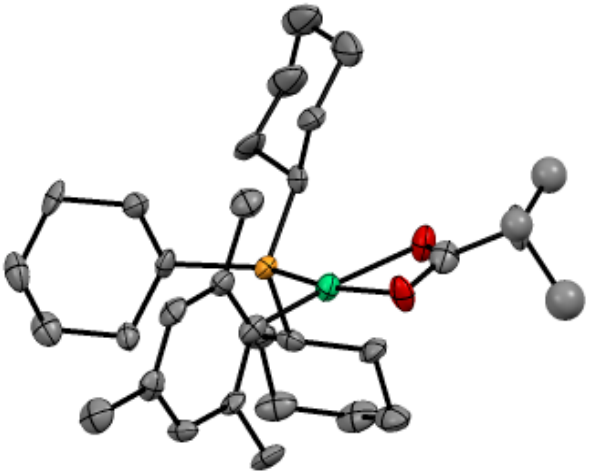

Figure S44. ORTEP Diagram of $(PCy_3)_2Ni(Mesityl)(OPiv)$ **8.** CCSD deposition number **2017444**

B Alert: The value of sine(theta_max)/wavelength is less than 0.575
RESPONSE: This B alert is caused by the weak diffraction power of the crystal due to its small size.

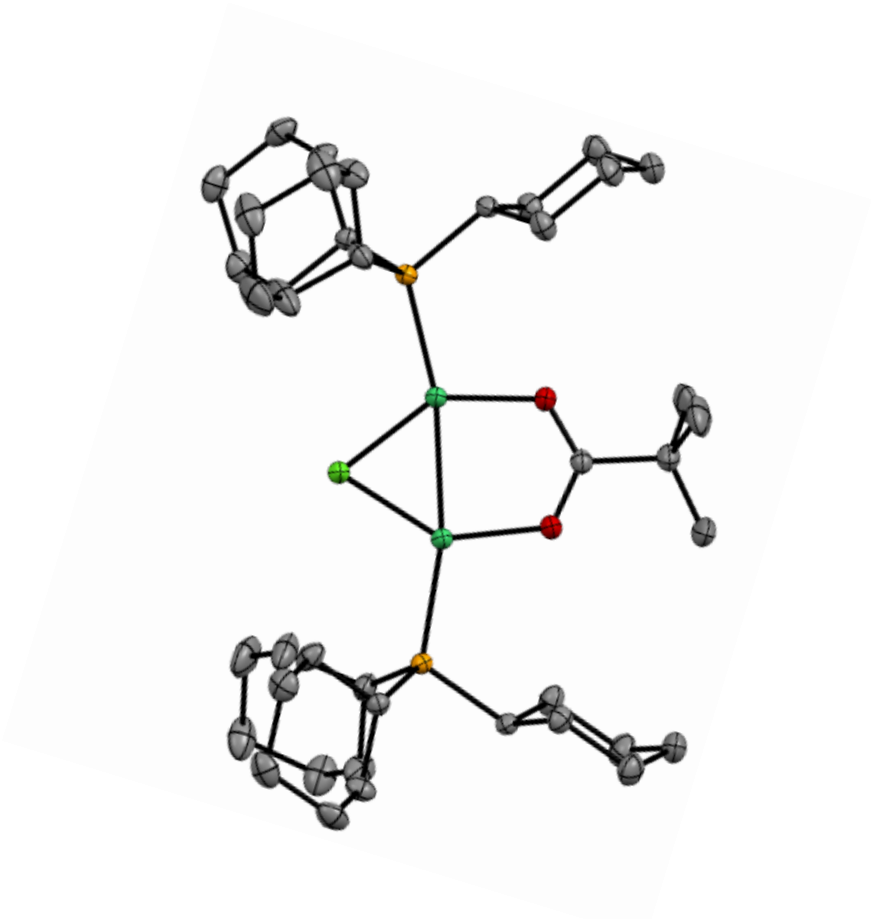

Figure S45. ORTEP Diagram of $[(PCy_3)_2Ni^{I}_2(\mu\text{-}Cl)(\mu\text{-}OPiv)]$ **10.** CCSD deposition number **2017446**

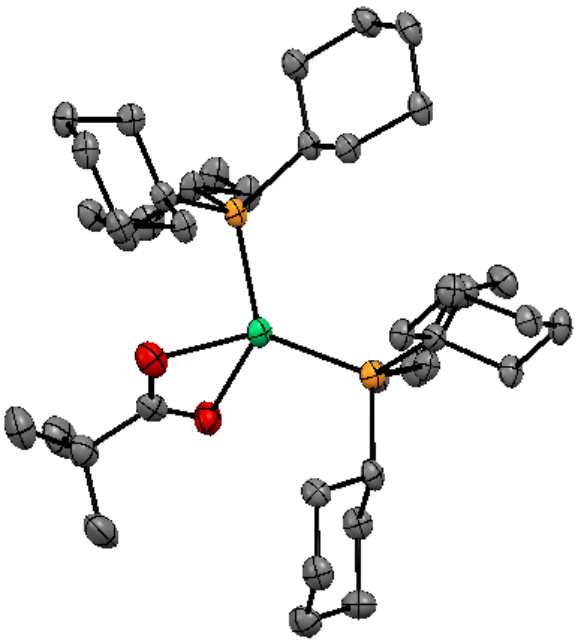

Figure S46. ORTEP Diagram of $(PCy_3)_2Ni^{I}(OPiv)$ **11**. CCSD deposition number **2017445**

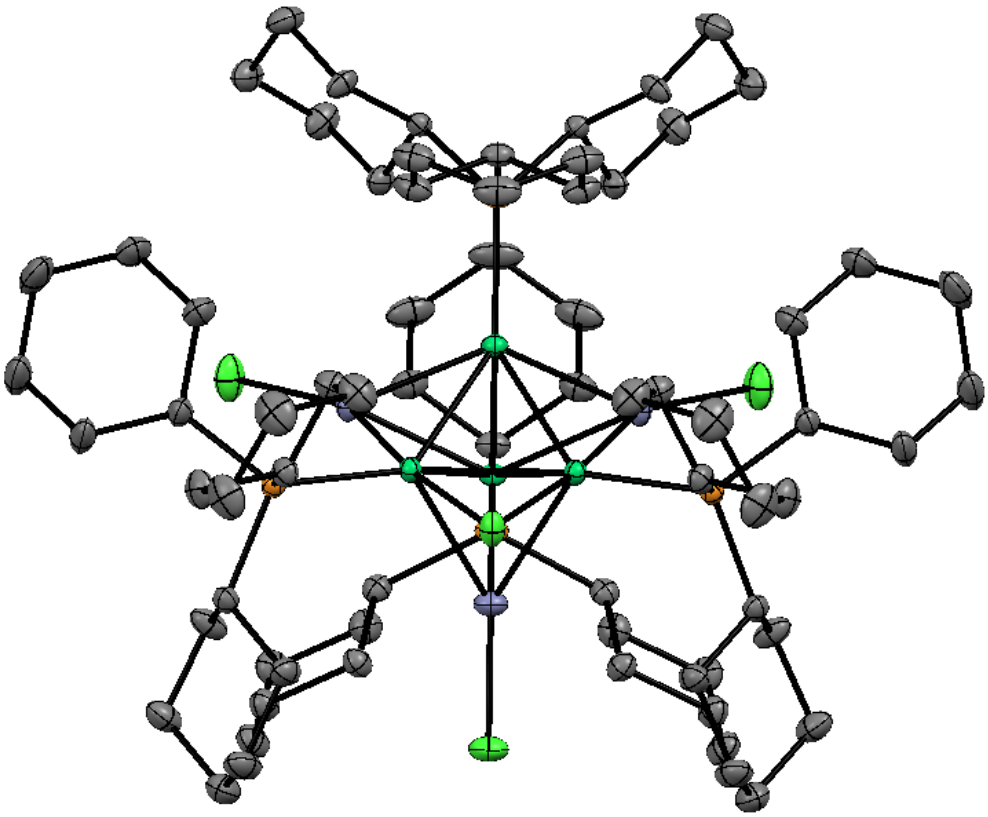

Figure S47. ORTEP Diagram of $Zn_3Ni_4Cl_4P_3C_{73}H_{99}$ **12**. CCSD deposition number **2017450**

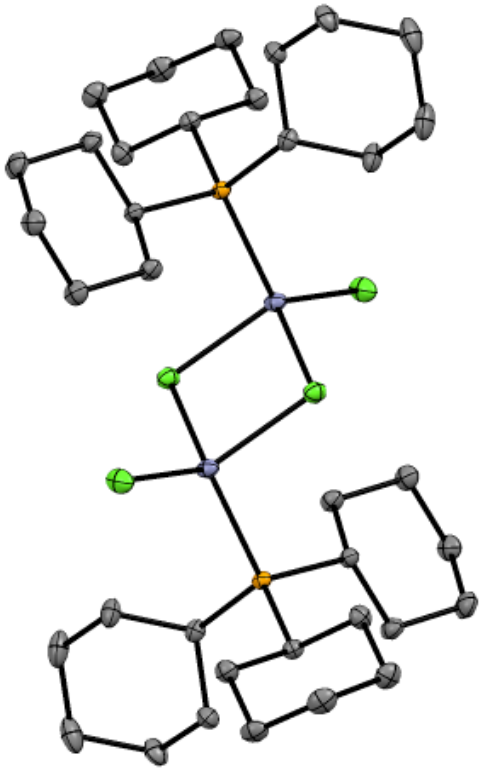

Figure S48. ORTEP Diagram of $[(PCy_3)ZnCl_2]_2$ **13**. CCSD deposition number **2017441**

B Alert: Ratio of Maximum / Minimum Residual Density .... 4.53 Report
RESPONSE: The values of the max and min residual densities are very weak, 0.761 e and 0.168 e, both within the atomic radius of the Zn atom, so they are negligible. Moreover, the R1 =1.8% denotes that the structure quality is unusually good.

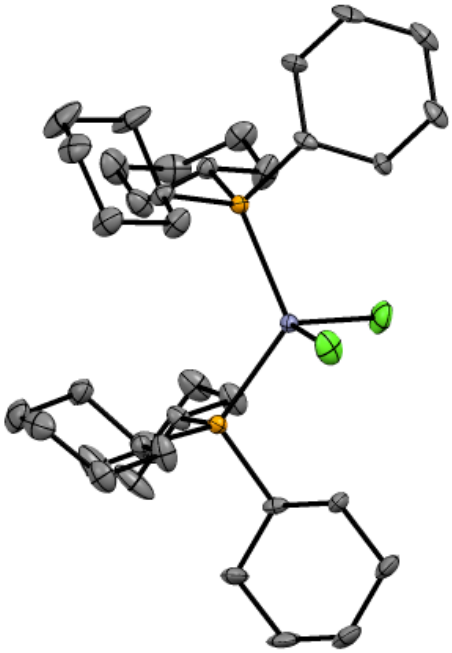

Figure S49. ORTEP Diagram of $(PCy_3)_2ZnCl_2$ **14**. CCSD deposition number **2017443**

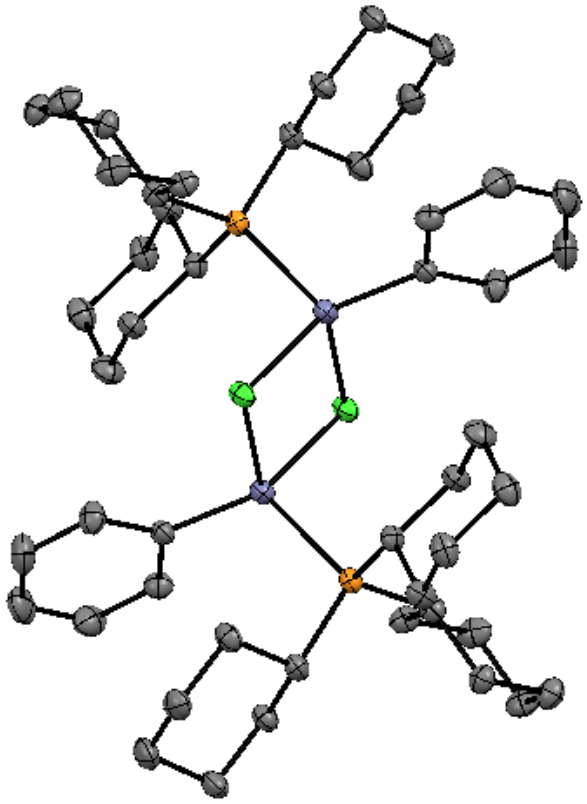

Figure S50. ORTEP Diagram of $[(PCy_3)Zn(Cl)(Ph)]_2$ **17**. CCSD deposition number **2017440**

Table S1. Crystallographic Data

	5a	**5b**	**5c**	**6a**
Formula	$C_{60}H_{102}NiO_2P_2$	$C_{52}H_{90}NiO_3P_2$	$C_{55}H_{87}F_3NiO_2P_2$	$C_{48}H_{82}Ni_2O_2P_2$
Formula weight	976.06	883.88	957.89	870.49
T (K)	100(2)	100(2)	100(2)	100(2)
Wavelength (Å)	0.71073	0.71073	0.71073	0.71073
Crystal system	monoclinic	triclinic	Triclinic	triclinic
Space group	P21/n	P-1	P-1	P -1
***a* (Å)**	11.3012(3)	9.8283(4)	9.791(2)	11.8307(4)
***b* (Å)**	28.9459(8)	13.2541(5)	13.449(3)	12.5291(3)
***c* (Å)**	17.2482(5)	20.5794(7)	20.225(5)	16.7277(4)
***a* (deg)**	90	94.4051(12)	87.810(8)	85.3982(19)
***b* (deg)**	90.0677(8)	103.5746(12)	78.269(7)	80.458(2)
***g* (deg)**	90	108.7519(12)	80.999(7)	68.699(3)
V (Å^3)	5642.3(3)	2433.58(16)	2575.4(10)	2277.61(12)
Z	4	2	2	2
Density (calc.) (Mg/m^3)	1.149	1.206	1.235	1.269
μ (mm^{-1})	0.440	0.505	0.489	0.933
F(000)	2144	968	1036	944
Crystal size (mm^3)	0.200 x 0.100 x 0.010	0.100 x 0.100 x 0.100	0.20 x 0.06 x 0.04	0.200 x 0.100 x 0.060
Theta range for data collection (deg)	1.837 to 31.545	1.032 to 29.717	1.533 to 32.616	2.116 to 33.151
Index ranges	-16<=h<=15,-20<=k<=42,-25<=l<=25	-12<=h<=13,-18<=k<=15,-28<=l<=24	-14<=h<=14,-20<=k<=20,-19<=l<=30	-18<=h<=17,-19<=k<=18,-25<=l<=25
Reflections collected	67764	40923	33336	58665
Independent reflections	18251[R(int) = 0.0464]	13603[R(int) = 0.0473]	16222[R(int) = 0.0451]	16246[R(int) = 0.0544]
Completeness to theta	96.7% 31.545°	98.2% 29.717°	86.2% 32.616	93.5% 33.151°
Absorption correction	Multi-scan	Multi-scan	Empirical	Multi-scan
Max. and min. transmission	0.74 and 0.70	0.74 and 0.69	0.981 and 0.893	1.00 and 0.66
Refinement method	Full-matrix least-squares on F^2	Full-matrix least-squares on F^2	Full-matrix least-squares on F^2	Full-matrix least-squares on F^2
Data / restraints / parameters	18251/ 345/ 774	13603/ 325/ 663	16222/ 129/ 636	16246/ 61/ 545
Goodness-of-fit on F^2	1.026	1.018	1.061	1.073
Final R indices [I>2sigma(I)]	R1 = 0.0447, wR2 = 0.0953	R1 = 0.0489, wR2 = 0.1132	R1 = 0.0459, wR2 = 0.0982	R1 = 0.0545, wR2 = 0.1493
R indices (all data)	R1 = 0.0710, wR2 = 0.1045	R1 = 0.0751, wR2 = 0.1251	R1 = 0.0708, wR2 = 0.1088	R1 = 0.0804, wR2 = 0.1633
Largest diff. peak and hole	0.451 and -0.368 e.Å^{-3}	1.138 and -0.564 e.Å^{-3}	0.551 and -0.490 e.Å^{-3}	1.693 and -1.172 e.Å^{-3}

Table S2. Crystallographic Data

	8	**10**	**11**	**12**
Formula	$C_{32}H_{53}NiO_2$ P	$C_{41}H_{75}ClNi_2O_2P_2$	$C_{41}H_{75}NiO_2P_2$	$C_{76}H_{142}Cl_4Ni_4OP_4Zn_3$
Formula weight	559.42	814.82	720.66	1768.52
T (K)	100(2)	100(2)	100(2)	100(2)
Wavelength (Å)	0.71073	0.71073	0.71073	0.71073
Crystal system	orthorhombic	monoclinic	triclinic	orthorhombic
Space group	P 21 21 21	C2/c	P-1	Pnma
***a* (Å)**	11.7200(9)	25.9197(8)	9.7969(8)	25.13988(19)
***b* (Å)**	14.0642(11)	10.0522(4)	14.2334(10)	22.16329(17)
***c* (Å)**	18.7889(15)	16.3147(6)	15.1145(12)	14.90732(11)
***a* (deg)**	90	90	89.972(2)	90
***b* (deg)**	90	98.3953(10).	78.236(2)	90
***g* (deg)**	90	90	77.843(2)	90
V (Å^3)	3097.0(4)	4205.2(3)	2015.1(3)	8306.10(11)
Z	4	4	2	4
Density (calc.) (Mg/m^3)	1.200	1.287	1.188	1.414
μ (mm^{-1})	0.703	1.067	0.593	1.984
F(000)	1216	1760	790	3744
Crystal size (mm^3)	0.080 x 0.050 x 0.040	0.200 x 0.100 x 0.020	0.100 x 0.050 x 0.020	0.500 x 0.400 x 0.400
Theta range for data collection (deg)	1.809 to 23.030	2.176 to 30.554	1.378 to 26.312	2.310 to 32.230
Index ranges	-12<=h<=10, -15<=k<=15, -20<=l<=20	-36<=h<=32, -14<=k<=14, -23<=l<=15	-12<=h<=11, -17<=k<=11, -18<=l<=18	-37<=h<=37, -33<=k<=33, -22<=l<=21
Reflections collected	33650	21619	18666	291377
Independent reflections	4325[R(int) = 0.1115]	6285[R(int) = 0.0266]	7794[R(int) = 0.0686]	14683[R(int) = 0.0355]
Completeness to theta	99.9% 23.030°	97.4% 30.554°	95.2% 26.312°	97.7% 32.230°
Absorption correction	Multi-scan	Multi-scan	Multi-scan	Multi-scan
Max. and min. transmission	0.74 and 0.56	0.74 and 0.65	0.74 and 0.58	1.00 and 0.68
Refinement method	Full-matrix least-squares on F^2	Full-matrix least-squares on F^2	Full-matrix least-squares on F^2	Full-matrix least-squares on F^2
Data / restraints / parameters	4325/ 54/ 370	6285/ 308/ 333	7794/ 0/ 418	14683/ 328/ 604
Goodness-of-fit on F^2	1.016	0.926	1.015	1.034
Final R indices [I>2sigma(I)]	R1 = 0.0438, wR2 = 0.0865	R1 = 0.0354, wR2 = 0.1126	R1 = 0.0559, wR2 = 0.1108	R1 = 0.0235, wR2 = 0.0621
R indices (all data)	R1 = 0.0656, wR2 = 0.0938	R1 = 0.0483, wR2 = 0.1241	R1 = 0.1130, wR2 = 0.1293	R1 = 0.0291, wR2 = 0.0642
Largest diff. peak and hole	0.233 and -0.282 e.Å^{-3}	0.951 and -0.414 e.Å^{-3}	0.746 and -0.616 e.Å^{-3}	0.583 and -0.541 e.Å^{-3}

Table S3. Crystallographic Data

	13	**14**	**17**
Formula	$C_{36}H_{66}Cl_4P_2Zn_2$	$C_{20}H_{37}ClO_{0.50}PZn_{0.50}$	$C_{48}H_{76}Cl_2P_2Zn_2$
Formula weight	833.36	384.60	916.66
T (K)	100(2)	100(2)	100(2)
Wavelength (Å)	0.71073	0.71073	0.71073
Crystal system	triclinic	orthorhombic	triclinic
Space group	P-1	Fdd2	P-1
***a* (Å)**	9.57195(10)	15.4056(4)	8.5343(3)
***b* (Å)**	10.25467(11)	30.9862(8)	11.3827(5)
***c* (Å)**	10.98752(12)	17.0438(6)	13.3897(5)
***a* (deg)**	93.4549(9)	90	102.806(3)
***b* (deg)**	110.8907(10)	90	95.261(3.
***g* (deg)**	91.0965(9)	90	106.887(3)
V (Å^3)	1004.82(2)	8136.0(4)	1196.57(8)
Z	1	16	1
Density (calc.) (Mg/m^3)	1.377	1.256	1.272
μ (mm^{-1})	1.563	0.843	1.211
F(000)	440	3328	488
Crystal size (mm^3)	0.200 x 0.100 x 0.100	0.100 x 0.100 x 0.050	0.200 x 0.100 x 0.050
Theta range for data collection (deg)	1.989 to 32.226	2.629 to 32.131	2.158 to 32.091
Index ranges	-14<=h<=14,-15<=k<=15,-16<=l<=16	-21<=h<=22,-45<=k<=45,-24<=l<=22	-12<=h<=12,-16<=k<=16,-19<=l<=19
Reflections collected	34210	23701	13348
Independent reflections	6742[R(int) = 0.0162]	6397[R(int) = 0.0225]	13348[R(int) = ?]
Completeness to theta	94.6% 32.226°	95.5% 32.131°	95.2% 32.091°
Absorption correction	Multi-scan	Multi-scan	Multi-scan
Max. and min. transmission	1.00 and 0.87	1.00 and 0.87	1.00 and 0.80
Refinement method	Full-matrix least-squares on F^2	Full-matrix least-squares on F^2	Full-matrix least-squares on F^2
Data / restraints / parameters	6742/ 0/ 199	6397/ 199/ 260	13348/ 0/ 245
Goodness-of-fit on F^2	1.039	1.019	1.036
Final R indices [I>2sigma(I)]	R1 = 0.0182, wR2 = 0.0520	R1 = 0.0249, wR2 = 0.0658	R1 = 0.0361, wR2 = 0.1075
R indices (all data)	R1 = 0.0194, wR2 = 0.0526	R1 = 0.0270, wR2 = 0.0668	R1 = 0.0408, wR2 = 0.1095
Largest diff. peak and hole	0.761 and -0.168 e.Å^{-3}	0.420 and -0.293 e.Å^{-3}	1.023 and -0.349 e.Å^{-3}

2.6.6 References for the Experimental Section

1. Quasdorf, K. W.; Tian, X.; Garg, N. K. Cross-Coupling Reactions of Aryl Pivalates with Boronic Acids. *J. Am. Chem. Soc.* **2008,** *130* (44), 14422-14423.

2. Zarate, C.; Martin, R. A Mild Ni/Cu-Catalyzed Silylation via C–O Cleavage. *J. Am. Chem. Soc.* **2014,** *136* (6), 2236-2239.

3. Guan, B.-T.; Wang, Y.; Li, B.-J.; Yu, D.-G.; Shi, Z.-J. Biaryl Construction via Ni-Catalyzed C−O Activation of Phenolic Carboxylates. *J. Am. Chem. Soc.* **2008,** *130* (44), 14468-14470.

4. Li, B.-J.; Li, Y.-Z.; Lu, X.-Y.; Liu, J.; Guan, B.-T.; Shi, Z.-J. Cross-Coupling of Aryl/Alkenyl Pivalates with Organozinc Reagents through Nickel-Catalyzed C−O Bond Activation under Mild Reaction Conditions. *Angew. Chem. Int. Ed.* **2008,** *47* (52), 10124-10127.

5. Liu, C.; Ni, Q.; Bao, F.; Qiu, J. A simple and efficient protocol for a palladium-catalyzed ligand-free Suzuki reaction at room temperature in aqueous DMF. *Green Chemistry* **2011,** *13* (5), 1260-1266.

6. Semba, K.; Ohtagaki, Y.; Nakao, Y. Arylboration of 1-Arylalkenes by Cooperative Nickel/Copper Catalysis. *Org. Lett.* **2016,** *18* (16), 3956-3959.

7. Christian, A. H.; Müller, P.; Monfette, S. Nickel Hydroxo Complexes as Intermediates in Nickel-Catalyzed Suzuki–Miyaura Cross-Coupling. *Organometallics* **2014,** *33* (9), 2134-2137.

8. Ceder, R.; Muller, G.; Sales, J.; Vidal, J.; Neibecker, D.; Tkatchenko, I. Catalytic dimerization of ethylene to 1-butene by square-planar nickel complexes. *J. Mol. Catal.* **1991,** *68* (1), 23-31.

9. Mohadjer Beromi, M.; Nova, A.; Balcells, D.; Brasacchio, A. M.; Brudvig, G. W.; Guard, L. M.; Hazari, N.; Vinyard, D. J. Mechanistic Study of an Improved Ni Precatalyst for Suzuki–Miyaura Reactions of Aryl Sulfamates: Understanding the Role of Ni(I) Species. *J. Am. Chem. Soc.* **2017,** *139* (2), 922-936.

10. Goel, R. G.; Henry, W. P.; Jha, N. K. Reinvestigation of tricyclohexylphosphine complexes of zinc(II) and cadmium(II) halides. Preparation, characterization, and phosphorus-31 nuclear magnetic resonance and vibrational spectroscopic studies. *Inorg. Chem.* **1982,** *21* (7), 2551-2555.

11. Moers, F. G.; Langhout, J. P. A spectroscopic study of zinc(II), cadmium(II) and mercury(II) complexes with tricyclohexylphosphine as ligand. *Recl. Trav. Chim. Pays-Bas* **1973,** *92* (9), 996-1002.

12. Krasovskiy, A.; Knochel, P. Convenient Titration Method for Organometallic Zinc, Magnesium, and Lanthanide- Reagents. *Synthesis* **2006,** *2006* (5), 0890-0891.
13. Burchat, A. F.; Chong, J. M.; Nielsen, N. Titration of alkyllithiums with a simple reagent to a blue endpoint. *J. Organomet. Chem.* **1997,** *542* (2), 281-283.

Chapter 3: A Room Temperature-Stable Magnesium Electride

Under review in: *Journal of the American Chemical Society*

Research carried out in collaboration with: Cuong Dat Do, Carlota Odena, Jordi Benet-Buchholz, Liang Xu, Cina Foroutan-Nejad, Kathrin H. Hopmann

Author Contribution: C.S.D. designed and carried out all of the experimental reactions and analyzed the data unless otherwise stated. C.O. performed quantitative ^{1}H NMR and EPR experiments on **3** and reductions of (bipy)$NiCl_2$ with KC_8. C. D. D., L. X., and C. F. N. performed computational investigations with C. F. N. and K. H. H guiding these investigations. J. B. solved the crystal structures. C.S.D. and R.M. conceived and designed the experiments and prepared the manuscript. All authors contributed to discussions, commented and edited the manuscript.

3.1 General Introduction

3.1.1 Bipyridine Ligands in Catalysis

Bipyridine ligands have historic and prosperous relationships with main group, transition metal, and materials chemistry.[1] Cited as “the most widely used ligand",[2] the popularity of bipyridines is ascribed to their robust synthesis, tunable steric and electronic properties, modular σ-donating ability of the nitrogen atoms, and π-accepting molecular orbitals. These ligands are involved in rich coordination chemistry with most bipyridine ligands coordinating as bidentate *N,N*- chelating ligands, however are known to also act as monodentate ligands or react by cyclometallation as a *C,N*-donor.[3] In addition, the redox non-innocent character of the bipyridyl core[4-8] and the involvement of metal-to-ligand charge transfer events have enabled new catalytic redox transformations of utmost synthetic relevance for our chemical portfolio (Scheme 3.1).[9-12]

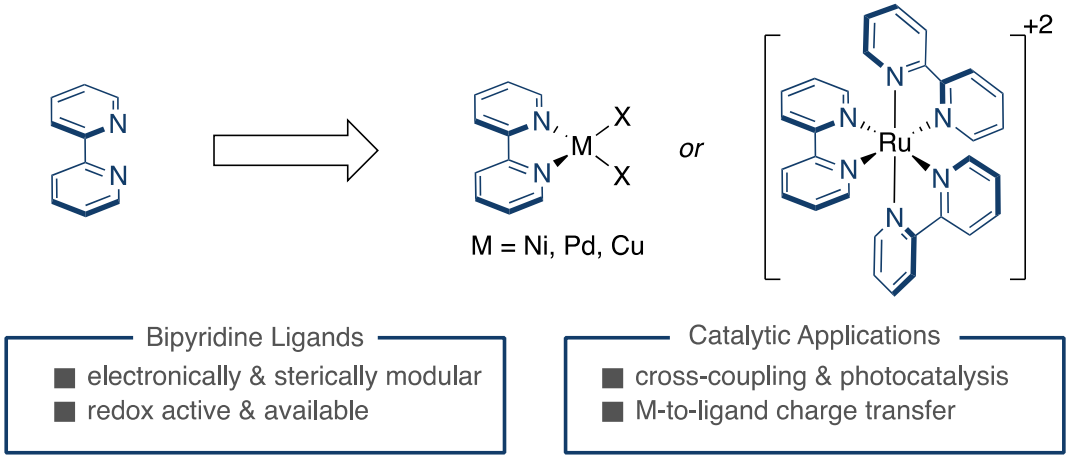

Scheme 3.1. Inherent interest of bipyridine scaffolds.

3.1.2 Bipyridine Ligands in Reductive Cross-Coupling Reactions

The incorporation of polypyridine ligands in Ni-catalyzed reductive coupling reactions has played a critical, yet not fully understood role in modulating both reactivity and selectivity.[13-15] A close inspection of the literature reveals an intriguing threshold in the reductants that are compatible in reductive cross-coupling reactions (Scheme 3.2). While milder Mn or Zn reductants have become routine in these processes with redox active ligands, stronger reductants such as Mg have only found utility in Ni-catalyzed reactions supported by redox-innocent NHC or PR_3 ligands.[16-18]

This apparent reactivity threshold in the use of stronger reductants, along with the mechanistic ambiguity surrounded by the use of heterogeneous metal reductants is particularly problematic as single electron transfer has been proposed as the turnover limiting step in many nickel-catalyzed reductive cross coupling reactions.[19-20]

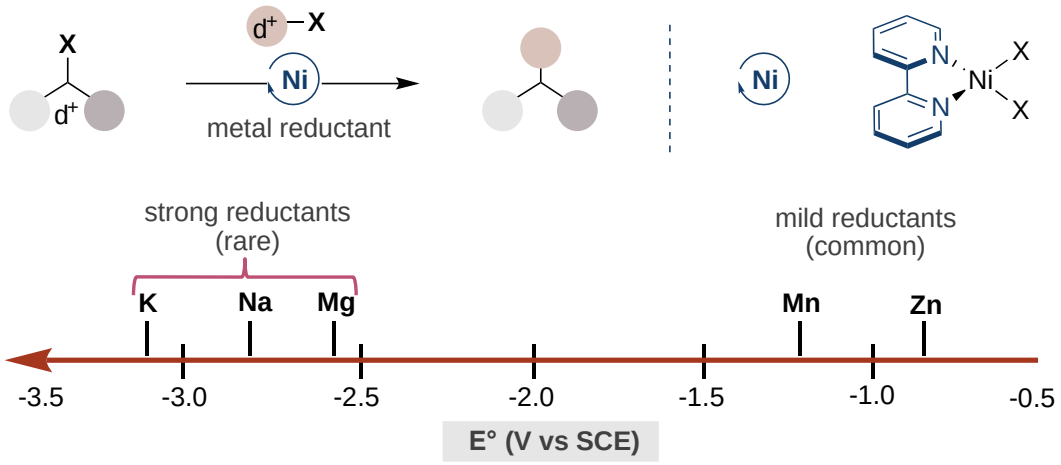

Scheme 3.2. Reductant compatibility with polypyridine ligands in nickel catalysis.

3.1.3 Reduced Bipyridine Ligands

Among various possible reactions between metal reductants and bipyridine ligands is their direct reduction which has long been established for the reaction between bipyridine ligands with reactive group 1 metals. Reports of this date back to the 1960's, in which the *in-situ* reduction of bipyridine by sodium metal was performed to generate the bipyridine radical anion as (bipy^{-})Na which was then later characterized by EPR spectroscopy.[21] Other reports found the bipyridine radical anion could be further reduced to the bipyridine dianion in the synthesis of (bipy^{-2})Na or (bipy)Li$_2$ complexes.[22-23] However, these reports also found that less reducing magnesium metal was only found to reduce bipyridine to the radical anion to give Mg(bipy)$_2$. Since these early reports, others have isolated and characterized both radical anions and dianions of group 1 metals such as (bipy^{2-})(Na^{+}(dme)}$_2$, (bipy^{2-}){Na^{+}(pmdta)}$_2$ and (bipy^{2-})Rb$_2$(en)$_2$.[24-25] Alternatively, the reduction of bipyridine ligated transition-metal complexes have also been reported for bipyridine radical anions and bipyridine dianion complexes. The first characterized example of a bipyridine radical anion was reported in the synthesis of [(CO)$_4$Cr(2,2-bipy)]$^{-}$ on the basis of spectroscopic studies[26] with a more comprehensive analysis provided of a transition-metal complex ligated by a bipyridine radial anion in [K(2,2,2-crypt)][Fe(bipy)(mes)$_2$].[27] Other recent examples include a series of [M(bipy)(mes)$_2$]^{x} complexes (x = 0, -1; M = Cr-Ni)[28] or

$(Cp^*)_2Yb(bipy)$[29] among others. Other reports of metal bipyridine dianions have been proposed as $[Al^{III}(bpy^{2-})_2]^-$,[30] $[Zr^{IV}(bpy^{2-})_3]^{2-}$,[31] and $[(\eta^5\text{-}Cp)_2Zr^{IV}(bpy^{2-})]^0$ (Figure 3.1).[32]

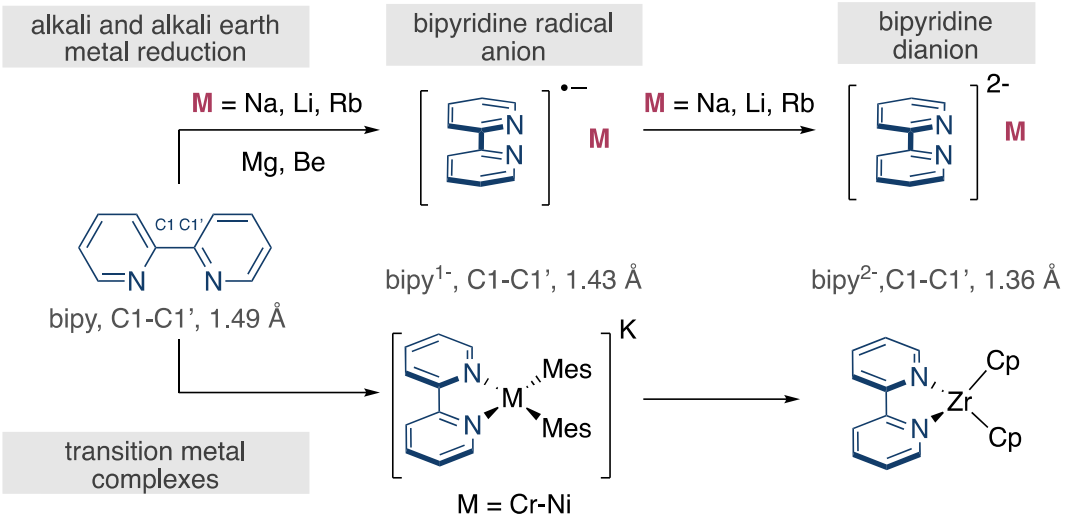

Figure 3.1. Alkali earth metal reduction of bipyridine ligands to the bipyridine radical anion and bipyridine dianion along with transition-metal complexes ligated by bipyridine radical anion or bipyridine dianion ligands.

3.2 General Aim of the Project

Spurred by the contrasting reactivity in nickel-catalyzed reductive cross-electrophile coupling reactions using redox active bipyridine ligands against redox innocent NHC or phosphine ligands, we aimed to better understand contributing factors for this incompatibility. As the redox nature of the bipyridine ligand is likely an origin of the divergent reactivity between these classes of ligands, a particular focus will be spent on determining the fate of the bipyridine ligand (Scheme 3.3). We anticipated that further investigations might uncover opportunities to explore inaccessible chemical transformations while leading to new knowledge in the Ni-catalyzed reductive coupling arena.

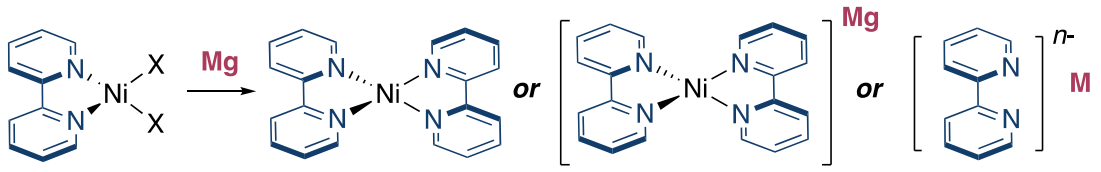

Scheme 3.3. Possible species generated from reduction of (bipy)$NiCl_2$ with magnesium.

3.3 A Room Temperature-Stable Magnesium Electride

3.3.1 Reduction of (bipy)$NiCl_2$ to $[(THF)_4Mg_4(\mu^2\text{-bipy})_4][(THF)_6Mg_2(\mu^2\text{-bipy})(Cl)]$ 3

We began our investigations by monitoring the stoichiometric reduction of (**L1**)$NiCl_2$ **1** (**L1** = 2,2'-bipyridine) with Mg powder ($Mg^{2+/0}$ = –2.61 V vs SCE) in THF-d_8 with additional ligands to stabilize unsaturated nickel species that might be generated upon reduction (Figure 3.2). Interestingly, upfield signals (δ = 6.7 – 4.1 ppm) were observed by ^{1}H NMR spectroscopy after 4 h, which we tentatively attributed to reduced, anionic [$(bipy)_2Ni$] entities. Such speciation is consistent with cyclic voltammetry studies performed by ourselves[33] and Bartak,[34] where reduction of low-valent $(bipy)_2Ni$ (**2**) occurs at ca –2.0 V to afford reduced bipy-Ni species. Analogous reports under strongly reducing conditions have accessed complexes [(bipy)$Ni(Mesityl)_2$][K(2,2,2-crypt)], [(triphos)$Co^{-1}N_2]_2Mg^{II}THF_4$, [$Ni(COD)_2]Li_2$, [K(crown)][(^{t}Bupyrox)$NiNs_2$]$^-$ or [K(crown)] [(^{t}Bupyrox)$Ni(DIPP)_2$]$^-$, supporting the notion that a [$(bipy)_2Ni$]Mg species could be sufficiently long-lived to isolate.[28,35-37] However, workup of the reaction mixture afforded a room temperature stable purple powder which upon crystallization from THF/pentane at –36 °C, led to the unambiguous characterization of an intriguing tetranuclear/dinuclear **3-Mg_4/3-Mg_2** couple $[(THF)_4Mg_4(\mu^2\text{-bipy})_4][(THF)_6Mg_2(\mu^2\text{-bipy})(Cl)]$ **3** by X-Ray crystallography which was reproducibly solved 16 times (Figure 3.2).[33] Interestingly, the ^{1}H NMR signals of **3** overlayed those observed *in-situ* upon stoichiometric reduction of (bipy)$NiCl_2$ **1** with Mg indicating our initial tentative prediction of an anionic $[(bipy)_2Ni]^-$ complex was incorrect. Furthermore, the formation of $(bipy)_2Mg(THF)_2$ competes with **3** if incomplete reduction occurs. Further information and the X-ray structure of this complex is included in the Supporting information. Direct reduction of bipy or other polypyridine ligands with magnesium did not generate ligand dianions of magnesium in high yields.

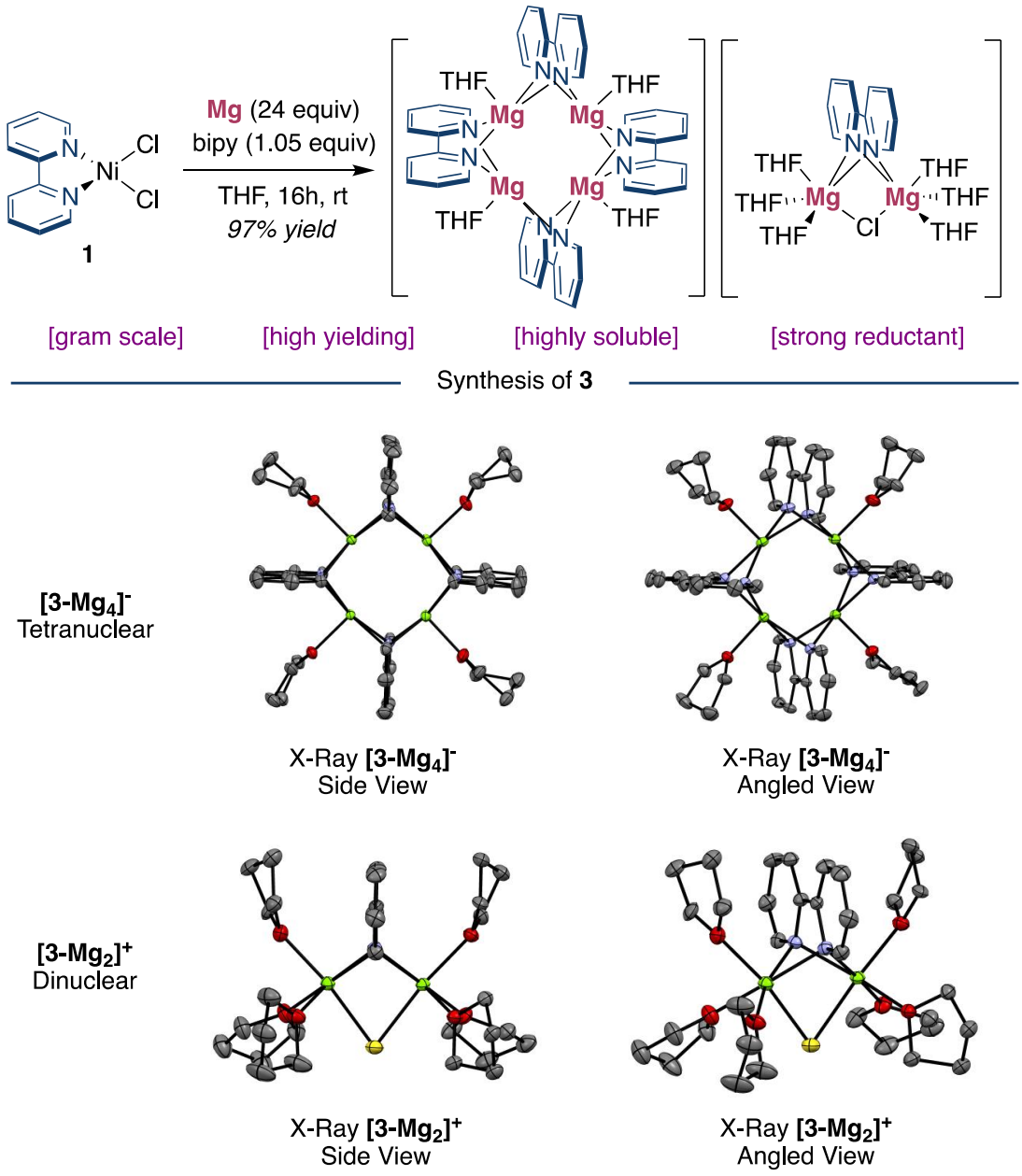

Figure 3.2 Synthesis, and crystal structure, of **3-Mg$_4$** and **3-Mg$_2$**. X-ray structures are shown with thermal ellipsoids drawn at the 50% probability level (see the Supporting Information for details and labeled structures). Selected distances (Å): C_{py}–C_{py}; C5B–C6B 1.374(5), C5A–C6A 1.382(5) Example Mg–Mg distance; Mg1B–Mg2B 2.8246(16).

Comparison of the interpyridyl C_{py}–C_{py} bonds of **3** with bipyridine radical anions (bipy^{1-}, 1.429 Å)[25] or free ligand (bipy, 1.494 Å),[38] reveals that **3** contains particularly contracted C_{py}–C_{py} linkages ranging from 1.369(5) Å to 1.382(5) Å (avg 1.376 Å). These interpyridyl C_{py}–C_{py} bond lengths of **3** are comparable to bipy^{2-} complexes of alkali metals[24-25] (Figure 3.3) with bond lengths similar to (bipy^{2-})(Na^{+}(dme)}$_2$ **Na-1**, [(bipy^{2-})$_2$] **Na-2** and its (bipy)Rb$_2$(en)$_2$ **Rb-1** analogue (Figure 3.3). This drastic

contraction reports directly on the localization of the electron density, suggesting electron occupation of the π^*-antibonding orbital and increased bonding character between the in-phase C_{py}–C_{py} bonds which results in an antiaromatic bipyridine ring system on the basis of the ring current analysis. Fragement charges were obtained to be 1.80 and 1.66 for bipyridine in **[3-Mg$_4$]**$^-$ and **[3-Mg$_2$]**$^+$. Current density analysis on **[3-Mg$_2$]**$^+$ sustains a paramagnetic current with a strength of 2.6 nA.T^{-1} that is characteristic of a weakly antiaromatic ring.[24-25,39]

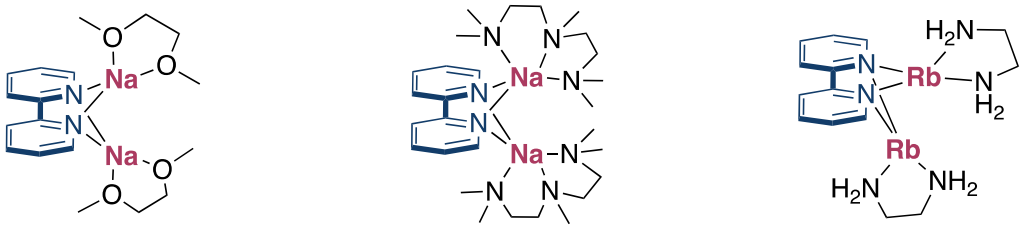

Na-1 C_{py}-C_{py} = 1.375 Å

Na-2 C_{py}-C_{py} = 1.375 Å

Rb-1 C_{py}-C_{py} = 1.399 Å

Figure 3.3. Alkali and alkali earth metal bipy complexes. X-ray structures of bipyridine dianions.[24-25]

The rare, symmetric binding mode of bipyridine ligands in **3** indicates that two bonding interactions are available from the N orbital lone pair and HOMO π^* orbital to magnesium, further advocating the notion that a bipy^{2-} entity is generated upon reduction of the bipyridyl core. The symmetric macrostructure and unique bond angles found in **3**, with Mg–N–Mg bond angles of 103° for the edges in **3-Mg$_4$** and 109° for the binuclear moiety **3-Mg$_2$** are among the few examples bearing symmetrically bridging μ^2-bipy ligands such as (**Na-1** and **Na-2**) or trinuclear species (Yb(μ^2-bipy)(THF)$_2$)$_3$[39] with no similar tetranuclear structures reported.

UV-VIS absorption and IR data corroborated the assignment of a bipyridine dianion in **3**.[33] Variable temperature ^{1}H NMR and DOSY spectroscopic experiments suggested that the multiple ^{1}H NMR signals observed at room temperature (Figure 3.4) originate from fluxional lower order and higher order species, which coalesced upon warming (ca. 55°C) to a single set of signals (Figure 3.4 – major signals). Quantitative EPR measurements of **3** also revealed the presence of a single electron with g = 2.00185.

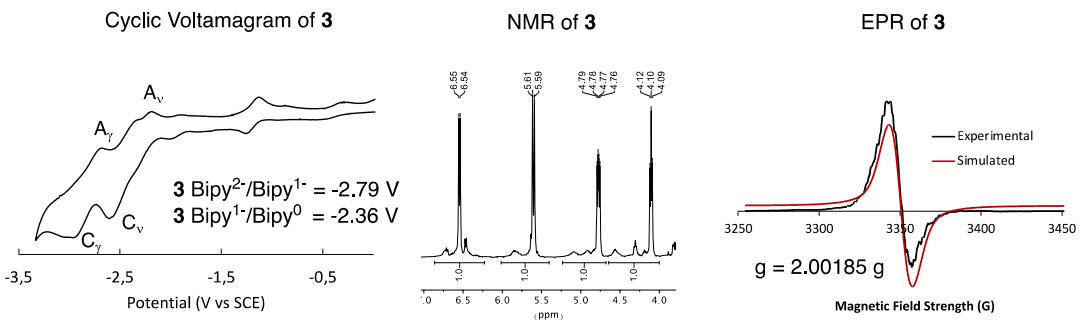

Figure 3.4. Characterization of **3-Mg$_4$** and **3-Mg$_2$**

3.3.2 Computational Analysis of 3

Initially, we visualized the electronic structure of **3** as a neutral **3-Mg$_4$** and a radical **3-Mg$_2$** unit with mixed valency Mg(I)–Cl and Mg(II) centers. However, density functional theory (DFT, PBE0-D3BJ/6-31+G(d,p)[IEFPCM:THF])[33] studies showed that the optimized geometries of the neutral **3-Mg$_4$/3-Mg$_2$** couple deviated significantly from the experimental X-ray structure. Further computation showed that an ion pair of singlet [**3-Mg$_2$**]$^+$ and radical [**3-Mg$_4$**]$^-$ is 11.7 kcal/mol more stable than the neutral structure, and shows bond distances closely matching experimental values (Figure 3.5). The ion-pair formation likely originates from the significant instability of Mg(I) atoms[40] which rapidly lose an electron to form the [**3-Mg$_4$**]$^-$/[**3-Mg$_2$**]$^+$ couple. Quantum theory of atoms in molecules (QTAIM) analysis[41] displayed high atomic charges (1.75 and 1.68 for [**3-Mg$_2$**]$^+$ and [**3-Mg$_4$**]$^-$, respectively) and QTAIM localization indices λ(Mg) close to 10, suggesting that all Mg atoms in **3** are Mg(II). Localization index is a less known QTAIM-based index that defines the population of an atomic basin minus the shared electrons. The difference between the localization index and atomic number provides an excellent measure of the charge of an atom after the ionic approximation for heteroatomic bonds corresponding to the IUPAC definition of oxidation state.

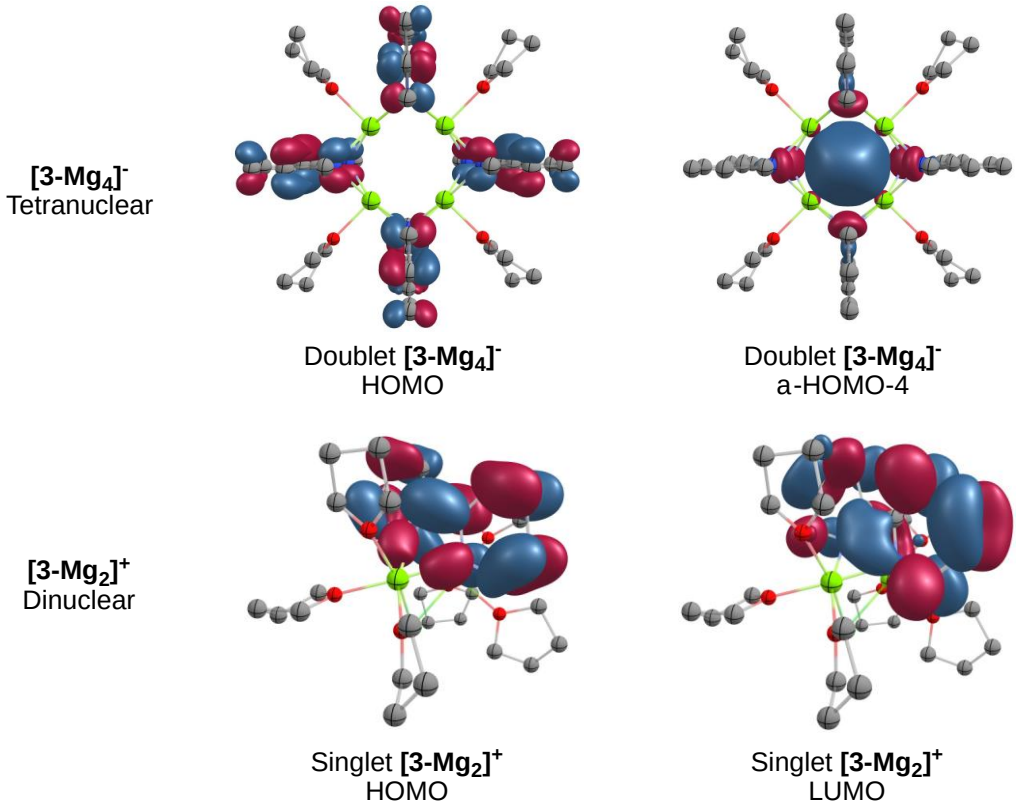

Figure 3.5. DFT orbital analysis of **3-Mg$_4$** and **3-Mg$_2$**. HOMO, LUMO and SOMO (HOMO-4) orbitals for **3-Mg$_4$** and **3-Mg$_2$** (PBE0-D3BJ/6-31+G(d,p)[IEFPCM:THF]).

While **3** contains short Mg–Mg distances that average 2.8533(17) Å, comparable to those reported in Jones's Mg(I)–Mg(I) dimer of 2.8457(8) Å;[42] no chemical bond between Mg(II) atoms is expected as they possess no valence electron to form a bond. QTAIM analysis on [**3-Mg$_4$**]$^-$ confirms this hypothesis.[33] Therefore we attribute the short distances to the bipyridine ligands templating the Mg atoms.[43]

With all Mg centres and bipy ligands of **3** assigned to Mg(II) and bipy^{2-}, respectively, the intriguing question arises of where the radical electron of [**3-Mg$_4$**]$^-$ is located. Interestingly, the crystallographic data consistently showed a residual electron density at the center of **3-Mg$_4$** (Figure 3.6), providing the fascinating possibility that this species is an electride. Electrides are materials that hold a free electron in a cavity formed by cations,[41,44] and to this date, only eight organic electrides have been experimentally characterized, of which only one is room temperature-stable.[45] Remarkably, QTAIM reveals the presence of a nonnuclear attractor (NNA) with a charge of -0.48 in the center of [**3-Mg$_4$**]$^-$, strongly supporting that it is an electride. The electride electron is topologically encaged by the interaction of 6/6' hydrogen atoms of bipyridine, within a capsule with an approximate length of 0.4 nm (Figure 3.6), akin to previously known organic electrides.[43] The NNA appears only in the α-electron (not

the β-electron) density and coincides with both the maximum of the spin density and the orbital HOMO-4, which we identify to be the SOMO of [**3-Mg$_4$]**$^-$, indicating SOMO-HOMO inversion.[33,46] The combined X-ray, DFT, and QTAIM results provide compelling evidence that [**3-Mg$_4$]**$^-$ is a room-temperature stable electride composed of [**3-Mg$_4$]** and a genuine free electron captured at its centre.

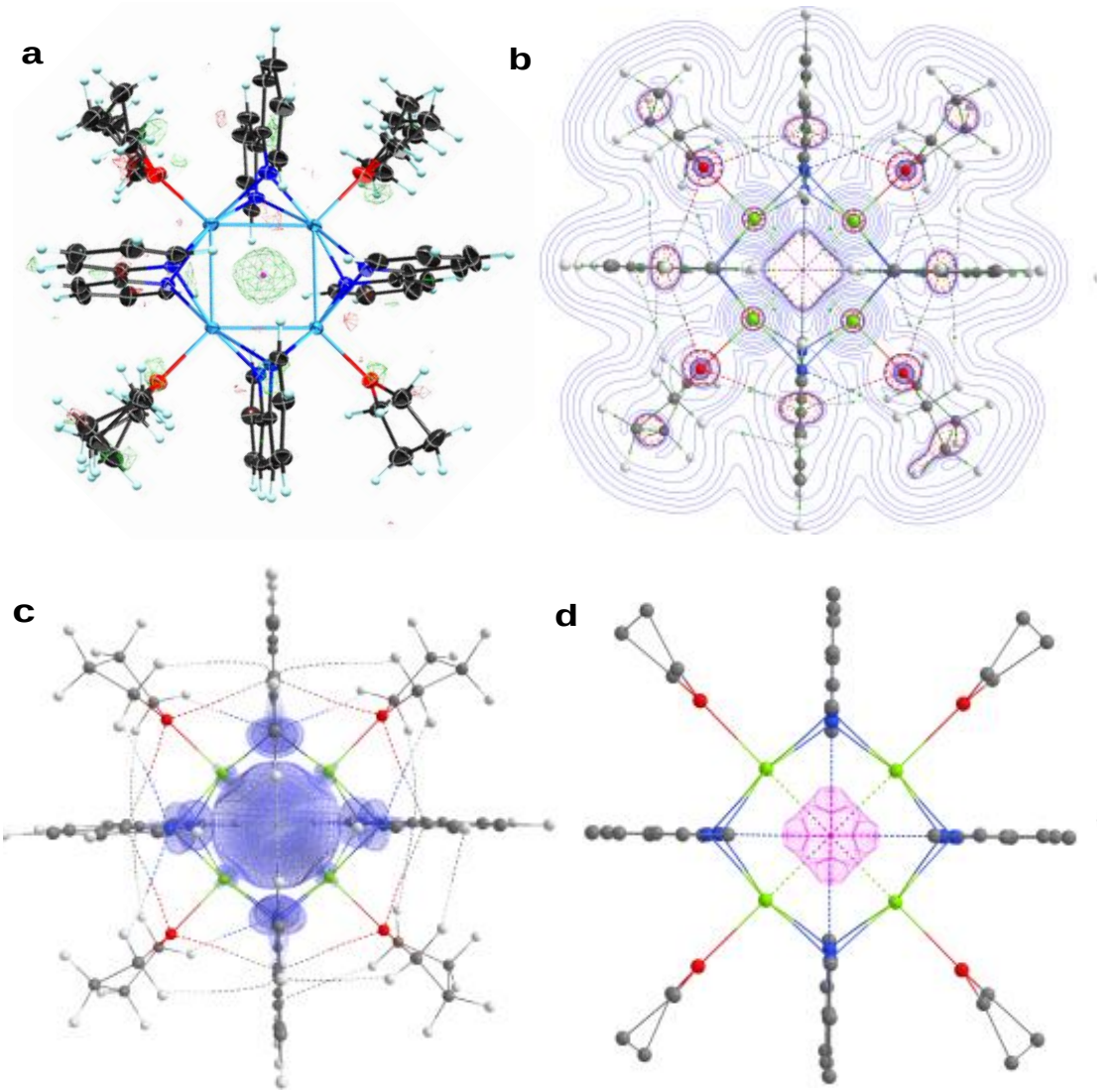

Figure 3.6. Topology of the electron density of **[3-Mg$_4$]**$^-$ containing an electride. **a**: X-ray structure showing residual electron density, **b**: QTAIM contour plots of the Laplacian of the electron density, and **c**: Its 3D- presentation with an isosurface of -0.005 au, **d:** QTAIM analysis showing that the spin density is concentrated in the middle of the Mg-cage and coinciding with the non-nuclear attractor.

Typically, organic electrides are synthesized by reacting nitrogen-donor ligands such as aza-crown ethers with alkali metals. However, these alkali cation-nitrogen systems form weak bonds, implying that most known organic electrides decompose at or above room temperature.[43] [**3-Mg$_4$]**$^-$ has strong Mg(II)–(bipy^{2-}), and four Mg(II) •••

e^- interactions, which stabilize the structure via electrostatic forces. To the best of our knowledge, **3-Mg$_4$** is the first experimentally known example of an Mg electride[47] as well as the first known example employing bipyridine as a stabilizing ligand in an electride.[44]

In light of these results, we believe **3** complements existing reports of bipyridine dianions with highly reducing alkali metals,[24-25] while offering (a) access to a room temperature-stable electride (b) new considerations into the redox chemistry of bipyridine ligands, (c) potential new applications of **3** as a mild, homogeneous reductant, and (d) the formation of macrostructures that group 1 analogs are not suited to. Slightly analogous macrostructures such as [$Na_4Mg_2(TMP)_6(C_6H_3OMe$-2,5)] (TMP = 2,2,6,6-tetramethylpiperidide) or [$KMg(TMP)_2{}^n$Bu] have demonstrated innovative solutions to C(sp^2) magnesiation and subsequent functionalization reactions.[48-51] In addition, the identification of **3** from the direct reduction of bipyridine-ligated nickel species demonstrates their susceptibility to participate in electron transfer processes. This observation is particularly important, tacitly suggesting that care should be taken when generalizing reactivity found in Ni-catalyzed processes, particularly within the context of catalytic reductive couplings that utilize either strong metallic reductants or homogenous photocatalysts.[4-8,10-15]

3.3.3 Reduction of sterically encumbered 6,6-disubstituted ligands

Taking into consideration the influence exerted by sterically encumbered 2,2-bipyridine ligands on reactivity,[52-58] we turned our attention to investigating the generality of accessing reduced polypyridine-Mg species other than **3**, as it might pave the way for future synthetic applications and an improved understanding. To this end, an otherwise similar route to that shown for **3** was followed for more sterically congested **L2** (6,6'-dimethyl-4,4'-diphenyl-2,2'-bipyridine), using (**L2**)$NiBr_2$ (**4**) as a precursor (Figure 4). Gratifyingly, we were able to isolate a moisture and oxygen-sensitive black powder which was characterized by X-Ray diffraction as the monomeric structure **5·THF**. The divergent structure of bis-ligated, monomeric magnesium complex **5**, when compared to **3** reinforces the modularity exerted by polypyridine ligands and the generality of ligand reduction but also the unique reactivity of **3** to stabilize a free electron. A comparison of the C_{py}–C_{py} bond length of **L2** and **5·THF** reveals a small contraction in the latter (1.496(3) Å vs 1.443(3) Å), suggesting each of the two bipy ligands in **5** bears one electron as a radical anion, bound to a Mg(II) centre.

This interpretation gains credence by observing an EPR signal at g = 2.00285, with DFT calculations supporting a biradical electronic state, with one unpaired electron on each bpy unit (Figure 3.7). While the preferred electronic state for **5** is a triplet, our calculations indicate that the open-shell singlet is only slightly higher in energy,[33] suggesting that **5** may behave as a spin crossover complex.

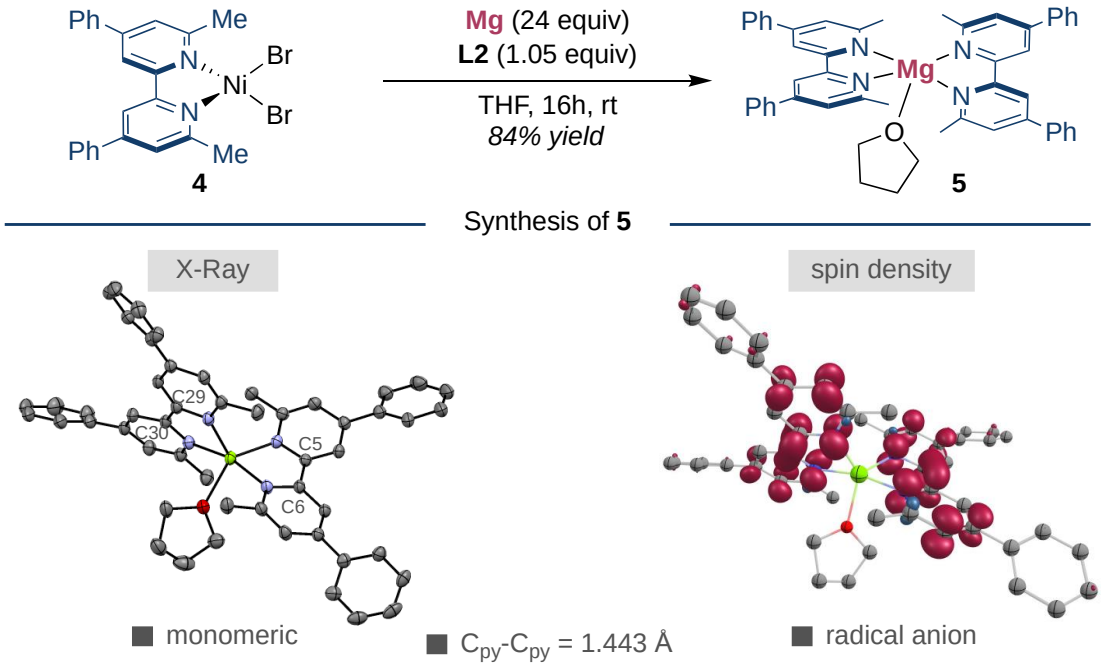

Figure 3.7. Reduction of Sterically Encumbered Ligand. Synthesis, DFT spin density, and X-ray structure of **5** with thermal ellipsoids drawn at the 50% probability level. Selected distances (Å) C_{py}–C_{py}; C5–C6 1.443(3), C29–C30 1.442(3).

3.3.4 Applications of Mg Complexes as Readily Handled Reductants

The rapid, reliable, and ease of synthesis of **3** and **5**, together with the wide range of redox potentials that could be accessed by fine-tuning the substituents on the bipyridyl core argues well for their utilization as homogeneous reductants.[59-62] Aimed at unraveling the potential of these complexes, we benchmarked their ease of handling and tunable reactivity by accessing low-valent $(bipy)_2Ni(0)$ complexes (Figure 3.4), compounds of utmost mechanistic relevance in Ni-catalyzed reactions.[4-8,10-15,63-64] Unlike their *ortho* substituted 2,2'-bipyridyl analogues,[65-66] the synthesis of $(bipy)_2Ni(0)$ (**2**) requires challenging experimental setups such as metal vapor synthesis,[34] or heterogeneous reductants such as Li metal, which suffer from competing overreduction, poor scalability, and irreproducibility. [42,59-62]

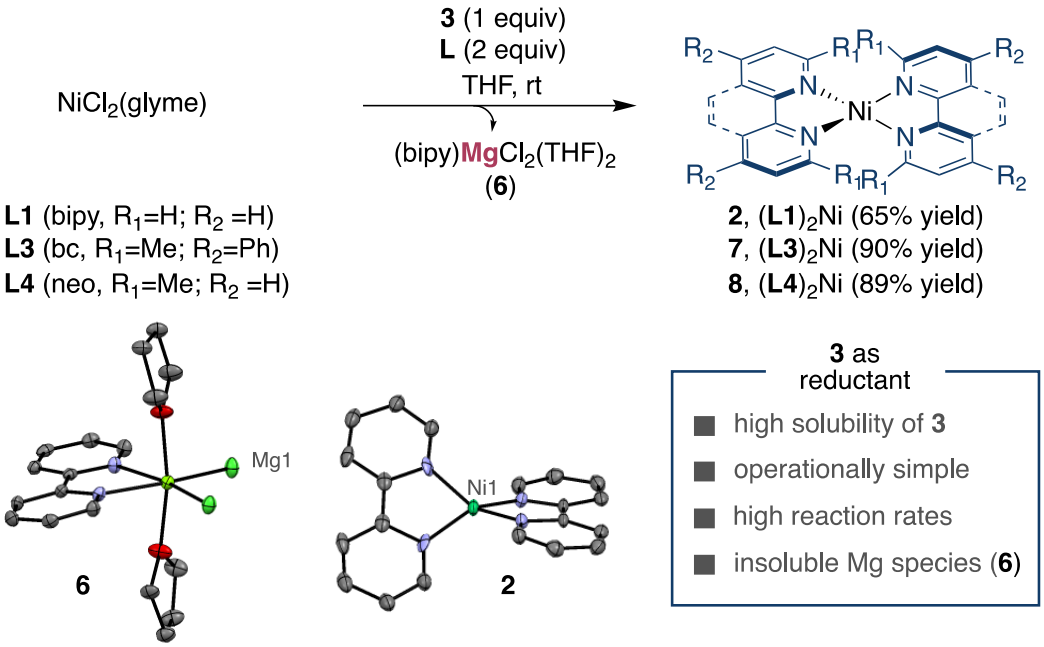

Scheme 3.4. Homoleptic Ni(0) polypyridine complexes.

Gratifyingly, the utilization of **3** as homogenous reductant cleanly delivered $(bipy)_2Ni(0)$ in 65 % yield after 1 h reaction time, together with the formation of insoluble $(bipy)MgCl_2(THF)_2$ (**6**) which was confirmed by X-ray diffraction (Scheme 3.4).[33] Notably, ligands other than bipy could be employed with equal ease, as **7** or **8** was easily within reach from $NiCl_2(glyme)$ and **L3** or **L4** (**L3** = bathocuproine, **L4** = neocuproine) with **3**.[69] Indeed, traces, if any, of **2** are observed after exposure of $Ni(COD)_2$ to bipy[67-68] or by reaction of **1** with Mn, Zn or Mg (Scheme 3.5, *left*).[33] Such lack of reactivity can tentatively be attributed to both slow electron transfer rates[19-20] and the deleterious impact that inorganic salts formed post-reduction (MCl_2; M = Mn, Zn, Mg) might have on the reaction outcome.

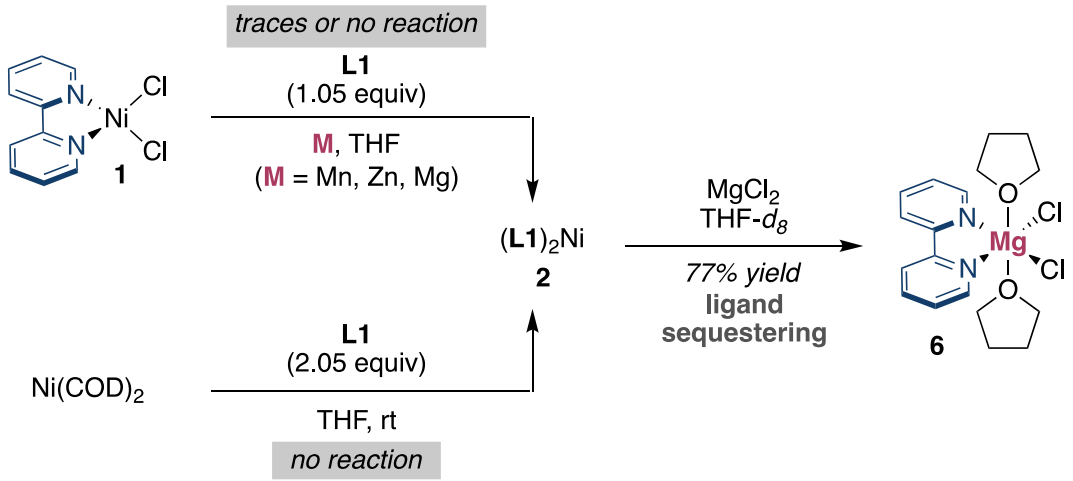

Scheme 3.5. Failed routes towards **2** and ligand sequestering.

Our hypothesis that $MgCl_2$ salts formed using heterogeneous Mg as a reductant would be deleterious was confirmed by reacting **2** with $MgCl_2$, leading to both rapid decomposition of the former and formation of **6** (Scheme 3.5, *right*). These findings highlight the importance of **3** forming highly coordinated and insoluble Mg complexes of type **6** en route to low-valent Ni(0) complexes, thus avoiding parasitic ligand sequestering events.

3.4 Conclusions

In summary, we have synthesized and isolated unorthodox Mg complexes that do not only represent the first example of group 2 metal reduction to bipyridine dianions and an unprecedented room-temperature stabilized electride by magnesium but also offer new opportunities for accessing elusive metal intermediates that were otherwise inaccessible by operationally simple techniques. We have additionally demonstrated the importance of ligand sequestering events in decomposition pathways, and solutions to overcome these limitations.

Future investigations into modifying the bipyridine backbone may provide insights into controlling the structural features of complexes like **3**. As seen with compound **5**, electron donating substituents such as alkyl groups may make the bipyridine ligands challenging to reduce to its dianion formulation but more easily reduced analogues such as 4,4'-diphenyl-2,2'-bipyridine may afford similar structures to **3**. Alternatively, combining the features of electrides to be conductive materials and the ability of bipyridine ligands to also readily transfer electronic information may offer the possibility that polymetric formulations based on **3** could act as highly conductive materials.

3.5 References

1. Constable; Housecroft The Early Years of 2,2'-Bipyridine—A Ligand in Its Own Lifetime. *Molecules* **2019,** *24* (21), 3951.

2. Kaes, C.; Katz, A.; Hosseini, M. W. Bipyridine: The Most Widely Used Ligand. A Review of Molecules Comprising at Least Two 2,2'-Bipyridine Units. *Chem. Rev.* **2000,** *100* (10), 3553-3590.

3. Constable, E. C.; Housecroft, C. E. More hydra than Janus – Non-classical coordination modes in complexes of oligopyridine ligands. *Coord. Chem. Rev.* **2017,** *350*, 84-104.

4. Lyaskovskyy, V.; de Bruin, B. Redox Non-Innocent Ligands: Versatile New Tools to Control Catalytic Reactions. *ACS Catal.* **2012,** *2* (2), 270-279.

5. Luca, O. R.; Crabtree, R. H. Redox-active ligands in catalysis. *Chem. Soc. Rev.* **2013,** *42* (4), 1440-1459.

6. Kaim, W. The Shrinking World of Innocent Ligands: Conventionaland Non-Conventional Redox-Active Ligands. *Eur. J. Inorg. Chem.* **2012,** *2012* (3), 343-348.

7. Butschke, B.; Fillman, K. L.; Bendikov, T.; Shimon, L. J. W.; Diskin-Posner, Y.; Leitus, G.; Gorelsky, S. I.; Neidig, M. L.; Milstein, D. How Innocent are Potentially Redox Non-Innocent Ligands? Electronic Structure and Metal Oxidation States in Iron-PNN Complexes as a Representative Case Study. *Inorg. Chem.* **2015,** *54* (10), 4909-4926.

8. Hu, X. Nickel-catalyzed cross coupling of non-activated alkyl halides: a mechanistic perspective. *Chem. Sci.* **2011,** *2* (10), 1867-1886.

9. Wang, C.-S.; Dixneuf, P. H.; Soulé, J.-F. Photoredox Catalysis for Building C–C Bonds from C(sp2)–H Bonds. *Chem. Rev.* **2018,** *118* (16), 7532-7585.

10. Twilton, J.; Le, C.; Zhang, P.; Shaw, M. H.; Evans, R. W.; MacMillan, D. W. C. The merger of transition metal and photocatalysis. *Nat. Rev. Chem.* **2017,** *1* (7), 0052.

11. McAtee, R. C.; McClain, E. J.; Stephenson, C. R. Illuminating photoredox catalysis. *Trends in Chemistry* **2019,** *1* (1), 111-125.

12. Shaw, M. H.; Twilton, J.; MacMillan, D. W. C. Photoredox Catalysis in Organic Chemistry. *J. Org. Chem.* **2016,** *81* (16), 6898-6926.

13. Everson, D. A.; Weix, D. J. Cross-Electrophile Coupling: Principles of Reactivity and Selectivity. *J. Org. Chem.* **2014,** *79* (11), 4793-4798.

14. Weix, D. J. Methods and Mechanisms for Cross-Electrophile Coupling of Csp^2

Halides with Alkyl Electrophiles. *Acc. Chem. Res.* **2015,** *48* (6), 1767-1775.

15. Diccianni, J.; Lin, Q.; Diao, T. Mechanisms of Nickel-Catalyzed Coupling Reactions and Applications in Alkene Functionalization. *Acc. Chem. Res.* **2020,** *53* (4), 906-919.

16. Liu, L.; Wang, Y.; Zeng, Z.; Xu, P.; Gao, Y.; Yin, Y.; Zhao, Y. Nickel(II)-Magnesium-Catalyzed Cross-Coupling of 1,1-Dibromo-1-alkenes with Diphenylphosphine Oxide: One-Pot Synthesis of (E)-1-Alkenylphosphine Oxides or Bisphosphine Oxides. *Adv. Synth. Catal.* **2013,** *355* (4), 659-666.

17. Li, R.-P.; Shen, Z.-W.; Wu, Q.-J.; Zhang, J.; Sun, H.-M. N-heterocyclic carbene ligand-controlled regioselectivity for nickel-catalyzed hydroarylation of vinylarenes with benzothiazoles. *Org. Lett.* **2019,** *21* (13), 5055-5058.

18. Zhang, J.; Lu, G.; Xu, J.; Sun, H.; Shen, Q. Nickel-catalyzed reductive cross-coupling of benzyl chlorides with aryl chlorides/fluorides: a one-pot synthesis of diarylmethanes. *Org. Lett.* **2016,** *18* (12), 2860-2863.

19. Lin, Q.; Diao, T. Mechanism of Ni-Catalyzed Reductive 1,2-Dicarbofunctionalization of Alkenes. *J. Am. Chem. Soc.* **2019,** *141* (44), 17937-17948.

20. Till, N. A.; Tian, L.; Dong, Z.; Scholes, G. D.; MacMillan, D. W. C. Mechanistic Analysis of Metallaphotoredox C–N Coupling: Photocatalysis Initiates and Perpetuates Ni(I)/Ni(III) Coupling Activity. *J. Am. Chem. Soc.* **2020,** *142* (37), 15830-15841.

21. Zahlan, A.; Heineken, F.; Bruin, M.; Bruin, F. ESR Spectrum of 2,2′Dipyridyl-Na Complex. *J. Chem. Phys.* **1962,** *37* (3), 683-684.

22. Herzog, S.; Taube, R. Neutralkomplexe des 2,2′-Dipyridyls Teil I Darstellung und Eigenschaften. *Zeitschrift für Chemie* **1962,** *2* (6-7), 208-214.

23. Taube, R.; Herzog, S. Neutralkomplexe des 2,2′-Dipyridyls Teil II Bindungsverhältnisse. *Zeitschrift für Chemie* **1962,** *2* (8), 225-237.

24. Bock, H.; Lehn, J.-M.; Pauls, J.; Holl, S.; Krenzel, V. Sodium Salts of the Bipyridine Dianion: Polymer $[(bpy)2^{-}\{Na^{+}(dme)\}_2]_\infty$, Cluster $[(Na_8O)^{6+}Na^{+}_6(bpy)_6{}^{2-}(tmeda)_6]$, and Monomer $[(bpy)^{2-}\{Na^{+}(pmdta)\}_2]$. *Angew. Chem. Int. Ed.* **1999,** *38* (7), 952-955.

25. Gore-Randall, E.; Irwin, M.; Denning, M. S.; Goicoechea, J. M. Synthesis and Characterization of Alkali-Metal Salts of 2,2′- and 2,4′-Bipyridyl Radicals and Dianions. *Inorg. Chem.* **2009,** *48* (17), 8304-8316.

26. Kaizu, Y.; Kobayashi, H. Complexes Coordinated by 2,2′-Bipyridine Negative Ion. I. Synthesis of Sodium 2,2′-Bipyridinetetracarbonylchromium. *Bull. Chem. Soc. Jpn.* **1970,** *43* (8), 2492-2494.

27. Irwin, M.; Jenkins, R. K.; Denning, M. S.; Krämer, T.; Grandjean, F.; Long, G. J.; Herchel, R.; McGrady, J. E.; Goicoechea, J. M. Experimental and Computational Study of the Structural and Electronic Properties of Fe^{II}(2,2′-bipyridine)$(mes)_2$ and [Fe^{II}(2,2′-bipyridine)$(mes)_2$]$^-$, a Complex Containing a 2,2′-Bipyridyl Radical Anion. *Inorg. Chem.* **2010,** *49* (13), 6160-6171.

28. Irwin, M.; Doyle, L. R.; Krämer, T.; Herchel, R.; McGrady, J. E.; Goicoechea, J. M. A Homologous Series of First-Row Transition-Metal Complexes of 2,2′-Bipyridine and their Ligand Radical Derivatives: Trends in Structure, Magnetism, and Bonding. *Inorg. Chem.* **2012,** *51* (22), 12301-12312.

29. Schultz, M.; Boncella, J. M.; Berg, D. J.; Tilley, T. D.; Andersen, R. A. Coordination of 2,2‘-Bipyridyl and 1,10-Phenanthroline to Substituted Ytterbocenes: An Experimental Investigation of Spin Coupling in Lanthanide Complexes. *Organometallics* **2002,** *21* (3), 460-472.

30. Nikiforov, G. B.; Roesky, H. W.; Noltemeyer, M.; Schmidt, H.-G. Reactivity of $Ti(bipy)_3$ and preparation of the $Li(THF)_4[Al(bipy)_2]$ complex with the dinegative bipy ligand. *Polyhedron* **2004,** *23* (4), 561-566.

31. Rosa, P.; Mézailles, N.; Ricard, L.; Mathey, F.; Le Floch, P. Dianionic Homoleptic Biphosphinine Complexes of Group 4 Metals. *Angew. Chem. Int. Ed.* **2000,** *39* (10), 1823-1826.

32. Nitschke, J. R.; Tilley, T. D. Novel Templating Effect in the Macrocyclization of Functionalized Diynes by Zirconocene Coupling. *Angew. Chem. Int. Ed.* **2001,** *40* (11), 2142-2145.

33. See the Supporting Information for more details.

34. Henne, B. J.; Bartak, D. E. Metal-vapor synthesis and electrochemistry of bis(bipyridyl)nickel(0). *Inorg. Chem.* **1984,** *23* (3), 369-373.

35. Nattmann, L.; Lutz, S.; Ortsack, P.; Goddard, R.; Cornella, J. A Highly Reduced Ni–Li–Olefin Complex for Catalytic Kumada–Corriu Cross-Couplings. *J. Am. Chem. Soc.* **2018,** *140* (42), 13628-13633.

36. Suslick, B. A.; Tilley, T. D. Mechanistic Interrogation of Alkyne Hydroarylations Catalyzed by Highly Reduced, Single-Component Cobalt Complexes. *J. Am. Chem. Soc.* **2020,** *142* (25), 11203-11218.

37. Wagner, C. L.; Herrera, G.; Lin, Q.; Hu, C. T.; Diao, T. Redox Activity of Pyridine-Oxazoline Ligands in the Stabilization of Low-Valent Organonickel Radical Complexes. *J. Am. Chem. Soc.* **2021,** *143* (14), 5295-5300.

38. Chisholm, M. H.; Huffman, J. C.; Rothwell, I. P.; Bradley, P. G.; Kress, N.; Woodruff, W. H. Bis(2,2'-bipyridyl)diisopropoxymolybdenum(II). Structural and spectroscopic evidence for molybdenum-to-bipyridyl π* bonding. *J. Am. Chem. Soc.* **1981,** *103* (16), 4945-4947.

39. Fedushkin, I. L.; Petrovskaya, T. V.; Girgsdies, F.; Köhn, R. D.; Bochkarev, M. N.; Schumann, H. Synthesis and Structure of the First Lanthanide Complex with the Bridging, Antiaromatic 2,2′-Bipyridine Dianion: [{Yb(μ_2-$N_2C_{10}H_8$)(thf)$_2$}$_3$]. *Angew. Chem. Int. Ed.* **1999,** *38* (15), 2262-2264.

40. Rösch, B.; Gentner, T. X.; Eyselein, J.; Langer, J.; Elsen, H.; Harder, S. Strongly reducing magnesium(0) complexes. *Nature* **2021,** *592* (7856), 717-721.

41. Bader, R. F. W., *Atoms in Molecules: A Quantum Theory.* Clarendon Press: Oxford, 1990.

42. Green, S. P.; Jones, C.; Stasch, A. Stable Magnesium(I) Compounds with Mg-Mg Bonds. *Science* **2007,** *318* (5857), 1754-1757.

43. Dye, J. L. Electrides: Early Examples of Quantum Confinement. *Acc. Chem. Res.* **2009,** *42* (10), 1564-1572.

44. Liu, C.; Nikolaev, S. A.; Ren, W.; Burton, L. A. Electrides: a review. *J. Mater. Chem. C* **2020,** *8* (31), 10551-10567.

45. Sitkiewicz, S. P.; Ramos-Cordoba, E.; Luis, J. M.; Matito, E. How Many Electrons Does a Molecular Electride Hold? *J. Phys. Chem. A* **2021,** *125* (22), 4819-4835.

46. Murata, R.; Wang, Z.; Abe, M. Singly Occupied Molecular Orbital−Highest Occupied Molecular Orbital (SOMO−HOMO) Conversion. *Aust. J. Chem.* **2021,** *74* (12), 827-837.

47. Saha, R.; Das, P.; Chattaraj, P. K. A Complex Containing Four Magnesium Atoms and Two Mg–Mg Bonds Behaving as an Electride. *Eur. J. Inorg. Chem.* **2019,** *2019* (38), 4105-4111.

48. Martínez-Martínez, A. J.; Kennedy, A. R.; Mulvey, R. E.; O'Hara, C. T. Directed Ortho-Meta′- and Meta-Meta′- Dimetalations: A Template Base Approach to Deprotonation. *Science* **2014,** *346* (6211), 834-837.

49. Martínez-Martínez, A. J.; Armstrong, D. R.; Conway, B.; Fleming, B. J.; Klett, J.; Kennedy, A. R.; Mulvey, R. E.; Robertson, S. D.; O'Hara, C. T. Pre-inverse-crowns: synthetic, structural and reactivity studies of alkali metal magnesiates primed for inverse crown formation. *Chem. Sci.* **2014,** *5* (2), 771-781.

50. Mongin, F.; Harrison-Marchand, A. Mixed AggregAte (MAA): A Single Concept

for All Dipolar Organometallic Aggregates. 2. Syntheses and Reactivities of Homo/HeteroMAAs. *Chem. Rev.* **2013,** *113* (10), 7563-7727.

51. Harrison-Marchand, A.; Mongin, F. Mixed AggregAte (MAA): A Single Concept for All Dipolar Organometallic Aggregates. 1. Structural Data. *Chem. Rev.* **2013,** *113* (10), 7470-7562.

52. Wang, Z.; Yin, H.; Fu, G. C. Catalytic enantioconvergent coupling of secondary and tertiary electrophiles with olefins. *Nature* **2018,** *563* (7731), 379-383.

53. Tortajada, A.; Juliá-Hernández, F.; Börjesson, M.; Moragas, T.; Martin, R. Transition-metal-catalyzed carboxylation reactions with carbon dioxide. *Angew. Chem. Int. Ed.* **2018,** *57* (49), 15948-15982.

54. Juliá-Hernández, F.; Moragas, T.; Cornella, J.; Martin, R. Remote carboxylation of halogenated aliphatic hydrocarbons with carbon dioxide. *Nature* **2017,** *545* (7652), 84-88.

55. Sun, S.-Z.; Talavera, L.; Spieß, P.; Day, C. S.; Martin, R. sp^3 Bis-Organometallic Reagents via Catalytic 1,1-Difunctionalization of Unactivated Olefins. *Angew. Chem. Int. Ed.* **2021,** *60* (21), 11740-11744.

56. Janssen-Müller, D.; Sahoo, B.; Sun, S.-Z.; Martin, R. Tackling Remote sp3 C−H Functionalization via Ni-Catalyzed “chain-walking” Reactions. *Isr. J. Chem.* **2020,** *60* (3-4), 195-206.

57. Tortajada, A.; Menezes Correia, J. T.; Serrano, E.; Monleón, A.; Tampieri, A.; Day, C. S.; Juliá-Hernández, F.; Martin, R. Ligand-Controlled Regiodivergent Catalytic Amidation of Unactivated Secondary Alkyl Bromides. *ACS Catal.* **2021,** *11* (16), 10223-10227.

58. Davies, J.; Janssen-Müller, D.; Zimin, D. P.; Day, C. S.; Yanagi, T.; Elfert, J.; Martin, R. Ni-Catalyzed Carboxylation of Aziridines en Route to β-Amino Acids. *J. Am. Chem. Soc.* **2021,** *143* (13), 4949-4954.

59. Bogdanovic, B. Magnesium anthracene systems and their application in synthesis and catalysis. *Acc. Chem. Res.* **1988,** *21* (7), 261-267.

60. Jones, C. Dimeric magnesium(I) β-diketiminates: a new class of quasi-universal reducing agent. *Nat. Rev. Chem.* **2017,** *1* (8), 0059.

61. Doni, E.; Murphy, J. A. Evolution of neutral organic super-electron-donors and their applications. *Chem. Commun.* **2014,** *50* (46), 6073-6087.

62. Murphy, J. A. Discovery and Development of Organic Super-Electron-Donors. *J. Org. Chem.* **2014,** *79* (9), 3731-3746.

63. Feng, Q.; Tong, R. Controlled photoredox ring-opening polymerization of O-carboxyanhydrides. *J. Am. Chem. Soc.* **2017,** *139* (17), 6177-6182.

64. Shrestha, R.; Dorn, S. C. M.; Weix, D. J. Nickel-Catalyzed Reductive Conjugate Addition to Enones via Allylnickel Intermediates. *J. Am. Chem. Soc.* **2013,** *135* (2), 751-762.

65. Powers, D. C.; Anderson, B. L.; Nocera, D. G. Two-Electron HCl to H_2 Photocycle Promoted by Ni(II) Polypyridyl Halide Complexes. *J. Am. Chem. Soc.* **2013,** *135* (50), 18876-18883.

66. van Gemmeren, M.; Börjesson, M.; Tortajada, A.; Sun, S.-Z.; Okura, K.; Martin, R. Switchable Site-Selective Catalytic Carboxylation of Allylic Alcohols with CO2. *Angew. Chem. Int. Ed.* **2017,** *56* (23), 6558-6562.

67. Dinjus, E.; Walther, D.; Kaiser, J.; Sieler, J.; Ngoc Thanh, N. 2,2′-dipyridyl-1,5-cyclooctadiennickel(0): kristall-und molekülstruktur. *J. Organomet. Chem.* **1982,** *236* (1), 123-130.

68. Mahmut, A.; Takakazu, Y. Kinetic Study of Ligand Exchange Reactions of Bis(1,5-cyclooctadiene)nickel(0) with 2,2′-Bipyridine, 4,4′-Dimethyl-2,2′-bipyridine, and 4,4′,5,5′-Tetramethyl-2,2′-bipyridine. *Bull. Chem. Soc. Jpn.* **1999,** *72* (6), 1255-1261.

69. The utilization of **5** as reductant resulted in **7** in unoptimized 29 % yield.

3.6 Experimental Section

3.6.1 General Considerations

Solvents. Reactions were carried out under N_2 in a glovebox or on a Schlenk line, in solvents (THF, Et_2O, toluene) that had been dried and degassed using an Innovative Technologies solvent purification system, then stored under N_2 over 4 Å molecular sieves for at least 16 h prior to use. Pentane was degassed by bubbling with N_2 and stored under N_2 over 4 Å molecular sieves for at least 16 h prior to use. C_6D_6, C_7D_8, CD_2Cl_2, THF-d_8, (Eurisotop) were freeze/pump/thaw degassed (4x) and likewise stored under N_2 over 4 Å molecular sieves for at least 16 h prior to use.

Reagents. Bipyridine and bathocuproine were purchased from Fluorochem. Magnesium powder (99 ≥%) and $MgCl_2$ (98 ≥%) were purchased from Sigma-Aldrich. Magnesium powder (99.8%) was purchased from Strem Chemicals. 1,3,5-Trimethoxybenzene (TMB) was purchased from TCI Chemicals. Complexes (bipy)$NiCl_2$,[1] (Bathocuproine)$NiCl_2$,[2] (Bathocuproine)$_2$Ni,[2] and ligand 6,6'-dimethyl-4,4'-diphenyl-2,2'-bipyridine[3] were synthesized according to literature procedures.

Analytical methods. Flash chromatography was performed with Sigma Aldrich technical grade silica gel 60 (230-400 mesh). Thin layer chromatography was carried out using Merck TLC Silica gel 60 F254. NMR spectra were recorded on Bruker Avance Ultrashield 300, 400, or 500 MHz spectrometers, with chemical shifts reported in parts per million (ppm) and coupling constants, *J*, reported in hertz. Quantitative NMR experiments were performed with d1 set to 10s (^{1}H). Gas chromatographic analyses were performed on an Agilent 6890N gas chromatograph with an FID detector. Continuous wave (CW) X-band EPR spectra were obtained using a Bruker EMX Micro X-band spectrometer using a Bruker ER 1164 HS resonator. Spectra were simulated using SpinFit within Xenon. The samples were cooled to 77 K in a Suprasil finger dewar (Wilmad-LabGlass) filled with liquid nitrogen. The spectral data were collected with the following spectrometer settings: microwave power = 0.56mW; centre field = 3250 G, sweep width = 2500 G, sweep time = 35.07 s, modulation frequency = 100 KHz, modulation amplitude = 10 G, power attenuation = 25 dB, time constant = 20.48 ms. Simulations, g values, and frequencies are provided alongside the characterization data

of the complexes. IR spectra were obtained with a Bruker FT-IR Alpha spectrometer. Elemental analysis and powder diffraction were unsuccessful in characterizing new Mg complexes in this work due to the reactivity and highly reduced nature of the species synthesized.

3.6.2 Synthesis and Characterization of Complexes

Synthesis of $[(THF)_4Mg_4(\mu^2\text{-bipy})_4][(THF)_6Mg_2(\mu^2\text{-bipy})(Cl)]$ 3

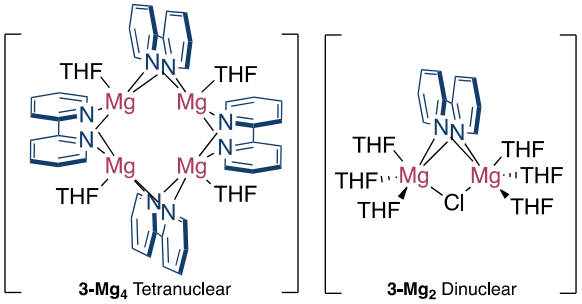

In a glovebox, $(bipy)NiCl_2$ (1.03 g, 3.62 mmol) was added to a 100 mL Schlenk flask with bipyridine (0.60 g, 3.82 mmol) and Mg powder (2.12g, 87.02 mmol). A stir bar was added, and the Schlenk flask was charged with 30 mL of THF turning the teal powder to a teal suspension and the resulting mixture left to stir overnight. After 16 hours the purple solution was filtered through a celite plug with a black solid and unreacted magnesium being filtered off and a purple solution collected. The solvent was then removed to afford a purple solid which was washed with pentane (15 mL x 3) to give $[(THF)_4Mg_4(\mu^2\text{-bipy})_4][(THF)_6Mg_2(\mu^2\text{-bipy})(Cl)]$ **3** (2.46 g, 98 % yield) as a purple powder.

Note: Mg source. We found that using Mg powder (99 ≥%) was important for faster reaction times (those noted) instead of Mg powder (99.8 %). **Stir rate.** A fast-stirring velocity was found to improve reaction times and mixing of the heterogeneous reductant. In the case of a slower reaction time/reduction, the reactions could be left longer with no loss in yield. **Incomplete reduction.** Syntheses conducted with shorter reaction times (ca. 4 h) showed incomplete reduction to **3** and crystals of $Mg(bipy)_2(THF)_2$ (See Fig 27 for X-Ray structure) formed. We were unable to isolate this structure from **3** under these short reaction times, but analogous reports from the reduction of bipyridine to the radical anion directly with magnesium are described.[4]

Stoichiometry of Magnesium. Likely lower stoichiometries of magnesium can be used if longer reaction times are employed. However, for a convenient and reproducible procedure an excess of magnesium is used. **Temperature.** While performing variable temperature ^{1}H NMR experiments (from rt to 55 °C – Figure S14) no decomposition was observed.

^{1}H NMR (400 MHz, THF-d_8): δ 6.55 (d, J = 6.8 Hz, 1H), 5.60 (d, J = 9.4 Hz, 1H), 4.77 (dd, J = 9.4, 5.2 Hz, 1H), 4.10 (t, J = 5.9 Hz, 1H). **^{13}C NMR** (101 MHz, THF-d_8): δ 149.3, 148.7, 148.6, 124.5, 124.4, 123.3, 119.7, 119.4, 119.0, 114.7, 114.3, 97.8, 97.4.

EPR = 2.00185 g (weak)

UV-VIS (nm) = 915, 813, 725, 530, 501, 383, 373

Key IR Stretches = 1557 cm^{-1} (C=C and C=N), 954 cm^{-1} (ring deformation stretch)

See Figure S7 for full IR Spectra

(6,6'-dimethyl-4,4'-diphenyl-2,2'-bipyridine)NiBr$_2$ 4

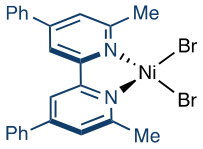

In a glovebox, NiBr$_2$diglyme (308 mg, 0.87 mmol) and 6,6'-dimethyl-4,4'-diphenyl-2,2'-bipyridine (301 mg, 0.90 mmol, 1.025 equiv.) were added to a 10 mL vial. A stir bar was added and charged with 6 mL of THF and left to stir overnight. After 16 h pentane (5 mL) was added to the suspension and the reaction mixture was filtered. The solid was washed with pentane (1 mL x 3) to afford (6,6'-dimethyl-4,4'-diphenyl-2,2'-bipyridine)NiBr$_2$ **4** as a pink powder (472 mg, 97 % yield).

^{1}H NMR (400 MHz, CD_2Cl_2): δ 74.3 (br s, 2H), 60.5 (br s, 2H), 20.2 (br s, 7H).

EA Calcd. C, 51.95; H, 3.63; N, 5.05; Found: C, 48.89; H, 3.83; N, 4.73 The deviation from the calculated EA values might be due to incomplete sample combustion and the formation of Ni black on the glass reaction tube during EA analysis. Alternatively, deviation may arise from contaminant during shipping or residual solvent or ligand.

Mg(6,6'-dimethyl-4,4'-diphenyl-2,2'-bipyridine)$_2$(THF) 5

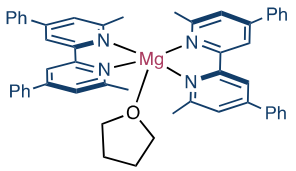

In a glovebox, (6,6'-dimethyl-4,4'-diphenyl-2,2'-bipyridine)$NiBr_2$ (145 mg, 0.26 mmol) was added to a 10 mL vial with 6,6'-dimethyl-4,4'-diphenyl-2,2'-bipyridine (93 mg, 0.28 mmol) and Mg powder (153 mg, 6.29 mmol). A stir bar was added, and the vial was charged with 4 mL of THF turning the powder into a suspension and left to stir overnight. After 16 h the solution was filtered through a celite plug with a black solid being filtered off and a dark brown solution was collected. The solvent was removed to afford a black solid which was washed with pentane (4 mL x 4) to give Mg(6,6'-dimethyl-4,4'-diphenyl-2,2'-bipyridine)$_2$(THF) **5** (169 mg, 84 % yield) as a black powder.

^{1}H NMR (500 MHz, THF-d_8, weak): δ 7.42 (d, J = 7.8 Hz, 5H), 7.23 (d, J = 7.9 Hz, 5H), 7.14 (t, J = 7.5 Hz, 7H), 7.05 (t, J = 7.6 Hz, 6H), 6.96 (t, J = 7.4 Hz, 3H), 6.81 (t, J = 7.3 Hz, 3H), 6.53 (s, 3H), 6.28 (s, 3H), 5.06 (s, 3H), 4.80 (s, 4H). The NMR samples were prepared from a saturated solution of **5** in THF-d_8 to improve signal intensity. However, due to the mainly paramagnetic nature of **5** and the resulting low intensity of the NMR signals obtained, no ^{13}C NMR signals were observed.

EPR = 2.00285 g (strong)

UV-VIS (nm) = 486, 406, 372

Note: Samples were unstable under UV-VIS conditions, where after one set of scans decomposition was observed (see Figure S8).

Key IR Stretches = 1573 cm^{-1} (C=C and C=N), 992 cm^{-1} (ring deformation stretch)

See Figure S7 for full IR Spectra.

3.6.3 Stochiometric Reactions

Synthesis of $(bipy)_2Ni$ 2 with 3

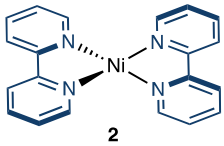

2

In a glovebox, $NiCl_2(glyme)$ (64 mg, 0.29 mmol) and bipyridine (91 mg, 0.58 mmol) were added to a 12 mL vial. A stir bar was added, and the vial was charged with 2 mL of THF forming a teal suspension. After 10 minutes, a solution of **3** (89 mg, 0.58 mmol) in 2 mL THF was added dropwise. After 55 minutes the green suspension was filtered through a celite plug with a black solid being filtered off and a green solution collected. The solvent was removed to afford a green solid which was washed with pentane (0.5 mL x 2) to give $(bipy)_2Ni$ **2** (70 mg, 65 % yield) as a green powder.

^{1}H NMR (400 MHz, C_6D_6): δ 10.20 (d, J = 5.7 Hz, 4H), 7.72 (ddd, J = 8.1, 6.8, 1.4 Hz, 4H), 7.24 (d, J = 8.5 Hz, 8H). **^{13}C NMR** (101 MHz, C_6D_6): δ 149.4, 140.4, 125.0, 121.1, 120.2.

Notes: Stoichiometry of **3** is determined by overall MW/# of reducing electrons (i.e 1683,29/11 = 153.0 g/mol per reducing equivalent) multiplied by 2 as two electrons are required to reduce Ni(II) to Ni(0). Crystals of **6** (see Figure S26) were formed from the crude reaction mixture. **Literature syntheses**. The syntheses of $(bipy)_2Ni$ **2** have been reported from metal-vapor synthesis,[5] lithium metal reduction[6] and through in situ or bulk electrochemical reductions.[1] A common theme in the synthesis of this complex are challenging experimental setups. Use of heterogeneous Li or KC_8 reductants (see below for synthesis using KC_8) can result in surface-retained over-reduction which lead to irreproducible results that suffer from poor scalability. Furthermore, reductions with Li cannot be performed in typical N_2 atmosphere gloveboxes due to the exothermic reaction of Li with N_2 and its low molecular weight complicates its use at small scales. In the reported lithium metal reduction, 14 mg of lithium metal are weighed to perform a stochiometric reduction at 1 mmol scale. The heterogeneous nature also results in longer reaction times with poor control over reaction rates. Alternatively, less well-defined procedures have been described from $K_4[Ni(CN)_4]$,[7] $Ni(COD)_2$,[8] and $(bipy)NiEt_2$.[9] In our hands, synthesis from $Ni(COD)_2$ were unsuccessful in forming (bipy)Ni(COD) (see synthesis below) and employing $(bipy)NiEt_2$ resulted in no

reaction, reflecting the general lack of literature reports implementing $(bipy)_2Ni$. Commonly, literature investigations of bipy-Ni complexes rely on *in-situ* generation of (bipy)Ni(COD) from $Ni(COD)_2$. These methods however generate a mixture of species[10] between $Ni(COD)_2$, (bipy)Ni(COD)[11] and $(bipy)_2Ni$, where the interactions of COD may complicate the desired outcome. This mixture of speciation also complicates isolation of $(bipy)_2Ni$ in pure form from $Ni(COD)_2$. **NMR Characterization.** To our knowledge only ^1H NMR characterization has been provided by Bartak[5] which is similar to those reported above. Fuller characterization is now reported with both ^1H and ^{13}C NMR data and corresponding spectra, in addition to unambiguous assignment by single crystal XRD.

Synthesis of $(bipy)_2Ni$ 2 from KC_8 Reduction

In a glovebox, $(bipy)NiCl_2$ (25.2 mg, 0.09 mmol), bipyridine (13.9 mg, 0.09 mmol), and KC_8 (13.5 mg, 0.10 mmol) were added to a 12 mL vial. A stir bar was added, and the vial was charged with 2 mL of THF turning the teal powder to a teal suspension. The initial dark pink solution gradually turned dark green over few minutes. (**Note.** Two identical reactions were carried out to be analyzed in different reaction times.) After 55 min and 3 hours, the green suspension was filtered through a celite plug with a black solid being filtered off and a green solution collected. The solvent was removed to afford a green solid which was washed with pentane (0.15 mL x 2). **Note.** Other experimental setups by adding KC_8 as a dropwise slurry in THF were unsuccessful.

- <u>After 55 min:</u> ^1H NMR analysis (C_6D_6) identified a mixture of $(bipy)_2Ni$ **2** and unreacted bipyridine (54:46 ratio – see Figure S1).
- <u>After 3 h:</u> $(bipy)_2Ni$ **2** (crude; 13.0 mg, 39 % yield – 10:1 ratio $(bipy)_2Ni$:free bipy) was obtained as a green powder. Significant spectral broadening is observed due to free ligand in equilibria with $(bipy)_2Ni$ (see Figure S1).

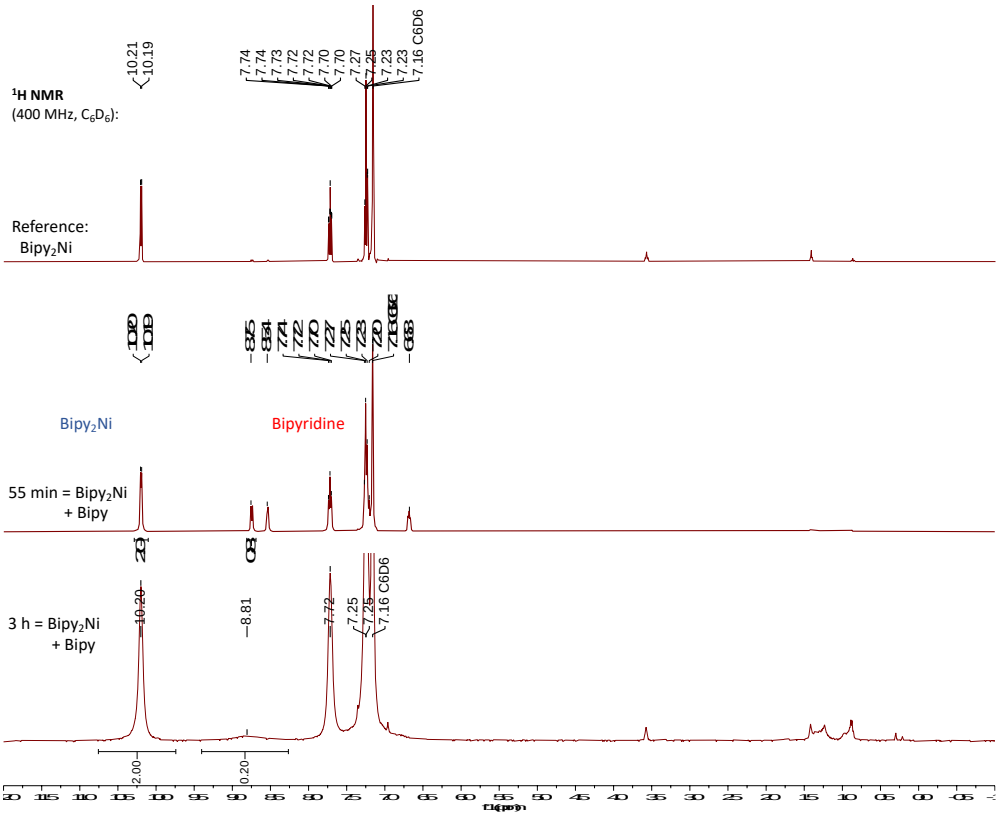

Figure S1. ^1H spectra (C_6D_6, 400 MHz) reducing $(bipy)NiCl_2$ with KC_8 (1.1 equiv.). After 55 min, a mixture of $(bipy)_2Ni$ **2** (blue) and unreacted bipyridine (red) is observed (54:46 ratio).

Synthesis of (bipy)Ni(COD) from $Ni(COD)_2$

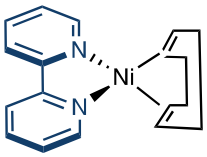

In a glovebox, $Ni(COD)_2$ (81 mg, 0.29 mmol) and bipyridine (96 mg, 0.62 mmol 2.1 equiv) were added to a 12 mL vial. A stir bar was added, and the vial was charged with 8 mL of pentane. After 16 h, the solution was filtered through a celite plug and the solvent was removed to afford a purple solid. The solid was washed with pentane (0.5 mL x 2) to give (bipy)Ni(COD) (75 mg, 92 % yield) as a purple powder with minor impurities of $(bipy)_2Ni$ **2** and COD.

^{1}H NMR (500 MHz, C_6D_6): δ 10.15 (d, J = 5.8 Hz, 2H), 7.29 (d, J = 3.9 Hz, 4H), 7.00 (d, J = 3.2 Hz, 2H), 3.92 (d, J = 3.4 Hz, 4H), 3.01 – 2.72 (m, 4H), 1.95 (d, J = 8.3 Hz, 4H). The spectroscopic data correspond to those previously reported in the literature.[11]

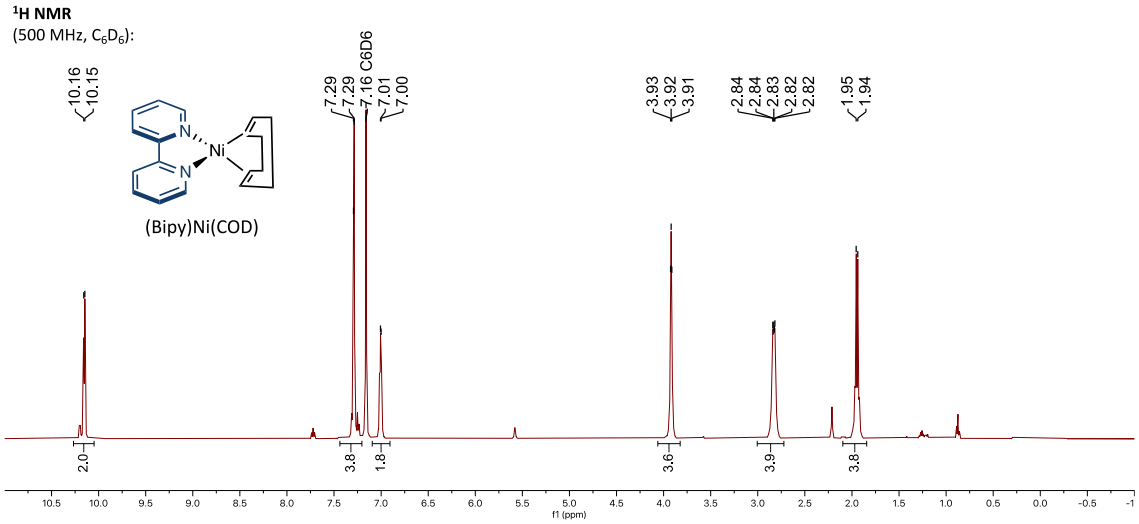

Figure S2. ^{1}H spectrum (C_6D_6, 500 MHz) of (bipy)Ni(COD) from $Ni(COD)_2$. bipy = bipyridine, COD = cyclooctadiene

Attempted Synthesis of $(bipy)_2Ni$ 2 with Mg, Mn, or Zn

In a glovebox, $(bipy)NiCl_2$ (25.2 mg, 0.09 mmol), bipyridine (13.9 mg, 0.09 mmol), and Mg powder (2.2 mg, 0.09 mmol) were added to a 12 mL vial. A stir bar was added, and the vial was charged with 2 mL of THF turning the teal powder to a teal suspension. The reaction remained a teal suspension that gradually began to darken over 7 days. After 7 days, an aliquot was taken from the suspension, filtered through a celite plug to remove unreacted $(bipy)NiCl_2$ and the solvent was removed. ^1H NMR analysis (C_6D_6) identified minor amounts of $(bipy)_2Ni$ **2**, and mainly unreacted bipyridine (15:85 ratio - below).

Note. Analogous Reactions with Mn or Zn afford no signals for $(bipy)_2Ni$.

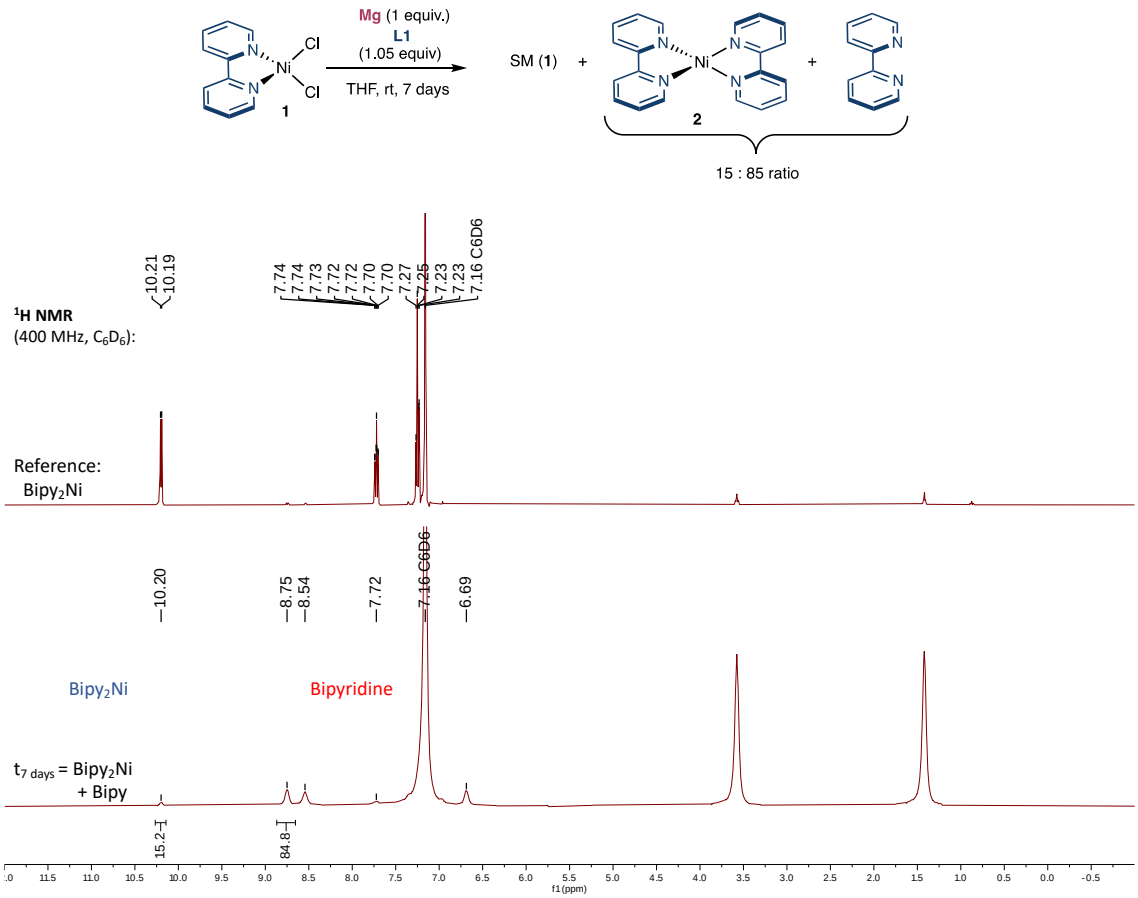

Figure S3. ^1H spectra (C_6D_6, 400 MHz) reducing $bipyNiCl_2$ with Mg powder (1 equiv.). After 7 days, very minor quantities of $(bipy)_2Ni$ **2** (blue) formed with largely unreacted bipyridine (red) remaining (15:85 ratio).

Synthesis of (Bathocuproine)$_2$Ni 7 with 3

In a glovebox, $NiCl_2$(glyme) (68 mg, 0.31 mmol) and bathocuproine (223 mg, 0.62 mmol) were added to a 12 mL vial. A stir bar was added, and the vial was charged with 4 mL of THF turning the powder to a suspension. After 5 minutes, a solution of **3** (95 mg, 0.62 mmol) in 4 mL THF was added dropwise. After 55 minutes the purple solution was filtered through a celite plug with a black solid being filtered off and a purple solution collected. The solvent was removed to afford a purple solid which was washed with pentane (1 mL x 2) to give (Bathocuproine)$_2$Ni **7** (216 mg, 90 % yield) as a purple powder. The spectroscopic data correspond to those previously reported and validated by independent synthesis using literature procedures from Ni(COD)$_2$.[2]

^{1}H NMR (500 MHz, C_6D_6) δ 7.96 (s, 2H), 7.86 (s, 2H), 7.67 (dd, *J* = 8.2, 1.3 Hz, 4H), 7.43 – 7.33 (m, 2H), 7.24 – 7.17 (m, 4H, slight overlap with C_6D_6), 2.49 (s, 6H).
^{1}H NMR (400 MHz, THF-d_8): δ 8.11 (s, 2H), 7.90 – 7.70 (m, 6H), 7.62 – 7.48 (m, 2H), 7.40 (t, *J* = 7.6 Hz, 4H), 2.45 (s, 6H).

Synthesis of (Neocuproine)$_2$Ni 8 with 3

In a glovebox, $NiCl_2$(glyme) (68 mg, 0.31 mmol) and neocuproine (129 mg, 0.62 mmol) were added to a 12 mL vial. A stir bar was added, and the vial was charged with 4 mL of THF turning the powder to a suspension. After 5 minutes, a solution of **3** (95 mg, 0.62 mmol) in 4 mL THF was added dropwise. After 55 minutes the brown solution was filtered through a celite plug with a black solid being filtered off and a brown solution collected. The solvent was removed to afford a brown solid and washed with pentane (1 mL x 2) to give (neocuproine)$_2$Ni **8** (131 mg, 89 % yield) as a brown powder. The spectroscopic data correspond to those previously reported and validated by independent synthesis using literature procedures from Ni(COD)$_2$.[12]

^{1}H NMR (500 MHz, C_6D_6) δ 9.00 (d, *J* = 7.3 Hz, 2H), 7.68 (d, *J* = 7.3 Hz, 2H), 7.32 (s, 2H), 2.24 (s, 6H).

Direct Reduction of Bipyridine, Neocurpoine, and Bathocuproine With Magnesium

An alternative synthesis to highly reduced polypyridine dianions could be envisioned via the direct reduction of the free ligand with magnesium. Attempts at the direct reduction of ligands bipyridine, neocuproine and bathocuproine with magnesium powder were attempted following the procedure for cluster **3**, however, none of the syntheses afforded the highly reduced ligand dianions of magnesium in high yields.

In-Situ Synthesis of (Bathocuproine)$_2$Ni 7

In a glovebox, bathocuproine (6.5 mg, 0.02 mmol) and trimethoxybenzene (1.8 mg, internal standard) were dissolved in 0.8 mL THF-d_8 in a 3 mL vial. The solution was then added to a J. Young NMR tube, and the initial integration ratio of bathocuproine and TMB was measured (below - t_0). The solution was brought back into the glovebox and added to a stirred solution of (bathocuproine)$NiCl_2$ (8.6 mg, 0.02 mmol) in 0.5 mL THF-d_8. **5** (16.6 mg, 0.02 mmol) was then added and a rapid color change to red was observed. After 30 minutes the solution was transferred into a J. Young NMR tube and analyzed by ^{1}H NMR spectroscopy (t_1 – Bc_2Ni, 27 % yield).

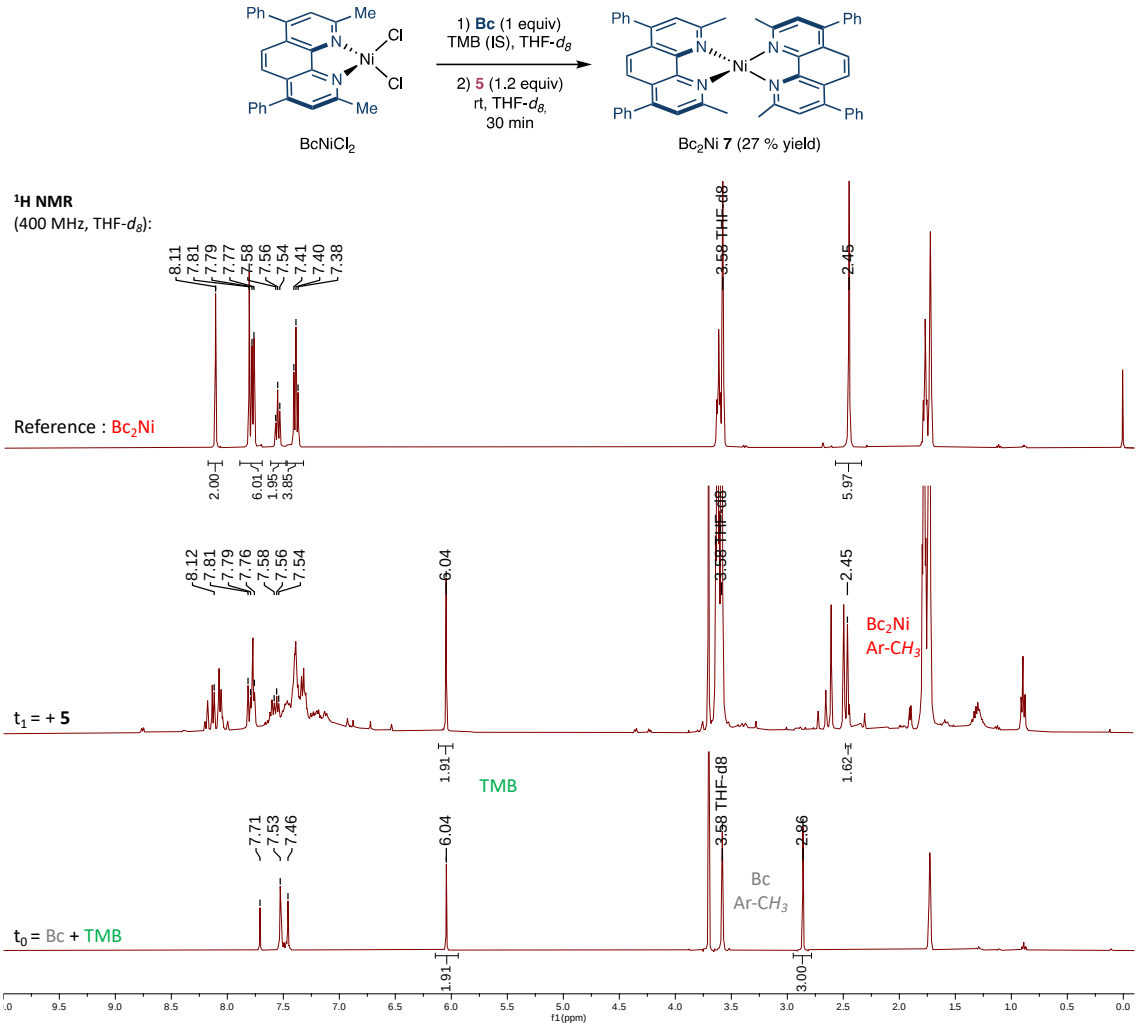

Figure S4. ^{1}H spectra (THF-d_8, 400 MHz) reducing (Bc)$NiCl_2$ to (Bc)$_2$Ni **7** (red) quantified from initial integration of bathocuproine (grey) using internal standard TMB (green).

Reaction of $(bipy)_2Ni$ 2 with $MgCl_2$

In a glovebox, $(bipy)_2Ni$ (9.8 mg, 0.03 mmol) and trimethoxybenzene (2.1 mg) were dissolved in 1 mL THF-d_8 in a 3 mL vial. The solution was then added to a J. Young NMR tube, and the initial integration ratio of $(bipy)_2Ni$ and TMB was measured (below - t_0). The solution was brought back into the glovebox and added to a stirred suspension of $MgCl_2$ (5.5 mg, 0.06 mmol) in 0.5 mL THF-d_8. After 1 h a suspension was formed and filtered through a pipette plug of celite where a black solid was filtered of and the filtrate was collected into a J. Young NMR tube and measured by quantitative ^1H NMR (t_1 – only TMB remaining in filtrate). The filtrate was brought back into the glovebox and added to a 3 mL vial where the solvent was removed. DMF-d_7 was added to the precipitate noted earlier and passed through the same celite plug dissolving the previously filtered solid into the vial of TMB and transfer to a J. Young NMR tube and measured by quantitative ^1H NMR (t_2 – ratio of $(bipy)MgCl_2(THF)_2$ **6** formed as a precipitate and TMB measured, 77 % yield).

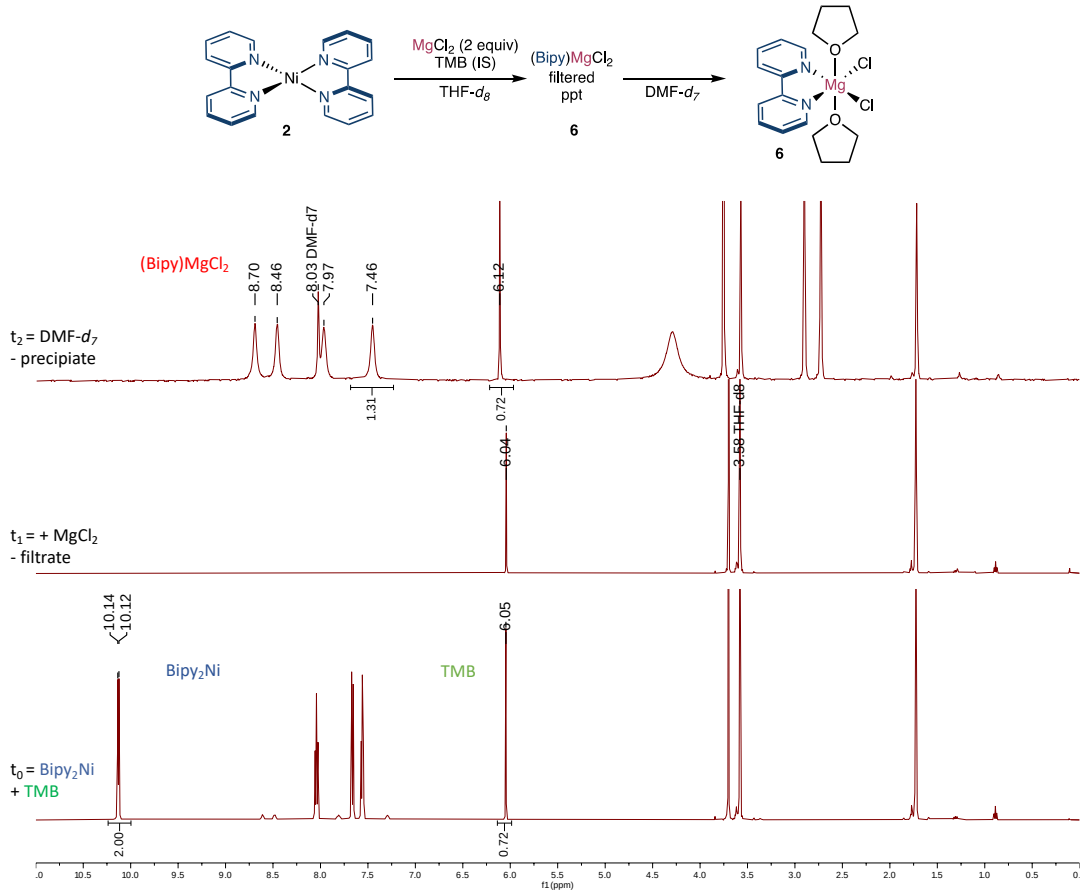

Figure S5. ^1H spectra (THF-d_8, 400 MHz and DMF-d_7) of $MgCl_2$ undergoing ligand scavenging of $(bipy)_2Ni$ **2** (blue) forming $(bipy)MgCl_2(THF)_2$ **6** (red) using internal standard TMB (green).

Independent formation of (bipy)$MgCl_2$

$MgCl_2$ (5.8 mg, 0.06 mmol) and bipyridine (9.6 mg, 0.06 mmol) were added to a 4 mL vial with 1 mL DMF-d_7. The solids were then sonicated until the solution was homogeneous (ca. 5 minutes) and then analyzed by ^{1}H and ^{13}C NMR spectroscopy. **^{1}H NMR** (400 MHz, DMF-d_7): δ 8.70 (br s, 2H), 8.45 (br s, 2H), 7.99 (br s, 2H), 7.47 (br s, 2H). **^{13}C NMR** (101 MHz, DMF-d_7): δ 156.6, 138.2, 125.2, 121.5.

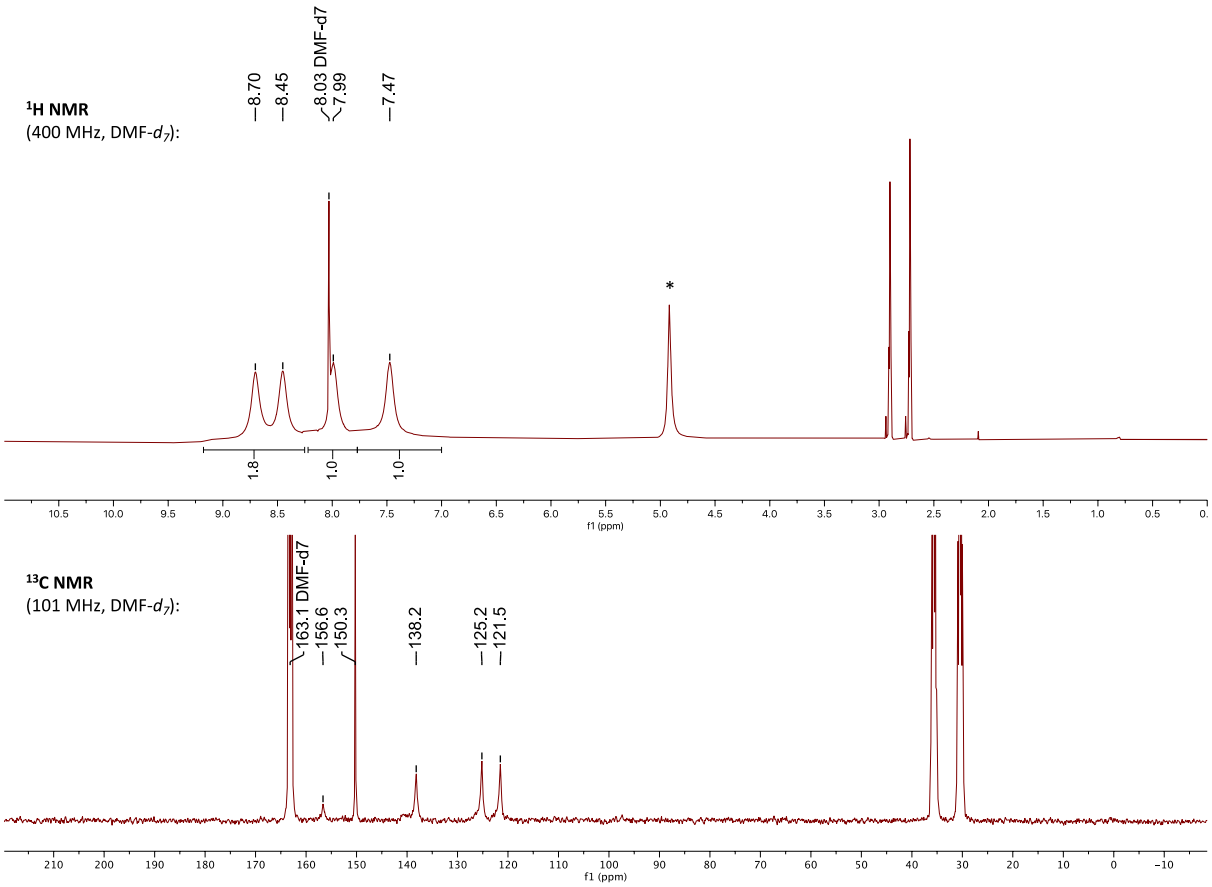

Figure S6. ^{1}H and ^{13}C spectra (DMF-d_7, 400/101 MHz) of (bipy)$MgCl_2$. *water

3.6.4 IR, UV-VIS, and Cyclic Voltammetry

Infrared Spectroscopy of 3 and 5

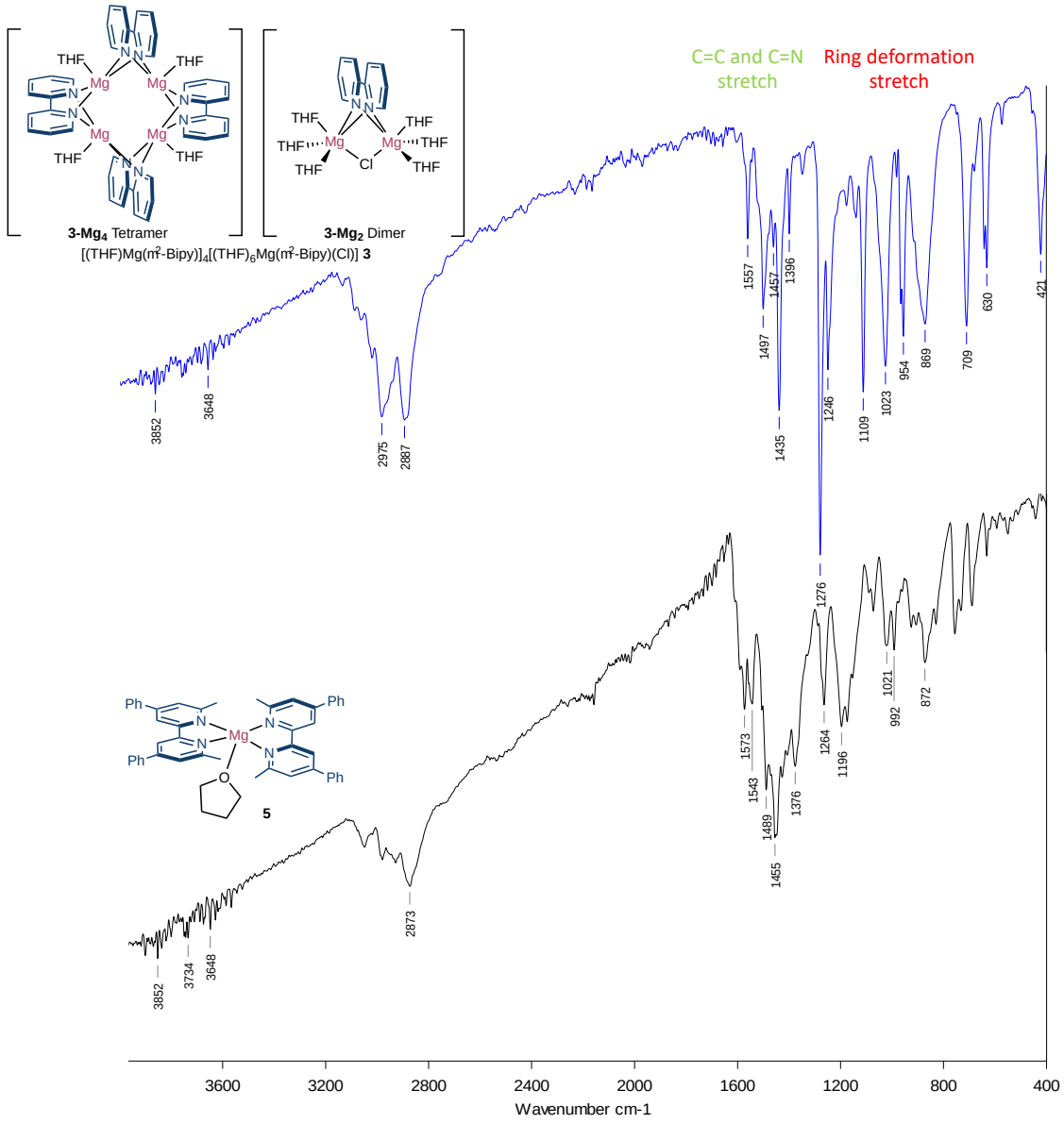

Figure S7. Stack IR spectra of **3** and **5**.

UV-VIS Spectroscopy of 3 and 5

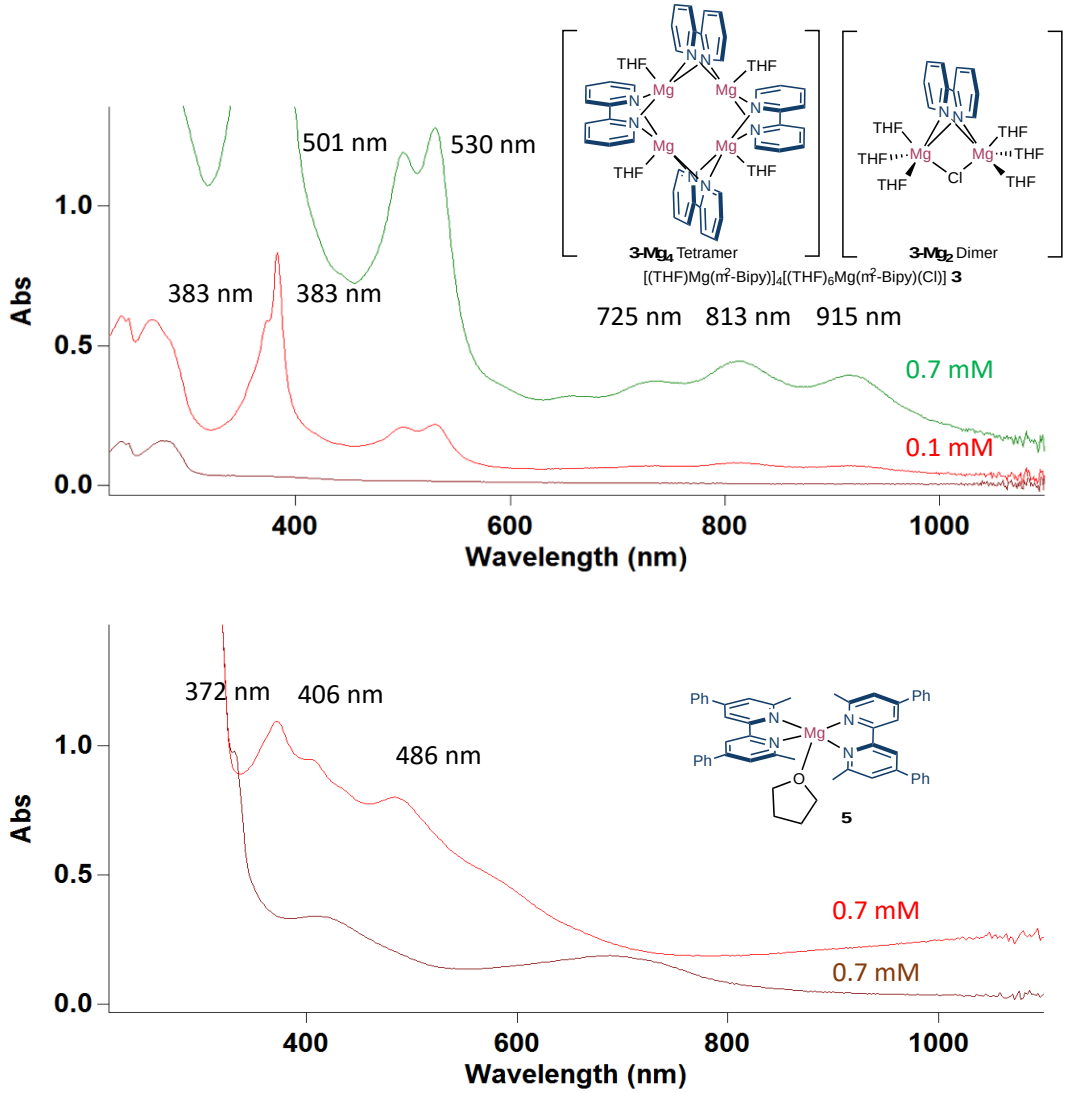

Figure S8. UV-VIS spectra of **3** and **5**. **5** showed instability with the initial scan (red) decomposing to the brown trace.

Cyclic Voltammetry of 1, 3 and 5

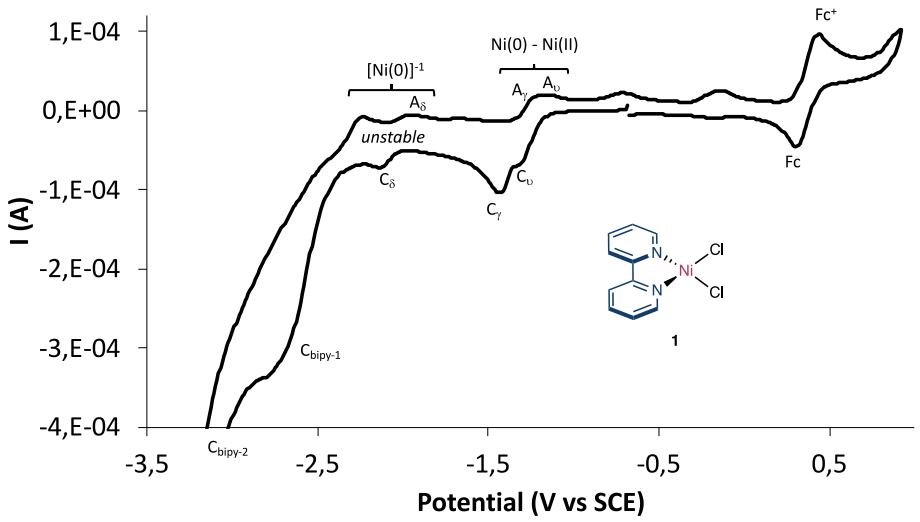

Figure S9. Cyclic voltammogram of (bipy)$NiCl_2$ **1**. Voltammograms were taken using a glassy carbon working electrode in a 0.1 M [^{n}Bu_4N][PF_6] supporting electrolyte DMF solution with a 50 mV/s scan rate and 0.01 M of sample referenced to Fc (+380 vs SCE). Scans were started at the open-circuit potential and scanned in the anode direction first; the second cycle is shown here. $E_{1/2}$ values for **1** are Ni^{2+}/Ni^0 = –1.33 V, $[Ni^0]^{1-}$ = –2.09 V and ligand reduction at –2.61 V. **Literature reports** CV of $(bipy)_2Ni$ or $(bipy)_3Ni(ClO_4)_2$ MeCN (0.2 M, TEAP)[5]; Ni^{2+}/Ni^0 = –1.27 V, $[Ni^0]^{1-}$ = –1.97 V, bipyridine radical anion reduction –2.40 V and dianion reduction –2.62 V among others.[1,9]

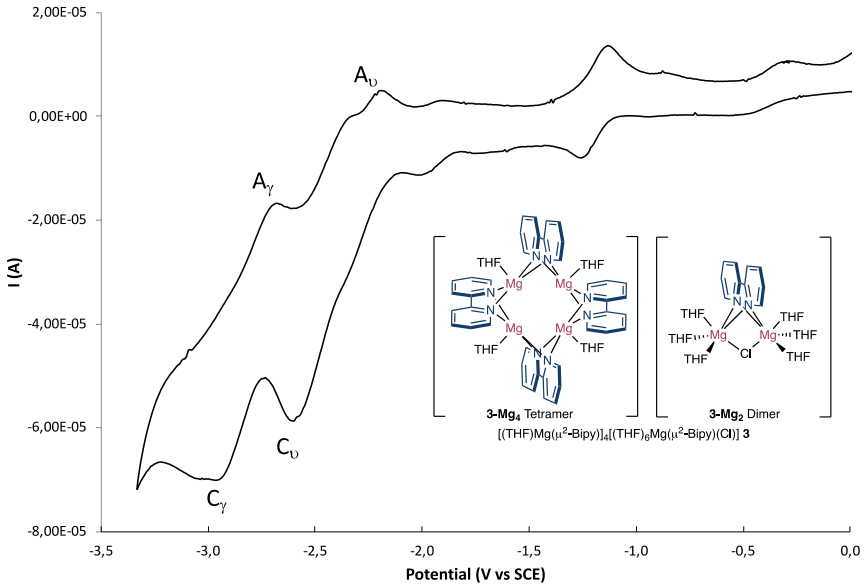

Figure S10. Cyclic voltammogram of **3**. Voltammograms were taken using a glassy carbon working electrode in a 0.1 M [^{n}Bu_4N][PF_6] supporting electrolyte THF solution with a 50 mV/s scan rate and 0.01 M of sample referenced to Fc (+380 vs SCE). Scans were started at the open-circuit potential and scanned in the anode direction first; the second cycle is shown here. $E_{1/2}$ values for **3** are Mg^{1-}/Mg^0 = –2.36 V, Mg^{-2}/Mg^{-1} = –2.79 V.

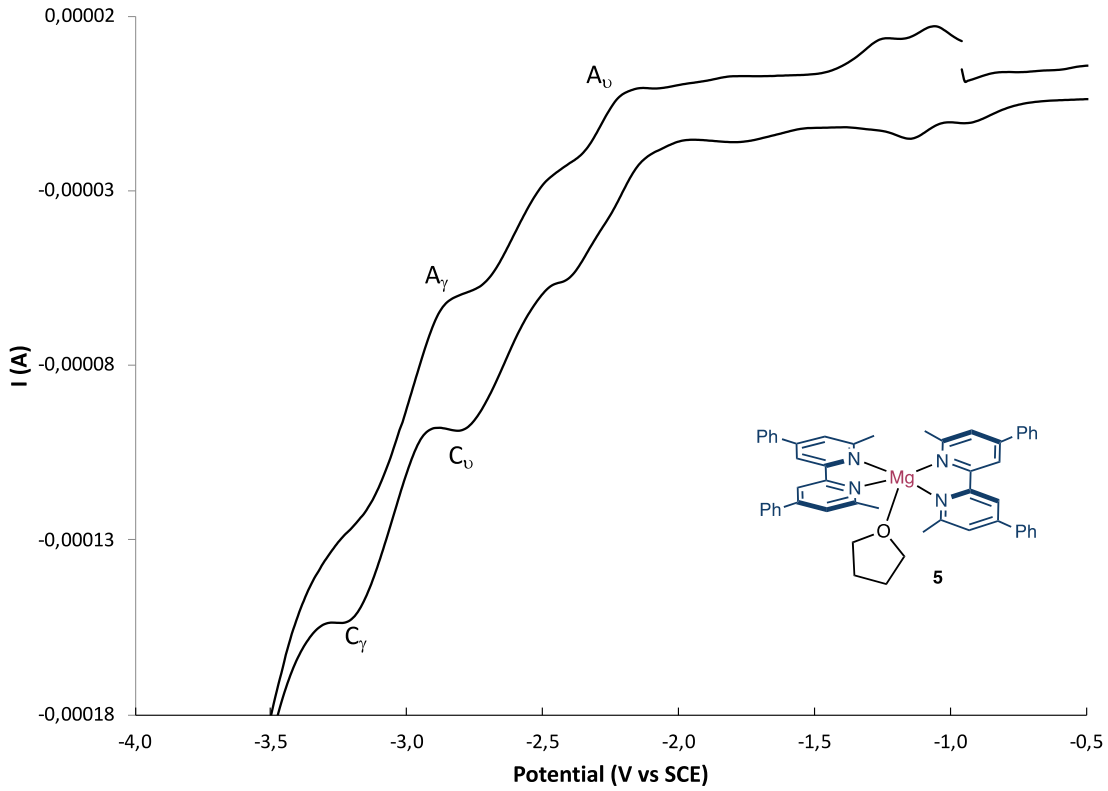

Figure S11. Cyclic voltammogram of **5**. Voltammograms were taken using a glassy carbon working electrode in a 0.1 M [$^{n}Bu_4N$][PF_6] supporting electrolyte THF solution with a 25 mV/s scan rate and 0.01 M of sample referenced to Fc (+380 vs SCE). Scans were started at the open-circuit potential and scanned in the anode direction first; the second cycle is shown here. $E_{1/2}$ values for **5** are Mg^0/Mg^{1-} = –2.29 V, $Mg^{1-}/Mg^{1□/1□}$ = –2.60 V $Mg^{1□/1□}/ Mg^{2□}$ = –3.04 V.

3.6.5 NMR and EPR Spectra of Synthesized Complexes

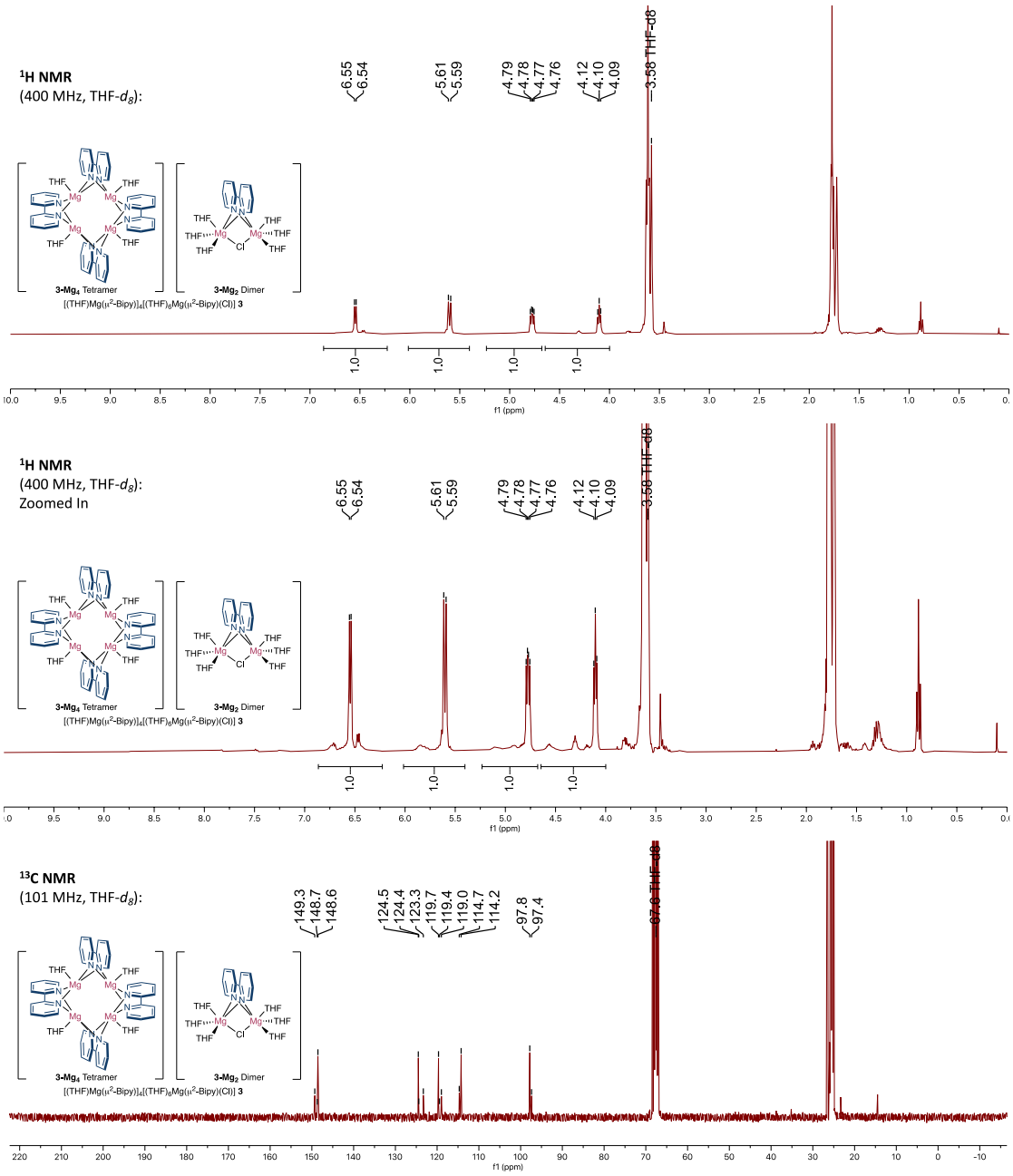

Figure S12. ^{1}H and ^{13}C NMR spectra (THF-d_8, 400/101 MHz) of **3**.

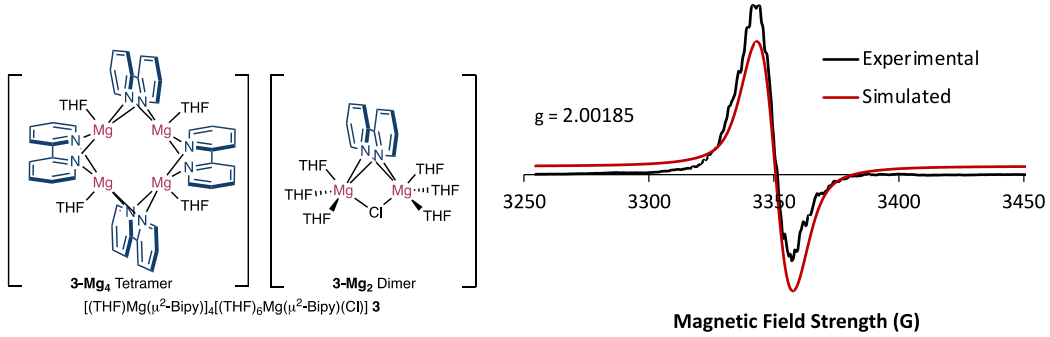

Figure S13. EPR spectrum of **3** (77K, THF), g = 2.00185.

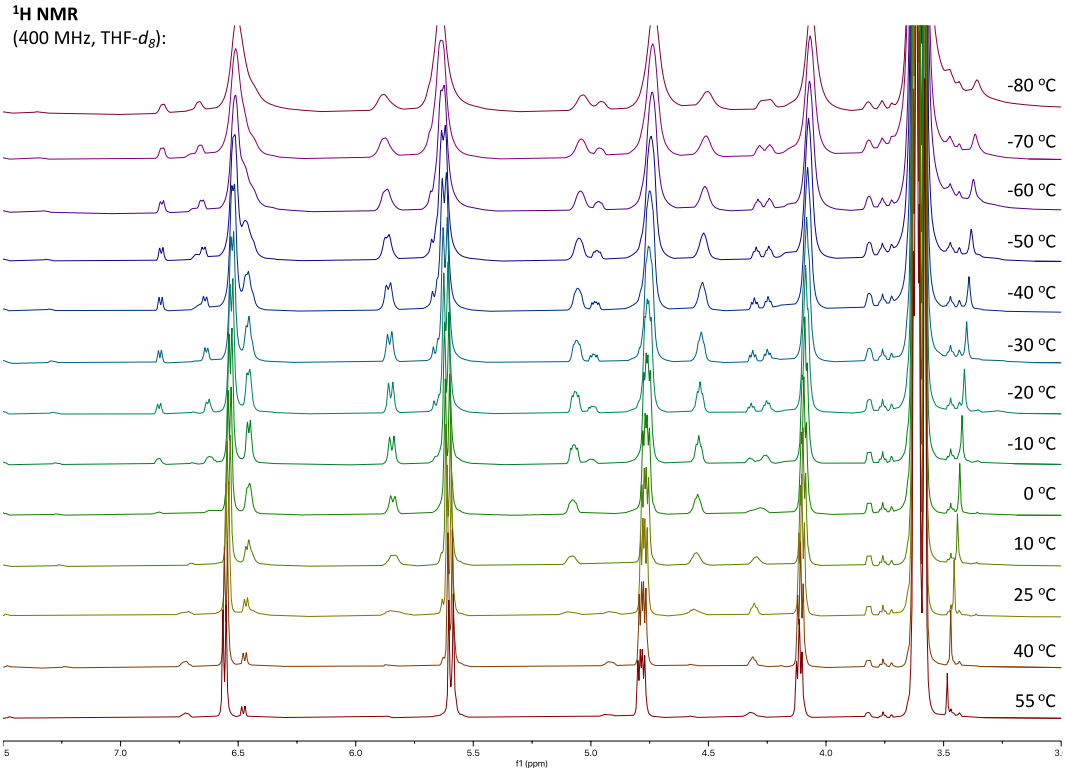

Figure S14. Variable temperature ^{1}H NMR spectra (THF-d_8, 400 MHz) of **3**.

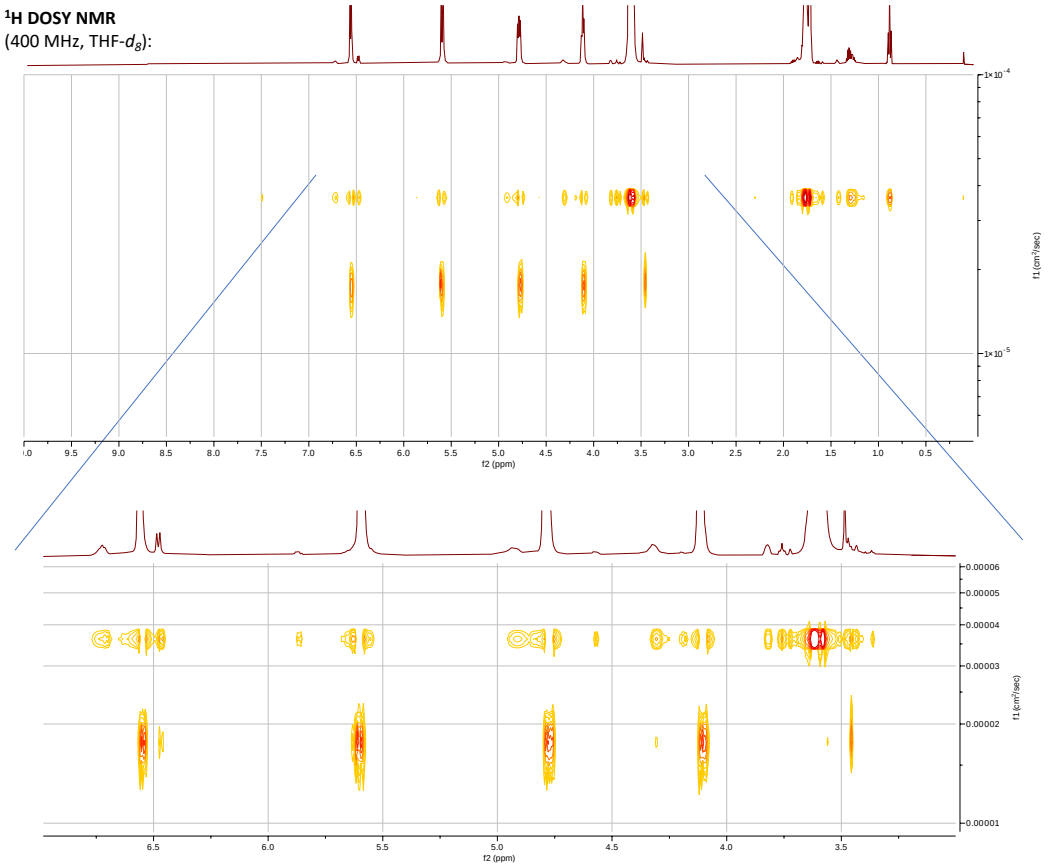

Figure S15. DOSY ^{1}H NMR spectra (THF-d_8, 400 MHz) of **3** illustrating both monomeric and higher order speciation exist in solution.

EPR quantification of 3

Two solutions of **3** in THF were prepared (1 and 3 mM) and quantified against a calibration curve of Cu(II). A minor concentration dependence was observed consistent with complex speciation, with slightly over 100 % (105 – 112 %, excluding a nonlinear calibration point) quantification of the unpaired electron of **3** was determined. We attribute this higher quantification to minor experimental error or minor paramagnetic impurities as the paramagnetic contribution of **3** is small compared to (1 electron over the whole complex of 236 atoms) the diamagnetic portion of the complex.

Calibration curve[1]		EPR quantification of 3					
c (mM)	Area[2]	Entry	Area[2]	Prepared c (mM)	EPR obtained c (mM)	3 (%)	Comment - Calibration curve:
0,9	17994,4	1	29033,677	1,0	1,3	122	Considering all the points
1,8	52139,8	2			1,2	112	Excluding 3rd point
2,7	57194,4	3	106316,29	3,0	3,5	115	Considering all the points
3,5	119341,9	4			3,2	105	Excluding 3rd point

[1]Calibration curve of $CuSO_4$ in H_2O/Ethylene glycol 1:1. [2]Area calculated in G=2450-3550

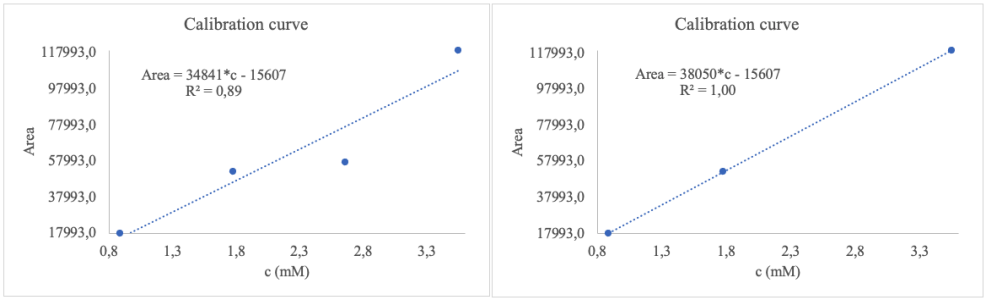

Figure S16. Calibration curve against Cu(II) and EPR quantification of **3**.

^{1}H NMR quantification of 3

Quantitative ^{1}H NMR experiments of **3** in THF-d_8 were conducted (1 and 3 mM solutions), using analytically pure [^{n}Bu$_4$][PF$_6$] as calibration standard. In both cases, 100±2 % of **3** was determined. [^{n}Bu$_4$][PF$_6$] was chosen as the internal standard since it is inert and **3** and cannot undergo redox reactions with it.

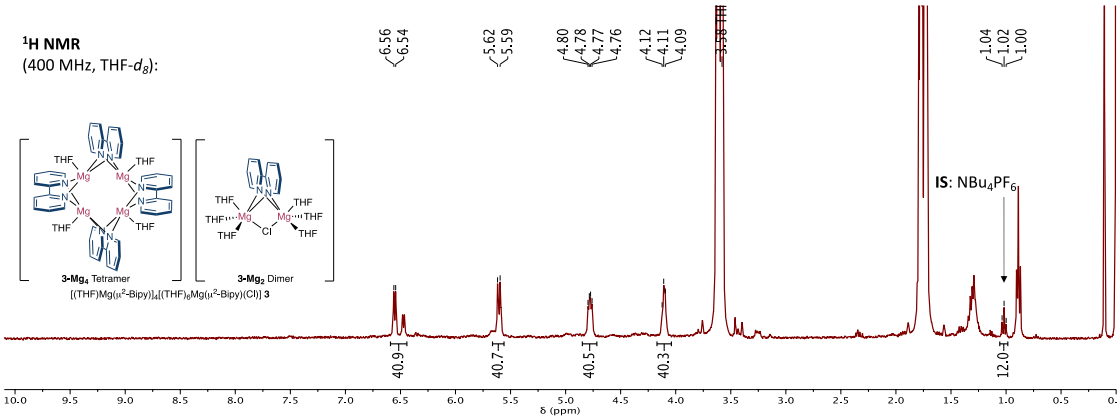

Figure S17. Quantitative ^{1}H NMR spectrum (THF-d_8, 400 MHz) of 3 mM solutions of **3**.

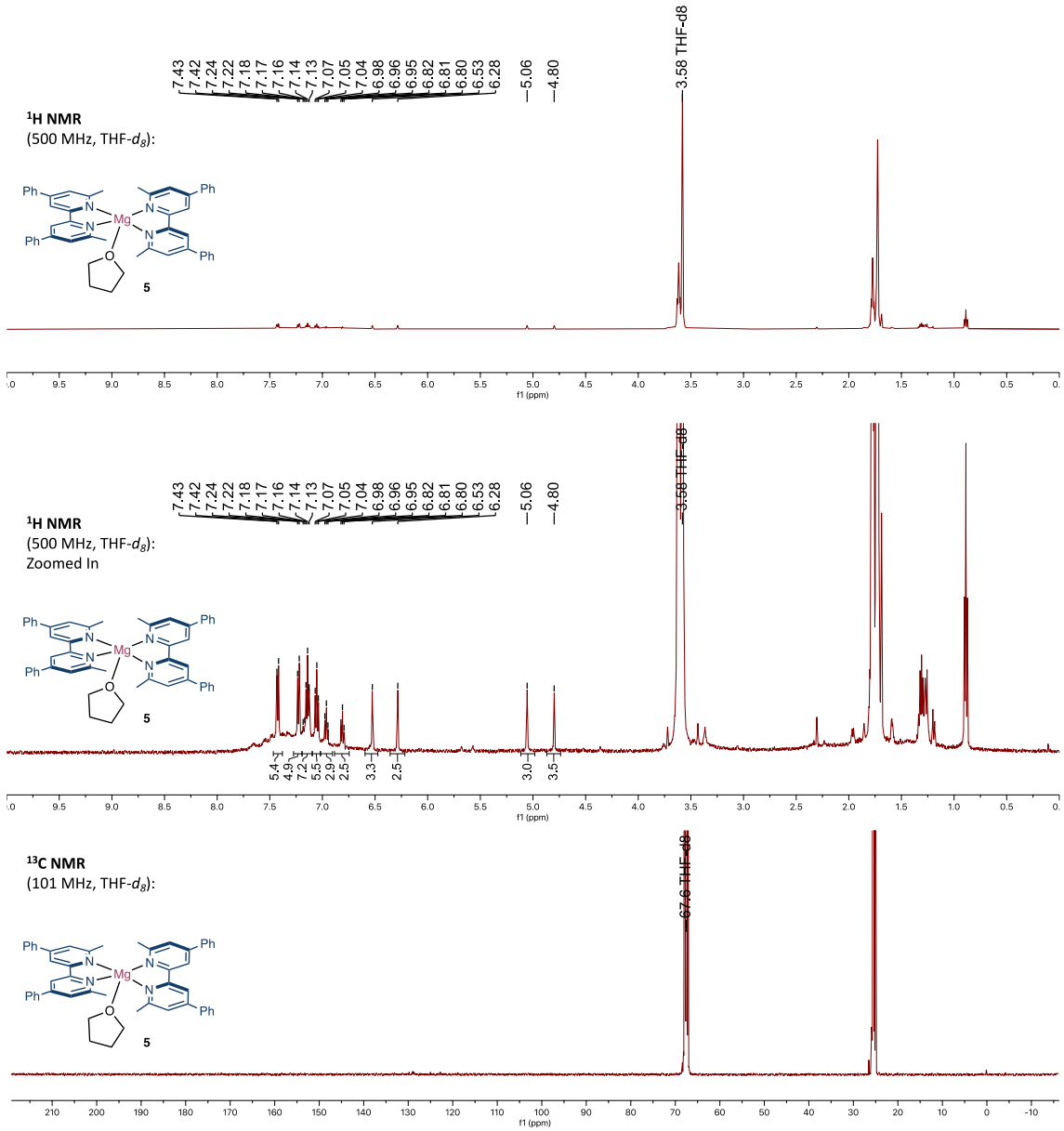

Figure S18. ^{1}H and ^{13}C NMR spectra (THF-d_8, 500 MHz) of **5**.

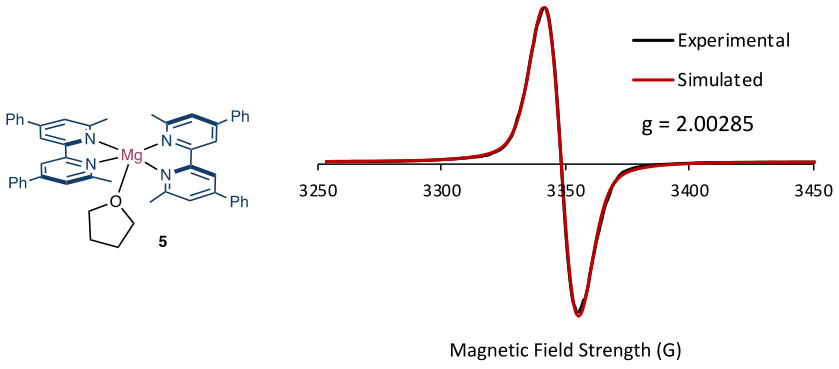

Figure S19. EPR spectrum of **5** (77K, THF), g = 2.00285.

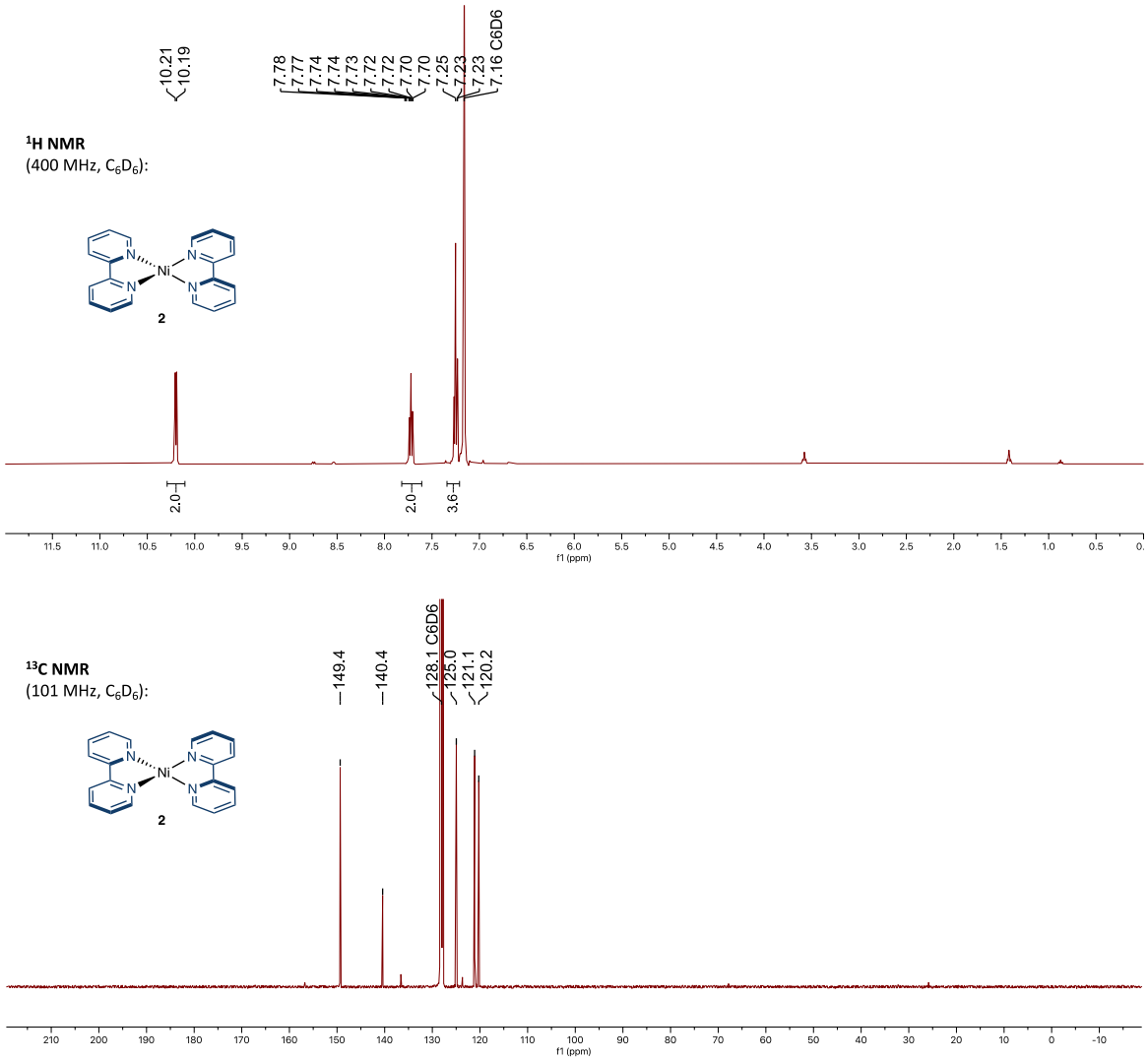

Figure S20. ^{1}H and ^{13}C NMR spectra (C_6D_6, 400 MHz) of $(bipy)_2Ni$ **2**.

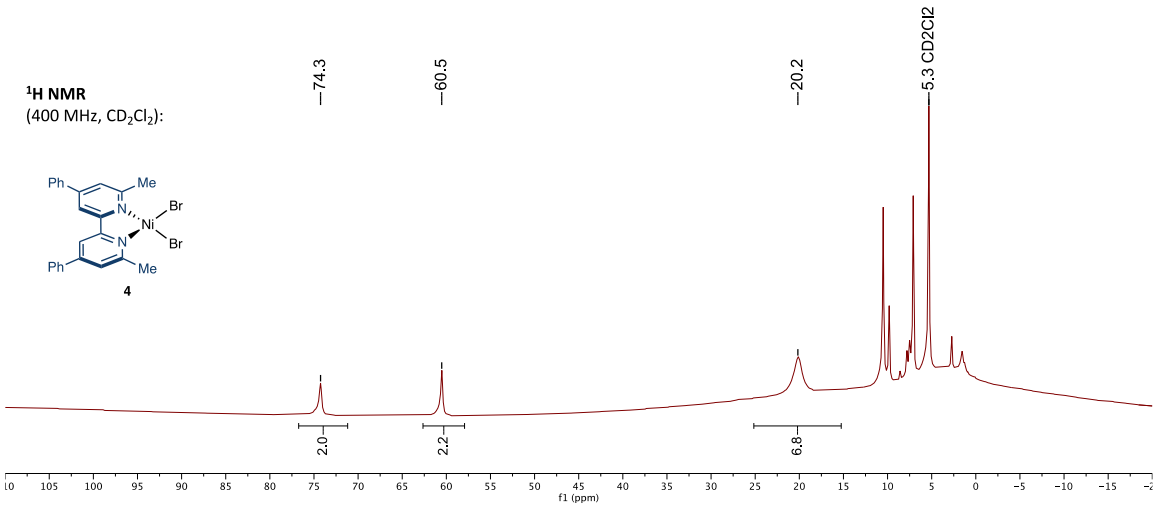

Figure S21. Paramagnetic ^{1}H NMR spectrum (CD_2Cl_2, 400 MHz) of (**L2**)$NiBr_2$ **4**.

3.6.6 Crystallographic Data

Data collection: The measured crystals were prepared under inert conditions immersed in perfluoropolyether as protecting oil for manipulation.

Crystal structure determination for compound **(bipy)$_2$Mg(THF)$_2$** was carried out using a Rigaku diffractometer equipped with a Pilatus 200K area detector, a Rigaku MicroMax-007HF microfocus rotating anode with MoK_α radiation, Confocal Max Flux optics and an Oxford Cryosystems low temperature device Cryostream 700 plus (T = -173 °C). Full-sphere data collection was used with ω and φ scans. *Programs used:* Data collection data reduction with CrysAlisPro[13] and absorption correction with Scale3 Abspack scaling algorithm.[14]

Crystal structure determination for **3** (crystal type C) was carried out using an Apex DUO Kappa 4-axis goniometer equipped with an APPEX 2 4K CCD area detector, a Microfocus Source E025 IuS using CuK_α radiation, Quazar MX multilayer Optics as monochromator and an Oxford Cryosystems low temperature device Cryostream 700 plus (T = -173 °C). Full-sphere data collection was used with ω and φ scans. *Programs used:* Data collection APEX-2,[15] data reduction Bruker Saint[16] V/.60A and absorption correction TWINABS.[17]

Crystal structure determination for **2**, **5**, **6** and **L2** was carried out using an Apex DUO Kappa 4-axis goniometer equipped with an APPEX 2 4K CCD area detector, a Microfocus Source E025 IuS using MoK_α radiation, Quazar MX multilayer Optics as monochromator and an Oxford Cryosystems low temperature device Cryostream 700 plus (T = -173 °C). Full-sphere data collection was used with ω and φ scans. *Programs used:* Data collection APEX-2,[15] data reduction Bruker Saint[16] V/.60A and absorption correction SADABS.[17]

Structure Solution and Refinement: Crystal structure solution was achieved using the computer program SHELXT.[18] Visualization was performed with the program SHELXle.[19] Missing atoms were subsequently located from difference Fourier synthesis and added to the atom list. Least-squares refinement on F^2 using all measured intensities was carried out using the program SHELXL 2015.[20] All non-hydrogen atoms were refined including anisotropic displacement parameters.

Comments for the structures:

Compound 3: Due to the difficulties in obtaining high quality single crystals for **3** and in order to confirm unambiguously this structure and specially the oxidation status of the metal atoms, several crystallizations and measurements were performed. While as

a powder, compound **3** is stable in a nitrogen glovebox, in the crystalline form is extremely sensitive to solvent loss (THF) and readily oxidizes under aerobic atmosphere (crystallizations were performed in a glovebox freezer), various methods of crystal preparation were performed (e.g chilling with dry CO_2, a N_2 stream at the microscope, etc.). Additionally, the preparation was further complicated as the colour of the crystals are very dark and opaque with a very dark mother liquor. The general tendence of this compound to also crystallize as multicomponent crystals or twins make this a very challenging compound to work with. Finally, 16 crystals were measured. Different cells in one crystal corresponded to different indexations of the same dataset (27 indexed datasets) containing the **3-Mg$_4$/3-Mg$_2$** couple. A summary of the dataset collected is shown in Table S1.

Table S1. Table of 16 different measured crystals, corresponding to each crystal code. Different cells correspond to different indexations of the same dataset (27 indexations). The dark grey marked line corresponds to the best dataset measured.

Crystal	Crystal code	Cell	Space group	a	b	c	α	β	γ	R1 (%)	Ratio reflect/par	Comments
A	mo_CSD0533_frag	monoclinic	*P*2/c	40.00	22.60	23.72	90.00	95.70	90.00	14.63	6.27	Initial structure obtained; highly disordered
		monoclinic	*C*2/c	23.70	22.60	37.40	90.00	90.06	90.00	25.10		TWIN 1 0 0 0 -1 0 0 0 -1
		monoclinic	*C*2/c	44.20	22.60	23.70	90.00	122.41	90.00	26.60		TWIN 1 0 2 0 1 0 0 0 -1
		orthorhombic	*P*bca	22.65	37.46	23.75	90.00	90.00	90.00	30.60		
		orthorhombic	*P*bcn	37.46	22.65	23.75	90.00	90.00	90.00	29.23		
		monoclinic	*C*2/m	23.75	22.64	37.36	90.00	90.06	90.00	24.92		
		orthorhombic	*I*bam	37.54	22.66	23.80	90.00	90.00	90.00	37.60		
A	58d-21 COJ311	orthorhombic	Pbcn	23,58	37,07	22,45	90,00	90,00	90,00	14,28	2,00	Extremly small crystal, not enough data
		orthorhombic	Pca2(1)	23,58	37,06	22,45	90,00	90,00	90,00	15,55	2,00	
D	58e-21 COJ311	triclinic	P1	17,93	18,43	18,98	97,83	92,07	118,07	14,76	4,80	Extremly disordered
D		triclinic	P-1	17,93	18,43	18,98	97,83	92,07	118,07	17,04	4,47	
D	58f-21 COJ311	triclinic	P-1	17,94	18,35	18,92	98,04	92,42	117,93			bad crystal
D	58ff-21 COJ311	triclinic	P-1	17,92	18,28	18,92	98,18	92,12	117,80			bad crystal
D	58ffff-21 COJ311	triclinic	P1	17,92	18,28	18,92	98,18	92,12	117,80	15,35	6,20	
D		triclinic	*P*-1	17.92	18.28	18.92	98.18	92.12	117.80	15.64	6.20	
D	247a-21 CSD08MgCluster	triclinic	P-1	18,00	18,41	18,96	98,33	92,13	117,73	20,00	3,50	
D	247b-21 CSD08MgCluster	triclinic	P-1	17,97	18,41	18,95	98,15	92,08	117,81	14,29	9,00	
C	58g-21 COJ311	monoclinic	C2/c	44,88	22,58	23,72	90,00	110,28	90,00	10,58	10,78	Multicomponent crystal with two domains
	58gg-21 COJ311	monoclinic	P21/c	42,99	22,64	23,81	90,00	101,05	90,00	24,08	9,69	
	58h-21 COJ311	triclinic	P1 / P2/m	22,64	23,81	43,06	79,31	90,04	89,97			bad crystal
C	58hh-21 COJ311	monoclinic	C2/c	45,00	22,67	23,76	90,00	110,26	90,00	24,45	3,08	twin5
C	58j-21 COJ311	monoclinic	C2/c	44,97	22,69	23,76	90,00	110,26	90,00	22,41	27,41	twin? Comprovar amb g
B	58i-21 COJ311	monoclinic	P2/c	39,92	22,61	23,70	90,00	90,80	90,00	19,66		TWIN 1 0 0 0 -1 0 0 0 -1
		monoclinic	P21/c	42,38	22,77	23.97	90,00	90,40	90,00	30,00		TWIN 1 0 0 0 -1 0 0 0 -1
B		orthorhombic	*P*bcn	42,34	22,71	23,88	90,00	90,00	90,00	13,38	5,51	
	58ii-21 COJ311	monoclinic	P2/c	39,98	22,64	23,76	90,00	95,87	90,00	24,00	3,70	
C	279a-21 CSD08Mgcluster	monoclinic	C2/c	45,10	22,64	23,80	90,00	110,20	90,00	7,15	13,78	TWIN 5 BASF 0.38

In general, it was observed that the crystal form measured depends on the crystallization conditions and on the speed by mounting the crystals. Generally, crystallizations of one same batch contained the same crystalline phase. Crystals mounted in a time below 5 seconds and directly form the suspension in the mother liquor under nitrogen, gave the best diffracting datasets but were difficult to clean up in relation of different crystalline domains. Crystals prepared first in the microscope under oil coating, presented different crystalline phases than the previous ones and showed a much higher mosaicity. In contrast, these were easier to select and clean up. In general, the loss of THF in the crystal leaded to changes in the crystal phase until it decomposed.

In the series of performed measurements a total of four different crystal structures (A, B, C and D) could be solved and refined which contained always the same organometallic core (**3-Mg_4/3-Mg_2** couple, see below); with a tremendous effort to obtain the best description of this new structure. For the description of this new compound in this paper the best dataset refined was selected (Structure type C). The complete description of all different structures obtained for this compound will be published elsewhere in a specialized journal.

Compound 3, crystal C:

A black crystal of compound **3** (crystal type C) was mounted directly extracted from the N_2-protected THF suspension without manipulation into the diffractometer at 100 K. The crystal was coated in perfluoropolyether as protecting oil and mounted in a time below 5 seconds. It resulted to be a multicomponent crystal from which two crystals could be indexed successfully. To reduce reflection overlapping the measurement was performed using Cu_{Ka}-radiation and the sample was processed with TWINABS[17] used for scaling and absorption correction of multicomponent crystals. The ratio of the two crystals after refinement (BASF value) achieved a value of 62:38. The structure obtained was of good quality (R1-value of 7.15 %) and for both crystals refined in the monoclinic space group *C*2/c an observed reflections to parameter ratio of 13,78 was reached.

The asymmetric unit contains one salt unit formed by a square Mg_4-cluster anion (3-Mg_4) and Mg_2Cl_1 cationic metal-complex molecule (3-Mg_2), and 6 ½ non-coordinated THF molecules. The 3-Mg_4 anion corresponds to a square Mg cluster coordinated to four bipyridine molecules and four THF molecules. The 3-Mg_2 cation corresponds to a bimetallic Mg complex with a chloro-bridge which is coordinated to one bipyridine molecule and six THF molecules. The 6.5 non-coordinated THF molecules are

disordered in 11 different locations. In the organometallic core most of the coordinated THF molecules are disordered in two orientations. Noteworthy a large residual electron density was located in the center of the four membered Mg-cluster which corresponds to a concentration of negative charge in the anionic part of the Mg-salt formed (1.9 $eÅ^{-3}$). This electron density is localized reproducibly in structures refined for crystal types A, B, C and D and is consistent with performed calculations.

Compound 2: The measured sample was formed by several crystals from which three could be indexed. Two minor crystals were ignored and only the larger crystal was used for integration. All samples tested were formed by several crystals and no better data could be collected. Although the structure is already known, the measured crystal corresponds to an unpublished polymorph of this compound. This structure unambiguously confirmed our assignment of **2** in its synthesis, which was lacking ^{1}H and ^{13}C NMR spectra in the literature. The refined crystal crystallized in the monoclinic space group *C*2/c as a real twin and the matrix -1 0 0 0 -1 0 1 0 1 (the minor twin component contribution was of 9 %; basf: 0.09) was applied. The asymmetric unit contains two half independent molecules of the metal complex which have *C*2 symmetry. Unusual residual densities and low bond precision were attributed to the presence of additional crystals in the sample measured and effects of twinning. The structure was considered of enough quality to be published.

Compound 5: Crystals measured for this sample were black and extremely difficult to select from the suspension. Mounted crystals were always formed by several single crystals (multi-component crystal or twin). The selected sample was also formed from several crystals in which five single crystals could be indexed (Crystals AA, BB, CC, DD and EE). Three different cells were identified. Crystal AA: a: 11.88 Å, b: 7.5 Å, c: 20.20 Å, α: 90º, β: 90º γ: 90º; Orthorhombic P. Crystal BB: a: 13.12 Å, b: 13.38 Å, c: 14.67 Å, α: 67.1º, β: 85.9º γ: 69.4º; Triclinic P. Crystal CC: a: 13.1 Å, b: 13.5 Å, c: 14.5 Å, α: 67.0º, β: 85.7º γ: 69.1º; Triclinic P. Crystal DD: a: 11.05 Å, b: 7.36 Å, c: 11.84 Å, α: 90º, β: 117.3º γ: 90º; Monoclinic P. Crystal EE: a: 11.07 Å, b: 7.38 Å, c: 11.86 Å, α: 90º, β: 117.0º γ: 90º; Monoclinic P. Crystals AA and EE were integrated, solved and refined. Both (AA and EE) corresponded to the structure of the ligand in two polymorphic forms (This ligand was used for forming the metal-complex structure; ligand: $C_{24}H_{22}N_2$). The structure corresponding to crystal EE was not added to this paper. Crystal AA is described as Compound L2. Crystal BB was also integrated, solved and refined and corresponded to the expected structure. The asymmetric unit of crystal

BB contains one molecule of the Mg metal complex and one non-coordinated THF molecule. Low bond precision on C-C bonds (0.00429) and deviations for the K values in the analysis of variance (C-alerts) were considered an effect of the presence of several crystals in the sample. Despite of the presence of the other crystals in the sample, the structure of crystal BB was of good quality and considered suitable for publication. The integration was performed using only the orientation matrix for crystal BB ignoring possible overlapping reflections of the other crystals present.

Compound L2: Compound L2 corresponds to crystal AA to the previous described multi-component crystal sample. The asymmetric unit contains half a molecule of the ligand which show *C*i-symmetry.

Compound 6: The two THF molecules attached to the Magnesium atom are disordered in two orientations (approximate ratio: 50:50).

Compound (Bipy)$_2$Mg(THF)$_2$: This compound crystallizes in the tetragonal group space *P*-42$_1$c. The asymmetric unit contains half molecule of the Mg metal complex.

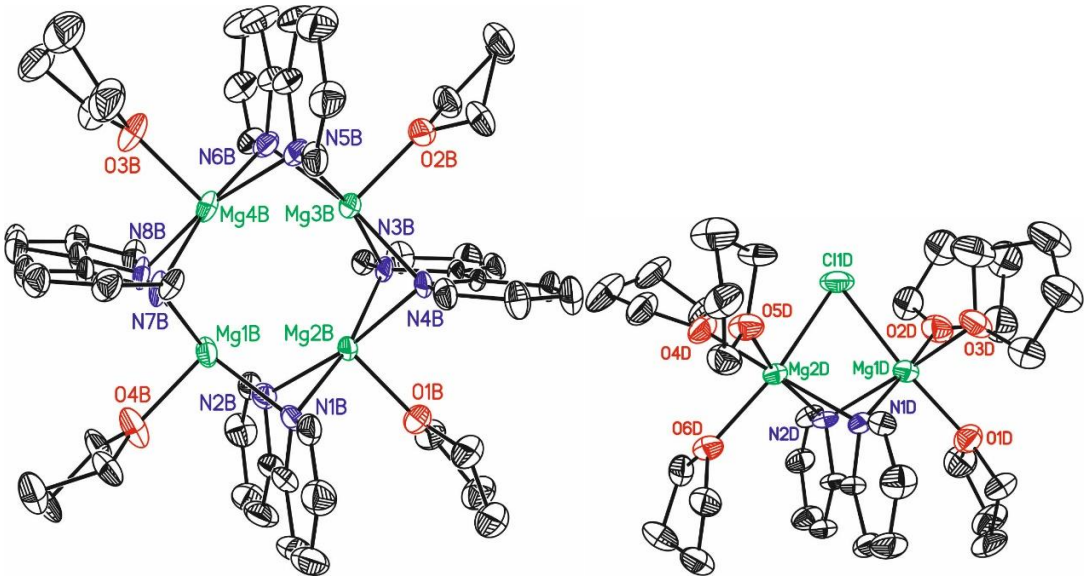

Figure S22. ORTEP drawing (50 %) showing one of the tetranuclear (**3-Mg$_4$**) and one of the binuclear groups (**3-Mg$_2$**) present in the structure of [(THF)$_4$Mg$_4$(□^{2}-bipy)$_4$][(THF)$_6$Mg$_2$(□^{2}-bipy)(Cl)] **3**. Non-coordinated solvent molecules (THF), disordered parts and hydrogen atoms have been omitted in the sake of clarity. CCDC deposition numbers **CCDC-2151121**.

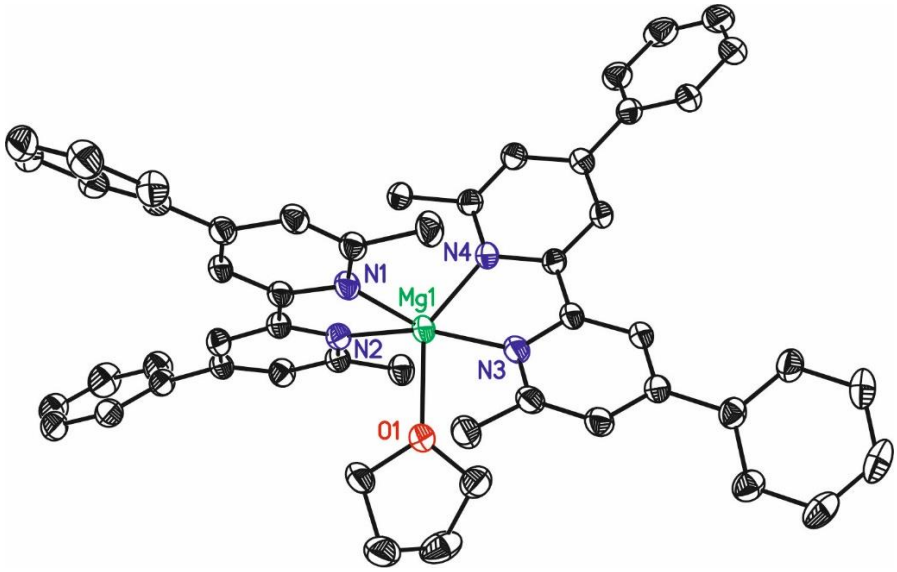

Figure S23. ORTEP drawing (50 %) showing Mg(4,4-phenyl-2,2-methyl-bipyridine)$_2$(THF) **5**. A non-coordinated THF molecule and hydrogen atoms have been omitted in the sake of clarity. CCDC deposition number **CCDC-2060212.**

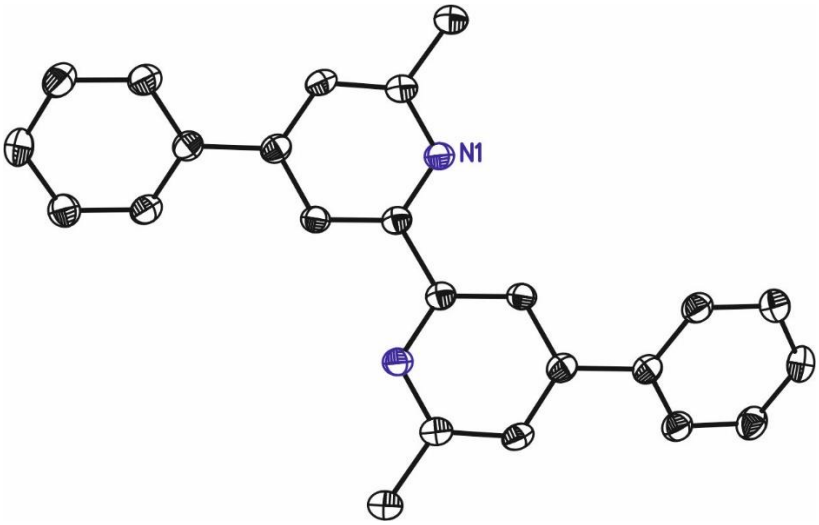

Figure S24. ORTEP drawing (50 %) showing 4,4-phenyl-2,2-methyl-bipyridine **L2**. Hydrogen atoms have been omitted in the sake of clarity. CCDC deposition number **CCDC-2060213.**

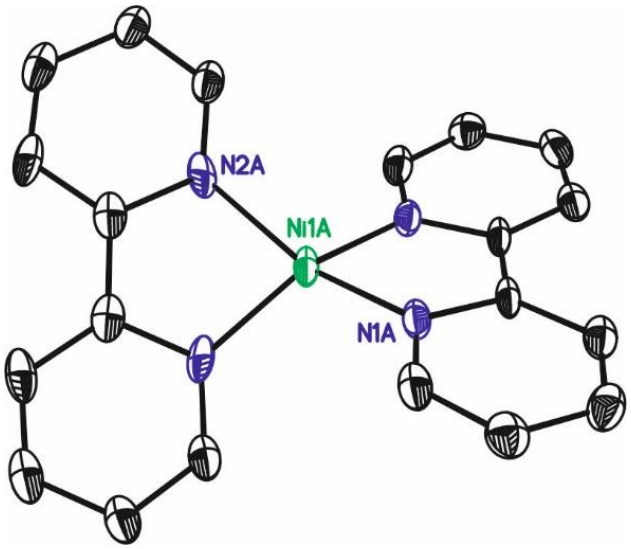

Figure S25. ORTEP drawing (50 %) showing one of the independent molecules contained in the structure of $(bipy)_2Ni$ **2**. Hydrogen atoms have been omitted in the sake of clarity. CCDC deposition number **CCDC-2060211.**

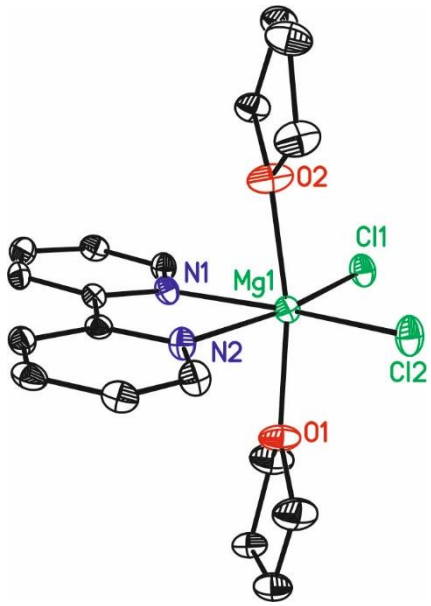

Figure S26. ORTEP drawing (50 %) showing $(bipy)MgCl_2(THF)_2$ **6**. Hydrogen atoms and disordered parts have been omitted in the sake of clarity. CCDC deposition number **CCDC-2060214.**

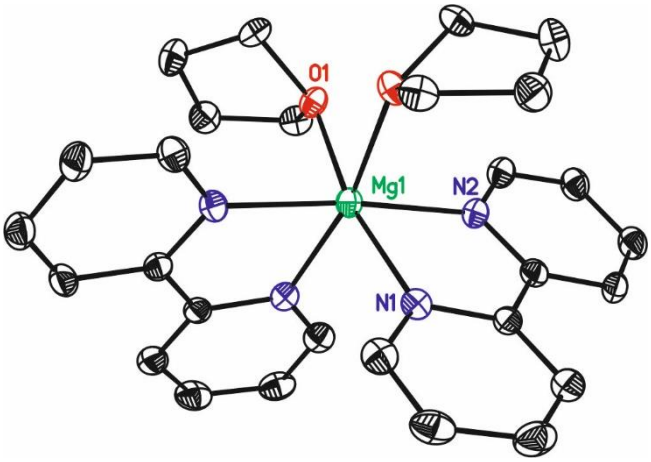

Figure S27. ORTEP drawing (50 %) showing $(bipy)_2Mg(THF)_2$. Hydrogen atoms have been omitted in the sake of clarity. CCDC deposition number **CCDC-2060210.**

Table S2. Crystallographic Data

	3 crystal type C	**6**	**$(bipy)_2Mg(THF)_2$**
Formula	$C_{115}H_{170}Cl_1Mg_6N_{10}O_{16.25}$	$C_{18}H_{24}Cl_2MgN_2O_2$	$C_{56}H_{64}Mg_2N_8O_4$
Formula weight	2133.91	395.60	961.77
T (K)	100(2)	100(2)	100(2)
Wavelength (Å)	1.54178	0.71073	0.71073
Crystal system	Monoclinic	Monoclinic	Tetragonal
Space group	*C*2/c	$P2_1/n$	$P\text{-}4\ 2_1c$
***a* (Å)**	45.107(5)	9.1946(9)	12.8507(4)
***b* (Å)**	22.640(2)	15.3698(13)	12.8507(4)
***c* (Å)**	23.805(3)	13.4637(12)	14.7557(10)
α (deg)	90	90	90
β (deg)	110.211(3)	97.066(3)	90
γ (deg)	90	90	90
V ($Å^3$)	22813(4)	1888.2(3)	2436.8(2)
Z	8	4	2
Density (calc.) (Mg/m^3)	1.243	1.392	1.311
μ (mm^{-1})	1.158	0.391	0.107
F(000)	9192	832	1024
Crystal size (mm^3)	0.50 x 0.20 x 0.20	0.080 x 0.040 x 0.010	0.200 x 0.020 x 0.020
Theta range for data collection (deg)	2.087 to 68.154	2.020 to 27.521	2.761 to 29.273
Index ranges	$-54 \le h \le 50$, $0 \le k \le 26$, $0 \le l \le 28$	$-11 \le h \le 11$, $-19 \le k \le 11$, $-17 \le l \le 17$	$-11 \le h \le 17$, $-17 \le k \le 10$, $-19 \le l \le 20$
Reflections collected	93425	16728	7037
Independent reflections	30367[R(int) = 0.0566]	4278[R(int) = 0.0889]	2741[R(int) = 0.0482]
Completeness to theta	96.1 % 68.154°	98.7 % 27.521°	93.0% 29.273°
Absorption correction	Multi-scan	Multi-scan	Multi-scan
Max. and min. transmission	0.75 and 0.51	0.74 and 0.67	1.00 and 0.59
Refinement method	Full-matrix least-squares on F^2	Full-matrix least-squares on F^2	Full-matrix least-squares on F^2
Data / restraints / parameters	30367/ 3441/ 1980	4278/ 318/ 480	2741/ 0/ 159
Goodness-of-fit on F^2	1.039	1.013	1.012
Final R indices [I>2sigma(I)]	R1 = 0.0715, wR2 = 0.1988	R1 = 0.0519, wR2 = 0.0914	R1 = 0.0429, wR2 = 0.0749
R indices (all data)	R1 = 0.0791, wR2 = 0.2080	R1 = 0.1175, wR2 = 0.1131	R1 = 0.0738, wR2 = 0.0831
Largest diff. peak and hole	1.897 and -0.642 $e.Å^{-3}$	0.420 and -0.342 $e.Å^{-3}$	0.210 and -0.220 $e.Å^{-3}$

Table S3. Crystallographic Data

	5	**L2**	**2**
Formula	$C_{56}H_{56}MgN_4O_2$	$C_{48}H_{40}N_4$	$C_{20}H_{16}N_4Ni$
Formula weight	841.35	672.84	371.08
T (K)	100(2)	100(2)	100(2)
Wavelength (Å)	0.71073	0.71073	0.71073
Crystal system	Triclinic	Orthorhombic	Monoclinic
Space group	*P*-1	*P*bca	*C*2/c
***a* (Å)**	13.082(3)	11.858(2)	10.837(2)
***b* (Å)**	13.520(3)	7.4875(14)	15.072(3)
***c* (Å)**	14.564(3)	20.191(4)	20.492(4)
□□(deg)	66.980(4)	90	90
□□(deg)	85.856(4)	90	105.33
□□(deg)	69.474(4)	90	90
V (Å^3)	2214.0(8)	1792.7(6)	3227.9(11)
Z	2	2	8
Density (calc.) (Mg/m^3)	1.262	1.246	1.527
μ (mm^{-1})	0.089	0.073	1.212
F(000)	896	712	1536
Crystal size (mm^3)	0.080 x 0.080 x 0.060	0.080 x 0.080 x 0.060	0.100 x 0.100 x 0.040
Theta range for data collection (deg)	1.667 to 29.064	2.017 to 26.429	1.030 to 26.884
Index ranges	$-17 \leq h \leq 17$, $-18 \leq k \leq 18$, $-19 \leq l \leq 19$	$-14 \leq h \leq 14$, $-9 \leq k \leq 9$, $-25 \leq l \leq 25$	$-13 \leq h \leq 13$, $-19 \leq k \leq 18$, $-25 \leq l \leq 25$
Reflections collected	33259	23556	46223
Independent reflections	11764[R(int) = 0.0934]	1841[R(int) = 0.0936]	3444[R(int) = 0.0993]
Completeness to theta	99.4 % 29.064 °	99.9 % 26.429 °	98.5 % 26.884 °
Absorption correction	Multi-scan	Multi-scan	Multi-scan
Max. and min. transmission	0.74 and 0.39	0.74 and 0.43	0.74 and 0.54
Refinement method	Full-matrix least-squares on F^2	Full-matrix least-squares on F^2	Full-matrix least-squares on F^2
Data / restraints / parameters	11764/ 0/ 572	1841/ 0/ 119	3444/ 0/ 228
Goodness-of-fit on F^2	1.032	1.083	1.080
Final R indices [I>2sigma(I)]	R1 = 0.0753, wR2 = 0.1857	R1 = 0.0469, wR2 = 0.1137	R1 = 0.0715, wR2 = 0.2199
R indices (all data)	R1 = 0.1247, wR2 = 0.2191	R1 = 0.0647, wR2 = 0.1257	R1 = 0.0874, wR2 = 0.2347
Largest diff. peak and hole	0.535 and -0.366 e.Å^{-3}	0.190 and -0.286 e.Å^{-3}	2.558 and -0.732 e.Å^{-3}

Table S4. Key Bond Lengths and angles

Cpy-Cpy Bonds 3			
C5B-C6B	1.374(5)	C25B-C26B	1.369(5)
C15B-C16B	1.380(4)	C35B-C36B	1.373(5)
C5A-C6A	1.382(5)		
Mg-Mg Bonds 3			
Mg1A-Mg2A	2.9418(17)	Mg1B-Mg4B	2.8332(18)
Mg1B-Mg2B	2.8246(16)	Mg2B-Mg3B	2.8288(18)
Mg3B-Mg4B	2.8379(17)		
Mg-bipy-Mg angles 3			
Mg1B-Bipy-Mg2B	103.4(2)	Mg4B-Bipy-Mg3B	103.5(2)
Mg3B-Bipy-Mg4B	104.0(2)	Mg2B-Bipy-Mg3B	102.9(2)
Mg1A-Bipy-Mg2A	108.8 (2)		
Mg-Mg-Mg angles 3			
Mg4B-Mg1B-Mg2B	90.0(2)	Mg2B-Mg3B-Mg4B	89.9(2)
Mg1B-Mg2B-Mg3B	90.1(2)	Mg3B-Mg4B-Mg1B	90.0(2)
Cpy-Cpy Bonds 5			
C5-C6	1.443(3)	C29-C30	1.442(3)
Cpy-Cpy Bonds L2			
C1-C1	1.496(3)		
Cpy-Cpy Bonds 6			
C5-C6	1.490(4)		
Cpy-Cpy Bonds 2			
C5B-C6B	1.443(9)	C1A-C1A	1.436(13)
C10A-C10A	1.425(14)		
Cpy-Cpy Bonds $(bipy)_2Mg(THF)_2$			
C5-C6	1.422(3)		

3.6.7 Computational Details

The molecular models were computed without truncations or symmetry constraints. Calculations were run using the Gaussian 16 program, Revision B.01.[21] Geometries were fully optimized (no imaginary frequencies) at the PBE0/6-31G+(d,p) level,[22-25] including the D3BJ empirical dispersion correction from Grimme[26] and the IEFPCM[27-28] solvent model with the parameters for tetrahydrofuran (THF). All energies are given at 298.15 K. For the orbital pictures (made with ChemCraft version 1.8 build 610b),[29] the isovalue was set to 0.03 for all LUMO/HOMO/SOMO orbitals and to 0.004 for all spin densities.

Dinuclear 3-Mg_2

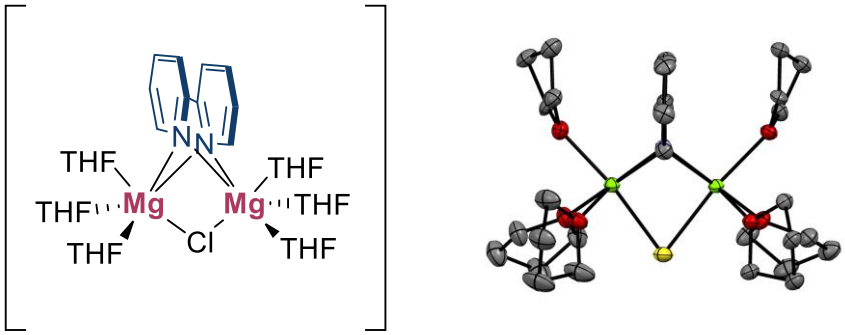

Figure S28. ChemDraw drawing (left) and X-ray structure (right) of dinuclear **3-Mg_2**

The dinuclear **3-Mg_2** species is comprised of one bipy ligand, one chloride, two Mg atoms and six THF molecules. If neutral, this amounts to a total of 101 atoms and 363 electrons and the system could *a priori* be doublet (one unpaired electron) or a quartet (three unpaired electrons). The complex was computed as a neutral species (doublet and quartet spin states), as a cation (singlet, assuming one electron was donated to **3-Mg_4**) and as an anion (singlet, assuming one electron was accepted from **3-Mg_4**). The starting geometry was taken from the experimental X-ray structure.

Charge	Spin state	Mg-N-Mg angle (average)	Mg-Mg distance (Å)	C(py)-C(py) distance (Å)	ΔG (kcal/mol)
0	Doublet	83.8	2.90	1.39	0.0
0	Quartet	83.7	2.91	1.43	13.8
-1	Singlet	82.7	2.94	1.38	-
+1	Singlet	83.2	2.95	1.38	-
X-ray structure		83.1	2.94	1.38	-

Table S5. Comparison of geometric parameters of the neutral (doublet/quartet), anionic and cationic **3-Mg$_2$**.

Table S5 shows that in terms of geometry, both charged forms of **3-Mg$_2$** have a Mg-Mg distance that is closer to the X-ray structure (2.94 Å, Table S4) than the computed neutral form.

Tetranuclear 3-Mg$_4$

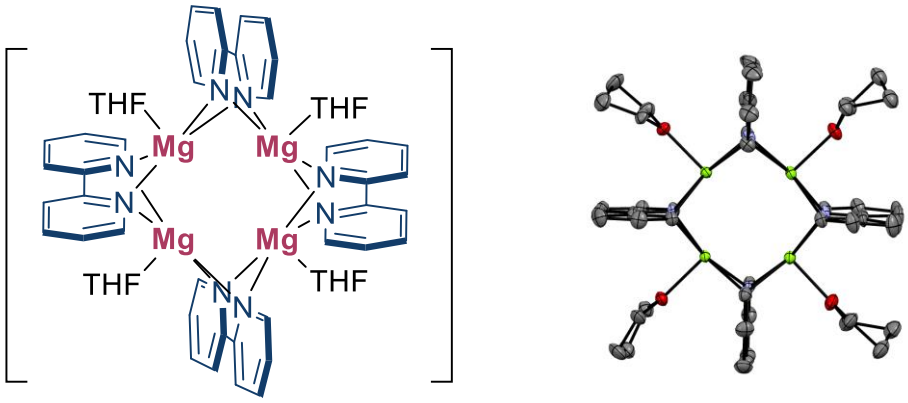

Figure S29. ChemDraw drawing (left) and X-ray structure (right) of the tetranuclear **3-Mg$_4$**

The full **3-Mg$_4$** structure was selected for computations, consisting of four bipy ligands, four Mg atoms, and four THF molecules. If neutral, this amounts to a total of 136 atoms and 536 electrons. Depending on the orbital distribution of the electrons, the system could be singlet (no unpaired electrons) or triplet (two unpaired electrons). The quintet (four unpaired electrons) and higher states were not considered in our calculations. Similarly to the dinuclear **3-Mg$_4$**, the anionic and cationic **3-Mg$_4$** were also computed (using the X-ray structure as starting geometry) and compared to the neutral one.

Charge	Multiplicity	Mg-Mg (Å)	C(py)-C(py) (Å)	dG (kcal/mol)
0	Singlet	3.04	1.38	0.0
0	Triplet	2.83	1.39	+12.5
-1	Doublet	2.82	1.38	-
+1	Doublet	3.05	1.39	-
X-ray structure		2.83	1.37	-

Table S6. Comparison between the neutral (singlet state), anionic and cationic **3-Mg$_4$**

There is a clear difference in Mg-Mg distance between the cationic and anionic forms of **3-Mg$_4$**. In the crystal structure, that distance is around 2.83 Å (Table S4), which is closer to the anion than the cation or neutral species.

In order to establish the preferred oxidation states of the **3-Mg$_2$** and **3-Mg$_4$** fragments, the Gibbs free energies were analyzed at the PBE0-D3BJ/6-31+G(d,p) level as follows:

$$[3-Mg_2]^0 + [3-Mg_4]^0 \rightarrow [3-Mg_2]^+ + [3-Mg_4]^- \qquad \Delta G = -11.7\ kcal/mol$$

$$[3-Mg_2]^0 + [3-Mg_4]^0 \rightarrow [3-Mg_2]^- + [3-Mg_4]^+ \qquad \Delta G = +67.1\ kcal/mol$$

These energies support that the **3-Mg$_2$/3-Mg$_4$** system most likely is an ion pair where **3-Mg$_2$** is the cation and **3-Mg$_4$** is the anion.

Bipy ligand

Given the propensity for the bipy ligand to act as a neutral, anionic (-1) or dianionic (-2) species depending on the system,[30-33] we analyzed the bipy ligands in both Mg clusters to determine their nature. The free bipy ligand was first computed separately with different oxidation states and then compared to the computed and experimental bipy ligand in the clusters.

Species	Charge	C(py)-C(py)
Bipy	0	1.49
	-1	1.44
	-2	1.39
[3-Mg$_2$]$^+$ (computed)	+1	1.38
[3-Mg$_4$]$^-$ (computed)	-1	1.38
[3-Mg$_2$] (X-ray)		1.38
[3-Mg$_4$] (X-ray)		1.37

Table S7. Calculated C(py)-C(py) distances in the isolated bipy ligand (neutral, anionic and dianionic) and the optimized [**3-Mg$_2$**]$^+$ and [**3-Mg$_4$**]$^-$ structures, as well as the crystal structure. For [**3-Mg$_4$**]$^-$ and the X-ray [**3-Mg$_4$**], the average C(py)-C(py) distance is reported.

The C(py)-C(py) distance varies significantly depending on the charge of the bipy, as shown in Table S7. The calculated C(py)-C(py) distances in [**3-Mg$_2$**]$^+$ and [**3-Mg$_4$**]$^-$ correlate well with the value for the free dianionic bipy, as well as the distance measured in the X-ray structure. This is consistent with an assignment where all Mg atoms in **3-Mg$_2$** and **3-Mg$_4$** are Mg(II).

Orbital analysis of **3-Mg$_2$** and **3-Mg$_4$**

For [**3-Mg$_2$**]$^+$, the HOMO and LUMO orbitals are nr. 181 and 182 respectively. The HOMO is localized on both sides of the bipy ligand, and so is the LUMO.

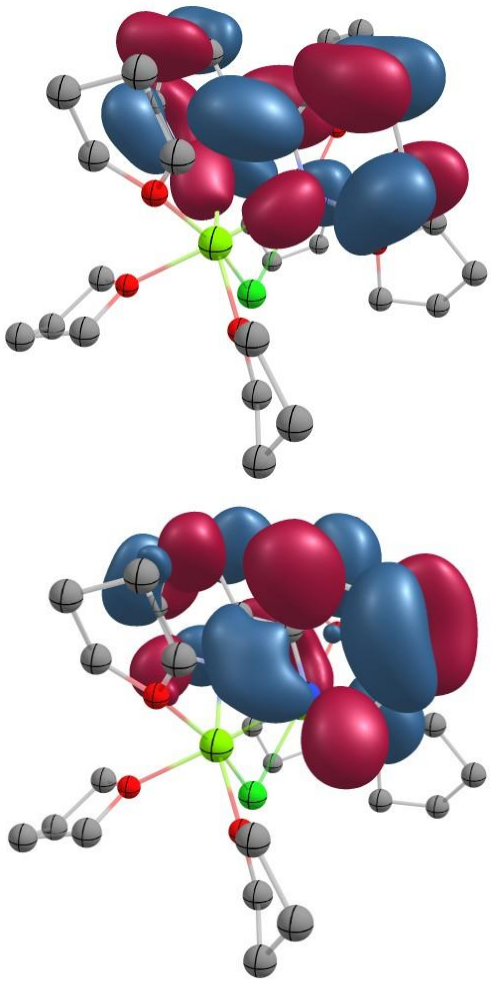

Figure S30. HOMO (left) and LUMO (right) of [**3-Mg$_2$**]$^+$

For [**3-Mg$_4$**]$^-$, the HOMO and LUMO were determined to be orbitals 269 and 270, respectively. Interestingly, the SOMO of [**3-Mg$_4$**]$^-$ is not the HOMO, but rather the α-HOMO-4 orbital. The α-HOMO-4 is localized in the middle of the square created by the four Mg atoms, in agreement with the assignment of the electride electron to this orbital. The same SOMO orbital was observed with other DFT functionals (ωB97XD, BP86), which supports that this result is not an artifact. The SOMO-HOMO inversion indicates that [**3-Mg$_4$**]$^-$ does not follow the Aufbau principle, however, we note that the electride electron is supposed to be free (not bound by an atom or molecule) and hence it should not enter into the molecular orbitals of 3-Mg$_4$. Therefore, one may view [**3-Mg$_4$**]$^-$ as two species, a neutral [**3-Mg$_4$**] part (which follows the Aufbau principle) and a free electron.

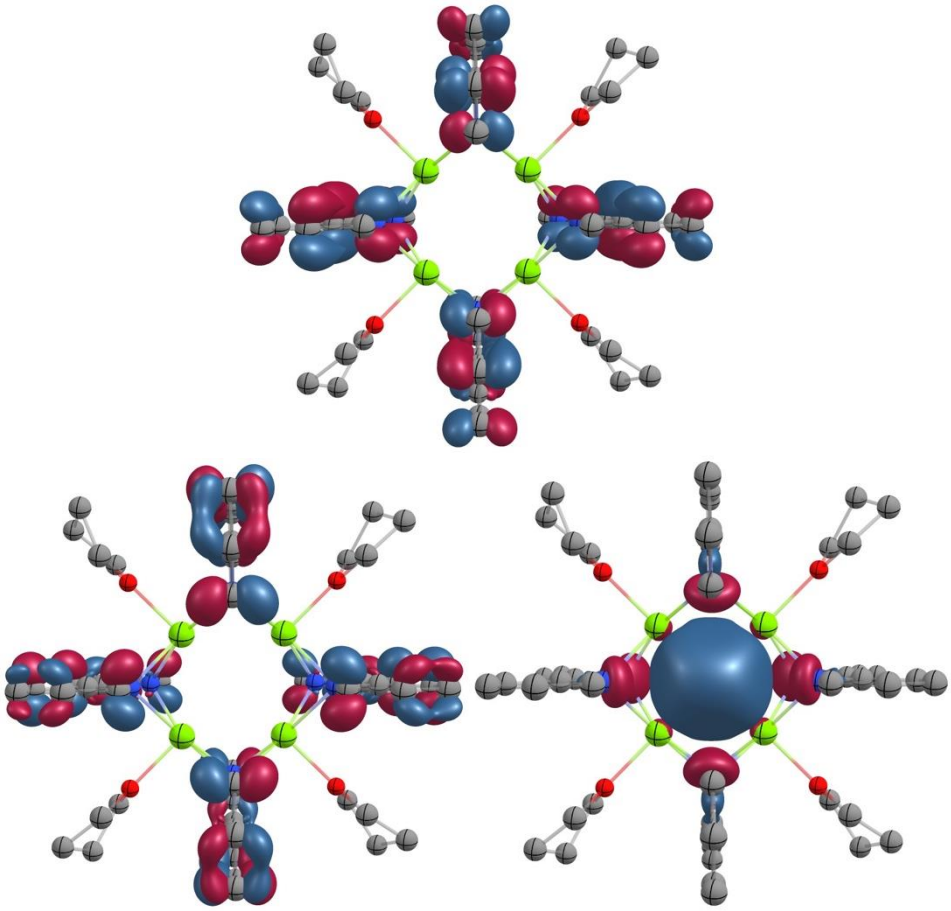

Figure S31. HOMO (top left), LUMO (top right) and SOMO (bottom) of [**3-Mg$_4$**]$^-$.

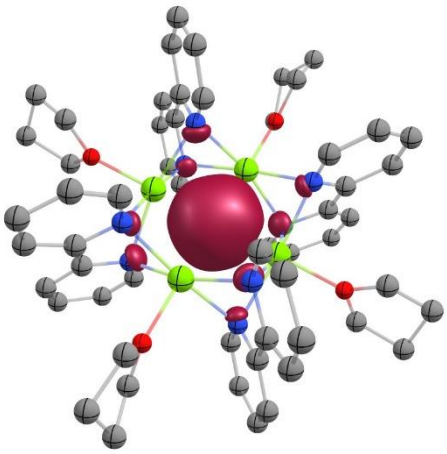

Figure S32. Spin density of [**3-Mg$_4$**]$^-$.

Structure **5**

The structure was optimized with the same computational protocol used for [**3-Mg$_2$**]$^+$ and [**3-Mg$_4$**]$^-$, in the closed-shell singlet (S = 0) and triplet (S = 1) state. The triplet is 13.7 kcal/mol more stable than the closed-shell singlet, indicating that **5** is a biradical.

Orbital analysis of the triplet system shows that the HOMO and LUMO orbitals are nr. 205 and 206, respectively. Similarly to [**3-Mg$_2$**]$^+$, the HOMO is located on the bipy ligands.

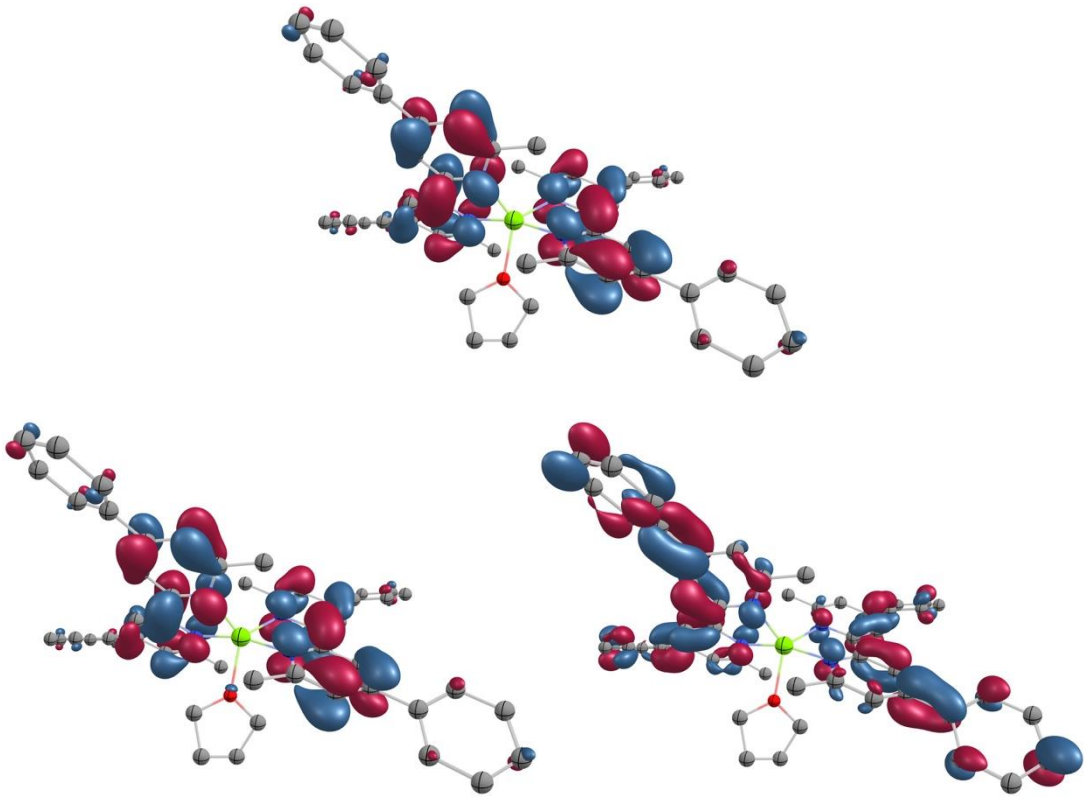

Figure S33. SOMO (orbital 204 top left, 205 top right) and LUMO (bottom) of structure **5** (triplet state)

The two SOMOs for this structure are orbitals 204 and 205, which follows the Aufbau principle. Both SOMOs have the same shape, but the main difference between the two is the inversion of phase on one of the bipy ligands.

Considering that the two spin sites in **5** are far away from each other (with one unpaired electron on each anionic bipy ligand), we also evaluated if the structure could be an open-shell singlet rather than a triplet. A broken symmetry singlet calculation was run using the triplet state geometry and wavefunction as starting guess, and the resulting optimized (M_S = 0) structure was only 0.7 kcal/mol higher in energy than the triplet (S = 1) structure. Analysis of the spin density shows that in the triplet state, each bipy ligand holds one α-spin, whereas in the broken symmetry singlet, one bipy has an α-spin and the other one has a β-spin (see Figure S34 below).

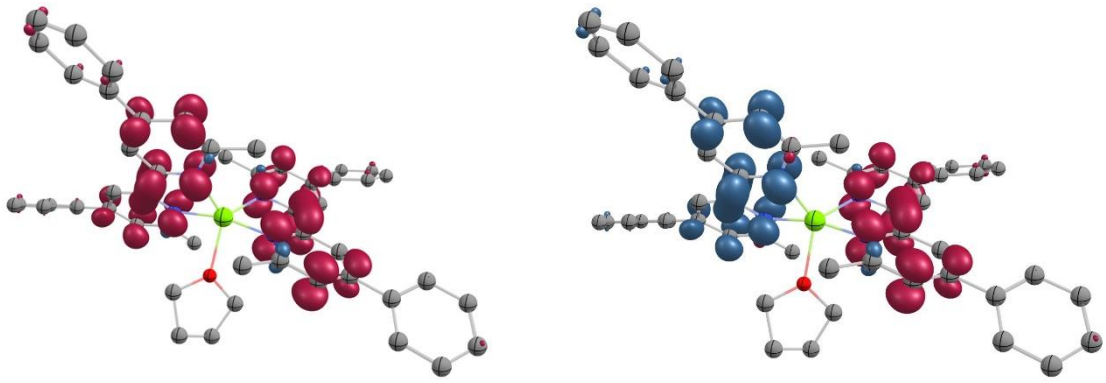

Figure S34. Comparison between the spin densities of structure **5** in the triplet state (left, S = 1) and in the broken symmetry singlet state (right, $M_S = 0$).

Given the small differences in energy between the triplet and the broken symmetry singlet state of **5**, it can be expected that both spin states would be thermally populated, which could make **5** a spin-crossover complex.

QTAIM analysis of [**3-Mg$_4$**]

The wave function of the molecules was extracted from the formatted checkpoint files of the PBE0/6-31G+(d,p) computations and was further analyzed within the framework of the quantum theory of atoms in molecules, QTAIM,[34] by AIMAll suite of programs.[35] The electron density, Laplacian of the electron density, and interatomic (zero-flux) surfaces were plotted by AIMStudio module, Figures S35, S36, and S37. The bonding between the Mg atoms in [**3-Mg$_4$**]$^-$ was examined by checking the electron delocalization index within the framework of QTAIM. The delocalization index values were found to be less than 0.01 au that is not even characteristic of a noncovalent interaction.

To assess aromatic/antiaromatic character of the bipyridine dianion, [**3-Mg$_2$**]$^+$ was selected and GIAO-NMR[36] computations at the PBE0/6-31G+(d,p) level were performed. The ring current intensity was measured as the integral of the current density passing through the interatomic surfaces between adjacent carbon atoms of the bipyridine ligands. The current density was assessed to be -2.6 nA.T^{-}, which is characteristic of a weakly antiaromatic system.

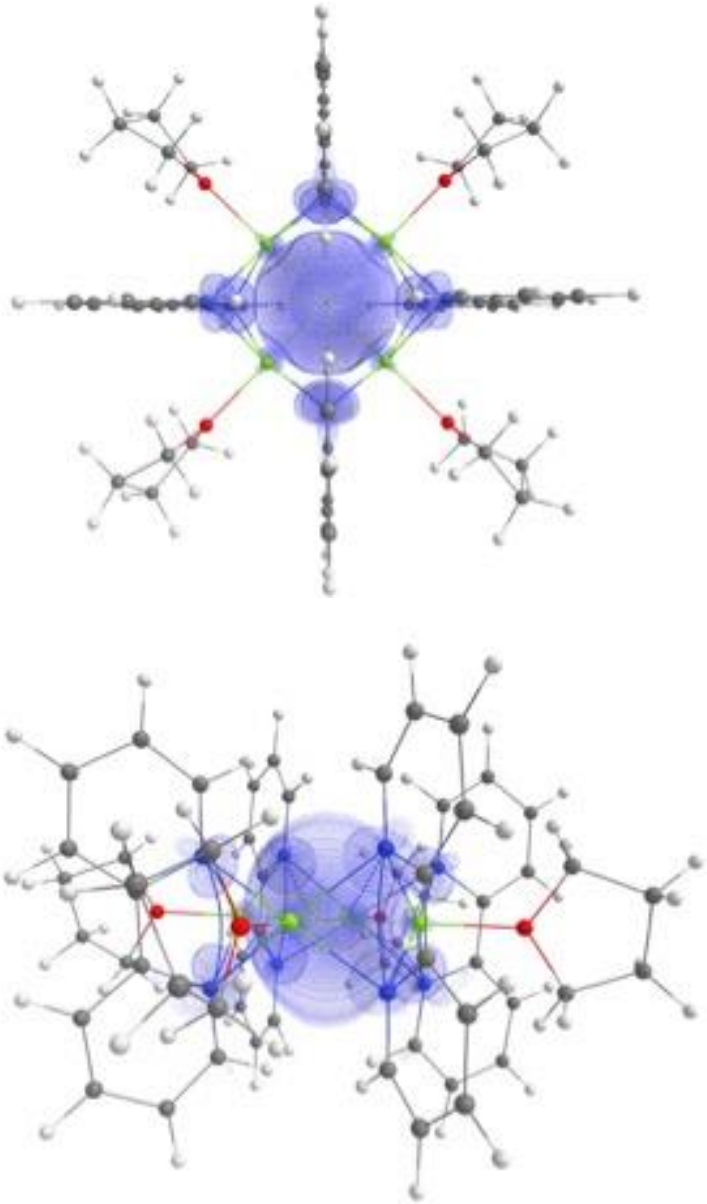

Figure S35. The spin density plots at 0.05 au isosurface.

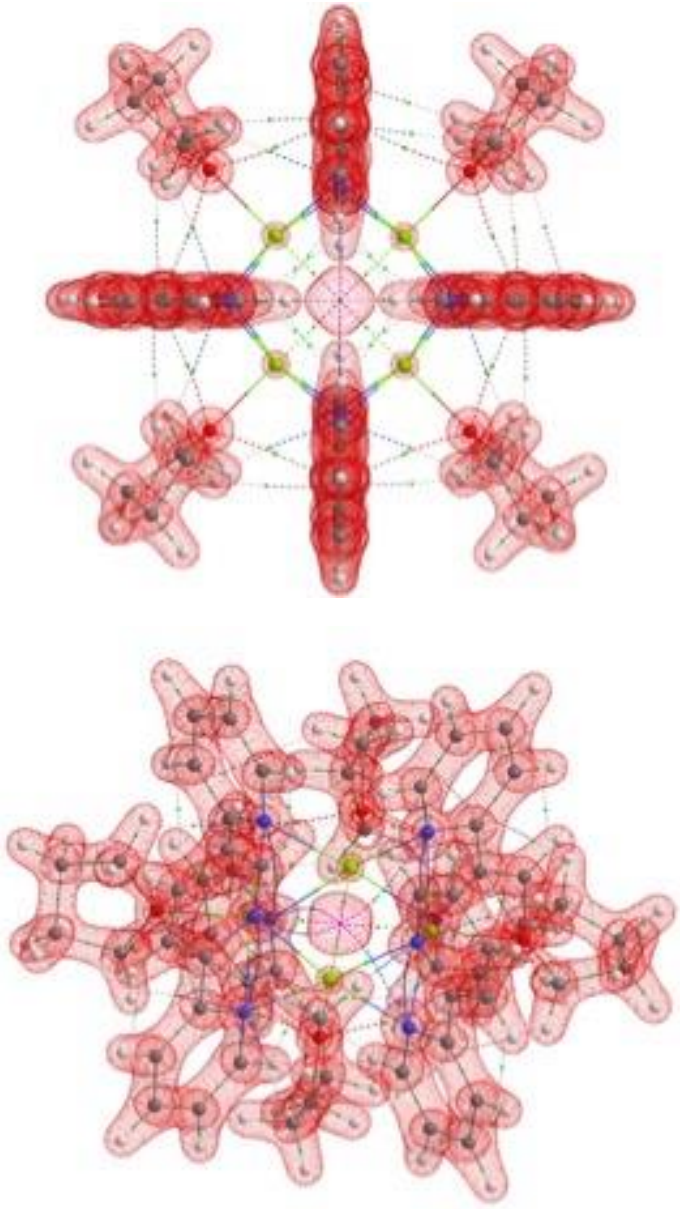

Figure S36. The 3D-isosurface of the Laplacian of the electron density at -0.005 au value from two directions. The central electron concentration corresponding to the electride electron is evident in both figures.

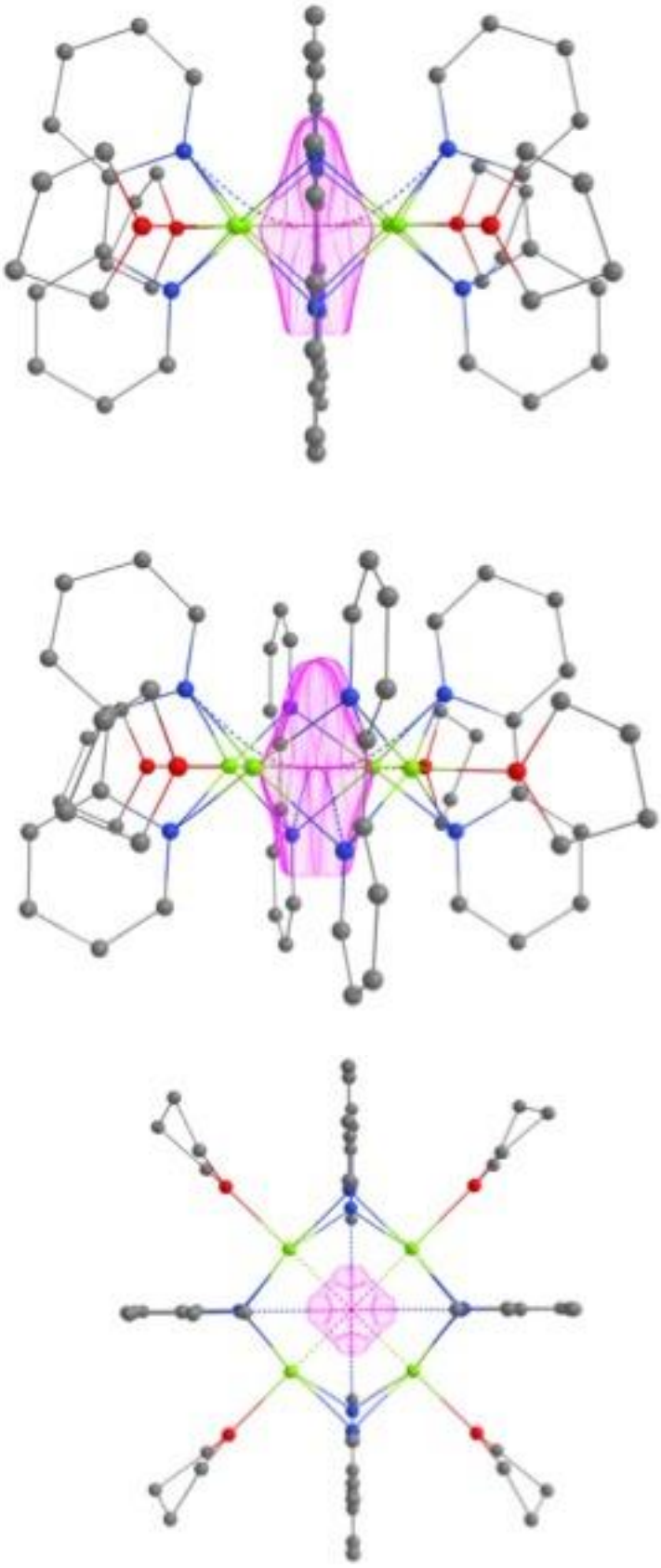

Figure S37. The atomic basin of the NNA enclosed in the interatomic zeroflux surfaces from different angles.

3.6.8 References for the Experimental Section

1. Yakhvarov, D. G.; Hey-Hawkins, E.; Kagirov, R. M.; Budnikova, Y. H.; Ganushevich, Y. S.; Sinyashin, O. G. Electrocatalytic reduction of aryldichlorophosphines with the (2,2′-bipyridine)nickel complexes. *Russ. Chem. Bull.* **2007,** *56* (5), 935-942.
2. Powers, D. C.; Anderson, B. L.; Nocera, D. G. Two-Electron HCl to H_2 Photocycle Promoted by Ni(II) Polypyridyl Halide Complexes. *J. Am. Chem. Soc.* **2013,** *135* (50), 18876-18883.
3. Tortajada, A.; Duan, Y.; Sahoo, B.; Cong, F.; Toupalas, G.; Sallustrau, A.; Loreau, O.; Audisio, D.; Martin, R. Catalytic Decarboxylation/Carboxylation Platform for Accessing Isotopically Labeled Carboxylic Acids. *ACS Catal.* **2019,** *9* (7), 5897-5901.
4. Creutz, C. Bipyridine Radical Ions. *Comments Inorg. Chem.* **1982,** *1* (5), 293-311.
5. Henne, B. J.; Bartak, D. E. Metal-vapor synthesis and electrochemistry of bis(bipyridyl)nickel(0). *Inorg. Chem.* **1984,** *23* (3), 369-373.
6. Wang, M.; England, J.; Weyhermüller, T.; Wieghardt, K. Electronic Structures of "Low-Valent" Neutral Complexes $[NiL_2]^0$ (S = 0; L = bpy, phen, tpy) – An Experimental and DFT Computational Study. *Eur. J. Inorg. Chem.* **2015,** *2015* (9), 1511-1523.
7. Behrens, H.; Müller, A. Zur Kenntnis der Chemie der Metallcarbonyle und der Cyanokomplexe in flüssigem Ammoniak, XIII. Zur Kenntnis der Reaktionsweisen der Cyanometallate(O) K6[Cr(CN)6] und K4[Ni(CN)4]. *Z. Anorg. Allg. Chem.* **1965,** *341* (3-4), 124-136.
8. Schunn, R. A.; Ittel, S. D.; Cushing, M. A.; Baker, R.; Gilbert, R. J.; Madden, D. P., Bis(1,5-Cyclooctadiene)Nickel(0). In *Inorg. Synth.*, 1990; pp 94-98.
9. Akira, M.; Yasuzo, U.; Takamichi, Y.; Hironori, K. The Electrochemical Behavior of the Low-valent Transititon-metal Complexes. I. Nickel-2,2′-Dipyridyl Complexes. *Bull. Chem. Soc. Jpn.* **1972,** *45* (5), 1438-1442.
10. Mahmut, A.; Takakazu, Y. Kinetic Study of Ligand Exchange Reactions of Bis(1,5-cyclooctadiene)nickel(0) with 2,2′-Bipyridine, 4,4′-Dimethyl-2,2′-bipyridine, and 4,4′,5,5′-Tetramethyl-2,2′-bipyridine. *Bull. Chem. Soc. Jpn.* **1999,** *72* (6), 1255-1261.
11. Dinjus, E.; Walther, D.; Kaiser, J.; Sieler, J.; Ngoc Thanh, N. 2,2′-dipyridyl-1,5-cyclooctadiennickel(0): kristall-und molekülstruktur. *J. Organomet. Chem.* **1982,** *236* (1), 123-130.
12. Davies, J.; Janssen-Müller, D.; Zimin, D. P.; Day, C. S.; Yanagi, T.; Elfert, J.; Martin, R. Ni-Catalyzed Carboxylation of Aziridines en Route to β-Amino Acids. *J. Am. Chem. Soc.* **2021,** *143* (13), 4949-4954.
13. Data reduction with CrysAlisPro 1.171.40.35 (Rigaku OD, 2018).
14. Empirical absorption correction using spherical harmonics implemented in Scale3 Abspack scaling algorithm, CrysAlisPro 1.171.40.35 (Rigaku OD, 2018).
15. Data collection with APEX II version v2013.4-1. Bruker (2007). Bruker AXS Inc., Madison, Wisconsin, USA.
16. Data reduction with Bruker SAINT version V8.30c. Bruker (2007). Bruker AXS Inc., Madison, Wisconsin, USA.

17. SADABS: V2012/1 Bruker (2001). Bruker AXS Inc., Madison, Wisconsin, USA. Blessing, Acta Cryst. 1995, A51, 33-38.
18. Sheldrick, G. M. SHELXT– Integrated space-group and crystal-structure determination. *Acta Crystallographica Section A Foundations and Advances* **2015,** *71* (1), 3-8.
19. Hübschle, C. B.; Sheldrick, G. M.; Dittrich, B. ShelXle: a Qt graphical user interface forSHELXL. *J. Appl. Crystallogr.* **2011,** *44* (6), 1281-1284.
20. Sheldrick, G. M. Crystal structure refinement withSHELXL. *Acta Crystallographica Section C Structural Chemistry* **2015,** *71* (1), 3-8.
21. Frisch, M. J.; Trucks, G. W.; Schlegel, H. B.; Scuseria, G. E.; Robb, M. A.; Cheeseman, J. R.; Scalmani, G.; Barone, V.; Petersson, G. A.; Nakatsuji, H.; Li, X.; Caricato, M.; Marenich, A. V.; Bloino, J.; Janesko, B. G.; Gomperts, R.; Mennucci, B.; Hratchian, H. P.; Ortiz, J. V.; Izmaylov, A. F.; Sonnenberg, J. L.; Williams; Ding, F.; Lipparini, F.; Egidi, F.; Goings, J.; Peng, B.; Petrone, A.; Henderson, T.; Ranasinghe, D.; Zakrzewski, V. G.; Gao, J.; Rega, N.; Zheng, G.; Liang, W.; Hada, M.; Ehara, M.; Toyota, K.; Fukuda, R.; Hasegawa, J.; Ishida, M.; Nakajima, T.; Honda, Y.; Kitao, O.; Nakai, H.; Vreven, T.; Throssell, K.; Montgomery Jr., J. A.; Peralta, J. E.; Ogliaro, F.; Bearpark, M. J.; Heyd, J. J.; Brothers, E. N.; Kudin, K. N.; Staroverov, V. N.; Keith, T. A.; Kobayashi, R.; Normand, J.; Raghavachari, K.; Rendell, A. P.; Burant, J. C.; Iyengar, S. S.; Tomasi, J.; Cossi, M.; Millam, J. M.; Klene, M.; Adamo, C.; Cammi, R.; Ochterski, J. W.; Martin, R. L.; Morokuma, K.; Farkas, O.; Foresman, J. B.; Fox, D. J. *Gaussian 16 Rev. C.01*, Wallingford, CT, 2016.
22. Adamo, C.; Barone, V. Toward reliable density functional methods without adjustable parameters: The PBE0 model. *J. Chem. Phys.* **1999,** *110*, 6158-6170.
23. Petersson, G. A.; Bennett, A.; Tensfeldt, T. G.; Al-Laham, M. A.; Shirley, W. A.; Mantzaris, J. A complete basis set model chemistry. I. The total energies of closed-shell atoms and hydrides of the first-row elements. *J. Chem. Phys.* **1988,** *89* (4), 2193-2218.
24. Clark, T.; Chandrasekhar, J.; Spitznagel, G. W.; Schleyer, P. V. R. Efficient diffuse function-augmented basis sets for anion calculations. III. The 3-21+G basis set for first-row elements, Li–F. *J. Comput. Chem.* **1983,** *4* (3), 294-301.
25. Petersson, G. A.; Al-Laham, M. A. A complete basis set model chemistry. II. Open-shell systems and the total energies of the first-row atoms. *J. Chem. Phys.* **1991,** *94* (9), 6081-6090.
26. Grimme, S.; Ehrlich, S.; Goerigk, L. Effect of the damping function in dispersion corrected density functional theory. *J. Comput. Chem.* **2011,** *32* (7), 1456-1465.
27. Cossi, M.; Barone, V.; Cammi, R.; Tomasi, J. Ab initio study of solvated molecules: a new implementation of the polarizable continuum model. *Chem. Phys. Lett.* **1996,** *255* (4), 327-335.
28. Lipparini, F.; Scalmani, G.; Mennucci, B.; Cancès, E.; Caricato, M.; Frisch, M. J. A variational formulation of the polarizable continuum model. *J. Chem. Phys.* **2010,** *133* (1), 014106.
29. Zhurko, G. A. *Chemcraft - graphical program for visualization of quantum chemistry computations.*, Ivanovo, Russia, 2005.
30. Bock, H.; Lehn, J.-M.; Pauls, J.; Holl, S.; Krenzel, V. Sodium Salts of the Bipyridine

Dianion: Polymer $[(bpy)2^{-}\{Na^{+}(dme)\}_2]_\infty$, Cluster $[(Na_8O)^{6+}Na^{+}_6(bpy)_6^{2-}(tmeda)_6]$, and Monomer $[(bpy)^{2-}\{Na^{+}(pmdta)\}_2]$. *Angew. Chem. Int. Ed.* **1999,** *38* (7), 952-955.
31. Gore-Randall, E.; Irwin, M.; Denning, M. S.; Goicoechea, J. M. Synthesis and Characterization of Alkali-Metal Salts of 2,2′- and 2,4′-Bipyridyl Radicals and Dianions. *Inorg. Chem.* **2009,** *48* (17), 8304-8316.
32. Chisholm, M. H.; Huffman, J. C.; Rothwell, I. P.; Bradley, P. G.; Kress, N.; Woodruff, W. H. Bis(2,2'-bipyridyl)diisopropoxymolybdenum(II). Structural and spectroscopic evidence for molybdenum-to-bipyridyl π* bonding. *J. Am. Chem. Soc.* **1981,** *103* (16), 4945-4947.
33. Fedushkin, I. L.; Petrovskaya, T. V.; Girgsdies, F.; Köhn, R. D.; Bochkarev, M. N.; Schumann, H. Synthesis and Structure of the First Lanthanide Complex with the Bridging, Antiaromatic 2,2′-Bipyridine Dianion: $[\{Yb(\mu_2\text{-}N_2C_{10}H_8)(thf)_2\}_3]$. *Angew. Chem. Int. Ed.* **1999,** *38* (15), 2262-2264.
34. Bader, R. F. W., *Atoms in Molecules: A Quantum Theory.* Clarendon Press: Oxford, 1990.
35. Keith, T. A. *AIMAll*, Version 19.10.12; TK Gristmill Software: Overland Park KS, USA, 2019.
36. London, F. Théorie quantique des courants interatomiques dans les combinaisons aromatiques. *J. Phys. Radium* **1937,** *8* (10), 397-409.

Chapter 4: Elucidating Electron Transfer Events for Polypyridine Ligated Nickel Complexes

Submitted to: *Nature Catalysis*

Research carried out in collaboration with: Ángel Rentería, Stephanie J. Ton, Achyut Gogoi, and Osvaldo Gutierrez

Author Contribution: C.S.D. designed and carried out all of the experimental reactions and analyzed the data unless otherwise stated. S.J.T performed the catalytic reactions and part of the electrochemical analysis. A. R., and A. G., performed computational investigations with O. G. guiding these investigations. C.S.D. conceived and designed the project. R.M. and C.S.D prepared the manuscript. R.M. guided the investigation. All authors contributed to discussions, commented and edited the manuscript.

4.1 General Introduction

4.1.1 Importance of Studying Electron Transfer

In recent years there has been an explosion of preparative methodologies in nickel catalysis with innovative solutions discovered to forge carbon-carbon and carbon-heteroatom bonds. The ability of nickel complexes to shuttle between odd and even oxidation states allows for classical two-electron processes, single electron processes or a powerful merger of the two.[1-5] While synthetic chemists have made significant advances into developing new bond forming reactions and increasing the chemical space accessible via nickel catalysis, a rational understanding of these catalytic systems lags behind, thus hampering further innovation in the field. Particularly problematic is that even general, fundamental steps within these catalytic reactions are often poorly defined (Figure 4.1). Among the least understood of these reactions are electron transfer events between nickel species such as comproportionation, disproportionation or reduction events. Nearly all nickel-catalyzed reactions are proposed to undergo redox changes and hence these electron transfer events are regularly encountered in catalysis.

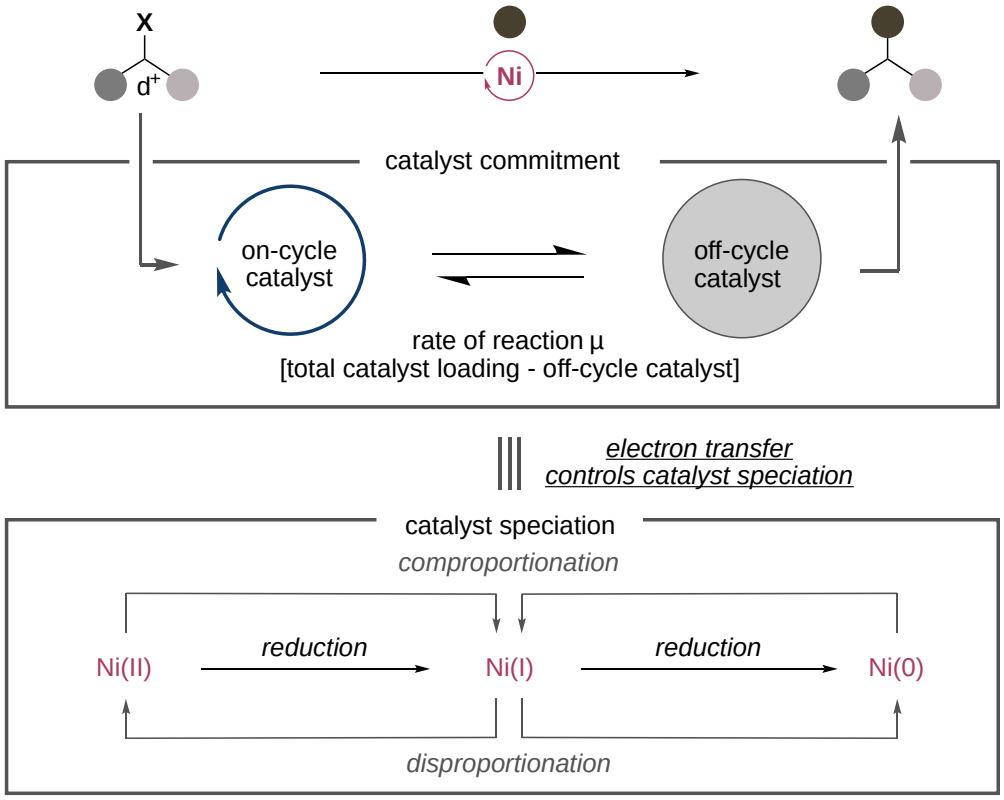

Figure 4.1. Implications of catalytic commitment on the rate of reaction and how electron transfer dictates catalyst speciation.

The insufficient knowledge regarding the intrinsic reactivity of on-cycle or off-cycle species can result in arduous screening efforts for successful reaction development as additives beneficial or poisonous to productive catalysis are challenging to differentiate. With increasing evidence of catalyst turnover or deactivation being dependent on the oxidation state of nickel,[6-10] the ability to select for the desired oxidation state is critical to achieve productive catalysis. Investigations by our group have disclosed that phosphine ligated Ni-catalyzed C-O cleavage reactions follow a Ni(II)/Ni(0) cycle, with generation of off-cycle Ni(I) species restricting catalysis.[11-12] On the other hand, the formation of Ni(I) complexes were essential to carboxylation with polypyridine ligated nickel alkyl species.[13] Other groups have likewise reported on the importance of forming the appropriate Ni(0), Ni(I), Ni(II), or Ni(III) species in catalysis.[6-10,14-18] These studies make it clear that understanding how oxidation states are interconverted (i.e. comproportionation, disproportionation, and reduction events) is critical to maintaining nickel complexes as the desired on-cycle intermediates and preventing the formation of off-cycle species. Catalytic reactions with poor control over the speciation would necessitate high catalyst loadings to counter slow reaction rates as an insufficient portion of the precatalyst is committed to on-cycle species.

4.1.2 Past studies into disproportionation and comproportionation

Studies into ancillary ligand effects on disproportionation and comproportionation reactions date back to the 1960's in which Ni(II)-halides and Ni(0) complexes ligated by triphenylphosphine ligands were shown to react by comproportionation to form Ni(I) complexes (Figure 4.2).[19] Interestingly, the reverse disproportionation reaction could be triggered by the addition of π-accepting phosphite ligands which has since been corroborated by others and it has been proposed that the driving force behind disproportionation is the ability of π-accepting ligands to stabilize the resultant Ni(0) complex.[20-23]

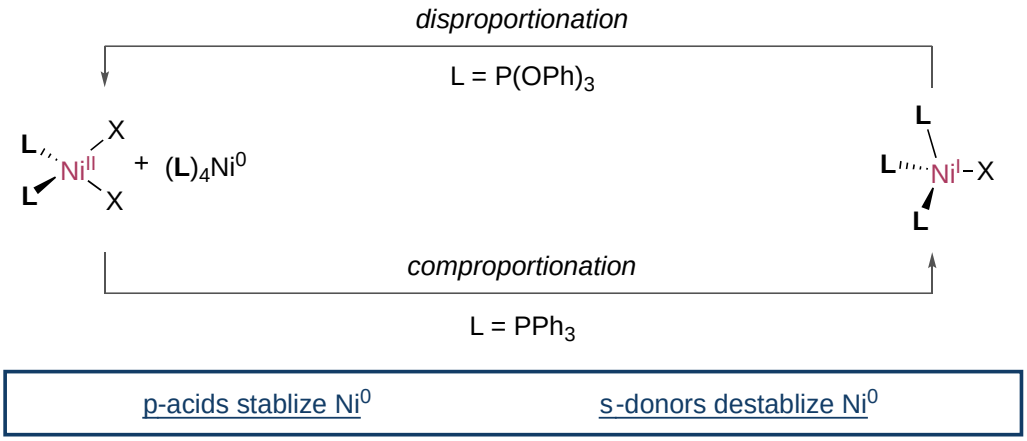

Figure 4.2. Ancillary ligand effect on the outcome of comproportionation or disproportionation.

Similar studies with nickel-halide complexes have since been extended to a range of ligands in which comproportionation between Ni(0) and Ni(II) halides generally occurs (Figure 4.3).[8,19-20,22,24-25] While polypyridine ligated Ni complexes have been routinely employed in Ni catalysis due to their facile merger in redox catalysis, and their unique reactivity profile; studies into their reactivity in comproportionation and disproportionation reactions remain relatively poorly defined which we aimed to study in more detail.[26-27]

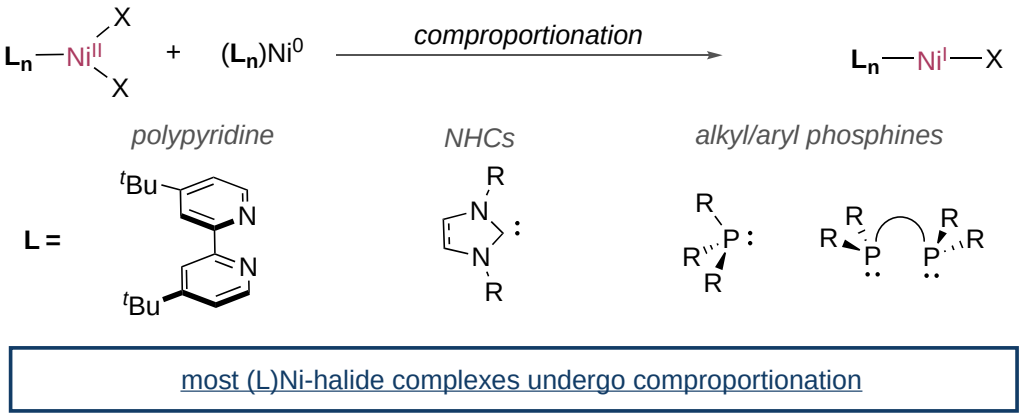

Figure 4.3. General trend for Ni(II)-halide complexes to react by comproportionation with Ni(0).

4.2 General Aim of this Project

In this chapter, we aim to understand factors responsible for key elementary steps of electron transfer in disproportionation, comproportionation and reduction events (Scheme 4.1). Representative examples of pseudohalide and halide ligated Ni(II) complexes are studied in which a change in anionic ligand results in significantly different reactivity towards electron transfer. While Ni(II)-halides react by comproportionation with Ni(0) complexes to form Ni(I) species, we identify that Ni(II)-pseudohalides are unreactive with Ni(0) and the corresponding Ni(I)-pseudohalides react by disproportionation. Furthermore, in stochiometric studies, we find commonly used metal reductants such as Zn or Mn are unable to reduce Ni(II)-pseudohalides to catalytically active Ni(I) or Ni(0) complexes. Factors responsible for disproportionation or comproportionation are further investigated electrochemically. The implications of these findings are studied under catalytic conditions which support that the formation of off-cycle pseudohalide complexes are inactive in catalysis but can be reactivated by inorganic salts. Together, these results provide rationalizations to previously overlooked and fundamental catalytic steps which will act a blueprint for the development of future nickel-catalyzed reactions.

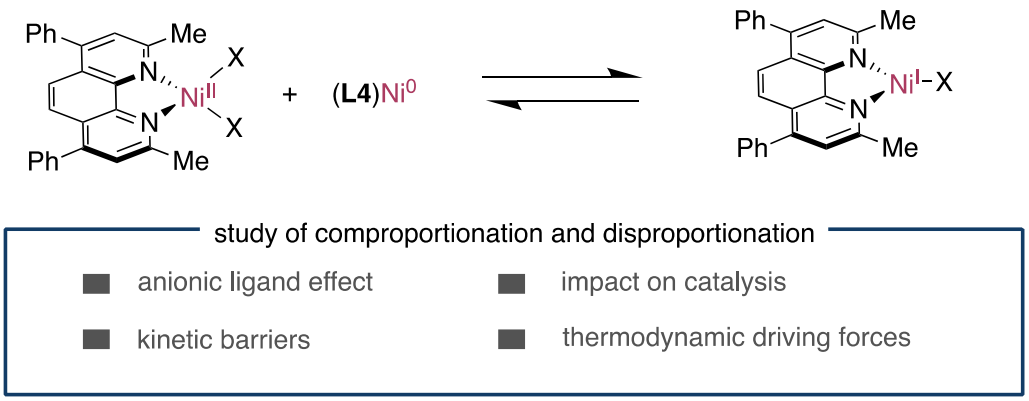

Scheme 4.1. General comproportionation/ disproportionation reaction being studied and the ambiguity surrounding catalytic activity.

4.3 Elucidating Electron Transfer Events for Polypyridine Ligated Nickel Complexes

4.3.1 Synthesis and Characterization of Ni(II) Complexes

At the onset of this investigation, we synthesized model nickel(II) complexes in order to investigate their reactivity in electron transfer. With the synthesis of bipyridine and phenanthroline ligated nickel complexes (**L**)$NiCl_2$ (2,2′-bipyridine = **L1**, 1,10-phenanthroline = **L2**), however, we encountered issues of insolubility in conventional organic solvents (Figure 4.4). There was also a tendency to form a mixture of higher order ligated nickel complexes of type $(\mathbf{L})_nNiCl_2$ (n = 0,1,2,3) or nickelate species such as $[(\mathbf{L1})_3Ni][NiCl_4]$.[28] Such complicated speciation would make definitive experimental interpretation difficult[29] and therefore we looked to simplify the mono-, bis-, and tris-ligated Ni mixture with **L1** or **L2** to a single species. This was achieved by substituting the positions adjacent to the nitrogen atom of the 1,10-phenanthroline backbone with neocuproine (**L3**). However, (**L3**)$NiCl_2$ still suffered from poor solubility (Figure 4.4). Modifying the backbone with additional phenyl groups (bathrocuproine, **L4**), resulted in a complex (**L4**)$NiCl_2$ with well-defined speciation and improved solubility. The structure of this complex was verified by single crystal XRD of the analogous (**L4**)$NiBr_2$.Reacting (**L4**)$NiCl_2$ with additional **L4** resulted in no change in the paramagnetic ^1H NMR or UV-VIS spectra, providing evidence for (**L4**)$NiCl_2$ existing as a single species. These 2,9-disubstituted 1,10-phenanthroline ligands (phen*) have found wide application in nickel-catalyzed reactions and are among the state-of-the-art in reductive coupling reactions, being employed in carboxylation, amidation, chain-walking, thiolation, and alkylation reactions, among others.[30-37]

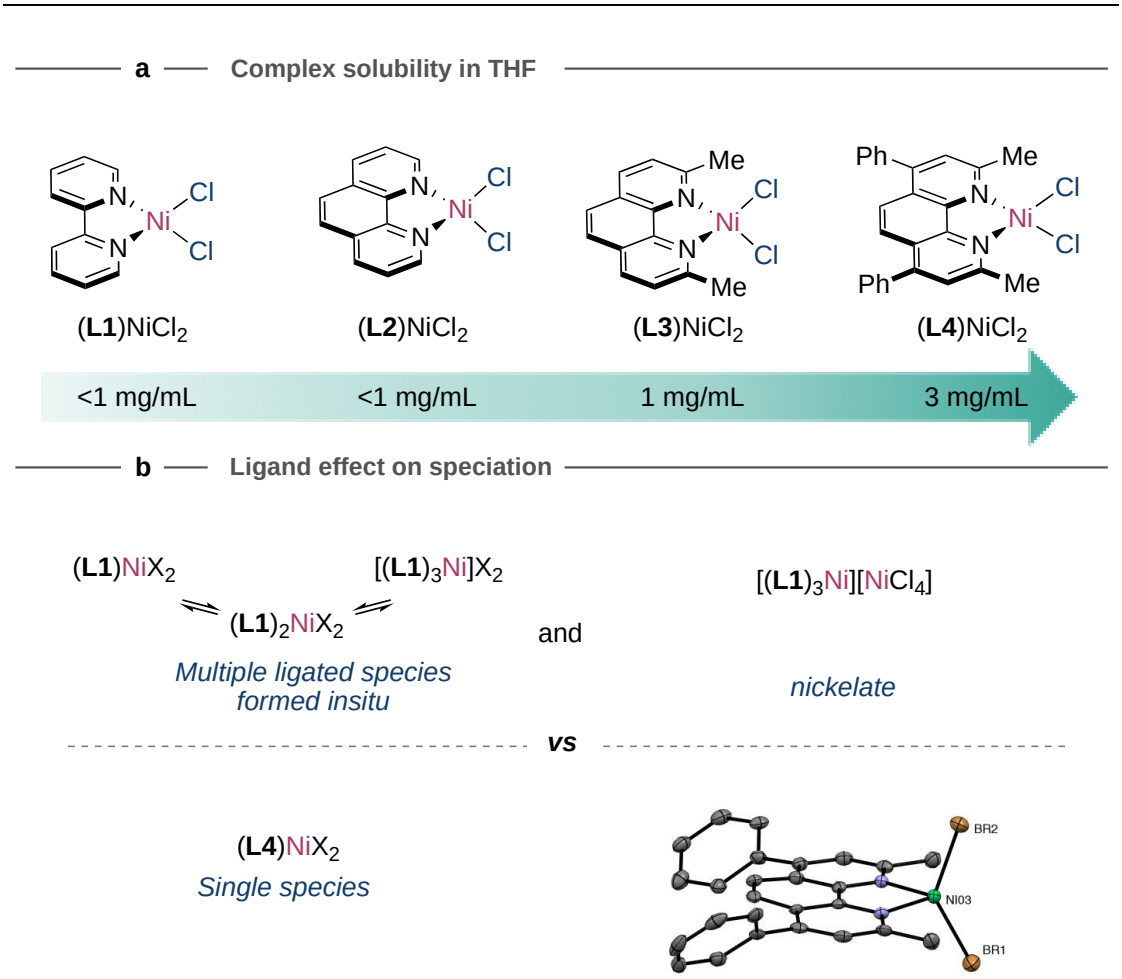

Figure 4.4. (a) Solubility of polypyridine ligated Ni(II) dichloride complexes in THF (b) the influence of ligand substitution of complex speciation.

Mechanistic studies of polypyridine bound Ni complexes are notoriously challenging due to the possibility of one electron or two electron pathways, the paramagnetism of many Ni(II) and Ni(I) complexes and the fact that Ni(II) complexes are X-band EPR silent. Nevertheless, there have been many important contributions to elucidate their reactivity. Surveying the literature of polypyridine ligated nickel halide complexes (**L**)$Ni^{II}X_2$ reacting in electron transfer reactions, they have been demonstrated to form Ni(I) or Ni(0) complexes by reduction (Figure 4.5).[10,13,27,38-42] Examples include: the direct reduction of (dtbbpy)$NiCl_2$ (E_p Ni(II/0) = -0.86 V vs SCE) to (dtbbpy)Ni(COD) with metallic Zn;[40] the reduction of (phen*)$NiBr_2$ ($E_p(Ni^{II}/Ni^{I})$ = -0.69 vs SHE) to (phen*)$Ni^{I}Br$ with Zn;[39] comproportionation between dtbbpy ligated Ni(II) and Ni(0) complexes to form $[(dttbpy)NiCl]_2$;[38,41] and the comproportionation between (phen*)NiX_2 (X = Cl or Br) and (phen*)Ni(COD) to form $[(phen^*)_2Ni^{I}]X$ or (phen*)$Ni^{I}X$ (X = Cl or Br).[13]

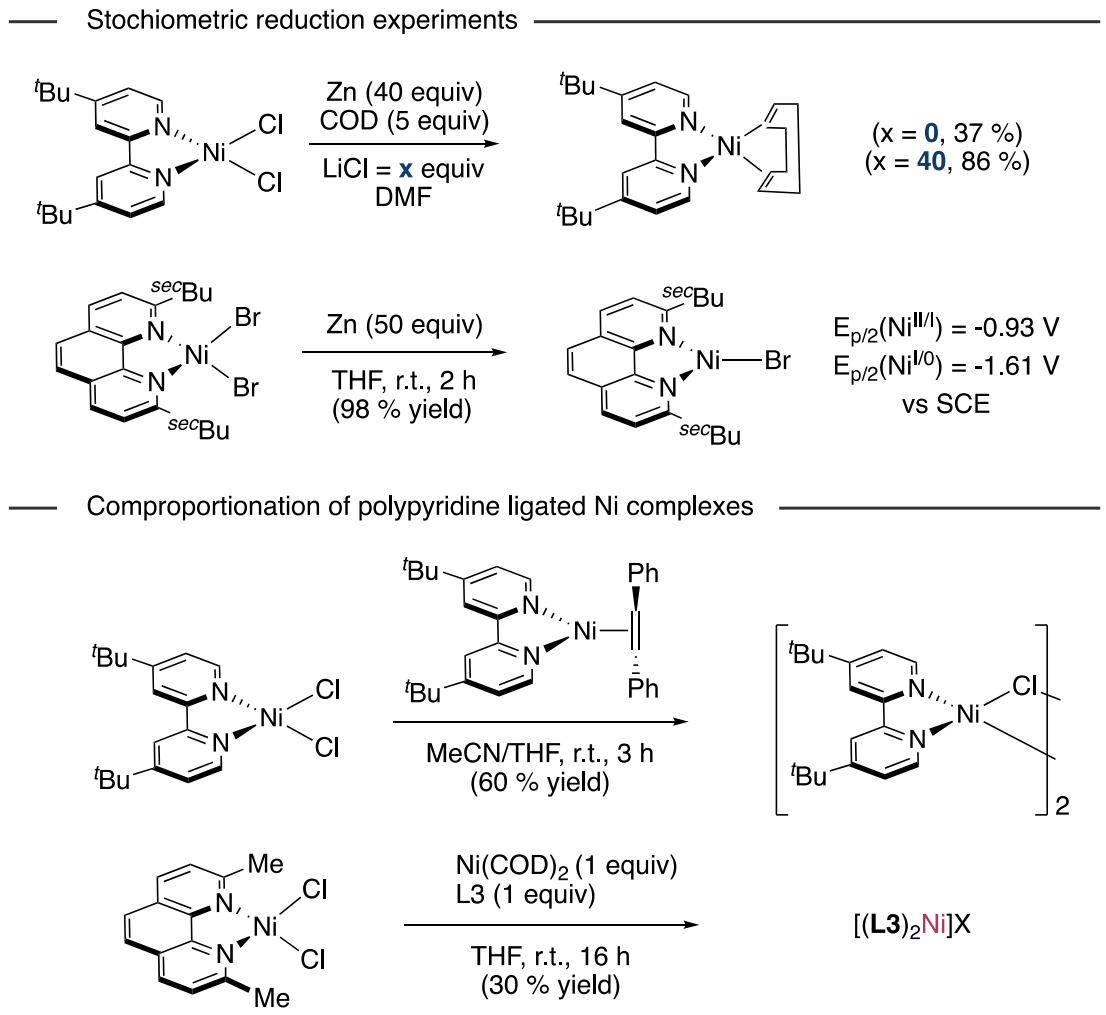

Figure 4.5. Stochiometric reduction of Ni(II)-polypyridine complexes and comproportionation reactions between Ni(II)-dihalide and Ni(0) complexes.

Undoubtedly, these reports provide invaluable information for reaction development as (**L**)Ni-halide complexes are commonly employed as precatalysts or proposed as intermediates in catalytic cross-coupling reactions. Conversely, a current lack of empirical evidence surrounding disproportionation reactions still remains, along with an incomplete understanding of electron transfer reactions and how disproportionation, comproportionation and reduction events are interconnected. Further ambiguity exists whether Ni-pseudohalides share the same reactivity trends with Ni-halide complexes. The involvement of Ni-pseudohalides in catalytic transformations such as Ni-phenoxide or Ni-carboxylate complexes cannot be understated as these species are readily formed when inorganic bases such as phenoxides or carboxylates are used or generated as on-cycle species such as in carboxylation reactions. This lack of clarity limits the full potential of nickel-catalyzed

reactions to maintain the desired on-cycle intermediates and prevent the formation of off-cycle complexes.

With the intention to investigate the electron transfer from Ni(II) to Ni(I) more generally, a representative set of (**L4**)$Ni^{II}X_2$ complexes were synthesized with systematic variation of the anionic (X) ligands. As previously discussed, using inorganic bases encountered in cross-coupling reactions such as sodium phenoxide or potassium pivalate, structurally varied nickel complexes **3a**-**3c** could be synthesized as (**L4**)NiX_2 (Figure 4.6. path i-iii, **3a**-**3c**, X = -OCO^{t}Bu, -OCOPh, -OPh). Interestingly, attempts at accesses Ni-alkoxide complexes by reacting LiOtBu with (**L4**)$NiCl_2$ saw formation of LiO^{t}Bu Ni-clusters in $[NiLi_3Cl_2(O^tBu)_3]_2$•4THF with loss of **L4**.

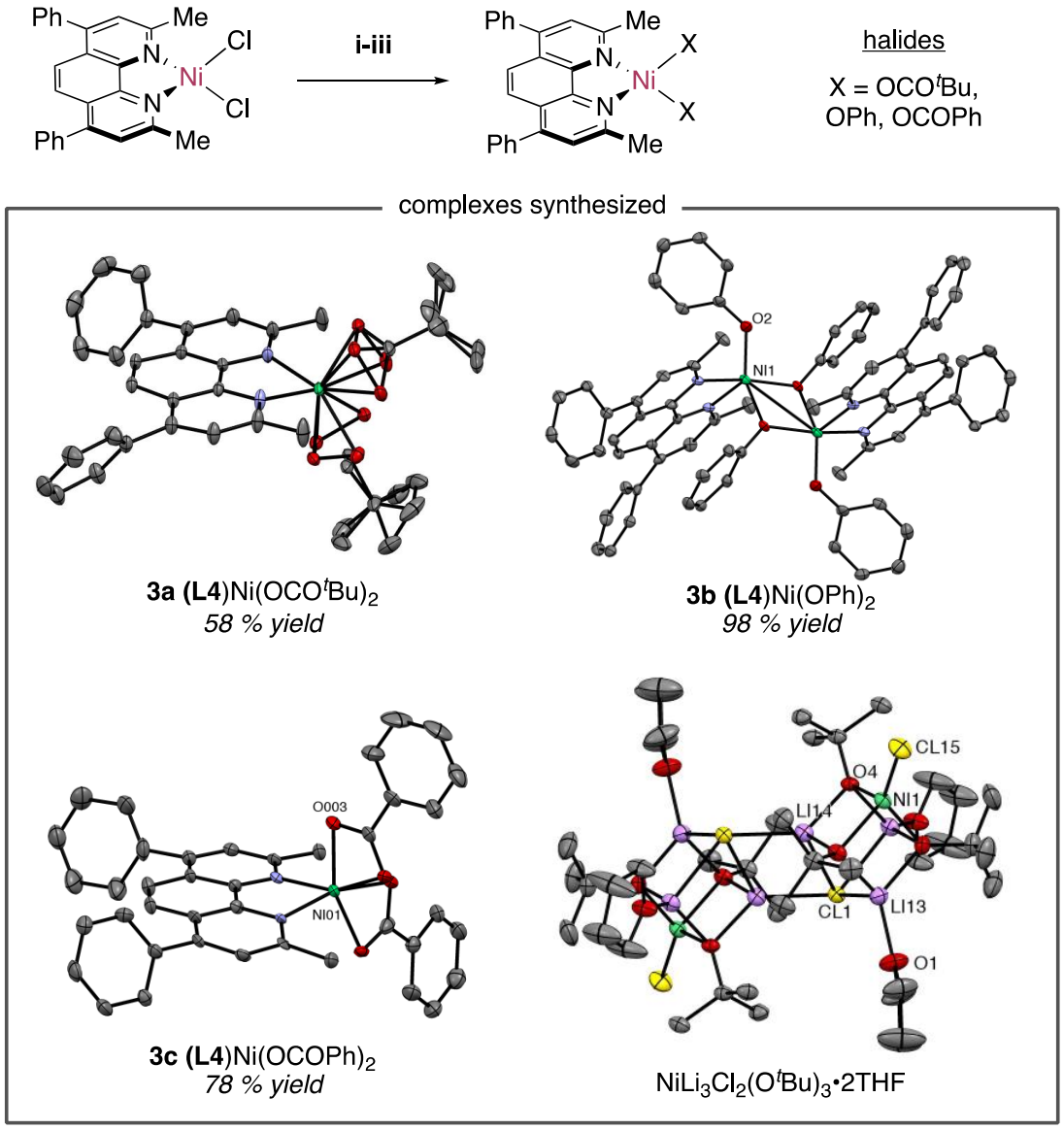

Figure 4.6. Synthesis of bathrocuproine, **L4** ligated Ni(II)-pseudohalides and alternative complexes formed.

4.3.2 Studying Comproportionation of Ni(II) Complexes

With these complexes in hand, we then evaluated their reactivity towards electron transfer. As expected, comproportionation between Ni(II) halides **3-Cl** and **3-Br** (**L4**)$Ni^{II}X_2$ (X = Cl, Br) and (**L4**)$_2Ni^0$ (**5a**) rapidly formed Ni(I) complexes **4a-Cl** and **4a-Br** [(**L4**)$_2Ni^I$]X (X = Cl, Br). Kinetic analysis by UV-Vis occurred within seconds consistent with rapid electron transfer where Ni(0) acts as a reductant and Ni(II) as an oxidant to form a stable Ni(I) species. Next, we extended this study to the reaction between Ni(0) and the corresponding Ni(II)-phenoxide, **3b** (X = OPh) or Ni(II)-carboxylate complexes **3a** and **3c** (X = OCOPh and OCO^{t}Bu). Intriguingly, *none* of these Ni(II) complexes underwent reaction with Ni(0) **5a** as judged EPR and paramagnetic ^{1}H NMR with no signal observed for Ni(I) species generated and isolation of starting materials **3a-3c** (Figure 4.7). To validate these results were not specific to **L4**, the **L3** analogue (**L3**)Ni(OCO^{t}Bu)$_2$ **3d** was prepared and characterized by single crystal XRD. Consistent with the previous results, when **3d** was treated with (**L3**)$_2Ni^0$ (**5b**), no reaction was observed.

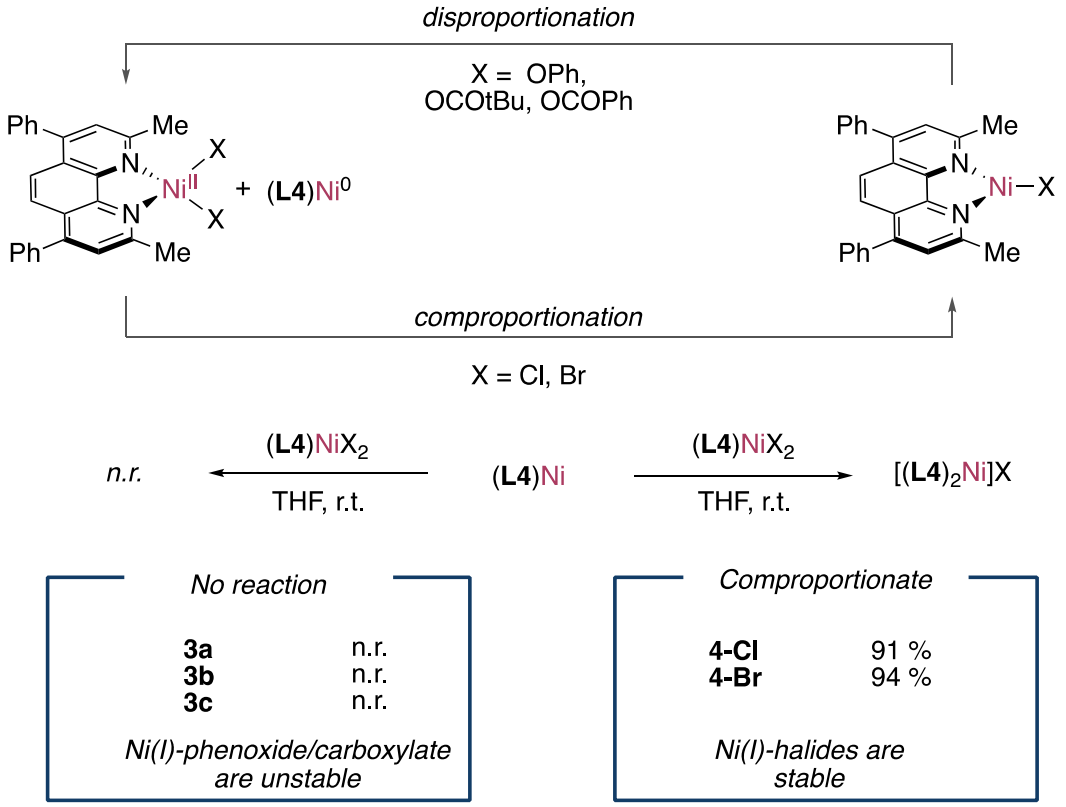

Figure 4.7. Disproportionation and comproportionation reactions with Ni(II)-halide and Ni(II)-pseudohalide complexes

4.3.3 Studying Disproportionation of Ni(I) Complexes

Considering that the reactions between Ni(0) and Ni(II) complexes are electron transfer events, we assumed they are under thermodynamic control. Therefore, if comproportionation between Ni(0) and Ni(II) does not occur, we believed that this indirectly supports that disproportionation of Ni(I) to Ni(0) and Ni(II) should occur spontaneously. Probing the viability of this hypothesis, [(**L4**)$_2$Ni]Cl (**4a-Cl**) was reacted with potassium pivalate to generate a Ni(I)-carboxylate (**L4**)Ni^{I}(OCO^{t}Bu) *in situ*. Monitoring this reaction, we were unable to detect the transiently formed Ni(I)-carboxylate by EPR and only the products of disproportionation (**L4**)Ni(OCO^{t}Bu)$_2$ and (**L4**)$_2$Ni^0 were generated, with (**L4**)$_2$Ni^0 formed in a quantitative yield (Figure 4.8). These findings are consistent with our proposal that Ni(I)-carboxylate complexes are unstable and react spontaneously by disproportionation. The same outcome occurred using potassium benzoate or sodium phenoxide, forming (**L4**)$_2$Ni^0 in 68 % and 97 % yields respectively along with the respective Ni(II) complex (**3b** or **3c**). Modifying the solvent to one with a higher dielectric constant such as MeCN ($\varepsilon = 37.5$) did not change the reaction outcome. We further extended the findings to **L3** with the reaction of [(**L3**)$_2$Ni]Cl **4b-Cl** with potassium pivalate which formed (**L3**)Ni(OCO^{t}Bu)$_2$ **3d** and (**L3**)$_2$Ni^0 in 96 % yield.

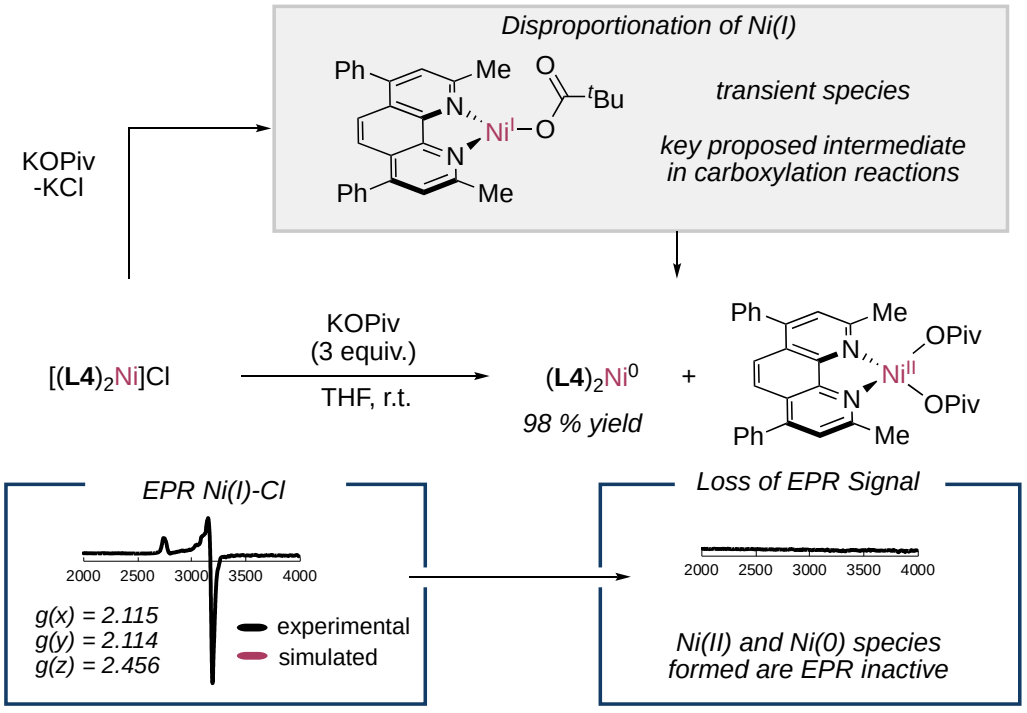

Figure 4.8. Studying disproportionation via in-situ generation of a Ni(I)-carboxylate complex by anion exchange.

4.3.4 Electrochemical Investigations of Ni(II) complexes

Having identified a model reaction with divergent reactivity imparted simply by changing the anionic ligand, we further studied the electron transfer events by comparing the cyclic voltammograms (CVs) of Ni(II)-halide complexes to the Ni(II)-carboxylate complex (Figure 4.9). The CVs of Ni(II)-halide complexes (**L4**)$Ni^{II}Cl_2$ and (**L4**)$Ni^{II}Br_2$ resulted in separated redox potentials between Ni(II)/Ni(I) (Cl = -0.86 V, Br = -0.71 V vs SCE) and Ni(I)/Ni(0) (Cl = -1.24 V, Br = -1.10 V vs SCE) oxidation states in MeCN. The separation of redox potentials and oxidation states is consistent with the ability to generate a stable Ni(I) oxidation state and that electron transfer and comproportionation between (**L4**)$Ni^{II}X_2$ and (**L4**)$_2$Ni. A striking distinction in the CV of Ni(II)-carboxylate (**L4**)$Ni^{II}(OCO^tBu)_2$ was observed where only two electron redox events occur, in which Ni(II) is directly reduced to Ni(0) (E_p = -1.55 V vs SCE, MeCN). The lack of a stable Ni(I) oxidation state is consistent with the previous stochiometric reactions, either between [(**L4**)$_2$Ni]Cl with $KOCO^tBu$ to disproportionate into Ni(II) and Ni(0) or no comproportionation observed between (**L4**)$_2$Ni and (**L4**)Ni(OCOtBu)$_2$.

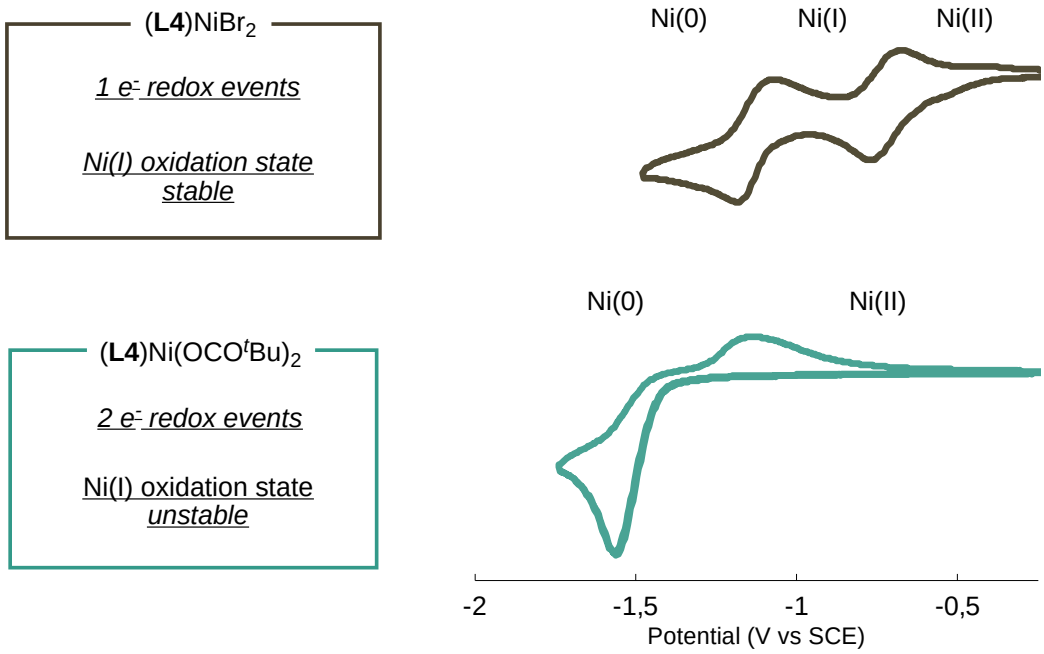

Figure 4.9. Comparison of cyclic voltammograms of Ni(II)-halide and Ni(II)-pseudohalide complexes.

As shown in Figure 4.9, the striking distinction in reduction potentials between Ni-halide and Ni-carboxylate complexes led us to question how these complexes would react with commonly employed metallic reductants. As Zn and Mn are among the most commonly used metallic reductants in cross-electrophile coupling reactions, we sought

to clarify their ability to engage in reduction with these complexes. Performing the CVs of $ZnCl_2$ (E_p = -1.57 V vs SCE, MeCN) and $MnCl_2$ (E_p = -1.77 V vs SCE, MeCN) it appeared that these reductants would be competent to undergo sequential reduction with (**L4**)Ni(II)-halides to first form Ni(I) complexes and then Ni(0). However, it was unclear if (**L4**)Ni(OCO^{t}Bu)$_2$ would be reduced due to the similar E_p values with Mn and Zn (Figure 4.10).

Tabulated redox potentials

(**L4**)$NiBr_2$	Ni(II/I) = -0.71 V		Ni(I/0) = -1.10 V
(**L4**)$NiCl_2$	Ni(II/I) = -0.86 V		Ni(I/0) = -1.24 V
(**L4**)Ni(OCO^{t}Bu)$_2$	———	Ni(II/0) = -1.55 V	———
$ZnCl_2$	———	Zn(II/0) = -1.57 V	———
$MnCl_2$	———	Mn(II/0) = -1.77 V	———

Figure 4.10. Tabulated redox potentials for Ni(II) complexes, Zn and Mn.

4.3.4 Stochiometric Reduction of Ni(II) Complexes

Investigating this hypothesis, the stochiometric reduction of (**L4**)$NiBr_2$ was first performed with 2.5 additional equivalents of **L4** to stabilize low-coordinate Ni species generated and bind Zn or Mn salts formed post reduction. By analysis of the reaction mixture after 1 h, we identified the formation of (**L4**)$_2$Ni^0 in 76 and 77 % yields with Zn and Mn respectively (Figure 4.11). On the other hand, repeating the reaction but using (**L4**)Ni(OCO^{t}Bu)$_2$ complex **3a** instead, no reaction was observed even after 24 h and **3a** was recovered. As reduction of Ni(II) to Ni(I) or Ni(0) complexes is a key step in many nickel-catalyzed reductive coupling reactions, we aimed to identify pathways to reduce **3a** to Ni(0) that would be applicable to common catalytic conditions. We hypothesized that the addition of inorganic salts such as LiBr or $ZnBr_2$ would generate *in situ* (**L4**)$NiBr_2$ from (**L4**)Ni(OCO^{t}Bu)$_2$ **3a** which we validated by the stochiometric reaction between **3a** and LiBr. Indeed, repeating the reduction of **3a** with Zn with additional LiBr forms (**L4**)$_2$Ni^0 in 80 % yield after 1 h.

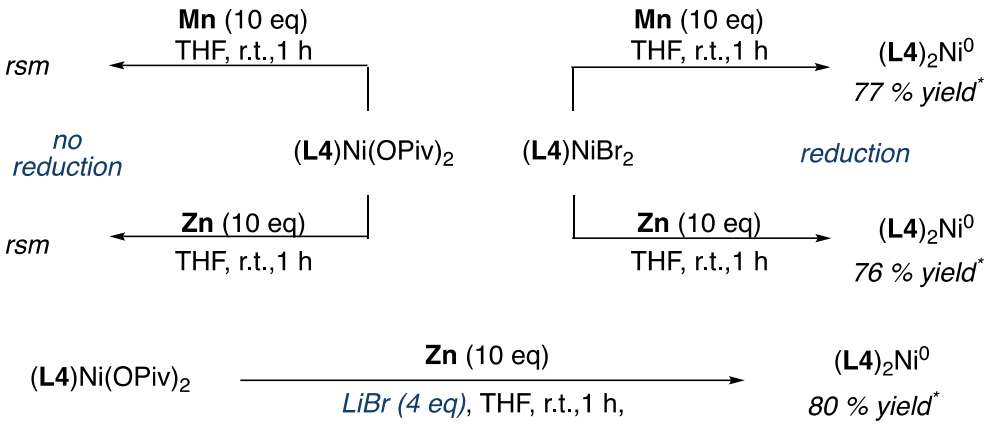

Figure 4.11. Reaction of Ni(II)-halide and pseudohalide complexes with reductants Zn and Mn.

These results highlight the importance of inorganic salts in aiding in reduction events when Ni(II)-pseudohalide complexes are formed during catalysis, either from on-cycle pathways such as in carboxylation reactions or when inorganic bases are present. As we had previously demonstrated rapid oxidation of PCy_3 ligated Ni(0) complexes to Ni(I) occurs with Zn(II),[11] we studied this heterobimetallic electron transfer of (**L4**)$_2$Ni^0 and Zn(II) or Mn(II) salts. In contrast to our previous findings, oxidation of (**L4**)$_2$Ni^0 was not observed in either case and ligand sequestering by Zn(II) was observed to form (**L4**)$ZnCl_2$ as the major side reaction. This alternative reactivity likely originates from **L4** acting as a less σ-donating ligand than PCy_3 and therefore the resultant Ni(0) complex is a weaker reductant.

4.3.5 Implication of Ni Speciation on Reductive Cross-Coupling Reactions

Through interrogating the fundamental reactivity of Ni-polypyridine complexes, we have identified new information about their reactivity in electron transfer which we believed to be directly relevant to nickel-catalyzed cross-coupling reactions. Most apparent was the possibility that pseudohalide bases that are employed in cross-coupling reactions may be influencing catalyst speciation and acting as a poison in reductive cross-coupling reactions by both inhibiting reduction from Ni(II) and preventing formation of Ni(I) species by disproportionation reactions. As such, we investigated model reactions using **L4** in reductive cross-coupling reactions or reactions that propose Ni(I) as a key oxidation state. The deleterious effect of pseudohalide bases on reductive coupling reactions was clear by addition of potassium pivalate while

monitoring the cross electrophile coupling of alkyl bromides and aryl bromides using **L4**, NiI_2, and Zn reported by Yin to access 1,1-diarylalkanes.[33] Addition of potassium pivalate at 1 h (Figure 4.12, teal trace) resulted in a significant reduction in both reaction rate and final yield when compared to the standard reaction (Figure 4.12, blue trace). Consistent with the retarded reaction rate during catalysis originating from the formation of inactive (**L4**)Ni(OCO^tBu)$_2$ complexes was MALDI-MS analysis of an aliquot from the reaction at 2 h which identified m/z fragments of (**L4**)Ni(OCO^tBu)$_2$ **3a**. The inability of **3a** to enter the catalytic cycle by direct reduction and the role of inorganic halide salts to transform **3a** into catalytically active Ni(II)-halide complexes was also clearly demonstrated by using **3a** as a precatalyst and omitting inorganic halide source nBu_4NBr. Monitoring of the reaction observed no product until nBu_4NBr was added after 1.5 h and catalyst activity was restored, all be it at a slower rate than the standard reaction due to the presence of pivalate anions (Figure 4.12, grey trace).

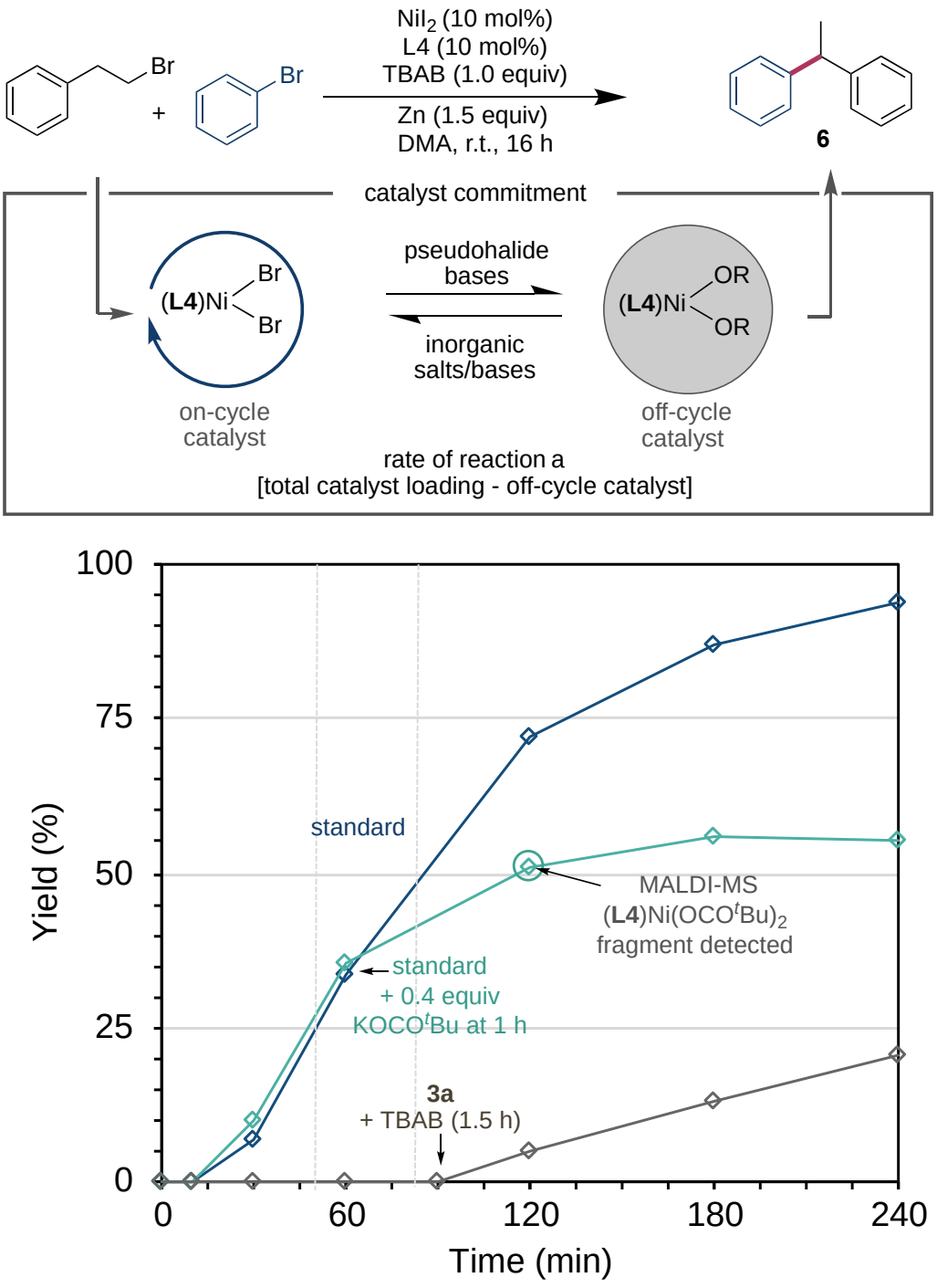

Figure 4.12. Monitoring the reductive cross electrophile coupling of alkyl and aryl bromides under: (i) the standard conditions, (ii) adding 0.4 equivalents of KOPiv at 1 h and (iii) using **3a** as a precatalyst and adding 1.0 equivalents of TBAB at 1.5 h.

Extending our investigation to reactions where Ni-pseudohalides are generated as on-cycle intermediates were studies into the reductive carboxylation reaction of allylic alcohols developed by our group.[35] Again **L4** was employed in combination with $NiBr_2$, Zn and $MgCl_2$ under CO_2 atmosphere to form the linear allylic carboxylic acid **8** (Figure

4.13). Consistent with inorganic halides being beneficial to catalysis by assisting in reduction via anionic ligand exchange of Ni-pseudohalides was the observation that removal of $MgCl_2$ from the standard reaction conditions resulted in a significant loss in yield to 15 %. The minor quantities of **8** formed can likely be attributed to a subtle feature of using nickel halide salts as precatalysts like $NiBr_2$. Upon reduction of $NiBr_2$ to Ni(0), catalytic quantities of $ZnBr_2$ are generated which would promote anion exchange of on-cycle species and regenerate (**L4**)$NiBr_2$ from (**L4**)Ni-pseudohalides to turnover of the catalytic reaction. This hypothesis was supported by experiments using $Ni(COD)_2$ as precatalyst in place of $NiBr_2$ and omitting halide sources ($ZnBr_2$ or $MgCl_2$) in which no product was observed.

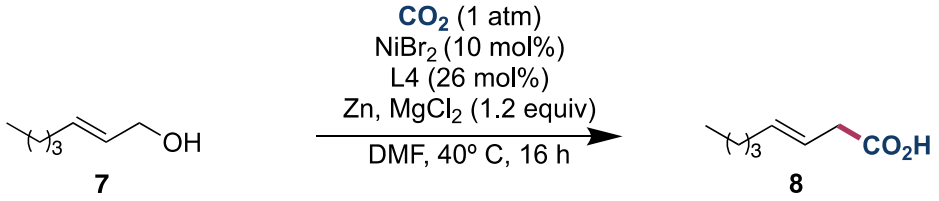

Entry	Deviation from standard conditions	Yield **8** (%)[a]
1	None	64
2	No $MgCl_2$	15
3	0.4 equiv KOPiv, No $MgCl_2$	9
4	(**L4**)$Ni(OPiv)_2$ instead of $NiBr_2$, No $MgCl_2$	0
5	Ni(COD) instead of $NiBr_2$, No $MgCl_2$	0

Figure 4.13. Carboxylation of allylic alcohol under varied reaction conditions.

Control experiments using $Ni(COD)_2$ confirmed its competence as a precatalyst when $MgCl_2$ was present which resulted in a 61 % yield (vs 64 % using $NiBr_2$). Consistent with our studies of the reductive arylation (Figure 4.12), the addition of substoichiometric quantities of potassium pivalate while omitting $MgCl_2$ resulted in a further decrease in yield from 15 % to 9 % and the use of preformed complex (**L4**)$Ni(OCO^tBu)_2$ without $MgCl_2$ resulted in a 0 % yield. Similar detrimental effects were also observed in migratory hydrothiolation reactions of alkenes which propose Ni(I) species to be central to the reaction outcome (Figure 4.14).[37]

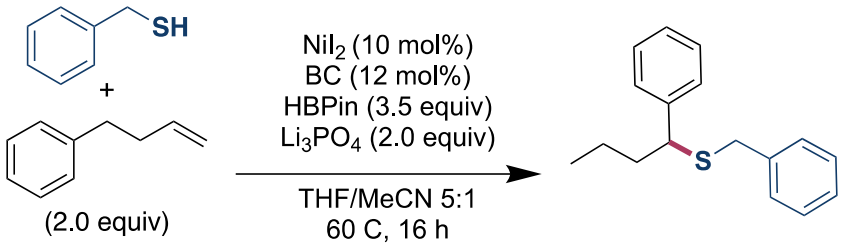

Entry	Deviation from standard conditions	Yield (%)[a]
1	None	76
2	0.4 equiv KOPiv	8
3	$Ni(OPiv)_2$ instead of $NiBr_2$	2
4	$Ni(OPiv)_2$ instead of $NiBr_2$ + 0.4 equiv LiI	34

Figure 4.14. Migratory hydrothiolation of alkenes. Impact of forming pseudohalide Ni species on the reaction outcome.

4.4 Conclusions

Together, these findings provide a greater understanding of electron transfer events and the factors contributing to comproportionation, disproportionation, and reduction of polypyridine ligated Ni species. We demonstrate that a change in anionic ligand from Ni-halides to Ni-pseudohalides has a significant effect on nickel speciation in which Ni-halides adopt stable Ni(0), Ni(I), and Ni(II) oxidation states and react in comproportionation reactions while Ni-pseudohalides are only stable as Ni(0) and Ni(II) complexes and react via disproportionation. This divergent reactivity provided an opportunity to investigate factors that influence comproportionation and disproportionation which were studied both experimentally and theoretically. Furthermore, modification of the anionic ligand to pseudohalides results in significantly harder to reduce complexes which do not undergo reduction with metallic reductants such as Zn or Mn. The impact of these findings were extended to studies of catalytic reductive coupling reactions where psuedohalide bases act as poisons as a result of generating off-cycle Ni-psuedohalide species, while reactions that generate Ni-pseudohalide species on-cycle necessitate inorganic halides to regenerate catalytically active Ni-halide complexes. These findings also support a modification of traditionally accepted reaction mechanisms such as in the carboxylation of alkyl halides where reduction of Ni(I)-carboxylates are proposed as a key step. Evidence provided within this work provides an alternative to this catalytic cycle by rapid disproportionation of the Ni(I)-carboxylate to form a Ni(II)-carboxylate and Ni(0), where the Ni(II)-carboxylate must undergo anion exchange by inorganic salts to re-enter the catalytic cycle. This in-depth understanding of electron transfer now provides increased control over on-cycle and off-cycle species and we believe will assist in the development of mechanistic understanding and novel preparative methodologies.

Future work into the studying the effect of anion ligands and redox active ancillary ligands on the outcome of comproportionation or disproportionation are needed to validate the generality of these conclusions and inform the general choice of ligand and additives on promoting or disfavoring these reactions. Considering the generally poorly defined nature of comproportionation and disproportionation reactions, revisiting redox innocent ligands and studying these reactions in more detail (for example in structure-activity relationships), either in the presence of π-acidic ligands or without these ligands will also provide important information about what governs these reactions. Similar

studies can be extended to other first row transition metal complexes (i.e Co, Fe) to identify trends in the propensity of each transition-metal to undergo these reactions.

4.5 References

1. Diccianni, J. B.; Diao, T. Mechanisms of Nickel-Catalyzed Cross-Coupling Reactions. *Trends in Chemistry* **2019,** *1* (9), 830-844.
2. Diccianni, J.; Lin, Q.; Diao, T. Mechanisms of Nickel-Catalyzed Coupling Reactions and Applications in Alkene Functionalization. *Acc. Chem. Res.* **2020,** *53* (4), 906-919.
3. Tasker, S. Z.; Standley, E. A.; Jamison, T. F. Recent advances in homogeneous nickel catalysis. *Nature* **2014,** *509* (7500), 299-309.
4. Hazari, N.; Melvin, P. R.; Beromi, M. M. Well-defined nickel and palladium precatalysts for cross-coupling. *Nat. Rev. Chem.* **2017,** *1* (3), 0025.
5. Everson, D. A.; Weix, D. J. Cross-Electrophile Coupling: Principles of Reactivity and Selectivity. *J. Org. Chem.* **2014,** *79* (11), 4793-4798.
6. Mohadjer Beromi, M.; Nova, A.; Balcells, D.; Brasacchio, A. M.; Brudvig, G. W.; Guard, L. M.; Hazari, N.; Vinyard, D. J. Mechanistic Study of an Improved Ni Precatalyst for Suzuki–Miyaura Reactions of Aryl Sulfamates: Understanding the Role of Ni(I) Species. *J. Am. Chem. Soc.* **2017,** *139* (2), 922-936.
7. Barth, E. L.; Davis, R. M.; Mohadjer Beromi, M.; Walden, A. G.; Balcells, D.; Brudvig, G. W.; Dardir, A. H.; Hazari, N.; Lant, H. M. C.; Mercado, B. Q.; Peczak, I. L. Bis(dialkylphosphino)ferrocene-Ligated Nickel(II) Precatalysts for Suzuki–Miyaura Reactions of Aryl Carbonates. *Organometallics* **2019,** *38* (17), 3377-3387.
8. Mohadjer Beromi, M.; Banerjee, G.; Brudvig, G. W.; Hazari, N.; Mercado, B. Q. Nickel(I) Aryl Species: Synthesis, Properties, and Catalytic Activity. *ACS Catal.* **2018,** *8* (3), 2526-2533.
9. Mohadjer Beromi, M.; Banerjee, G.; Brudvig, G. W.; Charboneau, D. J.; Hazari, N.; Lant, H. M. C.; Mercado, B. Q. Modifications to the Aryl Group of dppf-Ligated Ni σ-Aryl Precatalysts: Impact on Speciation and Catalytic Activity in Suzuki–Miyaura Coupling Reactions. *Organometallics* **2018,** *37* (21), 3943-3955.
10. Yanagi, T.; Somerville, R. J.; Nogi, K.; Martin, R.; Yorimitsu, H. Ni-Catalyzed Carboxylation of C(sp^2)–S Bonds with CO_2: Evidence for the Multifaceted Role of Zn. *ACS Catal.* **2020,** *10* (3), 2117-2123.
11. Day, C. S.; Somerville, R. J.; Martin, R. Deciphering the dichotomy exerted by Zn(ii) in the catalytic sp2 C–O bond functionalization of aryl esters at the molecular level. *Nat. Catal.* **2021,** *4* (2), 124-133.
12. Somerville, R. J.; Hale, L. V. A.; Gómez-Bengoa, E.; Burés, J.; Martin, R. Intermediacy of Ni–Ni Species in sp^2 C–O Bond Cleavage of Aryl Esters: Relevance in Catalytic C–Si Bond Formation. *J. Am. Chem. Soc.* **2018,** *140* (28), 8771-8780.
13. Somerville, R. J.; Odena, C.; Obst, M. F.; Hazari, N.; Hopmann, K. H.; Martin, R. Ni(I)–Alkyl Complexes Bearing Phenanthroline Ligands: Experimental Evidence for CO2 Insertion at Ni(I) Centers. *J. Am. Chem. Soc.* **2020,** *142* (25), 10936-10941.
14. Dürr, A. B.; Fisher, H. C.; Kalvet, I.; Truong, K.-N.; Schoenebeck, F. Divergent Reactivity of a Dinuclear (NHC)Nickel(I) Catalyst versus Nickel(0) Enables Chemoselective Trifluoromethylselenolation. *Angew. Chem. Int. Ed.* **2017,** *56* (43), 13431-13435.
15. Kalvet, I.; Guo, Q.; Tizzard, G. J.; Schoenebeck, F. When Weaker Can Be Tougher:

The Role of Oxidation State (I) in P- vs N-Ligand-Derived Ni-Catalyzed Trifluoromethylthiolation of Aryl Halides. *ACS Catal.* **2017,** *7* (3), 2126-2132.
16. Kapat, A.; Sperger, T.; Guven, S.; Schoenebeck, F. E-Olefins through intramolecular radical relocation. *Science* **2019,** *363* (6425), 391-396.
17. Yuan, M.; Song, Z.; Badir, S. O.; Molander, G. A.; Gutierrez, O. On the Nature of C(sp^3)–C(sp^2) Bond Formation in Nickel-Catalyzed Tertiary Radical Cross-Couplings: A Case Study of Ni/Photoredox Catalytic Cross-Coupling of Alkyl Radicals and Aryl Halides. *J. Am. Chem. Soc.* **2020,** *142* (15), 7225-7234.
18. Phapale, V. B.; Guisán-Ceinos, M.; Buñuel, E.; Cárdenas, D. J. Nickel-Catalyzed Cross-Coupling of Alkyl Zinc Halides for the Formation of C(sp2)□C(sp3) Bonds: Scope and Mechanism. *Chem. Eur. J.* **2009,** *15* (46), 12681-12688.
19. Heimbach, P. Changes in the Coordination Number of Ni(0) and Ni(I) Compounds. *Angew. Chem. Int. Ed.* **1964,** *3* (9), 648.
20. Tsou, T. T.; Kochi, J. K. Mechanism of oxidative addition. Reaction of nickel(0) complexes with aromatic halides. *J. Am. Chem. Soc.* **1979,** *101* (21), 6319-6332.
21. Cundy, C. S.; Nöth, H. Metal-boron compounds: XI. Complexes derived from reactions of bis(triphenylphosphine)(π-ethylene)nickel with alkyl and boron halides. *J. Organomet. Chem.* **1971,** *30* (1), 135-143.
22. Porri, L.; Gallazzi, M. C.; Vitulli, G. Complexes of nickel(I) with triphenylphosphine. *Chem. Commun.* **1967,** (5), 228-228.
23. Beattie, D. D.; Lascoumettes, G.; Kennepohl, P.; Love, J. A.; Schafer, L. L. Disproportionation Reactions of an Organometallic Ni(I) Amidate Complex: Scope and Mechanistic Investigations. *Organometallics* **2018,** *37* (9), 1392-1399.
24. Dible, B. R.; Sigman, M. S.; Arif, A. M. Oxygen-Induced Ligand Dehydrogenation of a Planar Bis-μ-Chloronickel(I) Dimer Featuring an NHC Ligand. *Inorg. Chem.* **2005,** *44* (11), 3774-3776.
25. Schunn, R. A. Preparation and reactions of triethylphosphine complexes of zerovalent nickel, palladium, and platinum. *Inorg. Chem.* **1976,** *15* (1), 208-212.
26. Twilton, J.; Le, C.; Zhang, P.; Shaw, M. H.; Evans, R. W.; MacMillan, D. W. C. The merger of transition metal and photocatalysis. *Nat. Rev. Chem.* **2017,** *1* (7), 0052.
27. Till, N. A.; Oh, S.; MacMillan, D. W. C.; Bird, M. J. The Application of Pulse Radiolysis to the Study of Ni(I) Intermediates in Ni-Catalyzed Cross-Coupling Reactions. *J. Am. Chem. Soc.* **2021,** *143* (25), 9332-9337.
28. Harris, C. M.; McKenzie, E. D. Nitrogenous chelate complexes of transition metals—III: bis-chelate complexes of nickel (II) with 1,10-phenanthroline, 2,2′-bipyridyl and analogous ligands. *J. Inorg. Nucl. Chem.* **1967,** *29* (4), 1047-1068.
29. Kawamata, Y.; Vantourout, J. C.; Hickey, D. P.; Bai, P.; Chen, L.; Hou, Q.; Qiao, W.; Barman, K.; Edwards, M. A.; Garrido-Castro, A. F.; deGruyter, J. N.; Nakamura, H.; Knouse, K.; Qin, C.; Clay, K. J.; Bao, D.; Li, C.; Starr, J. T.; Garcia-Irizarry, C.; Sach, N.; White, H. S.; Neurock, M.; Minteer, S. D.; Baran, P. S. Electrochemically Driven, Ni-Catalyzed Aryl Amination: Scope, Mechanism, and Applications. *J. Am. Chem. Soc.* **2019,** *141* (15), 6392-6402.
30. Davies, J.; Janssen-Müller, D.; Zimin, D. P.; Day, C. S.; Yanagi, T.; Elfert, J.; Martin, R. Ni-Catalyzed Carboxylation of Aziridines en Route to β-Amino Acids. *J. Am. Chem.*

Soc. **2021,** *143* (13), 4949-4954.
31. Tortajada, A.; Börjesson, M.; Martin, R. Nickel-Catalyzed Reductive Carboxylation and Amidation Reactions. *Acc. Chem. Res.* **2021,** *54* (20), 3941-3952.
32. Tortajada, A.; Menezes Correia, J. T.; Serrano, E.; Monleón, A.; Tampieri, A.; Day, C. S.; Juliá-Hernández, F.; Martin, R. Ligand-Controlled Regiodivergent Catalytic Amidation of Unactivated Secondary Alkyl Bromides. *ACS Catal.* **2021,** *11* (16), 10223-10227.
33. Peng, L.; Li, Y.; Li, Y.; Wang, W.; Pang, H.; Yin, G. Ligand-Controlled Nickel-Catalyzed Reductive Relay Cross-Coupling of Alkyl Bromides and Aryl Bromides. *ACS Catal.* **2018,** *8* (1), 310-313.
34. Juliá-Hernández, F.; Moragas, T.; Cornella, J.; Martin, R. Remote carboxylation of halogenated aliphatic hydrocarbons with carbon dioxide. *Nature* **2017,** *545* (7652), 84-88.
35. van Gemmeren, M.; Börjesson, M.; Tortajada, A.; Sun, S.-Z.; Okura, K.; Martin, R. Switchable Site-Selective Catalytic Carboxylation of Allylic Alcohols with CO2. *Angew. Chem. Int. Ed.* **2017,** *56* (23), 6558-6562.
36. Rezazadeh, S.; Devannah, V.; Watson, D. A. Nickel-Catalyzed C-Alkylation of Nitroalkanes with Unactivated Alkyl Iodides. *J. Am. Chem. Soc.* **2017,** *139* (24), 8110-8113.
37. Zhang, Y.; Xu, X.; Zhu, S. Nickel-catalysed selective migratory hydrothiolation of alkenes and alkynes with thiols. *Nature Communications* **2019,** *10* (1), 1752.
38. Ting, S. I.; Garakyaraghi, S.; Taliaferro, C. M.; Shields, B. J.; Scholes, G. D.; Castellano, F. N.; Doyle, A. G. 3d-d Excited States of Ni(II) Complexes Relevant to Photoredox Catalysis: Spectroscopic Identification and Mechanistic Implications. *J. Am. Chem. Soc.* **2020,** *142* (12), 5800-5810.
39. Lin, Q.; Diao, T. Mechanism of Ni-Catalyzed Reductive 1,2-Dicarbofunctionalization of Alkenes. *J. Am. Chem. Soc.* **2019,** *141* (44), 17937-17948.
40. Huang, L.; Ackerman, L. K. G.; Kang, K.; Parsons, A. M.; Weix, D. J. LiCl-Accelerated Multimetallic Cross-Coupling of Aryl Chlorides with Aryl Triflates. *J. Am. Chem. Soc.* **2019,** *141* (28), 10978-10983.
41. Mohadjer Beromi, M.; Brudvig, G. W.; Hazari, N.; Lant, H. M. C.; Mercado, B. Q. Synthesis and Reactivity of Paramagnetic Nickel Polypyridyl Complexes Relevant to C(sp^2)–C(sp^3)Coupling Reactions. *Angew. Chem. Int. Ed.* **2019,** *58* (18), 6094-6098.
42. Powers, D. C.; Anderson, B. L.; Nocera, D. G. Two-Electron HCl to H_2 Photocycle Promoted by Ni(II) Polypyridyl Halide Complexes. *J. Am. Chem. Soc.* **2013,** *135* (50), 18876-18883.

4.6 Experimental Section

4.6.1 General Considerations

Solvents. Reactions were carried out under N_2 in a glovebox or on a Schlenk line, in solvents (THF, Et_2O, toluene) that had been dried and degassed using an Innovative Technologies solvent purification system, then stored under N_2 over 4 Å molecular sieves for at least 16 h prior to use. Pentane was degassed by bubbling with N_2 and stored under N_2 over 4 Å molecular sieves for at least 16 h prior to use. C_6D_6, C_7D_8, THF-d_8, (Eurisotop) were freeze/pump/thaw degassed (4x) and likewise stored under N_2 over 4 Å molecular sieves for at least 16 h prior to use.

Reagents. Neocuproine and bathocuproine were purchased from Fluorochem. Zinc dichloride ($ZnCl_2$), and sodium phenoxide, lithium tert-butoxide, and manganese dichloride were purchased from Sigma-Aldrich. Potassium benzoate was purchased from Thermo Fisher. $ZnBr_2$ and potassium pivalate (KOPiv) were purchased from Alfa Aesar. [Ni(COD)$_2$] was purchased from Strem Chemicals. Trimethoxylbenzene (TMB) was purchased from TCI Chemicals. Salts $ZnBr_2$, $ZnCl_2$, and KOPiv were dried at 150 ^oC under high vacuum overnight. Complexes (bipy)$NiCl_2$,[1] (phen)$NiCl_2$,[1] (neocuproine)$NiCl_2$,[2] (bathocuproine)$NiCl_2$,[2] (neocuprooine)$_2$Ni,[2] and (bathocuproine)$_2$Ni,[2] were synthesized according to literature procedures.

Analytical methods. Flash chromatography was performed with Sigma Aldrich technical grade silica gel 60 (230-400 mesh). Thin layer chromatography was carried out using Merck TLC Silica gel 60 F254. NMR spectra were recorded on Bruker Avance Ultrashield 300, 400, or 500 MHz spectrometers, with chemical shifts reported in parts per million (ppm) and coupling constants, *J*, reported in hertz. Quantitative NMR experiments were performed with d1 set to 10s (^{1}H). Gas chromatographic analyses were performed on an Agilent 6890N gas chromatograph with an FID detector. Continuous wave (CW) X-band EPR spectra were obtained using a Bruker EMX Micro X-band spectrometer using a Bruker ER 1164 HS resonator. Spectra were simulated using SpinFit within Xenon. The samples were cooled to 77 K in a Suprasil finger dewar (Wilmad-LabGlass) filled with liquid nitrogen. The spectral data were collected with the following spectrometer settings: microwave power = 0.56mW; centre field = 3250

G, sweep width = 2500 G, sweep time = 35.07 s, modulation frequency = 100 KHz, modulation amplitude = 10 G, power attenuation= 25 dB, time constant = 20.48 ms. Simulations, g values, and frequencies are provided alongside the characterization data of the complexes. IR spectra were obtained with a Bruker FT-IR Alpha spectrometer. MALDI-TOF mass spectra were collected on a Bruker Autoflex MALDI-TOF mass spectrometer. Samples were prepared by the dried-droplet protocol, from solutions containing the charge-transfer matrix pyrene or DCTB in THF.

4.6.2 Synthesis and Characterization of Complexes

Synthesis of (L4)Ni(OCO^{t}Bu)$_2$

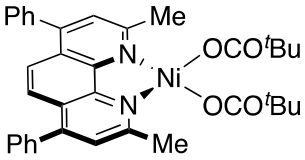

In the glovebox, (L4)NiCl$_2$ (224 mg, 0.46 mmol) was added to a 12 mL vial with potassium pivalate (206 mg, 1.66 mmol). A stir bar was added, and the vial was charged with 6 mL of toluene turning the pink powder to a pink suspension and let stir overnight. After 16 hours the green solution was filtered through a celite plug with salt being filtered off and a green solution collected. The solvent was then removed to afford a green solid and washed with pentane (1 mL x 3) to give (L4)Ni(OCO^{t}Bu)$_2$ (199 mg, 70 % yield) as a green powder.

Stability: Stable in air

^{1}H NMR (^{1}H NMR (400 MHz, C_6D_6) δ 49.57, 20.78, -9.05. **^{13}C NMR**, no signals are observed due to paramagnetism of (L4)Ni(OCO^{t}Bu)$_2$.

X-Band EPR = EPR Silent

UV-VIS (nm) = 685 nm

Key IR Stretches = 1619 cm^{-1} (weak), 1527 cm^{-1} (strong)

EA Calcd. C, 69.58; H, 6.16; N, 4.51; Found: C, 69.34; H, 6.14; N, 4.38

Cyclic Voltammetry = E_p values for (L4)Ni(OCO^{t}Bu)$_2$ are Ni(II)/Ni(0) = -1.55 V. The reduction appears chemically reversible (E_p oxidation = -1.27 V vs SCE) and electrochemically irreversible.

Single Crystal XRD

Synthesis of (L4)Ni(OCOPh)$_2$

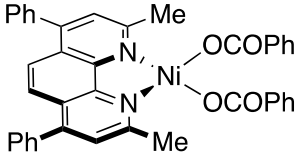

In the glovebox, (L4)NiCl$_2$ (122 mg, 0.25 mmol) and potassium benzoate (83 mg, 0.52 mmol, 2.08 equiv.) were added to a 10 mL vial. A stirbar was added and charged with

3 mL of THF and left to stir overnight in which a colour change from pink to orange to green is observed. The solvent was then removed and the solid was dissolved in DCM and filtered through a celite plug where a white solid was filtered off. The green filtrate was concentrated to dryness and filtered. The solid was washed with pentane (3 mL x 3) to afford (L4)Ni(OCOPh)$_2$ as a green powder (128 mg, 78 % yield).

Stability: Stable in air

^{1}H NMR (500 MHz, THF-d_8) δ 52.21, 21.77, -9.11. **^{13}C NMR**, no signals are observed due to paramagnetism of (L4)Ni(OCOPh)$_2$.

X-Band EPR = EPR Silent

UV-VIS (nm) = 700 nm

Key IR Stretches = 1593 cm^{-1} (weak), 1528 cm^{-1} (strong)

EA Calcd. C, 72.64; H, 4.57; N, 4.24; Found: C, 70.25; H, 4.90; N, 3.88

Single crystal XRD

Synthesis of [(L4)Ni(OPh)$_2$]$_2$

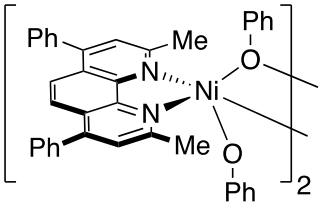

In the glovebox, (L4)NiCl$_2$ (158 mg, 0.32 mmol) and sodium phenoxide (116 mg, 1.00 mmol, 3.1 equiv.) were added to a 10 mL vial. A stirbar was added and charged with 5 mL of toluene and left to stir overnight. The solvent was then removed and redissolved in DCM (sparingly soluble) and filtered through a celite plug. The solvent was removed, filtered and washed with pentane (3 mL x 3) to afford (L4)Ni(OPh)$_2$ as a brown powder (88 mg, 45 % yield).

^{1}H NMR (400 MHz, CD_2Cl_2) δ 54.35, 49.37, 19.92, 18.28, 0.30, 0.09. **^{13}C NMR**, no signals are observed due to paramagnetism of [(L4)Ni(OPh)$_2$]$_2$.

X-Band EPR = EPR Silent

Key IR Stretches = 1256 cm^{-1} (strong)

EA Calcd. C, 75.40; H, 5.00; N, 4.63; Found: C, 76.54; H, 5.20; N, 5.49

Single crystal XRD

Synthesis of $NiLi_3Cl_2(O^tBu)_3$•2THF

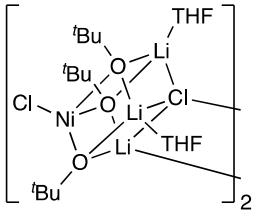

In the glovebox, $(L4)NiCl_2$ (113 mg, 0.23 mmol) and lithium tert-butoxide (41 mg, 0.51 mmol) were added to a 10 mL vial. A stirbar was added and charged with 3 mL of THF and left to stir overnight. The solvent was then removed and dissolved in minimal THF, and then filtered through a celite plug. The solvent was removed, filtered and washed with pentane (3 mL x 3) to afford $NiLi_3Cl_2(O^tBu)_3$•2THF as a blue powder (88 mg, quantitative).

Stability: Unstable in air

^{1}H NMR (400 MHz, THF-d_8) δ 33.31, 32.48, 13.01. **^{13}C NMR**, no signals are observed due to paramagnetism of $NiLi_3Cl_2(O^tBu)_3$•2THF.

X-Band EPR = EPR Silent

EA Calcd. C, 51.95; H, 3.63; N, 5.05; Found: C, 48.89; H, 3.83; N, 4.73

Single crystal XRD

Synthesis of $[(L4)_2Ni]Cl$

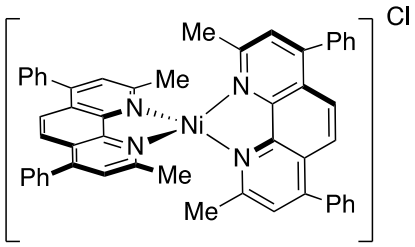

Following a modification of literature procedures,[3] in the glovebox, $(L4)NiCl_2$ (44 mg, 0.09 mmol), $Ni(COD)_2$ (25 mg, 0.09 mmol, 1 equiv) and L4 (96 mg, 0.27 mmol, 3 equiv) were added to a 10 mL vial. A stirbar was added and charged with 5 mL of THF and left to stir overnight. The solvent was removed, filtered and washed with pentane (1 mL x 3, cold -36 ºC) to afford $[(L4)_2Ni]Cl$ as a purple powder (132 mg, 91 % yield).

Stability: Unstable in air

^{1}H NMR (400 MHz, THF-d_8) δ 75.78, 53.72, 25.67, 18.75, 14.13. **^{13}C NMR**, no signals are observed due to paramagnetism of $[(L4)_2Ni]Cl$.

X-Band EPR = g(x) = 2.109, g(y) = 2.106, g(z) = 2.445

UV-VIS (nm) = 560 nm, 735 nm

Synthesis of $[(L4)_2Ni]Br$

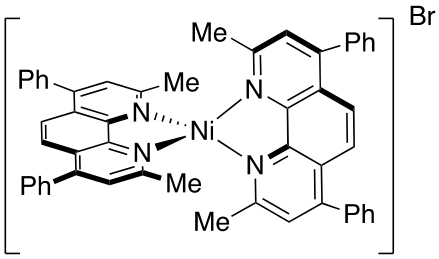

Following a modification of literature procedures,[3] in the glovebox, $(L4)NiBr_2$ (60 mg, 0.10 mmol), $Ni(COD)_2$ (29 mg, 0.10 mmol, 1 equiv) and L4 (112 mg, 0.31 mmol, 3 equiv) were added to a 10 mL vial. A stirbar was added and charged with 5 mL of THF and left to stir overnight. The solvent was removed, filtered and washed with pentane (1 mL x 3, cold -36 ºC) to afford $[(L4)_2Ni]Br$ as a blue powder (167 mg, 94 % yield).

Stability: Unstable in air

^{1}H NMR (400 MHz, THF-d_8) δ 24.45, 12.22. **^{13}C NMR**, no signals are observed due to paramagnetism of $[(L4)_2Ni]Br$.

X-Band EPR = g(x) = 2.115, g(y) = 2.114, g(z) = 2.456

UV-VIS (nm) = 560 nm, 690 nm

Single crystal XRD

Synthesis of $(L3)Ni(OCO^tBu)_2$

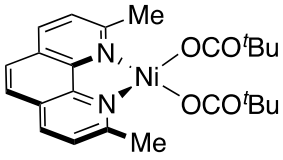

In the glovebox, $(L3)NiCl_2$ (97 mg, 0.29 mmol) was added to a 12 mL vial with potassium pivalate (143 mg, 1.15 mmol, 4 equiv). A stir bar was added, and the vial was charged with 7 mL of toluene turning the pink powder to a pink suspension and let stir overnight. After 16 hours the green suspension was filtered through a celite plug and washed with DCM (8 mL) with the salt being filtered off and a green solution collected. The solvent was then removed to afford a green solid and washed with pentane (1 mL x 3) to give $(L3)Ni(OCO^tBu)_2$ (123 mg, 90 % yield) as a green powder.

^{1}H NMR (^{1}H NMR (400 MHz, C_6D_6) δ 48.92, 18.43, 15.50, -9.49. **^{13}C NMR**, no signals are observed due to paramagnetism of (L3)Ni(OCO^tBu)$_2$.

X-Band EPR = EPR Silent

Single Crystal XRD

4.6.3 Stochiometric Reactions.

No reaction between (L4)Ni(OCO^{t}Bu)$_2$ and (L4)$_2$Ni

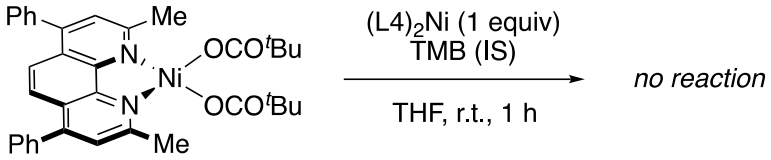

Monitored by quantitative ^{1}H NMR and paramagnetic ^{1}H NMR. In the glovebox, (L4)$_2$Ni (12 mg, 0.02 mmol) and TMB (1 mg, internal standard) were added to a 4 mL vial with 1 mL of THF-d_8. The solution was transferred to a J-Young NMR tube and the initial integration of (L4)$_2$Ni and TMB was recorded. The J-Young NMR tube was brought back into the glovebox and added to a vial containing (L4)Ni(OCO^{t}Bu)$_2$ (10 mg, 0.02 mmol) and stirred for 1 h before transferring back into the J-Young NMR tube and analyzed by ^{1}H NMR. No conversion of (L4)$_2$Ni was observed and paramagnetic signals of (L4)Ni(OCO^{t}Bu)$_2$ remained with no additional signals of paramagnetic species observed. Conclusion: This is consistent with no reaction between (L4)$_2$Ni and (L4)Ni(OCO^{t}Bu)$_2$.

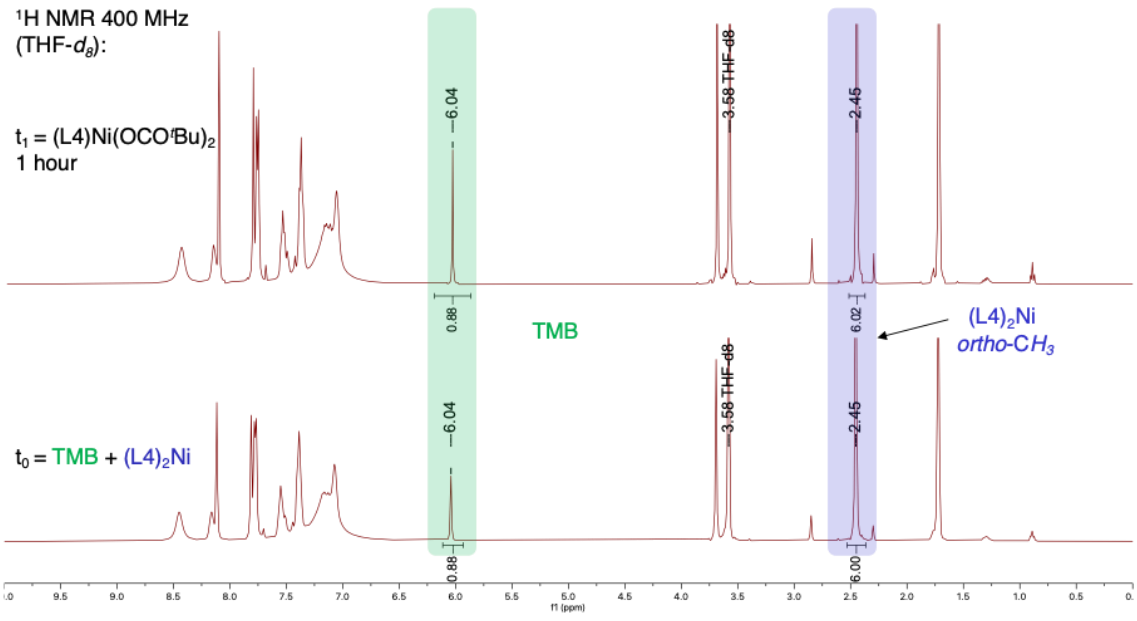

Figure S1. Quantitative ^{1}H NMR spectra of TMB and (L4)$_2$Ni indicating no conversion of (L4)$_2$Ni upon adding (L4)Ni(OCO^{t}Bu)$_2$. Internal standard trimethoxybenzene, TMB (green) and (L4)$_2$Ni (blue).

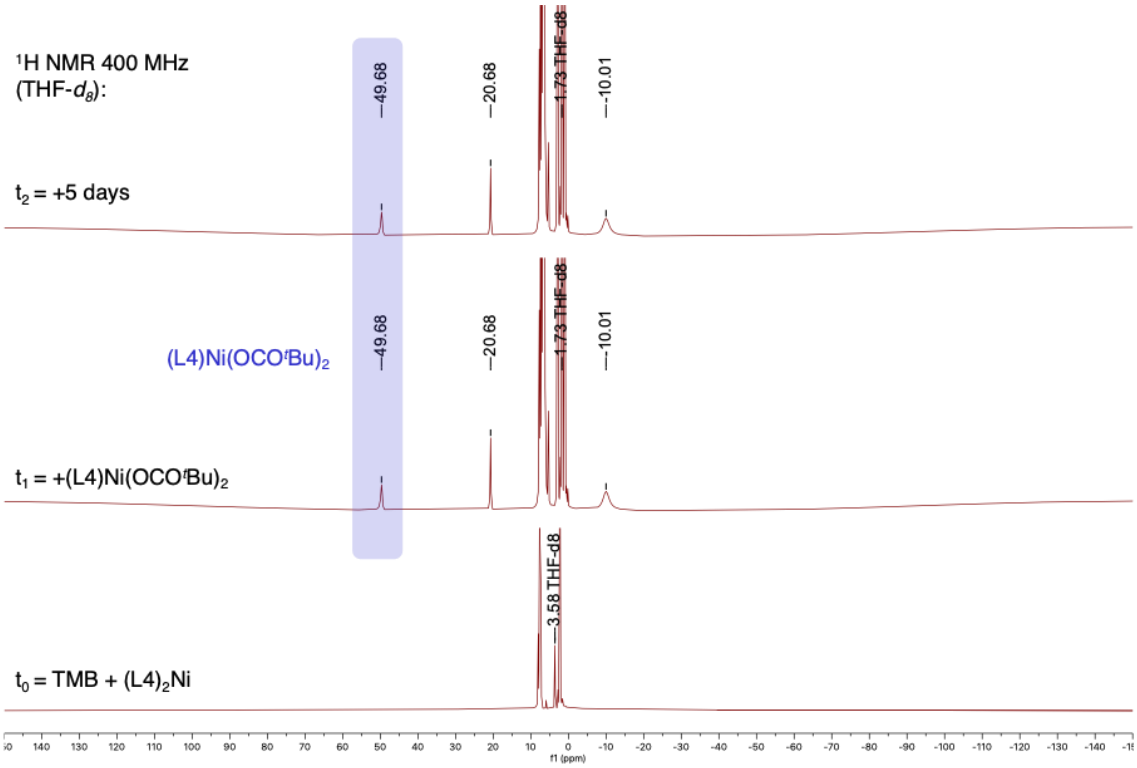

Figure S2. Paramagnetic ^{1}H NMR spectra upon mixing (L4)Ni(OCO^{t}Bu)$_2$ and (L4)$_2$Ni indicating no conversion of (L4)Ni(OCO^{t}Bu)$_2$. (L4)Ni(OCO^{t}Bu)$_2$ (blue).

Monitored by EPR. In the glovebox, a solution of (L4)$_2$Ni was prepared and the EPR spectrum of (L4)$_2$Ni was recorded which was EPR silent. Separately, (L4)Ni(OCO^{t}Bu)$_2$ (10 mg, 0.02 mmol) and (L4)$_2$Ni (12 mg, 0.02 mmol) were added to a 4 mL vial. A stir bar was added, and the vial was charged with 1 mL of THF. After 1 hour, a 100 uL aliquot was removed and diluted to 800 uL in THF and then analyzed by EPR, in which no EPR signals corresponding to Ni(I) species were observed. As described in the synthesis of (L4)Ni(OCO^{t}Bu)$_2$, this Ni(II) complex is X-band EPR silent.

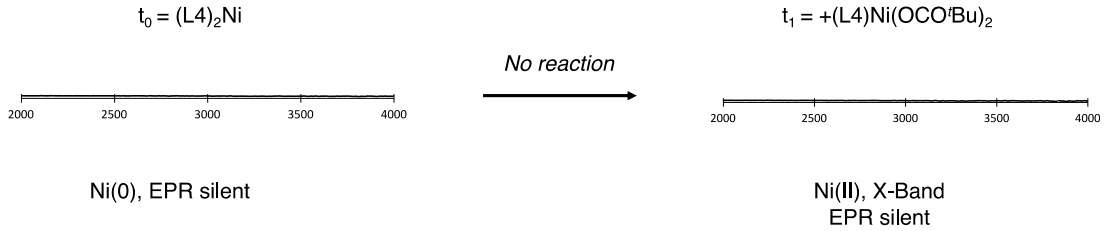

Figure S3. Continuous wave (CW) X-Band EPR spectra of (L4)$_2$Ni and upon mixing (L4)Ni(OCO^{t}Bu)$_2$ and (L4)$_2$Ni indicating no formation of Ni(I) species. (L4)$_2$Ni and (L4)Ni(OCO^{t}Bu)$_2$ are both X-Band EPR silent, while Ni(I) species would be EPR active.

No reaction between (L4)Ni(OCOPh)$_2$ and (L4)$_2$Ni

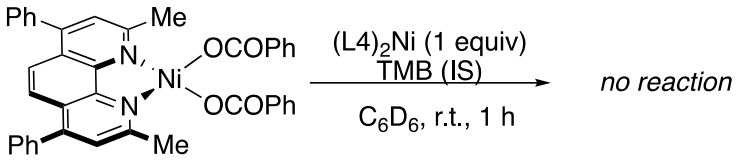

Monitored by quantitative ^{1}H NMR and paramagnetic ^{1}H NMR. In the glovebox, (L4)$_2$Ni (10 mg, 0.01 mmol) and TMB (1 mg, internal standard) were added to a 4 mL vial with 1 mL of C_6D_6. The solution was transferred to a J-Young NMR tube and the initial integration of (L4)$_2$Ni and TMB was recorded. The J-Young NMR tube was brought back into the glovebox and added to a vial containing (L4)Ni(OCOPh)$_2$ (9 mg, 0.01 mmol) and stirred for 1 h before transferring back into the J-Young NMR tube and analyzed by ^{1}H NMR. No conversion of (L4)$_2$Ni was observed and paramagnetic signals of (L4)Ni(OCOPh)$_2$ remained with no additional signals of paramagnetic species observed. Conclusion: This is consistent with no reaction between (L4)$_2$Ni and (L4)Ni(OCOPh)$_2$.

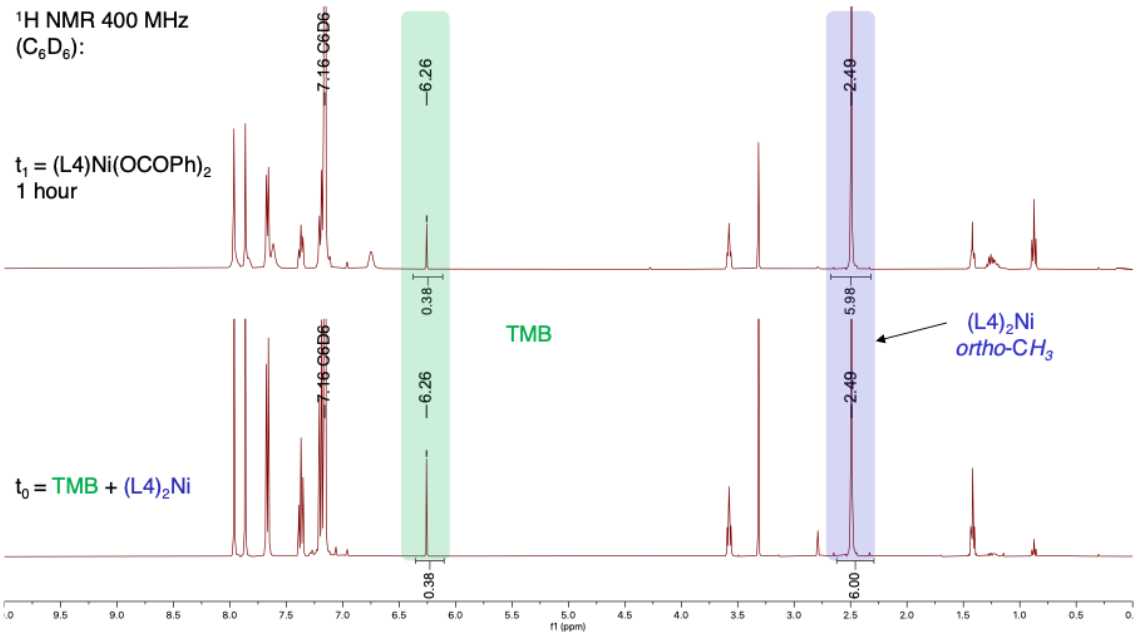

Figure S4. Quantitative ^{1}H NMR spectra of TMB and (L4)$_2$Ni indicating no conversion of (L4)$_2$Ni upon adding (L4)Ni(OCOPh)$_2$. Internal standard trimethoxybenzene, TMB (green) and (L4)$_2$Ni (blue).

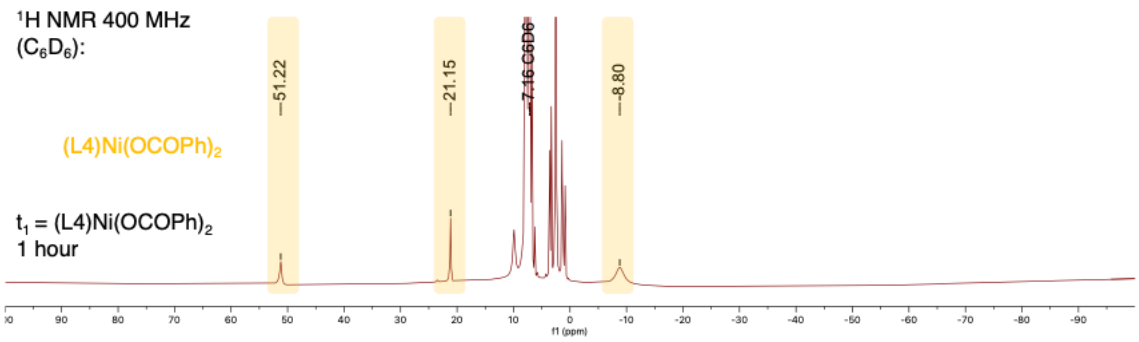

Figure S5. Paramagnetic ^{1}H NMR spectra upon mixing (L4)Ni(OCOPh)$_2$ and (L4)$_2$Ni indicating no conversion of (L4)Ni(OCOPh)$_2$. (L4)Ni(OCOPh)$_2$ (orange).

Monitored by EPR. In the glovebox, (L4)Ni(OCOPh)$_2$ (8 mg, 0.02 mmol) and (L4)$_2$Ni (9 mg, 0.01 mmol) were added to a 4 mL vial. A stir bar was added, and the vial was charged with 1 mL of THF. After 1 hour, a 100 uL aliquot was removed and diluted to 800 uL in THF and then analyzed by EPR.

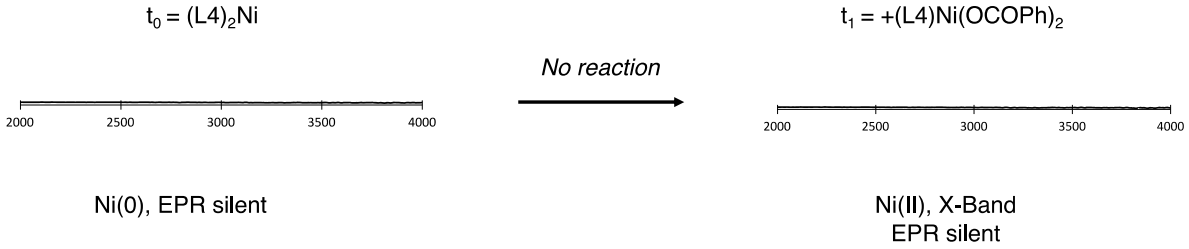

Figure S6. Continuous wave (CW) X-Band EPR spectra of (L4)$_2$Ni and upon mixing (L4)Ni(OCOPh)$_2$ and (L4)$_2$Ni indicating no formation of Ni(I) species. (L4)$_2$Ni and (L4)Ni(OCOPh)$_2$ are both X-Band EPR silent, while Ni(I) species would be EPR active.

No reaction between [(L4)Ni(OPh)$_2$]$_2$ and (L4)$_2$Ni

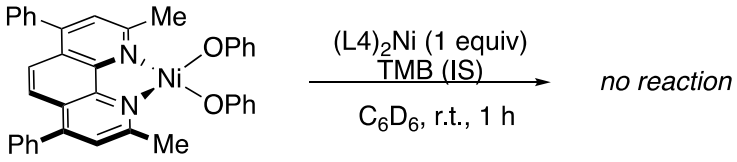

Monitored by quantitative ^{1}H NMR and paramagnetic ^{1}H NMR. In the glovebox, (L4)$_2$Ni (10 mg, 0.01 mmol) and TMB (1 mg, internal standard) were added to a 4 mL vial with 1 mL of C_6D_6. The solution was transferred to a J-Young NMR tube and the initial integration of (L4)$_2$Ni and TMB was recorded. The J-Young NMR tube was brought back into the glovebox and added to a vial containing [(L4)Ni(OPh)$_2$]$_2$ (8 mg, 0.01 mmol) and stirred for 1 h before transferring back into the J-Young NMR tube and analyzed by ^{1}H NMR. No conversion of (L4)$_2$Ni was observed with no additional signals of paramagnetic species observed, signals for [(L4)Ni(OPh)$_2$]$_2$ were observed

in low intensity due to the poor solubility in C_6D_6. Conclusion: This is consistent with no reaction between $(L4)_2Ni$ and $[(L4)Ni(OPh)_2]_2$.

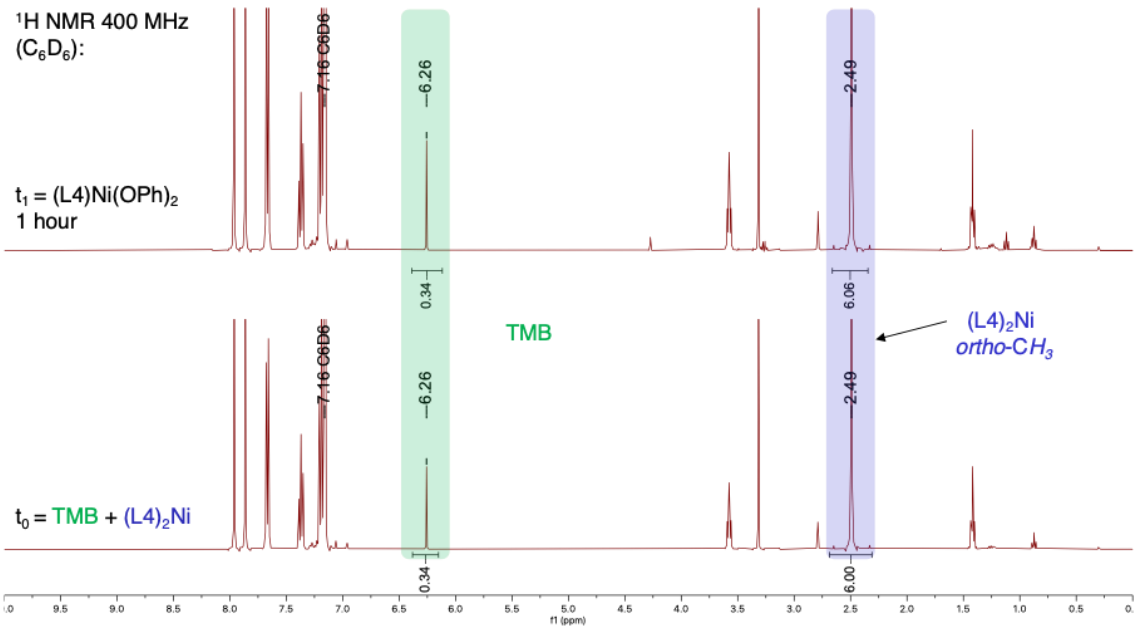

Figure S7. Quantitative ^1H NMR spectra of TMB and $(L4)_2Ni$ indicating no conversion of $(L4)_2Ni$ upon adding $[(L4)Ni(OPh)_2]_2$. Internal standard trimethoxybenzene, TMB (green) and $(L4)_2Ni$ (blue).

Monitored by EPR. In the glovebox, $[(L4)Ni(OPh)_2]_2$ (10 mg, 0.02 mmol) and $(L4)_2Ni$ (12 mg, 0.02 mmol) were added to a 4 mL vial. A stir bar was added, and the vial was charged with 1 mL of THF. After 1 hour, a 100 uL aliquot was removed and diluted to 800 uL in THF and then analyzed by EPR.

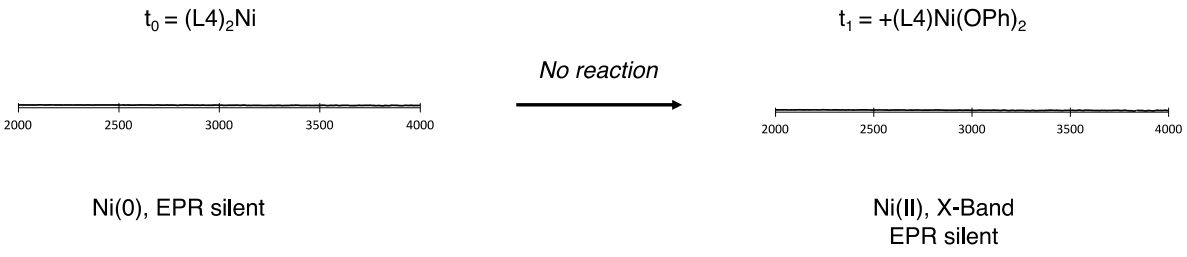

Figure S8. Continuous wave (CW) X-Band EPR spectra of $(L4)_2Ni$ and upon mixing $[(L4)Ni(OPh)_2]_2$and $(L4)_2Ni$ indicating no formation of Ni(I) species. $(L4)_2Ni$ and $[(L4)Ni(OPh)_2]_2$are both X-Band EPR silent, while Ni(I) species would be EPR active.

No reaction between (L3)Ni(OCO^{t}Bu)$_2$ and (L3)$_2$Ni

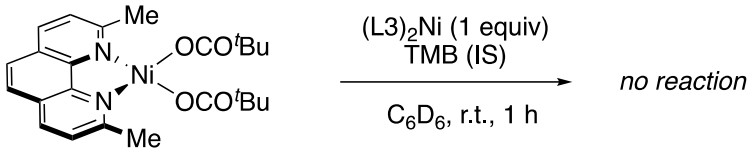

Monitored by quantitative ^{1}H NMR and paramagnetic ^{1}H NMR. In the glovebox, (L3)$_2$Ni (4.4 mg, 0.01 mmol) and TMB (1 mg, internal standard) were added to a 4 mL vial with 0.7 mL of C_6D_6 and filtered through a celite plug to remove traces of undissolved material and the filtrate was diluted further with 0.4 mL of C_6D_6 to prevent (L3)$_2$Ni from precipitating out of solution. The solution was transferred to a J-Young NMR tube and the initial integration of (L3)$_2$Ni and TMB was recorded. The J-Young NMR tube was brought back into the glovebox and added to a vial containing (L3)Ni(OCO^{t}Bu)$_2$ (4.3 mg, 0.01 mmol) and stirred for 1 h before transferring back into the J-Young NMR tube and analyzed by ^{1}H NMR. No conversion of (L3)$_2$Ni was observed and paramagnetic signals of (L3)Ni(OCO^{t}Bu)$_2$ remained with no additional signals of paramagnetic species observed. Conclusion: This is consistent with no reaction between (L3)$_2$Ni and (L3)Ni(OCO^{t}Bu)$_2$.

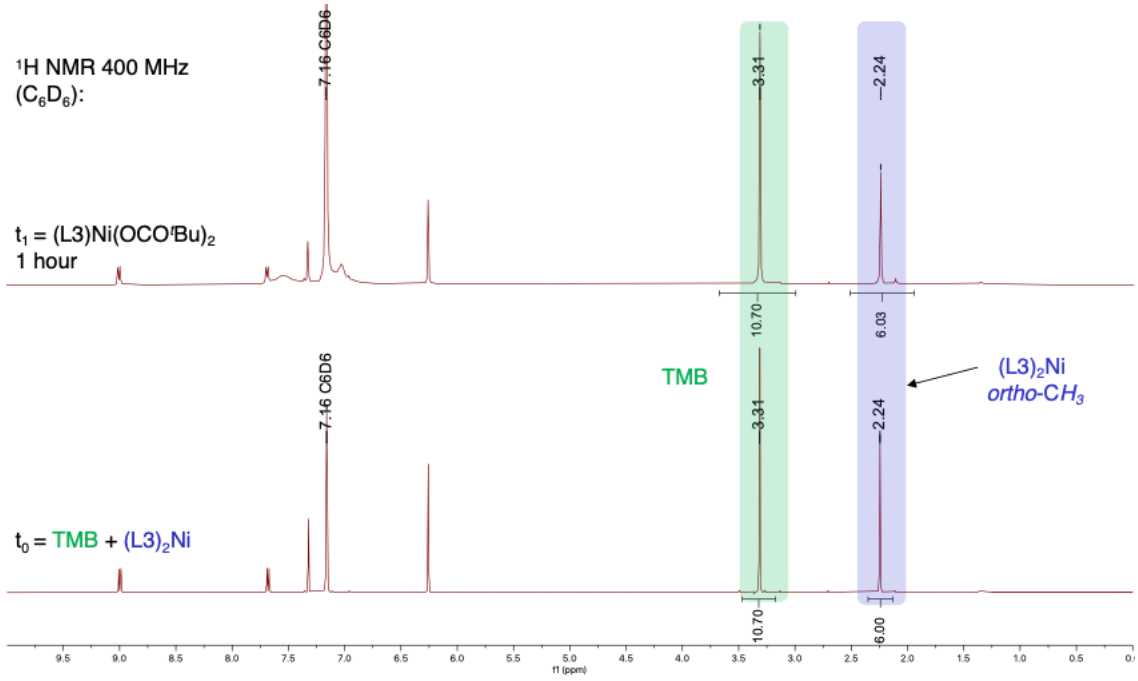

Figure S9. Quantitative ^{1}H NMR spectra of TMB and (L3)$_2$Ni indicating no conversion of (L3)$_2$Ni upon adding (L3)Ni(OCO^{t}Bu)$_2$. Internal standard trimethoxybenzene, TMB (green) and (L3)$_2$Ni (blue).

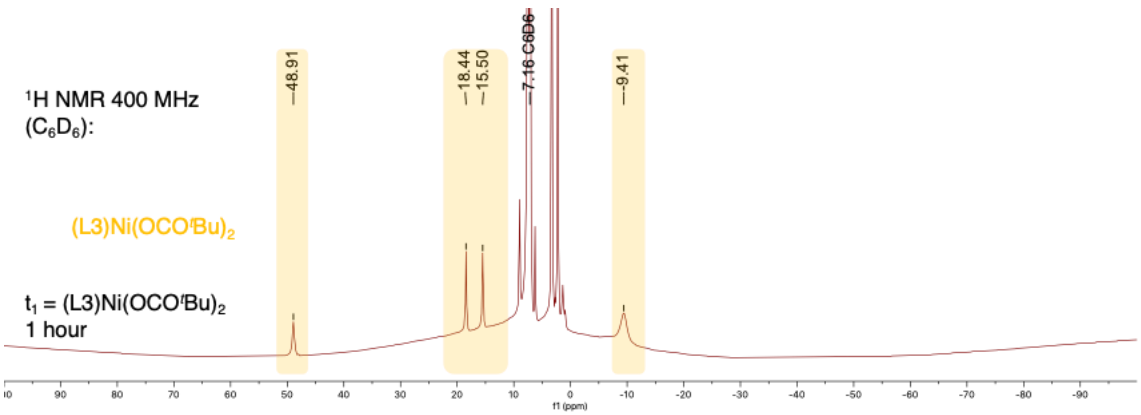

Figure S10. Paramagnetic ^{1}H NMR spectra upon mixing (L3)Ni(OCO^{t}Bu)$_2$ and (L3)$_2$Ni indicating no conversion of (L3)Ni(OCO^{t}Bu)$_2$. (L3)Ni(OCO^{t}Bu)$_2$ (orange).

Reaction between (L4)NiBr$_2$ and (L4)$_2$Ni

Monitored by quantitative ^{1}H NMR and paramagnetic ^{1}H NMR. In the glovebox, (L4)$_2$Ni (10 mg, 0.01 mmol) and TMB (1 mg, internal standard) were added to a 4 mL vial with 1 mL of THF-d_8. The solution was transferred to a J-Young NMR tube and the initial integration of (L4)$_2$Ni and TMB was recorded. The J-Young NMR tube was brought back into the glovebox and added to a vial containing (L4)NiBr$_2$ (7 mg, 0.01 mmol) and stirred for 1 h before transferring back into the J-Young NMR tube and analyzed by ^{1}H NMR. Full conversion of (L4)$_2$Ni was observed with additional signals of paramagnetic species observed. Conclusion: This is consistent with reaction between (L4)$_2$Ni and (L4)NiBr$_2$ to form Ni(I) complex [(L4)$_2$Ni]Br.

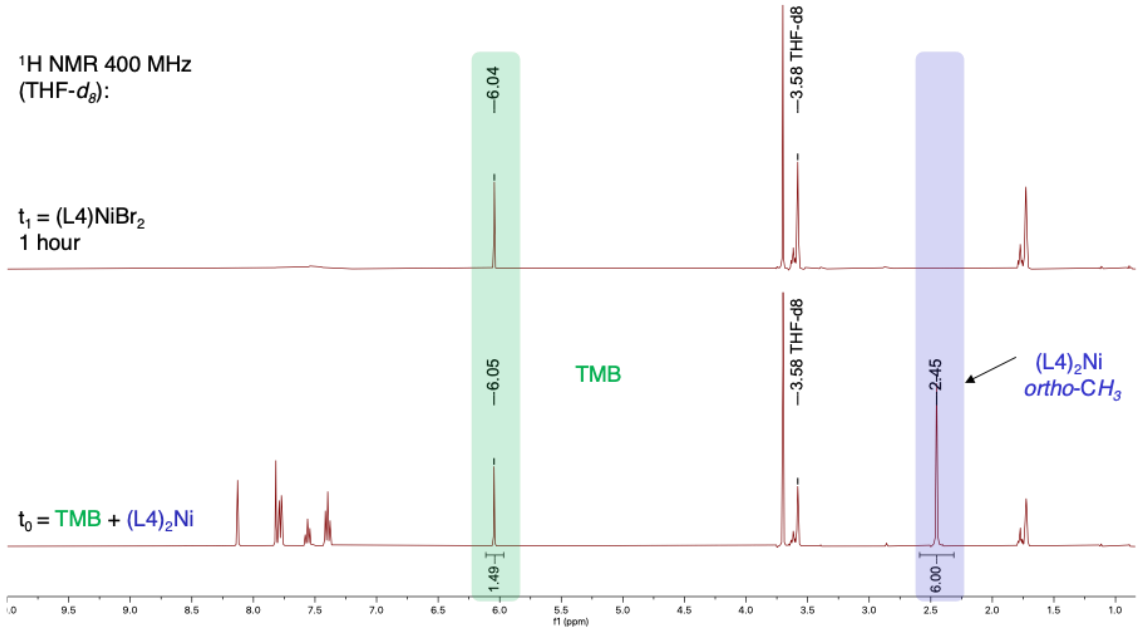

Figure S11. Quantitative ^{1}H NMR spectra of TMB and (L4)$_2$Ni indicating full conversion of (L4)$_2$Ni upon adding (L4)NiBr$_2$. Internal standard trimethoxybenzene, TMB (green) and (L4)$_2$Ni (blue).

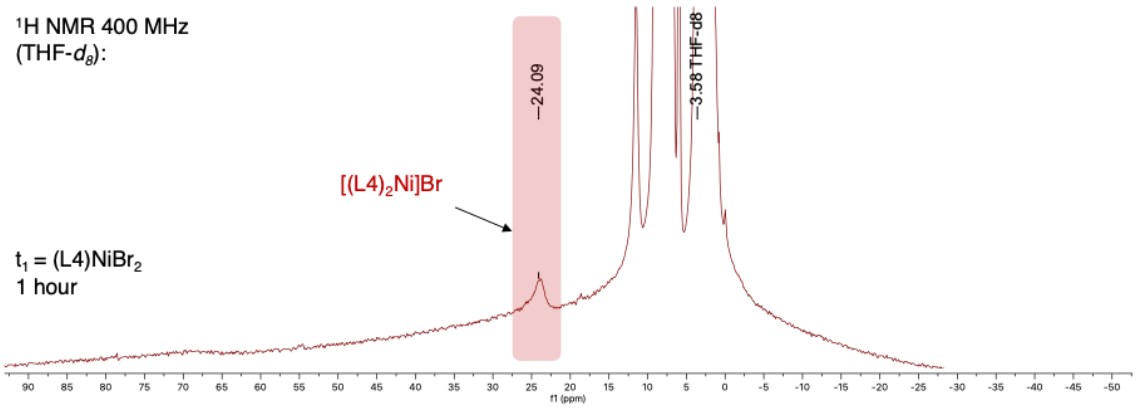

Figure S12. Paramagnetic ^{1}H NMR spectra upon mixing (L4)NiBr$_2$ and (L4)$_2$Ni indicating full conversion of (L4)$_2$Ni and formation of [(L4)$_2$Ni]Br. [(L4)$_2$Ni]Br (red).

Monitored by EPR. In the glovebox, (L4)NiBr$_2$ (8 mg, 0.01 mmol) and (L4)$_2$Ni (11 mg, 0.01 mmol) were added to a 4 mL vial. A stir bar was added, and the vial was charged with 1 mL of THF. After 1 hour, a 100 uL aliquot was removed and diluted to 800 uL in THF and then analyzed by EPR.

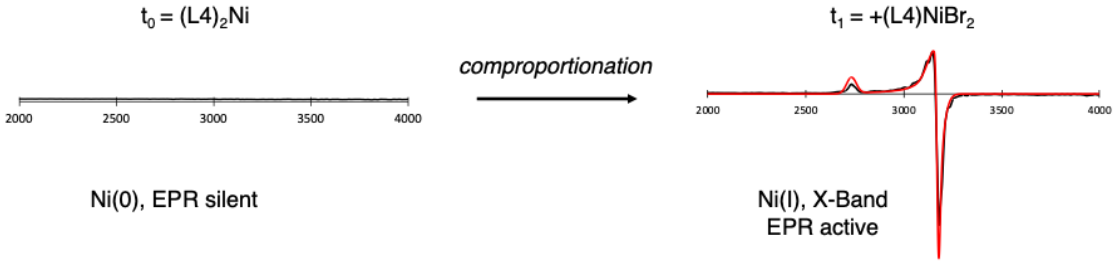

Figure S13. Continuous wave (CW) X-Band EPR spectra of (L4)$_2$Ni and upon mixing (L4)NiBr$_2$ and (L4)$_2$Ni indicating formation of Ni(I) species. (L4)$_2$Ni and (L4)NiBr$_2$ are both X-Band EPR silent, while Ni(I) species [(L4)$_2$Ni]Br would be EPR active.

Monitored rate of reaction by UV-VIS. In the glovebox, a solution of (L4)$_2$Ni (0.04 mM, 2.5 mL) in THF was transferred to a sealed cuvette. The UV-VIS spectra was monitored at 550 nm an a solution of (L4)NiBr$_2$ (0.4 mM, 0.25 mL) was injected via microsyringe in which the reaction was complete within 4 seconds. Noise from injecting the solution of (L4)NiBr$_2$ precluded accurate rate measurements. Conclusion: This is consistent with reaction between (L4)$_2$Ni and (L4)NiBr$_2$ to form Ni(I) complex [(L4)$_2$Ni]Br occurs rapidly.

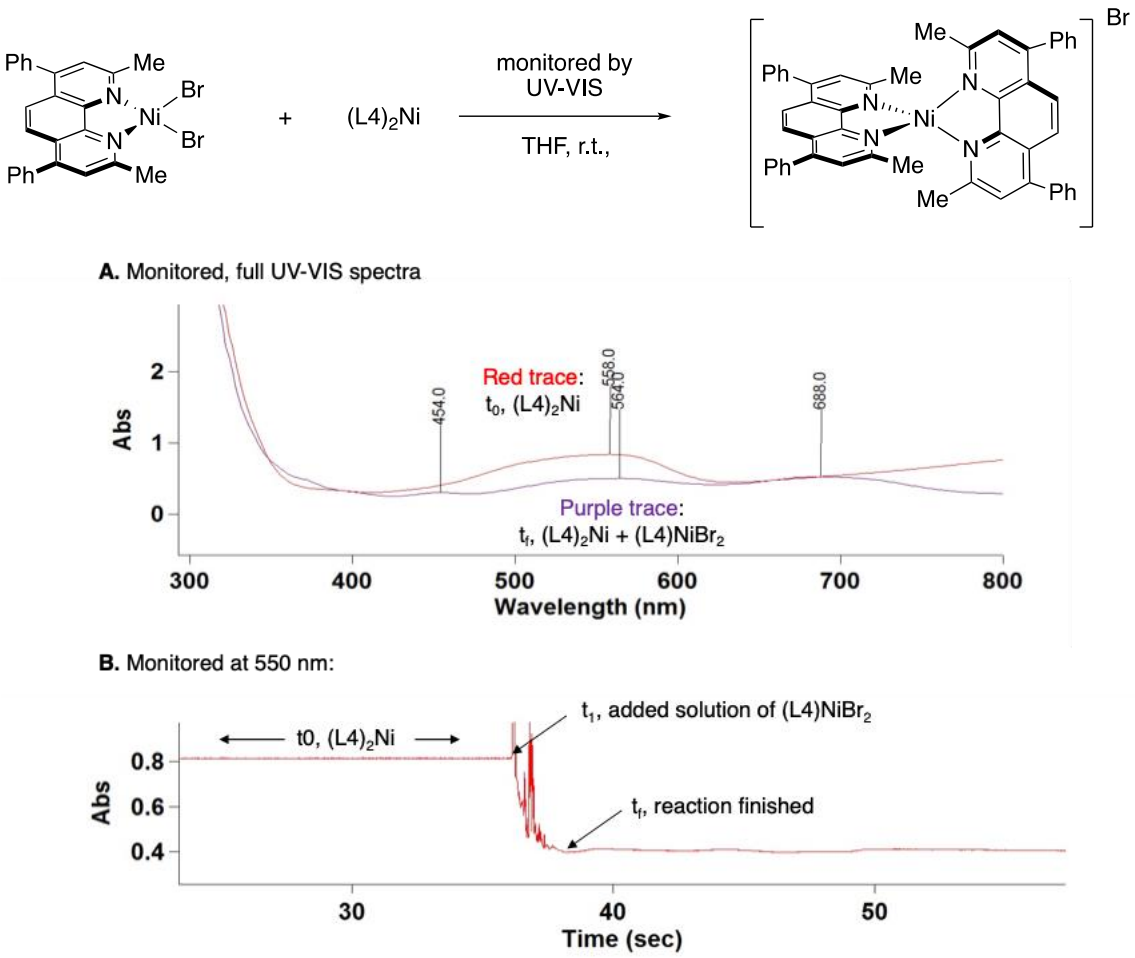

Figure S14. Monitoring the reaction of $(L4)_2Ni$ and $(L4)NiBr_2$ by UV-VIS spectroscopy. **A**. Initial UV-VIS spectrum of $(L4)_2Ni$ (red trace) and the resulting spectrum after addition of $(L4)NiBr_2$. **B**. Monitoring the reaction at 550 nm.

Reaction Between $[(L4)_2Ni]Cl$ and Potassium Pivalate in THF

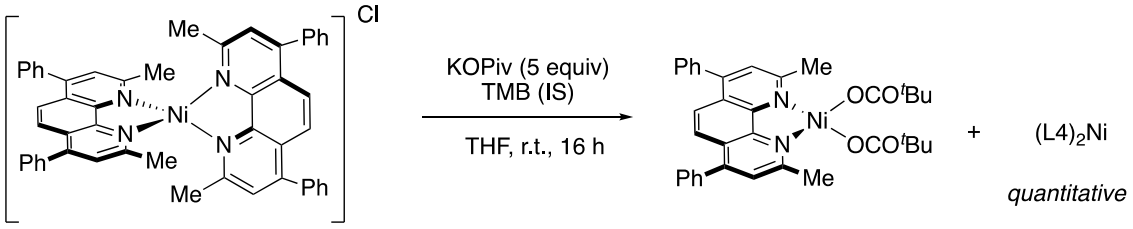

Monitored by quantitative ^{1}H NMR and paramagnetic ^{1}H NMR. In the glovebox, ($[(L4)_2Ni]Cl$ (22 mg, 0.03 mmol) and potassium pivalate (18 mg, 0.15 mmol, 5 equiv) were added to a 4 mL vial. A stir bar was added, and the vial was charged with 2 mL of THF. After 16 hour, the solvent was removed and redissolved in 3 mL of C_6D_6. To this solution, a stock solution of TMB in C_6D_6 was added and the integral ratio of TMB to $(L4)_2Ni$ was measured by ^{1}H NMR to determine $(L4)_2Ni$ had formed in quantitative yield and the only species observed in the paramagnetic NMR was $(L4)Ni(OCO^tBu)_2$.

Attempts to follow these reactions by EPR and paramagnetic NMR were performed to identify the formation of transient (L4)Ni^{I}-OCO^{t}Bu, however we were unable to identify any new signals that would correspond to this species suggested it undergo rapid disproportionation once formed. Conclusion: This is consistent with reaction between Ni(I) complex [(L4)$_2$Ni]Cl and potassium pivalate to form (L4)$_2$Ni and (L4)Ni(OCO^{t}Bu)$_2$.

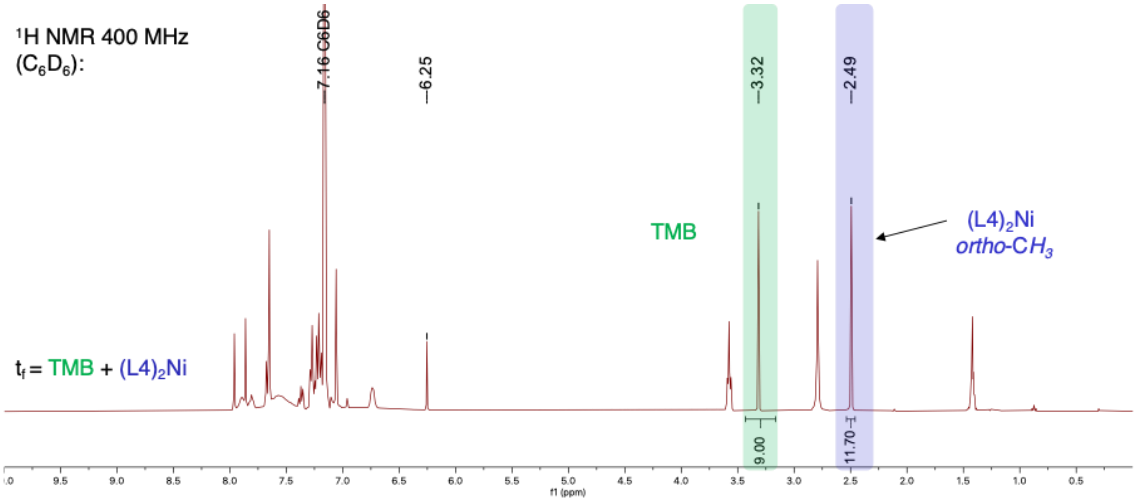

Figure S15. Quantitative ^{1}H NMR spectra of TMB and (L4)$_2$Ni after reacting [(L4)$_2$Ni]Cl with potassium pivalate. Internal standard trimethoxybenzene, TMB (green) and (L4)$_2$Ni (blue).

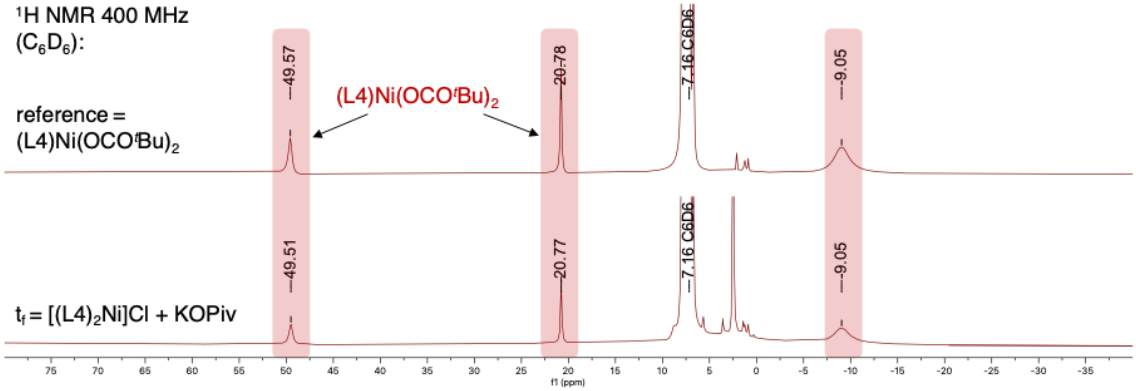

Figure S16. Paramagnetic ^{1}H NMR spectra upon mixing [(L4)$_2$Ni]Cl with potassium pivalate formation of (L4)Ni(OCO^{t}Bu)$_2$. (L4)Ni(OCO^{t}Bu)$_2$ (red).

Monitored by EPR. In the glovebox, [(L4)$_2$Ni]Cl (10 mg, 0.01 mmol) and potassium pivalate (8 mg, 0.06 mmol, 6 equiv) were added to a 4 mL vial. A stir bar was added, and the vial was charged with 1 mL of THF. After 16 hour, a 100 uL aliquot was removed and diluted to 800 uL in THF and then analyzed by EPR.

Figure S17. Continuous wave (CW) X-Band EPR spectra of $[(L4)_2Ni]Cl$ and upon mixing $[(L4)_2Ni]Cl$ with potassium pivalate indicating loss of Ni(I) species $[(L4)_2Ni]Cl$. $(L4)_2Ni$ and $(L4)Ni(OCO^tBu)_2$ are both X-Band EPR silent, while Ni(I) species $[(L4)_2Ni]Cl$ would be EPR active.

Reaction Between $[(L4)_2Ni]Cl$ and Potassium Pivalate in MeCN

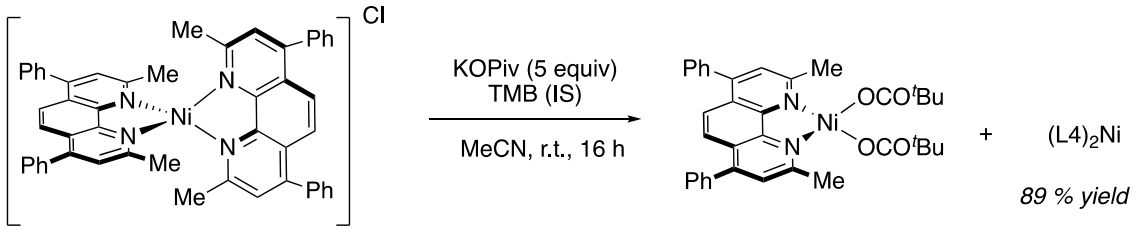

Monitored by quantitative ^{1}H NMR and paramagnetic ^{1}H NMR. In the glovebox, ($[(L4)_2Ni]Cl$ (18 mg, 0.02 mmol) and potassium pivalate (14 mg, 0.11 mmol, 5 equiv) were added to a 4 mL vial. A stir bar was added, and the vial was charged with 3 mL of MeCN. After 16 hour, the solvent was removed and redissolved in 3 mL of C_6D_6. To this solution, a stock solution of TMB in C_6D_6 was added and the integral ratio of TMB to $(L4)_2Ni$ was measured by ^{1}H NMR to determine $(L4)_2Ni$ had formed in 89 % yield and the only species observed in the paramagnetic NMR was $(L4)Ni(OCO^tBu)_2$. Conclusion: This is consistent with reaction between Ni(I) complex $[(L4)_2Ni]Cl$ and potassium pivalate to form $(L4)_2Ni$ and $(L4)Ni(OCO^tBu)_2$.

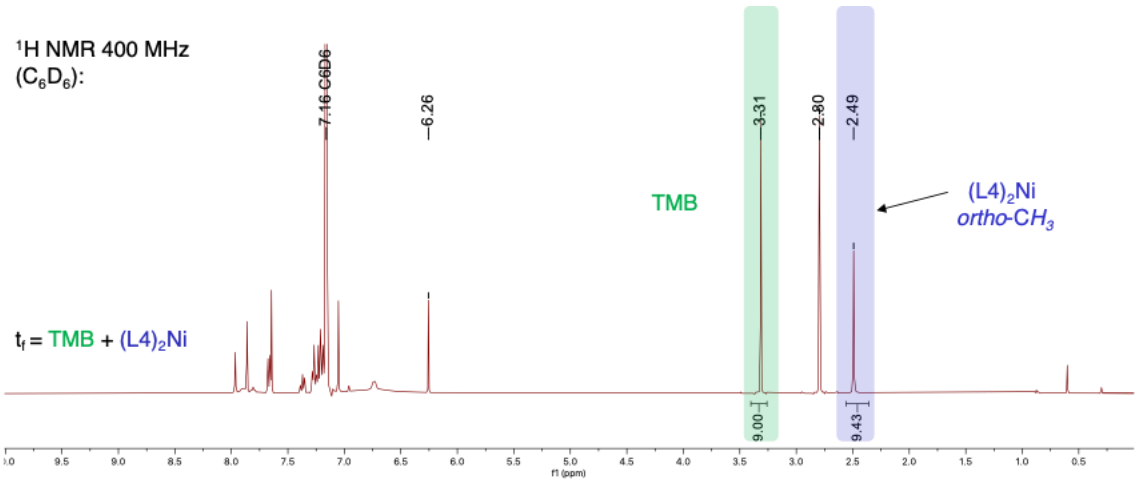

Figure S18. Quantitative ^{1}H NMR spectra of TMB and $(L4)_2Ni$ after reacting $[(L4)_2Ni]Cl$ with potassium pivalate. Internal standard trimethoxybenzene, TMB (green) and $(L4)_2Ni$ (blue).

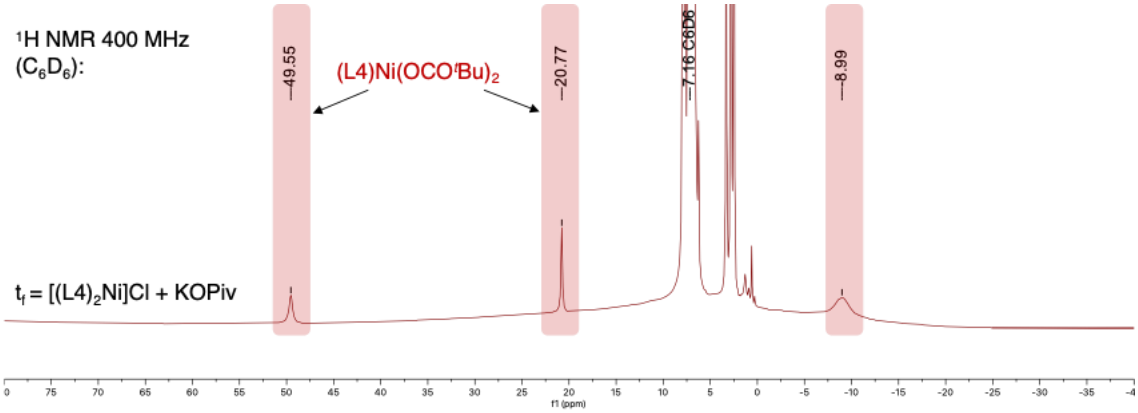

Figure S19. Paramagnetic ^{1}H NMR spectra upon mixing $[(L4)_2Ni]Cl$ with potassium pivalate formation of $(L4)Ni(OCO^tBu)_2$. $(L4)Ni(OCO^tBu)_2$ (red).

Reaction Between $[(L4)_2Ni]Cl$ and Potassium Benzoate

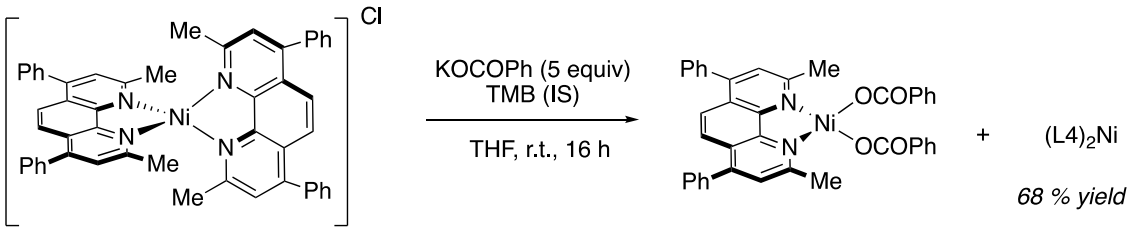

Monitored by quantitative ^{1}H NMR and paramagnetic ^{1}H NMR. In the glovebox, ($[(L4)_2Ni]Cl$ (10 mg, 0.01 mmol), potassium benzoate (10 mg, 0.06 mmol, 6 equiv), and L4 (5 mg, 0.01 mmol) were added to a 10 mL vial. A stir bar was added, and the vial was charged with 2 mL of THF. After 16 hour, the solvent was removed, redissolved in 3 mL of C_6D_6 and filtered through a celite plug. To this solution, a stock solution of

TMB in C_6D_6 was added and the integral ratio of TMB to $(L4)_2Ni$ was measured by ^1H NMR to determine $(L4)_2Ni$ had formed in 68 % yield and the only species observed in the paramagnetic NMR was $(L4)Ni(OCOPh)_2$. Conclusion: This is consistent with reaction between Ni(I) complex $[(L4)_2Ni]Cl$ and potassium benzoate to form $(L4)_2Ni$ and $(L4)Ni(OCOPh)_2$.

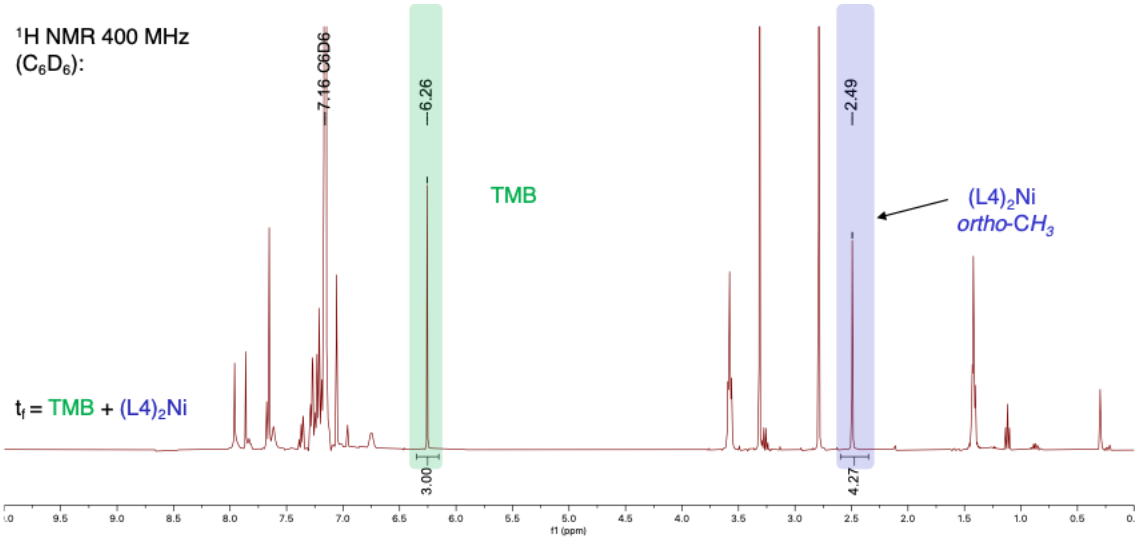

Figure S20. Quantitative ^1H NMR spectra of TMB and $(L4)_2Ni$ after reacting $[(L4)_2Ni]Cl$ with potassium benzoate. Internal standard trimethoxybenzene, TMB (green) and $(L4)_2Ni$ (blue).

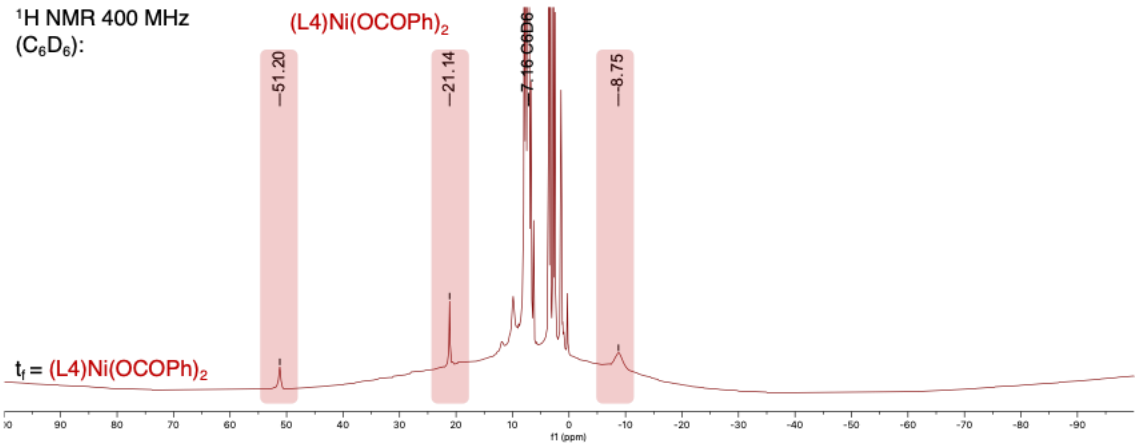

Figure S21. Paramagnetic ^1H NMR spectra upon mixing $[(L4)_2Ni]Cl$ with potassium benzoate and formation of $(L4)Ni(OCOPh)_2$. $(L4)Ni(OCOPh)_2$ (red).

Reaction Between $[(L4)_2Ni]Cl$ and Sodium Phenoxide

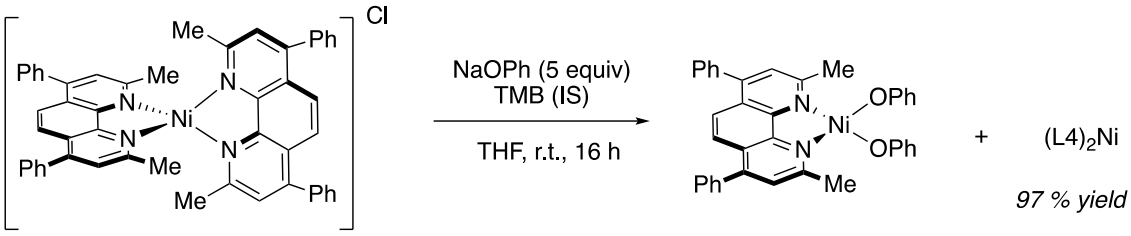

Monitored by quantitative ^{1}H NMR and paramagnetic ^{1}H NMR. In the glovebox, ($[(L4)_2Ni]Cl$ (21 mg, 0.03 mmol), sodium phenoxide (15 mg, 0.13 mmol, 5 equiv), and L4 (9 mg, 0.03 mmol) were added to a 10 mL vial. A stir bar was added, and the vial was charged with 2 mL of THF. After 16 hour, the solvent was removed, redissolved in 3 mL of C_6D_6 and filtered through a celite plug. To this solution, a stock solution of TMB in C_6D_6 was added and the integral ratio of TMB to $(L4)_2Ni$ was measured by ^{1}H NMR to determine $(L4)_2Ni$ had formed in 97 % yield and the only species observed in the paramagnetic NMR was $(L4)Ni(OPh)_2$. Due to the insolubility of $[(L4)Ni(OPh)_2]_2$ in C_6D_6, only faint traces of paramagnetic species are observed. Conclusion: This is consistent with reaction between Ni(I) complex $[(L4)_2Ni]Cl$ and sodium phenoxide to form $(L4)_2Ni$ and $[(L4)Ni(OPh)_2]_2$.

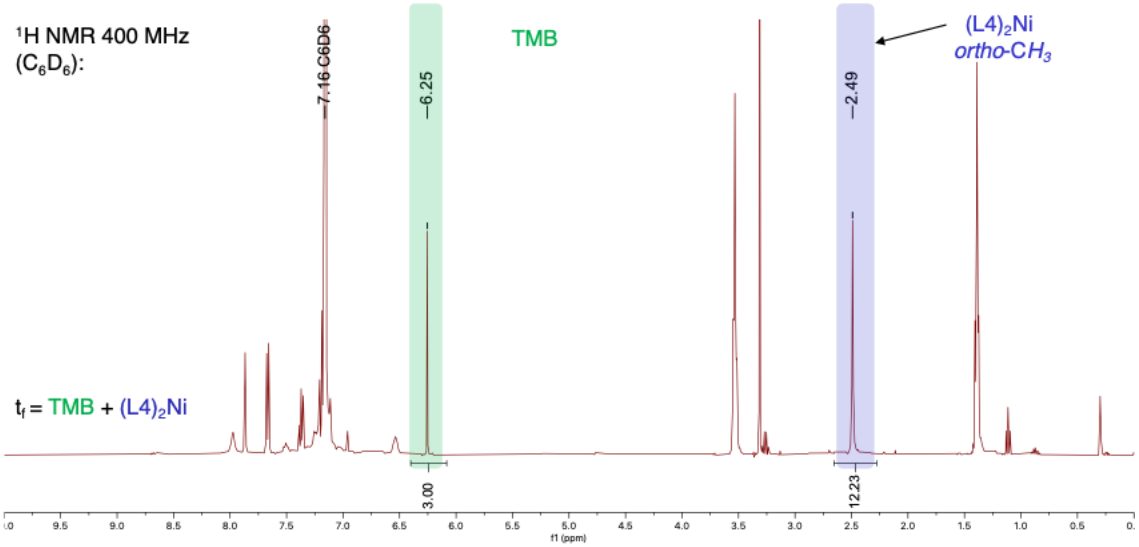

Figure S22. Quantitative ^{1}H NMR spectra of TMB and $(L4)_2Ni$ after reacting $[(L4)_2Ni]Cl$ with sodium phenoxide. Internal standard trimethoxybenzene, TMB (green) and $(L4)_2Ni$ (blue).

Reaction Between $[(L3)_2Ni]Cl$ and Potassium Pivalate

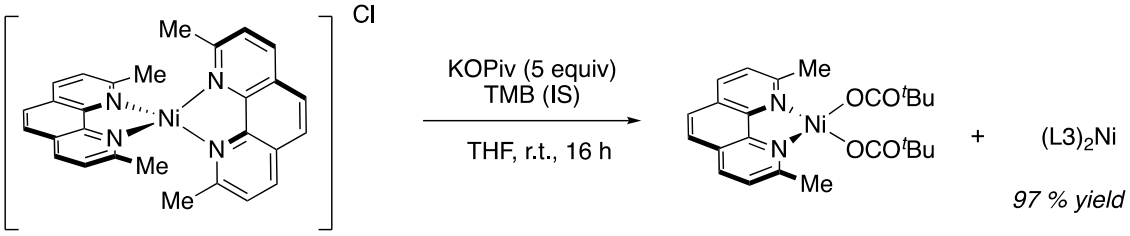

Monitored by quantitative ^{1}H NMR and paramagnetic ^{1}H NMR. In the glovebox, ($[(L3)_2Ni]Cl$ (10 mg, 0.02 mmol), potassium pivalate (12 mg, 0.10 mmol, 5 equiv), and L3 (4 mg, 0.02 mmol) were added to a 10 mL vial. A stir bar was added, and the vial was charged with 2 mL of THF. After 16 hour, the solvent was removed, redissolved in 3 mL of C_6D_6 and filtered through a celite plug. To this solution, a stock solution of TMB in C_6D_6 was added and the integral ratio of TMB to $(L3)_2Ni$ was measured by ^{1}H NMR to determine $(L3)_2Ni$ had formed in 96 % yield and the only species observed in the paramagnetic NMR was $(L3)Ni(OPiv)_2$. Conclusion: This is consistent with reaction between Ni(I) complex $[(L3)_2Ni]Cl$ and potassium pivalate to form $(L3)_2Ni$ and $(L3)Ni(OPiv)_2$.

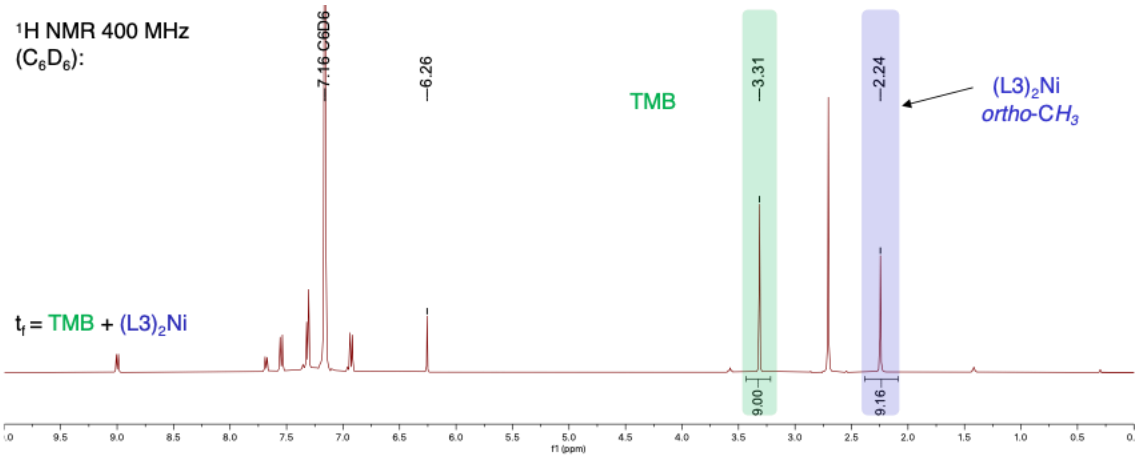

Figure S23. Quantitative ^{1}H NMR spectra of TMB and $(L3)_2Ni$ after reacting $[(L3)_2Ni]Cl$ with pottasium pivalate. Internal standard trimethoxybenzene, TMB (green) and $(L3)_2Ni$ (blue).

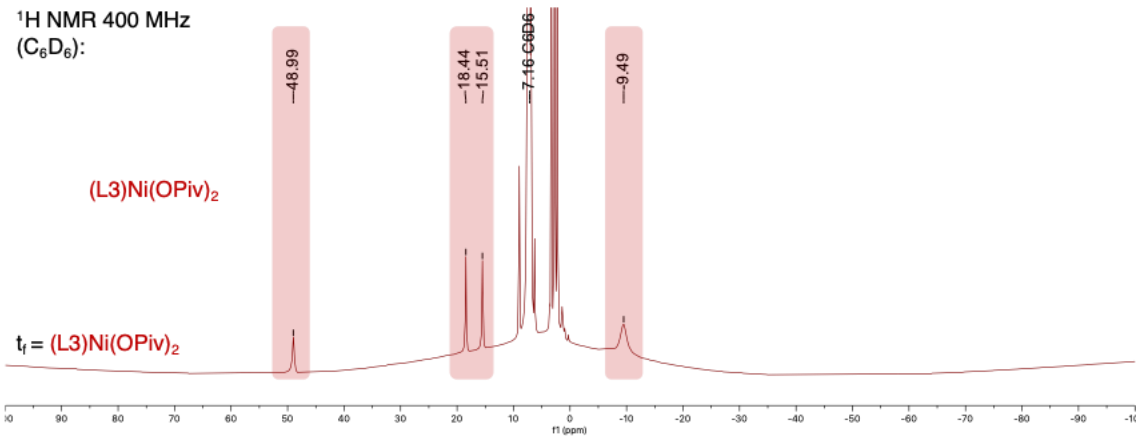

Figure S24. Paramagnetic ^{1}H NMR spectra upon mixing $[(L3)_2Ni]Cl$ with potassium pivalate and formation of $(L3)Ni(OPiv)_2$. $(L3)Ni(OPiv)_2$ (red).

Solubility of Ni(II) complexes

In the glovebox $(bipyridine)NiCl_2$ (25 mg) was added to a 10 mL vial. A stir bar was added, and the vial was charged with 3 mL of THF and stirred at 900 rpm. After 1 hour, a 1.5 mL aliquot was removed and filtered through a celite plug to afford a saturated solution of $(bipyridine)NiCl_2$ in which 1 mL was transferred to a tared vial. The solvent was removed to afford the resultant solid. This representative procedure was repeated for $(phenanthroline)NiCl_2$, $(neocuproine)NiCl_2$ and $(bathrocuproine)NiCl_2$.

Reaction Between (L4)NiBr$_2$ and Zinc

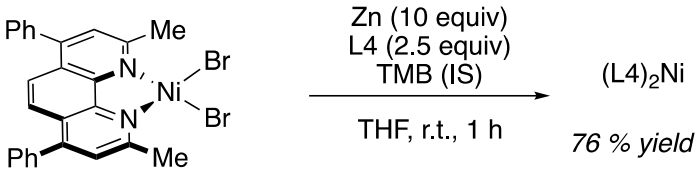

Quantified by ^{1}H NMR. In the glovebox, (L4)NiBr$_2$ (22 mg, 0.04 mmol), L4 (35 mg, 0.10 mmol, 2.5 equiv) and zinc (25 mg, 0.38 mmol, 10 equiv) were added to a 10 mL vial. A stir bar was added, and the vial was charged with 2 mL of THF and stirred at 900 rpm. After 1 hour, the suspension was filtered through a celite plug and the solvent was removed and redissolved in 3 mL of C_6D_6. To this solution, a stock solution of TMB in C_6D_6 was added and the integral ratio of TMB to (L4)$_2$Ni was measured by ^{1}H NMR to determine (L4)$_2$Ni had formed in 76 % yield. Conclusion: This is consistent with full reduction of Ni(II) to Ni(0) with Zn.

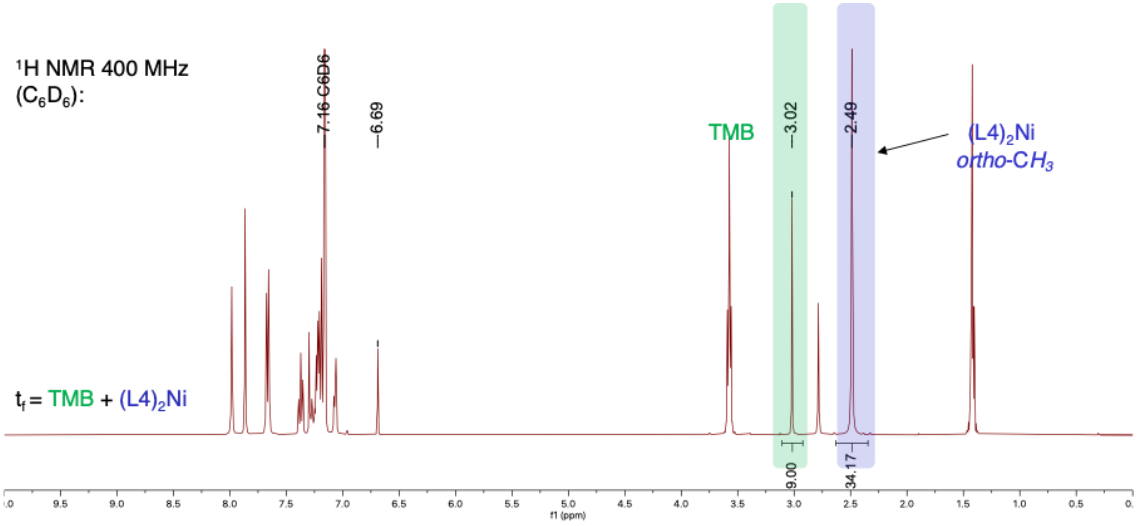

Figure S25. Quantitative ^{1}H NMR spectra of TMB and (L4)$_2$Ni after reacting (L4)NiBr$_2$ with zinc (10 equiv). Internal standard trimethoxybenzene, TMB (green) and (L4)$_2$Ni (blue).

Reaction Between (L4)NiBr$_2$ and Manganese

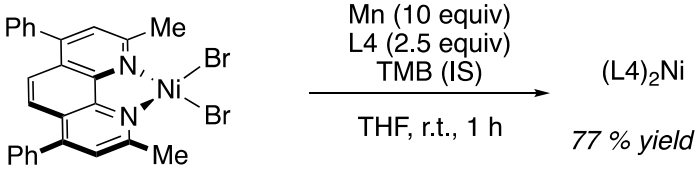

Quantified by ^{1}H NMR. In the glovebox, (L4)NiBr$_2$ (16 mg, 0.03 mmol), L4 (25 mg, 0.07 mmol, 2.5 equiv) and manganese (15 mg, 0.27 mmol, 10 equiv) were added to a

10 mL vial. A stir bar was added, and the vial was charged with 2 mL of THF and stirred at 900 rpm. After 1 hour, the suspension was filtered through a celite plug and the solvent was removed and redissolved in 3 mL of C_6D_6. To this solution, a stock solution of TMB in C_6D_6 was added and the integral ratio of TMB to $(L4)_2Ni$ was measured by ^1H NMR to determine $(L4)_2Ni$ had formed in 77 % yield. Conclusion: This is consistent with full reduction of Ni(II) to Ni(0) with Mn.

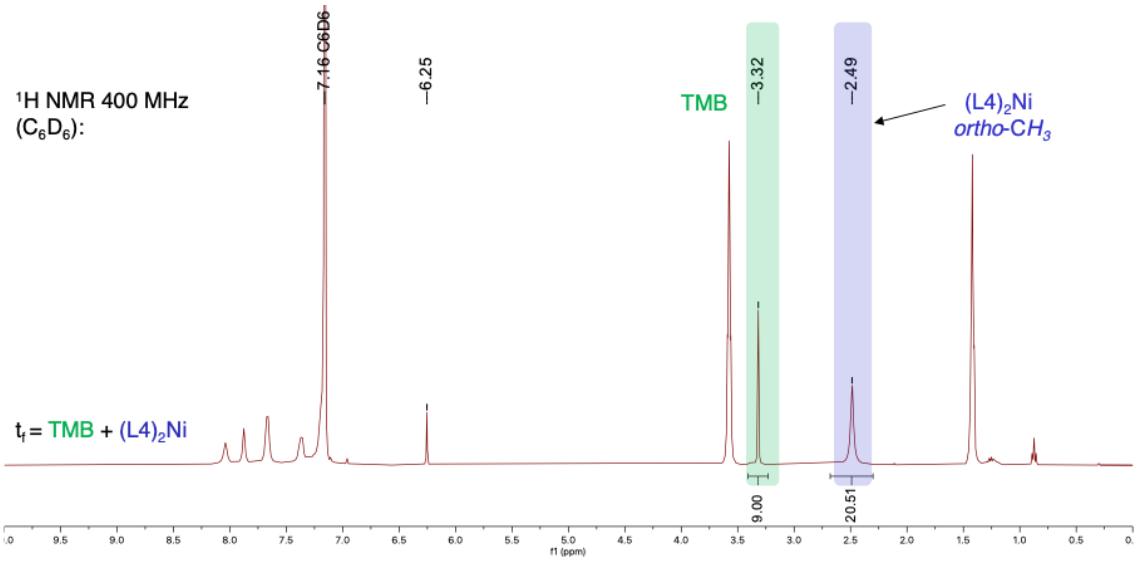

Figure S26. Quantitative ^1H NMR spectra of TMB and $(L4)_2Ni$ after reacting $(L4)NiBr_2$ with manganese (10 equiv). Internal standard trimethoxybenzene, TMB (green) and $(L4)_2Ni$ (blue).

No Reaction Between (L4)Ni(OCO^{t}Bu)$_2$ and Zn

Quantified by isolation. In the glovebox, $(L4)Ni(OCO^tBu)_2$ (19 mg, 0.03 mmol), and zinc (20 mg, 0.31 mmol, 10 equiv) were added to a 10 mL vial. A stir bar was added, and the vial was charged with 2 mL of THF and stirred at 900 rpm. After 1 hour, the suspension was filtered through a celite plug to afford a green filtrate in which the solvent was removed. The solid was then filtered to afford $(L4)Ni(OCO^tBu)_2$ as a green solid (18 mg, 92 % recovered yield). These reactions were performed without added L4 to assist in isolation. They were repeated with additional L4 as a control to verify this did not change the reaction outcome in which only starting material is observed, even at 16 h in which only starting material is observed (Figure S27). Conclusion: This is consistent with no reduction of Ni(II)-$(OCO^tBu)_2$ to Ni(0) with Zn.

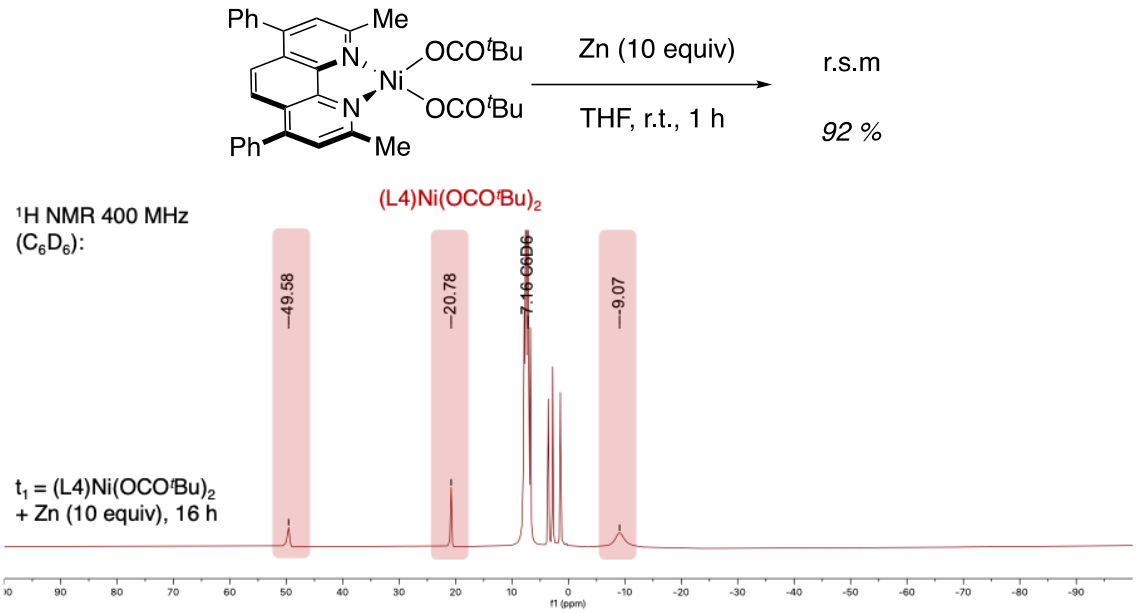

Figure S27. Paramagnetic ^{1}H NMR spectra upon mixing (L4)Ni(OCO^{t}Bu)2 with zinc (10 equiv) and isolating unreacted (L4)Ni(OCO^{t}Bu)$_2$ with no formation of (L4)$_2$Ni. (L4)Ni(OCO^{t}Bu)$_2$ (red).

No Reaction Between (L4)Ni(OCO^{t}Bu)$_2$ and Mn

Quantified by isolation. In the glovebox, (L4)Ni(OCO^{t}Bu)$_2$ (19 mg, 0.03 mmol), and manganese (17 mg, 0.30 mmol, 10 equiv) were added to a 10 mL vial. A stir bar was added, and the vial was charged with 2 mL of THF and stirred at 900 rpm. After 1 hour, the suspension was filtered through a celite plug to afford a green filtrate in which the solvent was removed. The solid was then filtered to afford (L4)Ni(OCO^{t}Bu)$_2$ as a green solid (18 mg, 97 % recovered yield). These reactions were performed without added L4 to assist in isolation. They were repeated with additional L4 as a control to verify this did not change the reaction outcome in which only starting material is observed, even at 16 h in which only starting material is observed (Figure S28). Conclusion: This is consistent with no reduction of Ni(II)-(OCO^{t}Bu)$_2$ to Ni(0) with Zn.

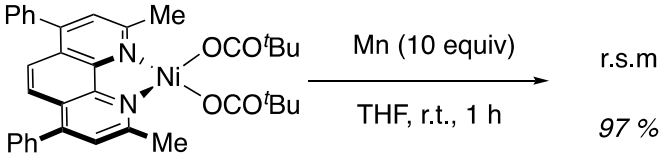

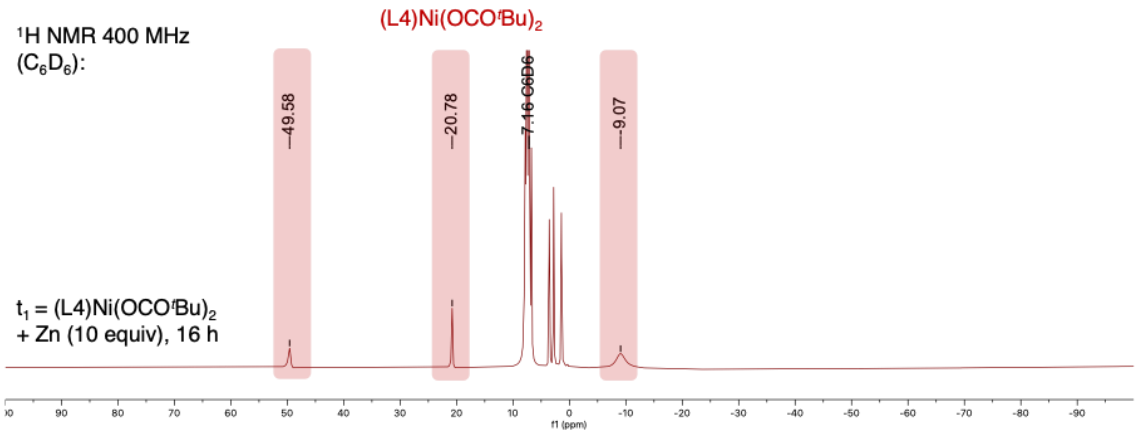

Figure S28. Paramagnetic ^{1}H NMR spectra upon mixing (L4)Ni(OCO^{t}Bu)$_2$ with manganese (10 equiv) and isolating unreacted (L4)Ni(OCO^{t}Bu)$_2$ with no formation of (L4)$_2$Ni. (L4)Ni(OCO^{t}Bu)$_2$ (red).

Reaction Between (L4)Ni(OCO^{t}Bu)$_2$ and LiBr

Quantified by isolation. In the glovebox, (L4)Ni(OCO^{t}Bu)$_2$ (31 mg, 0.05 mmol), and LiBr (17 mg, 0.20 mmol, 4 equiv) were added to a 10 mL vial. A stir bar was added, and the vial was charged with 2 mL of THF and stirred at 900 rpm. After 1 hour, the suspension was filtered through a celite plug to afford a pink filtrate from which the solvent was removed. The solid was then re-dissolved in toluene and filtered the solvent was again removed to afford (L4)Ni(Br)$_2$ as a pink solid (27 mg, 93 % yield). Conclusion: This is consistent with full conversion of Ni(II)-(OCO^{t}Bu)$_2$ to Ni(II)-(Br)$_2$ with LiBr.

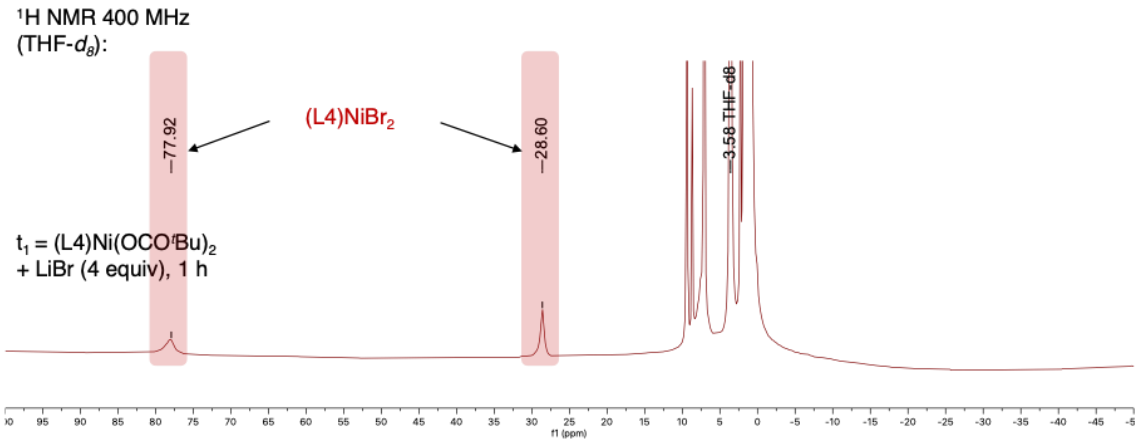

Figure S29. Paramagnetic ^{1}H NMR spectra upon mixing (L4)Ni(OCO^{t}Bu)$_2$ with LiBr (4 equiv) indicating full conversion of (L4)Ni(OCO^{t}Bu)$_2$ to (L4)NiBr$_2$. (L4)NiBr$_2$ (red).

Reaction Between (L4)Ni(OCO^{t}Bu)$_2$, Zinc and LiBr

Quantified by ^{1}H NMR. In the glovebox, (L4)Ni(OCO^{t}Bu)$_2$ (12 mg, 0.02 mmol), L4 (18 mg, 0.05 mmol, 2.5 equiv), LiBr (9 mg, 0.1 mmol, 4 equiv) and zinc (13 mg, 0.20 mmol, 10 equiv) were added to a 4 mL vial. A stir bar was added, and the vial was charged with 1 mL of THF-d_8 and stirred at 900 rpm. After 1 hour, the suspension was filtered through a celite plug. To this solution, a stock solution of TMB in THF-d_8 was added and the integral ratio of TMB to (L4)$_2$Ni was measured by ^{1}H NMR to determine (L4)$_2$Ni had formed in 80 % yield. Conclusion: This is consistent with full reduction of Ni(II) to Ni(0) with Zn. Excess ligand was used to prevent ligand sequestering by coordinatively unsaturated Zn salts.

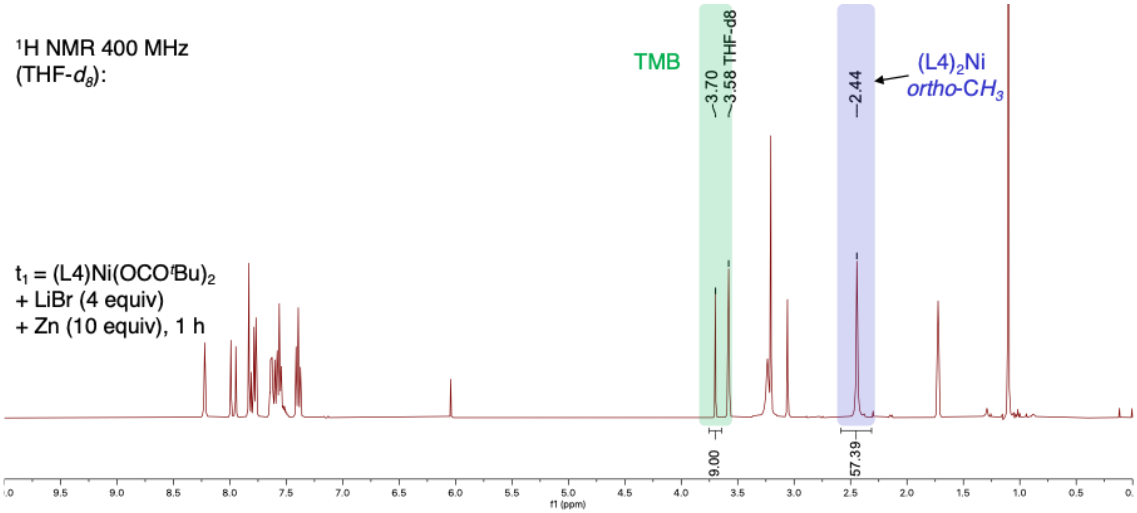

Figure S30. Quantitative ^{1}H NMR spectra of TMB and (L4)$_2$Ni after reacting (L4)Ni(OCO^{t}Bu)$_2$ with LiBr (4 equiv) and zinc (10 equiv). Internal standard trimethoxybenzene, TMB (green) and (L4)$_2$Ni (blue).

Reaction Between (L4)Ni(OCO^{t}Bu)$_2$, Zinc and ZnBr$_2$

Quantified by ^{1}H NMR. In the glovebox, (L4)Ni(OCO^{t}Bu)$_2$ (13 mg, 0.02 mmol), L4 (42 mg, 0.12 mmol, 5.9 equiv), ZnBr$_2$ (15 mg, 0.07 mmol, 3 equiv) and zinc (14 mg, 0.21 mmol, 10 equiv) were added to a 10 mL vial. A stir bar was added, and the vial was charged with 3 mL of THF and stirred at 900 rpm. After 3 hours, the solvent was removed and redissolved in 1.5 mL of C_6D_6 which was then filtered through a celite plug. To this solution, a stock solution of TMB in C_6D_6 was added and the integral ratio of TMB to (L4)$_2$Ni was measured by ^{1}H NMR to determine (L4)$_2$Ni had formed in a quantitative yield. Conclusion: This is consistent with ZnBr$_2$ undergoing anion exchange with Ni(II)-OCO^{t}Bu species which enables the full reduction of Ni(II) to Ni(0)

with Zn. Excess ligand was used to prevent ligand sequestering by coordinatively unsaturated Zn salts.

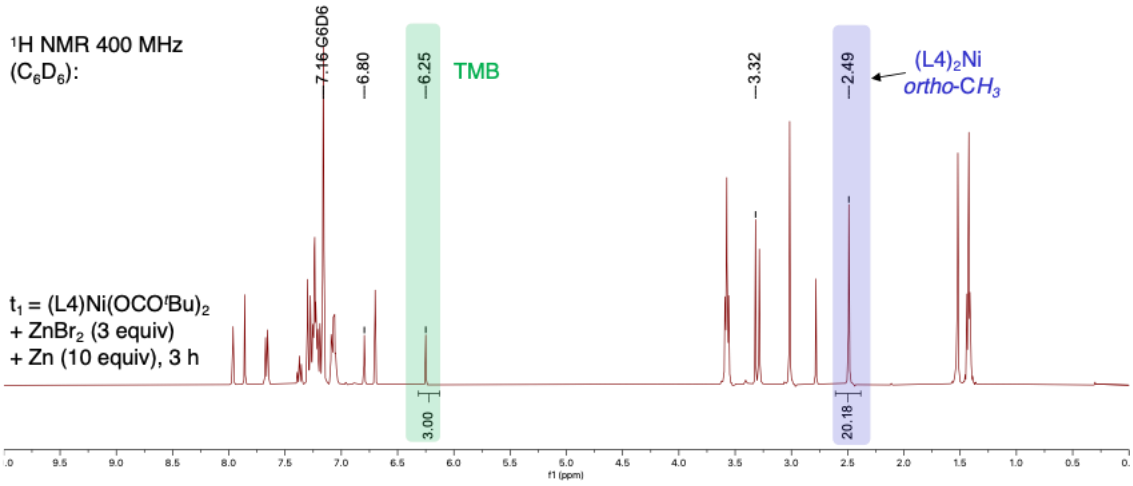

Figure S31. Quantitative ^{1}H NMR spectra of TMB and $(L4)_2Ni$ after reacting $(L4)Ni(OCO^tBu)_2$ with $ZnBr_2$ (3 equiv) and zinc (10 equiv). Internal standard trimethoxybenzene, TMB (green) and $(L4)_2Ni$ (blue).

Reaction Between $(L4)_2Ni$ and Zinc Chloride

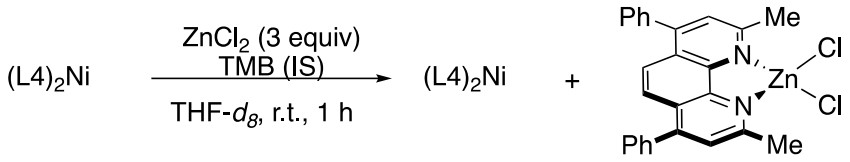

Monitored by quantitative ^{1}H NMR and paramagnetic ^{1}H NMR. In the glovebox, $(L4)_2Ni$ (11.2 mg, 0.01 mmol) and TMB (2 mg, internal standard) were added to a 4 mL vial with 1.5 mL of THF-d_8. The solution was transferred to a J-Young NMR tube and the initial integration of $(L4)_2Ni$ and TMB was recorded. The J-Young NMR tube was brought back into the glovebox and added to a vial containing $ZnCl_2$ (5.6 mg, 0.04 mmol) and stirred for 1 h before transferring back into the J-Young NMR tube and analyzed by ^{1}H NMR. After 1h, $(L4)_2Ni$ remained (46 %) along with formation of $(L4)ZnCl_2$ (39 %) with no paramagnetic species generated (Figure S32. t1. Conclusion: This is consistent with ligand sequestering of $ZnCl_2$ from $(L4)_2Ni$.

Independent synthesis of $(L4)ZnCl_2$. CSD0842 In the glovebox, $ZnCl_2$ (66 mg, 0.48 mmol), L4 (177 mg, 0.49 mmol, 1.02 eq) were added to a 10 mL vial with a stirbar. The vial was charged with THF (3 mL) to afford a yellow suspension that was stirred

overnight to afford a white suspension. After 16 h the suspension was filtered and washed with THF (1 mL) and pentane (3 ml x 2) and dried under vacuum to afford (L4)$ZnCl_2$ (88 mg, 37 % yield) as a white solid.

^{1}H NMR (400 MHz, THF-d_8) δ 7.99 (s, 2H), 7.93 (s, 2H), 7.74 – 7.45 (m, 11H), 3.17 (s, 6H).

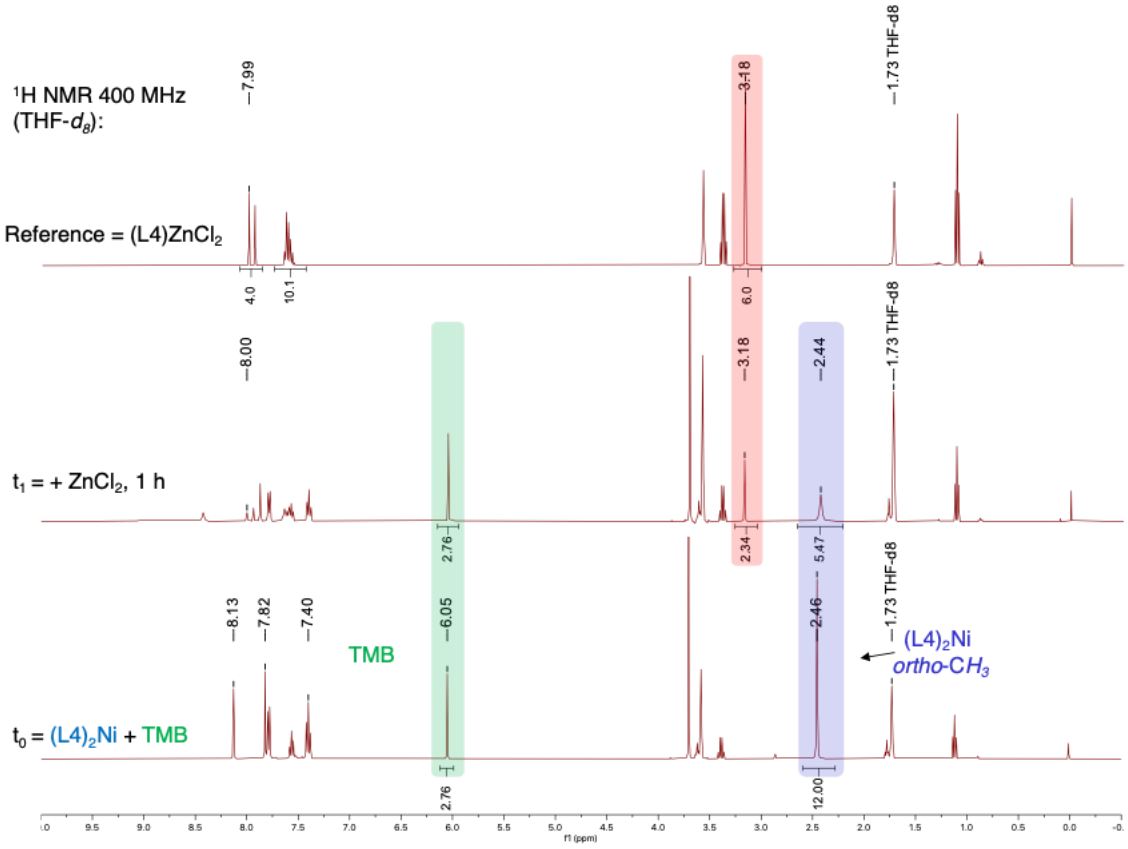

Figure S32. Quantitative ^{1}H NMR spectra of TMB and (L4)$_2$Ni indicating ligand sequestering by $ZnCl_2$ from (L4)$_2$Ni. Internal standard trimethoxybenzene, TMB (green) and (L4)$_2$Ni (blue), (L4)$ZnCl_2$.

Reaction Between (L4)$_2$Ni and Manganese Chloride

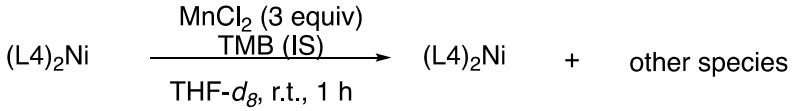

Monitored by quantitative ^{1}H NMR and paramagnetic ^{1}H NMR. In the glovebox, (L4)$_2$Ni (10.0 mg, 0.01 mmol) and TMB (2 mg, internal standard) were added to a 4

mL vial with 1.5 mL of THF-d_8. The solution was transferred to a J-Young NMR tube and the initial integration of $(L4)_2Ni$ and TMB was recorded. The J-Young NMR tube was brought back into the glovebox and added to a vial containing $MnCl_2$ (4.3 mg, 0.03 mmol) and stirred for 1 h before transferring back into the J-Young NMR tube and analyzed by ^1H NMR. After 1h, $(L4)_2Ni$ remained (71 %) with no paramagnetic species observable. Conclusion: This is consistent with ligand sequestering of $MnCl_2$ from $(L4)_2Ni$, in which the Mn complexes formed are either insoluble or have very broad paramagnetic ^1H NMR spectra. A very broad paramagnetic spectra would be consistent with low spin d^5 complex $(L4)MnCl_2$. The existence of these paramagnetic species is also consistent with extensive line broadening observed in the diamagnetic ^1H NMR spectra.

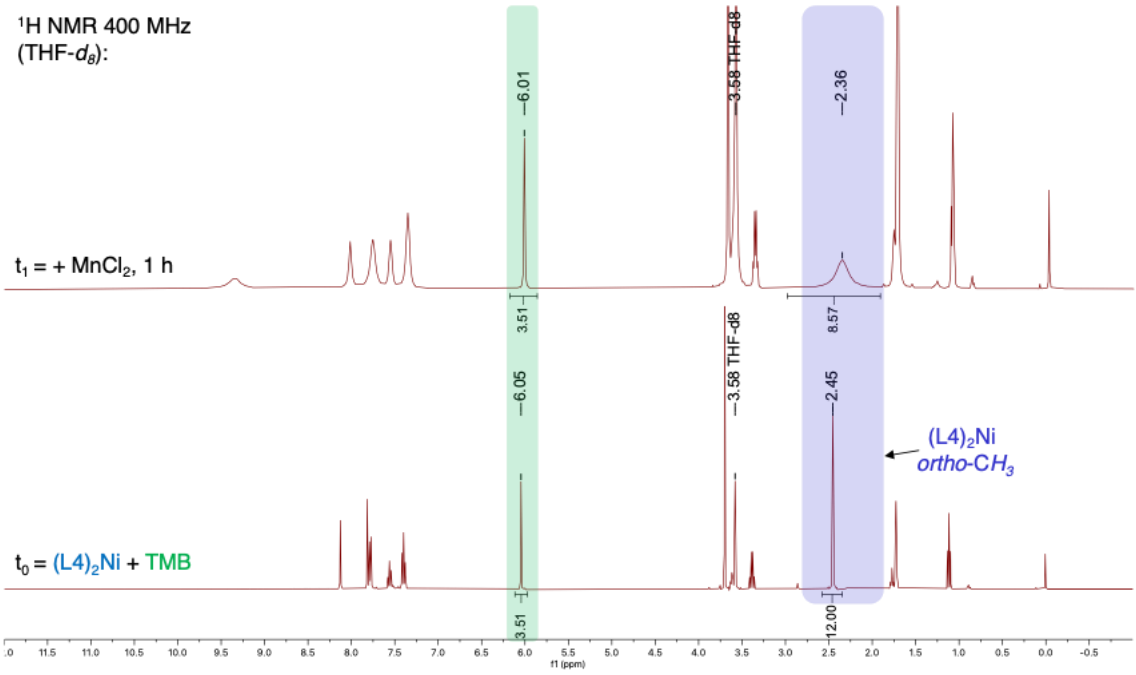

Figure S33. Quantitative ^1H NMR spectra of TMB and $(L4)_2Ni$ indicating ligand sequestering by $MnCl_2$ from $(L4)_2Ni$. Internal standard trimethoxybenzene, TMB (green) and $(L4)_2Ni$ (blue).

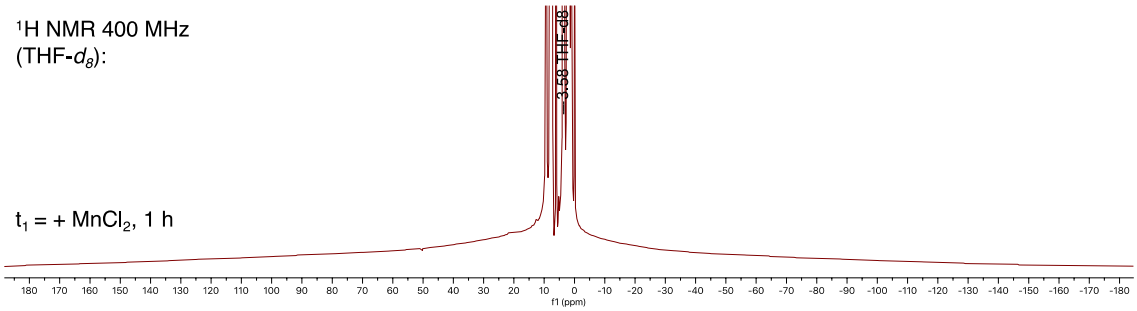

Figure S34. Paramagnetic ^1H NMR spectra indicating no oxidation of $(L4)_2Ni$ to $[(L4)_2Ni]Cl$.

4.6.4 Catalytic reactions

Representitive Procedure for Reductive Cross-Coupling of Alkyl Bromides and Aryl Bromide

In the glovebox NiI_2 (8 mg, 0.025 mmol, 10 mol%) and L4 (9 mg, 0.025 mmol, 10 mol%) or (L4)Ni(OCO^{t}Bu)$_2$ (16 mg, 0.025 mmol, 10 mol%) were added to a 10 mL vial. In addition, zinc dust (25 mg, 0.38 mmol, 1.5 equiv.), *n*-Bu_4NBr (81 mg, 0.25 mmol, 1.0 equiv.) and KOPiv (35 mg, 0.25 mmol, 1 equiv) when applicable, were added with DMA (1 mL). In a separate 4 mL vial a stock solution of decane (72 mg, 0.5 mmol) and (2-bromoethyl)benzene (93 mg, 0.5 mmol) was dissolved in 2 mL DMA from which 1 mL (0.25 mmol, 1 equiv.) was added to the reaction vial, additionally 50 µl aliquot of the stock solution was removed for GC-FID analysis to establish an initial ratio of starting material to internal standard. Finally, aryl bromide (39 mg, 0.6 mmol, 1.2 equiv.) was added to the reaction vial. The reaction was stirred at 900 rpm at room temperature for 5 h in the glovebox. At given time intervals reaction monitoring was carried out by quenching 50 µl aliquots with HCl, after dilution with EtOAc and filtration, samples were analyzed by GC-FID to determine conversion of starting material and yield of cross coupled product.

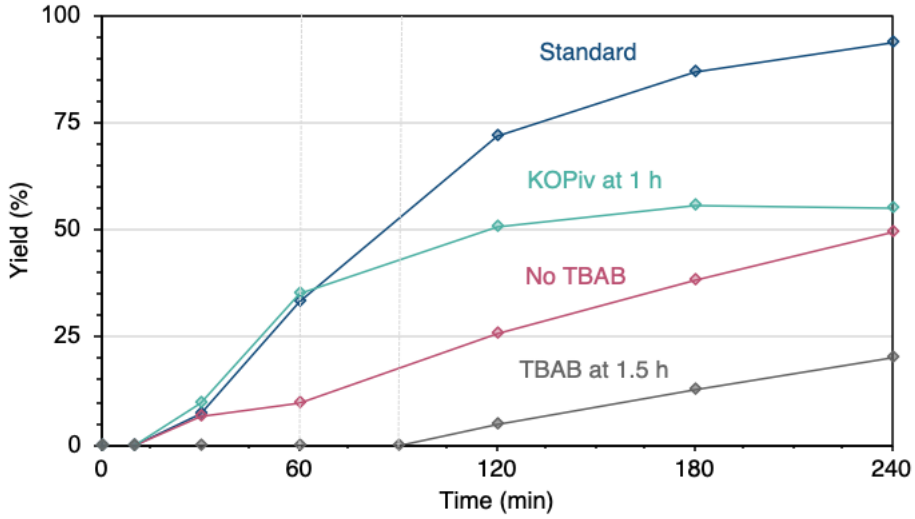

Figure S35. Monitoring the reductive cross-coupling of alkyl bromides and aryl bromides by GC-FID.

Catalytic Carboxylation of Allylic Alcohols with CO_2

In the glovebox to an oven-dried schlenk tube containing a stirring bar was added $NiBr_2DME$ (6 mg, 0.020 mmol, 10 mol%) and L4 (19 mg, 0.052 mmol, 26 mol%) or (L4)Ni(OCO^{t}Bu)$_2$ (12 mg, 0.020 mmol, 10 mol%) and L4 (12 mg, 0.032 mmol, 16 mol%). Additionally, Zn dust (14 mg, 0.240 mmol, 1.2 equiv.), $MgCl_2$ (19 mg, 0.200 mmol, 1 equiv.) and KOPiv (34 mg, 0.240 mmol, 1.2 equiv.) were added when applicable. The tube was taken out of the glovebox and connected to a Schlenk line where it was evacuated and back-filled under CO_2 flow 3 times. (E)-oct-2-en-1-ol (26 mg, 0.200 mmol, 1 equiv.), and DMF (2 mL) were added under CO_2 flow. Once added, the schlenk tube was closed under a flow of CO_2 (approx.. 1 bar overpressure) and stirred at 40 ºC for 16 h. The mixture was quenched with 2M HCl and diluted with EtOAc. An aliquot of the solution was analyzed by by ^{1}H-NMR spectroscopy using TMB as internal standard to determine the yield of the expected product.

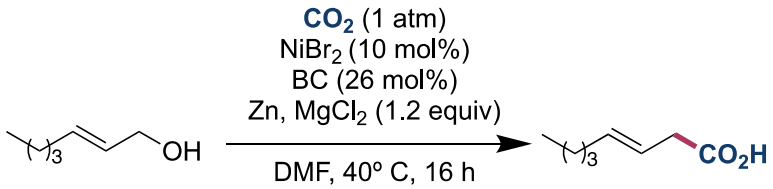

Entry	Deviation from standard conditions	Yield (%)[a]
1	None	64
2	No $MgCl_2$	15
3	0.4 equiv KOPiv, No $MgCl_2$	9
4	$Ni(OPiv)_2$ instead of $NiBr_2$, No $MgCl_2$	0
5	$Ni(OPiv)_2$ instead of $NiBr_2$	45
6	$Ni(COD)_2$ instead of $NiBr_2$, No $MgCl_2$	0
7	$Ni(COD)_2$ instead of $NiBr_2$	61

Figure S36. Various conditions of the reductive carboxylation of allylic alcohols with CO_2. [a] ^{1}H NMR yields using 1,3,5-trimethoxybenzene as internal standard

Migratory Hydrothiolation of Alkenes

In the glovebox NiI_2 (6 mg, 0.020 mmol, 10 mol%) and L4 (9 mg, 0.024 mmol, 12 mol%) or (L4)Ni(OCO^{t}Bu)$_2$ (12 mg, 0.020 mmol, 10 mol%) were added to a 10 mL vial. The solid was dissolved in THF (0.40 mL) and MeCN (0.20 mL). To this solution but-3-en-1-ylbenzene (53 mg, 0.40 mmol, 2.0 equiv.), benzyl mercaptan (25.0 mg, 0.20 mmol, 1.0 equiv.), HBpin (90 mg, 0.70 mmol, 3.5 equiv.) Li_3PO_4 (50 mg, 0.40 mmol, 2.0 equiv.) and KOPiv (11.2 mg, 0.080 mmol, 0.4 equiv.) when required, were added. The vial was stirred at 60 ºC for 24 h after which an aliquot of the solution solution was

analyzed by by ^{1}H-NMR spectroscopy using TMB as internal standard to determine the yield of the expected product.

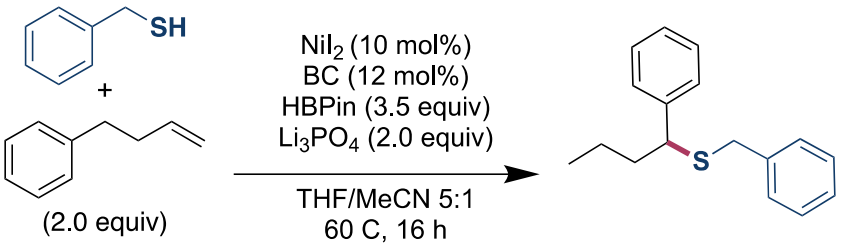

Entry	Deviation from standard conditions	Yield (%)[a]
1	None	76
2	0.4 equiv KOPiv	8
3	$Ni(OPiv)_2$ instead of $NiBr_2$	2
4	$Ni(OPiv)_2$ instead of $NiBr_2$ + 0.4 equiv LiI	34

Figure S37. Various conditions of the migratory hydrothiolation of alkenes. [a] ^{1}H NMR yields using 1,3,5-trimethoxybenzene as internal standard

4.6.5 IR, UV-VIS, and Cyclic Voltammetry

Infrared Spectroscopy

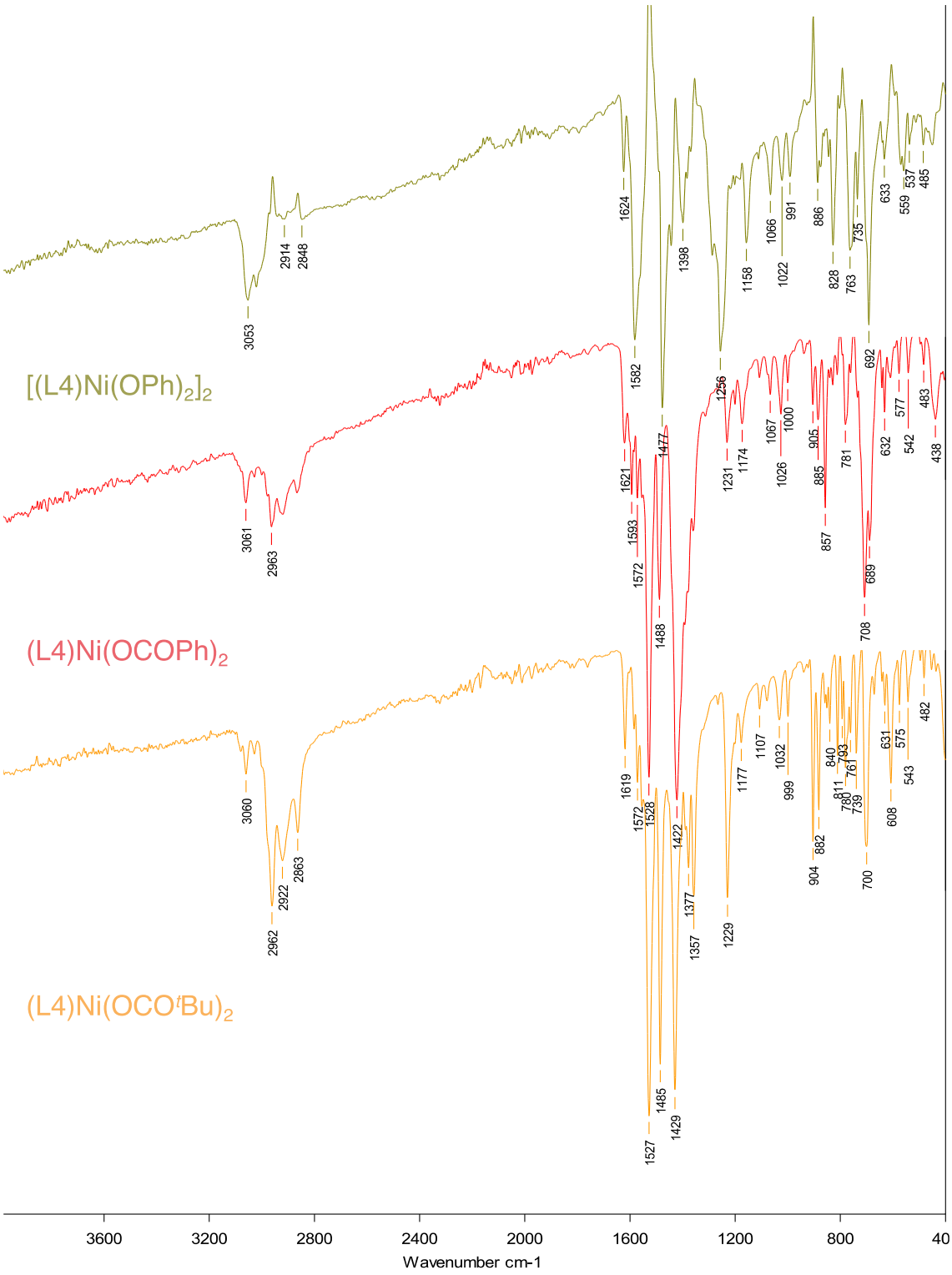

Figure S38. Stack IR spectra of $[(L4)Ni(OPh)_2]_2$, $(L4)Ni(OCOPh)_2$, and $(L4)Ni(OCO^tBu)_2$.

UV-VIS Spectroscopy

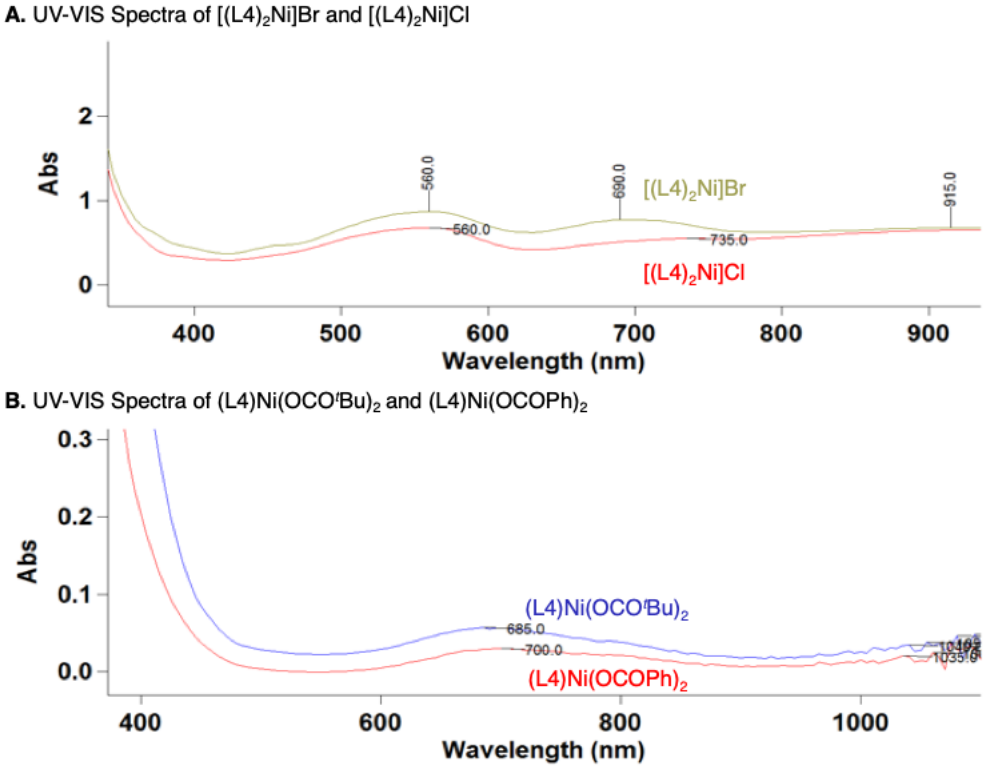

Figure S39. UV-VIS spectra of $[(L4)_2Ni]Br$, $[(L4)_2Ni]Cl$, $(L4)Ni(OCO^tBu)_2$ and $(L4)Ni(OCOPh)_2$.

Cyclic Voltammetry

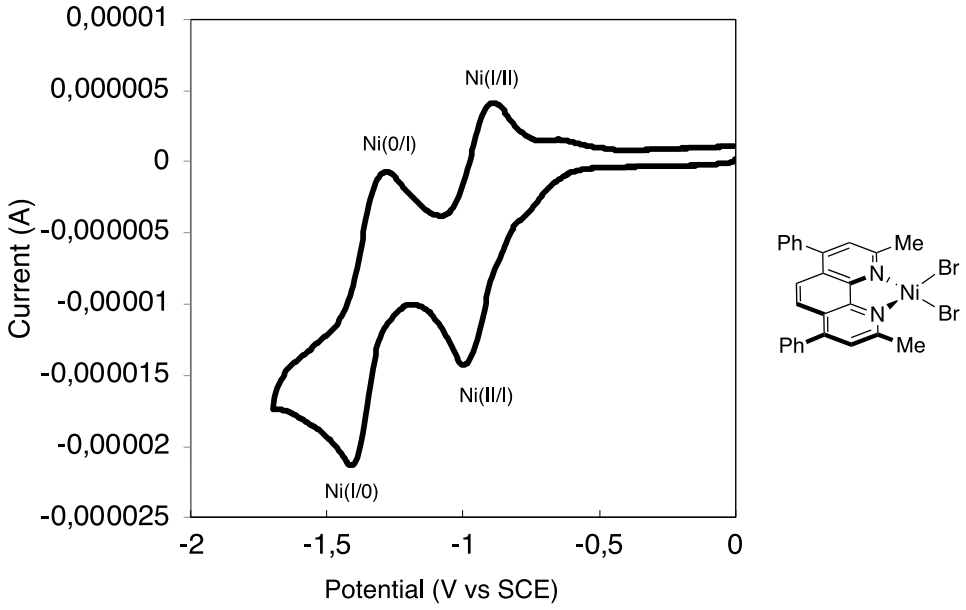

Figure S40. Cyclic voltammogram of (L4)$NiBr_2$. Voltammograms were taken using a glassy carbon working electrode in a 0.1 M [$^nBu_4N$][PF_6] supporting electrolyte MeCN solution with a 100 mV/s scan rate and 0.01 M of sample referenced to Fc (+380 vs SCE). Scans were started at the open-circuit potential and scanned in the anode direction first; the second cycle is shown here. $E_{1/2}$ values for (L4)$NiBr_2$ are Ni(II)/Ni(I) = -0.71 V, Ni(I)/Ni(0) = -1.10 V. **Literature reports** CV of 2,9-substituted phen ligated Ni complexes are reported with $E_{p/2}$ values of Ni(II)/Ni(I) = -0.69 V, Ni(I)/Ni(0) = -1.37 V vs SHE in THF.[4]

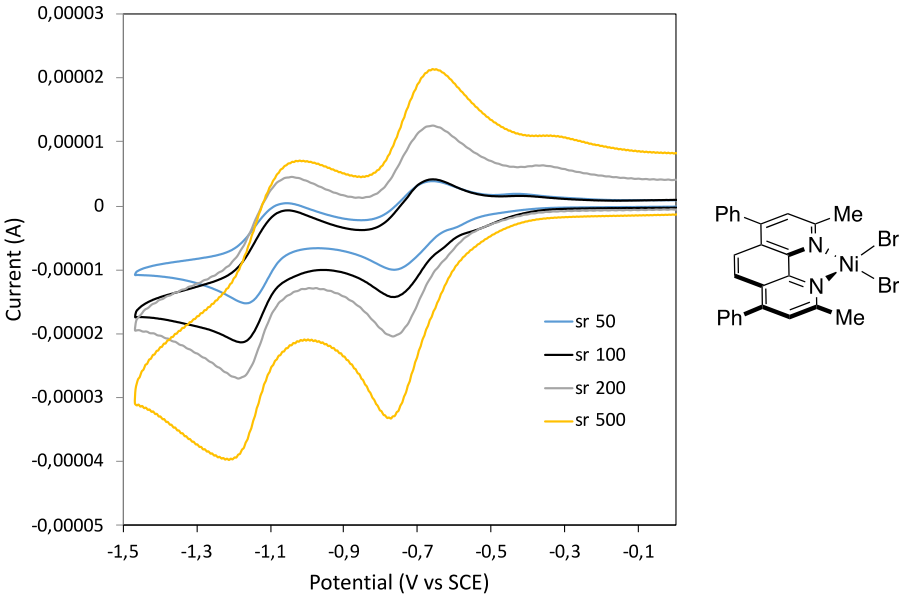

Figure S41. Cyclic voltammogram of (L4)$NiBr_2$. Voltammograms were taken using a glassy carbon working electrode in a 0.1 M [$^nBu_4N$][PF_6] supporting electrolyte MeCN solution with a varied scan rates and 0.01 M of sample referenced to Fc (+380 vs SCE).

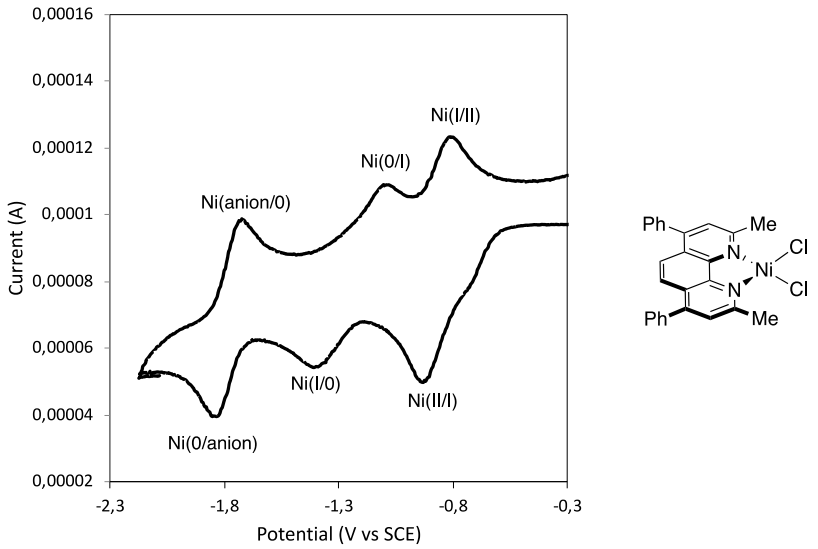

Figure S42. Cyclic voltammogram of (L4)$NiCl_2$. Voltammograms were taken using a glassy carbon working electrode in a 0.1 M [$^nBu_4N$][PF_6] supporting electrolyte MeCN solution with a 100 mV/s scan rate and 0.01 M of sample referenced to Fc (+380 vs SCE). Scans were started at the open-circuit potential and scanned in the anode direction first; the second cycle is shown here. $E_{1/2}$ values for (L4)$NiCl_2$ are Ni(II)/Ni(I) = -0.86 V, Ni(I)/Ni(0) = -1.24 V. While the first reduction $E_{1/2}$ ($Ni^{II/I}$) appears reversible, the second reduction $E_{1/2}$ ($Ni^{I/0}$) appears quasireversible. Reduction of the ligand or to an anionic complex is observed in further reduction.

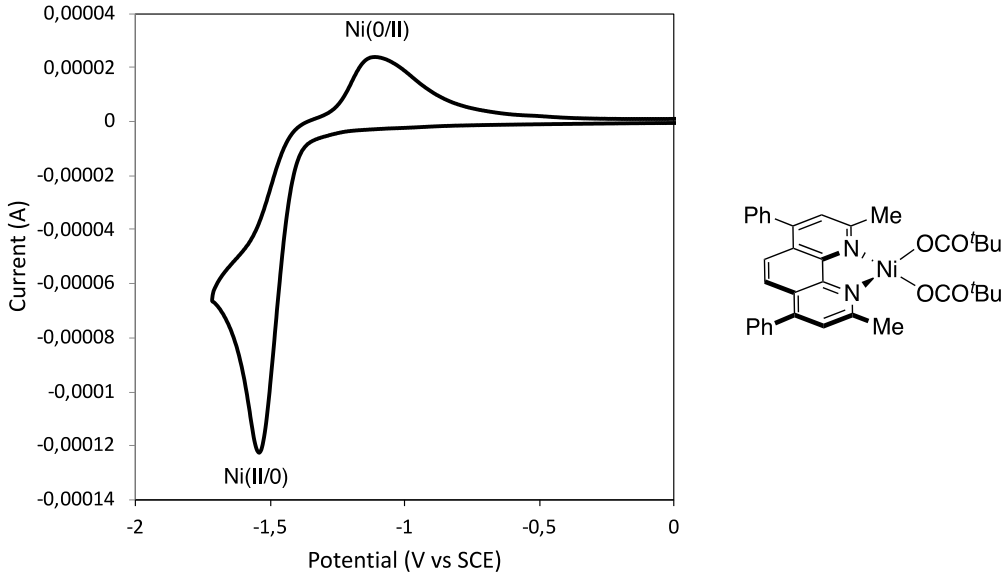

Figure S43. Cyclic voltammogram of (L4)Ni(OCO^tBu)$_2$. Voltammograms were taken using a glassy carbon working electrode in a 0.1 M [$^nBu_4N$][PF_6] supporting electrolyte MeCN solution with a 100 mV/s scan rate and 0.01 M of sample referenced to Fc (+380 vs SCE). Scans were started at the open-circuit potential and scanned in the anode direction first; the second cycle is shown here. E_p values for (L4)Ni(OCO^tBu)$_2$ are Ni(II)/Ni(0) = -1.55 V. The reduction appears chemically reversible (E_p oxidation = -1.27 V vs SCE) and electrochemically irreversible.

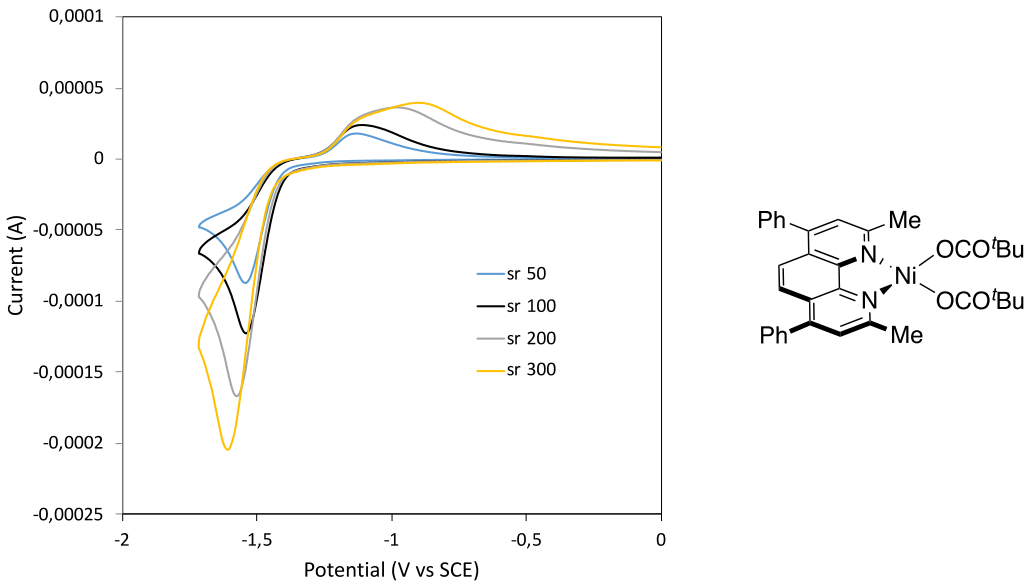

Figure S44. Cyclic voltammogram of (L4)Ni(OCO^{t}Bu)$_2$. Voltammograms were taken using a glassy carbon working electrode in a 0.1 M [^{n}Bu$_4$N][PF$_6$] supporting electrolyte MeCN solution with various scan rates and 0.01 M of sample referenced to Fc (+380 vs SCE).

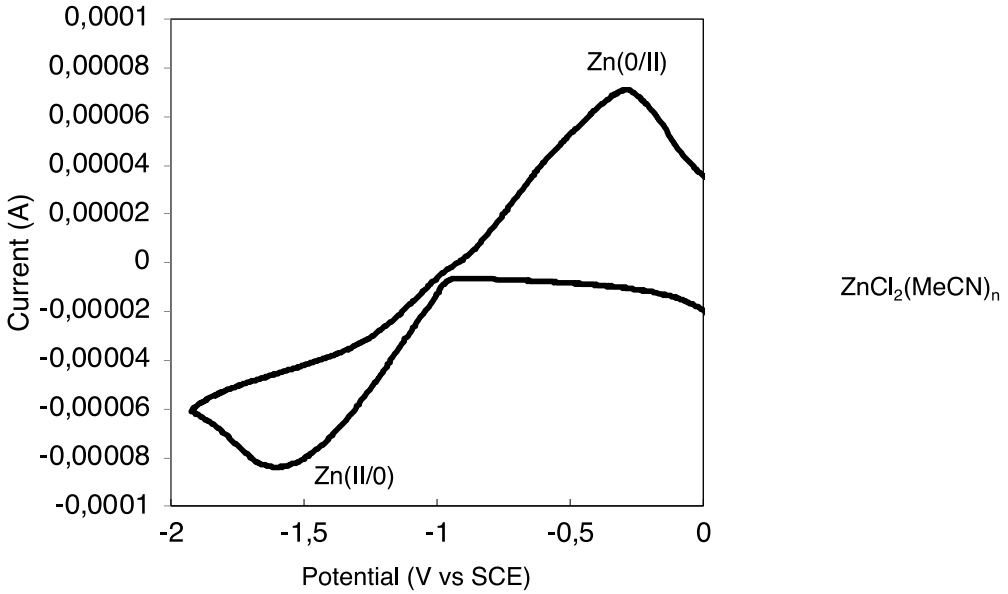

Figure S45. Cyclic voltammogram of $ZnCl_2$. Voltammograms were taken using a glassy carbon working electrode in a 0.1 M [^{n}Bu$_4$N][PF$_6$] supporting electrolyte MeCN solution with a 100 mV/s scan rate and 0.01 M of sample referenced to Fc (+380 vs SCE). Scans were started at the open-circuit potential and scanned in the anode direction first. E_p values for $ZnCl_2$ are Zn(II)/Zn(0) = -1.57 V. The reduction appears chemically reversible (E_p oxidation = -0.26 V vs SCE), and electrochemically irreversible. **Literature reports** CV of $ZnBr_2$ are reported with $E_{p/2}$ values of Zn(II)/Zn(0) = -1.26 V vs SHE, in DMA.[4]

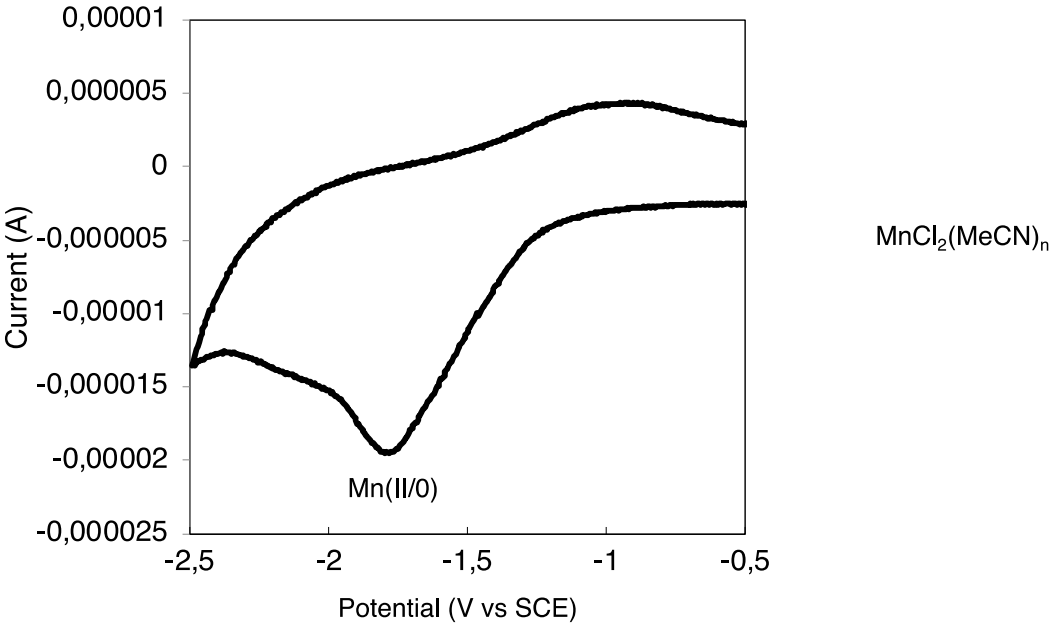

Figure S46. Cyclic voltammogram of $MnCl_2$. Voltammograms were taken using a glassy carbon working electrode in a 0.1 M [^{n}Bu$_4$N][PF_6] supporting electrolyte MeCN solution with a 100 mV/s scan rate and 0.01 M of sample referenced to Fc (+380 vs SCE). Scans were started at the open-circuit potential and scanned in the anode direction first. E_p values for $ZnCl_2$ are Zn(II)/Zn(0) = -1.77 V. Unlike the case of $ZnCl_2$, $MnCl_2$ reduction appears chemically irreversible and electrochemically irreversible.

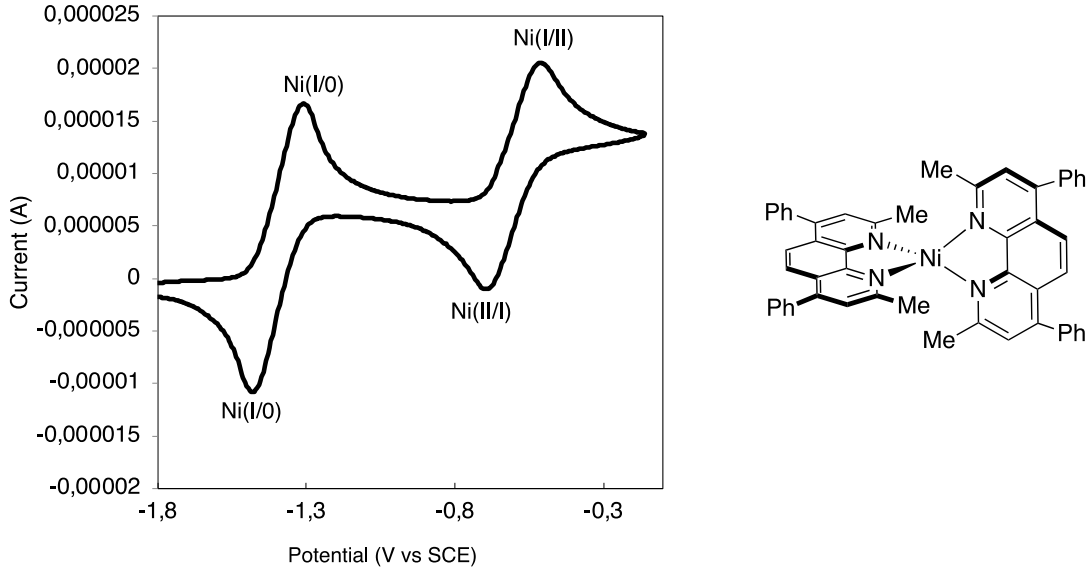

Figure S47. Cyclic voltammogram of $(L4)_2Ni$. Voltammograms were taken using a glassy carbon working electrode in a 0.1 M [^{n}Bu$_4$N][PF_6] supporting electrolyte THF solution with a 100 mV/s scan rate and 0.01 M of sample referenced to Fc (+380 vs SCE). Scans were started at the open-circuit potential and scanned in the anode direction first; the second cycle is shown here. $E_{1/2}$ values for $(L4)_2Ni$ are Ni(II)/Ni(I) = -0.59 V, Ni(I)/Ni(0) = -1.39 V. **Note:** This complex studied is poorly soluble in MeCN so CVs were performed in THF.

4.6.6 NMR and EPR Spectra of Synthesized Complexes

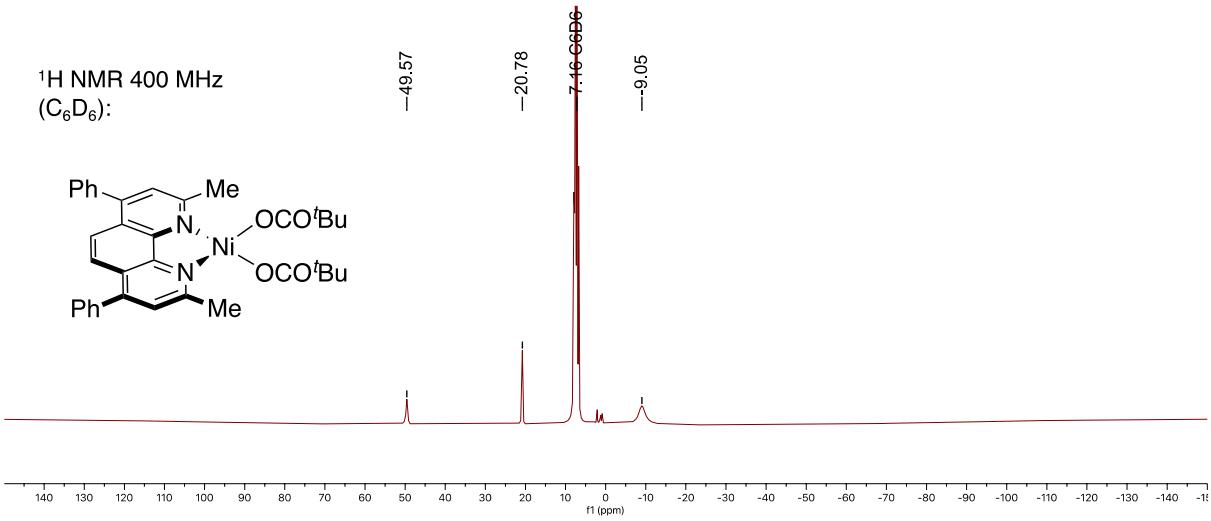

Figure S48. NMR spectra (C_6D_6, 400 MHz) of (L4)Ni(OCO^{t}Bu)$_2$.

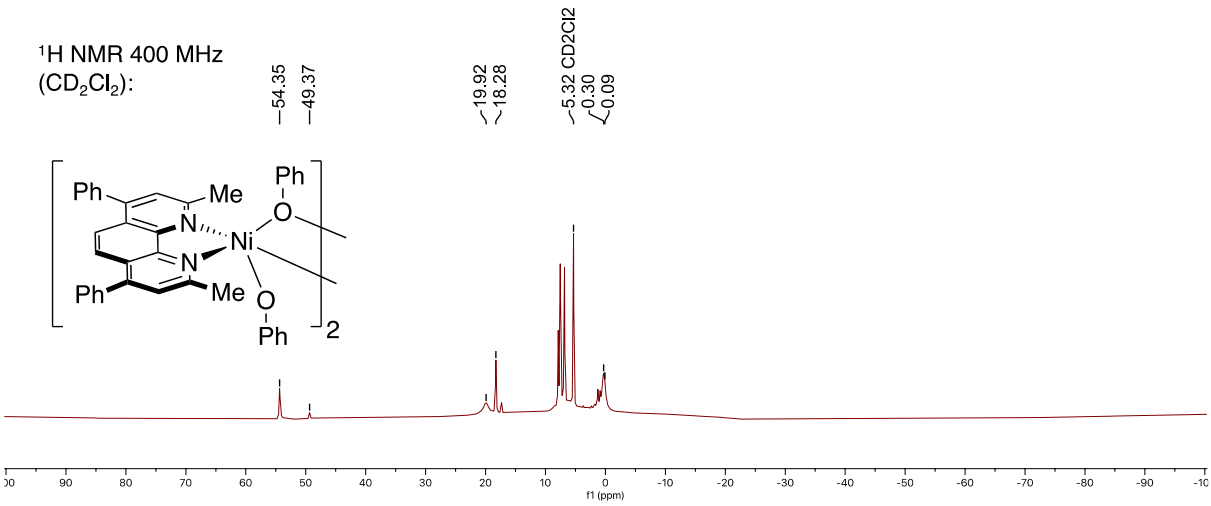

Figure S49. NMR spectra (CD_2Cl_2, 400 MHz) of [(L4)Ni(OPh)$_2$]$_2$.

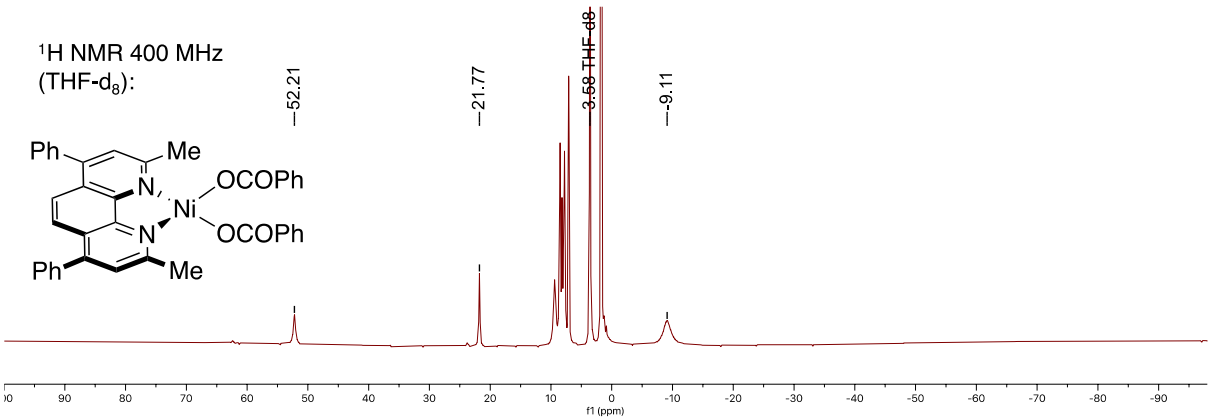

Figure S50. NMR spectra (THF-d_8, 400 MHz) of (L4)Ni(OCOPh)$_2$.

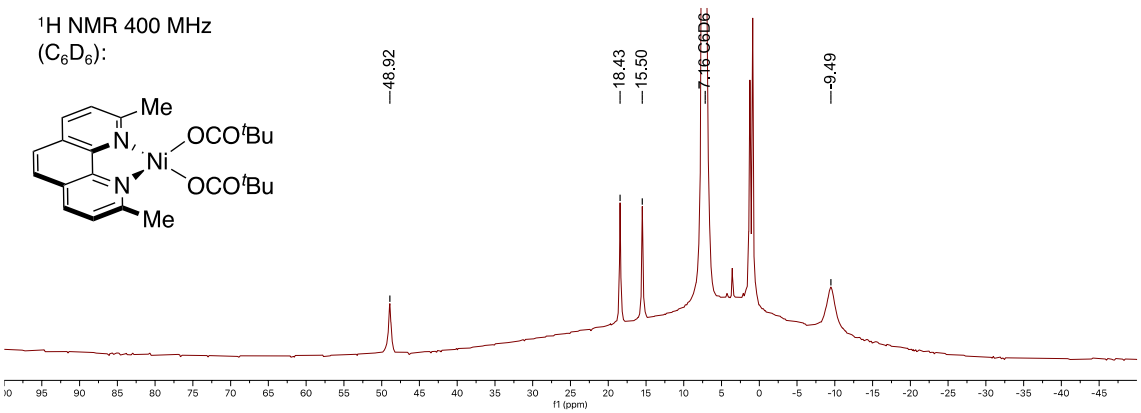

Figure S51. NMR spectra (C_6D_6, 400 MHz) of (L3)Ni(OCO^{t}Bu)$_2$

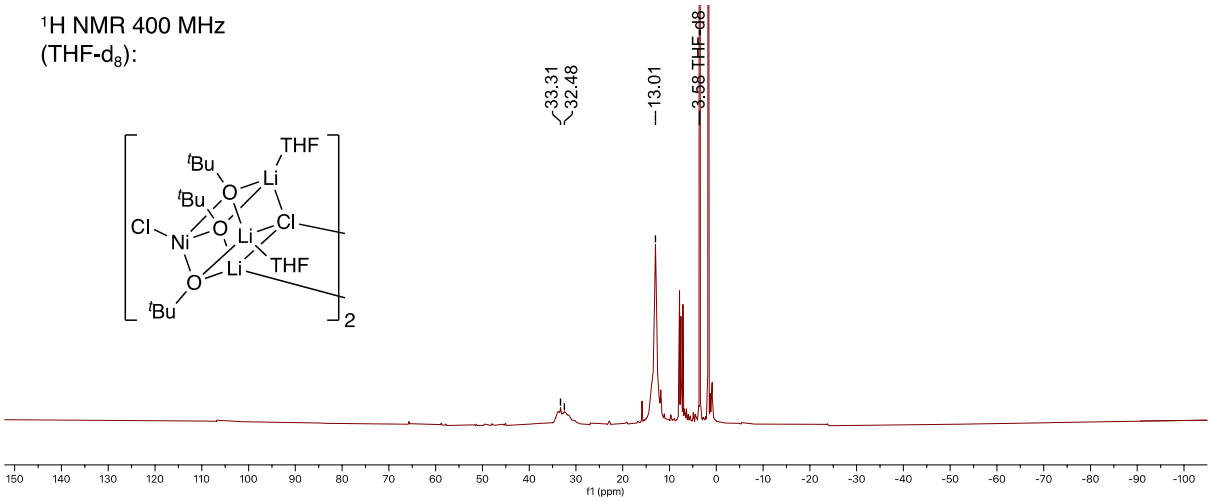

Figure S52. NMR spectra (THF-d_8, 400 MHz) of $NiLi_3Cl_2(O^tBu)_3$•2THF.

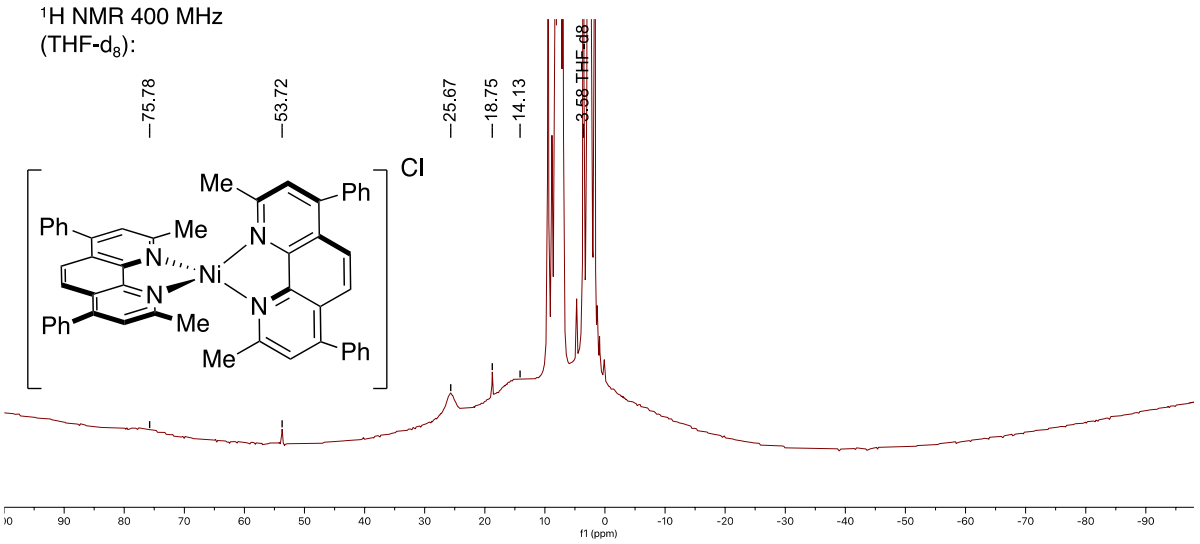

Figure S53. NMR spectra (THF-d_8, 400 MHz) of [(L4)$_2$Ni]Cl.

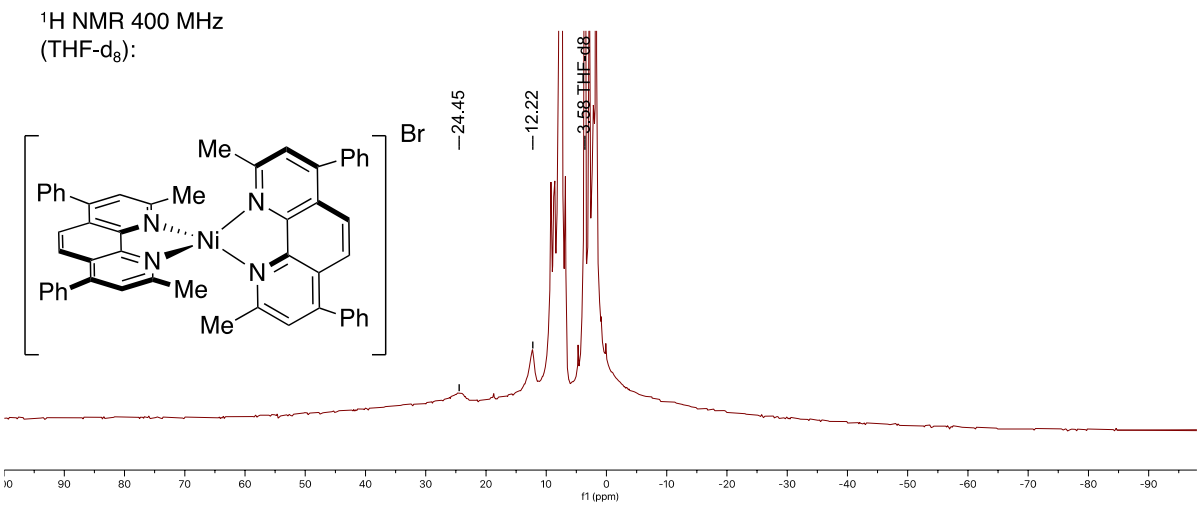

Figure S54. NMR spectra (THF-d_8, 400 MHz) of $[(L4)_2Ni]Br$.

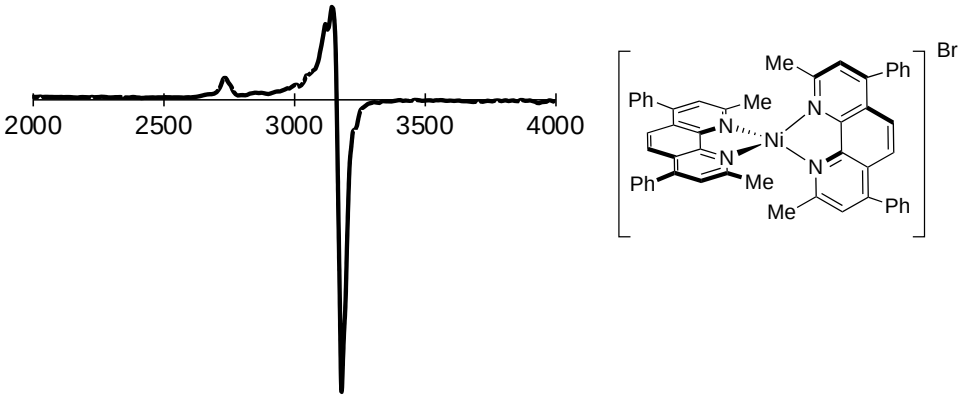

Figure S55. Continuous wave (CW) X-Band EPR spectra of $[(L4)_2Ni]Br$ with g values fit to g(x) = 2.115, g(y) = 2.114, g(z) = 2.456.

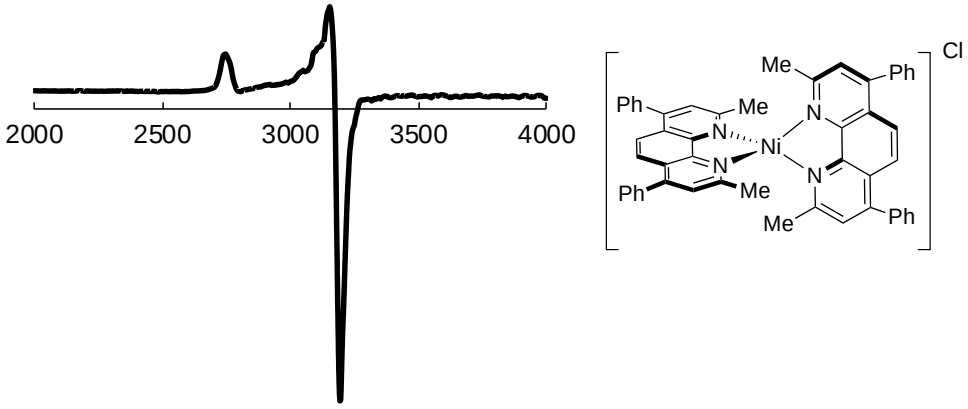

Figure S56. Continuous wave (CW) X-Band EPR spectra of $[(L4)_2Ni]Cl$ with g values fit to g(x) = 2.109, g(y) = 2.106, g(z) = 2.445.

4.6.7 Crystallographic Data

Data collection: The measured crystals were prepared under inert conditions immersed in perfluoropolyether as protecting oil for manipulation.

Crystal structure determination was carried out using a Rigaku diffractometer equipped with a Pilatus 200K area detector, a Rigaku MicroMax-007HF microfocus rotating anode with MoK_α radiation, Confocal Max Flux optics and an Oxford Cryosystems low temperature device Cryostream 700 plus (T = -173 °C). Full-sphere data collection was used with ω and φ scans. *Programs used:* Data collection data reduction with CrysAlisPro and absorption correction with Scale3 Abspack scaling algorithm.

Structure Solution and Refinement: Crystal structure solution was achieved using the computer program SHELXT. Visualization was performed with the program SHELXle. Missing atoms were subsequently located from difference Fourier synthesis and added to the atom list. Least-squares refinement on F^2 using all measured intensities was carried out using the program SHELXL 2015. All non-hydrogen atoms were refined including anisotropic displacement parameters.

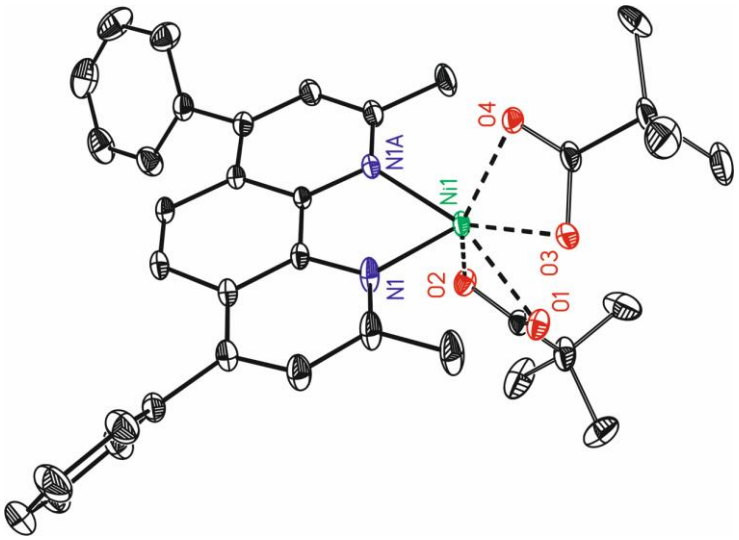

Figure S57. ORTEP drawing (50 %) showing (L4)Ni(OCO^tBu)$_2$. Hydrogen atoms and disordered parts have been omitted in the sake of clarity.

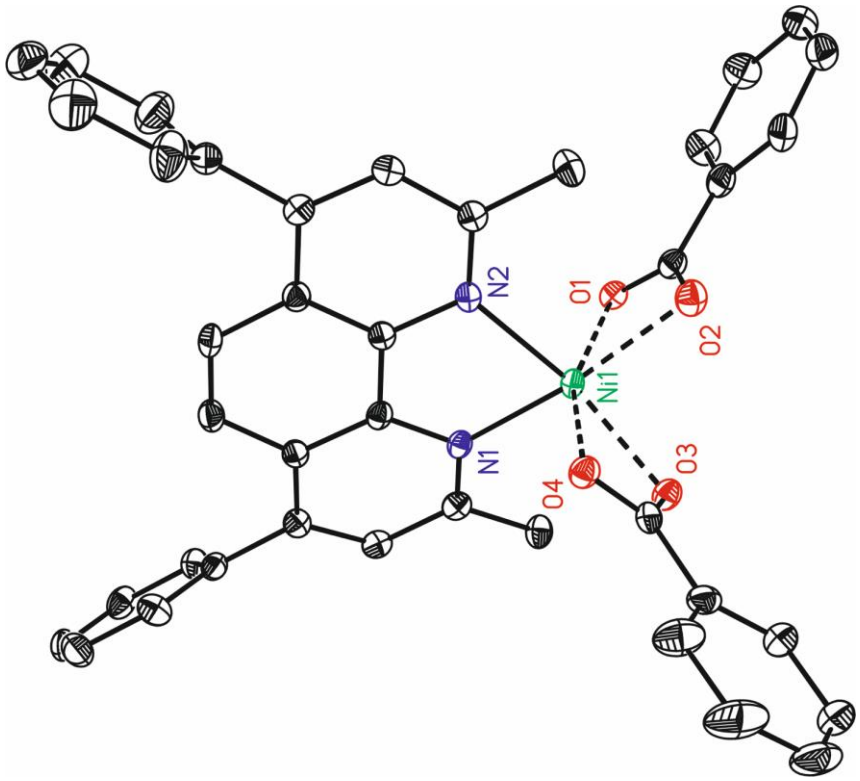

Figure S58. ORTEP drawing (50 %) showing (L4)Ni($OCOPh$)$_2$. Hydrogen atoms and disordered parts have been omitted in the sake of clarity.

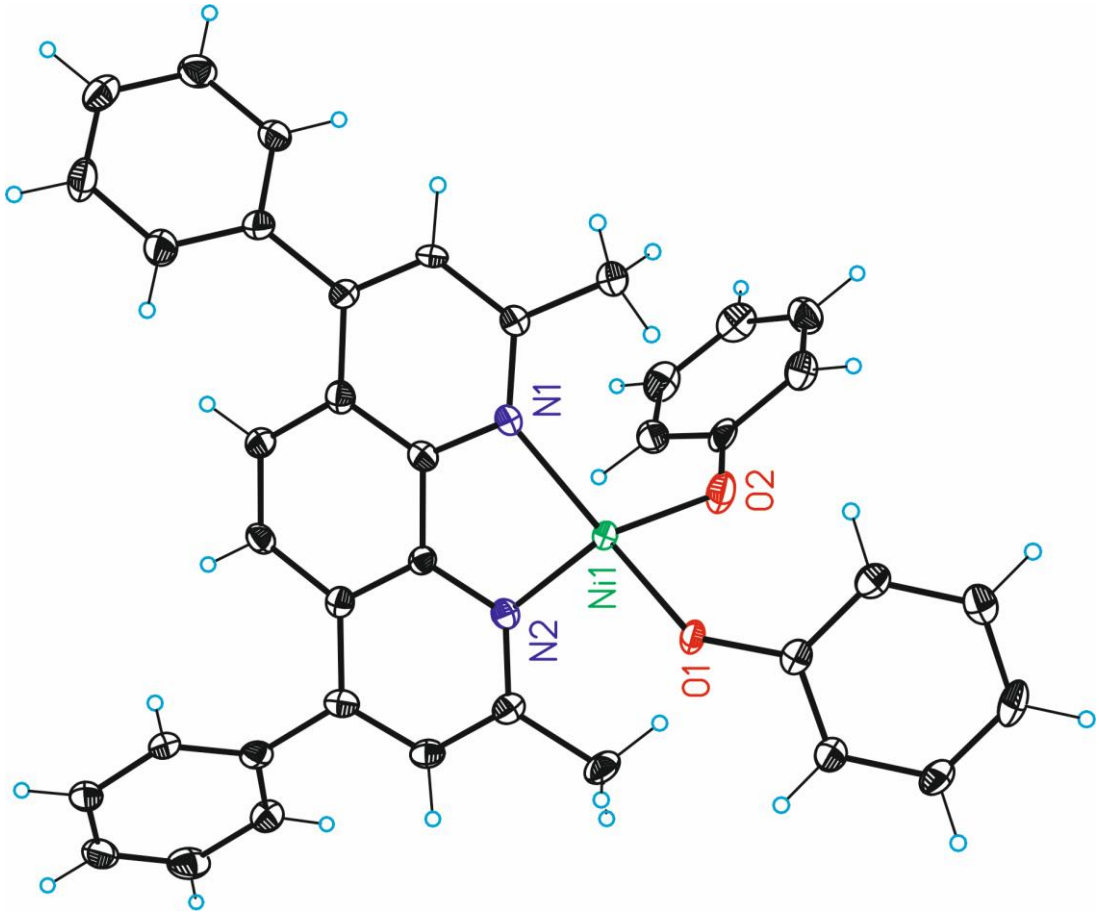

Figure S59. ORTEP drawing (50 %) showing (L4)Ni(OPh)$_2$ with half the symmetric half omitted for clarity. Hydrogen atoms and disordered parts have been omitted in the sake of clarity.

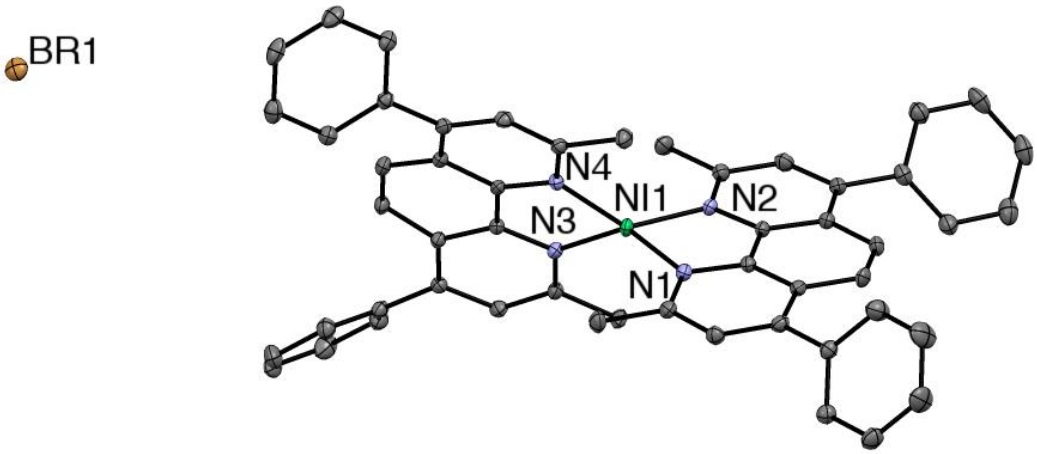

Figure S60. ORTEP drawing (50 %) showing [(L4)$_2$Ni]Br. Hydrogen atoms and disordered parts have been omitted in the sake of clarity.

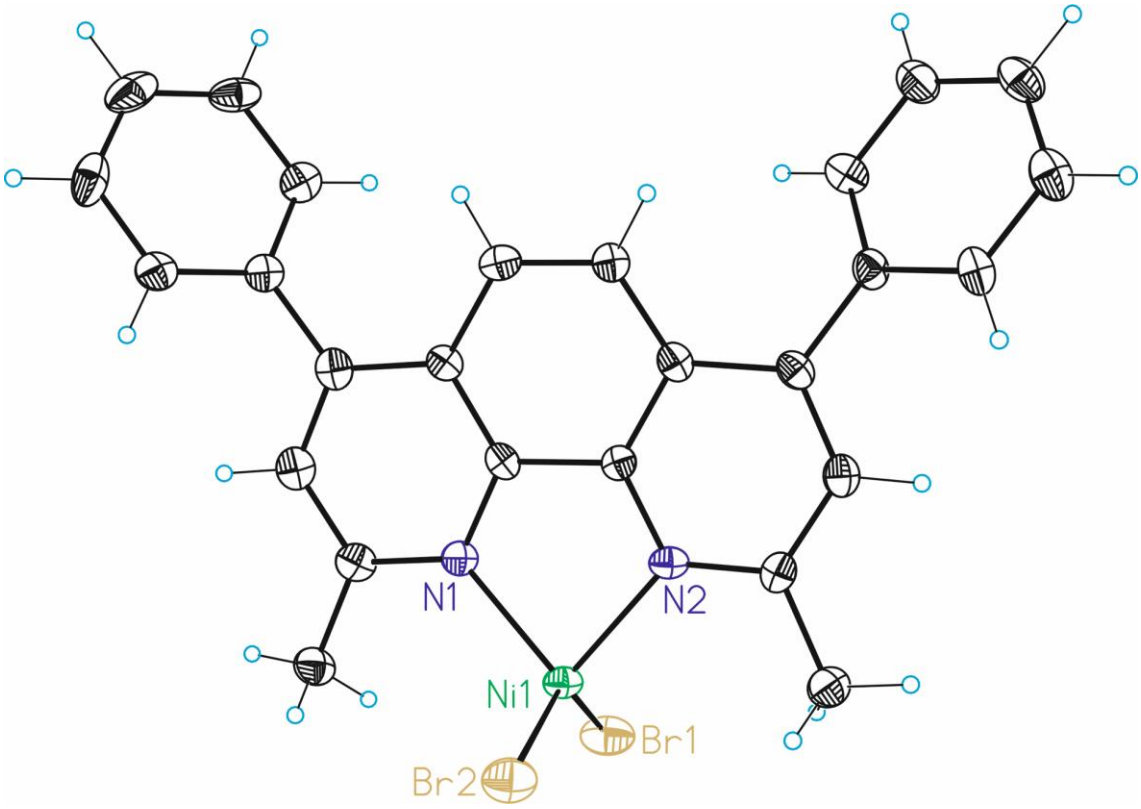

Figure S61. ORTEP drawing (50 %) showing (L4)$NiBr_2$. Hydrogen atoms and disordered parts have been omitted in the sake of clarity.

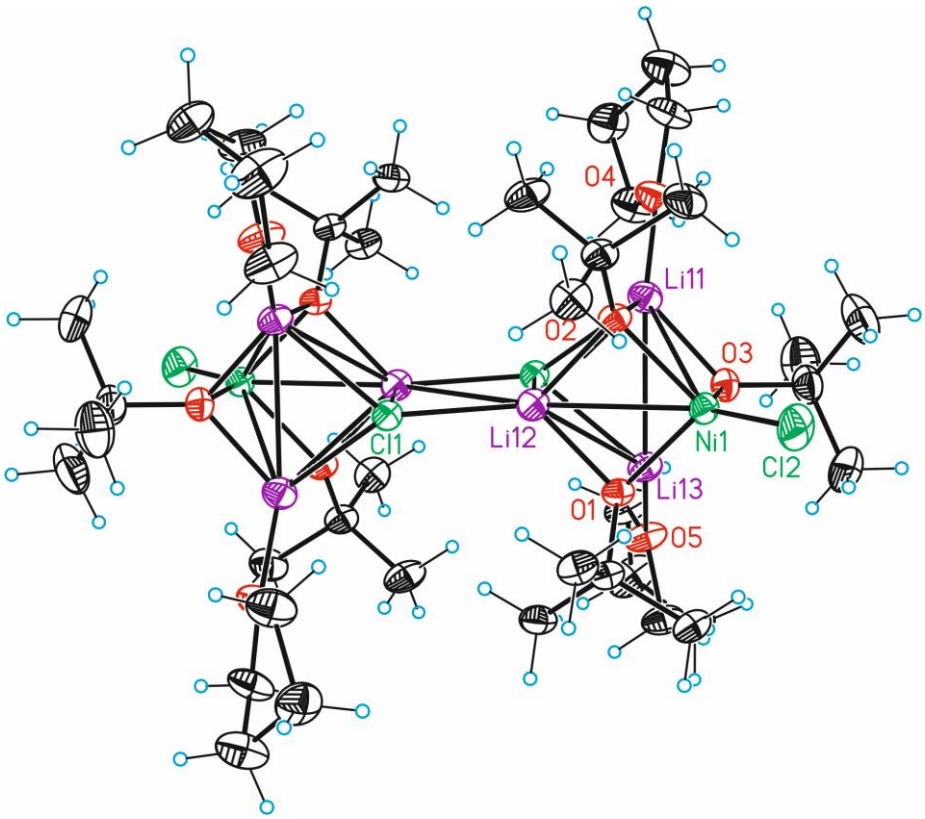

Figure S62. ORTEP drawing (50 %) showing $NiLi_3Cl_2(O^tBu)_3$•2THF. Hydrogen atoms and disordered parts have been omitted in the sake of clarity.

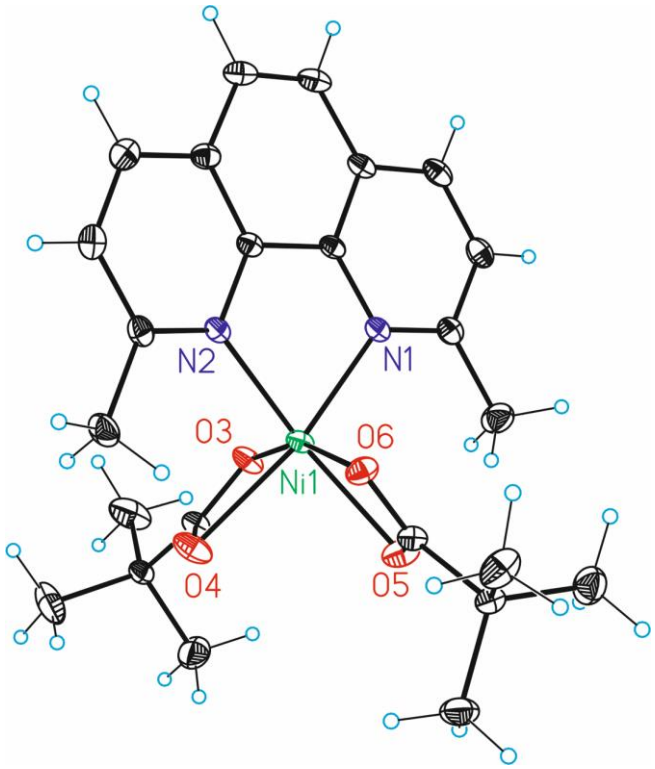

Figure S62. ORTEP drawing (50 %) showing (L3)Ni(OCO^{t}Bu)$_2$. Hydrogen atoms and disordered parts have been omitted in the sake of clarity.

Table S1. Crystallographic Data

	(L4)Ni(OCO^{t}Bu)$_2$	(L4)Ni(OCOPh)$_2$	(L4)Ni(OPh)$_2$
Formula	$C_{10.29}H_{10.86}N_{0.57}Ni_{0.29}O_{1.14}$	$C_{42}H_{34}N_2NiO_{4.50}$	$C_{21}H_{19}NNi_{0.50}O_{1.50}$
Formula weight	177.54	697.42	338.73
T (K)	100(2)	100(2)	100(2)
Wavelength (Å)	0.71073	0.71073	0.71073
Crystal system	Orthorhombic	Monoclinic	Triclinic
Space group	*P*nma	*C*2/c	*P*-1
***a* (Å)**	8.6390(3)	44.5471(15)	9.4680(15)
***b* (Å)**	17.4573(10)	11.9193(5)	12.252(2)
***c* (Å)**	20.8047(5)	12.5427(4)	14.803(3)
□□(deg)	90	90	100.401(5)
□□(deg)	90	96.780(3)	97.331(5)
□□(deg)	90	90	96.907(5)
V (Å^3)	3137.6(2)	6613.2(4)	1657.0(5)
Z	14	8	4
Density (calc.) (Mg/m^3)	1.315	1.401	1.358
μ (mm^{-1})	0.660	0.636	0.629
F(000)	1312	2912	712
Crystal size (mm^3)	0.040 x 0.040 x 0.020	0.090 x 0.060 x 0.010	0.050 x 0.030 x 0.010
Theta range for data collection (deg)	2.553 to 37.284	2.446 to 28.951	1.708 to 27.896
Index ranges	-13<=h<=14, -22<=k<=15, -35<=l<=19	-47<=h<=59, -12<=k<=16, -15<=l<=14	-11<=h<=12, -16<=k<=16, -19<=l<=19
Reflections collected	22056	28776	16033
Independent reflections	7206 [R(int) = 0.0375]	7433[R(int) = 0.0357]	7626[R(int) = 0.0715]
Completeness to theta	86.3% 37.284°	85.0% 28.951 °	96.2 % 27.896 °
Absorption correction	Multi-scan	Multi-scan	Multi-scan
Max. and min. transmission	1.00 and 0.85	1.00 and 0.46	0.74 and 0.65
Refinement method	Full-matrix least-squares on F^2	Full-matrix least-squares on F^2	Full-matrix least-squares on F^2
Data / restraints / parameters	7206/ 0/ 257	7433/ 194/ 494	7626/ 220/ 481
Goodness-of-fit on F^2	1.017	1.026	1.031
Final R indices [I>2sigma(I)]	R1 = 0.0397, wR2 = 0.0901	R1 = 0.0450, wR2 = 0.1049	R1 = 0.0666, wR2 = 0.1330
R indices (all data)	R1 = 0.0698, wR2 = 0.0993	R1 = 0.0762, wR2 = 0.1162	R1 = 0.1242, wR2 = 0.1557
Largest diff. peak and hole	0.475 and -0.468 e.Å^{-3}	1.038 and -0.659 e.Å^{-3}	0.703 and -0.692 e.Å^{-3}

Table S2. Crystallographic Data

	$[(L4)_2Ni]Br$	$(L4)NiBr_2$	$NiLi_3Cl_2(O^tBu)_3$ •2THF
Formula	$C_{58}H_{49}BrN_7Ni$	$C_{52}H_{40}Br_4N_4Ni_2$	$C_{20}H_{43}C_{l2}Li_3NiO_5$
Formula weight	982.66	1157.94	513.97
T (K)	100(2)	100(2)	100(2)
Wavelength (Å)	0.71073	0.71073	0.71073
Crystal system	Monoclinic	Monoclinic	Triclinic
Space group	*C*2/c	*P*21/c	*P*-1
***a* (Å)**	32.275(3)	12.861(5)	9.9981(3)
***b* (Å)**	11.1373(11)	22.587(8)	11.4148(4)
***c* (Å)**	27.385(3)	7.834(3)	13.5283(3)
α (deg)	90	90	103.805(2)
β (deg)	101.187(2)	98.804(11)	103.504(2)
γ (deg)	90	90	102.091(2)
V (Å^3)	9656.8(16)	2249.0(14)	1399.21(7)
Z	8	2	2
Density (calc.) (Mg/m^3)	1.352	1.710	1.220
μ (mm^{-1})	1.276	4.432	0.908
F(000)	4072	1152	548
Crystal size (mm^3)	0.500 x 0.030 x 0.020	0.200 x 0.100 x 0.010	0.080 x 0.060 x 0.050
Theta range for data collection (deg)	1.516 to 31.357	1.602 to 29.346	2.299 to 31.958
Index ranges	-42<=h<=43, -16<=k<=16, -39<=l<=40	-17<=h<=14, -28<=k<=31, -10<=l<=9	-14<=h<=14, -16<=k<=16, -20<=l<=19
Reflections collected	38133	23083	22057
Independent reflections	15247 [R(int) = 0.0431]	5709 [R(int) = 0.0814]	9056 [R(int) = 0.0452]
Completeness to theta	96.1% 31.357°	92.4 % 29.346 °	93.7 % 31.958 °
Absorption correction	Multi-scan	Multi-scan	Multi-scan
Max. and min. transmission	0.74 and 0.66	0.74 and 0.52	1.00 and 0.44
Refinement method	Full-matrix least-squares on F^2	Full-matrix least-squares on F^2	Full-matrix least-squares on F^2
Data / restraints / parameters	15247/ 0/ 611	5709/ 0/ 282	9056/ 480/ 381
Goodness-of-fit on F^2	1.020	1.031	1.027
Final R indices [I>2sigma(I)]	R1 = 0.0443, wR2 = 0.0918	R1 = 0.0555, wR2 = 0.1488	R1 = 0.0529, wR2 = 0.1353
R indices (all data)	R1 = 0.0735, wR2 = 0.1008	R1 = 0.0944, wR2 = 0.1723	R1 = 0.0692, wR2 = 0.1440
Largest diff. peak and hole	0.552 and -0.442 e.Å^{-3}	1.285 and -1.305 e.Å^{-3}	1.640 and -1.049 e.Å^{-3}

Table S3. Crystallographic Data

	(L3)Ni(OCO^{t}Bu)$_2$
Formula	$C_{24}H_{30}N_2NiO_4$
Formula weight	469.21
T (K)	100(2)
Wavelength (Å)	0.71073
Crystal system	Triclinic
Space group	*P*-1
***a* (Å)**	9.4391(3)
***b* (Å)**	9.6315(2)
***c* (Å)**	14.0382(3)
α (deg)	88.863(2)
β (deg)	82.422(2)
γ (deg)	62.883(2)
V (Å^3)	1124.87(5)
Z	2
Density (calc.) (Mg/m^3)	1.385
μ (mm^{-1})	0.895
F(000)	496
Crystal size (mm^3)	? x ? x ?
Theta range for data collection (deg)	2.378 to 33.032
Index ranges	-14<=h<=14, -14<=k<=13, -21<=l<=21
Reflections collected	22403
Independent reflections	7703 [R(int) = 0.0173]
Completeness to theta	90.4 % 33.032°
Absorption correction	Multi-scan
Max. and min. transmission	1.00 and 0.87
Refinement method	Full-matrix least-squares on F^2
Data / restraints / parameters	7703/ 0/ 288
Goodness-of-fit on F^2	1.044
Final R indices [I>2sigma(I)]	R1 = 0.0253, wR2 = 0.0699
R indices (all data)	R1 = 0.0284, wR2 = 0.0713
Largest diff. peak and hole	0.528 and -0.360 e.Å^{-3}

4.6.8 References for the Experimental Section

1. Yakhvarov, D. G.; Hey-Hawkins, E.; Kagirov, R. M.; Budnikova, Y. H.; Ganushevich, Y. S.; Sinyashin, O. G. Electrocatalytic reduction of aryldichlorophosphines with the (2,2'-bipyridine)nickel complexes. *Russ. Chem. Bull.* **2007,** *56* (5), 935-942.
2. Powers, D. C.; Anderson, B. L.; Nocera, D. G. Two-Electron HCl to H_2 Photocycle Promoted by Ni(II) Polypyridyl Halide Complexes. *J. Am. Chem. Soc.* **2013,** *135* (50), 18876-18883.
3. Yanagi, T.; Somerville, R. J.; Nogi, K.; Martin, R.; Yorimitsu, H. Ni-Catalyzed Carboxylation of C(sp^2)–S Bonds with CO_2: Evidence for the Multifaceted Role of Zn. *ACS Catal.* **2020,** *10* (3), 2117-2123.
4. Lin, Q.; Diao, T. Mechanism of Ni-Catalyzed Reductive 1,2-Dicarbofunctionalization of Alkenes. *J. Am. Chem. Soc.* **2019,** *141* (44), 17937-17948.

Chapter 5: Conclusions

5.1 Conclusions

In conclusion, the work summarised in this Doctoral Thesis provide mechanistic information about two main research lines in nickel-catalyzed C(sp^2)–O bond functionalisation reactions, and nickel-catalyzed reductive coupling reactions.

In Chapter 2, the nickel-catalyzed Negishi cross-coupling of non-π-extended aryl pivalates was investigated, in which we provide a comprehensive analysis into the catalytic cycle and disclose on-cycle catalysis and deactivation or decomposition events. Initially, the direct oxidative addition of PCy_3 bound Ni(0) complexes are demonstrated to form κ^1-O or κ^2-O bound $(PCy_3)_nNi(aryl)(OPiv)$ complexes which undergo decomposition to Ni(I) species $(PCy_3)_2Ni(OPiv)$. Studying into the role of Zn(II) salts provide evidence for zinc species undergoing halide exchange with on-cycle Ni-pivalate complexes, undergoing ligand sequestering events, facilitating decomposition or deactivation pathways, along with reacting by productive transmetallation. The multifaceted effect of zinc salts shows a significant reliance on solvent choice in which Zn(II) salts react with Ni(0) complexes in weakly ligating solvents, while the reaction between Zn(II) and Ni(0) are disrupted with more coordinating solvents. Given the general uptake zinc salts have found in reductive cross-electrophile coupling reactions, one may envision these processes follow similar reactivity to those described in this study. Taken together, we believe the results reported within this work will promote nickel-catalyzed cross-coupling reactions from a preparative and mechanistic standpoint.

Chapter 3, investigates an incompatibility of strong reductants in nickel-catalyzed reductive coupling reactions using redox active bipyridine ligands. From the reduction of $(bipy)NiCl_2$ with magnesium powder we have synthesized and isolated an unorthodox Mg complex that do not only represent the first example of group 2 metal reduction to bipyridine dianions but also an unprecedented room-temperature magnesium stabilized electride. This bipy-Mg complex also offers new opportunities for accessing elusive metal intermediates by operationally simple techniques. We have additionally demonstrated the importance of ligand sequestering events in decomposition pathways, and solutions to overcome these limitations.

Chapter 4, describes a detailed understanding of electron transfer events and the factors contributing to comproportionation, disproportionation, and reduction of polypyridine ligated Ni species. We demonstrate that a subtle change in anionic ligands from Ni-halides to Ni-pseudohalides has a significant effect on nickel speciation in which Ni-halides adopt stable Ni(0), Ni(I), and Ni(II) oxidation states and react in comproportionation reactions while Ni-pseudohalides are only stable as Ni(0) and Ni(II) complexes and react via disproportionation. This divergent reactivity provided an opportunity to investigate the factors that influence comproportionation and disproportionation which were studied both experimentally and theoretically. Furthermore, modification of the anionic ligand to pseudohalides results in significantly harder to reduce complexes which do not undergo reduction with standard reductants such as Zn or Mn. The impact of these findings are extended to studies of catalytic transformations where organic bases act as poisons in reductive coupling reactions, while reactions that generate Ni-pseudohalide species on-cycle necessitate inorganic salts to regenerate catalytically active Ni-halide complexes. These findings also support a modification of traditionally accepted reaction mechanisms such as in the carboxylation of alkyl halides where reduction of Ni(I)-carboylates are proposed as a key step. Evidence provided within this work provides an alternative to this catalytic cycle by rapid disproportionation of the Ni(I)-carboxylate to form a Ni(II)-carboxylate and Ni(0), where the Ni(II)-carboxylate must undergo anion exchange by inorganic salts to reenter the catalytic cycle. This more rigorous understanding of electron transfer now provides increased control over both on-cycle and off-cycle species and we believe will assist in the development of new mechanistic understanding and preparative methodologies.

UNIVERSITAT
ROVIRA i VIRGILI